UNIVERSITÀ DEGLI STUDI DI PADOVA

UNIVERSITÀ DEGLI STUDI DI PADOVA

Facoltà di Scienze Matematiche Fisiche e Naturali

Dipartimento di Fisica e Astronomia 'Galileo Galilei'

SCUOLA DI DOTTORATO DI RICERCA IN ASTRONOMIA XXV CICLO

PHYSICAL MODELLING OF HIGH REDSHIFT GALAXY SPECTRA: A NEW MULTIWAVELENGTH VIEW ON GALAXY FORMATION AND EVOLUTION

Director of the School: Prof. G. Piotto

Supervisor: Prof. A. Franceschini

Co-Supervisor: Dr. L. Silva

Referee: Prof. R. Maiolino

PhD candidate: Lo Faro Barbara

A thesis submitted for the degree of
"Doctor Philosophiae"

in
ASTRONOMY

"Two things fill the mind
with ever new and increasing wonder and awe,
the more often and the more intensely the reflection dwells on them:
the starry heavens above me and the moral law within me."

I. Kant - The Critique of Pure Reason

Sommario

Un importante passo avanti nella comprensione del meccanismo di formazione ed evoluzione delle galassie è dato dal recente sviluppo di potenti strumenti astronomici in grado di rilevare segnali estremamente deboli provenienti da distanze remote.

Uno degli ultimi sviluppi di particolare rilevanza è stata l'apertura di lunghezze d'onda maggiori della banda visibile all'osservazione astronomica dallo spazio. Dalla metà degli anni '80 con la pionieristica survey IRAS, fino ad oggi, con il telescopio spaziale Herschel operante nel lontano infrarosso e l'Atacama Large Millimetre Array (ALMA) nel millimetrico, una serie di iniziative sono state messe a punto per osservare il Cosmo a lunghezze d'onda lunghe. Tra le tante novità che emergono da tutto questo, è diventato sempre più evidente il ruolo del mezzo diffuso nelle galassie nel 'modellare' la loro emissione spettrale modificando il flusso emergente dalle stelle. Un effetto particolare è quello dovuto alla combinazione di polveri e gas nel mezzo interstellare della galassia (ISM): poiché le particelle di polvere hanno una elevata sezione d'urto rispetto ai fotoni ottici e UV tipicamente emessi dalle stelle, una frazione significativa dell' emissione stellare è assorbita dalla polvere e riemessa a lunghezze d'onda nella banda IR e millimetrica. Secondo l'evidenza osservativa e le previsioni teoriche, questo 're-shaping' degli spettri di emissione delle galassie ad opera del contenuto di polvere del loro ISM diventa sempre più importante quanto più ricco è il contenuto di gas e polvere primordiale della galassia. Ciò accade soprattutto quando si considerano le prime fasi della loro formazione ed evoluzione.

Scoperte importanti in questo senso sono state fatte utilizzando grandi telescopi millimetrici da terra (come SCUBA, IRAM, APEX tra gli altri), rivelando l'esistenza di una popolazione di galassie ad alto redshift estremamente luminose, con luminosità confrontabili a quelle dei quasar. La maggior parte della radiazione emessa da questi oggetti cade nel lontano infrarosso e sub-mm ed è visibile fortemente spostata verso il rosso alle lunghezze d'onda millimetriche. Nell'ottico queste galassie appaiono come estremamente deboli e rosse, per l'effetto combinato di estinzione da polvere e redshift.

Questa scoperta, in seguito confermata da osservatori spaziali infrarossi, ha dimostrato l'esistenza di fasi di intensa attività di formazione stellare già ad alto redshift, molto probabilmente legate alla formazione di galassie sferoidali massive (ellittiche, S0). Complessivamente, tutti questi recenti sviluppi richiedono nuovi approcci per studiare le proprietà fisiche delle galassie ad alto redshift, quindi vincolare la storia del loro assemblaggio e l'evoluzione iniziale. Al tempo in cui erano disponibili solo i dati ottici e UV, per galassie a basso redshift, i requisiti modellistici per interpretare i loro dati spettro-fotometrici consistevano semplicemente nel sommare linearmente i contributi di tutte le stelle presenti nella

galassia, indipendentemente dalla geometria della distribuzione stellare o opacità della polvere. Ora i nuovi dati a disposizione sulla ri-emissione della polvere forniti da osservatori infrarossi hanno dimostrato che, in particolare durante i principali episodi di formazione stellare, grandi o addirittura dominanti frazioni della emissione da stelle giovani vengono assorbite dalla polvere e riemesse come grandi picchi nel lontano infrarosso. Vi è quindi una chiara associazione tra la formazione stellare e l'estinzione della polvere, in quanto elevati tassi di formazione stellare richiedono mezzi altamente opachi affinché il gas possa collassare e formare stelle.

In una galassia 'star forming' reale stelle, gas e polvere sono mescolati in modo molto complesso, e l'estinzione della polvere è una forte funzione dell' età della popolazione stellare nella galassia. I nuovi dati a disposizione ci obbligano a considerare una nuova generazione di modelli di spettri sintetici di galassie, con radicali complicazioni rispetto al precedente modelling classico, che si verificano a due livelli: da un lato l'effetto di estinzione della non può essere trascurato e deve essere considerato in funzione dell'età della popolazione stellare nella galassia. Inoltre, l'effetto di estinzione differenziale fa sì che gli effetti geometrici nella distribuzione di stelle e polvere svolgano un ruolo fondamentale e debbano essere accuratamente modellati.

Vari tentativi sono stati fatti nel corso degli ultimi dieci anni per fornire approcci semplificati ai problemi di cui sopra. Il più semplice ampiamente utilizzato consiste nel calcolare lo spettro totale sommando i contributi di tutte le stelle estinguendolo poi con una legge di estinzione media possibilmente rappresentativa. Praticamente tutti i risultati delle analisi fisiche di popolazioni di galassie nell'universo si basano su codici numerici semplificati basati su questo approccio. Questo può fornire risultati ragionevoli per popolazioni di galassie caratterizzate da quantità trascurabili di gas interstellare e moderata estinzione, come nelle galassie del primo tipo nell'universo locale o nelle spirali 'moderately star forming'. Ma sappiamo già che si tratta di un approccio non corretto quando si considerano galassie caratterizzate da una più attiva formazione stellare o oggetti osservati durante le prime fasi di collasso del gas e quindi in presenza di un mezzo interstellare molto ricco. Queste corrispondono alle fasi più importanti ed interessanti della formazione ed evoluzione delle galassie.

Lo scopo del presente lavoro è quello di contribuire a superare le difficoltà e le limitazioni appena descritte, attraverso l'implementazione di una nuova modellistica e analisi fisica delle popolazioni di galassie sia nell' universo locale che ad alto redshift.

Più nello specifico il fulcro di questo progetto di ricerca di dottorato è quello di studiare la natura fisica e la storia di assemblaggio in massa di galassie oscurate dalla polvere, ad alto redshift ($0.8 < z < 2.5$) e con attività recente di formazione stellare, osservate con Herschel,

attraverso una modellizzazione auto-consistente delle loro principali proprieta fisiche tra cui massa stellare, del gas e della polvere, SFR e SFH e l'oscuramento da polvere.

Con tipiche luminosità infrarosse negli intervalli $10^{11} - 10^{12}$ $L_{\odot}$ e $\geq 10^{12}$ $L_{\odot}$, le galassie luminose e ultraluminose nell'IR [(U)LIRGs nel testo], rispettivamente, sono tra gli oggetti extra-galattici più luminosi e complessi che si possano concepire, comprendenti un'ampia varietà di popolazioni stellare giovani e vecchie, assorbimento da polvere, scattering, riemissione termica da parte dei grani e emissione AGN (Lonsdale et al., 2006). Sebbene questi oggetti siano abbastanza rari nell'Universo locale, essi dominano la rate di formazione stellare cosmica e il FIR background a $z > 1$. Percio' essi rappresentano i laboratori più adatti ove studiare i principali processi fisici che regolano la formazione ed evoluzione delle galassie.

La caratterizzazione fisica della fenomenologia delle (U)LIRGs richiede un approccio multi lunghezza d'onda e una trattazione dettagliata degli effetti della polvere. La tecnica di sintesi evolutiva delle galassie costituisce un potente strumento per interpretare gli spettri delle galassie. La distribuzione spettrale d'energia di una galassia (SED) contiene preziose informazioni sulle sue proprietà fisiche, che includono il contenuto in gas e in stelle, la distribuzione di età e di abbondanze della popolazione stellare che viene dalla storia di formazione stellare e la loro interazione con il mezzo interstellare. Lo studio della SED quindi costituisce il metodo più diretto per investigare la formazione ed evoluzione delle galassie, sia attraverso osservazioni dirette che attraverso corrispondenti modelli teorici.

Per modellare l'emissione da stelle e polvere in maniera consistente e ottenere stime affidabili dei principali parametri fisici della galassia è necessario risolvere le equazioni del trasferimento radiativo per distribuzioni geometriche idealizzate ma realistiche di stelle e polvere, così come trarre vantaggio da una copertura in lunghezza d'onda completa dal far-UV al radio.

La forza del nostro approccio sta nella combinazione di una completa copertura multi-lunghezza d'onda per la nostra selezione di galassie, che include il FIR 70-500 micron da Herschel PACS e SPIRE e gli spettri IRS di Spitzer, ove disponibili, con un codice di sintesi spettrale auto-consistente, GRASIL citep Silva1998, utilizzato per interpretare le SED delle galassie. Questo codice calcola le SED delle galassie, dal lontano UV al radio, includendo un trattamento dettagliato degli effetti di estinzione e ri-emissione della polvere basato sulla risoluzione delle equazioni del trasferimento radiativo. Le caratteristiche di questo modello, prima tra tutte l'attenuazione da polvere dipendente dall'età delle popolazioni stellari, diverse geometrie per la distribuzione di stelle e polvere nella galassia, calcolo della distribuzione delle temperature della polvere in funzione della tipologia dei grani insieme con la completa copertura spettrale, consentono un' approfondita analisi fisica delle SED osservate.

Abbiamo utilizzato un campione di (U)LIRGs locali come 'campione test' per esplorare lo spazio dei parametri e studiare come i diversi parametri di input possono influenzare le diverse regioni dello spettro della galassia. Sulla base della nostra esplorazione dei parametri abbiamo costruito diverse librerie di SED teoriche delle galassie che variano da quelle di starburst pure, sia a basso che ad alto redshift, a quelle di galassie cosiddette 'normal star forming' ad alto-z.

Siamo partiti focalizzando la nostra analisi fisica su un campione piccolo ma ben rappresentativo di (U)LIRGs ad alto redshift (selezionate dal campo GOODS-S), aventi l'insieme di dati fotometrici e spettroscopici attualmente più ricco a disposizione, disponibile per la prima volta a redshift $z \sim 2$, combinando immagini profonde da Herschel con spettri IRS da Spitzer ultra-profondi. La grande quantità di informazioni racchiusa in questi dati ci ha spinto ad indagare la natura e le principali proprietà fisiche - come massa stellare, luminosità bolometrica, storia di formazione stellare, estinzione, così come la storia di assemblaggio della massa - per ogni oggetto.

Data la forma dettagliata della SED a banda larga di queste galassie, la nostra analisi fisica sembra essere in grado non solo di dare una stima precisa della SFR istantanea, ma anche di dare importanti indicazioni circa la storia passata della sorgente (SFH). Quest'ultima, in particolare, sembra giocare un ruolo cruciale nella nostra interpretazione degli spettri delle galassie.

La calibrazione di Kennicutt (1998), ampiamente utilizzata in letteratura per stimare la SFR dalla luminosità totale infrarossa rest frame a 8-1000 μm, sembra corrispondere a un caso estremo in cui la SFR è costante in un intervallo di tempo di 100 milioni di anni e tutta la luce è supposta provenire dalle stelle più giovani. La nostra tipologia di galassie, invece, sembra includere un contributo significativo al riscaldamento della polvere da parte di stelle di età intermedia attraverso l'emissione di cirro. Questo fa sì che la calibrazione della SFR dalla L_{IR}, per le nostre galassie moderatamente star forming, sia un fattore ~ 2 più bassa della calibrazione di Kennicutt.

Un altro punto cruciale della nostra analisi è che l'oscuramento da polvere nelle galassie dipende fortemente dalla distribuzione geometrica sia delle stelle che della polvere in particolare in termini di età delle popolazioni stellari, nel senso che le stelle più giovani racchiuse nelle nubi molecolari (MCs) saranno anche più oscurate di quelle più vecchie. Dimostriamo che approcci estremamente idealizzati (schermo omogeneo di polvere + singola legge di estinzione), che non includono un'attenuazione da polvere dipendente dall'età delle popolazioni stellari e basati sul fit solo della SED ottica della galassia, possono generare SED stellari non attenuate incapaci di bilanciare energeticamente l'emissione infrarossa riprocessata dalla polvere contenuta nella galassia. Per gli oggetti più fortemente oscurati da polvere questo può portare ad una sottostima della massa stellare che può raggiungere un

fattore ~ 6. Al contrario, una geometria più realistica, come quella adottata in GRASIL, è in grado di spiegare, per esempio, le differenze tra la legge di attenuazione osservata di galassie starburst e la legge di estinzione galattica.

Un ulteriore aspetto interessante, relativo al trattamento degli effetti dovuti alla polvere in modelli di galassie, è l'ampio range di attenuazioni consentite dal modello rispetto ad assumere un' unica legge di attenuazione. Questa distribuzione più ampia di valori che caratterizza i modelli è stata studiata in dettaglio da Fontanot et al. (2009b) ed è dovuta alle diverse storie di formazione stellare, alla distribuzione geometrica delle stelle e della polvere e alla connessione tra popolazioni stellari di età diverse, con diversi ambienti polverosi .

La nostra analisi dimostra quindi che un trattamento corretto e auto-consistente dell' estinzione e riemissione da polvere assieme ad una copertura Multiwavelength completa (dal lontano-UV al radio), è essenziale per ottenere stime affidabili dei principali parametri fisici come la massa stellare, l'estinzione da polvere e la SFR. Mostriamo che un approccio fisico di questo tipo può avere un forte impatto sulla rivendicata relazione tra SFR e la massa stellare. Ciò è dovuto alle incertezze legate all'interpretazione dell' emissione dall' ottico al lontano IR in funzione dell'età delle popolazioni stellari responsabili del riscaldamento della polvere e ri-emissione. Osserviamo che l'aggiunta dell' emissione radio al fit spettrale multi-banda fornisce uno stretto vincolo alla SFR recente, dato che soltanto le stelle più giovani di circa 10 milioni di anni producono i raggi cosmici galattici responsabili dell'emissione radio non termica. Inoltre, poiché l'emissione radio sonda la SFH su tempi scala diversi rispetto all'emissione IR, la nostra analisi ci permette anche di capire meglio e vincolare SFH della sorgente, in particolare il numero di stelle massicce che contribuiscono alla componente non termica di emissione radio attraverso le 'core-collapse SNe'.

La forma della SED della galassia non è tuttavia sufficiente da sola a porre forti vincoli sulla massa totale e molecolare del gas delle galassie. Un vincolo più stretto su queste quantità è fornito dal confronto tra le nostre soluzioni fisiche e le stime di massa dinamica e molecolare derivate da osservazioni di righe del CO. Investigare le proprietà del gas molecolare contenuto nelle galassie 'star forming' ad alto redshift è essenziale per capire come evolve la formazione stellare nelle galassie lontane e far luce sull'origine della correlazione tra SFR, massa stellare e massa in gas poiché è il gas molecolare l'ingrediente base da cui si formano le stelle. Il nostro modello fisico sembra confermare le grandi quantità di gas molecolare osservate nelle galassie a $z \sim 1.5$ selezionate con il criterio BzK e, contemporaneamente, la loro emissione radio e le proprietà della polvere.

La tesi è organizzata come segue.

Chapter 1: Questo capitolo definisce il contesto scientifico entro il quale si pone il nostro lavoro rivedendo i concetti fondamentali alla base della formazione ed evoluzione delle

galassie, sia da un punto di vista osservativo che modellistico/intepretativo.

Chapter 2: In questo capitolo vengono discussi in dettaglio i concetti di base della sintesi spettrale delle popolazioni stellari, ingrediente di base della nostra analisi, con particolare enfasi su quegli aspetti che influenzano maggiormente le SED delle galassie e la loro interpretazione.

Chapter 3 In questo capitolo viene presentato il codice spettrofotometrico utilizzato nel lavoro di tesi per modellare in maniera auto-consistente le SED delle galassie.

Chapter 4: Dopo un' approfondita descrizione delle missioni spaziali IR Spitzer e Herschel, essenziali per l'analisi di oggetti ad alto z oscurati da polvere, viene presentato in maniera dettagliata il campione di galassie luminose e ultraluminose nell'IR analizzato in questo lavoro.

Chapter 5: In questo capitolo vengono prima presentati i risultati principali del nostro lavoro di ricerca recentemente pubblicati nel paper Lo Faro et al. (2013), dove vengono investigate, attraverso un modelling fisico, la natura e la storia di 'mass assembly' del campione di 'star forming' (U)LIRGs ad alto z oscurate da polvere. Successivamente viene presentata un'analisi complementare svolta sullo stesso campione che include una discussione dettagliata sui parametri best-fit del modello, efficienze di formazione stellare, tempi scala di esaurimento del gas,curve di attenuazione e relazione SFR-massa stellare.

Chapter 6: Questo capitolo presenta i risultati principali riguardanti la modellizzazione fisica dell'emissione radio e delle SFRs di galassie oscurate 'star forming' ad alto z.

Chapter 7: Vengono presentati in questo capitolo i primi risultati di un'analisi fisico-modellistica delle proprietà del gas molecolare e della polvere di un campione di galassie selezionate con il criterio BzK a redshift z$\sim$1.5.

Chapter 8: Conclusioni & Prospettive Future

Appendix A: Descrizione di un progetto portato avanti in parallelo al progetto di tesi, svolto presso l' Infrared Processing and Data analysis Center (IPAC) del Caltech, focalizzato sull'analisi dell'effetto Holmberg in coppie vicine di galassie interagenti ad alto z selezionate nel campo COSMOS

Appendix B: In questa appendice vengono presentati i risultati principali del paper Lo Faro et al. (2009) dove si mostra come il codice spettro-fotometrico GRASIL, usato in questo lavoro, possa essere interfacciato anche con modelli semi-analitici di formazione galattica per studiare le proprietà statistiche e fotometriche di galassie Lyman-Break a redshift $z \gtrsim 4$.

UNIVERSITÀ DEGLI STUDI DI PADOVA

Abstract/Summary

Scienze Matematiche Fisiche e Naturali
Dipartimento di Fisica e Astronomia 'Galileo Galilei'

Doctor of Philosophy

by Lo Faro Barbara

A major step forward in our understanding of the formation mechanism and evolution with cosmic time of galaxies is given by the recent development of powerful astronomical tools able to detect exceedingly faint signals from remote distances.

One of the latter developments of particular significance was the opening of wavelengths longwards the classical visual band to the astronomical observation from space. From the mid '80 with the pioneering IRAS survey, until today, with the operation of the Herschel Space Observatory in the far-infrared and the Large Atacama Millimetre Array (ALMA) in the millimetre, a variety of initiatives have been put in operation to observe the Cosmo at long wavelengths. Among the many novelties emerging from all this, it became more and more evident the role of diffuse media in galaxies in shaping their spectral emission and modifying the flux emerging from stars. A particular effect is that due to the mixing of dust and gas in the galaxy interstellar media (ISM): as dust particles have a large cross section with respect to the optical and ultraviolet photons typically emitted by stars, a large fraction of stellar emission is absorbed by dust and re-emitted at long wavelengths in the IR and millimeter bands. According to observational evidence and theoretical expectation, this re-shaping of galaxy emission spectra by the dust content of their ISM becomes more and more important the richer the galaxy content is of primeval gas and dust. This happens particularly when we consider the early phases of their formation and evolution.

Important discoveries in this sense have been made using large millimetric telescopes on ground (like SCUBA, IRAM, APEX among others), revealing the existence of a population of extremely luminous galaxies at high redshift, with luminosities comparable to those of quasars. Most of the light emitted by these objects falls in the far-infrared and sub-mm and is visible strongly redshifted at millimeter wavelengths. In the optical these galaxies appear as extremely faint and red, due to the combined effect of dust extinction and redshift.

This discovery, later confirmed by space infrared observatories, proved the existence of phases of enormous star formation activity already at high redshift, very likely related to

the formation of massive spheroidal galaxies (ellipticals, S0's). Altogether, all these recent developments require new approaches to investigate the physical properties of high-redshift galaxies, hence constraining the history of their assembly and early evolution. At the time when only visual (optical-UV) data were available on moderate-redshift galaxies the modellistic requirements to interprete their spectro-photometric data were most simply to add linearly the contributions of all stars present in the galaxy, quite independently on the geometry of the stellar distribution or dust opacities. Now the new data on dust re-radiations offered by infrared observatories showed that, particularly during major episodes of stellar formation, large or even dominant fractions of the emission by young stars are absorbed by dust and re-emitted as large far-infrared bumps. There is thus a clear association of star formation and dust extinction, because high star formation rates require highly opaque media for gas to collapse and form stars.

In a real star-forming galaxy stars, gas and dust are mixed in a very complicated way, and dust extinction is a strong function of the age of the stellar population in the galaxy. New data then force us to consider a new generation of models of galaxy synthetic spectra, with radical complications with respect to previous classical modelling, occurring at two levels: on one side dust extinction can not be neglected and should be considered as a function of the age of the stellar population in the galaxy. In addition, the effect of differential extinction entails that geometrical effects in the distribution of stars and dust play a fundamental role and have to be carefully modelled.

Various attempts have been made during the last decade to provide simplified approaches to the above problems. The simplest widely used is to calculate the summed spectrum of all stars and extinguish it with an average and possibly representative extinction law. Virtually all results of physical analyses of galaxy populations in the universe are based on simplified numerical codes based on this approach. This can provide sensible results in relation to galaxy populations characterized by the presence of negligible amounts of interstellar gas and modest extinction, like in early type galaxies in the local universe or moderately star-forming spirals. But we already know that this is an improper approach when considering more actively star-forming galaxies or objects detected during early phases of gas collapse hence in the presence of a very rich interstellar medium. These correspond to the most important and interesting phases of the formation and evolution of galaxies.

The aim of the present work is to contribute to overcome the difficulties and limitations described above, with a new effort of modelling and physical analysis of populations of galaxies, both in the local universe and at high redshifts.

More specifically, the main focus of my PhD research is to investigate the nature and mass assembly history of dusty star forming galaxies at high redshift ($0.8 < z < 2.5$), observed

with Herschel, through a self-consistent modelling of their main physical properties like stellar, gas and dust mass, SFR and SFH, and dust attenuation.

With total infrared luminosities between $10^{11} - 10^{12}$ $L_{\odot}$ and $\geq 10^{12}$ $L_{\odot}$, respectively, Luminous and Ultra luminous infrared galaxies [(U)LIRGs hereafter], are among the most luminous and complex extragalactic objects we can conceive, including all varieties of young and old stellar populations, dust absorption, scattering, grain thermal re-radiation, and AGN emission (Lonsdale et al., 2006). Although they are quite rare in the local universe, they dominate the cosmic star formation rate and the FIR background at $z > 1$. Therefore they are suitable laboratories to study the main physical processes which drive galaxy formation and evolution.

The physical characterization of the ULIRG phenomenon requires a multi-wavelength approach and a detailed treatment of dust effects. Galaxy Evolution Synthesis Technique seems to be a powerful tool to interpret galaxy spectra. The spectral energy distribution (SED) of a galaxy contains valuable information about its physical properties, including the stellar, gas and dust content, the age and abundance distribution of the stellar populations resulting from the SFH, and their interaction with the interstellar medium (ISM). The study of the SED therefore offers the most direct way to investigate galaxy formation and evolution, both through direct observations and corresponding theoretical modelling.

To model the emission from stars and dust consistently and get reliable estimates for the main galaxy physical parameters we need to solve the radiative transfer equation for idealised but realistic geometrical distributions of stars and dust, as well as take advantage of the full SED coverage from UV to sub-mm.

The power of our approach, here, lies in the combination of a full multi-wavelength coverage for our selected galaxies, including the FIR from 70 to 500 micron by Herschel PACS and SPIRE and the IRS Spitzer spectra where available, with a self-consistent spectral synthesis code GRASIL (Silva et al., 1998) used to interpret galaxy SEDs. This code computes the SEDs of galaxies from far-UV to radio including a state-of-the-art treatment of dust extinction and reprocessing based on a full radiative transfer solution. The characteristics of this model (e.g. accounting of diffuse and clumped dust and stars, realistic geometry, both giving rise to an age-dependent dust attenuation, and a full computation of dust temperature as a function of grain size and composition) together with the large spectral coverage, allows a thorough physical analysis of the observed SEDs.

We have used a sample of local (U)LIRGs as a 'test sample' to explore the parameter space and investigate how the different input parameters may affect the different regions of the galaxy spectrum. On the basis of our parameter exploration we have built several

libraries of theoretical galaxy SED ranging from pure starburst galaxies, both at low and high redshift, to more normal star forming galaxies at high-z.

We started focusing our physical analysis on a small but well representative sample of high-redshift (U)LIRGs (from the GOODS-S field), with the currently richest suite of photometric and spectroscopic data, available for the first time at redshift $z \sim 2$, combining deep *Herschel* imaging with ultra-deep IRS spectra from *Spitzer*. The information from these data has prompted us to investigate the nature and the main physical properties - like stellar mass, bolometric luminosity, star-formation history, extinction, as well as the mass assembly history - for every object.

Given the detailed shape of the broadband SED of these galaxies, our physical analysis seems to be able not only to give an accurate estimate of the instantaneous SFR but also to give important hints about the source's past SFH. The latter, in particular, seems to play a crucial role in our interpretation of galaxy spectra.

The Kennicutt's (1998) calibration, widely used in literature to estimate SFRs from the rest-frame 8-1000 μm total IR luminosity, appears to correspond to an extreme case in which the SFR is constant over a time interval of 100 Myr and all the the light comes from the youngest stars. Our typical galaxies, instead, seem to include significant contribution to the dust heating by intermediate-age stellar populations through "cirrus" emission. This brings to a factor $\sim$2 lower calibration of SFR from L_{IR}, for our moderately star-forming galaxies, with respect to the Kennicutt's calibration.

Another crucial point of our analysis is that dust obscuration in galaxies strongly depends on the geometrical distribution of both stars and dust particularly in terms of the age of stellar populations, in the sense the younger stars embedded in the dense molecular clouds (MCs) will be more extinguished than older stars. We demonstrate that extremely idealized approaches (homogeneous foreground screen of dust + single extinction law), not accounting for an age-dependent dust attenuation and based on optical-only SED-fitting procedures, may generate unextinguished stellar SEDs unable to energetically balance the reprocessed IR emission from the galaxy due to dust. For the most dust obscured objects this can result in stellar mass underestimates which may reach a factor $\sim$6. On the contrary a more realistic geometry, like the one adopted in GRASIL, is able to explain, for example, the differences between the observed attenuation law of starburst galaxies and the galactic extinction law, even adopting the galactic cirrus optical properties.

A further interesting aspect, related to the treatment of dust effects in galaxy models, is the wide range of attenuations allowed by the model with respect to assuming a single attenuation law. This larger spread characterizing the models was studied in detail by Fontanot et al. (2009b) and has to be ascribed to the accounting of the star formation

histories, the geometrical distribution of stars and dust and the connection between stellar populations of different ages with different dusty environments.

Our analysis thus demonstrates that a correct and self-consistent treatment of dust extinction and reprocessing together with a full multiwavelength coverage (from far-UV to radio), is essential to get reliable estimates of the main physical parameters like stellar mass, dust extinction and SFRs. We show that such a physical approach can have strong impact on the claimed relation between the SFR and stellar mass. This is due to the uncertainties related to the interpretation of the optical to far-IR emission depending on the age of stars responsible for the dust heating and reprocessing. We observe that the addition of radio emission to the spectral multi-band fitting offers a tight constraint on the current SFR, considering that only stars younger than about 10 Myr produce the galactic cosmic rays responsible for the non-thermal radio emission. Moreover as the radio emission probes the SFH on different timescales with respect to the IR emission, our analysis also allows us to better understand and constrain the source's past SFHs, in particular the number of massive stars contributing to the NT component of radio emission through core-collapse SNe.

The shape of the galaxy SED alone, however, is not sufficient to put strong constraints on the total and molecular gas mass of galaxies. A tighter constraint on these quantities is provided by comparing our physical solutions to dynamical and molecular gas masses derived from CO line observations. Probing the properties of molecular gas reservoirs of high-z star forming galaxies is essential to understand how galaxy formation proceeds in distant galaxies and shed light on the origin of the $M_\star$- and M_{gas}-SFR correlation since it is the molecular gas out of which stars form. We show that our physical model appears to confirm the presence of large molecular gas reservoirs in high-z BzK-selected galaxies characterized by quasi-steady long-lasting mode of SF, and simultaneously their radio and dust properties.

The thesis is organized as follows.

Chapter 1: The Chapter sets the scientific context of this work reviewing the current status of galaxy formation and evolution from both an observational and modellistic/interpretative point of view.
Chapter 2: Here the basic concepts of Stellar Population Synthesis, one of the building blocks of our analysis, are discussed in detail with particular emphasis on those aspects affecting galaxy SEDs and their physical interpretation.
Chapter 3 The spectro-photometric code used in this work to model in a self-consistent way galaxy SEDs is presented here. This code includes a state-of-the art treatment of dust extinction and reprocessing based on a full radiative transfer solution.
Chapter 4: After a detailed description of the Spitzer and Herschel IR space missions,

essential for the analysis of high-z dust obscured objects, the sample of high-z dusty star forming (U)LIRGs studied in this work is here presented in detail.

Chapter 5: Here we first present the main results of our research work recently published in the paper by Lo Faro et al. (2013), where we investigate the nature and mass assembly history of dusty star forming galaxies at high redshift through the physical modeling of their SEDs. Then we also present a complementary analysis on the same objects including a detailed discussion on the best-fit model parameters, SFEs, depletion timescales, dust attenuation curves and SFR-$M_\star$ relation.

Chapter 6: The Chapter presents our main results on the physical modelling of radio emission and SFRs of high-z dusty star forming galaxies.

Chapter 7: Here we report the first results on the physical modelling of molecular gas and dust properties of BzK selected SF galaxies at z$\sim$1.5.

Chapter 8: Conclusions & Future Perspectives

Appendix A: Parallel project performed at the Infrared Processing and Data analysis Center (IPAC) of Caltech focused on the analysis of the Holmberg effect in high-z close major merger pairs selected in the COSMOS field.

Appendix B: Here we present the main results of the paper published by Lo Faro et al. (2009) which shows how the GRASIL code used in this work can be interfaced also with semi-analytical models of galaxy formation to investigate both the statistical and photometric properties of $z \gtrsim 4$ Lyman-break galaxies.

Contents

List of Figures

List of Tables

Dedicated to my Parents

Chapter 1

Galaxy Formation & Evolution: the observational perspective

In this introductory chapter we outline the fundamental aspects of modern observational and interpretative cosmology particularly focusing on those concepts which will be useful in the research for, and detection of, high-redshift dusty star forming galaxies.

1.1 Observational Properties of Galaxies

Observational cosmology is concerned with the distribution of matter on scales much larger than those of individual galaxies. For many purposes, therefore, we can regard the basic building block of cosmology to be the galaxies. The study of the spatial distribution of galaxies allows us, by comparing the results from theories with observed data, to cast light on the process of galaxy formation. Let us see, therefore, some of the basic properties of galaxies.

1.2 Local Galaxies & Morphological Classification

The morphological classification of galaxies is due to Hubble and traces back to 1925. Galaxies can be divided, on the basis of this classification, into four basic types: *ellipticals*, including the S0 or *lenticulars*, *spirals* and *irregulars*. They are usually divided into two basic types: early-type galaxies including ellipticals and lenticulars, and those of the late-types including spirals and irregulars. The ellipticals, which account for only around 10% of the observed bright galaxies, are elliptical in shape and have no discernible spiral structure. They are usually red in color, due to the type of stars they are composed of, they have very little dust and show no sign of active star formation (i.e. they are poor in

ISM). The luminosity profile (i.e. the surface brightness measured along the major axis of the photometric image of the galaxy), of elliptical galaxies is well described by the De Vaucouleurs' law:

$$I(r) = I_0 \exp(-(r/r_0)^{1/4}) \tag{1.1}$$

where I_0 and r_0 are constants and r is the distance from the center. The scale-length r_0 is typically around $1 - 10Kpc$. They have various ellipticities and are classified on the basis of the ratio between the major and minor semiaxes of their sky projection into E_n different types. The integer n is defined by $n \simeq 10(1 - b/a)$, where a and b are the major and minor axes, respectively. Ellipticals show no significant rotational motions and their shape is thought to be sustained by the anisotropic 'hot' motions of the stars within them. These galaxies mainly host old stars characterized by a high metallicity, mostly red giants. These, however, dominate the light but not the mass of these galaxies which is mostly in little stars of the main sequence. Ellipticals occur preferentially in dense regions, e.g. inside clusters of galaxies. The distribution of stellar masses of elliptical galaxies is very broad, extending from 10^5 to $10^{12} M_\odot$.

Lenticular, or S0, galaxies were added later by Hubble to bridge the gap between normal spirals and ellipticals. Around 20% of galaxies we see present this morphology. They are more elongated than elliptical galaxies but have neither bars nor spiral structure. They present, thus, intermediate characteristics between spirals and ellipticals in term of their morphology, (thick disc and prominent bulge), but are very similar to the second ones in term of their stellar population. Spiral galaxies account for more than half the galaxies observed out to $100Mpc$ and brighter than $m = 14.5$. Hubble's division into normal (S) and barred (SB) spirals depends on whether the prominent spiral arms emerge directly from the nucleus, or originate at the ends of a luminous bar projecting symmetrically through the nucleus. Spirals often contain copious amounts of dust, and the spiral arms in particular show evidence of ongoing star formation (i.e. lots of young supergiant stars), giving the arms a blue color. The nucleus or bulge of a spiral galaxy resembles an elliptical galaxy in morphology, luminosity profile and color. Many spirals also demonstrate some kind of 'activity' (non-thermal emission processes connected to star formation). The intensity profile of spiral galaxies (outside the nucleus) does not follow Eq. 1.1 but can instead be fitted by an exponential form:

$$I(r) = I_0 \exp(-r/r_0). \tag{1.2}$$

The subdivision of S and SB into a, b or c depends on how tightly the spiral arms are wound up. Spirals show ordered rotational motion which can be used to estimate their

masses. Irregular galaxies have no apparent structure and no rotational symmetry. They are relatively rare, are often faint and small and are very hard to see. These galaxies can be usually divided into two groups: type I irregulars, displaying a rotation pattern similar to the spiral one, and those of type II showing an irregular kinematics. Less luminous galaxies are often called dwarfs and irregular galaxies are generally dwarfs.

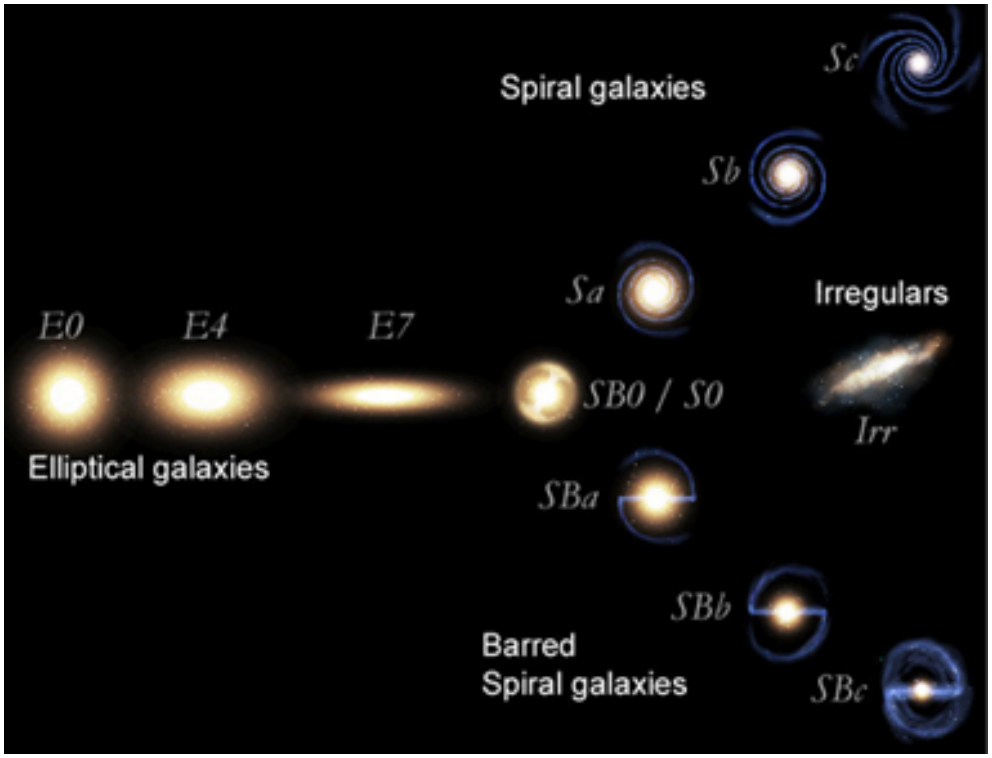

Figure 1.1 Hubble Galaxy morphological classification

1.3 Physical interpretation of the Hubble sequence

A coherent interpretation of the Hubble sequence suggests that the variation of the gas and stellar content which is observed in galaxies of different morphological type can be due to a different star formation history and efficiency. Star formation has, indeed, a central role in galaxy formation and evolution. Systems in which star formation is very efficient at the beginning, form preferentially spheroidal systems. This process occurs with little energy dissipation. If the formation process is slow and the gas dissipates part of its energy a disc can form. The initial star formation efficiency is thought to depend on the initial gas density and velocity dispersion. Therefore we expect spheroidal galaxies or galaxies with a prominent spheroidal component to form in high density and high velocity dispersion regions. This agrees with the observations, in fact elliptical galaxies usually are in dense

cluster with high dispersion velocity, while spirals are generally in low density and velocity dispersion regions.

Moreover, galaxies possess angular momentum whose amount depends on the morphological type: it is maximum for spirals and S0 galaxies, and minimum for ellipticals [1]. According to the model, the first version of which was created by Hoyle (1949), the acquisition of angular momentum by a galaxy is due to the tidal action of protogalactic objects around it, at the epoch when the protogalaxy is just about to form a galaxy. One finds that this tidal effect, due to all the surrounding objects, increases the angular momentum of the galaxy according to $\dot{J} \propto t^{-2}$ decreasing with time because the expansion of the Universe carries the protogalaxies away from each other.

The question of the angular momentum and the origin of the morphological types comes from the idea that dissipation is important for spiral galaxies but not for ellipticals, and all this can be explained as follows. The tidal action can generate a value of $\lambda \simeq 0.05 - 0.1$, not quite large enough to account for spiral galaxies but comfortable for ellipticals. It seems clear for spirals that dissipation must be important to explain why the luminous matter in a galaxy is concentrated in the middle of its dark halo. If the gas collapses through cooling, then its binding energy will increase while the mass and angular momentum are conserved. If the binding energy of a spherical cloud is $E \simeq GM^2/R$, as usual, then $E \propto 1/R$ as the gas cools and shrinks. This means that $\lambda \propto R^{-1/2}$, so cooling can increase the λ parameter. The problem with this is that, if the galaxy is all baryonic, the rate of increase is rather slow. If, however, there is a dominant dark halo, one can get a much more rapid increase in λ and a value of $\simeq 0.4 - 0.5$ is reasonable.

The problem of formation of elliptical galaxies is less well understood. For the ellipticals, differently from the spirals, it seems that there isn't significant dissipation. A possible explanation for this is that ellipticals formed earlier, when the Universe was denser and star formation more efficient. In this case, one could speak of biased galaxy formation in which the very highest density peaks, which collapse soonest, become ellipticals, while the smaller peaks become spirals. Ellipticals could also form through "major mergers" of disc galaxies, this model, however, cannot explain the mass metallicity relation of elliptical galaxies.

Elliptical galaxies are also characterized by a relation between color and absolute magnitude, that is, more luminous galaxies are redder. Redder colors are associated with older

[1] The conventional parametrisation of galactic angular momenta is in terms of the ratio between the observed angular velocity, ω, and the angular velocity which would be required to support the galaxy by rotation alone, ω_0:

$$\lambda \equiv \frac{\omega}{\omega_0} \simeq \frac{J/(MR^2)}{(GM/R^3)^{1/2}}$$

where the dimensionless angular momentum parameter λ is typically as high as $\lambda \simeq 0.4$ for spirals, but only $\lambda \simeq 0.05$ for ellipticals.

stellar populations, so a possible interpretation of the color-magnitude relation is that more massive galaxies have older stellar populations, i.e. they assembled their mass before less massive objects. This is in line with the downsizing scenario. However the interpretation of this color-magnitude relation is complicated by the age-metallicity degeneracy. The color of a stellar population is determined by the color of the main sequence turn-off. Unfortunately, if we consider two stellar populations, one older and a second one richer in metal, they show the same color of the main sequence turn-off. The relation between the metallicity index $Mg2$ and the velocity dispersion σ_{EL} can be interpreted as evidence of the fact that more massive ellipticals are richer in metals.

1.4 Galaxy Color Distribution

The colors of galaxies are strongly related with their stellar content. Recent observations indicate that galaxies at low redshift are characterized by a bimodal color distribution (Strateva et al. (2001); Baldry et al. (2004b)), which defines two classes of galaxies; a red population, largely contributed by non-star forming galaxies which have formed most of their stellar mass at high redshifts z, and a blue population consisting of galaxies actively forming stars.

The fraction of galaxies belonging to the red population grows with the luminosity L, being smaller than the blue fraction for $M_r > -19.5$ and dominating the distribution for $M_r > -21$. There is also a clear dependence on the galaxy environment, since red galaxies typically populate the overdense regions (Balogh et al. (2004)). The bimodal galaxy distribution is present at least up to $z \approx 1-2$ (Bell et al. (2004), Giallongo et al. (2005)). This well defined property of the galactic population must constitute a powerful constraint to the galaxy formation models aiming at deriving the galactic properties "ab initio". These connect the formation of stars in progenitor dark matter (DM) haloes (formed from the collapse of overdense regions in the primordial density field) with the assemblage of galaxies through repeated merging events involving the DM haloes.

According to galaxy formation models, the tendency of massive galaxies to be red and old, and of the low mass ones to be bluer and star-forming, is a natural outcome of the hierarchical scenarios. Indeed, the progenitors of present-day massive galaxies formed in biased, high-density regions that collapsed at higher z and contained denser gas.

The existence of a clear bimodality in the galaxy color distribution constitutes a finer probe for the physical processes included in the models, since it suggests a dichotomy in the star-formation histories of galaxies that should be originated by deep, fundamental properties of the galaxy formation process (Menci et al. (2005)).

1.5 Galaxy structural relations : The Fundamental Plane and Tully-Fisher

The Tully-Fisher (TF) (Tully & Fisher 1977) and the Fundamental Plane are two structural relations which link respectively the rotational velocity, for the spirals, and the central velocity dispersion, for the ellipticals, to the luminosity of a galaxy. The Fundamental Plane for the elliptical galaxies is a bi-dimensional surface defined by the following parameters: the velocity dispersion σ_0 , the effective radius r_e (defined as the major semiaxis of the isophote containing half the luminosity of the object) and the mean surface brightness I_e at the radius r_e. It is easy to show that if the virial theorem holds and the mass to light ratio M/L is kept constant in ellipticals, the following relation holds:

$$I_e r_e \propto \sigma_0. \tag{1.3}$$

indeed we have

$$r_e \propto \sigma^{1.4} I_e^{-0.9}. \tag{1.4}$$

Bender et al. (1992) showed that the precise inclination of the fundamental plane depends on the variation of M/L as a function of luminosity. In principle this relation can be applied up to redshift 1 corresponding at about $4 \times 10^3 Mpc$.

For spiral galaxies Tully & Fisher (1977) observed that a galaxy luminosity and rotational velocity at a given scale length linearly correlate in a log-log plane. The slope of this relation depends on the band in which one observes. This is due to variations in the mass-to-light ratios of disc with luminosity. The effect is stronger in the B-band, whereas it is smaller in the I-band. For this reason the I-band Tully-Fisher relation is considered more appropriate to be compared with models. We can conclude that the Tully-Fisher relation gives us information more on the structure of the disc than the nature of stellar populations.

This relation, however, cannot be applied to galaxies at redshift $z \geq 5$ as they do not have disks. Their morphology, in fact, does not follow Hubble classification and it shows a fragmentary structure probably due to the strong UV emission by young stars of O and B type contained.

1.6 Luminosity Function

The Luminosity Function $\Phi(L)$ is defined as the number density of galaxies per unit luminosity and it is directly observable. If dN is the number of galaxies present in a volume dV

with luminosity in the range $[L, L+dL]$, then $\Phi(L)$ is given by the relation $dN = \Phi(L)dVdL$. This function can be computed from a galaxy catalogue once the adopted objective selection criteria are specified and the distance of each object is known. This is empirically represented, in the local universe, by the Schechter function (1976):

$$\Phi(L)dL = \Phi^*\Big(\frac{L}{L^*}\Big)^{\alpha}\exp\Big(-\frac{L}{L^*}\Big)\frac{dL}{L^*} \tag{1.5}$$

The parameter Φ^* is related to the number of galaxies in the catalogue with typical luminosity L^* :

$$\Phi(L^*) = (\Phi^*/L^*)e^{-1} \tag{1.6}$$

The Schechter function is specified by the other two parameters L^* and α. It behaves as a power law with slope $\alpha \sim -1$ for $L \ll L^*$, for $L \gg L^*$, instead, an exponential cut-off dominates. The L^* parameter represents, therefore, the typical luminosity of a bright galaxy.

The classical form of the Schechter function is valid up magnitudes as faint as about -15 (Trentham et al. (2005)). Recent studies on the faint end of the LF (Blanton et al. (2005)) show an excess of faint objects with respect to the Schechter function fixed at $L \geq L^*$. Typical values of parameters in B-band ($M^* \sim -19.74$) are $\alpha = -1.16$, $L^* \sim 4 \times 10^{10} L_{\odot}$ and $\Phi^* = 0.0153 h^3 Mpc^{-3}$.

It is possible to show that the Schechter LF is the combination of various LFs, relative to the different morphological types (see e.g., Marinoni et al. 1999, Baldry et al. 2004a). The shapes of these LFs could be different from the Schechter form. In particular early type galaxies are characterized by a gaussian LF, turning into a Schechter function if we consider also dwarf ellipticals and lenticular galaxies. Analogue considerations hold for early type spirals; instead, late type spirals and irregulars have a Schechter LF with a steeper faint end. The sum of the different components gives rise to the observed Schechter LF.

If we move from the optical to other wavelengths the shape of the LF changes. In the NIR the LF is well described by a Schechter function, while in FIR and radio bands the LF shape does not follow the Schechter function anymore.

Fig.1.2 reports the luminosity function in B-band for a galaxy at $z = 0$. In general, it is observed that at brighter magnitude the luminosity function contribution is mainly given by giant ellipticals lying in the centre, while in the distribution tail spheroidal dwarfs or irregular galaxies lie. In the area corresponding to the L^* 'knee' we can mainly find spirals or lenticulars.

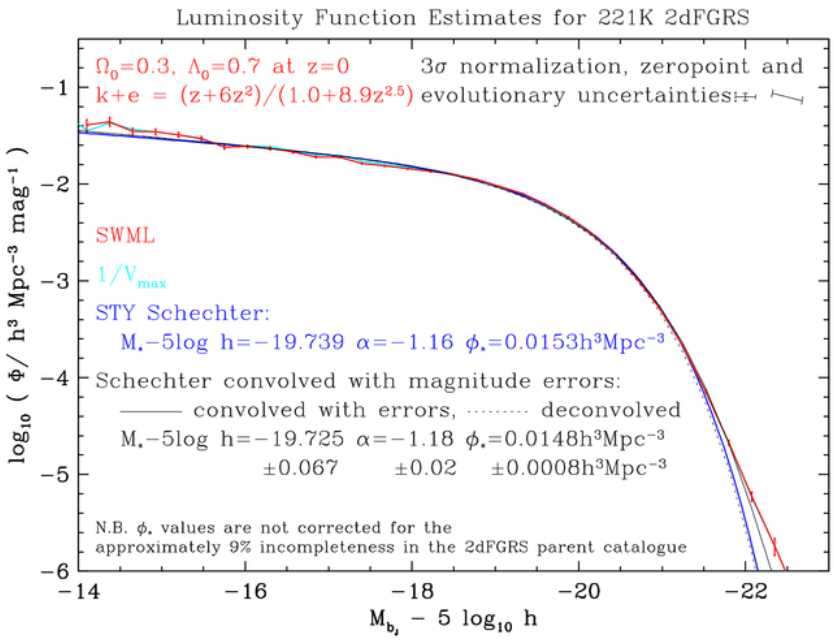

Figure 1.2 Luminosity Function in b_j band at $z = 0$ (from: 2dFGRS)

1.7 Gas content of galaxies

The study of the structure and evolution of the Inter Stellar Medium (ISM) is particularly important to understand the process of galaxy formation. The ISM of our Galaxy is concentrated, above all, on the galactic plane, though it is also present in some halo regions. It consists of two components: gas and interstellar dust. Dust is composed of very small solid particles with sizes lower than a micron. Just for its size, comparable to those of optical and ultraviolet radiations, ranging from 1 to 0.1 *micron*, dust absorbs (or scatters) preferably UV and blue light, letting the red light pass. This has the effect of reddening the spectrum of a source whose radiation is absorbed by the ISM.

Extinction and Reddening are the main effects due to dust which particularly influence Star Formation Rate (SFR) measures, fundamental to understand galaxy formation process. The first is the phenomenon for which the source light is absorbed by the ISM and then scattered from the line of sight. In the latter, reddening, the interstellar dust, preferentially absorbing UV and blue light, yields a reddening in the galaxy colors. Dust, moreover, is particularly abundant in strong star formation regions (starburst), and they nearly dim all the UV radiation emitted by young stars of O-B type. In this case, in fact, the radiation emitted in the UV is re-processed and re-irradiated by dust in the far IR. This makes such regions more visible in the IR rather than in the UV or blue.

Gas, the other component of the ISM, is composed of atoms and molecules scattered among stars. Differently from dusts, which radiates in a selective but continuous way, gas absorbs

stellar radiation only at certain well determined wavelengths characteristic of its composing elements and ionization state.

Inside galaxies we also find the so called HII regions where very bright O-B type stars are surrounded by ionized hydrogen regions emitting an emission line-dominated spectrum. When an O-B type massive star starts to shine it emits a large quantity of UV photons, mostly of wavelength shorter than the Lyman limit (912). The emitted photons ionize hydrogen in a neighboring sphere , called Stromgren sphere, corresponding to the HII region. These, moreover, are characterized by the so-called forbidden lines corresponding to metastable transitions , that is characterized by long decay times.

Recombinations in HII regions represent the original sources of most Lyα photons which give rise to Lymanα emission. The Lyα emission line is produced by electron transitions from the excited $2p$ state to the fundamental state $1s$ and it has a typical wavelength of $\lambda = 1216$ located in the UV band.

As to HI regions, namely neutral hydrogen regions, their study was possible thanks to radio observations. HI clouds emit and absorb a particular forbidden line at a wavelength of $21cm$ due to the transition related to the hydrogen hyperfine structure. The advantage in radio observation is that dust does not absorb radiation at all in this band.

1.8 Galaxy evolution at $z \gtrsim 1$

The morphological and photometric features of galaxies show time evolution. The best known effect is the evolution in color called Butcher-Oemler for which, in clusters at $z \gtrsim 0.1$ a higher fraction of blue galaxies is observed, compared to local clusters, interpreted as evidence of the evolution of galactic population.

A further evolution effect, theoretical and not observed, as the previous one, is the so called passive evolution on the basis of which red galaxies (ellipticals) appear brighter and bluer at higher redshift. This effect is due to the fact that the farther the distance the younger the star population is , therefore bluer.

The simplest way to measure galaxy distribution is to count them in function of flux. B-band counts, for example, sensitive to young stars, show an excess of galaxies. First it was thought that these might be proto-galaxies at $z \sim 3$, but later observations confirmed that indeed they were forming dwarf galaxies at $z \sim 1$.

If one observes the evolution of the luminosity function for different spectral types, at $z \sim 1$, one can note that, while more luminous galaxies evolve nearly passively, the less luminous ones seem to increase in blue and decrease in red.

Observations conducted by HDF (Williams et al. (1996)), GOODS (Dickinson et al. (2003)), HUDF (Panagia (2003)), COSMOS (Schinnerer et al. (2004)), DEEP2 (Davis et al. (2000)), COMBO17 (Wolf et al. (2004a)) surveys (etc.), only to mention some, confirm that up to $z \sim 1$ bright galaxy evolution seems almost passive, but at $z \sim 3$ galaxies appear essentially different.

In particular at redshift $z \gtrsim 3$ galaxies do not follow Hubble sequence and they appear irregular and fragmentary. This last effect might be due, in part at least, to the fact that high redshift galaxies are composed mostly by very young stars of O B type emitting in the UV. Local galaxies too, if observed in the UV, show a fragmentary structure because in this band star formation areas are pointed out. This effect is also known as morphological K-correction.

During the last decade considerable progress has been made in studying galaxy populations at high redshift and characterizing their cosmic evolution. Galaxy evolution is currently quite precisely known between redshift 0 and approximately 1, mostly based on deep optical imaging and spectroscopy (see, among others projects, DEEP-2, Faber et al. 2007; COMBO-17, Bell et al. 2004; K20, Cimatti et al. 2002; COSMOS, Scoville et al. 2007; VVDS, Le Fèvre et al. 2005). One important aspect of these investigations concerns the fraction of optical-UV radiation emitted by young stellar populations, which is absorbed by dust in the ISM and re-emitted at long wavelengths. It has been shown that, while it is modest for evolved galaxies like early-type spirals, and negligible in E/S0 galaxies, this fractional energy may become strong or even dominant during active phases of star formation, galaxy assembly, and nuclear activity (Franceschini et al., 1994, Kormendy & Sanders, 1992, Sanders & Mirabel, 1996). Mid- and far-infrared observations of the high-redshift universe are then needed to quantify dust-extinction effects: without a direct observation of the dust-reradiated part of the young stellar population emission, a reliable estimate of the star formation rate and even of the stellar mass is difficult (e.g. Poggianti et al. 2001, Poggianti & Wu 2000).

In the redshift interval from local up to $z \sim 1$, relatively deep IR observations have been carried out with early space infrared missions like IRAS (Soifer, 1988) and ISO (Genzel & Cesarsky, 2000). Based on the fair sensitivity and moderate spectral coverage of the latter, the galaxy and AGN evolution in the redshift interval $0 < z < 1$ has been mapped (Chary & Elbaz 2001, Elbaz et al. 2002, Franceschini et al. 2001, Lagache et al. 2004, Pozzi et al. 2004, Rowan-Robinson 2001, 2009), but there was insufficient sensitivity at higher redshifts to put any significant constraint.

For a long time, both theoretical expectations (Blain & Longair, 1993, Franceschini et al., 1997, 1994) and preliminary observational results by millimetric and sub-millimetric surveys with SCUBA (Blain et al., 2002, Chapman et al., 2005, Hughes et al., 1998, Smail

et al., 2002) and IRAM (Bertoldi et al., 2007, Greve et al., 2005) have provided evidence that major events of star formation in the universe happened at high redshifts, z> 1, and are likely responsible for the origin or assembly of the most massive present-day galaxies. Such events would be accompanied by major energy release, but, due to heavy dust extinction, would be detectable only through far-infrared observations. Sub-millimetric surveys indeed have identified sources that are extremely luminous at long wavelength, but almost undetectable in the optical (e.g. Chapman et al. 2005, Rodighiero et al. 2007).

A significant improvement in our knowledge of the infrared emissivity of source populations at redshifts z > 1, corresponding to the the era of peak star formation and AGN activity, has recently been made possible with the deep sky exploration by the Spitzer Space Telescope (SST, Werner et al. 2004). The Multiband Imaging Photometer (MIPS, Rieke et al. 2004) on SST combined sensitivity and spectral coverage, particularly with the $\lambda_{eff} = 24\ \mu m$ band, well suited for identifying and characterizing substantial numbers of far-IR galaxies up to z ∼ 3 (Caputi et al., 2007, Dole et al., 2006, Le Floc'h et al., 2005, Lonsdale et al., 2004, Rowan-Robinson et al., 2005). The MIPS instrument also includes photometric imagers at λ_{eff}= 70 and 160 μm (although the latter was limited by source confusion). A further crucial contribution of the SST mission was the capability provided by the Infrared Spectrometer (IRS, Houck et al. 2004) to obtain high-quality far-IR spectra of high-redshift sources for the first time.

The historical difficulty in identifying and interpreting luminous high-redshift sources, i.e. the difficult association of the optical counterparts to the IR-mm sources due to the poor spatial resolution and the large IR error-boxes, is also largely overcome by observations with the Spitzer Infrared Array Camera (IRAC, Fazio et al. 2004. IRAC deep multiwavelength imaging at 3 to 10 μm allows continuous band-merging and association of far-IR and optical/near-IR source catalogues in this critical spectral transition region (e.g. Egami et al. 2004).

The multiwavelength observations by Spitzer have fully confirmed previous expectations of numerous populations of luminous galaxies and active nuclei at high redshifts. MIPS surveys at longer wavelengths (70 and 160 μm) have produced more limited samples of distant sources (Frayer et al., 2006a,b, 2009), because of the much longer integration times required and lower mapping speed at faint flux levels. These faint far-IR Spitzer sources are also more difficult to identify, because of the poor Spitzer resolution at such long wavelengths.

Recent results, by Rodighiero et al. (2010), obtained exploiting deep MIPS 24 μm data are reported in Fig. 1.3 (top panel) which shows the evolution of the star formation rate density as a function of redshift. This plot clearly shows a quick increase of the star formation activity from $z = 0$ to $z \sim 1$ where we can observe a wide peak, it remains nearly

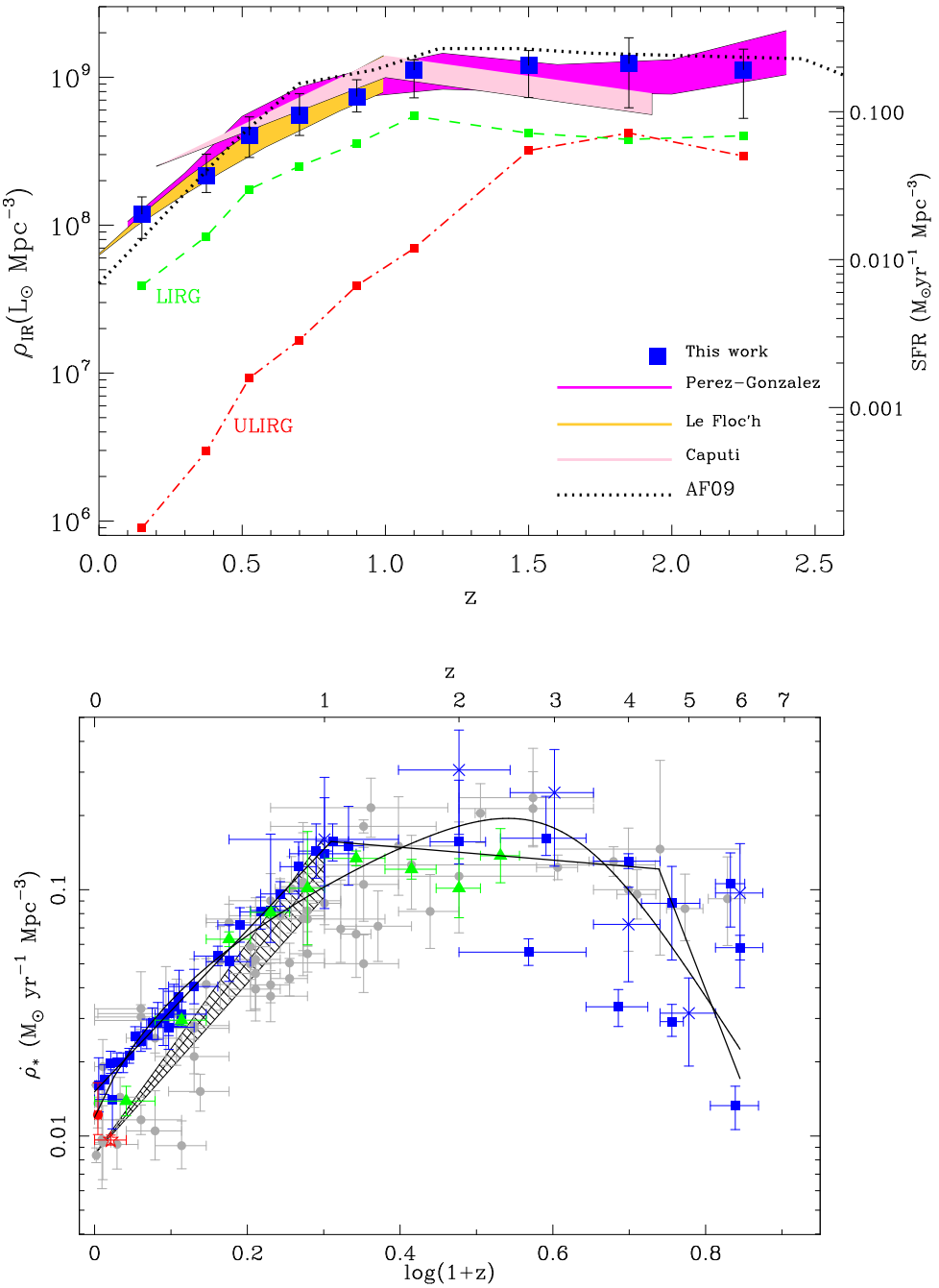

Figure 1.3 Evolution of the star formation rate density as from IR (top) and UV (bottom) luminosity function estimates. **Top**: Evolution of the comoving bolometric IR luminosity density with redshift by Rodighiero et al. (2010). The right-hand axis contains the conversion to star-formation rate based on a scaling law by Kennicutt (1998). See the paper for a detailed description of the plot; **Bottom**: Evolution of the SFR density with redshift by Hopkins & Beacom (2006) where the grey point fitted by the filled black line peaking at $z \sim 2$ are UV selected data by Hopkins (2004).

constant up to $z \sim 3$ to decrease, then, at higher redshifts. A complete different scenario is drawn by studies based only on UV selected data, such as Hopkins (2004) whose results

are presented in the bottom panel of Fig. 1.3. Here the peak of the SFR is shifted to z$\sim$ 2 followed by a rapid decrease at higher redshift.

It is worth stressing that both these solutions come from strong over-extrapolation on data, especially at high redshift, and are thus affected by large uncertainties. To really understand what happens at high redshift we need a multi-wavelength approach in combination with deeper and more precise observations at FIR wavelengths, essential to directly probe the SFR activity in a wide range of redshift.

A major step forward, for this kind of studies, has been recently made possible by the Herschel Space Observatory

The published works based on the first data collection undertaken with Herschel have already proved the great potential of this innovative instrument particularly with the Herschel Multi-tiered Extra-galactic Survey (HerMES) (Oliver et al., 2012). HerMES is detecting over 100,000 sources using two instrument, PACS and SPIRE sampling 70/100/160 and 250/350/500 μm respectively (see Section 4.3 for more details). The SED fitting over this broad wavelength range is essential to determine the role of obscured AGN with respect to starburst and to explore the nature of dust emission, the chemical and physical properties of dust together with its production and destruction mechanisms and obviously the bulk of stellar population and massive episodes of star formation.

By analysing a SDSS sample of AGN, Hatziminaoglou et al. (2010) find that one third are detected by SPIRE, with the long wavelength colours undistinguishable from star forming galaxies. The Modelling of the full SED required, instead, the combined contribution of both AGN and starburst components, with the former dominating the emission at the MIR wavelengths and the latter contributing mostly to the FIR wavelengths. This may be an indication that SPIRE detects the star formation in AGN, with little contamination from any dusty torus, providing a powerful tool to disentangle nuclear and star formation activity.

The wealth of data in these fields allows us to explore the FIR properties of many known samples, among which also the so-called Lyman-Break galaxies.

Thanks to the rich database built within HerMES we can now investigate the global relationship between FIR and optical galaxies. First results comparing HerMES and GALEX data (Buat et al., 2010) confirm that the total infrared luminosity accounts for $\sim$90 per cent of the total star formation rate, although this reduces to 70 per cent when considering the lower star formation rate systems ($\dot{M}_\star < 1 M_\odot/yr$).

The exploration, with Herschel, of galaxy morphologies at 2 ¡ z ¡ 3 has revealed that the average SFR for the spheroidal galaxies is about a factor of three lower than that of disk like galaxies (Cava et al., 2010).

Herschel is thus revealing of extreme importance to improve our understanding of galaxy formation and evolution.

1.9 Star formation rate diagnostics in galaxies

Accurate estimates of star formation rates (SFRs) in galaxies are crucial in nearly all fields of extragalactic astronomy. Multiwavelength galaxy surveys, recently made available by combined ground-based and space-based observations, provide the necessary tools to cross calibrate SFR indicators at different wavelengths and to test the physical assumptions underlying each indicator (Calzetti et al., 2007).

Currently, a large variety of SFR diagnostics are commonly used in literature (e.g., Kennicutt 1998, each of which has its strengths and drawbacks.

Easy accessibility has traditionally favoured the use of the ultraviolet (UV) stellar continuum and of the optical nebular recombination lines as SFR indicators, the former mainly at intermediate- to high-redshift (as it gets redshifted into the optical observer frame) and the latter mostly in low-redshift surveys. Both indicators only probe the radiant energy released by unobscured young massive stars. While directly related to the massive star formation process, observations at UV and optical wavelengths are heavily affected by dust extinction which varies enormously within and among galaxies. This makes extremely problematic the characterization of the evolution of the SFR density with redshift as galaxies dominating the stellar mass assembly between $1 \lesssim z \lesssim 3$ appear to be dusty starbursts with infrared luminosities in the range $10^{10}\,L_{\odot} \lesssim L_{IR} \lesssim 10^{13}\,L_{\odot}$ (Bouwens et al., 2009, Chary & Elbaz, 2001, Murphy et al., 2011a,b, Takeuchi et al., 2005). In this IR-bright galaxies more than 90% of the UV emission can be obscured (e.g. Buat et al. 2010, Howell et al. 2010, Murphy et al. 2011a,b).

Among the optical recombination lines, H_{α} is the most widely used, due to a combination of its intensity and a lower sensitivity to dust attenuation than bluer nebular lines. However it strongly depends on the assumptions made on the underlying stellar absorption and on the form of the high-end stellar initial mass function (IMF; e.g.

Infrared SFR indicators are complementary to UV-optical indicators because they measure star formation via the dust-reprocessed UV/optical stellar light that emerges beyond a few microns. Although IR emission does not suffer significantly from dust extinction,

its interpretation is also complex. The FIR emission, in fact, depends on the dominant population of stars heating the dust. There are in fact few issues concerning the SFR estimates based on the FIR: first of all, dust may also be heated by older stellar populations (i.e., the cirrus component; Bendo et al. 2010, Helou 1986, Hirashita et al. 2003, Li et al. 2010, Lonsdale Persson & Helou 1987), as confirmed by our work which will be presented in Chapter 6. Then there could be a fraction of the UV-optical emission escaping the galaxy and so not re-processed by the dust.

Radio continuum emission is also widely used as a tracer of star formation in galaxies both at low and high redshifts as the result of the tight empirical correlation between their optically thin synchrotron emission at 1.4 GHz and their FIR radiation (e.g., de Jong et al. 1985, Helou et al. 1985). Although the FIR/radio correlation is one of the tightest correlation in Astrophysics, its physical origin is still debated. It is natural when the synchrotron mechanism dominates over the inverse Compton, and the electron cooling time is shorter than the fading time of the supernova rate. Both conditions are met in star forming galaxies, from normal spirals to obscured starbursts.

Spitzer revealed local correlations in the spatial distributions of 70 μm and non-thermal radio emission in the disks of galaxies that seem to reflect an age effect indicating the complexities of using non-thermal radio continuum emission as an SFR diagnostic (Murphy et al., 2006, 2008).

Higher-frequency radio continuum emission, which becomes dominated by thermal (freefree) radiation beyond $\sim$30 GHz for globally integrated measurements of star-forming galaxies (e.g., Condon 1992), is largely extinction free and can be directly related to the ionizing photon rate arising from newly formed massive stars. Evidence for this has been provided by detailed studies of star-forming regions in the Galaxy (e.g., Mezger & Henderson 1967), nearby dwarf irregulars (e.g., Klein & Graeve 1986), the nuclei of normal galaxies (e.g., Turner & Ho 1983, 1994), and starbursts (e.g., Klein et al. 1988, Turner & Ho 1985). This is usually considered an ideal measure for the current star formation activity in galaxies, however the presence of an "anomalous" dust emission component in excess the freefree emission between $\sim$10 and 90 GHz, generally attributed to rapidly rotating ultrasmall grains with a non-zero electric moment, may complicate this picture (see Murphy et al. 2011b and references therein).

The specific calibrations for the most commonly used SFR diagnostics are here below itemized (see review by Kennicutt 1998 and Ellis 2008).

- The rest-frame ultraviolet continuum (1250-1500 $\AA$) has the advantage of being directly connected to well-understood high mass ($> 5M_{\odot}$) main sequence stars. Kennicutt suggests the following calibration for the UV luminosity:

$$\mathrm{SFR}(M_{\odot}yr^{-1}) = 1.4 \times 10^{-28} L_{\nu}(ergss^{-1}Hz^{-1}) \tag{1.7}$$

  with L_{ν} being the rest-frame luminosity at 1500 $\AA$. For young starbursts the proportionality constant can be significantly different; using this calibration the SFR would be overestimated (Madau et al., 1998).

- For redshifts $z \lesssim 2.5$, nebular emission lines such as H_{α} and [OII] are also available, for example as a natural by-product of faint redshift surveys. Gas clouds are photoionized by very massive ($> 10M_{\odot}$) stars. Dust extinction can often be evaluated from higher order Balmer lines under various radiative assumptions depending on the escape fraction of ionizing photons. The sensitivity to the initial mass function is strong.

$$\mathrm{SFR}(M_{\odot}yr^{-1}) = 7.9 \times 10^{42} L(H_{\alpha})\ (ergs\,s^{-1}) \tag{1.8}$$

$$\mathrm{SFR}(M_{\odot}yr^{-1}) = 1.4 \pm 0.4 \times 10^{41} L(OII)\ (ergs\,s^{-1}) \tag{1.9}$$

- The rest-frame luminosity at 24 μm is also a reliable SF tracer and avoids extrapolations to the whole IR range. Differently from the 8 μm flux which comes from diffuse regions, the 24 μm flux peaks in point-like regions closely related to the star formation. The calibration suggested by Calzetti et al. (2007) is:

$$\mathrm{SFR}(M_{\odot}yr^{-1}) = 1.27 \times 10^{-38} L(24\mu m)^{-0.8850}\ (ergs^{-1}) \tag{1.10}$$

- Far infrared emission (10-300 μm) includes two different contributions: a) young stars in star forming regions (warm, $\lambda \sim 60\,\mu m$) and b) an "infrared cirrus" component (cooler, $\lambda > 100\mu m$), associated with more extended dust heated by the interstellar radiation field. It acts as a valuable complementary probe to the UV continuum. As we have seen in previous section, luminous far infrared galaxies are also seen to high redshift. However, not all dust heating is due to young stars and the bolometric far infrared flux (integrated over 8-1000 micron), L_{FIR}, is needed for an accurate measurement. Kennicutt (1998) suggest the following calibration:

$$\mathrm{SFR}(M_{\odot}yr^{-1}) = 4.5 \times 10^{-44} L_{FIR}\ (ergss^{-1}) \tag{1.11}$$

  It is defined in the limit of complete dust obscuration and dust heating fully dominated by young stars and assumes a constant SF lasting 100 Myr computed using the Starburst99 spectral synthesis code by Leitherer & Heckman (1995). A powerful

strategy usually consists in adding UV and IR measurements to estimate the SFRs (see e.g. Bell et al. 2003, 2005, Daddi et al. 2004, Iglesias-Páramo et al. 2006).

- The radio emission, e.g. at 1.4 GHz, is thought to arise from synchrotron emission generated by relativistic electrons accelerated by supernova remnants following the rapid evolution of the most massive stars. Its great advantage is that it offers a dust-free measure of the recent SFR. Sullivan et al. (2001) proposed the following calibration

$$\mathrm{SFR}_{1.4\mathrm{Ghz}}(M_{\odot}yr^{-1}) = 1.1 \times 10^{28} L_{1.4Ghz}\ (ergss^{1}Hz^{1}) \tag{1.12}$$

for bursts of duration > 100 Myr. As in Chapter 6 we will compare our SFR estimates with those based on Bell et al. (2003) radio empirical calibration, we report here also this relation.

$$\mathrm{SFR}^{\mathrm{Bell}}_{1.4\mathrm{Ghz}}(M_{\odot}yr^{-1}) = 5.52 \times 10^{22} L_{\nu,1.4GHz}\ (WHz^{-1}) \tag{1.13}$$

where the proportionality coefficient is corresponding to a Salpeter IMF in the range (0.1-100 $M_{\odot}$). This calibration is based on the IR-radio correlation; it assumes that non thermal radio emission directly tracks the SFR, and is chosen so the radio SFR matches the IR SFR for $L \geq L_{\star}$ galaxies.

1.10 Star formation histories and stellar mass growth out to z∼2: the SFR-M$_{\star}$ relation

A major step forward in characterizing the nature of star formation in distant galaxies is given by the recent evidence of a tight correlation between the SFR of galaxies and their stellar mass $M_{\star}$ along a main sequence (MS) relation which evolves with redshift with the bulk of star formation occurring earlier in massive galaxies than in less massive systems (e.g., Guzman et al. 1997; Brinchmann & Ellis 2000; Bauer et al. 2005; Bell et al. 2005; Papovich et al. 2006; Reddy et al. 2006; Noeske et al. 2007a; Elbaz et al. 2007; Daddi et al. 2007b; Pannella et al. 2009; Rodighiero et al. 2011, 2010; Karim et al. 2011). This correlation has been estimated to have a slope of 0.7-1.0 in log space and a dispersion of a factor of only ∼2 from redshifts $z \sim 0.1$ to $z \sim 3$. Its normalization is found to evolve strongly with redshift raising as $(1+z)^{\sim 3.5}$ from z=0 to z∼2.5 and then flattening all the way to the highest redshifts (e.g. Daddi et al. 2007b; Rodighiero et al. 2011, 2010; Karim et al. 2011). The range of log (SFR) remains constant to z∼2, while the MS as a whole moves to higher SFR as z increases. The range of the SFR along the MS constrains the amplitude of episodic variations of SF and the effect of mergers on the SFR. Slope and normalization of the SFR-M$_{\star}$ relation both play a crucial role in the growth of galaxies and

in the evolution of their mass function (Renzini 2009; Peng et al. 2010, 2012). According to Noeske et al. (2007a) the slope and evolution of the MS can be understood as gradual gas exhaustion in a model in which galaxy age and SF timescale are function of galaxy mass, and the dispersion of the MS is interpreted as resulting from a spread in age and SF timescales at a given mass. Observations of the CO molecular gas content of MS galaxies indicate that their star formation efficiency does not depend strongly on cosmic epoch to z $\sim$ 2, with the SFR increase being due to higher molecular gas fractions (Daddi et al. 2010a, 2008; Tacconi et al. 2010).

All the galaxies having very high specific SFR (SSFR) compared to normal MS galaxies (by a factor $\times$4, $\times$8 higher), such as local ultraluminous infrared galaxies and some of the submillimeter-selected galaxies at $1 < z < 4$ are usually classified as "outliers" and/or starbursts. MS galaxies and outliers appear to be in different star formation regimes: a quasi-steady, longlasting mode for disks and a more rapid, starburst mode in galaxies dominated by gas-rich major mergers. According to Scoville (2012) definitions for starburst classification which compare the sSFR to the galaxy age or better, using the timescale for exhausting the ISM (i.e. the depletion timescale defined as M_{ISM}/SFR) should be used in place of those simply involving the dispersion about the main sequence, as more physically meaningful. This is justified by the following consideration: "The sSFRs of MS galaxies at z $\sim$ 2 are found to be higher by a factor $\sim$15 than those at low redshift, so the discriminant between the two star formation modes is evolving in time - without a clear physical basis, be it a higher gas content, smaller stellar mass at early epochs or an increasing efficiency/rate in converting existing gas to stars. And, of course, if the definition of the main sequence is evolving in time, the fraction of galaxies found to be 'bursting' will depend entirely on how far off the main sequence a galaxy must be to be so classified. If most galaxies at high redshift were, in fact, bursting, then the 'main-sequence' SSFR would be elevated as observed and the dispersion would simply reflect the range of burst activity." So we should be careful when distinguishing between MS and starburst systems; it would be fundamental at this point, for example, to analyse the morphologies of the so-called main-sequence galaxies to classify the merging/interacting versus undisturbed percentages.

According to Noeske et al. (2007a) the dominant mode of SF evolution since z $\sim$ 1 is apparently a gradual decline of the average SFR in most individual galaxies, not a decreasing frequency of starburst episodes, or a decreasing factor by which SFRs are enhanced in starbursts. More recently Rodighiero et al. (2011) have shown, by using Herschel/PACS observations, that the merger enhanced SFR phases account for only 10% of the cosmic SFR density at $z \sim 2$. This is a further indication that the most of the stellar mass forms in continuous mode of SF. Under this picture luminous infrared galaxies (LIRGs) at z $\sim$ 1 seem to mostly reflect the high SFR typical for massive galaxies at that epoch, so they are not brief stochastic starbursts as their local counterpart. They simply represent the early

gas-rich phase of smoothly declining SFH of $\geqslant L_\star$ galaxies. Anyway, as we have seen in Chapter 1, measuring SFR diagnostics is not trivial and various systematics remain poorly understood (Noeske et al., 2007b). The SFR-$M_\star$ relation vs z is therefore fundamental to understand SF and baryon physics of galaxies.

Figures 1.4 top and bottom (see captions for details), show the evolution of the SFR-$M_\star$ relation discussed above, up to redshift $\sim$ 1 and 2, respectively as estimated by Noeske et al. (2007b), Daddi et al. (2007b) and Rodighiero et al. (2011).

In oder to make further progress in understanding how galaxy formation proceeds in distant galaxies, and to shed light on the origin of the SFR-$M_\star$ correlations we need to start probing the main physical properties of these galaxies including their SFR, SFHs, $M_\star$, Av and also M_{gas}. The redshift range $1 \lesssim z \lesssim 2.5$ represents the crucial epoch where much of the present day stellar mass was assembled in massive galaxies, heavy elements were produced, the number density of QSOs peaked and the Hubble sequence was established. It's also known that most of the energy radiated during this epoch by newly formed stars was heavily obscured by dust. So long-wavelength observations are crucial.

1.11 Deep Multiwavelength Surveys: a census of galaxy SF out to z∼3

The Great Observatories Origins Deep Survey (GOODS; Giavalisco et al. 2004) is an astronomical survey designed to gather the best and deepest multiwavelength data for studying the formation and evolution of galaxies and active galactic nuclei, the distribution of dark and luminous matter at high redshift, the cosmological parameters from distant supernovae, and the extragalactic background light. It combines extremely deep observations from NASA's Great Observatories, Spitzer, Hubble, and Chandra, ESA's Herschel and XMM-Newton, and from the most powerful ground-based facilities, to survey the distant universe to the faintest flux limits across the electromagnetic spectrum. The survey covers a total of roughly 320 square arcminutes subdivided in two fields centered on the Hubble Deep Field North (GOODS-N) and the Chandra Deep Field South GOODS-S or CHDF-S). Subdividing the survey area provides insurance against cosmic variance due to galaxy clustering, and guarantees that astronomers in both hemispheres can carry out related observations. It incorporates a Spitzer Space Telescope Legacy Program (P.I. M. Dickinson) to carry out the deepest observations with that facility at 3.6 to 24 microns, a Hubble Space Telescope Treasury Program (P.I. M. Giavalisco) for deep high-resolution optical imaging, and a Herschel Space Observatory open time Key Program (Elbaz et al., 2011) with the deepest far-infrared observations at 100 to 500 microns. The complementary ground-based

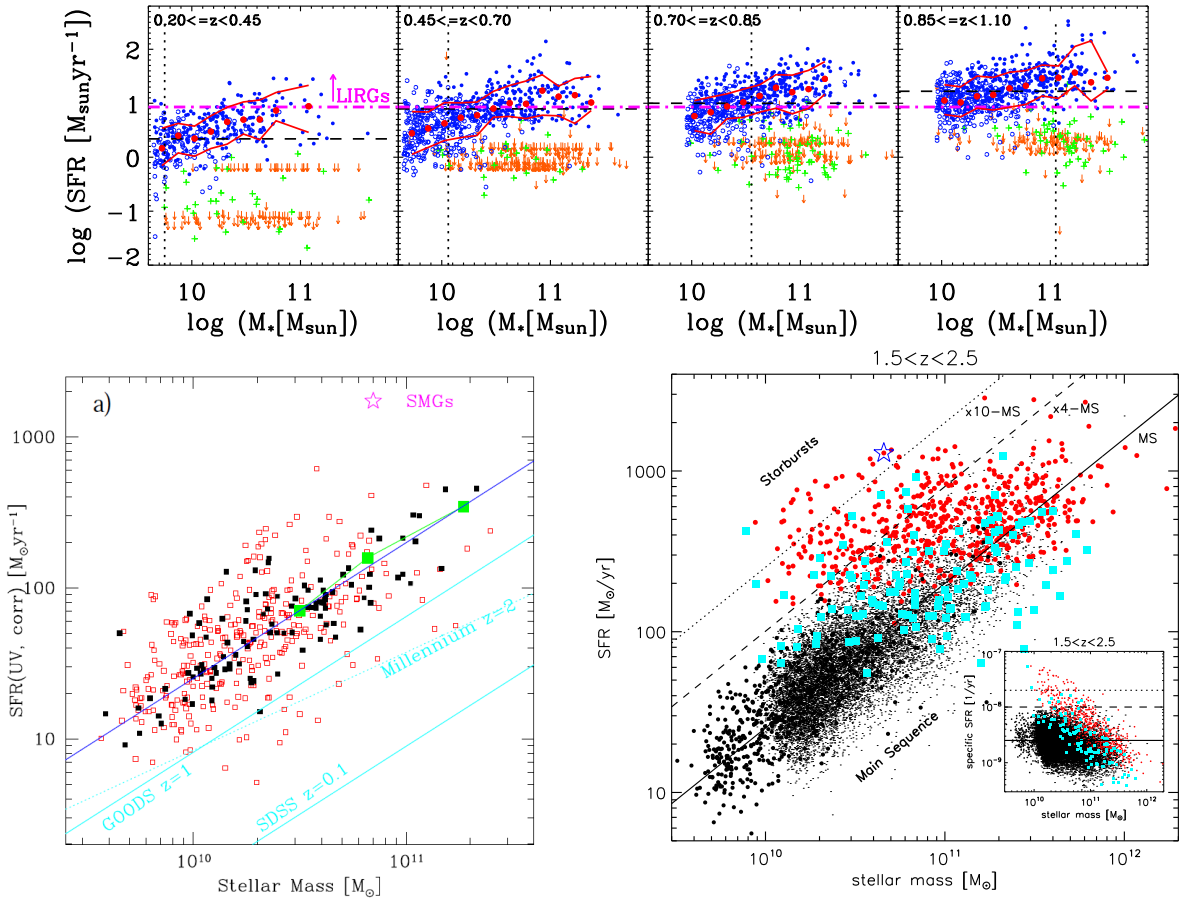

Figure 1.4 TOP: SFR vs. $M_\star$ for 2905 galaxies in the Extended Groth Strip, in the M range where the data are $> 80\%$ complete. The dotted vertical line marks $> 95\%$ completeness. *Filled blue circles:* Combined SFRs from MIPS 24 μm and DEEP2 emission lines. *Open blue circles:* No 24 μm detection, blue U-B colors, SFR from extinction-corrected emission lines. *Green plus signs:* Same as open blue circles, but red U-B colors, mostly LINER/AGN candidates. *Orange downward arrows:* No robust detection at 24 μm and no emission lines; conservative SFR upper limits shown. There is a distinct sequence formed by fiducial SF galaxies (*open and filled circles*); galaxies with little or no SF lie below this sequence. *Red circles* show the median of log (SFR) in mass bins of 0.15 dex for MS galaxies (blue circles). *Red lines* include 34% of the MS galaxies above and 34% below the median of log (SFR), $\pm 1\sigma$ in the case of a normal distribution. *Horizontal black dashed line:* SFR corresponding to the 24 μm 80% completeness limit at the center of each z bin; 24 μmdetected galaxies above the *magenta dot-dashed line* are LIRGs [image and caption from Noeske et al. (2007b)].
BOTTOM: SFR-$M_\star$ relation at $1.5 < z < 2.5$. *Red filled circles* represent the "shallow" PACS-COSMOS sources, the *cyan squares* the deeper PACS-GOODS South, the *black filled circles* the BzK-GOODS sample, and the *black dots* are the BzK-COSMOS sources. The *solid black line* indicates the MS for star-forming galaxies at $z \sim 2$ defined by Daddi et al. (2007b), while the *dotted* and *dashed lines* mark the loci 10 and 4 times above the MS (along the SFR axis), respectively. The star indicates the PACS source detected by Aztec at 1.1 mm in the COSMOS field. In the smaller inset, the stellar mass as a function of SSFR (SFR/$M_\star$) is shown. [image and caption from Rodighiero et al. (2011)]

imaging and spectroscopy include extensive commitments of ESO and NOAO observing time.

The combined GOODS data from HST, Spitzer, Herschel, Chandra, and ground-based observatories allow us to map the evolution of the Hubble sequence with redshift, reconstructing the history of galaxy mass assembly, star formation and nuclear activity. By observing at lambda $> 3\mu m$, Spitzer for example, is able to sample the rest-frame near- and mid-infrared light from objects at $1 < z < 6$ allowing us to measure the stellar mass distribution of galaxies through most of cosmic history. Moreover, MIPS observations offer the best opportunity to detect emission from dust-obscured star formation in ordinary galaxies out to z$\sim$2.5, as we will see in next sections in relation to the samples analysed in this work. Complementary, by observing the sky area of about 300 square arcminutes with Herschel-PACS, it is possible to detect some of the faintest objects, and galaxies in the earliest stages of the Universe. The observations are done with both SPIRE and PACS instruments: PACS very deep imaging of the GOODS fields (330 hours); SPIRE deep imaging of the GOODS-N Field (30 hours). The HST data will also provide a powerful tool to study the dark matter mass around galaxies using gravitational lensing, to search for low-mass stars in our own galaxy, and perhaps to detect moving objects in the outer solar system.

Chapter 2

Population Synthesis models: a powerful tool to interpret galaxy spectra

The spectral energy distribution (SED) of a galaxy contains valuable information about its physical properties, including the stellar, gas and dust content, the age and abundance distribution of the stellar populations resulting from the star formation history (SFH), and their interaction with the interstellar medium (ISM). The study of the SED therefore offers the most direct way to investigate galaxy formation and evolution, both through direct observations and corresponding theoretical modelling. The main goal of stellar population synthesis (SPS) is, therefore, to deconvolve and interpret all the information contained in the SED in terms of the SFH and galaxy evolution in general. To extract such information, models are necessary in order to connect the physical properties of the galaxy with the observed SED.

In this chapter I summarize all the basic ingredients and steps necessary to build a composite stellar population through spectral synthesis technique starting from its building blocks, i.e. simple stellar populations (SSPs). For a more detailed discussion about stellar population synthesis and its application to modeling SEDs we defer the reader to the foundational review by Tinsley (1980).

Figure 2.1 gives an overview of the entire process of constructing composite stellar populations.

2.1 Simple Stellar Populations & Isochrones

A galaxy can be simply thought as a collection of stars ranging from numerous, low-luminosity, low-mass stars, to the bright, short-lived, massive OB stars. The method of creating a galactic spectrum through the sum of the spectra of its stars is called stellar

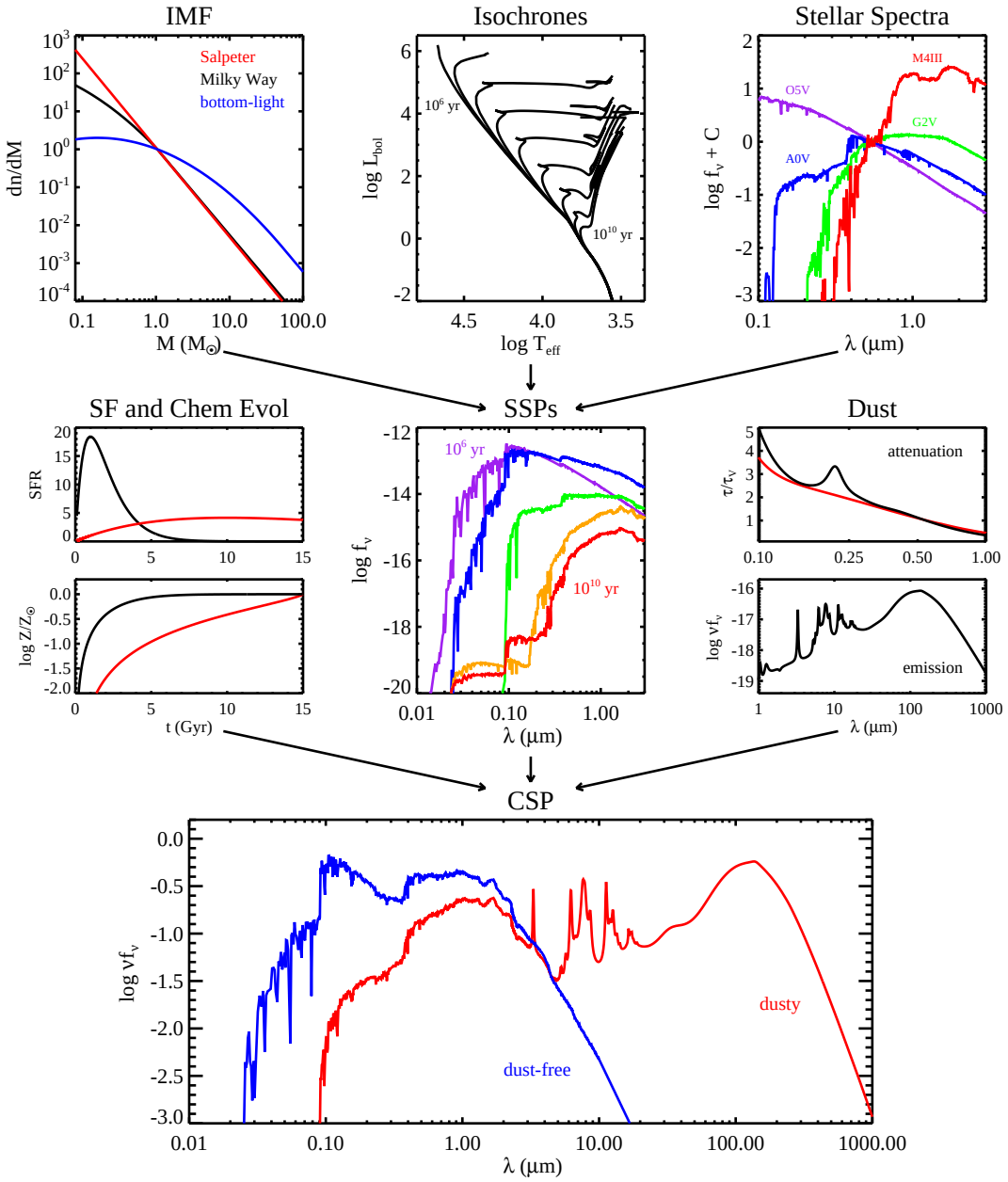

Figure 2.1 Overview of the stellar population synthesis technique. The upper panels highlight the ingredients necessary for constructing simple stellar populations: an initial mass function (IMF), isochrones for a range of ages and metallicities, and stellar spectra spanning a range of T_{eff}, L_{bol}, and metallicity. The middle panels highlight the ingredients necessary for constructing composite stellar populations (CSPs): star formation histories and chemical evolution, SSPs, and a model for dust attenuation and emission. The bottom row shows the final CSPs both with (red solid line) and without (blue solid line) dust obscuration. [Figure courtesy of C. Conroy].

population synthesis and was pioneered in works by Searle et al. (1973), Tinsley (1972) and Larson & Tinsley (1978). Simple Stellar Populations (SSPs) are the building-blocks of

any galaxy model. Each SSP describes the evolution in time of the SED of a single, coeval population of stars having the same initial elemental composition (metallicity). There are two main methods currently used to compute the SEDs of SSPs: The first one, which is the one adopted by the majority of stellar population models (included the one used in this work), is called "isochrone synthesis" and was first established by Chiosi et al. (1988); Maeder & Meynet (1988) and more recently Charlot & Bruzual (1991). This method is here below summarized:

Stars of different masses follow different evolutionary tracks. For fixed mass and chemical composition, the evolutionary track represents the path that the star follows across the Hertzsprung Russell Diagram (HRD) during its evolution, it is therefore a curve that instantaneously identifies the temperature and luminosity of a star. In a theoretical HRD, stars of an SSP are located along an isochrone, from the Greek word meaning "same age". This line connects the points belonging to the various theoretical tracks at the same age. The specific shape of an isochrone depends, of course, on the properties of the underlying evolutionary tracks, while the relative number of stars in different portion of the isochrone is governed by the assumed Initial Mass Function (IMF) and the lifetimes of the stars present in the isochrone in different evolutionary stages. By integrating the contribution of each isochrone element along the whole isochrone, and coupling the isochrones with libraries of stellar spectra and an IMF, one can derive the spectral energy distribution of an SSP of any age and metallicity.

To build an SSP we therefore need three basic ingredients: (a) stellar evolution theory in the form of isochrones, (b) stellar spectra libraries and (c) an IMF. These components are usually combined according to the following relation:

$$f_{\rm SSP}(t, Z) = \int_{m_{\rm lo}}^{m_{\rm up}(t)} f_{\rm star}[T_{\rm eff}(M), \log\, g(M)|t, Z]\Phi(M)\mathrm{d}M, \tag{2.1}$$

where M is the zero-age main sequence stellar mass (ZAMS), Φ(M) is the initial mass function, $f_{\rm star}$ is the stellar spectrum and $f_{\rm SSP}$ is the resulting time- and metallicity-dependent SSP spectrum. The lower limit of integration, $m_{\rm lo}$, is usually taken to be the hydrogen burning limit (either 0.08 or 0.1 $M_\odot$ depending on the stellar population synthesis code), while the upper limit is imposed by stellar evolution. The isochrones determine the relation between $T_{\rm eff}$, log g and M for a given t and Z (Conroy, 2013).

The second approach used to compute SSP SEDs uses the so-called "fuel consumption theorem" (Renzini & Buzzoni 1986, Maraston 1998). Basically we can split the total bolometric luminosity of an SSP into two terms, one for the contribution of stars still burning hydrogen in their core (those still in their MS phase) and one for stars in their

post-MS phases. The main idea is that the luminosity of the post-main sequence stars, which are the most luminous, is directly linked to the fuel available to stars at the turnoff (TO) mass. In other words: *" the contribution to the bolometric light of an SSP by stars in any post-MS stage is proportional to the amount of fuel burned during that stage "* (Greggio & Renzini, 2011).

One of the problems of the isochrone synthesis method was that isochrones are usually calculated in discrete steps in time and therefore phases where stellar evolution is more rapid than these time-steps were not well represented (the most famous example of the last years being the thermally pulsing asymptotic giant branch stars). Modern sets of isochrones are now relatively immune to these effects (Charlot & Bruzual, 1991). Models using the fuel consumption theorem circumvent this problem by changing the integration variable above the main sequence TO to the stellar fuel, i.e. the amount of hydrogen and helium used in nuclear burning. The fuel is integrated along the evolutionary track (Walcher et al., 2011).

Over the past few decades, much work has been done to provide large grids of stellar isochrones covering a wide range of stellar parameters in terms of ages (initial masses - usually from ∼0.1 $M_{\odot}$ to ∼120 $M_{\odot}$), chemical compositions and most relevant evolutionary phases. Among the most popular stellar models we recall, the Padova models (Bertelli et al., 1994, Bressan et al., 1998, Girardi et al., 2000, Marigo & Girardi, 2007, Marigo et al., 2008), which are the ones use in this work and the BaSTI models (Pietrinferni et al., 2009). In addiction we also recall the Geneva (Lejeune & Schaerer, 2001, Schaller et al., 1992), Yale (Demarque et al., 2004) and MPA models (Weiss & Schlattl, 2008). The Geneva models, for example, are tailored specifically to follow high-mass stars through advanced evolutionary phases, including the Wolf-Rayet (WR) phase, but they do not model low mass stars. It is common to combine the Padova isochrones covering the bulk of age and metallicity range with the Geneva models for young ages. Less attention is usually paid to the lowest mass portion of the isochrones, since low mass stars contribute only ∼ 1% of the total light of an old stellar population. An exception in this regard is the model of Conroy & van Dokkum (2012), who paid special care to the modeling of low-mass stars for SPS (Conroy, 2013).

2.1.1 How "macrophysics" shape stellar isochrones

The particular assumptions at the basis of the evolutionary models used to construct the isochrones may account for major differences in the resulting stellar population synthesis models (e.g. Maraston et al. 2006, M06 hereafter). These concern the assumptions made, among the others, on physical processes such as convection, rotation, mass-loss, thermal pulses during the AGB evolution phase and close binary interactions.

Convection

Let's compare, for example, two of the most popular stellar population models currently used, i.e. the Maraston (2005, M05 hereafter) and the Bruzual & Charlot (2003, BC03 hereafter) models. They differ mainly in the three following aspects: (1) the stellar evolutionary models used to build the isochrones, (2) the treatment of the TP-AGB phase and (3) the procedure used to compute the integrated spectra. Concerning the input stellar models, the BC03 models rely on the Padova stellar tracks (Fagotto et al., 1994), whereas M05 rely on the Frascati stellar tracks (e.g. Cassisi et al. 1997). The two sets differ mostly for two aspects, first the Padova stellar tracks include a certain amount of "convective overshooting" on the main sequence (MS), while the Frascati tracks were constructed with no overshooting; second, they also differ for the temperature distribution of the Red Giant Branch (RGB) phase, which is shifted towards cooler temperatures in the Padova tracks for solar metallicity and above, due to the different calibration of the mixing-length theory used for modelling the envelope convection.

Typically high MS stars, more massive than $M_\star \sim 1.1\ M_\odot$ (Conroy, 2013), have a convective core, since at least part of the hydrogen burning occurs through the CNO cycle, whose energy generation rate is extremely sensitive on temperature. Low mass stars, instead, burn hydrogen through the p-p chain, whose reaction rate is not extremely sensitive on temperature, so that these stars possess a radiative core and a convective envelope due to the high opacity (low temperatures) of outer layers. Of course, due to the proximity to the Hayashi line, also evolved giants have convective envelopes (see e.g Greggio & Renzini 2011 for more details). Classically, the boundary between convective and radiative regions is specified by the Schwarzschild criterion, i.e., all over $\bigtriangledown_{\rm rad} > \bigtriangledown_{\rm ad}$ convection develops. This is effectively defined as the 'point' where the acceleration of a convective fluid element is zero. However the fluid element will likely have a non-zero velocity as it crosses this boundary, and so some amount of 'overshooting' is expected.

Concerning convective-core overshooting, this can have two main effects on stellar models. First it prolongs (by $\sim$ 25%) the MS lifetime for a given stellar mass, while leaving the effective temperature almost unchanged. This is due to the extended convective core ensuring more fresh hydrogen to fuel to the central regions where nuclear burning takes place. Thus isochrones constructed from models with overshooting (like the Padova ones) are hotter, and therefore bluer, than those that do not include overshooting (the Frascati ones). Second, overshooting delays the appearance of stars with a degenerate helium core and the corresponding RGB phase. For example the RGB phase develops at an age of $t \sim 0.5 Gyr$ in the Frascati models and at an age of $t \gtrsim 1 Gyr$ in the Padova models (Ferraro et al. 2004; M05; M06). The appearance of the RGB makes the SED redder, this means that in the age range between $\sim$ 0.5-1 Gyr models with overshooting are bluer because they

do not have yet a well developed RGB. The net effect is that the theoretical SEDs based on models with overshooting are bluer and therefore give systematically older ages than the models without overshooting. Moreover having a lower contribution by RGB, they will also have lower luminosity (by $\sim 40\%$ with respect to M05, as assessed by M06) for given age and mass in stars which results in higher M/L ratios and therefore higher galaxy masses for given luminosity. Of course this applies to ages younger than a few Gyr for which MS stars do have a convective core (see M06).

Figure 2.2 compares the evolutionary tracks from different groups with and without convective-core overshooting.

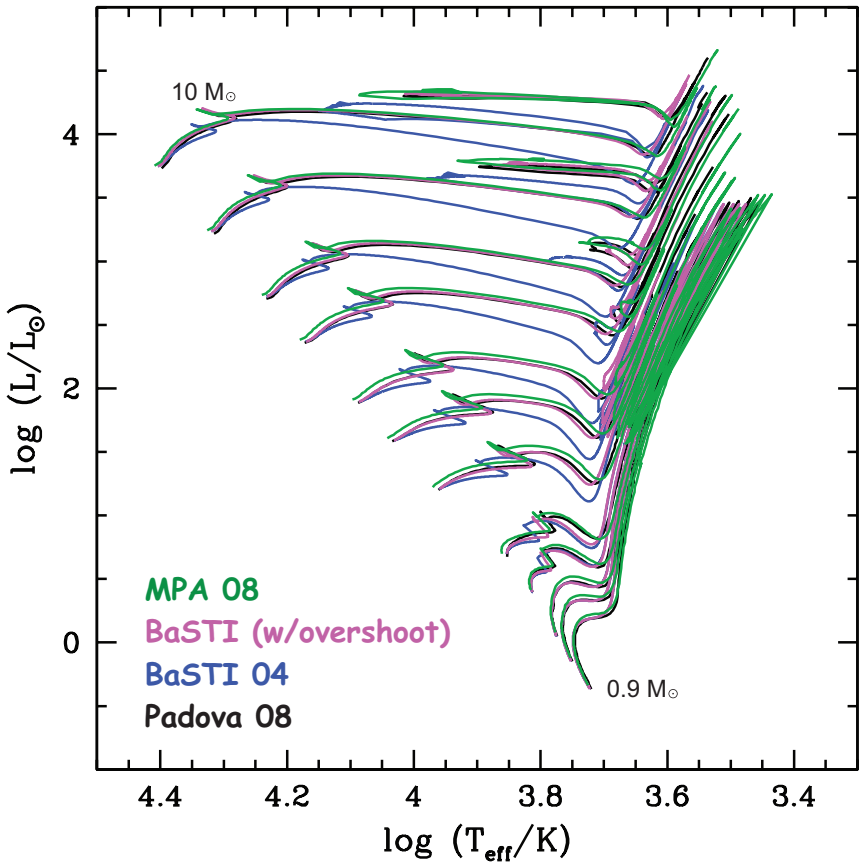

Figure 2.2 Comparison between the evolutionary tracks of solar composition low mass stars (0.9 - 10 $M_\odot$) of four different models (as labelled): MPA08 (Weiss & Schlattl, 2008) (green line), BaSTI04 (with (magenta)/without (blue) overshooting; Pietrinferni et al. 2009), and Padova08 (Marigo & Girardi 2007; Marigo et al. 2008)[courtesy S. Charlot]

There are a lot of observational evidences in favour of a moderate amount of convective-core overshooting in the mass range between 1.1 and 7 $M_\odot$ (see e.g. Keller & Wood 2006, Nordstroem et al. 1997, Stothers 1991, VandenBerg & Stetson 2004) and almost all stellar population models now include it in the isochrones, with the exception of Maraston models.

Convection in the outer envelope of evolved red giants is usually not so efficient, mostly because the thermal content of (cool) convective elements is lower than in the (hot) interior, and the actual gradient tends to be intermediate between the radiative and the adiabatic gradients ($\bigtriangledown_{\rm ad} < \bigtriangledown < \bigtriangledown_{\rm rad}$) (Greggio & Renzini, 2011). The amount of overshooting in the convective envelopes is therefore less constrained as discussed in Cassisi (2004). However it may affects the ratio of red to blue helium-burning giants (Renzini et al., 1992) and also the location of the luminosity bump in the RGB luminosity function. The latter has been recently used by Cassisi et al. (2011) to argue for a modest amount of overshooting in the convective envelopes.

The TP-AGB phase

The first appearance of thermally-pulsating asymptotic giant branch (TP-AGB) stars in the life of a stellar population has been called AGB-phase transition (RenziniBuzzoni1986), and its direct effect is a strong increase of the near-IR flux, as TP-AGB stars emit most of their radiation at $\lambda > 1\mu$m. According to Maraston (1998) TP-AGB stars can contribute up to $\sim$ 40% of the bolometric light, and up to $\sim$ 80% of the near-IR emission in stellar populations with ages between 0.2 and 2 Gyr. The importance of TP-AGB stars and their effect on deriving stellar population parameters has been discussed in detail in M06 and has since become a controversial topic. The TP-AGB phase represents the late stage of AGB phase for low and intermediate mass stars (M *le* 5-7 $M_{\odot}$). It culminates in stellar populations of age 0.3-2 Gyr and is characterized by thermally unstable thin He-burning shell. This shell periodically produces burst of energy which manifest as thermal pulses, from which 'thermally pulsing' AGB phase. Pulses typically happens every $\sim 10^4$ yr, for a C-O core mass of $\sim$ 0.6-0.8 $M_{\odot}$, during which time the star is quiescent. Pulses create convective zones in the He-burning shell. Consequences of pulses are therefore important to both the chemistry and structure of stars (e.g. through the so-called "third dredge-up"). During thermal pulses phase mass-loss may become catastrophic, thereby terminating the life of the star.

The contribution of TP-AGB stars to the integrated light of a synthetic stellar population critically depends on what is adopted for the stellar mass loss occurring during this phase. The higher the assumed mass loss, the sooner the star loses its envelope, and the sooner the TP-AGB phase is terminated. Since there is no theory relating the mass-loss rate to the basic stellar parameters one has to rely on empirical calibrations. The treatment of the TP-AGB phase is, indeed, one of the main difference between the M05 and BC03 models. While BC03 calibrate the duration of the TP-AGB phase, the prescription of M05 calibrates the fractional luminosity contribution to the total bolometric light. Although both prescriptions are based on the calibration of the same set of data (Frogel et al., 1990),

M05 models appear to include a larger contribution of the TP-AGB phase with respect to BC03 ones (see also Maraston et al. 2006).

The Padova group has recently developed a new set of isochrones including an updated treatment of TP-AGB calibrated against observations in the Large Magellanic Cloud (LMC Marigo & Girardi (2007), Marigo et al. (2008)). According to Conroy & Gunn (2010) these new models fail in reproducing the colors of intermediate-age Magellanic Cloud star clusters, by as much as 0.5 mag in some cases. In order to match the LMC data, these authors have provided recalibrated stellar population models in which the weight given to TP-AGB stars has been reduced. In addition, Melbourne et al. (2012) find that the latest Padova model predictions for the luminosity contributed by red core helium burning stars is a factor of two higher than observed in dwarf galaxies. This problem in the models may be related to the treatment of convection in the envelopes of evolved giants discussed above.

For what concern the implementation of the AGB-phase, including the dusty envelopes produced during the TP-AGB phase, in our stellar population models we postpone the discussion to section 3.3 where the SSP spectral library used in our stellar population synthesis code is described in detail.

Mass-loss

Mass-loss is another critical parameter in stellar evolution models. For low and intermediate mass stars ($M_\star \lesssim 8$ $M_\odot$) it determines when a star will end its life as a white dwarf, and its final size. At higher masses ($M_\star > 40$ $M_\odot$) it can have strong effects on the advanced evolutionary phases. In high mass stars the mass loss mechanism is thought to be via line-driven winds, while in lower mass stars ($\lesssim 8$ $M_\odot$) it is believed to be due to pulsation-induced dust-driven winds (Willson, 2000). In any event, the mass-loss prescription is another free parameter in these models and it is crucial because it strongly affects the lifetimes of advanced (and luminous) evolutionary phases. For example, the lifetime of TP-AGB stars and the number of thermal pulses they undergo depend strongly on the mass-loss prescription (Ventura & Marigo, 2010).

Rotation & binary interactions

Other important physical processes which may affect the evolutionary models implemented in stellar population synthesis are stellar rotation and binary interactions. The former has been widely investigated by the Geneva group during the last two decades (see Maeder & Meynet 2012 and reference therein for details). One of its main effects is an increasing of the main sequence lifetimes (by ~ 25 %) due to rotation-induced mixing bringing fresh fuel

to the convective core. Rotation is also likely to generate magnetic fields, which usually are ignored in the calculations of stellar evolution. According to Leo Mestel, one of the founders of stellar magnetism, these magnetic field can actually make things simpler when dealing with stellar rotation. We know that stars are believed to born with quite high angular momentum which is then transferred to the wind accompanying mass-loss. Magnetic fields cause such winds to co-rotate up to a certain distance from the star, hence transfer much more angular momentum to the wind than in the case of no co-rotation. Moreover, inside stars magnetic fields dynamically connect layers in differential rotation, thus exchanging angular momentum among them. The net effect is that magnetic fields extract angular momentum from the stellar interior, transfer it to the wind, and the wind disperses it into space. The outcome is that stars rapidly lose most of their angular momentum, and the non-rotating, spherically symmetric approximation becomes quite viable. This should be particularly true for advanced stellar evolution stages, such as red giants, which lose a significant fraction of their mass, and virtually all their residual angular momentum along with it. So, with the exception of some fast rotating massive stars, rotation does not appear to play a leading role in shaping stellar isochrones. This detailed explanation is taken from the book by Greggio & Renzini (2011).

More than 50% of stars (and most massive stars) are found to be in binary or multiple systems, and a large fraction of them strongly interact with their companions in the course of their evolution. Mass transfer can take place, common-envelope stages in close binaries can result in envelope ejection, and this can dramatically affects the subsequent evolution and observational properties. According to Eldridge & Stanway (2012) stellar population models including binary star evolution give a better fit to UV spectra of star-forming galaxies. Regardless of the details, it is clear that where massive stars matter in galaxy SEDs, the effects of both rotation and binary evolution can play an important role. Currently there are not popular stellar population models including the effects of binary star evolution.

2.2 Stellar Spectra

In order to compute the total flux (SED) of an SSP we need to integrate the spectra of all stars, covering the necessary parameter space in log T_{eff}, log g, metallicity etc., along the isochrone. In the last two decades the libraries of stellar spectra have seen significant improvements, with both fully theoretical (e.g. Kurucz 1992; Westera et al. 2002; Smith et al. 2002; Coelho et al. 2005; Martins et al. 2005; Lançon et al. 2007) and empirical, e.g. STELIB (Le Borgne et al., 2007), MILES (Sánchez-Blázquez et al. 2006; Cenarro et al. 2007), Indo-US (Valdes et al., 2004), ELODIE (Prugniel & Soubiran 2001; Prugniel et al. 2007), HST/NGSL (Gregg et al., 2004) libraries covering much greater parameter spaces

and increasing in both spectral and parameter resolution. Figure 2.3 emphasizes the large improvements in both spectral resolution and library size, seen among the optical spectra from both theoretical and empirical stellar libraries from the 1979 to present.

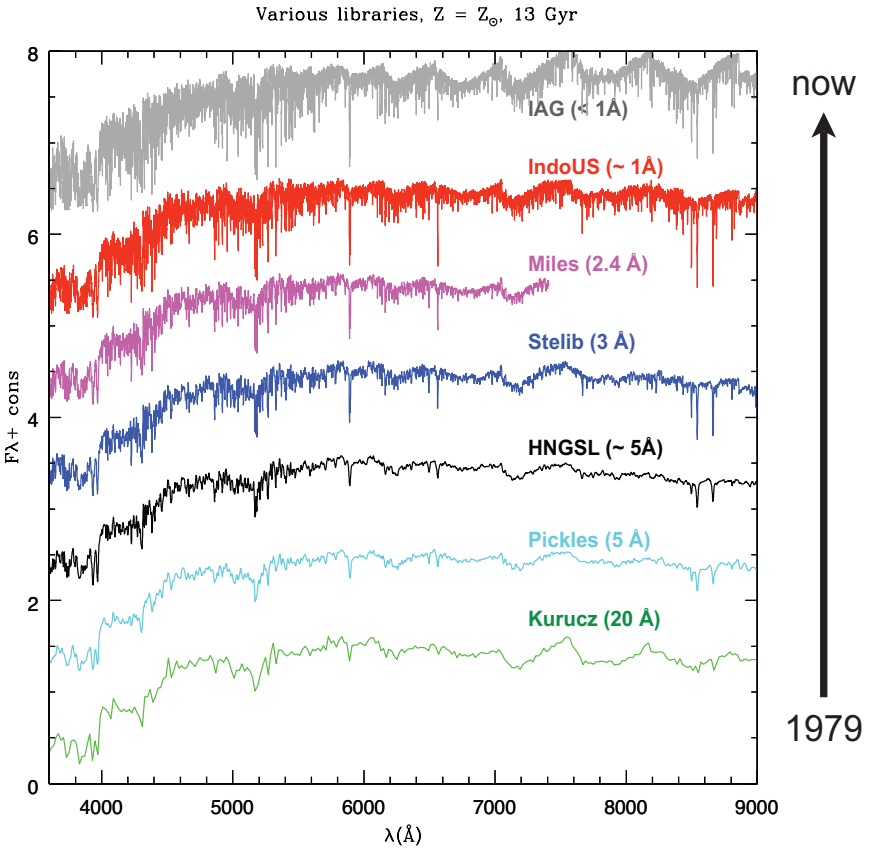

Figure 2.3 Walcher2011–[courtesy S. Charlot]

Compared to the optical, the UV still suffers from incomplete libraries which are particularly important for fully exploiting data on high redshift galaxies (see e.g. Pellerin & Finkelstein 2010). Significant improvements in this context have been recently achieved by Leitherer et al. (2010) and collaborators who provided a comprehensive set of theoretical ultraviolet spectra of hot, massive stars using the radiation-hydrodynamics code WM-Basic (Pauldrach et al., 2001). This code is optimized for computing the strong P-Cygni type lines originating in the winds of hot stars, which are the strongest features in the ultraviolet spectral region. The chosen stellar parameters cover the upper left H-R diagram at L $\gtrsim 10^{2.75}$ $L_{\odot}$ and T_{eff} $\gtrsim$ 20,000 K. The adopted elemental abundances are 0.05 $Z_{\odot}$, 0.2 $Z_{\odot}$, 0.4 $Z_{\odot}$, $Z_{\odot}$, and 2 $Z_{\odot}$. The spectra cover the wavelength range from 900 to 3000 $\AA$ and have a resolution of 0.4 $\AA$. The full paper presenting the work by Leither & collaborators, of which I am a co-author, can be found in the Appendix.

There is, however, no single spectral library, whether theoretical or empirical, that covers the entire range of parameter space necessary for constructing SPS models. Combining

together various libraries, often of widely varying quality, is therefore necessary. The question about which of empirical or theoretical libraries is preferable is still matter of debate and depends on the specific application (for a short review see Coelho 2009). The benefits and drawbacks of these two approaches are here below briefly discussed (source: Walcher et al. 2011).

The main benefit of empirical libraries is that they are based on real stars and thus avoid uncertainties in stellar atmosphere structure or opacities. On the other hand, due to the observational limits they cover a restricted parameter space biased towards Milky way compositions (see e.g. Cenarro et al. 2007). Moreover the determination of their fundamental parameters can be difficult for some types of stars and is itself based on stellar models. Conversely theoretical libraries can cover a much larger parameter space and at any chosen resolution (see e.g. Martins et al. 2005). There are still known problems in the comparison between observed and theoretical stellar spectra (Martins & Coelho, 2007). Among the problems related to theoretical models there are: incomplete line lists (Kurucz, 2005), problematic particularly at high spectral resolution, and the modelling of the IR emission (Lançon et al., 2007), which is especially difficult for stars in the luminosity classes I and II. A possible way to overcome these difficulties may be a synthesizing approach, as suggest by Walcher et al. (2009), aimed at using the strengths of both kinds of libraries. As with the evolutionary tracks, most libraries are limited to single compositions for a given metallicity. However recently this also has been changing, with stellar libraries exploring abundance changes such as α-enhancement as well (e.g. Coelho et al. 2007).

2.3 IMF

The third basic ingredient to build a simple stellar population is the initial mass function which provides the initial distribution of stellar masses along the main sequence. The IMF is usually defined through the so-called *birthrate function*, $B(m,t) = \Phi(M)\psi(t)dmdt$, which represents the number of stars formed in the mass interval m, $m + dm$ and in the time interval t, $t + dt$. Given the lack of a detailed understanding of star formation processes, the stellar birthrate is usually separated in two independent functions, $\psi(t)$ representing how many solar masses of the ISM are converted into stars per unit time and unit area (i.e. the star formation rate (SFR)) and $\Phi(M)$ being the IMF. The latter is defined in such a way that $\Phi(M)dM$ specifies the fraction of stars in the mass interval of width dM around M, where the distribution is normalized as

$$\int_{M_{low}}^{M_{up}} M\Phi(M)dM = 1M_{\odot} \tag{2.2}$$

where M_{low} and M_{up} are the lower and upper mass cut-off of the initial mass function. Typically, one puts $M_{low} \sim 0.1$ $M_\odot$ because less massive stars do not ignite their hydrogen (and are thus brown dwarfs), and $M_{up} \sim 100$(or120) $M_\odot$, because more massive stars have not been observed. Normally the upper limit can be equally choose as 100 or 120 $M_\odot$, because there are few high mass stars, compared to the whole population of stars. The lower limit, instead, is a delicate issue, because if one decreases this limit, the amount of low mass stars increases, with respect to the number of high mass stars. This effect reflects on the study of the integrated light of the single stellar populations, since SSPs less luminous (for mass unity) can be created. One solar mass of SSPs with more very low mass stars will be less luminous. Although much more attention is usually paid to the lower limit of the initial mass function, the IMF above 1 $M_\odot$ can also strongly affect the shape of the SED of composite stellar populations. In composite stellar populations the SED is influenced by stars with a range of masses (see Section 2.4), and so the IMF must play an important role.

The IMF has been studied extensively for decades (e.g Chabrier 2003, Kroupa 2001, Salpeter 1955, Scalo 1998, 1986). It is generally represented by a power-law of the form:

$$\Phi(M) = AM^{-(1+x)} \tag{2.3}$$

With $x = 1.35$ over the entire mass range one has the classical Salpeters IMF, whereas a bottom-light IMF with $x = 0.35$ for M < 0.5 $M_\odot$ and x $= 1.35$ above is now adopted quite extensively and is known as the Salpeter-diet IMF. Table 2.1 summarizes the typical values of some of the most popular IMF (of power-law form), implemented in current stellar population models.

Reference	Power law slope x			
	$0.1 - 0.5$ $M_\odot$	$0.5 - 1$ $M_\odot$	$1 - 10$ $M_\odot$	$10 - 100$ $M_\odot$
Salpeter (1955)	1.35	1.35	1.35	1.35
Kennicutt (1983)	0.4	0.4	1.5	1.5
Scalo (1986)	0.15	1.1	2.05	1.5
Scalo (1998)	0.2	0.2	1.7	1.3
Kroupa (1998)	0.5	1.2	1.7	1.7
Kroupa (2001)	-0.7	0.3	1.3	1.7
Franceschini et al. (2001) *Top-heavy 1*	1.0	1.0	1.0	1.0
Franceschini et al. (2001) *Top-heavy 2*	0.85	0.85	0.85	0.85

Table 2.1 Table of the most popular power-law IMFs. Part of the numbers reported here come from the reference papers and some from Tab. 2 of Baldry & Glazebrook (2003)

In addiction to the ones shown in Tab. 2.1, here below we report other two popular and largely used IMFs which are not described by a simple power law, but by a different more sophisticated functional form:

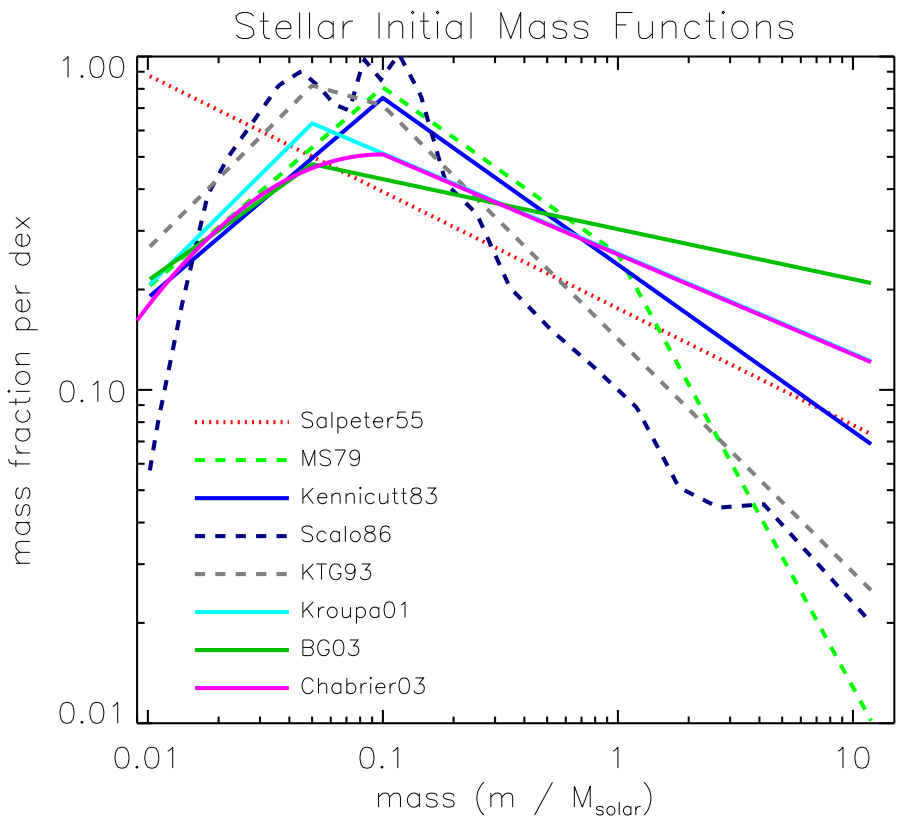

Figure 2.4 This figure compares the IMFs by plotting the mass fraction per dex versus mass, i.e., normalized so that the integral under each curve is unity. They are assumed to be valid from 0.1 to 120 solar masses. [Figure courtesy of I. Baldry]

- **Larson (1998) IMF.** Larson (1998) proposed an IMF in which the relative percentage of very low mass stars and sub-stellar objects is decreased due to the presence of an exponential cut-off. It is defined as:

$$\Phi(\mathrm{M}) \propto \mathrm{M}^{-1.35} \exp\left(-\frac{\mathrm{M_L}}{\mathrm{M}}\right) \tag{2.4}$$

  This IMF recovers the Salpeter IMF at high masses, whereas at low masses the exponential cut-off determines the steep downfall after the peak mass $\mathrm{M}_P = \mathrm{M}_L/1.35 = 0.25\ \mathrm{M}_\odot$. It is computed for the typical mass range $[0.01 - 100\ \mathrm{M}_\odot]$ and allows for a high number of intermediate-high mass stars.

- **Chabrier (2001) IMF.** On the same line of Larson (1998), Chabrier (2001) proposed the following IMF:

$$\Phi(\mathrm{M}) \propto \mathrm{M}^{-2.3} \exp\left[\left(-\frac{\mathrm{M_C}}{\mathrm{M}}\right)^{\frac{1}{4}}\right] \tag{2.5}$$

  with a mass range $[0.01 - 100\ \mathrm{M}_\odot]$ and $\mathrm{M}_C = 716.4$.

Figure 2.4 compares the different IMFs discussed above with the addiction of those from,

Baldry & Glazebrook (2003, BG03 in the figure), Kroupa et al. (1993, KTG93 in the figure) and Miller & Scalo (1979, MS79 in the figure). The Kennicutt (1983), Kroupa (2001), BG03 and Chabrier (2003) IMFs are the best option for reasonable mass-to-light ratios and galaxy colors (solid lines). The BG03 analysis favoured a slope shallower than Salpeter at the high-mass end based on constraints from local luminosity densities and cosmic star-formation history; IMFs with high-mass slopes steeper than Kennicutt's were ruled out as a universal IMF. The Salpeter IMF has too many low mass stars (dotted line). It was never measured down to 0.1 solar masses by Salpeter. The MS79, Scalo and KTG93 IMFs have too few high mass stars (dashed lines). They were based on galactic disk measurements which cannot be used to accurately infer the high-mass end because of the complicated SFH of the galaxy. Measured IMFs within star clusters generally give a shallower IMF close to the Salpeter value. Elmegreen (2006) finds that galaxy-averaged IMFs are not in general steeper than this.

2.4 Composite stellar populations: basic concepts & ingredients

Galaxies are complex systems made up of stars of different ages and metallicities contributing in different way to the integrated galaxy luminosity and contain dust. We refer to such systems as composite stellar populations (CSPs). The spectral synthesis technique, for the starlight alone, consists in summing up the spectra of each stellar population provided by an SSP of appropriate age and metallicity (Z), weighted by the star-formation rate (SFR) $\Psi(t)$ at time of the star's birth (Bressan et al., 1994):

$$F_{CSP_\lambda}(t_G) = \int_0^{t_G} f_{SSP_\lambda}(t_G - t, Z(t)) \times \Psi(t) dt \tag{2.6}$$

where t_G is the age of the galaxy, t is the birth age of an individual SSP and f_{SSP} is the SSP spectrum as defined in eq. 2.1. Of course here we assume that the IMF does not change with time. By definition, the properties of a CSP depend on the SFR and on the initial chemical composition (or Age-Metallicity Relation - AMR) of the stars. The SFR and AMR together define the star formation history (SFH). If the SFH is known, together with the IMF, the CSP of a system (e.g., a galaxy or its bulge) is then determined. But in general, the SFH is not known a priori, because it depends on the gas accretion and removal from this system as well as the star formation efficiency and the stellar mass ejection back to the ISM (stellar feedback). None of these processes are well understood. The stellar feedback itself can in principle be inferred from the stellar evolution modeling, although how it affects the other processes is still unclear. Therefore, through the study of the CSP we can get important hints on both stellar evolution and galaxy formation; thus it stands

at a boundary between these two major areas of astronomical research. (source: lessons by Prof. Daniel Wang).

2.4.1 Modeling the SFH of galaxies

As widely discussed in Conroy (2013), the SFH can in principle be arbitrarily complex, although simple forms are usually adopted. By far the most popular is the exponentially declining SFR, or $\tau-$model, where SFR $\propto e^{-t/\tau}$. This form arises naturally in scenarios where the SFR depends linearly on the gas density in a closed-box model (Schmidt (1959): $\Psi(t) = \Psi_0 \mathrm{M}^n_{\mathrm{gas}}$, with n=1). Recently, rising SFHs have been proposed to explain the SEDs of high-redshift galaxies (Maraston et al., 2010, Papovich et al., 2011). Rising SFHs at early times seem to be a natural consequence of galaxy evolution in a hierarchical universe (Finlator et al. (2007); Lee et al. (2010)). Functional forms that incorporate an early phase of rising SFRs with late-time decay, such as SFR $\propto t^{\beta} e^{-t/\tau}$ (similar in the form to the one used in our work), may therefore become more popular amongst modelers.

Figure 2.5 (from Conroy (2013) - top-panels) shows the fractional flux contribution from stars in different evolutionary phases for three representative SFHs, from a steeply falling SFH to a rising one. At late times ($t_G \sim 13Gyr$ - solid lines) the RGB and red HB dominate the red and NIR flux of $\tau-$model SFHs. While, at young ages ($t_G \sim 1Gyr$ - dashed lines) and/or for rising SFHs, the red and NIR are also influenced strongly by AGB stars, suggesting that the NIR can be affected by large uncertainties (due to uncertainties in the modeling of the AGB, as discussed in detail in section 2.1.1). The lower left panel of Fig. 2.5 shows the fractional flux contribution from stars more massive than 20 $\mathrm{M}_{\odot}$ and 60 $\mathrm{M}_{\odot}$ for an exponentially declining SFH with τ = 10 Gyr. Massive star evolution is uncertain due to the complicating effects of rotation and binarity, and so this panel gives an idea of how the uncertainties in massive star evolution affect SED modeling. Finally, the lower right panel shows the light-weighted age as a function of wavelength, again for a τ = 10 Gyr SFH. The dashed line indicates the mass-weighted mean age. As you can see from the figure, already by 0.5 μm (approximately the V-band), the light-weighted age reaches its maximal value, again suggesting that going to redder rest-frame wavelengths is not providing substantial new information on the SFH. We also note that the maximum light-weighted age never reaches the mass-weighted age. This is simply due to the fact that young stars outshine the more numerous, older low mass stars.

We have seen in section 1.9 that there exists a large variety of observational tracers, from the UV to the radio, which can be used to measure the SFRs in galaxies. Each indicator is sensitive to a different SFR timescale, with the ionizing radiation (e.g., the ricombination lines) being sensitive to the shortest timescale, $\sim 10^6$ yr, and the UV and total IR being

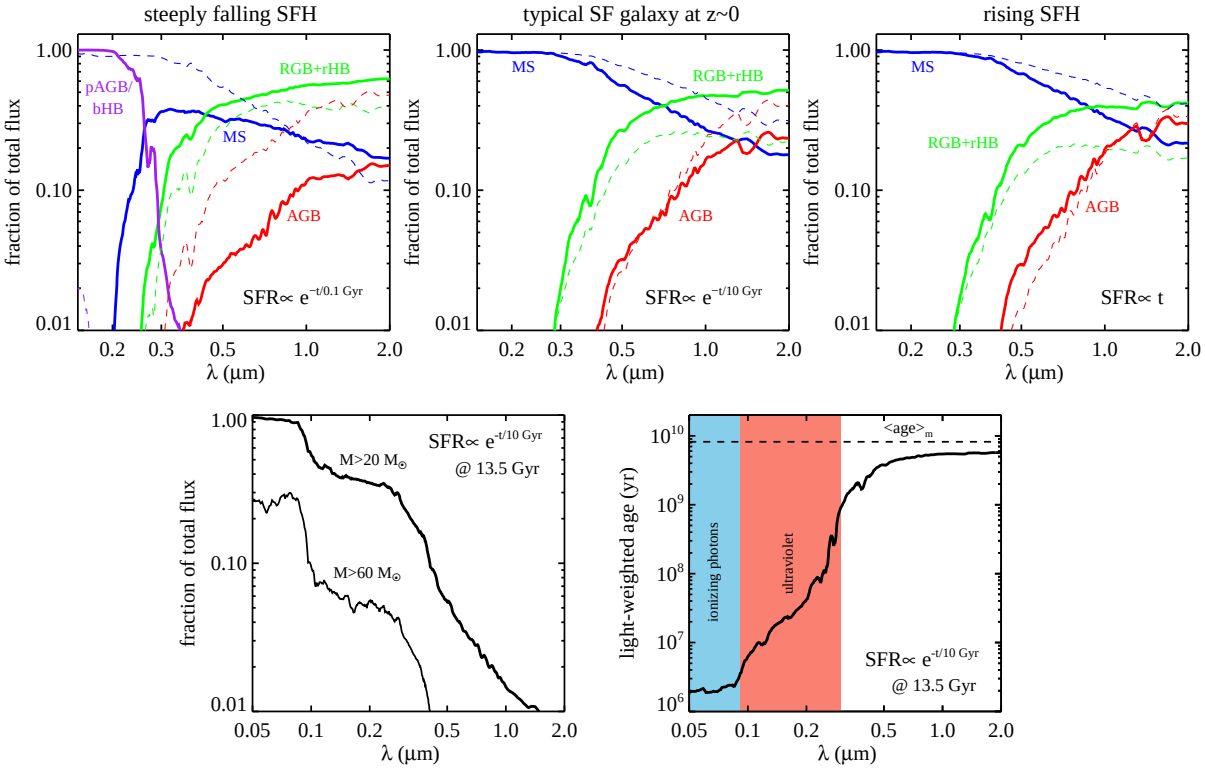

Figure 2.5 Top Panels: Fractional contribution to the total flux from stars in various evolutionary phases, for three different SFHs. The left panel is representative of a galaxy that formed nearly all of its stars very rapidly at early times, the middle panel is representative of a typical star-forming galaxy at $z \sim 0$, and the right panel may be representative of the typical galaxy at high redshift. Flux contributions are at 13 Gyr (solid lines) and 1 Gyr (dashed lines) after the onset of star formation; all models are solar metallicity, dust-free, and are from FSPS (v2.3; Conroy, Gunn & White 2009). Labeled phases include the main sequence (MS), red giant branch (RGB), asymptotic giant branch (AGB, including the TP-AGB), post-AGB (pAGB), and the blue and red horizontal branch (bHB and rHB). Bottom Left Panel: Fractional flux contributions for stars more massive than 20 $M_\odot$ and 60 $M_\odot$ for the SFH in the middle panel of the top row. Bottom Right Panel: Light-weighted age as a function of wavelength for the same SFH. The dashed line indicates the corresponding mass-weighted age. [Figure courtesy of C. Conroy]

sensitive to longer timescales, e.g. $\sim 10^8$ yr. Measuring the detailed SFH of a galaxy from the observed SED is, indeed, one of the most critical and challenging issue of spectral synthesis models, especially if high quality data are not available. Moreover the age-dust-metallicity degeneracy together with the choice of model priors on dust model and SFH library contribute to make things even more complicated often biasing the resulting ages and SFRs. This has been clearly emphasized, recently, by Wuyts et al. (2011) who compared the SFRs of galaxies at $z \sim 3$ computed with three different methods: Hα−based SFRs, SED-fitting based SFRs, and a mixed SFR indicator based on the UV and IR emission. They found that for SFRs $\lesssim 100$ $M_\odot yr^{-1}$, the three indicators agreed reasonably well (no

systematic offsets were detected), provided that extra attenuation was included toward HII regions when modeling the Hα-based SFRs. They also found that at the highest SFRs $\gtrsim$ 100 $M_{\odot} yr^{-1}$ the SED-based values tended to underpredict the SFR, compared to the mixed indicator (see also Santini et al. 2009). They argued that this was due to their assumption of a uniform dust screen, (see section 2.5 for more details), which at high column density becomes an increasingly poor representation of reality.

Another important probe of SFH is given by the mean stellar ages of galaxies. We can distinguish here among mass- and light- weighted ages. While the former offer a direct probe of the integrated SFH, the latter are more directly measurable from the SEDs. As emphasized in Fig. 2.5 (bottom-right panel) mass-weighted ages will always be larger than light-weighted ones, due to the fact that young stars outshine older stars. In the local Universe the "standard" indicator of the mean age of a stellar population is the strength of the $Dn(4000)\mathring{A}$ HK continuum break (e.g., Kauffmann et al. 2003) often used in combination with the Balmer absorption line index $H\delta_A$, to constrain also the star formation history of the galaxy. Together these two spectral indices allow to distinguish recent star formation histories dominated by bursts from those that are more continuous (Kauffmann et al., 2003). The break at 4000 $\mathring{A}$ (Balogh et al., 1999, Bruzual A., 1983) is the strongest discontinuity observed in the optical spectrum of a galaxy and is due to the accumulation of a large number of spectral lines in a narrow wavelength region. The main contribution to the opacity comes from ionized metals. In hot stars, the elements are multiply ionized and the opacity decreases, so the 4000 $\mathring{A}$ break will be small for young stellar populations and large for old, metal-rich galaxies. Strong $H\delta$ absorption lines arise in galaxies that experienced a burst of star formation that ended $\sim$ 0.1-1 Gyr ago. The peak occurs once hot O and B stars, which have weak intrinsic absorption, have terminated their evolution.

Mean ages of quiescent galaxies have been estimated largely by fitting single-age SSP models to these two spectral features. However several authors have demonstrated that these derived ages are only a lower limit to the true mass-weighted and even the light-weighted ages (see Conroy 2013 and references therein). This is due to the sensitivity of Balmer lines to $\sim$ 1 Gyr old stars. It is therefore more likely that the ages estimated through this method based on single-age SSPs are mostly measuring the residual star formation over $\sim$ 1 Gyr timescales. Similar conclusions have been obtained by Ferreras et al. (2009) who estimated the mean ages of early-type galaxies at z$\sim$1 by fitting models to *HST* grism spectra. They found no correlation between the ages estimated from single-age models and those estimated with composite models. In principle, as suggested by Renzini & Buzzoni (1986), also the onset of the AGB phase in $\sim$ 0.1-1 Gyr old populations could be used to age-date galaxies in the NIR. Subsequent modeling efforts by Maraston (2005) have confirmed that NIR spectral features due to oxygen-rich and carbon-rich AGB stars vary strongly over the range $\sim$ 0.1-1 Gyr, and may be used as an independent constraint on the

presence of intermediate-age stellar populations. However the uncertainties related to the modeling of this particular phase of stellar evolution including mass-loss and convection make this "age-indicators" quite uncertain.

Summarizing, one of the fundamental limitation of "classical" (see next sections) SED-modeling is that young stars tend to outshine older, less luminous stars (see Maraston et al. 2010 for an interesting discussion about this). This results in an underestimation of galaxy stellar mass when single-component SFH models are used (e.g. Daddi et al. 2004, Papovich et al. 2001, Pforr et al. 2012) and has effects also on stellar ages and SFR estimates. By analysing the SEDs of high-z mock galaxies Lee et al. (2009) concluded that the use of single-component exponentially-decreasing SFHs ($\tau-$models) may result in underestimated SFRs and overestimated mean ages (by factors of two for both parameters). This has been explained as due to the fact that mock galaxies tended to have rising SFHs in contrast to the declining model SFHs. Subsequent works by Lee et al. (2010), Maraston et al. (2010), Wuyts et al. (2011) and Pforr et al. (2012) largely confirmed these findings, and further concluded that models with rising SFHs (both inverted and delayed $\tau-$models) tend to provide a better fit to observed high redshift SEDs and produce SFRs in better agreement with the other indicators. Similar results for high-z sub-mm galaxies (SMGs) have been recently obtained by Michałowski et al. (2012) by considering a double component SFH allowing for a second burst whose effect is similar to the one obtained by using a rising SFH. The main conclusion of this discussion is that a model library of SFHs used to fit, in particular star forming galaxies, must include a large variety of possibilities from one component to two-component SFHs from a constant one to the classical $\tau-$model and more recent inverted and delayed $\tau-$models. Model SFHs that are too restricted in parameter space will inevitably lead to biased results.

2.5 Accounting for the effects of Dust

In chapter 1 we have briefly introduced the general properties of dust and its main effects in terms of absorption and re-emission at longer wavelengths. Here we review its role in shaping galaxy spectra in the context of SPS models.

Dust plays a dual role in spectral synthesis models, heavily affecting our view of galaxies: it absorbs and scatters photons, mostly at wavelengths $\lesssim 1$ μm, that is nearly the dust grains dimension, and thermally emits the absorbed energy in the IR ($\lambda \sim$ 5-1000 μm). The resulting SED of galaxies is often substantially changed and in many relevant cases radically modified by the presence of dust (see Fig. 2.1 bottom panel). This effect is particularly critical in galaxies with strong star formation episodes, which preferentially occur within dense molecular clouds. It is found, in fact, that the fraction of the energy emitted in

the IR increases as a function of the strength of the star-formation activity. Dust is also important for its catalytic action on molecular Hydrogen. It is, in fact, thought that the combination of HI into molecules probably requires the catalytic action of dust grains. The star formation is particularly favoured by the presence of dust, which shields dense clouds from the stellar UV radiation and thus keeps them to temperatures low enough to start the gravitational instability process. So dust plays a fundamental role in the star formation process of a galaxy.

The importance of dust effects for building a complete picture of galaxy formation is now well established: in order to understand the history of star formation in the universe from observational data, one must have a unified picture that covers all wavelengths from the far-UV to the sub-mm, but especially the UV and the far-IR, since young stellar populations emit most of their radiation in the rest-frame UV, and the part of this radiation that is absorbed by dust is then re-radiated mostly in the rest-frame far-IR, so that luminosities in these two wavelength ranges are the best tracers of the SFR at different redshifts. The modeling of these two components (absorption in the UV and re-emission in the IR) is often decoupled in most approaches being dust obscuration more sensitive to geometry while dust emission is more sensitive to the interstellar radiation field. This results, in some cases, in an inconsistency between what is absorbed at shorter wavelengths and what is then re-emitted at longer wavelength. This may lead to inconsistent stellar mass estimates and ages (due to the age-dust degeneracy), and therefore questionable cosmological interpretations (see e.g. Lo Faro et al. 2013).

Let's now briefly review (following Conroy 2013), more specifically, the two main contributions of dust in terms of attenuation and emission in the context of spectral synthesis models.

ATTENUATION

As we have seen in chapter 1, dust particles interact with photons emitted by astrophysical sources by absorbing, scattering, and polarizing the light (the combined effect of absorption and scattering takes the name of *extinction*). By comparing the observed spectrum of individual stars to the expected one in absence of dust one can measure the total extinction (i.e. total loss of energy) along the line of sight. The average extinction curve along many line-of-sights in the Milky Way (MW) has been studied by many authors (see references in Hoyle & Wickramasinghe 1991; and see Fig 2.6). We recall its main properties: *(a)* a growth in the optical–near UV, more than linear with frequency, $\tau \propto \nu^{1.6} \propto \lambda^{-1.6}$ $(0.6 - 5\ \mu m)$; *(b)* a bump around 2175 Å; *(c)* a steeper rise in the far–UV; *(d)* two features in the mid–IR at 9.7 and 18μm.

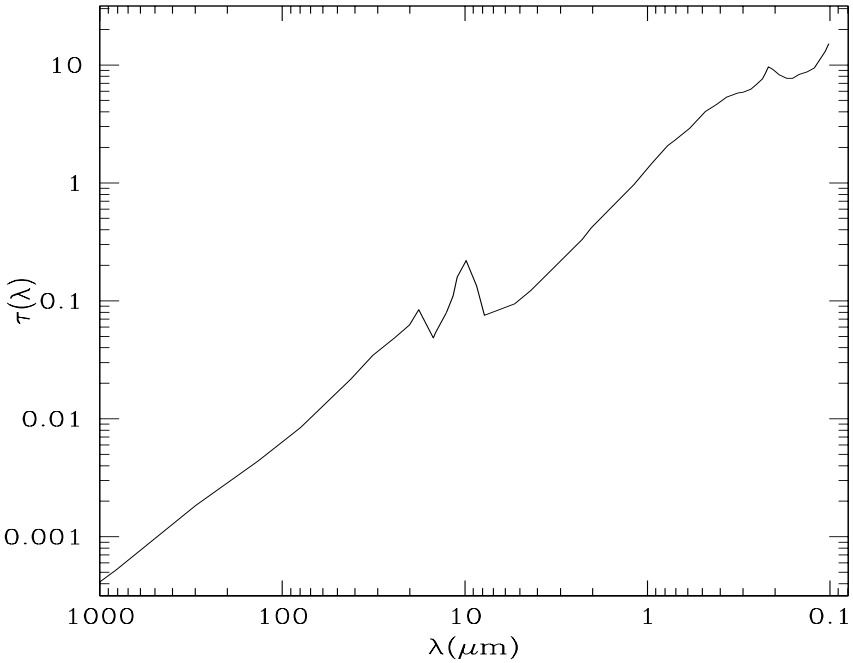

Figure 2.6 The galactic extinction curve, in optical depth per unit value of E(B-V). The two silicate features at 10 and 18 μm and that of carbonaceous grains at 2175 $\AA$ can be recognised.

The extinction curve, however, is not universal: in the MW it depends on the line of sight. Data on other stellar systems (Large and Small Magellanic Clouds (LMC and SMC, respectively, for example) also suggest a variable behaviour, in particular in UV. In fact in the MW and LMC the only striking feature in the extinction curve is the broad absorption at 2175 $\AA$. This feature is absent in three out of four line of sight to the SMC, and it is weaker in the LMC than in the MW. The grain population responsible for this feature may be polycyclic aromatic hydrocarbons (PAHs) as suggested by Draine (2003). In general, dust extinction is a consequence of the optical properties of the grains and the grain size and shape distribution.

When modeling galaxy SEDs, the relevant concept is dust attenuation, which differs from extinction in two important respects: (1) light can be scattered both out of and into a given line of sight; (2) the geometrical distribution of dust with respect to the stars strongly affects the resulting SED (see Calzetti 2001, for an extensive discussion of these issues). The total dust attenuation in a galaxy can be estimated by analogy with dust extinction. Having to deal with the geometrical effects of dust, estimating dust attenuation is considerably more complex than estimating dust extinction.

Although the shape of the dust attenuation curve depends on the star-dust geometry, grain size distribution, etc., in a complex manner, several simple empirical rules can be adopted. The simplest dust geometry is that of a homogeneous foreground screen of dust,

lying between us and the stellar population of the galaxy. This simple geometry yields an attenuation curve whose shape depends only weakly on the total dust column density (the weak dependence arises from the scattered light component). If we indicate with $\Delta\tau$ the thickness of the screen we have:

$$I(\lambda)_{obs} = I_{star}(\lambda)e^{-a_\lambda \Delta\tau} \tag{2.7}$$

with a_λ being the wavelength dependent reddening law.

More complex geometries generally yield attenuation curves that become greyer (i.e., shallower) as the column density increases. Clumpy interstellar media also result in greyer attenuation curves than their homogeneous counterparts. In all cases, the total attenuation optical depth is less than the amount of extinction that would be produced by the same column density because some scattered light is always returned to the line-of-sight. Finally, because the 2175 $\AA$ dust feature is believed to be due to pure absorption, the effects of radiative transfer will cause this feature to respond differently to geometrical effects compared to the rest of the attenuation curve. The use of a single dust attenuation curve for analysing a wide range of SED types is therefore without theoretical justification.

Calzetti et al. (2000) proposed a universal shape for the dependence of the attenuation on wavelength (function of $1/\lambda$), such that the UV light is the most affected by dust. This so called Calzetti law is based on observations of 39 nearby UV-bright starburst galaxies, and is the most currently used for high-redshift galaxies. They found a law much greyer than the extinction laws of the MW and LMC demonstrating the effects of geometry and mixing compared to simple extinction. However, the Calzetti law provides a poor fit to the UV colours of larger samples of nearby galaxies that have a range of star formation rates (e.g. Conroy 2010; Buat et al. 2011a). Other observational studies also find that, at least for part of the UV-selected galaxies at $1 < z < 4$, the attenuation is not well described by the Calzetti law (Noll et al. 2009; Buat et al. 2011b, 2012; Lee et al. 2012).

In the literature we can find many different reddening laws studied by different authors each describing a particular environment (galaxy, clusters, etc.). Figure 2.7 summarizes the the most popular reddening laws currently used in galaxy spectral synthesis.

DUST EMISSION

Beyond $\lambda \sim$ 5-10 μm the SED of normal galaxies is dominated by emission from dust grains which have been radiatively heated by a range of interstellar radiation field strengths. The observed dust emission spectrum thus depends on both the optical properties and size distribution of grains and on the interstellar radiation field. At long wavelengths

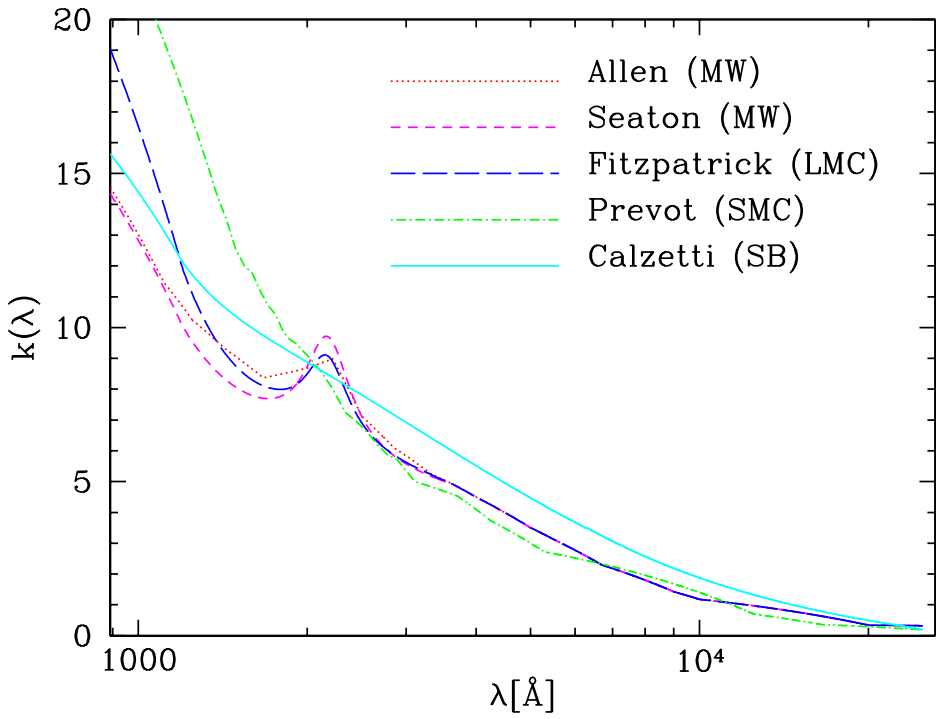

Figure 2.7 Extinction curves k(λ) for different reddening laws. The absence of the 2175 $\AA$ bump and the slower rise in the far-UV characterizing the Calzetti attenuation law, may be due to the fact that the starburst has modified the grain distribution, in particular suppressing the 2175 $\AA$ feature observed in the MW. [Figure courtesy of M. Bolzonella]

($\lambda > 50\mu$m) the emission is dominated by big grains in thermal equilibrium at a temperature of $\sim$ 15-20 K and contributes $\sim 2/3$ of the total IR luminosity. At shorter wavelengths the IR emission arises from single photon heating of dust grains (including PAHs) and accounts for the remaining $\sim 1/3$ of the total IR emission (see the review by Draine 2003, for details). The IR emission at the shortest wavelengths ($\lambda < 12\mu$m) is supplied almost entirely by PAHs. More in general the mid-IR region of the spectrum (3-30 μm) is characterized by continuum emission by hot dust, coming from regions mainly located near hot stars, in the active galactic nuclei (AGN) torii and dense circumstellar envelopes of cool evolved stars, and by the presence of strong emission generally ascribed to PAHs.

A detailed modelling of the entire SED of galaxies from UV to sub-mm, taking into account also the effects of dust, is therefore very complex. Several different approaches have been proposed, depending on the purpose of the applications. Some works (e.g. Devriendt et al. 1999; Chary & Elbaz 2001; Dale et al. 2001; Dale & Helou 2002; Galliano et al. 2003; Lagache et al. 2003; Burgarella et al. 2005a, da Cunha et al. 2008) have proposed semi-empirical treatments of the SEDs. The aim of these works is in general to interpret large samples of data, requiring fast computing times making use of observationally or physically motivated SEDs. There are then other codes, as Hyperz (Bolzonella et al., 2000) or LePhare (Arnouts et al., 1999) which usually perform a template-based SED fitting procedure based

on a standard χ^2 minimization method. Usually here dust effects are accounted for by computing the attenuation of the light from a source placed behind a foreground screen of dust and assuming different extinction curves.

Other works are based, instead, on theoretical computations in order to have a more general applicability in terms of interpretative and predictive power. Several papers deal with the radiative transfer (RT) in spherical geometries, mainly aimed at modelling starburst galaxies (e.g. Rowan-Robinson 1980; Rowan-Robinson & Crawford 1989; Efstathiou et al. 2000; Popescu et al. 2000; Efstathiou & Rowan-Robinson 2003; Takagi et al. 2003a; Takagi et al. 2003b; Siebenmorgen & Krügel 2007; Rowan-Robinson 2012). Early models of this kind did not include the evolution of stellar populations. Silva et al. (1998) were the first to couple radiative transfer through a dusty ISM and the spectral (and chemical) evolution of stellar populations. Now a variety of models exist that combine grain size distributions and grain optical properties with models for starlight (or simply the radiation field) to predict IR emission (Dale et al., 2001, Draine & Li, 2007, Groves et al., 2008, Jonsson, 2006, Piovan et al., 2006, Popescu et al., 2011). With respect to the semi-empirical approaches described above, these models based on theoretical computations are not always well-suited for interpreting large numbers of observed IR SEDs because they contain a large number of parameters, require knowledge of the star-dust geometry, and/or require radiative transfer calculations. In chapter 3 we will show how powerful, from a predictive point of view, this kind of approach can be. Specifically we will present the spectro-photometric + radiative-transfer code used in this work by which with a limited number of free parameters and a larger number of photometric bands we have been able to investigate in detail the physical properties of high-z dusty star-forming galaxies including their star formation history.

2.6 Fitting SED-Models to Data: Physical parameters

By fitting the population synthesis models described above to the detailed shape of the broadband SED of galaxies (as well as moderate-resolution optical/NIR spectra, or spectral indices), one is able to infer the main physical parameters of stellar populations, such as stellar, gas and dust mass, SFR and average extinction A_V. This procedure usually requires several input parameters. The library of SSPs (based on a particular set of isochrones, stellar spectra and IMF), is generally given. The SSPs span a wide range in age and metallicity to realistically reproduce the mix of age and composition of the stellar content of galaxies. Then the SFH of the galaxies, including the histories of the star formation rate, of the IMF, of the metallicity and the residual gas fraction, is defined by varying two or more parameters depending on whether or not a second burst superimposed on the quiescent SFH is considered. Dust attenuation and related additional parameters also need

to be specified if IR data are available. As we have seen in previous section, there are different fitting procedures available but most of them are generally limited to grid-based χ^2 minimization techniques.

As emphasized in Conroy (2013), in a standard SED-fitting procedure only the shape of the SED is being used to constrain model parameters such as M/L, specific SFR (SSFR=SFR/M), dust attenuation and metallicity.

2.6.1 Mass-to-light ratios and Stellar Masses

The stellar mass of a galaxy is directly linked to its luminosity, so the most direct way to derive this important parameter is to convert a luminosity measure into a stellar mass estimate. This is usually done by multiplying the mass-to-light ratio by the observed luminosity L. While the uncertainties on L depend on the quality of the data, the estimate of M/L and its associated uncertainties depend mostly on the SED fitting procedure performed and its basic assumptions. The best strategy in this case is to search for a reference band that minimizes the effects of M/L variations due to stellar populations (age, metallicity, chemical abundances) and due to dust absorption. Although the commonly adopted band is the NIR (e.g. the H-band at 1.65 μm), problems can arise because of thermally pulsing asymptotic giant branch stars (discussed in section 2.1) for stellar ages between 0.3-2 Gyr. This is the critical range where different tools give larger discrepancies due to the peak of the TP-AGB phase.

Before proceeding with the discussion about the uncertainties related to the estimate of M/L from SED-fitting let's briefly review, following Longhetti & Saracco (2009), the different definitions of stellar mass currently used in literature.

There are three different way to define the mass of a galaxy (see Renzini 2006) when it is related to the output of models.

- (i) The mass of gas burned into stars from the epoch of its formation to the time corresponding to its age, resulting from the integration over time of its SFR:

$$M_{SFR}(t) = \int_0^t dt^{'} SFR(t^{'}) \tag{2.8}$$

- (ii) The mass contained at any epoch into stars, both those still surviving and those which are dead remnants:

$$M_{star}(t) = \int_0^t dt^{'} SFR(t^{'}) - \int_0^t dt^{'} M_{loss}(t^{'}), \tag{2.9}$$

whereMloss(t$^{'}$) is the mass of gas returned to the interstellar medium from stars at any time t$^{'}$

- (iii) The mass that at any epoch is contained into still surviving stars:

$$M_{alive}(t) = \int_0^t dt^{'} SFR(t^{'}) - \int_0^t dt^{'} M_{loss}(t^{'}) - M_r(t), \tag{2.10}$$

where $M_r(t)$ is the mass of dead remnants at the time t.

While M_{SFR} is the same for different models since it depends only on the selected SFH, M_{star} depends on the assumed IMF and on the stellar evolution picture contained in the isochrones. Fig. 2.8 shows the differences between the three definitions of stellar mass for the same model of galaxy and their dependence on the assumed IMF (Salpeter and Chabrier), in the case of a declining SFR with $\tau = 0.4$ Gyr. As reported by Longhetti & Saracco (2009), for ages greater than few Gyr the mass still locked into stars is about 67% (50%) of the total mass involved in the past SF activity, and only the 57% (35%) is that still locked into surviving stars for Salpeter (Chabrier) IMF. Smaller differences are produced by the assumption of different stellar tracks. If we consider the M05 models in place of BC03 and a Salpeter IMF, we have that for ages between 12-15 Gyr the percentage of the total mass involved into past SF still locked into stars is 72% and that one locked into still alive stars is 61%. The definition adopted here to indicate the total stellar mass of a galaxy, inferred from the spectral synthesis models, is the one from equation 2.9, M=M_{star}, which is, as a matter of fact, the most currently used in works on stellar mass determinations.

To convert a luminosity measure into a stellar mass estimate we can used the following equation (Longhetti & Saracco, 2009):

$$M_{gal}[M_\odot] = L_\lambda^{gal} M/L_\lambda \tag{2.11}$$

where M_{gal} is the stellar mass of the galaxy expressed in solar masses, L_λ^{gal} is the luminosity of the galaxy at λ in solar luminosities and M/L_λ is the mass to light ratio at λ in solar units. The luminosity of the galaxy L_λ^{gal} can be calculated from the relation

$$L_\lambda^{gal}[L_\odot] = 10^{[0.4(M_\lambda^{gal} - M_\lambda^{sun})]}, \tag{2.12}$$

where M_λ stands for the absolute magnitude at λ. Combining the two equations above and writing the absolute magnitude M_λ^{gal} as a function of the apparent magnitude m_λ^{gal} we get

$$log(M_{gal}) = logM/L_\lambda + 0.4k - corr_\lambda + 2log(d_{pc}) - 2.0 + 0.4M_\lambda^{sun} - 0.4m_\lambda \tag{2.13}$$

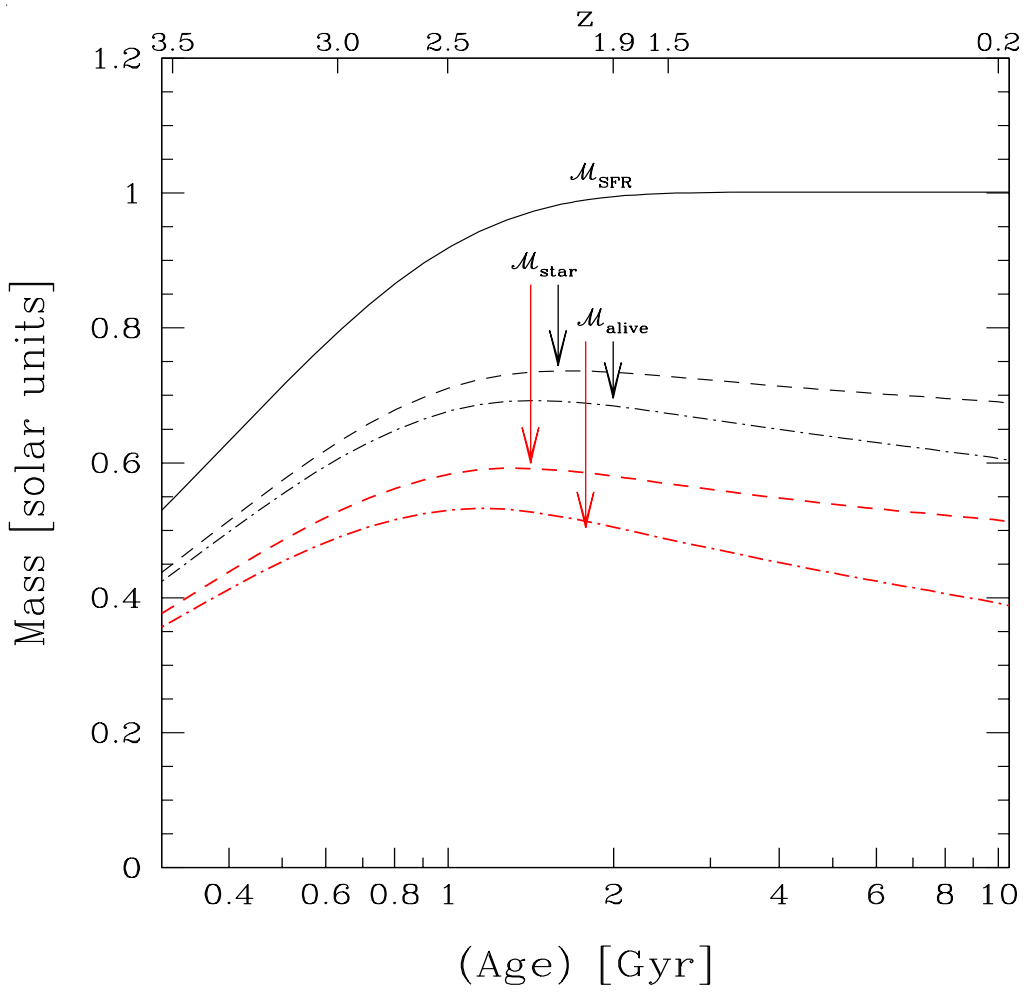

Figure 2.8 Figure 1 from Longhetti & Saracco (2009). It shows the mass content of a simulated galaxy plotted as function of its age (bottom axis) and z (assuming $z_{form} = 4$, top axis). The solid black line represents the mass obtained by integration over the age of the model of a declining SFR with $\tau = 0.4\,$Gyr, normalized to the final total mass. Short dashed lines represent the stellar mass still kept into stars at any age (i.e. it takes into account the stellar mass loss of some evolutionary phases). Dottedshort dashed lines stand for mass still kept into surviving stars alone (mass of dead remnants is subtracted). Black lines refer to models built with the Salpeter IMF, while red (grey) lines represent models obtained with Chabrier IMF (both assuming solar metallicity). [Figure courtesy of M. Longhetti]

where d_{pc} is the luminosity distance in pc that depends on the assumed cosmology and it is a function of z, M_λ^{sun} is the absolute magnitude of the Sun in the chosen filter centred at λ, while m_λ is the apparent magnitude of the galaxy in the observed filter centred at λ.

Spectrophotometric models play a crucial role in the determination of the conversion factor M/L and the k-correction necessary to compute the luminosity of the galaxy.

Uncertainties in M/L from SED-fitting

As first emphasized by Bell & de Jong (2001) and Bell et al. (2003), some of the largest uncertainties in derived M/L ratios arise from uncertainties in the assumed SFHs, in particular the presence of bursty SF episodes. As we have seen in section 2.4.1, the combination of Balmer lines with other age and metallicity-sensitive features, such as the 4000$\AA$ break, can help in constraining the burstiness of the SFH. Optical spectra therefore provide stronger constraints on the M/L ratio. Kauffmann et al. (2003) modeled the Hδ and Dn4000 spectral features measured from SDSS spectra in order to constrain SFHs and M/L ratios. They obtained 95% confidence limits on stellar masses of ~ 0.2 dex and ~ 0.3 dex for quiescent and star-forming galaxies, respectively. Typically the stellar masses of 'normal' galaxies, that is to say those not including eccentric SFHs, can be recovered at the ~ 0.3 dex level (σ uncertainty). This uncertainty, however, does not include potential systematics in the underlying SPS models.

The particular choice of the SFH, whether it is rising, declining or bursty, can significantly change the best-fit stellar mass, by as much as 0.6 dex in extreme cases (Pforr et al., 2012). A general rule of thumb is that M/L ratios estimated via simple SFHs (or single-age models) will be lower limits to the true M/L ratios (see Conroy 2013 and reference therein). This is a consequence of the fact that young stars outshine older ones, with the effect of 'hiding' old stellar populations in galaxies with a large number of young stars. This also explains why color-M/L relations are so uncertain for very blue colors.

The uncertainties related to particular phases of stellar evolution, such as the TP-AGB phase, can also affect the derived stellar masses. We have seen in section 2.1.1, how the different prescriptions on the TP-AGB phase can bring up to a factor of two difference in stellar mass and age estimates. An extreme case is represented by M05 models which predict much more luminosity arising from TP-AGB stars than previous models (e.g., Fioc & Rocca-Volmerange 1997, BC03). The effect is maximum at ages $3 \times 10^8 - 2 \times 10^9$ yr, where the TP-AGB phase peaks, with the M05 models giving stellar masses lower by a factor of 2 with respect to BC03. Subsequent work has largely confirmed the sensitivity of estimated stellar masses to the adopted SPS model (Wuyts et al. 2007, Kannappan & Gawiser 2007, Cimatti et al. 2008, Muzzin et al. 2009, Longhetti & Saracco 2009, Conroy et al. 2009), all works focusing on the comparison between the two most popular M05 and BC03 models. A detailed discussion about the main differences between these two spectral synthesis models is given in section 2.1.1. Many authors have found a maximum factor of $\sim 2-3$ difference in derived M/L ratios between the two models, in particular when NIR data are included. Kannappan & Gawiser (2007) have shown that the differences between M05 and BC03 models are relatively modest ($\lesssim 1.3$) when, instead, NIR data are excluded.

As we have already said, the contribution of TP-AGB stars to the integrated light of a synthetic stellar population peaks at $\sim 0.3 - 2$ Gyr, depending on metallicity, and so the importance of this phase to modeling SEDs will depend on the SFH of the galaxy. M06 found in passively evolving galaxies at z$\sim$2 the suitable sample to characterize the influence of TP-AGB stars on galaxy SEDs. The mid-UV spectra of these galaxies, in fact, exhibit features typical of A- or F-type stars which are indicative of ages in the range $\sim$ 0.3-2 Gyr. In addition to high-redshift quiescent galaxies, Lançon et al. (1999) suggested that post-starburst galaxies should also have a star formation history dominated by a burst in the exact age range where TP-AGB stars are expected to have the strongest impact. Their optical spectra show strong Balmer lines together with a well-developed Balmer Dn4000 break and little or no emission lines, indicative of large numbers of $10^8 - 10^9$ yr old stars and no active star formation. The 'debated' influence of TP-AGB stars on the SED of galaxies with ages in this range has recently been exploited by Zibetti et al. (2012). These authors, by analysing a sample of post-starburst galaxies at $z \sim 0.2$, find evidence for a low contribution from TP-AGB stars, and in particular they argue that M05 models predict significantly too much flux in the NIR for these objects, thus favouring more "TP-AGB light" models instead of the extreme predictions of M05.

The correct accounting for the TP-AGB stars is extremely complex due to the fact that this phase is so sensitive to age and metallicity. Moreover, as emphasized by Conroy (2013), using galaxy SEDs to constrain the relevance of this phase is difficult because many parameters among which metallicity, SFH, and dust, have to be simultaneously constrained. The situation reaches the maximum level of complexity at higher redshifts where dust also plays a crucial role in shaping galaxy spectra. It is worth mentioning that also the dusty envelopes with surround these stars during the TP-AGB phase may play a critical role.

However, we should take into consideration, that the effect of TP-AGB stars is limited to galaxies which are dominated by stars with ages in the range $\sim 3 \times 10^8 - 2 \times 10^9$ yr such as post-starburst galaxies, which are rare at most epochs, or quiescent galaxies at $z \gtrsim 2$. For typical galaxies at $z \sim$0, the treatment of this phase seems to be less relevant for estimating stellar masses, at least on average.

Chapter 3

Population Synthesis models in presence of dust: GRASIL

The SED of a normal star-forming disk-like galaxy is usually affected by dust mainly associated with the diffuse ISM, while for starburst galaxies most of the IR luminosity comes from the central ($\lesssim 1$ kpc) molecular-rich regions where the starburst is embedded. The computation of the SED of star-forming galaxies therefore requires an adequate treatment of the radiative transfer through a dusty medium. Moreover, in order to reproduce the infrared part of galaxy SEDs we need to model the thermal emission of dust grains, eventually accounting for the thermal fluctuations of smaller grains. As the dust emission spectrum depends on the optical properties and size distribution of grains and on the interstellar radiation field we need to build an appropriate dust-model which is able to reproduce the observed properties of galaxies.

Up to a few years ago, the importance of including dust effects in spectral synthesis models was generally under-appreciated mainly because of the level of complexity involved. The most striking difficulty is that while the integrated photometric properties of a hypothetical dust-free galaxy are geometry independent, the inclusion of dust introduces a strong dependence on the geometrical distribution of both dust and stars. Furthermore, the optical properties of dust grains and their dependence on environmental conditions have not yet been fully understood. Finally, the effects of scattering, absorption and emission of grains, which may not be in radiative equilibrium with the radiation field, make the solution of the radiative transfer equation in a complex geometry even more complicated.

However a more realistic and complete computation of the spectrophotometric galaxy models including dust effects is required, particularly at high redshift, to avoid erroneous estimates of fundamental quantities such as the star formation rate, stellar mass and age of stellar populations. The latter, in fact, can be affected by the degeneracy between the colors

of an old galaxy and those of an extinguished young galaxy, complicating the well-known age-metallicity degeneracy (Silva 1999, PhD thesis).

In other words, to model the emission from stars and dust consistently in order to get reliable estimates for the main galaxy physical parameters, like stellar mass, star formation rate and average extinction, one needs to solve the radiative transfer equation for idealised but realistic geometrical distributions of stars and dust, as well as taking advantage of the full SED coverage from UV to sub-mm.

Silva et al. (1998) were the first, with the GRASIL code for spectrophotometric evolution of galaxies, to couple radiative transfer through a dusty ISM with the spectral (and chemical) evolution of stellar populations.

In this chapter, I summarize the main features of the spectro-photometric code, GRASIL, we used to investigate the nature and mass assembly history of dusty star forming galaxies at high redshift. This code is able to predict the SEDs of galaxies from far-UV to radio including a state-of-the-art treatment of dust extinction and reprocessing based on a full radiative transfer solution. This chapter is mainly based on the seminal work by Silva (1999), Silva et al. (1998).

3.1 GRASIL

The problem of estimating the SED of a galaxy at age t_{gal}, including dust effects, is divided in GRASIL in two steps: (1) the determination, by means of a chemical evolution code, of the history of the star formation rate, of the IMF, of the metallicity, and of the residual gas fraction and then (2) the prediction, through stellar population synthesis, of the integrated galaxy SED taking into account all the stars and the gas present at t_{gal}.

If the effects of dust are neglected, the second step simply involves a sum of all the spectra of stars. But, when dust effects are included more complex aspects come into play. First, a dust model (i.e. chemical and physical properties and size distribution of grains) needs to be defined in order to model consistently both the absorption at UV-optical wavelengths and thermal re-emission in the infrared. Then a specific geometry for gas, stars and dust has to be included in galaxy models to compute the radiative transfer of the radiation emitted by the stars in the dusty medium of the galaxy.

The first step includes a number of possible choices that can be easily interfaced to the GRASIL code in order to describe the evolution of the SED (see section below).

3.2 The Chemical Evolution Code

The chemical evolution code, providing the input SFHs for GRASIL, is a preliminary and fundamental step for the spectro-photometric model. It has been written by L. Silva and G. L. Granato basically following the guidelines given by Tantalo et al. (1996). The code describes one-zone (no dependence on space, only on time) open models including the infall of primordial gas, according to the equations of galactic chemical evolution, in order to simulate the collapse phase of galaxy formation.

The SFH of a galaxy is parametrized as a sum of two terms: a first term representing the continuously varying part of SF given by the Schmidt-type law with efficiency $\nu_{\rm Sch}$, and when needed, a superimposed second analytical term, f(t), explicit function of time (i.e. constant or exponential), representing transient bursts possibly related to a galactic merger.

$$\Psi(t) = \nu_{\rm Sch} M_{\rm gas}(t)^k + f(t) \quad M_{\odot} yr^{-1} \tag{3.1}$$

where M_{gas} is the available mass of gas at the time t.

In order to simulate the chemical evolution of galaxies the time variation of the gas mass is expressed in the code as a function of three different contributions: (a) the depletion of gas due to star formation, (b) the injection to the ISM of processed gas by dying stars (feedback) and (3) the infall of primordial gas forming the galaxy. The processed gas returned from stars to ISM is computed under the assumption that it takes place when the stars died. It is calculated by estimating the rate of death of stars more massive than 5-8 $M_{\odot}$, and assuming an instantaneous recycling of ejected gas. The adopted stellar ejecta in the code is from Portinari et al. (1998).

In order to quantify the number of massive stars, the code have to adopt an initial mass function. The one used here is a power law, $\Phi(m) \propto m^{-x}$, with different mass intervals, and normalized to unitary total mass. Of course since the purpose is spectral synthesis we usually adopt here the same IMF used to build the SSPs. For the gas accretion into the galaxy, the code assumes an exponential infall of gas according to the equation:

$$dM_{inf}/dt = A_{inf} \cdot exp(-t/\tau_{inf}) \tag{3.2}$$

normalized in order to accrete a mass of gas M_{inf} at time t_{inf}. M_{inf} thus represents the total mass infelt in the system at time t_{inf} while τ_{inf} is the characteristic infall timescale.

By varying the two parameters ν_{Sch} and τ_{inf} the code allows for a wide range of different SFHs, from a more smooth and classical SFH characterized by longer phases of gas accretion and corresponding to large values of τ_{inf}, to a more 'monolithic-like' one characterized by very short infall timescales. A very short τ_{inf} can be used to have a so-called close box chemical evolution model, which ensures that the gas going to form the galaxy is all available at the beginning. Figure 3.1 shows some examples of the possible SFHs which can be implemented in the chemical evolution code. As you can see from the figure, by coupling the gas accretion phase with the depletion due to star formation we get SFHs which closely resemble, in their functional form, the so-called delay τ-models of Lee et al. (2010) already discussed in section 2.4.1. These are in fact usually characterized by an early phase of rising SFRs with late-time decay (SFR $\propto t^{\beta}e^{-t/\tau}$) and are probably the most suitable to explain the SEDs of high-redshift galaxies.

The code also allows for the possibility of interrupting the star formation activity and the gas infall at time t_{wind}. The computation is usually performed by igniting galactic winds when the amount of thermal energy from supernova explosions and stellar winds into the ISM exceeds the gravitational binding energy of the gas. This kind of chemical evolution model is particularly suited to reproduce the chemical and spectro-photometric properties of elliptical galaxies (see Matteucci 1996).

Table 3.1 summarizes the main input parameters of the chemical evolution code. Most of CHE_EVO parameters are usually left to their default value while the IMF is fixed to standard Salpeter. This reduces the number of free parameters of the model to two parameters, nu_{Sch} and $\tau_{\rm inf}$, when dealing with normal SFHs and 5 parameters (nu_{Sch}, $\tau_{\rm inf}$ for the continuous part of the SFH + t_{burst}, $\%M_b$, t_b for the analytic superimposed term) when including an analytic burst of SF on top of the Schmidt-type SFR. t_{burst} is usually fixed, what changes, actually, is the burst duration (Δ t_{burst}) together with the e-folding time of the burst. The exponential analytical term used to mimic merger effects has the form of $f(t) \sim exp(\Delta\ t_{burst}/t_b)$.

Par.	Unit	Description	class
$\nu_{\rm Sch}$	$\rm Gyr^{-1}$	SF efficiency	SFH: Quiescent
$\tau_{\rm inf}$	Gyr	infall timescale	SFH: Quiescent
$\%M_{\rm b}$	—	% of gas mass involved in the burst at $t_{\rm burst}$	SFH: burst
$t_{\rm b}$	Myr	burst e-folding time	SFH: burst
t_{burst}	Gyr	burst age	SFH: burst
IMF	m_{low}, m_{sup}, x	lower, upper limit and slope of power law IMF	

Table 3.1 Main CHE_EVO input parameters and their range of values.

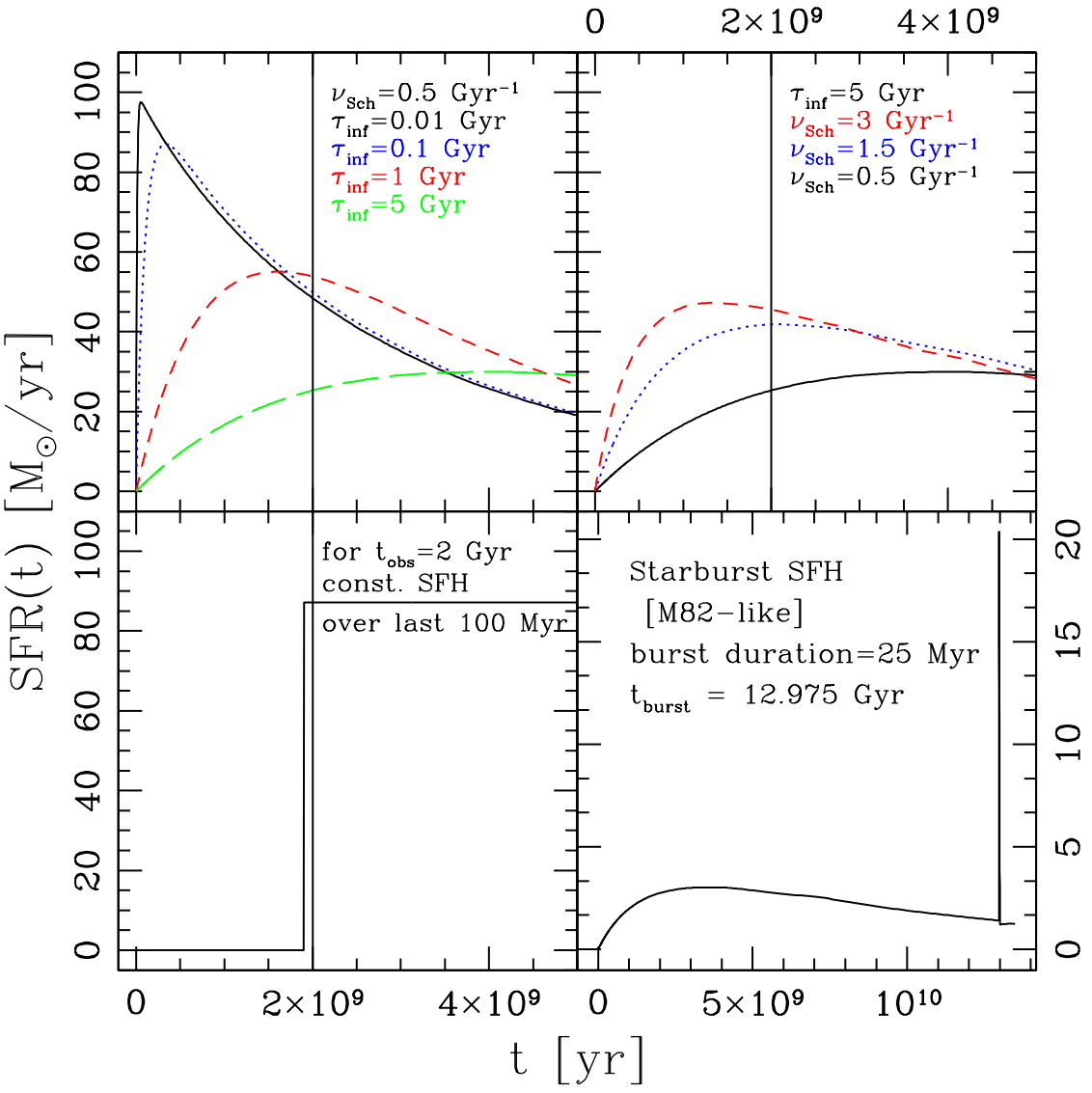

Figure 3.1 SFHs from chemical evolution code: from top-left to bottom-right we show, as an example several SFHs obtained with our chemical evolutio code. Top: exponentially declining SFHs at fixed ν_{Sch} for increasing values of τ_{inf} (left), then at fixed τ_{inf} and decreasing values of ν_{Sch} (right). When we consider longer infalla timescales and lower efficiencies our SFHs assume the form of a classical delay-τ model (see text for details). When, instead a shorter infall timescale is considered, a more rapidly declining SFH resembling the so-called τ-models, is obtained. Bottom-left panel shows a constant SFR while the bottom-right panel shows a typical 'starburst' SFH. Solid black vertical lines highlight an assumed observing time of 2 Gyr. In the bottom-right panel the time at which the galaxy is observed is highlighted in the figure.

3.3 Synthesis of starlight spectrum

The reference library of SSPs used here relies on the Padova stellar isochrones first developed by Bertelli et al. (1994) and then updated by Bressan et al. (1998, 2002) and Silva et al. (1998). One of the most interesting feature of this library is that it directly includes the

effects of dusty envelopes around AGB stars according to the prescriptions by (Bressan et al. 1998, hereafter B98) here below briefly summarized.

The effects of dust in the envelopes of evolved stars have long been neglected in the spectrophotometric synthesis of a composite population, basically due to the assumption that its contribution to the integrated bolometric light is negligible. We know now (see section 2.1.1), that this cannot be justified for intermediate age population clusters, whose brightest tracers are AGB stars. Bressan et al. (1998) were the first to account in a consistent way for the effect of dusty envelopes around AGB stars in isochrones at different ages and metallicity.

As we have seen in section 2.1.1, mass-loss along the AGB is a crucial parameter for the evolution of these stars because it affects the lifetime and the average luminosity of the phase. Both these quantities bear on the contribution of the whole phase to the integrated light because higher mass-loss rates imply shorter lifetimes of the phase and dimmer brightest stars, thus a lower contribution to the total light of the population (B98, Silva 1999). The mass-loss rate also affects the core mass of the subsequent post-AGB phase stars, hence the ultraviolet properties of the stellar population. A great effort has been devoted to clarify the role of mass-loss on the evolution of AGB stars but the actual mechanism which drives it is still not completely understood. It has been shown from both theory and empirical relations, (Bowen & Willson 1991; Vassiliadis & Wood 1993; Marigo 1998, Marigo et al. 1996) that the mass-loss rate rises almost exponentially with time (i.e. luminosity or period) during the AGB phase until it turns into a superwind that completely evaporates the envelope of the star, leaving a core which evolves towards very high temperatures. For the mass-loss here they adopt the empirical relations of Vassiliadis & Wood (1993) where the mass-loss rate grows exponentially with the pulsation period until a constant upper limit is reached at about 500 days, corresponding to the superwind phase. These empirical relations are based on observational determinations of mass-loss rates for Mira variables and pulsating OH/IR stars both in the Galaxy and LMC.

By adopting these empirical relations for the mass-loss rate and the wind terminal velocity in combination with analytical relations to describe the evolution of these stars in the HR diagram, they are able to model the effects of the dusty envelope around evolved stars, with a minimal number of parameters.

The infrared emission of late-type stars is modelled by solving the radiative transport equations inside a spherically symmetric stationary flow of matter (surrounding the star), which allows to derive the extinction and the emission of the dust as a function of wavelength. The radiative transfer is solved by means of the code described by Granato & Danese (1994). The envelope parameters, in particular its optical thickness, which is straightforwardly linked to the mass-loss rate and to the expansion velocity, are derived as a function

of basic stellar parameters (mass, luminosity, radius, and metallicity) combining hydrodynamic model results and empirical relations. Several envelope models are constructed as a function of the optical depth in such a way to assign the suitable dust envelope to the stars along the AGB.

The new isochrones are then computed at different age and metallicity and compared to existing infrared colors of M giants and Mira stars and to IRAS PSC data. The former data were fairly well reproduced by the models, though a possible inadequacy of the adopted atmospheric models was indicated. Though being characterized by different metallicity, the isochrones follow a single path in the IRAS two color diagram, fixed by the composition and optical properties of the dust mixture. The bulk of the data in the latter diagram is delimited by the curves corresponding to a mixture of silicate grains and one of carbonaceous grains. The emission in the mid-infrared is found to be about one order of magnitude larger when dust is taken into account in an intermediate age population, irrespective of the particular mixture adopted. The dependence of the integrated colors on the metallicity and age is also discussed, with particular emphasis on the problem of age-metallicity degeneracy showing how a suitable pass-band in the mid infrared can allow a fair separation of the two effects.

Finally we want to stress again that contrary to previous models here the mass-loss rate, which establishes the duration of the AGB phase, also determines the spectral properties of the stars. The contribution of these stars to the integrated light of the population is thus obtained in a consistent way.

The SSPs, built using the isochrones described above, span a wide range in age, from 1 Myr to 18 Gyr, and metallicity, Z = 0.0004, 0.004, 0.008, 0.02, 0,05, 0.1, to realistically reproduce the mix of age and composition of the stellar content of the galaxies. The library of SSPs has been computed for several IMFs, including Salpeter (1955), Scalo (1986), Miller & Scalo (1979), Kennicutt (1983) and the Chabrier (2003). As we have seen in previous chapter, in order to compute the total flux (SED) of an SSP we need to integrate the spectra of all stars, covering the necessary parameter space in log T_{eff} , log g, metallicity etc., along the isochrone. The core of the spectral library is the atlas by Kurucz (1993). This low resolution spectral library has the advantage of covering a wide range in parameter space and it is suitable for broad-band studies. Anyway high-resolution atmospheric stellar spectra can also be implemented when required (see for example Panuzzo et al. 2003). At temperatures higher than T_{eff} = 50000 K pure black-body spectra are adopted, whereas for stars cooler than T_{eff} = 3500 K the catalog of stellar fluxes by Fluks et al. (1994) is implemented. The latter library is based on stars of solar metallicity (Z $\sim$ 0.02) whereas the library of SSPs presented here spans the range of metallicity $0.0004 \leqslant Z \leqslant 0.05$. To account for a dependence on the metal content even for M giants, we adopted the same

library at different metallicities but assigned the spectral class, identified by the (V-K) color, adopting the (V-K)-T_{eff} relation of Bessell et al. (1991) which depends on the metallicity (see Bressan et al. 1998 for more details).

A summary of inputs used for the SSP models is given in Tab. 3.2.

Stellar flux library	Kurucz (1993) stellar atmosphere models
M Giant spectra	Straizys & Sviderskiene (1972) Lançon & Rocca-Volmerange (1992) Fluks et al. (1994)
Metallicity Z	0.02 $Z_\odot$ - 5 $Z_\odot$
IMF	Salpeter (1955); Kennicutt (1983); Scalo (1986); Miller & Scalo (1979); Chabrier (2003)
Age	1 Myr - 18 Gyr
$BC_{V_\odot}$	-0.08
$M_{bol_\odot}$	4.72
Initial star mass	0.1 - 120 $M_\odot$

Table 3.2 Inputs to the Single Stellar Population Models

As we have seen in Chapter 2, the spectral synthesis technique for the starlight alone, consists in summing up the SSPs of different age and metallicity, weighted by the SFR at time of the star birth. If we want to include also dust effects we need to specify a dust model and a geometrical arrangement for stars and dust and solve the radiative transfer equation in the different phases of the ISM.

3.4 Dust model

As already pointed out, the effects of dust on galaxy SEDs strongly depend on the physical and chemical properties of grains which affect the way they absorb and emit photons, as well as on the geometrical distribution of dust and stars. We know from observations that these properties are found to be function of the particular environment in which grains happen to live. At least three different dusty environments must be taken into account in order to properly understand the UV to sub-millimeter properties of galaxies: (i) circumstellar dust shells produced by the windy final stages of stellar evolution (further subdivided into the chemical subgroups of oxygen rich and carbon rich dust), (ii) dust in interstellar HI clouds heated by the general interstellar radiation field (ISRF) of the galaxy (the "cirrus" component), and (iii) dust associated with star-forming molecular clouds and HII regions (dense component). These environments have different importance in different galactic systems at various evolutionary stages. The stellar outflow dust, (i), is already included in the library of isochrones used to build the SSP as specified above and therefore it is fixed in GRASIL. This means that only the dust in the diffuse and dense component are allowed

to be varied by the user in the code. So, hereafter, when talking about dust in GRASIL we will refer to these two components.

The dust model used in GRASIL find its basis in the so called *standard model* for dust in the diffuse ISM developed by Draine & Lee (1984, hereafter DL84). Despite of the large efforts devoted to derive this model the precise composition of dust remains controversial. Significant clues have been derived from observations. ISO observations of the diffuse medium have contributed to establish that the prominent absorption features at 9.7 and 18 μm are due to the different vibration modes of amorphus silicates. The origin of the 2175 $\mathring{A}$ feature is somewhat debated, although graphite seems to be the most attractive solution (see Mathis 1990). The emission bands in the $3 - 20\mu m$ region are related to the presence of Polycyclic Aromatic Hydrocarbons (PAHs), while small thermally fluctuating grains are responsible for the very warm mid-IR (MIR) continuum. The remaining IR emission is due to the classical big grains in thermal equilibrium with the radiation field. All these components have been included in the diffuse dust model of GRASIL. Given the lack of information about the dust composition of the dense medium, the same mixture is adopted also for MCs, only decreasing the fraction of PAH molecules (see below).

The optical properties of graphite and silicate grains have been computed by Laor & Draine (1993) for spherical shapes using Mie theory, the Rayleigh-Gans approximation and geometrical optics. In particular GRASIL uses the cross sections of graphite and silicate grains computed by B.T. Draine for 81 grain sizes from 0.001 to 10 μm, in logarithmic steps of $\delta\log(a) = 0.05$.

In order to get the overall radiative properties of the dust mixture we need to specify the abundance and size distribution of grains. GRASIL uses as reference the distribution proposed by DL84, tuned to reproduce the optical-UV extinction law of the galactic diffuse ISM. A severe limitation of this model is the inability to reproduce the MIR cirrus emission at $\lambda \leq 60\mu m$ because of the presence of dust grains always big enough to maintain a low temperature thermal equilibrium in the general interstellar radiation field (ISRF) (Silva et al., 1998). This emission requires instead reprocessing of the radiation field by very small grains and/or PAH molecules, reaching temperatures higher than those given by thermal equilibrium. This can be achieved by decreasing the lower limit of the graphite grain distribution. Since the abundance of these grains must be higher than the simple extrapolation of the DL84 power law, Silva et al. (1998) have introduced a break to a steeper power law below a_b. These adjustments to the DL84 model have the effect of enhancing the MIR cirrus emission but at the same time tend to degrade the agreement with the observed extinction law in the optical-UV region. However, a reasonable compromise has been found

and, for graphite grains, the following size distribution is adopted in the code:

$$\frac{dn_i}{da} = \begin{cases} A_i n_H a^{\beta_1} & \text{if} \quad a_b \leq a \leq a_{max}, \\ A_i n_H a^{\beta_1 - \beta_2} a^{\beta_2} & \text{if} \quad a_{min} \leq a \leq a_b, \end{cases} \tag{3.3}$$

where a is the radius of the grain, $a_{min} = 8$ $\mathring{A}$, $a_{max} = 0.25$ μm, $a_b = 50$ $\mathring{A}$, β_1 = -3.5, β_2 = -4.0, and $A_{graphite} = 10^{-25.22} cm^{2.5}/H$. This last value is set in order to maintain the same volume of graphite grains as the DL84 model. For silicate grains the same size distribution as in DL84 is adopted here, i.e. a single power law with a_{min}=50 $\mathring{A}$, a_{max}=0.25 μm, a_b=50 $\mathring{A}$, β_1=-3.5 and $A_{silicate} = 10^{-25.11} cm^{2.5}/H$

Adopting these parameters for the distribution of graphite grains, the number of small thermally fluctuating dust particles with radius a $\leq a_b$ is enhanced by a factor of $\sqrt{\frac{a_b}{a}} \sim 2$ with respect to the DL84 law extrapolated below a_b and their corresponding MIR cirrus emission. In this model, the 2175 $\mathring{A}$ bump appears for $a \leqslant 300\mathring{A}$, and the silicate feature at 9.7 μm seems to be due to grains with $a \leqslant 1\mu$m. This model reproduces reasonably well both, the extinction from IR to UV and the whole cirrus emission (see e.g. figure 3 of Silva 1999, Silva et al. 1998).

Once the bathing radiation field is specified, the emissivity of grains with radius $a \geq 100\mathring{A}$ is computed assuming that they achieve thermal equilibrium, so that all grains of a given composition and radius emit as graybodies at a single temperature:

$$j_\lambda^{big} = \int_{a_{flu}}^{a_{max}} \pi a^2 Q_{abs}(a,\lambda) B_\lambda(T(a)) \frac{dn}{da} da = \sum_{i, a_i > a_{flu}} \omega_i Q_{abs}(a_i,\lambda) B_\lambda(T(a_i)) n_H \frac{erg}{cm^3 sst\mathring{A}} \tag{3.4}$$

T(a), the equilibrium temperature for grain a, is given by the energy balance between absorption from the radiation field J_λ and emission:

$$\int Q_{abs}(a,\lambda) J_\lambda d_\lambda = \int Q_{abs}(a,\lambda) B_\lambda(T(a)) d\lambda \tag{3.5}$$

here a_{flu} is set to 100 $\mathring{A}$. As specified in Silva et al. (1998) the maximum grain size for thermal fluctuations to be important depends on the intensity and shape of the radiation field but 100 $\mathring{A}$ seems to be a reliable value regardless of radiation field properties. Below this limit a temperature distribution for each size bin and composition is computed following Guhathakurta & Draine (1989), and then the emissivity is obtained by integrating over this distribution.

The total dust content (i.e. cirrus + MCs) of a galaxy ISM, depends on the residual gas mass, provided at each epoch by the chemical evolution code described above, and on the dust-to-gas ratio (δ=D/G). Measurements of the D/G in our Galaxy and in nearby galaxies typically range from 1/100 to 1/600 (e.g Dunne et al. (2000)). So, when the model is compared with nearby galaxies, it is common to use $D/G = 1/110$, which is the standard value of the DL84 model. However, being GRASIL a code conceived to model objects of very different nature and in different evolutionary stages, it also allows the possibility to use a general recipe to scale the dust-to-gas ratio with the metallicity Z of the system. The simplest way to do this is to assume D/G $\propto$ Z, with the proportionality constant chosen in order to have the standard 1/110 for Z=$Z_{\odot}$ (Dwek, 1998).

3.4.1 PAH emission: [based on Silva et al. (1998) + Vega et al. (2005)]

Besides the hot continuum emission, due to a strong radiation field that heats dust at the required temperatures, the MIR spectra of many dusty galactic and extragalactic sources are also characterized by strong emission features at 3.3, 6.2, 7.7, 8.6, 11.3 and 12.7 μm. These features are most commonly ascribed to aromatic C-C and C-H vibrations in large planar Polycyclic Aromatic Hydrocarbons (PAH) molecules, with size $\sim$ 10 $\AA$ and containing $\sim$ 50-100 C atoms (Leger & Puget 1984, Puget & Leger 1989, Tielens et al. 1999). Detailed observations with ISO have allowed deep investigations of the properties and variations of PAH features in different Galactic environments - post-AGB stars, planetary nebulae, reflection nebulae, young stellar objects, HII regions and photo-dissociation regions (PDR), diffuse interstellar medium -, as well as in different galaxies.

To model the effects of polycyclic aromatic hydrocarbons on the MIR SED of galaxies, a population of planar PAHs has been included in GRASIL. The PAH treatment in GRASIL was originally based on pre-ISO data so, it just computed the five emission bands at 3.3, 6.2, 7.7, 8.6, and 11.3 μm (see Silva et al. 1998). ISO observations have subsequently revealed the presence of also strong emission features at 11.9, and 12.7 μm, relevant sub-structure in the 6.2, 7.7 and 8.6 μm bands (Peeters et al., 2004), weaker features at 3.4, 5.4, 8.2, 11 etc., and hints of strong features for $\lambda > 13$ μm (e.g. Sturm et al. 2000). Based on these new evidences and adopting the main features of the model proposed by Li & Draine (2001), Vega et al. (2005) worked on an updated treatment of PAH emission in GRASIL including further emission bands and a different abundance of PAHs in the cirrus and MC component. We start presenting the original model introduced by Silva et al. (1998) followed by the updates introduced by Vega et al. (2005).

3.4.1.1 PAH treatment in GRASIL

This section is mainly based on Silva (1999). As we have already said above, the original treatment of PAH emission in GRASIL included five emission bands at 3.3, 6.2, 7.7, 8.6, and 11.3 μm. The adopted optical-UV absorption cross-section, σ_{PAH} is shown below in the Fig. 3.2. This has been obtained by Leger et al. (1989) by averaging the cross sections of six different PAH mixtures measured in laboratory above 1200 $\AA$, and joining the resulting mean curve to the coronene cross section below this limit. The same cross section is assumed by GRASIL to take into account the effect of PAHs on the extinction curve. Desert et al. (1990) also proposed an analytical description of σ_{PAH} derived from the observed interstellar extinction curve in the 1200-3300 $\AA$ range, assuming that these particles dominate its extreme UV (EUV) rise. The EUV rise can be also ascribed to small grains. In the dust emission model adopted in GRASIL in fact, (i.e. DL84), the EUV part of the extinction curve is due to the small grains. Therefore, the Leger et al. (1989) σ_{PAH} gives a better description of the PAH absorption and subsequent IR emission in the local interstellar radiation field than that one by Desert et al. (1990).

In order to compute the IR emission of PAHs, their heat capacity, $\mathrm{C_{PAH}(T)}$ must be specified. GRASIL adopts the $\mathrm{C_{PAH}(T)}$ estimate given by Leger et al. (1989) for which a numerically convenient and accurate representation is:

$$\frac{C_{PAH}(T)}{C_{max}} = \begin{cases} 9.25 \times 10^{-4} T & \text{if} \quad T < 800K \\ 2 \times 10^{-4} T + 0.58 & \text{if} \quad 800 \leq T < 2100K \\ 1 & \text{if} \quad T \geq 2100K, \end{cases} \tag{3.6}$$

where $\mathrm{C_{max}} = 3[N_t - 2]k$, $\mathrm{N_t} = \mathrm{N_C} + \mathrm{N_H}$ is the total number of atoms (carbon plus hydrogen) in the PAH molecule, and k is the Boltzmann constant.

There is an indication that small PAH molecules (with $\mathrm{N_C} \lesssim 20$) are easily destroyed by UV photons (e.g. Omont 1986). Thus, GRASIL adopts a population of PAHs with a continuous power-law distribution, $\frac{dn}{dN_C} \propto N_C^{-2.25}$ ranging from $\mathrm{N_C}$=20 to $\mathrm{N_C}$=280 (atoms), similar to those adopted by other authors, e.g. Dwek et al. (1997).

The typical observed flux ratios of the 11.3 and 7.7 μ m bands, i.e. between the C-H and C-C bands, suggest that PAHs in the ISM are partially dehydrogenated, probably due to the large UV flux in the typical PAH emission regions (Mattila et al. (1996)). The number of H atoms in a molecule is thus written as $N_{\mathrm{H}} = x_{\mathrm{H}} N_{\mathrm{s,H}}$, where $N_{\mathrm{s,H}}$ is the number of available hydrogen sites, and x_{H} is the hydrogen coverage. The relationship between $N_{\mathrm{s,H}}$ and N_{C} depends on the arrangements of hexagonal cycles in the molecule.

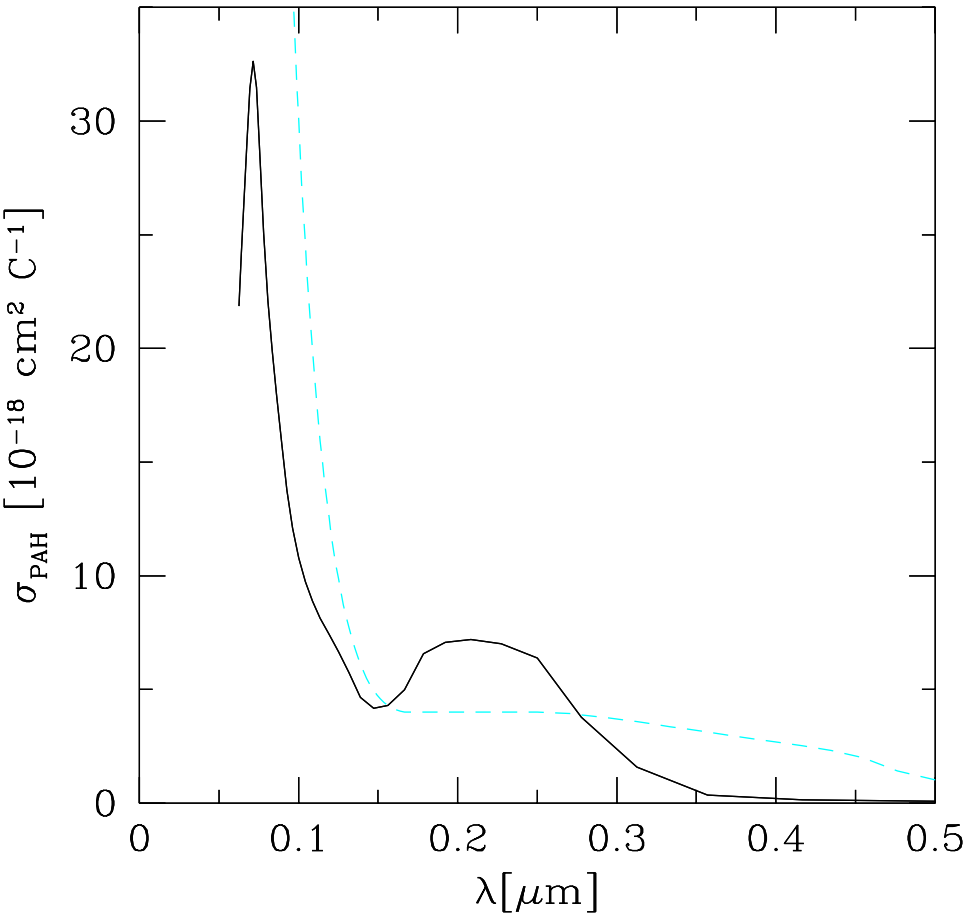

Figure 3.2 From Silva et al. (1998). Solid line: Cross section of PAH per carbon atom, derived from laboratory measurements taken from Leger et al. (1989). Dashed line: The analytical law assumed by Desert et al. (1990) for molecule with N_C = 50 C atoms. The one adopted here by GRASIL is from Leger et al. (1989). See text for details.

Although the actual carriers of PAH emission are still unknown, the structure of typical interstellar PAHs is likely to be close to that of catacondensed PAHs (Omont, 1986), which are the most compact and stable PAH configurations and have the general formula $C_{6p^2}H_{6p}$, i.e. $N_{s,H} = (6N_C)^{0.5}$. These quasi-circular molecules are usually assumed to represent the gross features of interstellar PAHs and have a radius a=0.9$\sqrt{N_C}\mathring{A}$ if $N_C \gg 1$, which translates in sizes ranging from $a = 4$ to 15 $\mathring{A}$ in our distribution of PAH molecules. In order to reproduce the typical flux ratios between CH and C-C bands observed in the Galactic cirrus, the hydro-coverage x_H in GRASIL, has been fixed to 0.2.

The PAH emissivity is then computed following Xu & de Zotti (1989). The abundance of

carbon atoms locked in PAHs in the GRASIL dust model, was originally set to 18 ppM in the cirrus, and was 10 times lower in the MCs to account for PAH destruction in strong UV fields. These abundances have then been updated by Vega et al. (2005) based on results from ISO observations (see next section for details). Once emitted, PAH bands are absorbed by MCs and/or cirrus dust before emerging from the model galaxy. This treatment provides a rigorous computation of the total energy carried by these features.

For what the profile of the features is concerned, due to the lack of theoretical information, the observed PAH profiles from the Ophiuchus MC by Boulanger et al. (1998) have been adopted. These authors found that the PAH bands are well fitted by Lorentz profiles, characterized by wide wings accounting for a large fraction of the continuum between the features (see also Vega et al. (2005)).

3.4.2 The updated PAH emission model: Vega et al. (2008, 2005)

As already specified in section 3.4.1, ISO data have allowed a great step forward in our understanding of PAH phenomenology. In particular, the detection of new emission bands together with the subsequent study of their profiles in different environments and galaxies, have contributed to put several constraints on their modeling. However the overall properties of astrophysical PAHs are still uncertain, so that, as in the case of dust models in general, their modeling still requires ad-hoc settings of parameters to better reproduce the observations.

In order to reproduce the properties of starburst galaxies in the MIR, region strongly influenced by the presence of polycyclic aromatic hydrocarbons, Vega et al. (2005) have worked to an updated treatment of PAH emission in both the cirrus and MC component of GRASIL modeled ISM. In the cirrus component they have introduced the new quantitative prescription of PAH emission in the diffuse ISM, given by Li & Draine (2001, LD01 hereafter). In addiction to the 3.3, 6.2, 7.7, 8.6, 11.3 μ m bands already included in GRASIL, Vega et al. (2005) have introduced the 11.9, 12.7, 16.4, 18.3, 21.2, and 23.1 μ m bands. Absorption and emission from PAHs are computed following the treatment described in section 3.4.1.1 but adopting Drude profiles with the FWHM and the emission cross sections taken from LD01. As stressed by the authors, available laboratory data on PAHs differ by large factors among different groups, and also between experimental results and theoretical calculations. Therefore, LD01 modified laboratory data for the emission cross sections in order to reproduce observations (the Galactic cirrus emission).

Once again, only after ISO it has been possible to define a clearer picture of PAH emission in different environments revealing a general lack of such features in regions associated with star formation processes. Observations in our Galaxy, for example, have shown a clear

depletion of PAH emission near hot stars or when passing inward from PDRs to HII regions (e.g. Boulanger et al. 2000, Contursi et al. 2000). At the same time Hony et al. (2001) observed a high degree of de-hydrogenation in star forming regions. The observational evidence of a lack of PAH emission in regions characterized by strong UV radiation fields, forced Vega et al. (2005) to reduce the PAH abundance in the dense MC component, by a large factor ($\sim$ 1000 times less than in the cirrus component). This updated model has been tested against observations by comparing the modeled SEDs with a selected sample of star-forming galaxies, for which both accurate MIR narrow-band, NIR, FIR and radio observations were available. This comparison have probed successfully over the wide range of FIR luminosities of the selected galaxies.

When dealing with PAH emission in GRASIL we will always refer, hereafter, to the updated treatment described above.

3.5 The Radiative transfer in dusty media

As already pointed out in previous sections the effects of dust on galaxy SEDs strongly depends on the relative distribution of dust and stars. In order to describe galaxies of all morphological types, GRASIL assumes a general geometry consisting of a composite disk + bulge (spheroidal component) system. In any case the galaxy is approximated as a system having azimuthal symmetry as well as planar symmetry with respect to the equatorial plane as shown in Figure 3.3.

Three different components are taken into account:

1. Star forming molecular cloud complexes, MCs, including dusty gas in a dense phase, HII regions and very young stars embedded in it (young stellar objects [YSOs]);
2. Stars already escaped from their parent MCs (*free stars*)
3. Diffuse gas or cirrus component

The relative distribution of these three components must be then specified before solving the radiative transfer equation for each case. More specifically, once defined a geometrical distribution for stars and gas, according to the formalism presented in section 3.5.1, a fraction f_{MC}, of the model gas mass M_{gas} at age t_{gal}, is assigned to MCs subdivided into clouds of given mass and radius (i.e. optical depth). The remaining gas goes in the diffuse phase. The energy source inside the MCs is due to newly born stars which gradually escape from their parent MCs as they get older. The RT computation for this dense phase is described in section 3.5.2. The starlight from older stars (free stars) and the emission

from MCs constitute the energy source for the diffuse dust whose RT effects are accounted for according to the formalism presented in section 3.5.3: the volume emissivities $j_\lambda^\star$ and j_λ^{mc} (erg cm^{-3} s^{-1} st^{-1} $\mathring{A}^{-1}$) of the galaxy at each point determine the local radiation field heating the diffuse dust in all the other volume elements, thus the local dust emission j_λ^c. The galaxy volume integral yields the observed flux (Silva, 1999).

The assumed geometry and galaxy components are shown in Fig. 3.3.

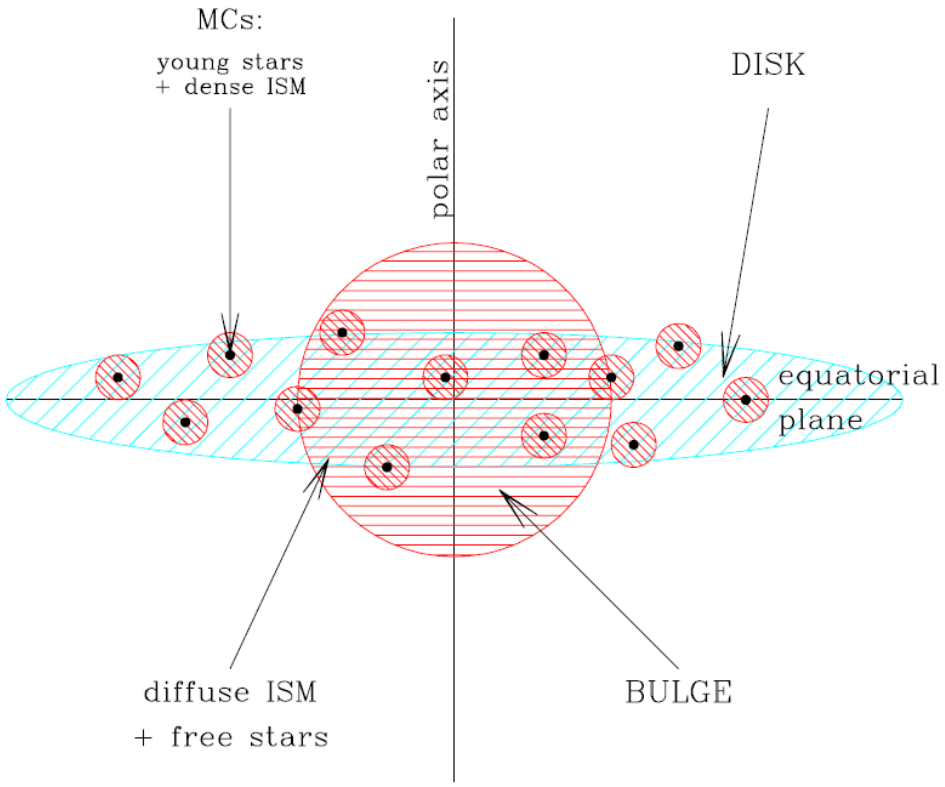

Figure 3.3 Scheme of the components included in GRASIL model computations and their adopted geometry.

3.5.1 Geometry & Distributions

GRASIL works in spherical coordinates (r, θ, ϕ). Therefore the densities of the three component, ρ_{mc}, $\rho_\star$, and ρ_c, depend on r and θ through analytical functions. In the following, unless otherwise explicitly stated, ρ_{mc} and $\rho_\star$ are assumed to have identical spatial dependence.

Depending on the specific nature of the objects we have to model, a different geometry can be considered. For disk-like systems, GRASIL uses a double exponential of the distance

from the polar axis R = r sin θ and from the equatorial plane z = r cos θ:

$$\rho_D = \rho_0 exp(-R/R_d) exp(-|z|/z_d). \tag{3.7}$$

In the code the scale lengths R_d and z_d can be independently set for the three components. Nevertheless an adequate simplification is to assume identical values for them, thus reducing the number of free parameters in case of disk geometry to two: $R_d^\star$=R_d^{mc}=R_d^c and $z_d^\star$=z_d^{mc}=z_d^c as for the models described in Chapter 6. Observations in our Galaxy suggest $z_d^\star \sim 0.35$ kpc.

In the case of spheroidal systems, a spherical symmetric distribution with King profile is adopted for both stars and dust (only for stars in the case of bulges):

$$\rho_B = \rho_0 (1 + (r/r_c)^2)^{-\gamma}, \tag{3.8}$$

extended up to the tidal radius r_t of the galaxy. This truncation radius is required in King models since $M(r)$, the mass contained within r, diverges as $r \to \infty$. As for the stellar component γ is set equal to 3/2. Also in the case of spheroidal geometry it is possible to simplify the problem by choosing $r_c^\star$=r_c^{diff}, thus assuming that stars and dust are equally spatially distributed. This reduces the number of free parameters for this geometry to only one.

The volume emissivity (erg cm^{-3} s^{-1} st^{-1} $\mathring{A}^{-1}$) of the galaxy at each point is the sum of three terms arising from the three components listed above:

$$j_\lambda = j_\lambda^{mc} + j_\lambda^\star + j_\lambda^c. \tag{3.9}$$

In the next sections I will describe how these quantities are computed within the spectrophotometric code.

3.5.2 Radiation Transfer in the MC component

All known star formation in low-redshift galaxies occurs in molecular gas clouds. In our Galaxy, most of the massive star formation activity is produced within giant molecular clouds (GMCs). Observations of CO and higher density tracers like HCN or CS indicate that the GMCs are non-uniform, highly structured objects, with a relatively dense ($n_{H_2} \sim 10^3 cm^{-3}$) envelope traced by CO, and density enhanced regions ($n_{H_2} \geqslant 10^4 cm^{-3}$), or cores, traced by molecules as HCN or CS, wherein star formation actually occurs (Lada & Adams, 1992). This clustering of young stars at different locations inside GMCs is confirmed by infrared imaging.

The first evolutionary stages are typically hidden at the uv-optical wavelengths, and a significant fraction, if not all, of the energy of these young objects is reprocessed by dust, and re-emitted in the IR, with only a minor fraction of the energy being reradiated as recombination lines. These MCs are usually destroyed on a time-scale comparable with the typical lifetime of massive OB stars ($\sim 10^6 - 10^7$ yr) due to the combined action of powerful stellar winds and outflows, and the ionizing flux from massive stars. In this way stars gradually get rid of their parent MCs and become visible at optical wavelengths. The typical dust densities in this objects are so high that even the IR photons are self-absorbed. So, the radiative transfer equation has to be solved in order to compute the emitted SED.

The complex evolution described above is simulated as follows. Given the total mass of gas available at t_{gal}, the gas mass in the dense component, which is the one involved in the star formation process, is computed by multiplying the f_{mc} parameter (see Tab.3.3), by the total gas mass as $M_{mc} = f_{mc}M_{gas}$. The molecular gas is then subdivided into spherical molecular clouds of assigned mass, m_{mc}, and radius, r_{mc} ranging in the typical observed intervals $\sim 10^5 - 10^6 M_\odot$ and $\sim 10 - 50pc$ respectively. It is then supposed in the code that each generation of stars, represented by an SSP, is born within each MC and then progressively escapes it. This is parametrized in the model by linearly decreasing the fraction f of SSP energy radiated inside the cloud as a function of its age t:

$$f = \begin{cases} 1 & \text{if} \quad t \leq t_{esc}, \\ 2 - t/t_0 & \text{if} \quad t_{esc} < t \leq 2t_{esc}, \\ 0 & \text{if} \quad t > 2t_{esc}. \end{cases} \tag{3.10}$$

where t_{esc} is the model parameter representing the typical time-scale for young stars to escape from their parent MCs. The time dependence of the above function gives rise to one of the most distinctive features of GRASIL, the age-dependent dust attenuation, where younger stellar populations are more extinguished than older ones. As we will see in the next chapters this feature becomes fundamental when dealing with high-z star forming galaxies.

The optical depth of the cloud ($\tau_{mc} \propto M_{mc}/(G/D)/r_{mc}^2$) is the real parameter shaping the cloud spectrum. The emerging SED is obtained by considering the total stellar content of the cloud as an emitting point source, and by solving the radiative transfer through the cloud with the code described by Granato & Danese (1994) whose main features are here briefly summarized.

This code was originally developed for interpreting AGN spectra in particular to model the dusty tori around these objects, but it is useful to treat more generally radiative transfer in thick media. The transfer of radiation originating from a central point source in an axisymmetric dust distribution is solved with the lambda-iteration method (see also section

1): at each iteration the local temperature of dust grains is computed from the condition of thermal equilibrium with the radiation field estimated at the previous iteration. The convergence is speeded up with respect to this simple scheme following the prescriptions given by Collison & Fix (1991). Moreover, in the present case (as for the AGB envelopes discussed in section 3.3), the computing times are reduced by about two order of magnitude taking advantage of the spherical symmetry of the clouds (Silva, 1999).

To simplify the problem we have assumed a central stellar point source for the MCs. The distribution of stars in real GMCs is indeed characterized by a dust temperature distribution with many hot spots and cooler regions randomly distributed. An obvious drawback of this approach is an overestimation of the amount of very hot dust around the source with respect to the more realistic approximation in which the stars are split in many sources at different locations. However Krugel & Siebenmorgen (1994) have shown that the output IR spectra resulting from the two approximations are very similar if the emission from the whole cloud is considered. Moreover the treatment of many hot spots within the cloud would introduce many other geometrical parameters slowing down considerably the code due to the loss of symmetry. The compromise solution found by Silva et al. (1998) consists of introducing a new parameter, the sublimation temperature of dust grains (T_{GRA}, T_{SIL}), which summarizes all the geometrical parameters relative to the "many hot spots" approach, while keeping the original central point source in the code. The real value of dust sublimation temperature is typically ~ 1000 K. Lowering the grain sublimation temperature produces a lower average temperature with a less opaque cloud. This makes the overall spectrum very close to the one predicted with a proper treatment of the hot spots. So, the code has been proved to be able to reproduce the MIR spectra of galaxies by fixing T_{GRA}=T_{SIL}=400 K.

It is worth mentioning that although the description given above assumes all MCs to be equal, GRASIL also allows the possibility to account for two or more populations of MCs characterized by different masses, radii and escape times. However the feasibility of using two or more populations of MCs has to be investigated case to case, given the increased number of free parameters and computational time consuming.

3.5.3 Propagation in the diffuse ISM: cirrus emission

Before escaping the galaxy, the light arising from the free stars and from molecular clouds interacts with the diffuse dust component. GRASIL adopts a simplified treatment of radiative transfer in this component which ignores dust self-absorption ($\tau_{IR} \ll 1$). This simplification is justified by the fact that in most astrophysical cases, the diffuse medium

is transparent to its own photons, and a complete treatment would imply a significant increase of the number of free parameters and of computational time.

Here the effects of optical-UV scattering are approximated by means of an *effective optical depth*, given by the geometrical mean of the absorption and scattering efficiencies $\tau^2_{eff} = \tau_{abs}(\tau_{abs} + \tau_{scatt})$ (Rybicki & Lightman 1979, p. 36). This approximation for combined scattering and absorption processes is rigorously applicable only to an infinite homogeneous medium and isotropic scattering. However Silva et al. (1998) tested this approximation by comparing their results with others obtained by means of Monte Carlo RT codes, and found excellent agreement, concluding that this approximation is good enough for the purposes of the code. Moreover in the GRASIL clumpy medium the optical-UV extinction is in most cases strongly dominated by MCs, where there is a better treatment of scattering than in the diffuse phase.

The galaxy is then subdivided into small volume elements V_i. The local (angle averaged) radiation field in the i-th element due to the extinguished emission of free stars and MCs from all the other elements is computed from the relation:

$$J_{\lambda,i} = \sum_k \frac{V_k(j^{mc}_{\lambda,k} + j^{\star}_{\lambda,k})exp(-\tau_{eff,\lambda}(i,k))}{r^2(i,k)} \frac{erg}{cm^2 sst\mathring{A}}, \tag{3.11}$$

where $\tau_{eff,\lambda}(i,k)$ and $r(i,k)$ are the effective optical thickness and the distance between the elements i and k respectively ($r^2(i,k)$ is a volume average of the square of the distance from i to all points within the volume k, see Silva 1999 for more details). The local dust emissivity is then computed according to the equation 3.4.

The volume emissivity of the galaxy at each point is the sum of three terms:

$$j_\lambda = j^{mc}_\lambda + j^{\star}_\lambda + j^{c}_\lambda \frac{erg}{cm^3 sst\mathring{A}} \tag{3.12}$$

Finally the specific flux measured by an external observer in a given direction θ is derived as a sum over the galaxy, of the extinguished emissivity of free stars, MCs, and diffuse dust:

$$F_\lambda(\theta) = 4\pi \sum_k V_k j_{\lambda,k} exp(-\tau_{eff,\lambda}(k,\theta)) \frac{erg}{s\mathring{A}}, \tag{3.13}$$

where $\tau_{eff,\lambda}(k,\theta)$ is the optical thickness from the element k to the outskirts of the galaxy along the direction θ (when only stars are considered this equation corresponds to the equation 2.6). Deviations from the energy balance between dust absorption and emission, which mainly depend on the number of volume elements in which the galaxy is subdivided, are kept within less than 2%-5% (see Silva 1999).

All the main GRASIL input parameters discussed in this Chapter are summarized in Tab. 3.3. As we will see in the next Chapters the number of GRASIL free parameters can be reduced to 4 or 5 depending on the particular geometry considered and the nature of galaxies under investigation.

D/G	dust-to-gas ratio. It can be fixed or $\propto Z$
f_{mc}	fraction of in the dense phase (MCs)
M_{mc}, r_{mc}	mass and radius of MCs. They define the optical depth of MCs as $\tau_{mc} \propto M_{mc}/(G/D)/r_{mc}^2$
t_{esc}	escape time of young stars from their parent MCs
$T_{GRA,SIL}$	sublimation temperature for graphite and silicate grains in MCs
$r_c^{\star,c,mc}$	core radii of King profiles for stars and dust
$R_d^{\star,c,mc}$	scale-lengths of the exponential disks for stars and dust
$z_d^{\star,c,mc}$	scale-lengths of the exponential disks for stars and dust
β	sub-mm spectral slope

Table 3.3 Main GRASIL input parameters. Note that the actual number of free parameters for the disk-like geometry is 2, since in general R_d and z_d are assumed to have the same values for all the three components (as discussed in section 3.5.1). Moreover the real fitting parameter shaping the MC spectrum is the optical depth, τ_{mc}. This means that identical SEDs from the MCs are produced by keeping constant the ratio $(M_{mc}/(G/D))/r_{mc}^2$. The sublimation temperature for graphite and silicate dust grains inside MCs affects their short wavelength ($\lesssim 10$ μm) emission from the clouds. This parameter is needed because of the simplified geometry of a central point source inside MCs. Fixing its value to 400 K, the code is able to reproduce the MIR spectra of galaxies.

3.6 Modeling the radio emission

As we have seen in Chapter 1, the existence of a tight correlation between the FIR and radio emission for nearby galaxies was discovered early in the 70's by van der Kruit. Initially both the infrared and radio emission were thought to be synchrotron radiation from relativistic electrons accelerated by 'nuclear monsters' (e.g. massive black holes in Seyfert galaxies or AGNs). A couple of years later Harwit & Pacini (1975) proposed that the infrared is thermal reradiation from dusty HII regions, while the radio luminosity is dominated by sinchrotron radiation from relativistic electrons accelerated in SNRs from the same population of massive stars that heat and ionize the HII regions. This FIR/radio correlation is now locally well established over a significant range of luminosity, from normal spirals ($\sim 10^8 L_\odot$) to the most extreme ULIRGs (up to $\sim 10^{13} L_\odot$) (see e.g. Condon 1992, Condon et al. 1991, Helou et al. 1985, Hummel et al. 1988, Wunderlich et al. 1987). Its validity has been successively confirmed also at higher redshift (up to $z \sim 1.3$ e.g. Appleton et al. 2004, Carilli & Yun 2000, Garrett 2001, 2002, Garrett et al. 2003 and up to $z \sim 2$ more recently by Sargent et al. (2010). The FIR/radio correlation is often expressed in terms of the q

parameter introduced by (Helou et al., 1985)and defined as:

$$q_{1.49Ghz} \equiv log\left(\frac{F_{FIR}}{3.75\times10^{12}Wm^{-2}}\right) - log\left(\frac{S_{1.49Ghz}}{Wm^{-2}Hz^{-1}}\right) \simeq 2.35 \pm 0.2 \tag{3.14}$$

This narrow distribution in $q_{1.49Ghz}$ suggests that the non-thermal (NT) emission, which in normal star forming galaxies may account $\sim 90\%$ of the radio emission (Condon, 1992), is related to the recent star formation, as traced by the FIR, and the most likely mechanisms could be synchrotron emission from relativistic electrons accelerated into the shocked ISM by core collapse supernova (CCSN) explosions.

Bressan et al. (2002) has extended the predictions of the continuum emissivity beyond the sub-millimeter regime, up to 316 Mhz, revisiting the model of radio emission by Condon & Yin (1990) for GRASIL. Here, the radio emission is assumed to be the sum of two different contributions: the thermal emission from free electrons in the HII regions, and synchrotron emission from relativistic electrons accelerated by SNe.

The thermal emission (L_ν^T) is proportional to the number of H ionizing photons (Q_H) derived from the SSPs and scales as $\approx \nu^{-0.1}$:

$$L_\nu^T(erg/s/Hz) = \frac{Q_H}{5.495\times10^{25}}\left(\frac{T_e}{10^4K}\right)^{0.45}\left(\frac{\nu}{1.49Ghz}\right)^{-0.1} \tag{3.15}$$

The non-thermal component (L_ν^{NT}) has been computed by Bressan et al. (2002) calibrating the NT emission/CCSN (type II SNe) rate relation on the observed properties of our Galaxy, thus using the SN rate ($\nu_{SNII}^{MW} \simeq 0.015$) and synchrotron luminosity of the MW and accounting for the small contribution, $\approx 6\%$, of SN remnants (SNR):

$$L_\nu^{NT}(10^{30}erg/s/Hz) = \left(E_{1.49}^{SNR}\left(\frac{\nu}{1.49}\right)^{-0.5} + E_{1.49}^{el}\left(\frac{\nu}{1.49}\right)^{-\alpha}\right)\times\frac{\nu_{SNII}}{yr^{-1}}, \tag{3.16}$$

where E^{SNR} is the average non thermal luminosity from SNR per supernova event, and E^{el} is the injected energy of the electrons also per SN event, which is taken ≈ 1.38 in order to reproduce the non-thermal energy per SN event in our Galaxy, and ν_{SNII} is the SN rate of the model. In order to reproduce the observed averaged slope of NT radio emission in normal spirals (≈ 0.8), Bressan et al. (2002) have adopted a value of $\alpha \approx 0.9$.

Although the calibration with our Galaxy is quite uncertain, the model reproduces very well the FIR-to-radio correlation of normal star forming galaxies, namely $q_{1.49Ghz}$=2.3.

Bressan et al. (2002) also found that the tightness of the FIR/radio correlation is natural when the synchrotron mechanism dominates over the inverse Compton, and the electron cooling time is shorter than the fading time of the SN rate. Observations have shown that both these conditions are met in star forming galaxies, from normal spirals to obscured

starbursts the latter being characterized by even shorter synchrotron electron lifetimes. In brief, the NT radio luminosity of a galaxy is proportional to the integral of the synchrotron power over the electron lifetime, and an increase of the former in a larger magnetic field is compensated by a shortening of the latter. However since the radio non-thermal emission is delayed, deviations are expected both in the early phases of a starburst, when the radio thermal component dominates, and in the post-starburst phase, when the bulk of the NT component originates from less massive stars. The authors have also shown that this delay allows the analysis of obscured starbursts with a time resolution of a few tens of Myrs, unreachable with other SF indicators.

With respect to the original calibration of the $L^{NT}_{1.4Ghz}/\nu_{CCSN}$ (i.e. non thermal radio emission/SN rate) ratio by Bressan et al. (2002) we used here the revised one by Vega et al. (2008) which consists of enhancing the calibration factor by 30-40%. This is required to reproduce the radio emission of normal star forming galaxies at high redshift as well as that one of both local and high-z (U)LIRGs. The new calibration factor is a consequence of the subsequent improvements on the SSP libraries adopted here and in Vega et al. (2008) with respect to those used in the original work of Bressan2002. The updated SSPs are characterized by a finer time sampling of the ages typical of non thermal emission. This results in a lower SNII rate ($dn/dt = dn/dm \times dm/dt = IMF \times dm/dt$) with respect to previous SSPs and therefore, for the same calibration, lower non thermal radio emission.

The inclusion of radio emission in galaxy modeling is challenging because it offers an additional and independent way to further constrain the current SFR of galaxies and the relative proportion of young and old stars contributing in different way to the IR and radio part of galaxy SED. In Chapter 6 we will explore its importance in reproducing the physical properties of high-redshift star forming galaxies.

3.7 SED-fitting with GRASIL

The models used to reproduce the observed SEDs are selected from different libraries generated with GRASIL which includes thousands of spectra corresponding to different combinations of model parameters. As discussed below we have been able, through the study of the parameter space of GRASIL, to reduce the number of free parameters to only 6-9 (discussed below) depending on the hypothesis made, among the others, on the SFH of the galaxies. The multiwavelength dataset considered in our analysis includes more than 18 photometric datapoints thanks to the availability of a full IR coverage by Spitzer and Herschel in addiction to a complementary multiwavelength dataset from far-UV to NIR.

The best-fit solution is obtained through a standard χ^2 minimization procedure by comparing the observed SED of a given galaxy to the set of modeled spectra:

$$\chi^2 = \frac{1}{n-1} \sum_{i=1}^{n} \frac{(F_{mod}(i) - F_{obs}(i))^2}{\sigma^2(i)} \tag{3.17}$$

where $F_{mod}(i)$, $F_{obs}(i)$, and $\sigma^2(i)$ are the model and observed fluxes and the observational errors, respectively. n represents the number of photometric datapoints used for the fit and it is always greater than the number of free parameters of the model (see above). Therefore the best fit galaxy model is always well constrained. We recall that this procedure is not based on a simple template rescaling but each model solution, corresponding to a specific set of parameters, is self-consistent and physically motivated.

When spectral information is also available, as for example the IRS spectra in our case, the best-fit solution to the photometry only is then compared to the spectrum and if necessary the specific parameters influencing that region of the spectrum are fine-tuned in order to reproduce both the photometry and the spectrum. This is done for all the solutions having a reliable χ^2 value.

3.8 Parameter Exploration

We have used a sample of local (U)LIRGs, already analysed with GRASIL by Vega et al. (2008), as a 'test-sample' to become familiar with the code and explore its parameter space. In particular we have used this sample to investigate how the different input parameters may affect the different regions of the spectrum of actively star forming galaxies (both normal star forming and starbursts). This exploration of parameter space allowed us to limit the number of free input parameters of the model to 7 when dealing with merger-induced starburst galaxies whose SFH is fixed a priori (usually local (U)LIRGs, while for high-z starburst galaxies we prefer to allow for different SFHs) and the geometry considered is the simplest one (i.e. King's profile), 9 when the SFH is left free and about 6 when considering normal star forming galaxies with varying SFHs (these objects at high-z will be discussed in detail in Chapter 5). The 7 main input parameters affecting the typical SED of starburst galaxies are here below briefly discussed and highlighted with different colors in Fig. 3.4. It is worth saying that indeed most of these parameters are in common with the other kind of objects investigated in this work. The parameters whose effect is not shown here are the two parameters ruling the SFH of galaxies, namely ν_{Sch} and τ_{inf} already discussed in detail in section 3.2. For pure starburst galaxies (where AGN contribution is negligible), the SED is found to be mainly affected by the optical depth of the dust ($\tau_{1\mu m}$ - marine oval), the

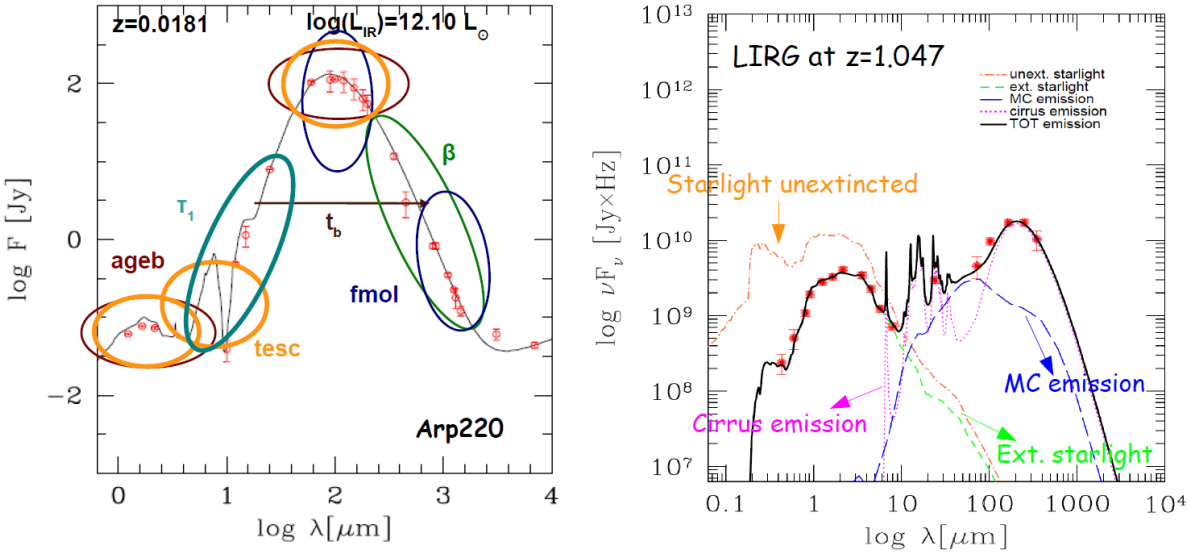

Figure 3.4 Left: figure shows the main GRASIL input parameters affecting the SED of starburst galaxies. On the background the best-fit (solid line) to *Arp220* photometric data (red open circles) is shown. Coloured ellipses emphasize the spectral regions affected by the specific parameter. For a brief description of how these parameters influence galaxy spectra see the text. Right: Figure highlights with various colors the different components contributing to the composite best-fit SED (black solid line) computed by GRASIL, namely the un-extinguished starlight (orange dot-dashed), the extinguished starlight (green dashed), the cirrus emission (magenta dotted) and finally the MC emission (blue long-dashed).

escape time (t_{esc} - yellow ovals), the age of the burst (age$_b$ - dark red), the e-folding time of the burst (t_b - brown arrow), the fraction of gas in molecular clouds (f_{mc} - blue ovals) and the sub-mm dust spectral index (β - green oval).

The optical depth mainly affects the MIR spectral range by varying the contribution of the MC emission in the MIR and the depth of the Silicate feature at 9.7 μm. For instance, an increase of the MC optical depth has the effect of strengthening the 9.7 μm silicate absorption feature. t_{esc} affects the NIR region, the PAH emission, and FIR colour by changing the contribution of un-extinguished young red supergiants to the NIR, by the heating of the cirrus from un-extinguished young stars, and by the heating of MCs from extinguished young stars, respectively. age_b mainly affects the radio spectral index, and in combination with t_b can be used to define the evolutionary phase of the starburst as shown by Vega et al. (2005). Higher values of the ratio age_b/t_b, indicating more evolved starbursts, are associated with higher NIR fluxes and cooler FIR colour (see Vega et al. 2005 for a thorough discussion). f_{mc} affects the FIR colour and the sub-millimetre region, while β mainly affects the sub-millimetre region.

In order to find the best-fit combination of model parameters describing the sample of local ULIRGs we have built several starburst libraries, (depending on the number of possible values each parameter can assume), considering almost all the possible combinations of

the seven parameters seen before. This library has been tested also against other samples of local starburst galaxies as for example those discussed in da Cunha et al. (2010). Our predictions, in terms of the main physical parameters of local starburst galaxies ($M_\star$, SFR, A_V, etc.), have been found to be in agreement with estimates from other works (e.g. da Cunha et al. 2010, Vega et al. 2008).

Chapter 4

Herschel and complementary observations of representative high-redshift galaxy samples

A powerful approach to understand the physical processes driving galaxy formation and evolution is to directly witness the growth of the stellar content in galaxies as a function, for example, of both redshift and stellar mass, thus focusing on the active phases of their evolution history. Since during active phases of star formation the bulk of the UV flux by young hot massive stars is strongly absorbed by dust and re-emitted at long wavelengths, we need FIR and sub-millimetre (SMM) data for this study, in addition to the optical/UV/NIR ones. Observations at long wavelengths, from a few to 1000 μm, are essential to study the diffuse medium in galaxies, including all kinds of atomic, ionic and molecular gases and dust grains. Hence they are particularly suited to investigate the early and active phases of galaxy evolution, when a very rich ISM is present in the forming systems.

During the last few years a variety of observational campaigns in the far-IR/sub-mm, exploiting both ground-based and space instrumentation, have started to provide results of relevant cosmological impact. Most crucial among these have been the discovery of an intense diffuse background in the far-IR/sub-mm of extragalactic origin, and the deep explorations from space in the far-IR and with large millimetric telescopes on ground. These results challenge those obtained from optical-UV observations, by revealing luminous to very luminous phases in galaxy evolution at substantial redshifts, likely corresponding to violent events of star-formation in massive systems. This is bringing to significant refinements of the present schemes of galaxy formation, as far as the history of baryon transformations is concerned (Franceschini, 2000).

In the local Universe the infrared emission accounts for about 1/3 of the total light emitted from galactic sources (Soifer & Neugebauer, 1991). At higher redshifts this contribution increases significantly due to the corresponding increase in dust-obscured star formation and/or gas accretion (e.g. Dole et al. 2006). From the Cosmic Infrared Background (CIRB), in fact, it can be easily inferred, that about 2/3 of the energy generation in the history of the Universe took place in dusty, obscured regions. Sub-millimetre surveys have contributed to identify the brighter sources responsible for some of this background. It is now clear, in fact, that dust enshrouded galaxies play a major role in galaxy evolution. Among these bright infrared sources an important role is played by sub-millimetre galaxies (SMGs), which are thought to be the high redshift equivalents of local Ultra Luminous Infrared Galaxies, lying at redshifts $z \sim 2-3$ and hosting starbursts forming stars at $10^2 - 10^3$ $M_{\odot} yr^{-1}$. These objects are likely to be the progenitors of massive elliptical galaxies seen in the local Universe today.

Many of the problems related to the sources responsible for this background can be addressed through the analysis of their broad-band SED from optical through the MIR and into the FIR, and the Herschel space observatory (Pilbratt et al., 2010), operating with its instruments between 55 and 671 μm has been, during the last three years, of great advantage allowing us to investigate regions of the spectrum for which until then we had only few data points.

The main focus of my current and PhD research project is to investigate the nature and mass assembly history of dusty star forming galaxies at high redshift observed with Herschel. So in this Chapter, after a brief review of the main features of the infrared spectral region of galaxies and the Spitzer & Herschel extragalactic surveys, we will present the galaxy sample analysed in this work. We will focus here on the redshift range $1 < z < 3$ (z$\sim$1-2) which represents the crucial epoch where much of the present-day stellar mass was assembled in massive galaxies, heavy elements were produced, the number density of QSOs peaked and the Hubble sequence was established. It's also known that most of the energy radiated during this epoch by newly formed stars was heavily obscured by dust. Long-wavelength observations are therefore crucial.

4.1 The Infrared Spectral Region

With Infrared (IR) we usually refer to the region of the electromagnetic spectrum spanning the wavelength range between 1 μm and 300 μm, with longer wavelengths ascribed to the sub-millimetre (SMM, 300 μm - 1 mm) and millimetre (mm) regions. It is usually subdivided into 3 different spectral regions: near, mid and far-infrared (i.e. NIR-MIR-FIR). The boundaries between NIR, MIR and FIR are not agreed upon and can vary. The main

factor that determines which wavelengths are included in each of these three regions is the type of detector technology used for gathering the infrared light.

Any source which has a temperature (i.e. radiates heat), emits in the infrared. So, basically all celestial objects emit some infrared. The wavelength at which an object radiates most intensely depends on its specific temperature. Here below the main features of the three IR regions are briefly summarised:

(1) The near-IR extends from (0.7-1) to (3-5) μm and cover the temperature range between 740 - (3000-5200) K. Large red giant stars and cooler low mass red dwarfs dominate in the near-infrared. Red giants are large reddish or orange stars which are running out of their nuclear fuel. They can swell up to 100 times their original size and have temperatures which range from 2000 to 3500 K. Red dwarfs are the most common of all stars. They are much smaller than our Sun and are the coolest of the stars having a temperature of about 3000 K which means that these stars radiate most strongly in the near-infrared. Many of these stars are too faint in visible light to even be detected by optical telescopes, and have been discovered for the first time in the near-infrared. The near-infrared is also the region where interstellar dust is transparent to infrared light.

(2) The mid-infrared extends from (3-5) to (25-40) μm and is characterized by temperatures ranging from (92.5-140) to 740 K. This regions is mostly contributed by continuum emission by warm dust (heated by starlight) and by the presence of strong emission features generally ascribed to PAHs. More in general this region of the electromagnetic spectrum is usually dominated by objects cooler than the red stars dominating the NIR, among which planets, comets and asteroids.

(3)The far-infrared, ranging from (25-40) to 300 μm sample very cold matter with temperatures ranging from (10.6-18.5) to (92.5-140) K. Here we find the contribution of emission from cold dust ('cirrus' emission), from the central regions of galaxies and from very cold molecular clouds.

Near-infrared observations have been made from ground based observatories since the 1960's. They are done in much the same way as visible light observations for wavelengths less than 1 micron, but require special infrared detectors beyond 1 micron. Mid and far-infrared observations can only be made by observatories which can get above our atmosphere due to the presence of water vapour and carbon dioxide which contribute to make the atmosphere completely opaque over large wavelength ranges from almost all ground-based observing sites. Moreover the atmosphere itself emits molecular lines and a very broad thermal continuum, which at each wavelength is proportional to the product of the emissivity and the Planck function evaluated at the temperature of the atmosphere. These

observations thus require the use of special cooled detectors containing crystals like germanium whose electrical resistance is very sensitive to heat. The thermal emission from the telescope also contributes significantly to the thermal continuum emission at wavelengths longer than a few μm. For these reasons, when observing in these bands, it is necessary to pay attention also to the noise due to the structure of the telescope which can be reduced, for example, by using an efficient cooling system.

A detailed discussion about the origin of infrared emission and infrared galaxies can be found in Chapter 1 & 2.

4.2 The Spitzer Space Telescope contribution to the analysis of IR luminous galaxies

The launch of the Spitzer Space Telescope (Werner et al., 2004) marked the beginning of a new era for infrared astronomy. Its higher sensitivity with respect to previous observatories both space- and ground- based, brought to significant improvements. The satellite was launched in August 2003 and was inserted into an Earth-trailing heliocentric orbit. Spitzer is constrained to point no closer than 80 deg toward and no further than 120 deg from the Sun, but even with these constraints 35% of the sky is visible at any time, and the entire sky is visible every six months.

The Spitzer Space Telescope is the final mission in NASA's Great Observatories Program - a family of four space-based observatories, each observing the Universe in a different kind of light. The other missions in the program include the visible-light Hubble Space Telescope (HST), Compton Gamma-Ray Observatory (CGRO), and the Chandra X-Ray Observatory (CXO).

Spitzer is designed to detect infrared radiation, which is primarily heat radiation. It incorporates two major components: The Cryogenic Telescope Assembly (CTA), which contains an 85 cm telescope cooled to 5.5 K, and three scientific instruments providing imaging and spectroscopy at wavelengths from 3.6 to 160 μm.

The telescope, cryostat, and associated shields and shells make up the CTA, built by Ball Aerospace, who also built the Multiband Imaging Photometer for Spitzer (MIPS) and Infrared Spectrograph (IRS) instruments. The third instrument, the Infrared Array Camera (IRAC), was built at NASA's Goddard Space Flight Center. The Spitzer flight hardware consists of a spacecraft that operates at roughly room temperature and the CTA that is cooled by a combination of superfluid liquid helium, helium boil-off gas, and radiative cooling and operates at much lower temperatures.

Its highly sensitive instruments allow scientists to investigate cosmic regions that are hidden from optical telescopes, including dusty stellar nurseries, the centers of galaxies, and newly forming planetary systems. Spitzer's infrared eyes also allows astronomers to see cooler objects in space, like brown dwarfs, extrasolar planets, giant molecular clouds, and organic molecules that may hold the secret to life on other planets.[1]

4.2.1 Spitzer Imaging Instruments

Spitzer comprises two imaging instruments, IRAC and MIPS, operating in the NIR and MIR and an IR spectrograph, IRS (Infrared Spectrograph), providing both high- and low-resolution spectroscopy at mid-infrared wavelengths (from 5 to 40 microns). A brief description of the three scientific instruments is given below:

- IRAC: InfraRed Array Camera (Fazio et al., 2004). It is a four-channel imaging camera that provides simultaneous $5.2' \times 5.2'$ images at 3.6, 4.5, 5.8 & 8 μm. Thanks to the low background available in space, it can reach faint limiting fluxes in modest exposure times. In fact, IRAC can reach similar depths (19th magnitude) as the 10 m W. M. Keck Telescope with the NIRC2 camera at 3.6 μm in only one-hundredth of the exposure time and does so with a far larger field of view: $5' \times 5'$ versus $40'' \times 40''$. The IRAC bands are only weakly affected by dust extinction and are well suited to probe stellar mass at fairly high redshifts and therefore to detect elliptical/spheroidal galaxies, Surace et al. (2005).

- MIPS: Multiband Imaging Photometer for Spitzer (Rieke et al., 2004). It produces imaging and photometry in three broad spectral bands, centered nominally at 24, 70 and 160 μm, and low-resolution spectroscopy between 55 and 95 μm. The instrument contains three separate detector arrays each of which resolves the telescope Airy disk with pixels of size $\lambda/2D$ or smaller. While the IRAC bands probe the stellar mass, the MIPS bands are sensitive to on-going star formation and cooler highly dusty regions. The high sensitivity at 24 μm of the MIPS instrument allows infrared-luminous galaxies to be traced to high redshifts. Sensitivity to obscured starbursts at $z \sim 2$ is enhanced due to redshifting of the 7.7 μm feature into the 24 μm band [source `http://irsa.ipac.caltech.edu`].

- IRS: Infrared Spectrograph (Houck et al., 2004). Consists of four separate modules (Short- Low, Short-High, Long-Low, Long-High) which provided low (R $\sim$ 60 - 130) and moderate (R $\sim$ 600) resolution spectroscopic capabilities from 5.2 to 38 μm. Spectra could be obtained in either staring or mapping mode. In addition,

[1] [source `http://www.spitzer.caltech.edu`]

the IRS provided imaging in two filters (13-18 and 18-26 μm) and onboard software to autonomously identify point sources and accurately place them (by offsetting the telescope) in any of the IRS slits.

Table 4.1 summarizes the main characteristics of the scientific instruments discussed above.

λ [μm]	λ/Dλ	FoV	Pixel	Sensitivity [μJy]
IRAC: InfraRed Array Camera				
3.6	4.7	$5.21' \times 5.21'$	1.2	1.6 (3.4)
4.5	4.4	$5.18' \times 5.18'$	1.2	3.1 (4.3)
5.8	4.0	$5.21' \times 5.21'$	1.2	20.8 (21)
8.0	2.8	$5.21' \times 5.21'$	1.2	26.9 (27)
MIPS: Multiband Imaging Photometer for Spitzer				
24	5	$5.4' \times 5.4'$	2.55	110
70	4	$2.7' \times 1.4'$	5.20	14.4 mJy
55-95	15-25	$0.32' \times 3.8'$	10.1	57, 100, 307 mJy (60, 70, 90 μm)
160	5	$0.5' \times 5.33'$	16×18	29 (40) mJy
IRS: Infrared Spectrograph				
5.2-14.7	64-128	$3.7'' \times 57''$	1.8	250
13-18.5	$\sim$3	$54'' \times 80''$	1.8	116 (80)
9.9-19.5	$\sim$600	$4.7'' \times 11.3''$	2.3	$1.2 \times 10 - 18$ W/m^2
14.3-35.1	64-128	$10.6'' \times 168''$	5.1	1500
18.9-37.0	$\sim$600	$11.1'' \times 22.3''$	4.5	$2 \times 10 - 18$ W/m^2

Table 4.1 Spitzer science instrument main characteristics, from the Spitzer telescope handbook [2]. The sensitivities reported in the table are for point sources, and are only representative; IRAC sensitivity is given for intermediate background for both cases without (first number) and with confusion (number in parenthesis); IRS sensitivity is given for low background at high ecliptic latitude (note that for IRS, sensitivity is a strong function of wavelength); MIPS sensitivity is given for low background; 70 observations can be confusion limited; Because of a bad readout at one end of the slit, spectral coverage for 4 columns in MIPS SED is reduced to about 65-95 μm; 160 μm is often confusion limited, 29 mJy refers to no confusion and 40 mJy refers to the estimated confusion limit.

4.2.2 The Spitzer Legacy Science Program

The Spitzer MIPS 24μm band offers the possibility to explore the Universe well up to $z = 2.5$. Due to a better sensitivity and increased efficiency in large areal coverage, the 24μm observations with Spitzer significantly improved the quality and statistics of number counts in the mid-infrared (Marleau et al. 2004). As infrared member of NASA's family of Great Observatories, Spitzer has been widely and successfully used in multi-spectral studies in combination with its companion observatories, the Chandra X-Ray Observatory and the HST. Spitzer has also observed objects currently accessible only in the infrared, most notably detecting radiation from extrasolar planets for the first time (Werner et al. 2006). Most of the extragalactic works comes from Spitzer surveys of areas of the sky

ranging in extent from tens of square arcminutes to tens of square degrees. Most of these surveys cover areas which have been well investigated also by many other observatories, thus proving a unique multi-wavelength view of the universe. The most popular scientific projects comprised within the Spitzer Legacy Science Program are here below itemized:[3]

- SWIRE: The Spitzer Wide-Area Infrared Extragalactic Survey (Cycle 0 Legacy), observed ~ 50 deg^2 broken down into six separate regions with IRAC and MIPS.
- FLS: The First Look Survey (extragalactic component) (Cycle 0 DDT) observed 4 deg^2 with IRAC and MIPS.
- SDWFS: The Spitzer Deep Wide-Field Survey (Cycle 4) observed about 8.5 deg^2 in the NOAO Deep Wide-Field Survey Bootes area with IRAC, following major GTO programmes using IRAC and MIPS.
- S-COSMOS: The Spitzer Cosmic Evolution Survey (Cycle 2 & 3) observed the 2 deg^2 Cosmic Evolution Survey field with IRAC and MIPS.
- SPUDS: (Cycle 4), The Spitzer Ultra Deep Survey extended the 1 deg^2 field UKIDSS Ultra Deep Survey with an IRAC and MIPS deep imaging survey.
- SIMPLE: The Spitzer IRAC/MUSYC Public Legacy in E-CDFS (Cycle 2), images 0.25 deg^2 around the Chandra Deep Field South with IRAC.
- GOODS: The Great Observatories Origins Deep Survey (Cycle 0 Legacy) observed 320 $'^2$ centered on the Hubble Deep Field North and the Chandra Deep Field South fields with IRAC and MIPS (at 24 μm). Spitzer's deepest observations have been made over portions of the GOODS field. A number of GO programmes and The Far-Infrared Deep Extragalactic Legacy Survey (Cycle 3) in part extends this imaging to 70 μm.
- SINGS/LVLS: The Spitzer Infrared Nearby Galaxies Survey (Cycle 0 Legacy) carried out an imaging and spectroscopic study of 75 nearby galaxies with IRAC, MIPS and IRS. The Local Volume Legacy Survey (Cycle 4) extends IRAC and MIPS imaging to a volume complete sample of 258 galaxies within 11 Mpc.

The surveys (with the exception of SINGS/LVLS which targeted individual objects) are ordered according to the increasing depth of Spitzer observations.

Spitzer was originally built to last for a minimum of 2.5 years, but with the expectation to last for around 5.5 years before running out of coolant. This occurred on 15 May 2009.

[3] http://irsa.ipac.caltech.edu/data/SPITZER/docs/spitzermission/observingprograms/legacy/

With the progressive exhaustion of the onboard cryogen used to cool the telescope to the very cold temperatures needed to operate, most of the longer wavelength instruments are no longer usable. However, the two shortest wavelength modules of the IRAC camera, at 3.6 and 4.5 μm, are still operable with the same efficiency and sensitivity as before the cryogen was exhausted, and will continue to be used in the Spitzer Warm Mission. The Spitzer Warm mission has therefore focused on the so called Spitzer Exploration Science Programme, whose observations require more than 500 hours of Spitzer observing time, providing an opportunity for large-scale investigations not possible during the cryogenic mission.

The Spitzer Extended Deep Survey (SEDS) of a few very small fields observed by HST and The Spitzer Extragalactic Representative Volume Survey (SERVS) of about 1/3 of the SWIRE footprint are examples of Exploratory Science projects which have allowed to better sample the IRAC depth-area parameter space. [4]

The main focus of this ambitious extragalactic observing program includes understanding galaxy formation and evolution processes in passive and actively star forming galaxies as well as mapping AGN, starbursts, spirals and spheroids out to high redshifts. Moreover it also aimes at studying the influence of environment on all scales, the history of star formation, the assembly of stellar mass and the role of gravitational accretion processes in AGN. While ISO's sensitivity was such that very few sources were detected beyond $z \sim 1$, Spitzer is able to detect sources up to the highest redshifts thus allowing a more detailed investigation of the mechanisms regulating galaxy evolution.

Deep Spitzer observations, in fact, have allowed direct measurement of star formation activity in galaxies up to $z \sim 3$. The 24 μm luminosities of galaxies gauge their bolometric IR luminosities, and hence obscured star formation rate, which represents ∼75% of the total star formation in the Universe. The bolometric IR luminosity, can be linked in turn, to the recent SFR through the well known Kennicutt (1998) calibration (defined in the limit of complete dust obscuration and dust heating fully dominated by young stars + constant SFR over ~ 100 Myr; see Chapter 1). The latter shows a dependence of the star formation activity on redshift, with a peak around $z \sim 1$, an approximately constant rate to $z \sim 2.5$ and a possible decline in the SFR per unit volume at higher redshift. Luminous Infrared Galaxies (LIRGS: $10^{11} L_{\odot} < L_{\rm IR} < 10^{12} L_{\odot}$) typically dominate the comoving star-formation rate density at $z < 1.5$. The Ultra Luminous Infrared Galaxies (ULIRGs: $10^{12} L_{\odot} < L_{\rm IR} < 10^{13} L_{\odot}$) at $z \sim 2$ represent ∼40% of the massive ($> 10^{11} M_{\odot}$) galaxies at that epoch and are undergoing their final mass accretion. The specific star-formation rate of massive galaxies ($\dot{M}/M_{\star}$) is found to increase by more than an order of magnitude from

[4] http://irsa.ipac.caltech.edu/data/SPITZER/docs/spitzermission/observingprograms/es/

$z \sim 0.8$ to $z \sim 2$. Fig. (4.1) shows the evolution of the IR luminosity density (SFR) as a function of redshift.

With the advent of Herschel, sampling typical wavelengths well beyond 200 μm, it is possible to extend the capabilities of Spitzer enabling direct measurements of the bolometric luminosities of higher-redshift objects where Spitzers 24 μm observations sample rest-frame emission at $\lambda < 10 \mu m$. In addition, the long-wavelength spectroscopic capabilities of Herschel also provide new insights into the physical conditions in very dusty systems. All these aspects will be presented in detail in the next sections.

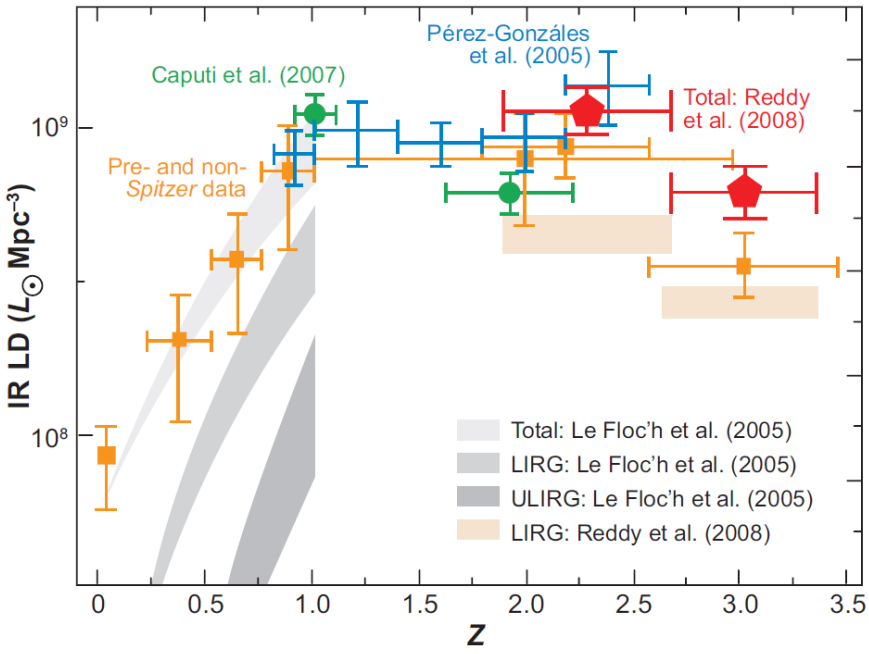

Figure 4.1 The infrared luminosity density (IR LD) as a function of redshift z up to $z = 3.5$. The orange points represent pre- and non-Spitzer data. The Spitzer-based data include results from Reddy & Steidel (2008), Caputi et al. (2007), Pérez-González et al. (2005), and Le Floc'h et al. (2005). The differently coloured strips indicate the total, LIRG, and ULIRG contribution to the total IR LD at $z < 1$, as determined by Le Floc'h et al. (2005) [image from Soifer et al. (2008)].

4.3 Herschel Space Observatory and Extragalactic Surveys

Herschel is the fourth 'cornerstone' mission in the ESA science programme [5]. With a 3.5 m Cassegrain telescope it is the largest space telescope ever launched. It performs photometry and spectroscopy in the 55-671 μm range, bridging the gap between earlier infrared space missions and ground-based facilities.

[5] http://herschel.esac.esa.int/,http://herschel.cf.ac.uk/

Figure 4.2 highlights the contribution to the extragalactic background measurements from different observations and its interpretation in terms of resolved sources. As we have seen above, cosmological background radiations are a fundamental channel of information about cosmic high redshift sources. As evident from the figure, the Extragalactic Background radiation in the range 0.1-1000 μm presents two maxima: one in the optical and one in the FIR, with roughly equal brightness and with a minimum around 5 μm due to the presence of dust and AGN non thermal emission in the thermal IR which contributes to decrease the brightness of stars. The CIRB is usually defined as the cosmic background at wavelengths longward of this minimum. This figure also shows that the optical and infrared cosmic backgrounds are well separated. The first surprising result is that the power in the infrared is comparable to the power in the optical, even if, locally, the infrared output of galaxies is only one third of the optical output. This implies that infrared galaxies grow more luminous with increasing z faster than do optical galaxies.

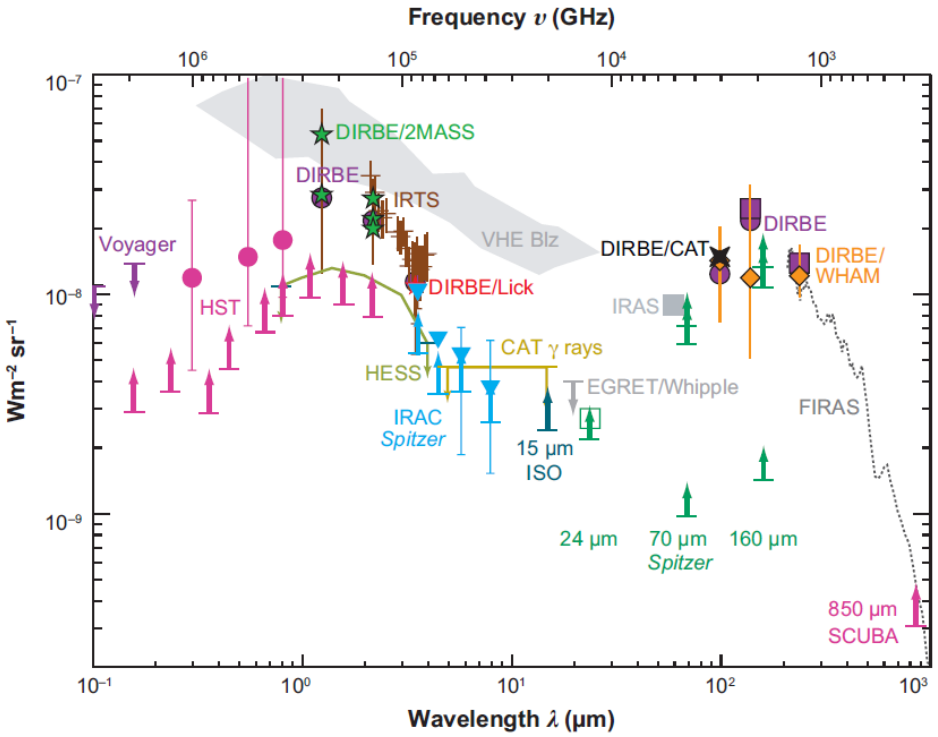

Figure 4.2 The extragalactic background light spectral energy distribution from 0.1 to 1000 μm, adapted from Dole et al. (2006). At Spitzer wavelengths from $24 - 160\,\mu$m, the green arrows are lower limits based on directly observed sources. The higher green arrows at 70 and 160 μm are based on stacking numerous 24 μm detections, as discussed in Dole et al. (2006) whereas the highest green arrows at these wavelengths reflect the estimated contribution of all 24 μm sources, including those beyond the sensitivity limit of the stacking analysis. The green open square is the estimated 24 μm background when these faint sources are included. Note that the corrected 70 and 160 μm background estimates from the MIPS data are essentially equal to the backgrounds estimated at these wavelengths by other techniques. See Dole et al. (2006) for identification of the other datasets and background estimates included in this figure. Image from Soifer et al. (2008).

The important role played by Herschel is emphasized in Fig. 4.2: covering with its instruments the wavelength range between 55-671 μm, it well samples the CIRB peak, therefore it is crucial to resolve it in galaxies.

Herschel has been specifically designed to observe the 'cool universe'; the main project goals include investigating the structure formation in the early universe, resolving the far infrared cosmic background, and revealing cosmologically evolving AGN/starburst symbiosis and galaxy evolution at the epochs when most stars in the universe were formed, unveiling the physics and chemistry of the interstellar medium and its molecular clouds, the wombs of the stars, and unravelling the mechanisms governing the formation of and evolution of stars and their planetary systems, including our own solar system, putting it into context. In other words, Herschel has opened a new window to study how the universe has evolved to become the universe we see today, and how our star the Sun, our planet the Earth, and we ourselves fit in.

Herschel is an ESA facility available for the worldwide astronomical community. Herschel has been designed to provide 3 years of routine science operations. The observing time consists of Guaranteed Time (GT) and Open Time (OT), the fraction GT is 32%, the remainder is OT. The GT is owned by contributors to the Herschel mission, mainly the science payload consortia. The OT is, instead, awarded in a standard competitive proposal procedure in response to Announcements of Opportunity (AO) issued by the Herschel Science Centre (HSC) managed by the Herschel Project Scientist on behalf of the Director of Science and Robotic Exploration [source: http://herschel.esac.esa.int/]. Herschel was successfully launched on 14 May 2009. However, it was conceived almost 30 years earlier as the Far InfraRed and Submillimetre Space Telescope (FIRST), which was formally proposed to ESA in November 1982. It was incorporated in the ESA 'Horizon 2000' long-term plan for implementation and in November 1993 ESA decided that FIRST would be implemented as the fourth 'cornerstone' mission.

4.3.1 The Herschel Telescope & Focal-Plane Instruments

The optical design of the Herschel Space Observatory is that of a classical Cassegrain telescope with a 3.5 m physical diameter primary and an 'undersized' secondary, yielding an effective primary diameter of 3.28 m. The telescope is the largest of its kind and utilises a novel silicon carbide technology. The primary mirror has been made out of 12 segments while the secondary mirror is a single piece. As for ISO, a fully passive design has been adopted.

Tab. 4.2 summarizes the main features of the telescope.

Telescope	
Primary physical/effective diameter	3.5 / 3.28 m
Secondary diameter	30.8 cm
System/primary f-number	8.70 / 0.5
Wave front error best-focus (centre/edge)	4.8 / 5.5 μm
Angular resolution	$\sim 7" \times (\lambda_{\rm obs}/100\ \mu{\rm m})$
Operational temperature	~85 K

Table 4.2 Herschel telescope main characteristics.

The Herschel science payload comprises three instruments which have been conceived and optimised with the prime science goals in mind. The instruments offer a wide range of capabilities for different observing programs and are led by different PIs. Here below a brief summary of their main features:

- PACS: The Photodetector Array Camera and Spectrometer, Poglitsch et al. (2010), PI: A. Poglitsch, Max-Planck-Institut für extraterrestrische Physik (MPE), Garching. PACS is a camera and low to medium resolution spectrometer for wavelengths in the range 55-210 μm. It employs four detector arrays, two bolometer arrays and two Ge:Ga photoconductor arrays. The bolometer arrays are dedicated for wideband photometry, while the photoconductor arrays are to be employed exclusively for spectroscopy with a resolution of a few thousand. PACS can be operated either as an imaging photometer, or as an integral field line spectrometer.

- SPIRE: The Spectral and Photometric Imaging REceiver, Griffin et al. (2010), PI: M. J. Griffin, Cardiff University. SPIRE is a camera and low to medium resolution spectrometer complementing PACS for wavelengths in the range 194-672 μm. It comprises an imaging photometer and a Fourier Transform Spectrometer (FTS), both of which use bolometer detector arrays. There are a total of five arrays, three dedicated for photometry and two for spectroscopy.

- HIFI: The Heterodyne Instrument for the Far Infrared, de Graauw et al. (2010), PI: T. de Graauw, in late 2008 succeeded by F. Helmich, SRON Netherlands Institute for Space Research, Groningen. HIFI is a very high resolution heterodyne spectrometer covering the 490-1250 GHz and 1410-1910 GHz bands. It utilises low noise detection using superconductor-insulator-superconductor (SIS) and hot electron bolometer (HEB) mixers, together with acousto-optical and autocorrelation spectrometers. HIFI is not an imaging instrument, it observes a single pixel on the sky at a time.

The three instruments allow for broad band photometric imaging capability in six bands with centre wavelengths of 70, 100, 160, 250, 350, and 500 μm, imaging spectroscopy over

HIFI	**Heterodyne spectrometer**
Wavelength coverage	157−212 & 240−625 μm
Field-of-view (FOV)	single pixel on sky
Detectors	5×2 SIS & 2×2 HEB mixers
Spectrometers	auto-correlator & acousto-optical
Spectral resolving power	typically 10^6
PACS	**2-band imaging photometer**
Wavelength coverage	60−85 or 85−130, 130−210 μm
Field-of-view (FOV)	$0.5F\lambda$ sampled $1.75' \times 3.5'$
Detectors	64×32 & 32×16 pixel bol. arrays
Diffraction limited beams	5.5", 7.7", 12" respectively
PACS	**integral field spectrometer**
Wavelength coverage	55–210 μm
Field-of-view (FOV)	(5×5 pixel) 47" $\times$ 47"
Detectors	two 25×16 pixel Ge:Ga arrays
Spectral resolving power	1000−4000
SPIRE	**3-band imaging photometer**
Wavelength bands ($\lambda/\Delta\lambda \sim 3$)	250, 350, 500 μm
Field-of-view (FOV)	$2F\lambda$ sampled 4' x8'
Detectors	139, 88 & 43 pixel NTD bol. arrays
Diffraction limited beams	18", 25", 36" respectively
SPIRE	**imaging fourier transf. spectrometer**
Wavelength coverage	194−324 & 316−671 μm
Field-of-view (FOV)	$2F\lambda$ sampled circular 2.6'
Detectors	37 & 19 pixel NTD bol. arrays
Spectral resolving power	370−1300 (high) / 20−60 (low)

Table 4.3 Herschel science instrument main characteristics. Acronyms relating to the detectors: superconductor-insulator-superconductor (SIS), hot electron bolometer (HEB), gallium-doped germanium (Ge:Ga), and neutron transmutation doped (NTD).

the entire Herschel wavelength coverage, and very high resolution spectroscopy over much of this range.

A number of observing modes are provided, including point source photometry, small, and large area photometric imaging, and the observation of a single spectral line, or one or more spectral ranges, in either a single position or in various mapping modes.

Table 4.3 summarizes the most important features of each Herschel science instrument (Pilbratt et al., 2010).

4.3.2 The Herschel Multi-tiered Extragalactic Survey (HerMES) Project

Herschel is carrying out surveys of unprecedented size and depth, vastly improving the state of observations in the under-explored FIR and Sub-mm wavebands. The objects under investigation range from comets in the Solar System to galaxies in the distant reaches of

the Universe. The science areas are subdivided into six broad categories: *Solar System*, *Planet Formation and Planetary system*, *Star and their environments*, *Interstellar Medium and Star Formation*, *Galaxies*, *Cosmology*.

As in this work we are mainly interested on extragalactic and cosmological observations, we will report here only the key programme extragalactic surveys within Herschel Guaranteed Time (GT) and Open time (OT). A more detailed description of the whole Herschel observing programme can be found at http://herschel.cf.ac.uk/mission/key-programmes/.

- HerMES: the Herschel Multi-tiered Extragalactic Survey (GT KP, Oliver et al. (2012),[6]). HerMES is an astronomical project aimed to study the evolution of galaxies in the distant Universe (up to 3-4 billion years after the big bang), now accessible thanks to the sub-mm coverage provided by Herschel. It is the biggest project on Herschel, the observations are done with both SPIRE and PACS instruments, surveying $\sim 70\mathrm{deg}^2$ from $20' \times 20'$ to $3.6^\circ \times 3.6^\circ$ (for a total of 900 hours observing time) and 12 clusters.

- The Dusty Young Universe (GT KP, [7]). Observations of some of the most distant quasars in the far-infrared shows that a substantial amount of dust was created in the first billion years after the Big Bang. However, the wavelengths observed to date haven't been able see the bulk of the emission, which is now possible using SPIRE and PACS. By observing over 100 of the most distant quasars it is possible to analyse their properties. In addition, PACS spectroscopy of four of the brightest quasars will allow the different origins of the far-infrared emission to be disentangled.

- PEP: PACS Evolutionary Probe (GT KP, Lutz et al. (2011) [8]. It is aimed to study the restframe far-infrared emission of galaxies in the past 11 billion years (up to redshifts of about 3) as a function of environment. The survey will shed new light on the constituents of the cosmic IR background and their nature, as well as on the co-evolution of AGN and starbursts. The observation are PACS only but PEP is coordinated with SPIRE observations of the same fields in the HerMES programme. It surveys 2.7 deg^2 from $10' \times 10'$ to $85' \times 85'$ (550 hours of observing time) and 10 clusters.

- Herschel-ATLAS (OT KP, Eales et al. (2010) [9]. The Herschel ATLAS is the Herschel survey covering the largest total area, it surveys 550 deg^2 of sky in five far-infrared and sub-mm bands, i.e. one eightieth of the sky.

  There are five main science programmes. The principal one is a survey of dust emission in 50,000 nearby galaxies. This wants to be a follow up of the highly successful Sloan

[6] http://hermes.sussex.ac.uk/
[7] http://www.mpia.de/Public/Forschung/Instrumentation/DustyYoungUniverse/index.html
[8] http://www.mpe.mpg.de/ir/Research/PEP/index.php
[9] http://www.h-atlas.org/

Digital Sky Survey, an optical survey that surveyed hundreds of thousands of galaxies in the nearby universe. However, Sloan missed the objects that were hidden by dust and did not provide any information about the gas in the galaxies out of which the stars form. H-ATLAS will do both. The observations are done using both SPIRE and PACS instruments.

- GOODS: Great Observatories Origins Deep Survey (OT KP, Elbaz et al. (2011)). The GOODS fields are small regions of the sky which have been observed very deeply in all available wavebands from X-ray to radio by many of the greatest space observatories, including Hubble, Chandra and Spitzer. By observing a sky area of about 300 square arcminutes with PACS, the project aims at detecting some of the faintest objects, and galaxies in the earliest stages of the Universe. The observations are done with both SPIRE and PACS instruments: PACS very deep imaging of the GOODS fields (330 hours); SPIRE deep imaging of the GOODS-N Field (30 hours).

Most of the results presented in this work were taken within the HerMES collaboration of which I am an official member. So below I give some more details about this survey.

The Herschel Multi-tiered Extragalactic Survey (HerMES:Oliver et al. (2012)), is a legacy program designed to map a set of nested fields totalling ~ 380 deg^2. Fields range in size from 0.01 to ~ 20 deg^2, using Herschel-SPIRE (at 250, 350 and 500 μm), and Herschel-PACS (at 100 and 160 μm), with an additional wider component of 270 deg^2 with SPIRE alone. These bands extensively probe the peak of the redshifted thermal spectral energy distribution from interstellar dust and thus well sample the dust re-processed optical and ultra-violet radiation arising from star formation providing accurate estimates of the infrared luminosity, $L_{\rm IR}$. In combination to complementary far-UV to MIR photometry these bands are therefore crucial for a complete multi-wavelength understanding of galaxy formation and evolution. The survey has been devoted to detect of order 100,000 galaxies at 5σ in some of the best studied fields in the sky. In order to optimize the wavelength coverage, HerMES is often combined with the PACS Evolutionary Probe survey.

HerMES samples both the higher luminosity objects, which are bright but rare, in the wide shallow fields, and the lower luminosity galaxies, which are faint but very numerous and marginally confused, in the deep narrow-fields. The total time allocated for HerMES is 909.3 hours. This comes from the Guaranteed Time awarded to the SPIRE instrument team (850 hr), from one of the Herschel Mission Scientists (M. Harwit, 10 hr) and from members of the Herschel Science Centre (B. Altieri, L. Conversi, M. Sanchez Portal and I. Valtchanov, 40hr). ESA also effectively contributed 9.3 hours as we agreed for our Abell 2218 observations in the Science Demonstration Phase to be made public immediately and so were not charged for these observations.

Confusion is a serious issue in particular for the Herschel-SPIRE instrument and strongly affects the survey depth. To estimate the confusion level several galaxy models (e.g. Lagache et al. 2003) are usually assembled and compared to existing survey data. Then the confusion limit is calculated using the criteria for source density of 30 beams per source and width of the sky intensity distribution. A number of techniques are employed to overcome the problem of confusion. With the availability of a full multiwavelength coverage (including ancillary data), it is possible to limit the confusion problem at the moment of source identification.

In order to pursue multi-wavelength analysis, the HerMES survey collects all the fields which are the most intensively observed at all wavelengths (see Fig. 4.3). These include: radio (VLA, WRST, GMRT, ATCA); sub-mm (SCUBA, Bolocam, AzTEC, MAMBO); mid and far infrared (Spitzer, ISO, AKARI); near-infrared (UKIRT, VISTA); optical (HST, Subaru SuprimeCAM, CFHT MegaCAM, KPNO Mosaic1, CTIO MOSAIC2, INT WFC); UV (GALEX) and X-ray (XMM-Newton,Chandra).

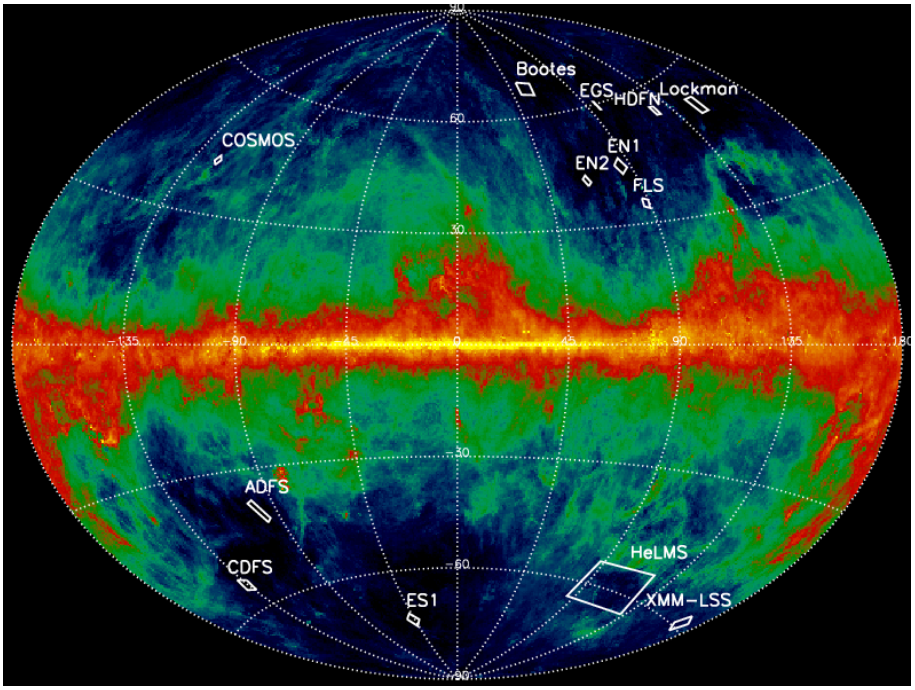

Figure 4.3 Dust emission map from the Galaxy, with HerMES fields over-plotted. The image is the 100 μm *COBE*-normalized, *IRAS* map of extended emission by (Schlegel et al., 1998). The Sky brightness is plotted on a false-colour logarithmic scale, with regions of very low Galactic emission highlighted in black and the Galactic plane highlighted in yellow. In addiction to the marked blank fields, HerMES has also observed 12 known clusters [image from Oliver et al. (2012)].

Extensive redshift and/or photometric redshift surveys are either available or underway for most of these fields. Another important requirement is that the contamination from Galactic emission (or cirrus) should be minimal. The use of a larger mirror makes the

cirrus less problematic for extra-galactic surveys with Herschel than it was for Spitzer, as discussed in Oliver et al. (2012). This means that the requirement for low-levels of cirrus are automatically satisfied by the criteria of good ancillary data, as illustrated in Fig. 4.3. The defining criterion was coverage at mid/far infrared wavelengths not accessible to Herschel, or where Herschel is relatively inefficient due to its warm mirror. Specifically it was required a Spitzer MIPS coverage at 24 and 70 μm. The only exception was the AKARI Deep Field South, which did not have Spitzer coverage but did have coverage at 65, 90, 140, and 160 μm from AKARI (Matsuura et al., 2011). The HeLMS field, added later in 2011 for studying large-scale structure and the bright end of the number counts, does not have ancillary data from Spitzer. However, being located on the SDSS Stripe 82 region, HeLMS does have ancillary coverage from many other facilities. The cumulative area of all major Herschel-SPIRE extra-galactic Key Program surveys as a function of instrumental noise and for the HerMES fields is shown in Fig. 4.4.

All these data, belonging to different databases, have been then collected together in a unique and homogeneous dataset well described in Chapter 4 of L. Marchetti PHD thesis.

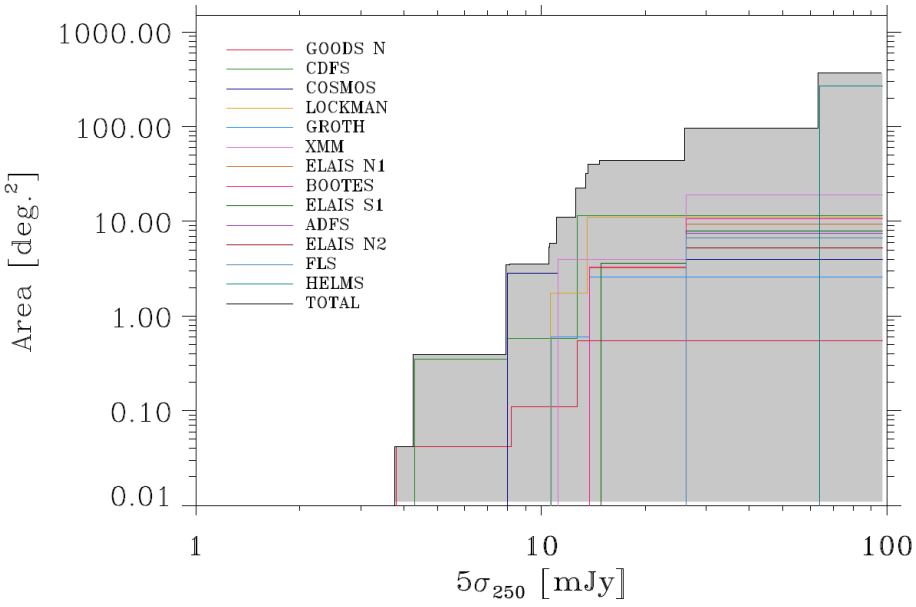

Figure 4.4 Cumulative area against 5-σ instrumental noise level at 250μm for the HerMES blank-field surveys with SPIRE (Oliver et al., 2012). The colour-coding breaks this down into individual survey fields.

4.3.3 Catalogue construction details: HerMES XID Method

Getting accurate estimates of flux densities for sources in astronomical images dominated by confusion noise can be really challenging when dealing with data coming from next generation telescopes at far-IR to radio wavelengths. The large improvements achieved in

the sensitivity of instruments at these long wavelengths (FIR/SUBMM/Radio) has meant that the blended signal from numerous, unresolved, faint sources now form a non-negligible fraction of the observed telescope background. Hence confusion noise, i.e. fluctuations in this background, is now the dominant source of noise in deep imaging. The first effect of confusion is that of increasing the positional uncertainty of sources dramatically (e.g. Hogg 2001), making cross-identifications with other wavelengths problematic. Secondly, correlations between the confusing background and sources above the confusion limit result in, at best, flux boosting of detected sources above the confusion limit and, at worst, complex blends of correlated confusion noise, resulting in spurious sources (Scheuer 1957, Condon 1974).

Up to now there have been two different approaches to dealing with these issues. More traditional source detection methods, combined with probabilistic approaches for flux boosting and source identification have been used to good effect on sub-mm surveys performed with SCUBA (e.g. Ivison et al. (2007)); and more statistical approaches ignoring individual sources and looking at the aggregate properties of sources via either stacking (e.g. Dole et al. (2006)), or the map statistics themselves via the pixel intensity distribution, the so-called $P(D)$ (e.g. Patanchon et al. (2009)).

Both approaches have advantages and disadvantages. Working with individual sources allows a proper investigation of the true variation of sub-mm galaxy properties and their correlations with other observables. However, finding multi-wavelength identifications for individual sub-mm sources is usually difficult, and generally reliable identifications can be found for only a fraction of sources (Ivison et al., 2007, Roseboom et al., 2009). Statistical approaches, on the other side, have the advantage of using all the available data, and hence provide greater precision in the parameters of interest. However, interpretation of these statistically-derived quantities is sometimes complicated, and highly dependent on the choice of parametrisation (Roseboom et al., 2010).

The cross-identification (XID) and source photometry techniques used to process Herschel SPIRE imaging data within HerMES have been discussed in detail in the paper by Roseboom et al. (2010). Here below we give only a brief overview of the XID method, which is based on a combination of the methods described above.

The method performs cross-identification and source photometry in map-space so as to minimize source-blending effects. It makes use of a combination of linear inversion and model selection techniques to produce reliable cross-identification catalogues based on Spitzer MIPS 24 μm source positions. Testing conducted on both simulations and real Herschel observations show that this approach gives robust results for even the faintest sources ($S_{250} \sim$ 10 mJy). This technique has been applied to HERMES SPIRE observations taken as part of the science demonstration phase of Herschel. Compared to more traditional approaches

of source detection and catalogue based cross identification, the map-based approach of Roseboom et al. (2010) is found to give significantly greater accuracy in the flux density and recovers a much larger fraction of faint SPIRE sources. Moreover for real SPIRE observations of bright unconfused sources Roseboom et al. (2010) find good agreement between their flux density estimates and those of SussExtractor (Savage & Oliver 2007) derived source catalogues by Smith & Spire Sag2 Consortium (2011). However the use of a 24 μm prior input list can introduce an additional incompleteness which is strongly dependant on the relative depth of the existing 24 μm catalogues and SPIRE imaging SPIRE data. By combining the deep SPIRE and Spitzer 24 μm observations in GOODS-N the incompleteness due to the shallow 24 μm limit in the other SDP fields is estimated to be $\sim$20 per cent at 250 μm, increasing to $\sim$ 40 per cent at 500 μm. However this incompleteness is dominated by the faintest SPIRE sources (i.e. less than 30-40 mJy), so that these catalogues can be considered complete at bright fluxes.

The strong point of this approach is its simplicity; the only assumptions are that all sources are unresolved by the telescope, and that the positions of all sources are known. If these assumptions hold, then in the limit of infinite signal-to-noise ratio in the image the resulting flux density measurements would be perfect, irrespective of source density.

4.4 Dusty star forming galaxies at high redshift: Observational properties and sample definition

In the next sections we will review the main observational properties of a sample of high-z dusty star forming (U)LIRGs whose ultra-deep MIR IRS spectra have been deeply investigated by Fadda et al. (2010, F10 hereafter) and whose physical properties have been accurately modeled with our self-consistent spectro-photometric code (see Chapter 6).

4.4.1 The (U)LIRG data sample

With total infrared luminosities between $10^{11} - 10^{12}$ $L_{\odot}$ and $\geq$ 10^{12} $L_{\odot}$, respectively, Luminous and Ultraluminous Infrared Galaxies [(U)LIRGs hereafter] are among the most luminous and complex extragalactic objects we can conceive, including all varieties of young and old stellar populations, dust absorption, scattering, grain thermal re-radiation, and AGN emission (Lonsdale et al., 2006). Although they are quite rare in the local universe, they dominate the cosmic star formation rate and the FIR background at z $\gtrsim$ 1. Therefore they are suitable laboratories to study the main physical processes which drive galaxy formation and evolution.

Observations of local ULIRGs have shown that they are dominated by strong interactions and mergers and the fraction of mergers/interactions among them has been found to be strongly correlated with their IR luminosity, such that lower luminosity LIRGs ($L_{IR} \lesssim 10^{11.5}$ $L_{\odot}$) are ordinary disks while the highest luminosity ULIRGs are advanced stage mergers.

High-z LIRGs and ULIRGs seem to be, instead, not equivalents of ULIRGs in the nearby universe, but rather upscaled versions of normal galaxies (Elbaz et al. 2011; Nordon et al. 2012; Symeonidis et al. 2009; Rujopakarn et al. 2011). An implication is that high-z ULIRGs could well have gradually evolving SFHs, and be not necessarily associated with merger events as they are at z∼0.

A still open question about luminous and ultraluminous IR galaxies is the quantification of the contamination by AGN emission to their bolometric luminosity. Standard multi-wavelength criteria can be used (involving X-ray emission, optical spectroscopy, IRAC photometry) but none of them is able to determine the relative AGN and starburst contributions to the bolometric luminosity of IR-luminous galaxies (Fadda et al., 2010). A very efficient way to probe dust obscured AGN emission, is through deep mid-IR spectroscopy. The difference between the mid-IR spectra of a starburst and an AGN is striking. Starbursts are often characterized by strong, low-excitation, fine-structure lines, prominent PAH features and a weak 10 μm continuum whereas AGN display weak or no PAH features, plus a strong mid-infrared continuum (see, e.g., Voit (1992)). To directly determine the AGN fraction at the lowest IR luminosity possible, F10 carried out an observational program to obtain low resolution, mid-IR spectra of 48 galaxies, (24 at $z \sim 1$ and 24 at $z \sim 2$), with 24 μm flux densities between 0.1-0.5 mJy. The main goal of F10 analysis was to provide the first observational data to characterize the spectral properties of LIRGs and ULIRGs that are responsible for the bulk on the CIRB and output energy at high redshifts ($z \sim 0.7$ - 2.5). Combining their deep mid-IR spectra with the available optical and near-IR data in CDFS, F10 compared global properties such as colors, morphologies, and stellar masses of these high-z (U)LIRGs with those of optically selected galaxies to provide observational constraints on the mid-IR properties of optically selected IR faint galaxies at $z \sim 1$ - 2.

In their analysis F10 adopted $\Omega_M = 0.27$, $\Omega_\Lambda = 0.73$ and $H_0 = 71$ km s^{-1} Mpc^{-1} cosmology.

4.4.2 Sample Selection

The sample of high-z (U)LIRGs presented here is a sample of 48 IR-luminous galaxies selected in GOODS-S by Fadda et al. (2010, F10 hereafter). It includes the faintest 24 μm sources observed with the Spitzer Infrared Spectrograph (IRS) ($S_{24} \sim 0.15 - 0.45$ mJy) in the two redshift bins ($0.76 - 1.05$ and $1.75 - 2.4$) to sample the major contributors to

the cosmic infrared background at the most active epochs. At these redshifts, the 24 μm fluxes translate to infrared luminosities roughly in the ranges for LIRGs at $z \sim 1$ and ULIRGs at $z \sim 2$. This sample is therefore crudely luminosity selected (with the S_{24} limits corresponding to different luminosity ranges for the z$\sim$ 1 LIRGs and z$\sim$ 2 ULIRGs) and F10 did not apply any other selections. Figure 4.5 shows the 24 μm fluxes of these IRS targets compared to the flux distribution of all the 24 μm sources in the GOODS-S field.

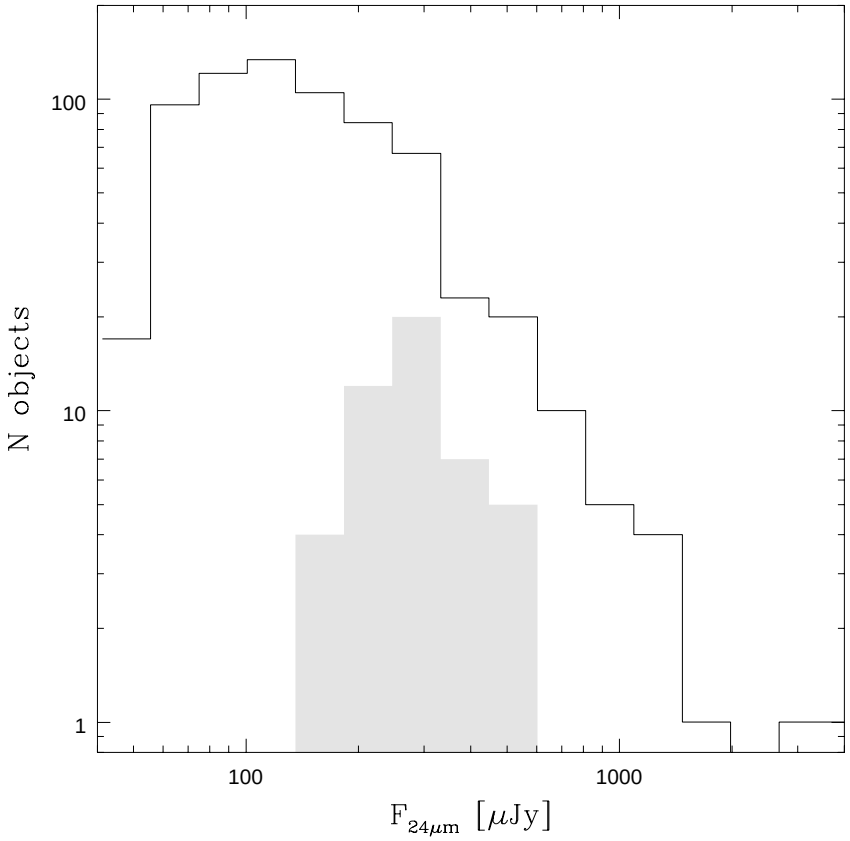

Figure 4.5 24 μm fluxes of IRS targeted (U)LIRGs (shaded histogram) compared to the flux distribution of all the 24 μm sources in the GOODS-CDFS field [image from Fadda et al. (2010)].

These objects have been selected by F10 mostly using the photometric redshifts computed by Caputi et al. (2006) since only 50% and 10% of them had spectroscopic-z in the z $\sim$ 1 and 2 bins, respectively. The selected ULIRGs represent *all* the 24 μm sources in the Chandra Deep Field-South (CDFS) area with S(24μm) $\sim$ 0.14-0.55 mJy at z = 1.75-2.4, excluding three sources too close to a neighbour source to obtain unblended spectra. The LIRGs have been selected among 24 μm sources with S(24μm) $\sim$ 0.2-0.5 mJy at z = 0.76-1.05 in order to avoid a large-scale structure localized at z = 0.734 (Szokoly et al., 2004). To make this sample more representative of LIRGs, spanning different luminosities within the LIRG range, F10 included in the selection also sources from the "extended CDFS" area. Figure

4.6 shows the spatial distribution of the targets relative to the available Advanced Camera for Surveys (ACS) images. Figure 4.7 quantitatively shows that the targeted (U)LIRGs

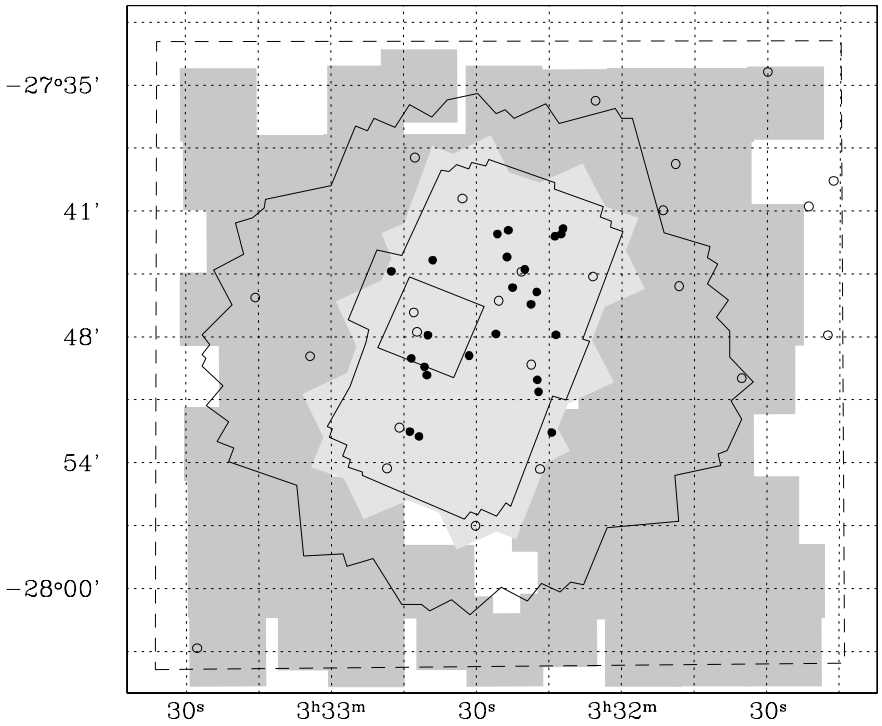

Figure 4.6 IRS targeted (U)LIRGs overlapped on ACS images from GOODS (light gray shaded) and GEMS (gray shaded). Open and filled circles represent the z $\sim$ 1 and 2 samples, respectively. The two internal contours mark the border of the 16 μm imaging (deep and ultra-deep observations). The external solid contour highlights the coverage of deep Chandra imaging (Luo et al., 2008), while the external dashed contour marks the field covered by COMBO17 (Wolf et al., 2004b) [image from Fadda et al. (2010)].

are energetically well representative of the population of IR luminous galaxies at those redshifts, dominating the energy productions at these cosmic epochs.

As emphasized by F10, except for having higher dust obscuration, these galaxies do not have extremely deviant properties in the rest-frame UV/optical compared to galaxies selected at observed optical/near-IR band (see e.g Fig. 4.8). Their observed optical/near-IR colors are very similar to those of extremely red galaxy (ERG) populations selected by large area K-band surveys.

Figure 4.8 shows the most recently published stellar mass functions at redshift 1-2 by Ilbert et al. (2010) with superimposed, as dashed vertical lines, the stellar masses derived by F10 for the galaxies in the sample. These stellar masses have been estimated following the method described in Wuyts et al. (2009a). It assumes a Kroupa's initial mass function (Kroupa, 2001), stellar population synthesis models by BC03 and the reddening law of Calzetti et al. (2000) and uses the Hyperz code (Bolzonella et al., 2000) for SED-fitting.

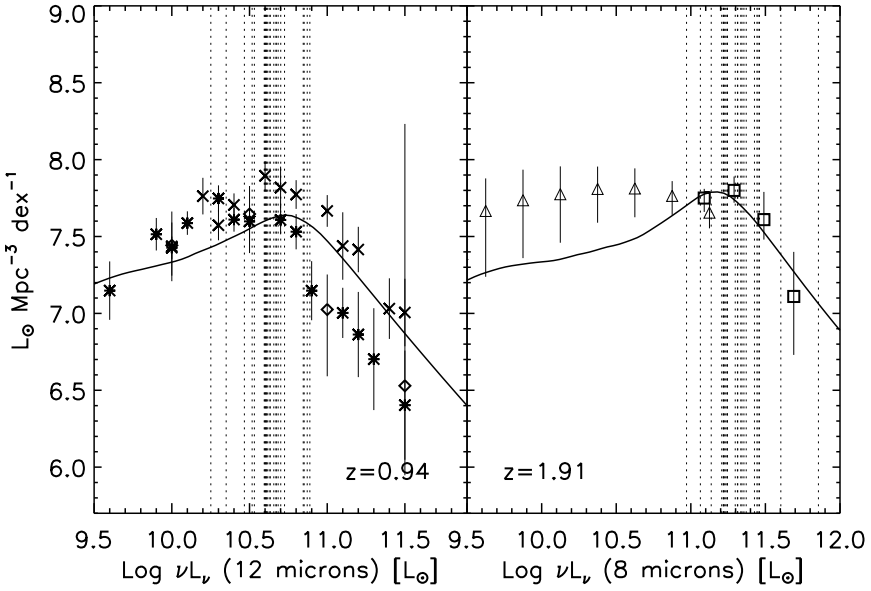

Figure 4.7 Co-moving 12 and 8 μm energy output per dex of 12 and 8μm luminosity (L dN/dLogL) at $z = 0.94$ and $z = 1.91$, corresponding to the mean redshifts of the two (U)LIRG bins. Continuous lines are from the model of Lagache et al. (2004). Diamonds, squares, and triangles are from Caputi et al. (2007), Le Floc'h et al. (2005), Reddy & Steidel (2008), respectively. At $z \sim 1$, stars and crosses are derived using the $0.7 < z < 1$ and $1 < z < 1.3$ 15 μm luminosity functions from Magnelli et al. (2009). Dotted lines represent the rest-frame 12 and 8 μm luminosities of our 48 targets computed from their 24 μm fluxes. No color correction has been applied. This Figure clearly shows that these galaxies dominate the energy output at the most active epochs [image from Fadda et al. (2010)].

The same set of assumptions are also used by Ilbert et al. (2010). This figure shows that the $z \sim 1$ LIRGs mostly have stellar masses near or a bit lower than $M_\star$, the turn-over of the mass function, thus probing the most representative and important mass scales at this redshift. The $z \sim 2$ ULIRGs reach much lower masses, $\lesssim 10^{11} M_\odot$, than those published by Ilbert et al. (2010) using COSMOS data. This is due to the fact that the catalogue used by Ilbert et al. (2010) to build these mass functions has a cut at $i_{AB} \lesssim 25.5$. This therefore suggests that many of the $z \sim 2$ ULIRGs have fainter optical magnitudes ($i_{AB} > 25.5$).

4.4.3 IRS spectra and Ancillary Data

The IRS spectra collected for these objects by F10, sample important PAH features at 6.2 and 7.7 μm, with the observed coverage of 7-21 μm and 14-35 μm for the z $\sim$ 1 and 2 sample, respectively. As we have already seen in section 1.11, the CDFS field allows for a large set of ancillary data publicly available. This includes the Chandra X-ray data, deep HST images at optical/UV, ground-based NIR data, and the Spitzer images taken

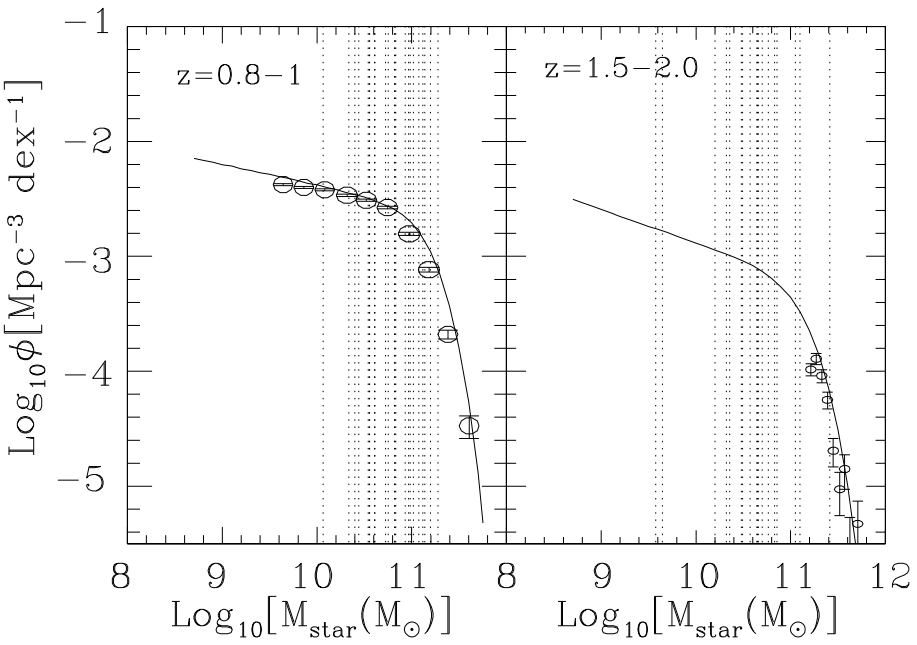

Figure 4.8 Stellar mass functions at $z \sim 1$ - 2 published by Ilbert et al. (2010) using the COSMOS data. The dashed lines mark the stellar masses of our sources estimated as in Wuyts et al. (2009b).[image from Fadda et al. (2010)].

with MIPS (24 μm and 70 μm), IRS (16 μm) and IRAC (8 μm). F10 and collaborators reduced the Spitzer data by themselves and directly took the reduced HST images from the GOODS (Giavalisco et al., 2004) and GEMS (Rix et al., 2004) surveys, as well as the recent FIREWORKS (Wuyts et al., 2008) and MUSYC multiwavelength photometric catalogues (Gawiser et al., 2006). F10 made also use of the X-ray catalogue from Luo et al. (2008) for their analysis.

F10 found published optical spectra for 17/24 ULIRGs and 9/24 LIRGs, 8 of which are included in the CDFS 'not extended' field analysed in our work. All the spectra with good redshift estimates (according to the published references), based on spectral features as [OIII],Ca, G-band, are shown in Fig. 4.9. Most of the available optical spectra are compatible with those of normal star forming galaxies at high redshifts.

Here we intend to give only a brief description of the main observational properties computed by F10 for these high-z (U)LIRGs without going in detail on the MID-IR data reduction performed by the authors. We defer the reader interested in the details of the data reduction to the original work by Fadda et al. (2010) (see §3).

4.4.4 Observed properties of MIR selected high-z (U)LIRGs

Following the procedure described in Section 3 of Fadda et al. (2010), F10 computed the observed MIR spectra for the 24 LIRGs at $z \sim 1$ and 24 ULIRGs at $z \sim 2$. These are shown

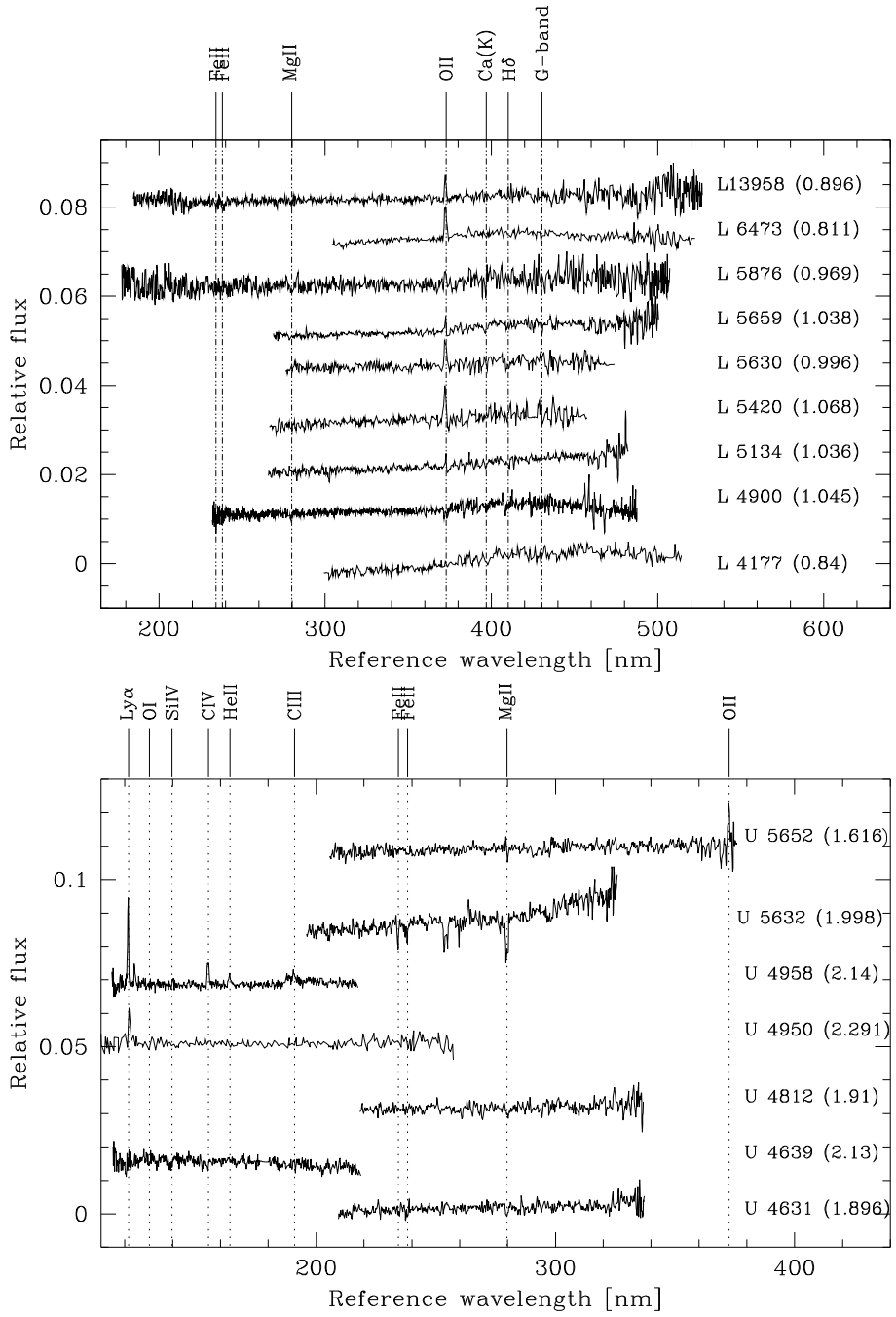

Figure 4.9 Optical spectra with good redshift estimates available for the z∼1 LIRGs (top) and z∼2 ULIRGs (bottom). The main absorption and emission features are highlighted. Estimated optical redshifts are reported between brackets. [image from Fadda et al. (2010)].

in Figure 4.10 and 4.11, respectively. The smoothed spectrum in the rest-frame wavelength is shown, in each panel of Fig. 4.10 and 4.11, as a red solid line, a local spectral template as dashed line and the unsmoothed spectrum with errorbars as an orange histograms. In each panel the broad band fluxes at 8, 16 and 24 μm, the object name and the redshift based on the MIR spectrum (or optical redshift when the MIR spectrum does not give a redshift, which is only the case for 3 LIRGs) are shown. Downward arrows mark the 5σ

upper limits. The spectral template shown as dashed line in the panels is either the average starburst spectrum obtained by Brandl et al. (2006) based on the Spitzer spectra of 22 local starburst galaxies, or the AGN template by Spoon et al. (2007) if the observed spectrum has no obvious PAH emission feature. Redshifts are estimated from the MIR spectra by cross-correlating these two templates to the data.

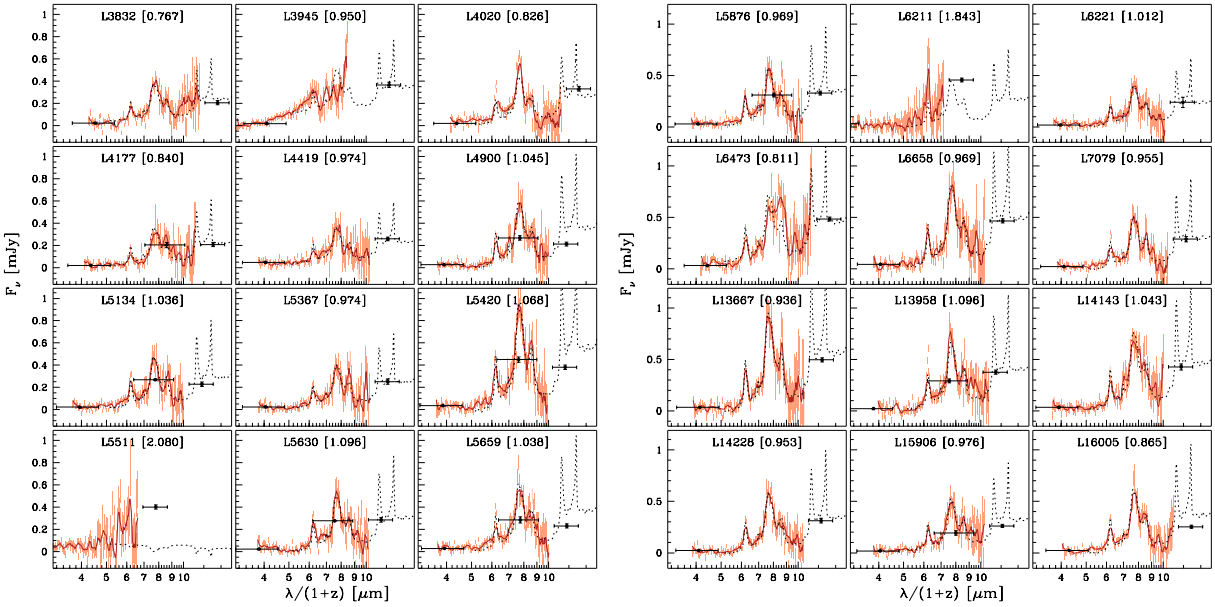

Figure 4.10 Observed MIR spectra of 24 z ∼ 1 LIRGs. The solid line, corresponding to the data with a smoothing of 5 pixels, is on the top of the shaded 1 σ error bars for each pixel. Broadband fluxes are overplotted. Dotted lines represent either the averaged local starburst template from Brandl et al. (2006) or the hot dust dominated spectrum from Spoon et al. (2007) rescaled to the data. Source names and redshifts appear on the top of each panel. [image from Fadda et al. (2010)].

As hinted above, based on the PAH emission and silicate absorption features visible in their MIR spectra, F10 were able to estimate the redshifts for 44/48 sources in their sample by cross-correlating the average starburst template of Brandl et al. (2006). For the remaining three sources in the LIRG sample, due to the absence of evident features, they were not able to measure a reliable spectroscopic redshift. Two of these three sources were also then re-classified as ULIRGs by F10 after a deeper spectroscopic analysis. Anyway these three objects were part of the extended CDFS field not included in our analysis. So as we will see in the next Chapter, for all the (U)LIRGs investigated in our work reliable spectroscopic redshifts have been measured from the IRS spectra.

F10 compared the MIR spectroscopic redshifts with photometric estimates from both Wuyts et al. (2008) and Caputi et al. (2004). The MIR spectroscopic redshifts were found to be consistent with the available optical spectroscopic and photometric redshifts within 20% with the photometric z having larger uncertainties than the MIR spectroscopic ones. They

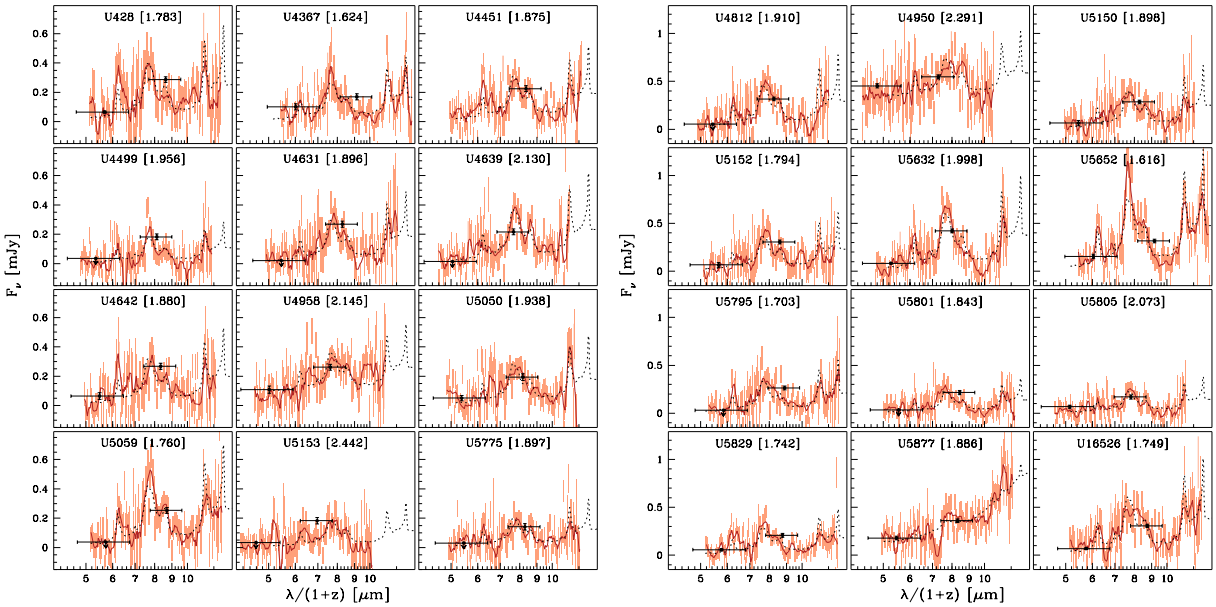

Figure 4.11 Same as Fig. 4.10 but for the 24 z∼2 ULIRGs. [image from Fadda et al. (2010)].

concluded that their sample selection based on optical photometric redshifts has proven to be effective.

4.4.5 AGN contamination

One of the scientific goals of F10 paper, was that of using MIR spectral diagnostics to measure the contribution of AGN to the total energy output of z∼1 LIRGs and z∼2 ULIRGs, particularly the obscured AGN which may not be detected by X-rays. The important point here is that, although in some cases the AGN can completely dominate the bolometric luminosity, there is an entire galaxy population with enshrouded AGN whose bolometric luminosity is dominated by star formation. To objectively classify AGN F10 used different indicators such as: broad and high ionization lines in optical spectra, lack of a 1.6 μm stellar bump in the SED, X-ray bright sources, low mid-IR 6.2 μm EW and optical morphology.

Most of the LIRGs and all the ULIRGs in F10 sample were covered by 2Ms Chandra X-ray Survey. Six of them (5 ULIRGs and 1 LIRG), had X-ray counterparts from the catalogue of Luo et al. (2008). Two of them, **U4950** and **U5877** were clearly detected in the (2-8)keV hard X-ray band. Another one, **U4642**, was detected at limit of sensitivity of the survey. Two more ULIRGs, **U428** and **U5775** were detected only in the soft X-ray and the remaining LIRG (**L5420**) was detected at a low-σ level in the soft X-ray.

Combining the broadband photometry and the mid-IR spectra for the six sources having X-ray counterparts F10 found that only two objects, **U4950** and **U5877**, have IRS spectra

compatible with a power law and broadband photometry typical of an AGN, i.e., absence of the 1.6 μm stellar bump and a power-law spectrum over the entire wavelength range. These objects also have HST morphologies showing compact, unresolved nuclei, further supporting the AGN classification from both X-ray and mid-IR spectra. The other source detected in the hard X-ray (**U4642**) has, on the contrary, a more complicated morphology with multiple clumps. According to F10, one clump can host the AGN, but the AGN does not dominate the optical-IR emission. All the other sources (**U5775, U428**, and **L5420**) have a softer X-ray emission, the mid-IR spectra have obvious PAH emission and their broadband SEDs reveal a strong stellar bump at rest-frame wavelength 1.6 μm, suggesting that although these three sources may have low luminosity AGNs, their host galaxies dominate the stellar emission in optical to near-IR. The X-ray luminosity of the fainter X-ray sources is also compatible with star formation using the relationships from Ranalli et al. (2003).

Looking at the optical spectra of the sources shown in Fig. 4.9 we can see that the spectrum of **U4958** shows a broad CIII line and strong NV and CIV emission lines. Based also on its rather featureless IR spectrum, F10 classified this source as AGN dominated. Being the 6.2 μm PAH feature relatively isolated its rest-frame EW can be cleanly measured and used to classify starburst-dominated systems. This is further supported by the evidence of a broad anti-correlation of the $EW_{6.2\mu m}$ with the flux ratios [NeV]/[NeII] and [OV]/[NeII] (Armus et al., 2006, Genzel et al., 1998, Lutz et al., 1996, Veilleux et al., 2009), where the detections of [NeV] $\lambda 14.3\,\mu m$ and [OIV] $\lambda 25.9\,\mu m$ indicate the excitation of the ionized gas by black hole accretion due to their extremely high ionization potentials (97.1 eV and 59.4 eV respectively).

F10 used the PAHFIT code (Smith et al., 2007) to fit lines and dust features together with a continuum from dust and stellar emission to the IRS spectra. To measure the EW of the 6.2 μm PAH, F10 used a Chiar-Tielens silicate profile and added an absorption component (following Veilleux et al. 2009) to take into account the water ice and hydrocarbon features at 5.7-7.8 μm. The addition of these absorption features is important mainly in strongly absorbed local ULIRGs and neglecting this in high-z ULIRG spectra does not significantly change the $EW_{6.2\mu m}$ estimates. For the $z \sim 1$ LIRGs the signal-to-noise ratio of the spectra is high enough to allow direct measurements of the EW of the 6.2 μm PAH feature. For the z,~ 2 ULIRGs instead, the low continuum combined with the higher noise of the spectra lead to large errors in the estimates of $EW_{6.2\mu m}$, with the error being dominated by the uncertainty in the estimate of the continuum from the spectrum. To get reliable estimates for individual sources F10 used the 16 μm fluxes as estimates of the continuum since they have a much lower uncertainty. They had 16 μm fluxes for 14 ULIRGs and upper limits for additional 9. As emphasize by F10, although, in general, most of the 16 μm flux is due to the continuum, the contribution of the 6.2 μm PAH is increasingly important at redshifts lower than 1.7. To compensate for this effect, they applied a multiplicative correction to

the 16 μm flux equal to the ratio of the 5.8 μm flux and the expected 16 μm of the averaged starburst spectrum moved at the redshift of the ULIRG. This correction ranges from 0.6 at $z \sim 1.6$ to 0.9 at $z \sim 2$ and it is found to not vary significantly by using different templates as the average HII-like ULIRG spectrum which better describes ULIRGs around the Si absorption feature. Following this approach F10 were able to measure the $EW_{6.2\mu m}$ for all the sources at $z \sim 2$ with the exception of U4958 already classified as AGN dominated on the basis of its optical spectrum.

Studies based on the analysis of the spectra of local LIRGs and ULIRGs have shown that the percentage of AGN contribution to the total energy output well correlates with $EW_{6.2\mu m}$. In F10 work they assumed that $EW_{6.2\mu m} < 0.2\mu m$ are AGN-dominated.

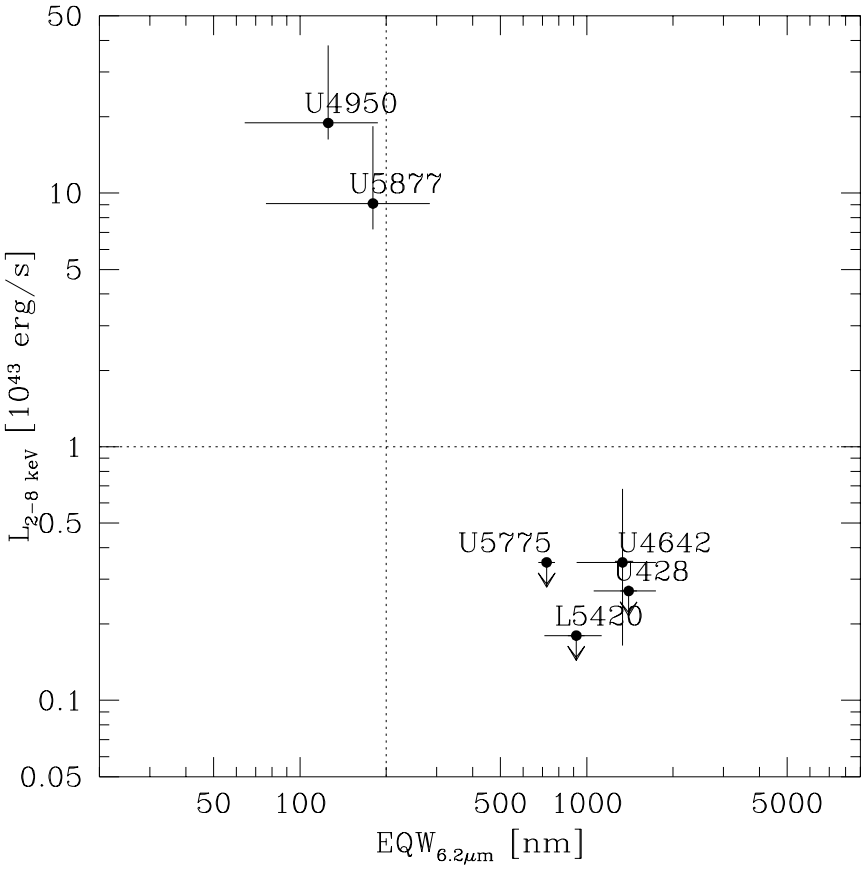

Figure 4.12 Hard X-ray 28 keV luminosity vs. EW of the 6.2 μm PAH feature for the IRS sources with X-ray counterparts. The infrared output of the objects on the left of the vertical line is dominated by AGN emission (Armus et al., 2007, Veilleux et al., 2009). Objects above the horizontal line are typically AGN-dominated sources (see, e.g., Fadda et al. (2002)). The dashed vertical line marks $EW_{6.2\mu m} = 0.2\ \mu m$, below which galaxies are AGN dominated. [image from Fadda et al. (2010)].

The application of mid-IR 6.2 μm PAH equivalent criteria yielded the same conclusions of the analysis performed above on the broad-band + MIR spectra of the six objects having

X-ray counterparts, namely that the two X-ray sources **U4950** and **U5877** are strong AGNs while the remaining 4 have their infrared emission dominated by star formation. This is highlighted in Figure 4.12. F10 analysed the 6.2 μm EWs of the entire sample of 48 sources. They found that the infrared emission of almost all the LIRGs and the majority of the ULIRGs are dominated by star formation. Among LIRGs, only one source is dominated by the AGN emission (5% of the sample) while for the ULIRGs, only 12% (3/25) have a dominant AGN. One result from F10 paper is that the AGN fraction for z $\sim$ 2 galaxies is small for $L_{IR} \sim 10^{12.6} L_{\odot}$, which implies that at high-z, the AGN-starburst transitional luminosity must be higher than $L_{IR} \sim 10^{12.6} L_{\odot}$.

4.4.6 Stacked MIR spectra and comparison with local IR galaxies

As evident from Figures 4.10 and 4.11, the individual MIR spectra of these high-z (U)LIRGs are very similar to the averaged z$\sim$0 starburst spectrum (Brandl et al., 2006), however, they are typically not deep enough to individually probe the silicate absorption feature at 9.7 μm. So in order to compare them with the spectra of local IR galaxies, F10 produced stacked spectra at the redshift 1 and 2 of the two bins. They excluded from the staking the few sources whose emission is dominated by an AGN and normalized the spectra to their 24 μm rest-frame luminosity which correlates with their total infrared luminosity. The rest-frame 24 μm luminosity has been computed differently for the two sample at redshift $\sim$ 1 and 2. For the z$\sim$1 LIRGs they simply interpolated the 8, 24, and 70 μm fluxes in the log(λ) versus log(νF_{ν}) plot. They did not take into account the 16 μm flux because it is severely affected by the 7.7 μm PAH complex. In the case of z$\sim$2 ULIRGs, the MIPS 70 μm flux is very close to the rest-frame 24 μm flux. Unfortunately, for many ULIRGs they had only upper limits of the 70 μm fluxes. In these cases, the rest-frame 24 μm fluxes were estimated by scaling a series of templates, including the averaged starburst from Brandl et al. (2006) and the composite ULIRGs from Veilleux et al. (2009), to fit the spectrum. The rescaled templates are shown in Figure 4.13. Table 4.4.6 reports the main physical quantities computed by F10 for these sources included the estimated total IR luminosities.

The result of the staking performed by F10 is shown in Fig. 4.14.

The averaged spectra clearly show the typical features of starburst-dominated galaxies with weak dust continuum at 4-14 μm and strong PAH emission at 6.2, 7.7, 8.6, and 11.3 μm. Weak PAH features at 5.25 and 5.70 μm are also visible, particularly in the LIRG spectrum. These spectra are also compared to local average spectra normalized to the data (by minimizing the χ^2 of the residuals). The average LIRG is surprisingly close to the average starburst spectrum from Brandl et al. (2006). As for the ULIRGs their spectrum has been compared to both the average starburst spectrum of Brandl et al. (2006) and to

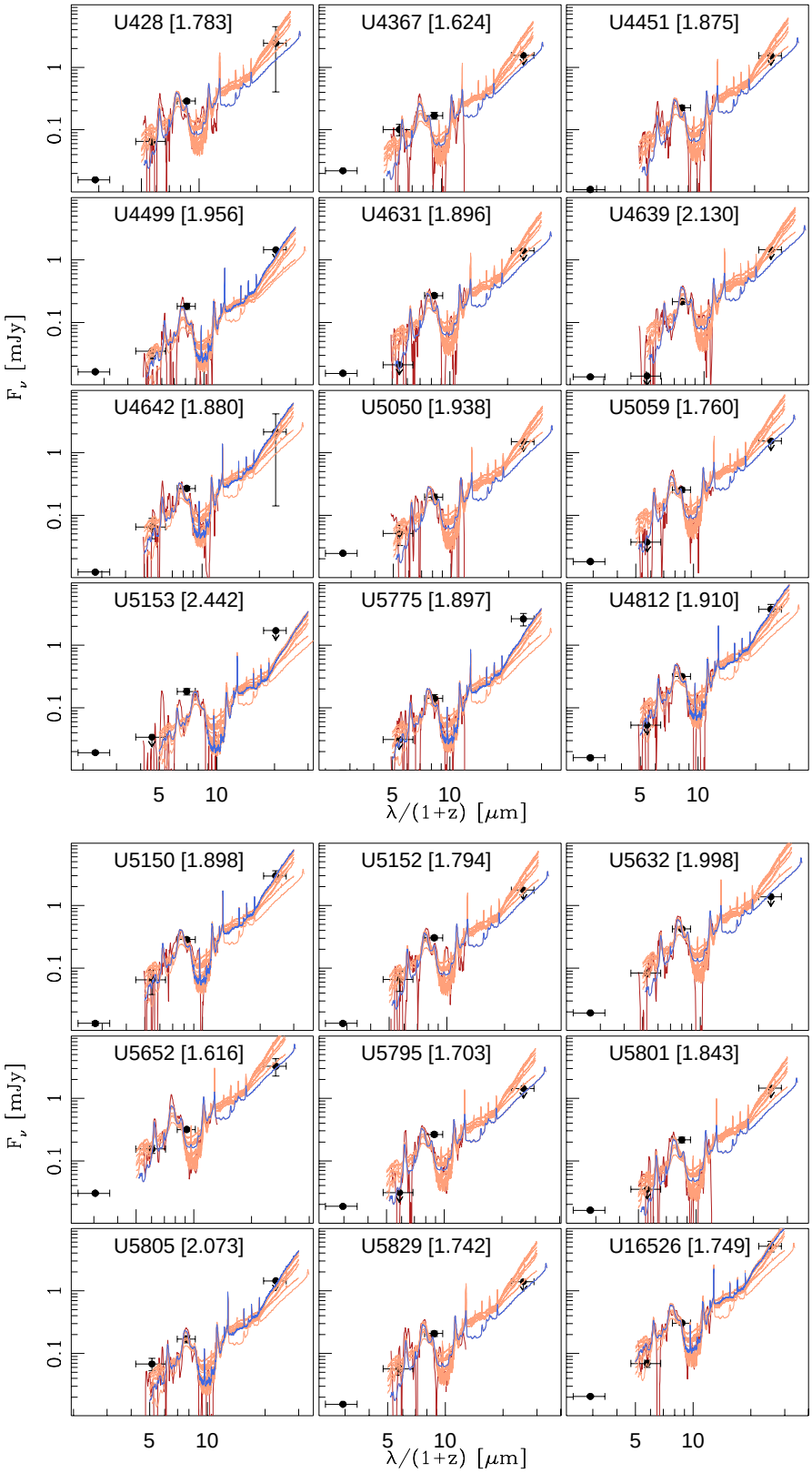

Figure 4.13 Templates of average starburst (Brandl et al., 2006) and ULIRG composites (Veilleux et al., 2009) rescaled to the smoothed IRS spectra (red line) of non-AGN-dominated ULIRGs. Blue lines represent the best fit compatible with the 70 μm flux. [image from Fadda et al. (2010)].

Table 4.4. Measured Fluxes, Redshifts and stellar masses of Fadda et al. (2010) sample [Tab. from Fadda (2010)]

ID	$S_{8\mu m}$		$S_{16\mu m}$		$S_{24\mu m}$		$S_{70\mu m}$		z_{IRS}	z_{opt}	*	$\log(L_{24\mu m})$	M_*
	[μJy]	SN	[μJy]	SN	[μJy]	SN	[mJy]	SN				[$L_\odot$]	[$10^{10}M_\odot$]
U428	15.9	68	65	24	287	38	2.43	3	1.783	(1.664)	a	11.47	4.09
U4367	22.2	79	101	12	169	20	<1.55		1.624	(1.762)	a	11.23	13.10
U4451	11.1	38			225	28	<1.53		1.875	(1.684)	a	11.40	3.47
U4499	16.3	77	< 35		182	23	<1.45		1.956	(1.909)	a	11.58	11.90
U4631	15.4	60	< 21		269	33	<1.40		1.841	1.896	1	11.39	9.61
U4639	13.5	57	< 14		216	27	<1.45		2.112	2.130	5	11.58	3.57
U4642	12.3	60	65	7	268	32	2.14	3	1.898	(1.748)	a	11.82	2.50
U4812	15.9	42	< 53		317	41	3.75	13	1.930	1.910	1	12.00	6.63
U4950	163.3	598	453	54	547	67	<1.68		2.312	2.291	4	11.79	10.41
U4958	16.4	62	109	11	262	33	<1.67		2.118	2.145	5	11.51	8.50
U5050	24.6	97	51	7	194	22	<1.50		1.938	(1.726)	a	11.40	18.93
U5059	18.1	64	< 37		253	31	<1.53		1.769	(1.543)	a	11.49	6.59
U5150	13.1	35	65	6	286	37	2.98	12	1.898	(1.738)	a	11.92	2.17
U5152	13.1	43	66	7	305	38	<1.77		1.794	(1.888)	a	11.44	2.75
U5153	19.2	68	< 34		183	21	<1.71		2.442	(2.030)	b	11.73	
U5632	19.2	86	83	35	421	52	<1.38		2.016	1.998	1	11.75	6.79
U5652	30.3	153	154	17	316	44	3.24	8	1.618	1.616	1	11.68	15.73
U5775	9.6	51	< 31		141	16	2.64	11	1.897	(1.779)	a	11.61	5.30
U5795	18.7	63	< 31		264	33	<1.43		1.703	(1.524)	a	11.36	5.63
U5801	16.2	57	< 35		216	24	<1.45		1.841	(1.642)	a	11.25	13.68
U5805	8.0	25	68	11	170	19	<1.45		2.073	(2.093)	a	11.74	1.16
U5829	15.4	69	57	12	208	26	<1.40		1.742	(1.597)	a	11.32	9.21
U5877	31.7	120	179	23	360	48	3.88	19	1.886	(1.708)	a	11.77	3.54
U16526	20.6	66	69	18	306	45	5.17	13	1.749	(1.718)	a	12.00	4.05
L3832	23.5	61			207	28	<1.90		0.767	(0.763)	b	10.53	4.39
L3945	19.0	18			367	39	3.81	11		(0.950)	b	11.08	0.37
L4020	20.8	30			332	38	4.22	21	0.826	(0.779)	b	10.90	3.10
L4177	20.5	70	204	22	208	27	<1.78		0.842	0.840	3	10.62	3.71
L4419	46.8	159			259	38	4.06	13	0.974	(0.995)	b	11.08	11.23
L4900	26.8	95	267	32	213	31	<1.82		1.047	1.045	5	10.91	6.75
L5134	22.6	106	269	110	229	28	<1.42		1.039	1.036	1	10.84	5.02
L5367	24.3	27			252	26	<1.92		0.974	(0.868)	b	10.86	5.79
L5420	36.7	135	450	48	381	46	2.76	5	1.068	1.068	3	11.15	4.42
L5511	38.6	50			401	54	2.22	5		(2.08)	c	11.87	25.90
L5630	22.8	104	277	149	286	36	2.06	3	0.997	0.996	3	10.93	2.27
L5659	28.6	129	285	25	231	30	2.41	9	1.044	1.038	1	11.00	4.57
L5876	29.2	103	310	41	330	43	2.54	15	0.971	0.969	1	10.98	7.16
L6211	31.5	84			457	62	<1.88		1.843	(1.840)	c	11.70	
L6221	19.1	14			239	12	<2.87		1.012	(0.989)	b	11.02	
L6473	32.3	44			484	63	2.78	8	0.816	0.811	1	10.83	
L6658	45.2	60			467	59	<1.87		0.969	(0.963)	b	10.94	12.54
L7079	23.3	20			289	27	3.21	8	0.955	(0.884)	b	11.00	
L13667	33.8	30			496	64	<2.65		0.936	(0.924)	b	11.00	
L13958	21.8	83	292	39	376	47	3.31	13	0.891	0.896	2	10.96	2.10
L14143	34.8	22			427	35	4.71	8	1.043	(0.965)	b	11.29	
L14228	23.8	23			313	35	<2.12		0.953	(0.961)	b	10.89	3.02
L15906	18.4	63	193	23	262	41	3.23	8	0.976	(1.045)	a	11.02	0.44
L16005	24.2	32			253	42	3.29	9	0.865	(0.984)	b	10.86	1.59

*Spectroscopic redshifts from: (1) Vanzella et al. (2008, 2006), (2) Mignoli et al. (2005), (3) Le Fèvre et al. (2004), (4) Szokoly et al. (2004), (5) Popesso et al. (2009), Photometric redshifts from: (a) Wuyts et al. (2008), (b) Caputi et al. (2004), (c) Fadda et al. (2010).

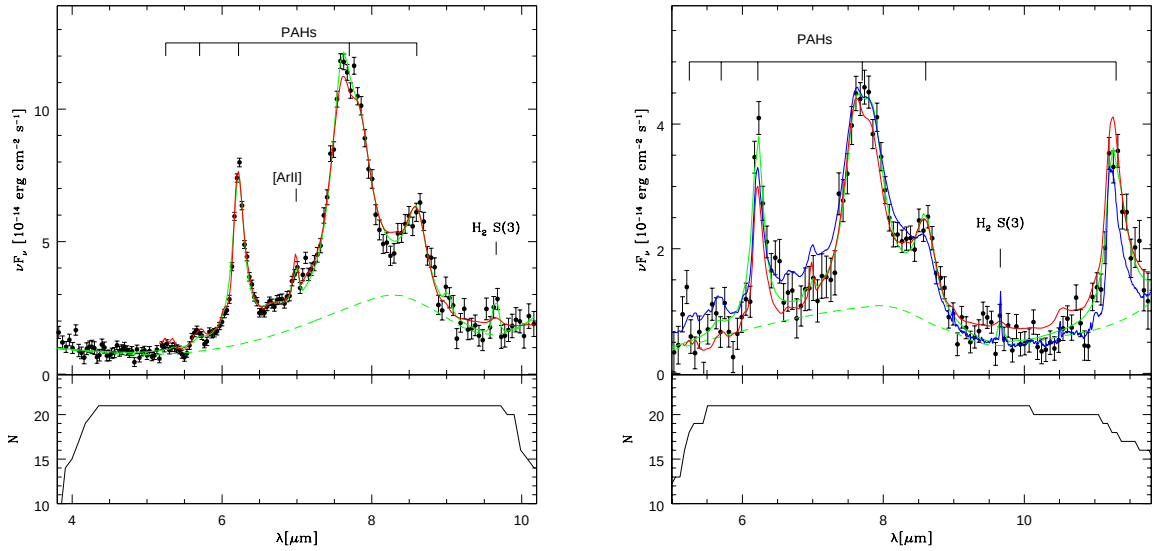

Figure 4.14 Averaged z $\sim$ 1 LIRG (left) and z $\sim$ 2 ULIRG spectrum (right) obtained by stacking all the spectra which are not AGN-dominated. The spectra have been normalized to the 24 μm rest-frame luminosity before stacking them. The lower panel shows the number of spectra used for each wavelength. The solid and dashed green lines correspond, respectively, to the total flux and continuum fitted with PAHFIT. The red and blue lines correspond, respectively, to the averaged starburst from Brandl et al. (2006) and the average local HII ULIRG from Veilleux et al. (2009) normalized to the stacked spectra [image from Fadda et al. (2010)].

several average local ULIRG spectra from Veilleux et al. (2009) obtained using the HII-like ULIRG average spectrum. As evident from Fig. 4.14, although the average starburst spectrum fits well to the relative PAH strength in the averaged spectrum of z $\sim$ 2 ULIRG, the local average ULIRG reproduces better the 9.7 μm silicate absorption. This implies that high-z ULIRGs have more dust extinction than lower luminosity LIRGs.

F10 also computed the composite spectra of LIRGs and ULIRGs by weighting the individual spectra of all the sources not dominated by AGN, by their total infrared luminosities. The same procedure has been applied to the IRAC and MIPS fluxes of the sources. The composite SED plus IRS spectra were then compared to four different models, among the most popular (i.e. Dale & Helou 2002; Chary & Elbaz 2001; Lagache et al. 2004; Franceschini et al. 2009). Using the composite spectra plus the IRAC and MIPS fluxes, F10 also tried to estimate how much the presence of PAH features boosts the detection of infrared galaxies in the 24 μm filter as a function of redshift. They fitted the composite LIRG and ULIRG with PAHFIT to estimate the continuum. Then, they computed the ratio of the flux in the 24 μm filter for the total spectrum and for the continuum only. The ratio of these two fluxes has two clear peaks approximately at z = 0.9 and z = 1.8 which corresponds to the redshifts where the 24 μm filter includes the two main PAH complexes

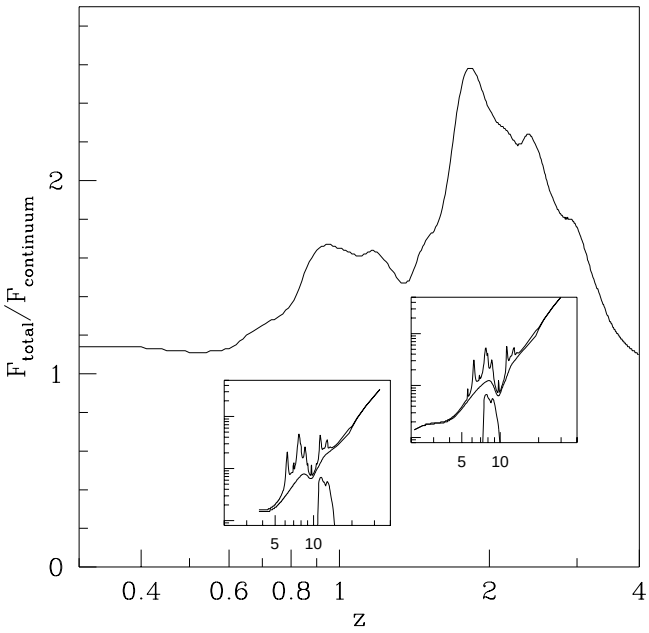

Figure 4.15 Fraction of the total over continuum 24 μm flux for luminous galaxies in the redshift range between 0 and 4, based on the composite LIRG and ULIRG spectra. The presence of PAH features boosts the detection of 24 μm sources around z $\sim$ 0.9 and z $\sim$ 1.8, the median redshifts of the two subsamples. The insets show the decomposition of the two composite spectra in PAH plus continuum and the locations of the 24 μm filter at the two sensitivity peaks [image from Fadda et al. (2010)].

(11.3 and 7.7 μm). This is highlighted in Fig. 4.15. For comparison, the median redshifts of the two samples are 0.95 and 1.87. *Figure 4.15 seems to suggest that at z$\sim$ 2, the 24 μm broadband filter selection will preferentially select galaxies with strong PAH emission rather than power-law sources, and this bias can be as high as a factor of 2.*

F10 explored the relationship between the restframe 24 μm monochromatic luminosity $(\nu L_\nu)_{24\mu m}$ and the EW of the 6.2 μm PAH feature which are both quantities linked to star formation. The authors found a maximum value of $\sim$ 1 μm for $EW_{6.2\mu m}$ for all infrared galaxies, independent of redshift and luminosity. This 'upper limit' in the 6.2 μm PAH strength is due to the fact that, for pure starbursts, the strength of the PAH line and of the underlying continuum are both proportional to the luminosity due to star-forming activity. At $L_{24\mu m} \gtrsim 10^{11} L_\odot$, there is a clear anti-correlation between the rest-frame 24 μm luminosity and 6.2 μm PAH EW. The 6.2 μm PAH EW of the z$\sim$1 sources is systematically greater than that of the local luminous galaxies in the same luminosity range. *In other words among high luminosity sources ($L_{24\mu m} \gtrsim 10^{11} L_\odot$), at a given luminosity, high-redshift sources have PAH emission stronger than that of local ULIRG. This is likely due to an AGN contribution in high-redshift galaxies lower than that of local IR luminous galaxies.*

4.4.7 Red Optical Colours of high-z (U)LIRGs

Many of the sources belonging to the F10 sample have very red optical SEDs, as evident from Figure 4.16. With the extremely red galaxies (ERG) and the distant red galaxies (DRG) defined by the criteria $(i-K)_{Vega} \gtrsim 4.0$ and $(J-K)_{Vega} \gtrsim 2.3$, respectively (Franx et al., 2003, van Dokkum et al., 2004, Yan et al., 2005, 2000), F10 find that among the 24 ULIRGs at z$\sim$2, 63% (15/24) are ERGs and 33% (8/24) are DRGs. These near-IR color selected DRGs have very faint optical magnitudes, and their redshifts are difficult to obtain with optical/near-IR spectroscopy (Kriek et al., 2008). Eight new redshifts have been provided by F10, based on the analysis of IRS spectra, which did not have optical spec-z. These have been used by Wuyts et al. (2009c) to check the reliability of DRG color selections. The finding of eight z $\sim$ 2 ULIRGs having very red (J-K) colors suggests that a significant fraction of DRGs selected by K-band surveys are dusty star-forming galaxies, not passively evolving stellar populations at z $\sim$ 2-3. This is consistent with previously published studies, which found as many as 50% of color-selected DRGs being dusty starbursts (Kriek et al., 2008, Labbé et al., 2005, Wuyts et al., 2007, 2009c).

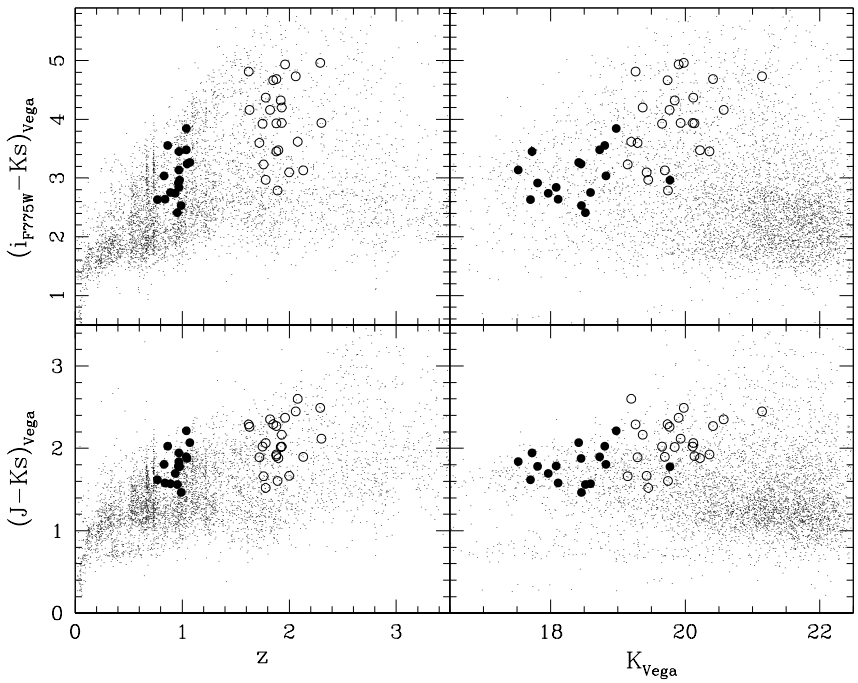

Figure 4.16 Color-color plots for galaxies in the GOODS field (dots) and galaxies of F10 sample. Filled and open circles mark, respectively, the z$\sim$1 LIRGs and z$\sim$2 ULIRGs of F10 sample [image from Fadda et al. (2010)].

Moreover, all the z$\sim$2 ULIRGs also satisfy the BzK ((z-B) vs (K-z)) color selection criteria first introduced by Daddi et al. (2004) to select star-forming and passively evolved galaxies

at $z \gtrsim 1.4$. These BzK color cuts are shown as lines in Figure 4.17 (left). As evident from the figure, the z ∼ 2 ULIRGs fall into the star-forming BzK region on the (z-B) versus (K-z) colorcolor diagram. As expected, their red BzK colors are mostly due to the dust absorption of the UV photons from O, B young stars produced by recent starbursts. Figure 4.17 also reports the IR excess (measured from the ratio SFR(IR+UV)/SFR(UV

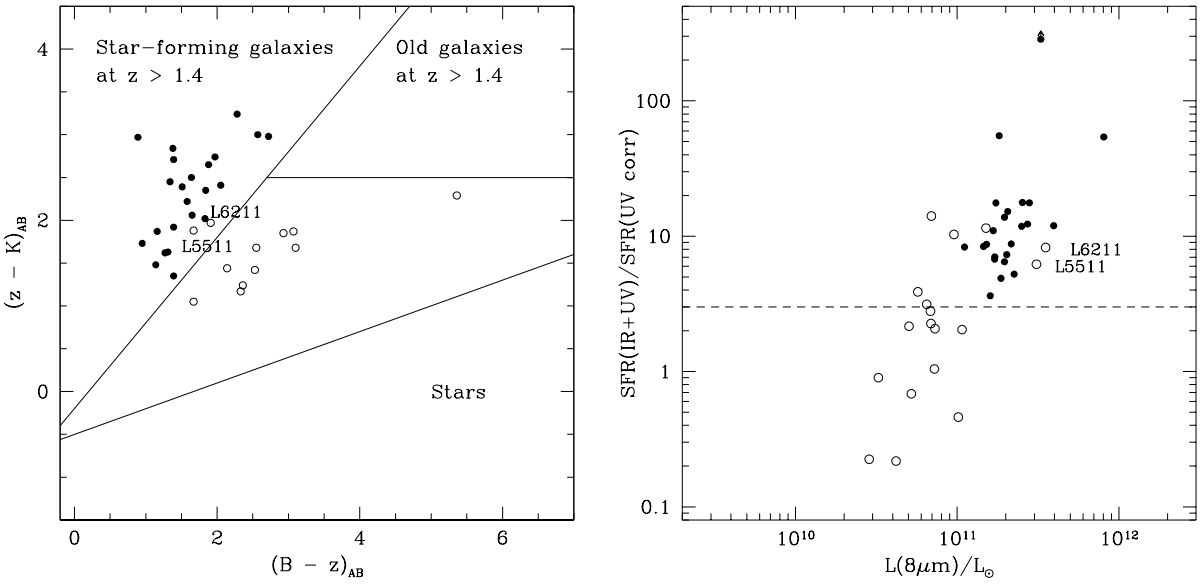

Figure 4.17 Left: optical/near-IR color plot; right: IR excess vs. rest-frame 8 μm luminosity. Filled and open circles represent, respectively, ULIRGs and LIRGs. The names indicate the two sources from the LIRG sample which are actually at redshift ∼ 2 [image from Fadda et al. (2010)].

corr.)) as a function of the rest-frame $L_{8\mu m}$ computed as in Daddi et al. (2004). All the $z \sim 2$ ULIRGs and a few LIRGs are IR excess galaxies according to the definition of Daddi et al. (2004) ($SFR_{IR} + SFR_{UV,uncorr.} \gtrsim 3.16 \times SFR_{UV,corr.}$). F10 also checked the position of these IR selected galaxies in the IRX-β diagram of Meurer et al. (1999) to investigate weather they follow the same dust extinction scaling relationship as optically selected objects with low dust content.

Figure 4.18 shows the far-infrared to 1600 $\mathring{A}$ monochromatic luminosity ratio as a function of UV spectral index β, where $f_\lambda \sim \lambda^\beta$, $1000\mathring{A} < \lambda < 2500\mathring{A}$. The ratio $L_{FIR}/L_{1600\mathring{A}}$ measures how much energy is re-distributed from UV to infrared, and β measures the UV SED slope, i.e., UV reddening. Studies of local UV selected starbursts have shown that dust absorption is correlated with UV reddening (Meurer et al., 1999, 1995). This correlation provides a powerful empirical tool, particularly for high-z UV/optical surveys, to recover the total, dust-absorption corrected, UV fluxes, using UV photometry alone. In Figure 4.18 the positions of F10 (U)LIRGs in the $L_{FIR}/L_{1600\mathring{A}}$ vs β diagram, are compared to those of local galaxies (Meurer et al., 1999) and high-redshift galaxies (Chapman et al.,

2005, Reddy et al., 2006). For the F10 (U)LIRGs, $L_{1600\mathring{A}}$ have been computed using the available optical magnitudes from U to R and interpolating in νF_ν, while β has been computed using the relations from Papovich et al. (2006). The L_{FIR} is derived from the rest-frame 24 μm luminosity using the relationship from Rieke et al. (2009) to compute the total IR luminosity and from Elbaz et al. (2002) to pass from total IR luminosity to far-IR luminosity. In the case of SMG galaxies from Chapman et al. (2005), F10 used the available B and R magnitudes to compute β and $L_{1600\mathring{A}}$. The relation from Papovich et al. (2006) was used after applying median corrections to the B and R magnitudes to transform them in the appropriate bands.

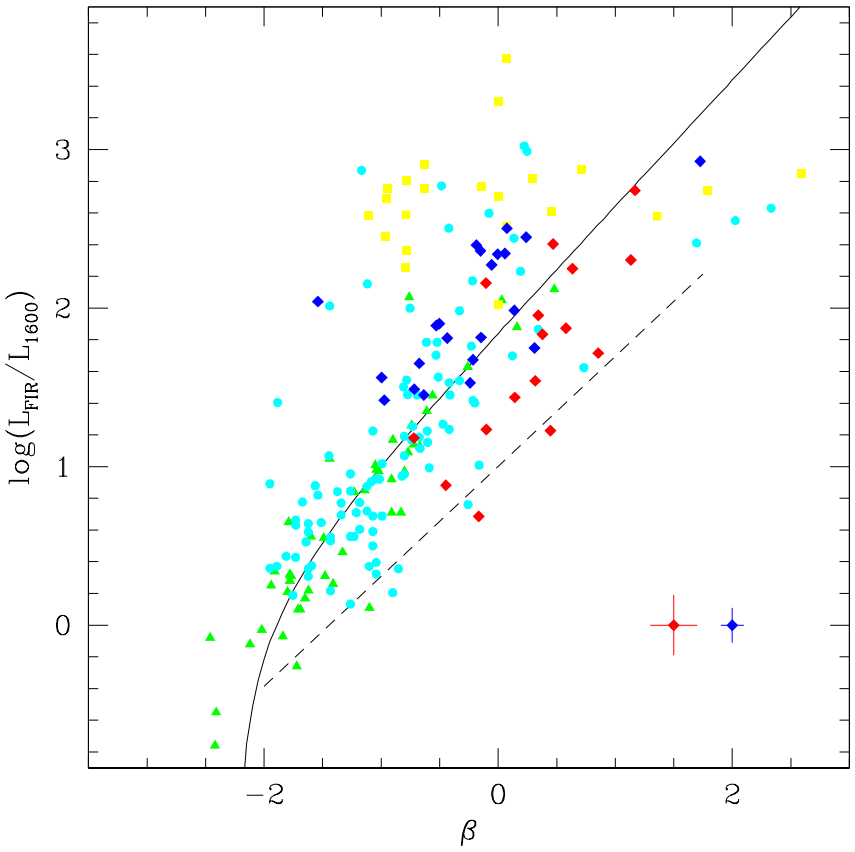

Figure 4.18 Ratio of far-IR to UV flux at 1600 $\mathring{A}$ versus the UV spectral slope β for F10 (U)LIRGs and some published comparison galaxies. The solid line shows the linear fit to the $A_{1600\mathring{A}}$-β relationship by Meurer et al. (1999). The dashed line shows the relation for normal star-forming galaxies (Cortese et al., 2006). The samples from Meurer et al. (1999), Reddy et al. (2006), and Chapman et al. (2005) are marked with green triangles, cyan dots, and yellow squares, respectively. F10 z $\sim$ 1 and z $\sim$ 2 sample are marked with red and blue diamonds, respectively. The typical error of the points is shown in the bottom right corner of the plot. Most of the z $\sim$ 2 ULIRG lie above the curve, in the region occupied by SMGs and HLIRGs [image from Fadda et al. (2010)].

The UV luminosities and β of z $\sim$ 1 LIRGs are poorly constrained because F10 did not have

UV observations for these galaxies. These sources appear to scatter between the normal star-forming galaxies and the UV selected starburst relations, which can be attributed to a range of UV extinction slopes (Fadda et al., 2010). Most of the z $\sim$ 2 ULIRGs, tend to lie above the Meurers relation, although usually not quite so far as the SMGs and HLIRGs (hyper-luminous IR galaxies). However, as emphasized by F10, the large scatter in this diagram, and the strong dependence on the UV slope of the unknown extinction curve serve as caveats in applying standard UV dust corrections. Boquien et al. (2009) have cautioned that applying the wrong extinction law to the UV would result in over- or underestimating the true SFR by factors of up to $\sim$ 7.

According to Daddi et al. (2004), $\sim$ (20-30)% of $1.4 < z < 2.5$ BzK selected galaxies with $K_{Vega} \lesssim 22$ have IR excess (as defined above). As we have seen above, all the z$\sim$2 ULIRGs of F10 sample are BzK galaxies satisfying the IR excess criteria (see Figure 4.17). This IR excess could be due to either (1) non-negligible Compton-thick AGN contribution to total luminosities, or (2) underestimation of UV extinction corrections, or (3) incorrect estimate (overestimates) of L_{IR}. Daddi et al. (2007a) have argued that this IR excess is primarily due to Compton-thick AGN heating of mid-IR luminosities, causing the overestimation of L_{IR}, thus 'excess' of SFR_{IR} + $SFR_{UV,uncorrected}$ (in principle in fact, assuming to know the correct relation to estimate L_{IR} from the rest-frame $L_{8\mu m}$, the correct UV extinction and assuming a negligible contribution by AGN, we should get $SFR_{UV,corrected}$ = SFR_{IR} + $SFR_{UV,uncorrected}$). The analysis of the MIR spectra of F10 (U)LIRGs suggest instead that most z$\sim$2 ULIRGs (92%) have strong PAH emission and low AGN contribution to their L_{IR}. However due to the presence of broad, strong PAH emission the rest-frame $L_{8\mu m}$ luminosity estimated from observed broadband 24 μm photometry will be overestimated. Finally, another important factor responsible for this 'IR excess' is the underestimated UV dust extinction correction. This is further supported by Figure 4.17, where the z $\sim$ 2 ULIRGs are systematically offset above the local relationship defined by low luminosity, low extinction star-forming galaxies. It is worth stressing that the UV dust extinction of heavily obscured ULIRGs is, indeed, only a lower limit because, for a mixed distribution of stars and dust, increasing amounts of dust will further absorb stellar emission, but the reddening of the integrated colors of a galaxy will saturate as the most obscured spectral regions have less weight in the integrated SED (Fadda et al., 2010, Wuyts et al., 2009b).

Based on the analysis of their IRS spectra, F10 concluded that the IR excess of these 24 μm selected $z\,sim\,2$ ULIRGs is mainly due to the strong PAH contribution (in particular the 7.7 μm feature), to the rest-frame mid-IR luminosity which leads to an overestimation of L_{IR} and to an underestimation of the UV dust extinction. This excess, therefore, is not due to dust being heated by obscured, Compton thick AGNs as claimed by Daddi et al. (2007a).

Stacking all the sources whose infrared flux is not dominated by AGN emission, F10 provided quantitative estimates of the obscured AGN luminosities contributing at the rest-frame 6 μm. By subtracting from the spectra around the 6.2 μm PAH feature the scaled averaged starburst spectrum of Brandl et al. (2006), F10 measured the average AGN powered continuum at 6 μm. Then from this, by using the relation $logL_{5.8\mu m} = 1.209 logL_{2-10keV} 8.667 erg/s$ (Bauer et al., 2010, Lutz et al., 2004), they estimated an average intrinsic X-ray AGN luminosity of $L_{2-10keV} = (0.1 \pm 0.6) \times 10^{43} ergs^{-1}$, a value substantially lower than that inferred from the X-ray stacking analysis in Daddi et al. (2007a) ($L_{2-8Kev} \sim (1-4) \times 10^{43} erg/s$). A similar analysis on the LIRG sample suggests that their emission is mostly powered by star formation.

From the F10 analysis of IRS spectra we can therefore conclude that the infrared emission of the majority of $z\sim 2$ ULIRGs, (21/24, i.e., 88%), is dominated by star formation. For the LIRGs hold similar conclusions, here only 5% (1/24) of the total sample is dominated by AGN.

4.4.8 (U)LIRG morphologies

In order to address the outstanding question about the power source responsible of the high IR luminosities of high-z LIRGs and ULIRGs ($10^{44} - 10^{46} erg/s$), whether it is dominated by major mergers as in the case of local (U)LIRGs or cold gas accretion, F10 examined the morphologies of their sources using high resolution images from HST.

Figures 4.19 and 4.20 show image cutouts for ULIRGs and LIRGs, respectively, in the HST *F435W* (B), *F606W* (V), *F775W* (i), *F850LP* (z) bands and the ground-based J and K images. Each cutout has a size of $10'' \times 10''$. These two figures show the steep variation of the spectral energy distribution from B to K, and clearly indicate that many of F10 sources have extremely red optical-to-NIR colors. Colors and morphologies are also highlighted in Figure 4.21 which shows three-color images of the galaxies which have been observed with ACS in the *F435W*, *F606W*, and *F850LP* bands. The angular size of the images is $3''$ and $4''$ for ULIRGs and LIRGs, respectively, corresponding to 25.2 kpc and 31.2 kpc at the median redshift of 1.9 and 0.9, respectively.

Many extended sources, such as U4367, U4451, U5652, and U5829, are also very red, suggesting that dust obscuration could be in play. Only four sources (U428, U4950, U4958, U5877) have very compact or nearly unresolved morphologies. Two of these sources (U4958 and U5877), also show very blue compact cores in Figure 4.21 and are AGN-dominated systems with weak or no PAH emission as shown in Figure 4.11. This correspondence between the rest-frame optical compact morphologies and the mid-IR AGN-dominated

spectra has also been found among a large sample of 24 μm selected ULIRGs in the Spitzer First Look Survey (Dasyra et al., 2008).

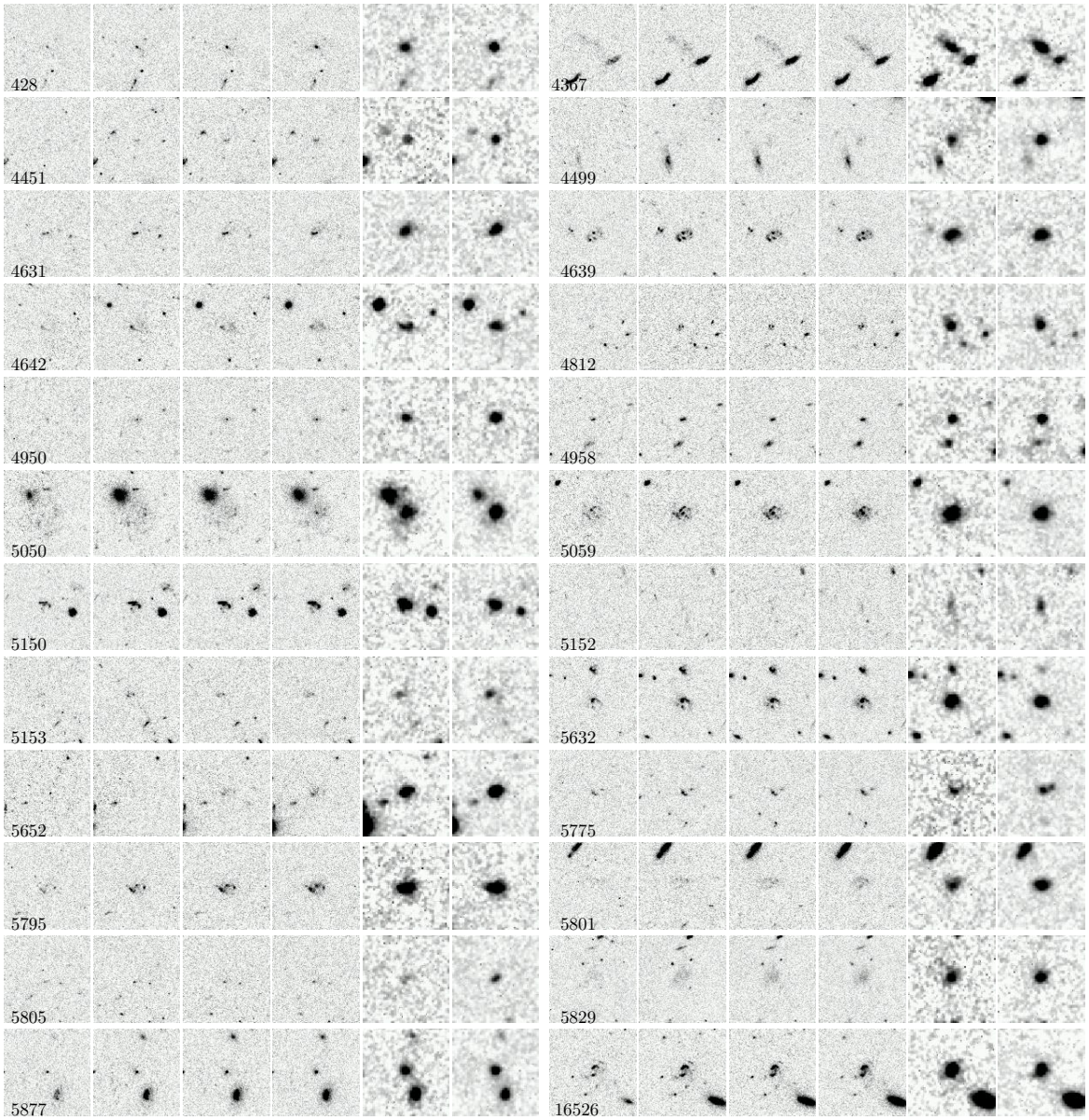

Figure 4.19 Image cutouts for each ULIRG are in the filters *F435W*, *F606W*, *F775W*, *F850LP* from HST ACS images of the GOODS treasury survey. *J* and *Ks* images are from the public EIS survey done with ISAAC on the VLT telescopes. The object ID is labeled on the *F435W* image. Each image stamp is $10'' \times 10''$ [image from Fadda et al. (2010)].

In order to quantify the morphological differences between high-z (U)LIRGs and faint infrared galaxies in the same redshift range, F10 computed the Gini coefficient and M_{20} for both samples. The Gini coefficient, G, is a statistic to measure the distribution of flux within the galaxy and M20 is the second-order moment of the brightest 20% of the galaxys flux. These two non parametric statistics were originally introduced by Lotz et al. (2004)

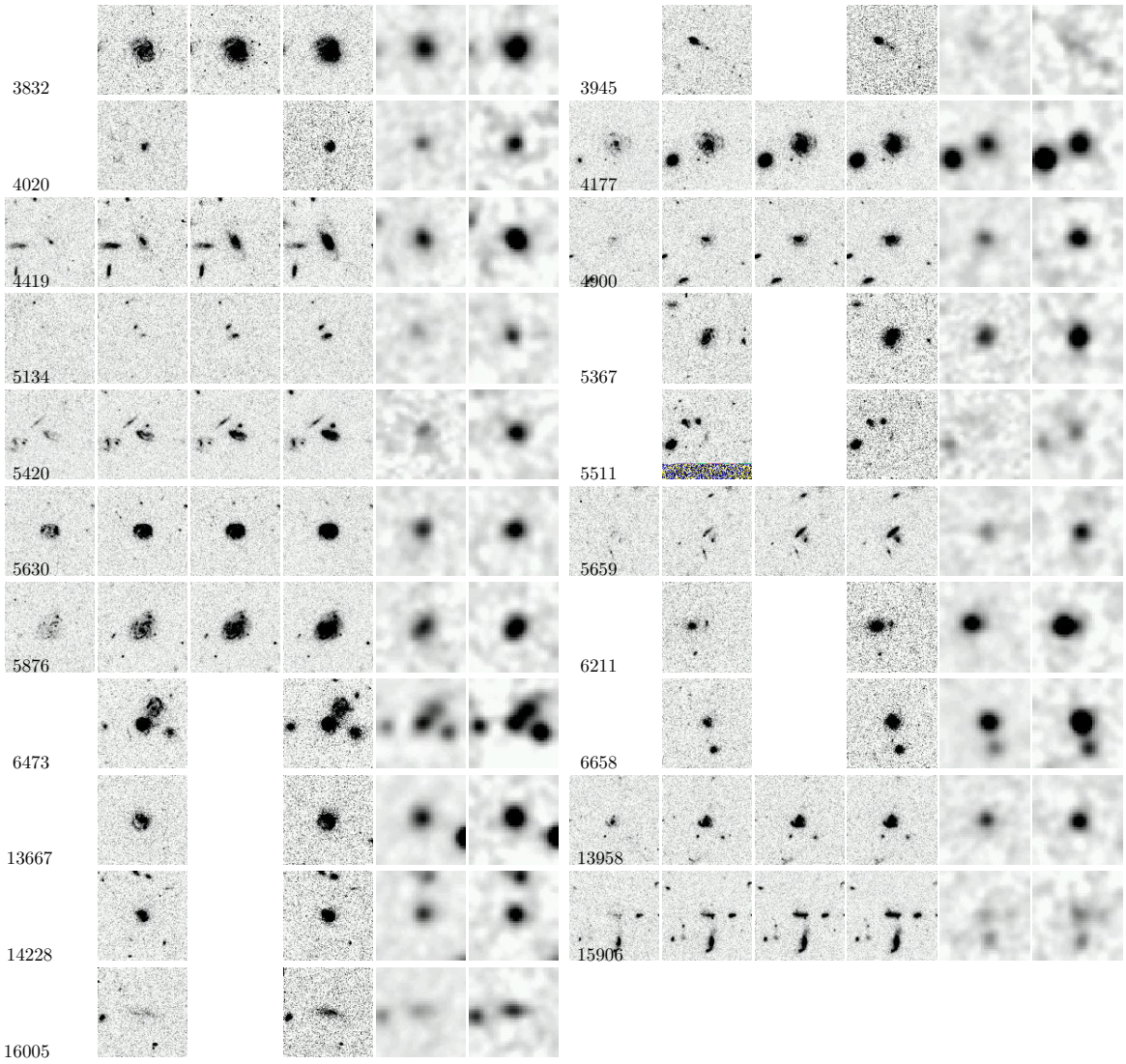

Figure 4.20 Similar to Figure 4.19 but for the 21 LIRGs at $z \sim 1$. Here all of the available observations in HST/ACS *F606W* and *F850LP* filters for LIRGs within the GEMS survey, and *F435W*, *F606W*, *F775W*, and *F850LP* for LIRGs within the GOODS region, have been used. For objects in the GOODS region, *J* and *Ks* images are from the EIS survey. Otherwise, they are from the MUSYC survey (Gawiser et al., 2006) [image from Fadda et al. (2010)].

to quantify galaxy morphology. Normal galaxies form a sequence in the G-M_{20} plot and, in the local universe, ULIRGs lie above this sequence.

The G and M_{20} statistics have been computed by F10 using the *F850LP* and *F606W* images for ULIRGs at $z \sim 2$ and LIRGs at $z \sim 1$, respectively, to be roughly at the same 3100 Årest-frame wavelength. The pixel size of the galaxies at the specific redshift correspond to a similar physical scale (0.24 and 0.25 kpc for LIRGs and ULIRGS, respectively). The errors on the coefficients have been computed using Monte Carlo simulations. Details about the exact procedure followed by F10 can be found in Fadda et al. (2010). The measured errors

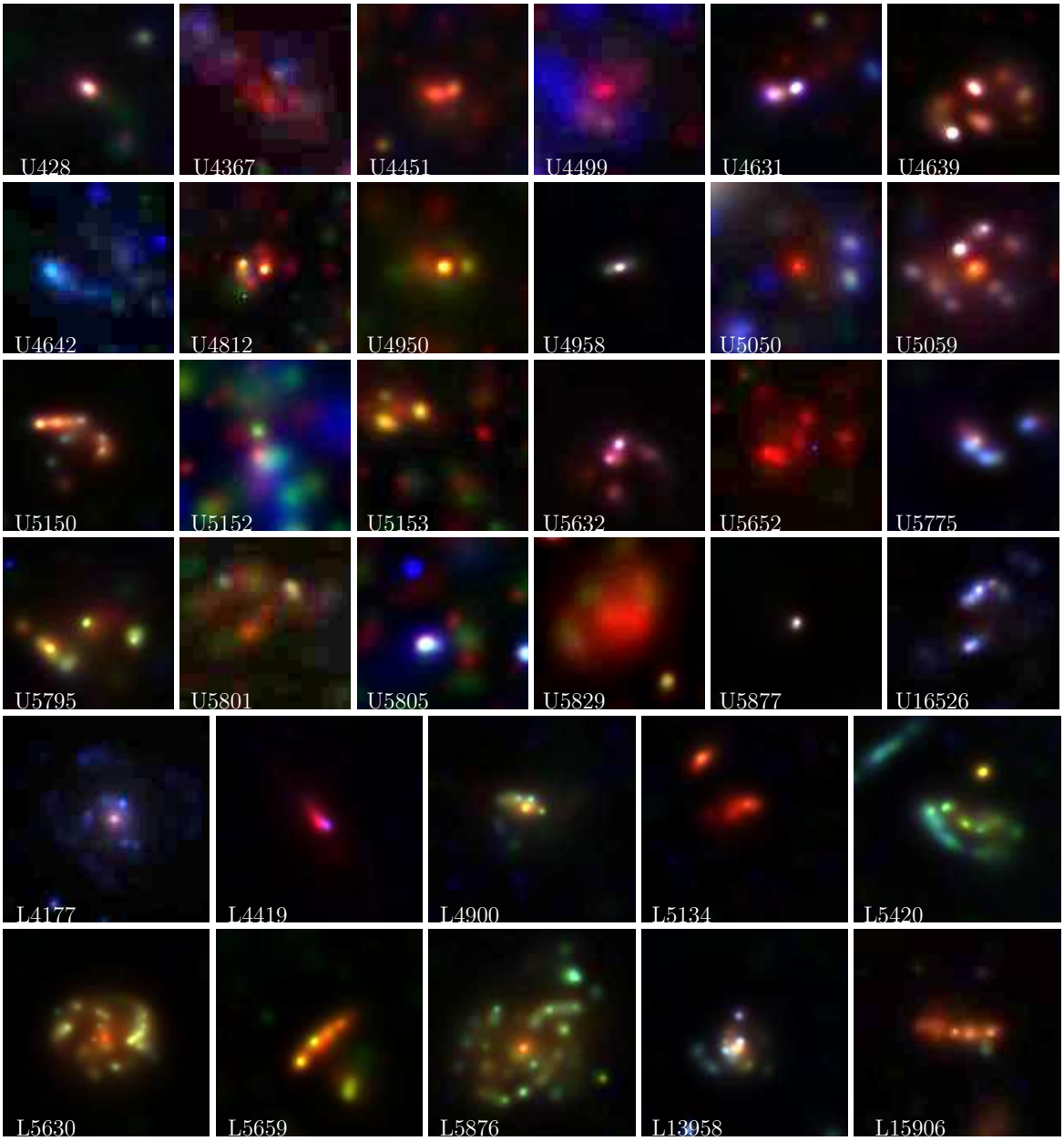

Figure 4.21 Three color images for 24 ULIRGs and 10 LIRGs of F10 sample with F435W, F606W, and F850LP ACS coverage. The field of view is $3'' \times 3''$ and $4'' \times 4''$ for ULIRGs and LIRGs, respectively. The composed image was obtained by giving the same weight to each band [image from Fadda et al. (2010)].

are 0.014 ± 0.011 and 0.04 ± 0.04 for the G and M_{20} coefficients, respectively. Figure 4.22 report the G and M_{20} values for the high-z (U)LIRGs for which the signal-to-noise was sufficient to compute them and also for a control sample of galaxies with faint infrared emission (less than 20 μJy at 24 μm) in the redshift ranges 0.8-1 and 1.8-2 typical of the (U)LIRGs of F10 sample. The typical $1\,\sigma$ error is reported in the lower right corner. A gray shaded region highlights the G-M_{20} sequence locally populated by "normal" galaxies while ULIRGs are found above that sequence. The three regions of the plot defined by Lotz

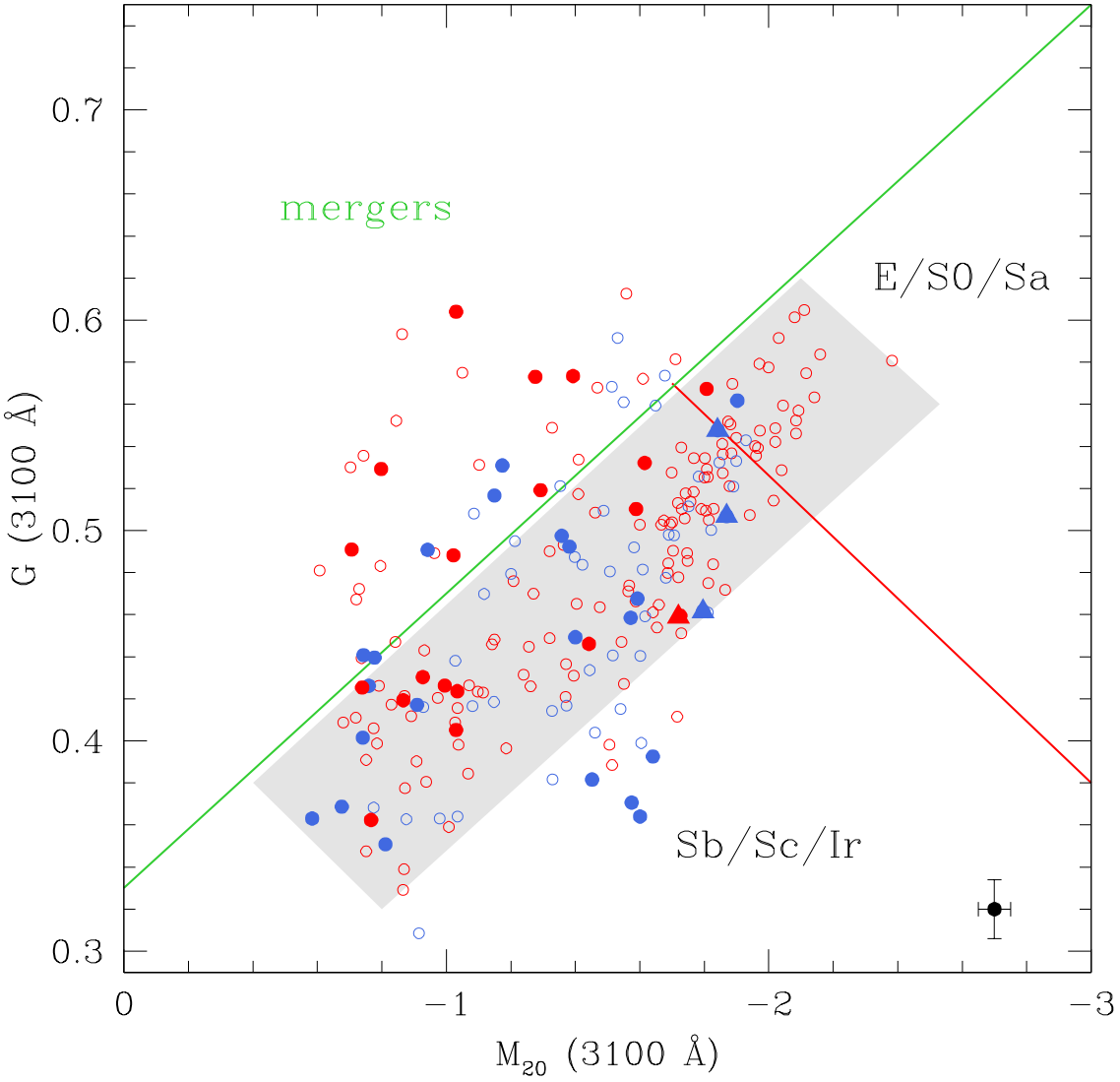

Figure 4.22 Gini coefficient and M_{20} statistic for the sample of $z \sim 1$ LIRGs (red filled dots), $z \sim 2$ ULIRGs (blue filled dots) and faint infrared sources in the redshift range $1 < z < 2$ (red and blue open dots, respectively). The triangles correspond to the sources whose mid-IR emission is AGN-dominated. The gray shaded region highlights the Gini-M_{20} sequence which, locally, is populated by "normal" galaxies while local ULIRGs lie above the sequence. The three regions defined in Lotz et al. (2008) are marked with solid lines. The statistics have been computed by F10 from ACS images in the bands *F606W* and *F850LP* for galaxies at $z \sim 1$ and $z \sim 2$, respectively, to be approximately at the rest-frame wavelength of 3100 *Å* [image from Fadda et al. (2010)].

et al. (2008) populated by merger, earlytype, and late-type galaxies are marked with solid lines. The G-M_{20} sequence found by Lotz et al. (2008) in the Groth strip at $0.2 < z < 1.2$ in the rest-frame blue band is well reproduced by F10 study, although at a bluer rest-frame wavelength. The separation between infrared-active and infrared-quiet galaxies is not so clear as for normal and IR-luminous local galaxies.

This quantitative analysis of (U)LIRG morphology based on ACS images reveals that most of the IR-luminous galaxies of this sample do not differ significantly from the majority of the IR-quiet galaxies at the same redshift range. At the 3100 $\mathring{A}$ rest frame, 37^{+22}_{16} % of the z$\sim$1 LIRGs and 21^{+15}_{10} % of the z$\sim$2 ULIRGs have Gini coefficients higher than those of normal IR-quiet galaxies. In the blue rest frame, 10^{+14}_{7} % of the z$\sim$1 LIRGs fall in the merger region of the Gini-M_{20} plot. This percentage is compatible with the 15% found by Lotz et al. (2008) among infrared galaxies with $L_{IR} > 10^{11} L_{\odot}$ at $0.4 < z < 1.0$.

4.4.9 Conclusions

In conclusion, the mid-IR spectra of LIRGs and ULIRGs at z$\sim$1 and 2 reveal that the majority of these galaxies have strong PAH emission and are starburst dominated. The Compton-thick AGN contribution to bolometric luminosity for this sample selected with $S_{24\mu m} \sim$ 0.15-0.5 mJy is small. The so-called IR excess for these faint 24 μm selected ULIRGs at z $\sim$ 2 is mainly due to the strong PAH contribution to the rest-frame mid-IR luminosity which leads to overestimations of L_{IR} and to underestimation of the UV dust extinction.

Chapter 5

The complex physics of dusty star-forming galaxies at high redshifts as revealed by Herschel and Spitzer

Modelling the emission from stars and dust consistently in order to get reliable estimates for the main galaxy physical parameters, like stellar mass ($M_\star$), star formation rate (SFR) and the average extinction (A_V), involves solving the radiative transfer equation for idealised but realistic geometrical distributions of stars and dust, as well as taking advantage of the full SED coverage from UV to sub-mm. The full SED of a galaxy allows the total luminosity of the galaxy to be robustly constrained without relying on extrapolations based on optical data alone. While the shape of the optical-UV SED indicates some level of dust extinction, there may be stellar populations (typically the newly born) completely obscured by dust. The only way to overcome this problem and quantify how much stellar light (and therefore mass) is missing from the optical, is to consider the dust-absorbed galaxy luminosity through the dust re-emitted spectrum in the IR, and model it together with the optical spectrum with a complete radiative transfer method.

With total infrared luminosities between $10^{11} - 10^{12}$ $L_\odot$ and $\geq 10^{12}$ $L_\odot$, respectively, Luminous and Ultraluminous Infrared Galaxies [(U)LIRGs hereafter] are among the most luminous and complex extragalactic objects we can conceive, including all varieties of young and old stellar populations, dust absorption, scattering, grain thermal re-radiation, and AGN emission ((Lonsdale et al., 2006)). Although they are quite rare in the local universe, they dominate the cosmic star formation rate and the FIR background at z > 1. Therefore they are suitable laboratories to study the main physical processes which drive galaxy formation and evolution. Observations of local ULIRGs have shown that they are dominated by strong interactions and mergers and the fraction of mergers/interactions among them

has been found to be strongly correlated with their IR luminosity, such that lower luminosity LIRGs ($L_{IR} \lesssim 10^{11.5}$ $L_{\odot}$) are ordinary disks while the highest luminosity ULIRGs are advanced stage mergers.

High-z LIRGs and ULIRGs seem to be, instead, not equivalents of ULIRGs in the nearby universe, but rather upscaled versions of normal galaxies (Elbaz et al. 2011; Nordon et al. 2012; Symeonidis et al. 2009; Rujopakarn et al. 2011). An implication is that high-z ULIRGs could well have gradually evolving SFHs, and be not necessarily associated with merger events as they are at z∼0.

This Chapter is based on our recent paper, (Lo Faro et al., 2013), which is the first of a series dedicated to a detailed physical investigation of the spectrophotometric properties of dusty high-redshift (U)LIRGs in an attempt to achieve a deeper understanding of the nature and mass assembly history of these sources.

Here we concentrate on a small sample of high-z (U)LIRGs with the currently richest suite of photometric and spectroscopic data, available for the first time at redshift $z \sim 2$, combining deep *Herschel* imaging (from both PACS and SPIRE) with ultra-deep IRS spectra from *Spitzer*. The data is analysed with a state-of-art chemo-spectro-photometric model (GRASIL: Silva et al. 1998) including a self-consistent treatment of dust absorption and reprocessing based on a full radiative transfer solution.

Our cosmological model assumes H_0=71 km s^{-1} Mpc^{-1}, Ω_Λ=0.73, Ω_M=0.27.

5.1 The (U)LIRG data sample

Our high-z (U)LIRGs have been selected from the sample of 48 IR-luminous galaxies in GOODS-S presented by Fadda et al.(2010 F10 hereafter) and described in detail in Section 4.4.1. It includes the faintest 24 μm sources observed with IRS ($S_{24} \sim 0.15 - 0.45$ mJy) in the two redshift bins ($0.76 - 1.05$ and $1.75 - 2.4$) and samples the major contributors to the cosmic infrared background at the most active epochs. At these redshifts, the 24 μm fluxes translate to infrared luminosities roughly in the ranges for LIRGs at $z \sim 1$ and ULIRGs at $z \sim 2$. This sample is therefore crudely luminosity selected (with the S_{24} limits corresponding to different luminosity ranges for the z∼ 1 LIRGs and z∼ 2 ULIRGs) and F10 did not apply any other selections.

These objects have been selected by F10 mostly using the photometric redshifts computed by Caputi et al. (2006) since only 50% and 10% of them had spectroscopic-z in the z∼ 1 and 2 bins, respectively. As emphasized by F10, except for having higher dust obscuration, these galaxies do not have extremely deviant properties in the rest-frame UV/optical compared to

galaxies selected at observed optical/near-IR band. Their observed optical/near-IR colors are very similar to those of extremely red galaxy (ERG) populations selected by large area K-band surveys.

In this paper we concentrate on galaxies powered by star formation. Therefore we excluded from our present analysis objects previously classified by F10 as AGN-dominated on the basis of several indicators such as broad and high ionization lines in optical spectra, lack of a 1.6 μm stellar bump in the SED, X-ray bright sources, low mid-IR 6.2 μm EW and optical morphology (see also Pozzi et al. 2012). We also excluded the sources falling outside the multiwavelength MUSIC catalogue (Santini et al., 2009), which is our reference for complementary optical/near-IR photometry. Among the 31 (U)LIRGs fulfilling these requirements, 10 are at $z \sim 1$ (all in the nominal LIRG regime) and 21, mostly ULIRGs, are at $z \sim 2$. The GOODS-S field was observed in 2010 with both *Herschel* (Pilbratt et al., 2010) SPIRE (Griffin et al., 2010) and PACS (Poglitsch et al., 2010), giving a total of six bands from 70 to 500 μm. SPIRE and PACS data are taken, respectively, from the Herschel Multi-tiered Extragalactic Survey (HerMES: Oliver et al. 2012) and the PACS Evolutionary Probe (PEP: Lutz et al. 2011) programs. Typical noise levels are ~ 1 mJy for PACS $70 - 160$ μm and ~ 6 mJy for SPIRE $250 - 500$ μm, including confusion.

5.2 Modeling the SEDs of high-z (U)LIRGs

Par.	Unit	Description	class	range
$\nu_{\rm Sch}$	$\rm Gyr^{-1}$	SF efficiency	SFH: Quiescent	$[0.3 - 2.0]$
$\tau_{\rm inf}$	Gyr	infall timescale	SFH: Quiescent	$[0.01 - 3.0]$
$\%M_{\rm b}$	—	% of gas mass involved in the burst at $t_{\rm burst}$ [1]	SFH: burst	$[0.1 - 15]$
$t_{\rm b}$	Myr	burst e-folding time	SFH: burst	$[10 - 80]$
$f_{\rm mol}$	—	fraction of gas in MC with respect to the diffuse comp.	basic	$[0.05 - 1.0]$
τ_1	—	MC optical depth at 1 μm	basic	$[5.0 - 108]$
$t_{\rm esc}$	Myr	escape time of newly born stars from their parent MCs	basic	$[1 - 90]$
β	—	sub-mm dust spectral slope	basic	$[1.5 - 2.0]$
$r_{\rm c}$	kpc	core radius	geometrical: King's profile	$[0.01 - 2.0]$

Table 5.1 Main GRASIL parameters and their range of values (see Silva et al. (1998) for a full description).

A physical characterization of the ULIRG phenomenon requires a multi-wavelength approach and a detailed treatment of the effects of dust. The spectro-photometric + radiative transfer code GRASIL (Silva et al., 1998, 2011) satisfies these requirements. It computes the SED of galaxies from far-UV to radio including a state-of-the-art treatment of dust

reprocessing. A detailed description of the code is given in Chapter 3, here we provide only a brief summary of its main features. It includes the radiative transfer effects of different dusty environments - star forming molecular clouds (MCs), diffuse dust (cirrus), dusty envelopes around AGB stars, and a geometrical distribution of stars and dust in a bulge-like (King profile) and/or a disk (double exponential) profile. In the following we adopt the simplest possible geometry, that is to say, a King's profile (i.e. a spherically symmetric profile) as it appears to be a reliable description of (U)LIRGs and in order to limit the number of free parameters. The accounting of the clumping of young stars and dust within the diffuse medium together with a realistic geometrical distribution for stars and dust gives rise to the age-dependent attenuation. The dust model consists of grains in thermal equilibrium with the radiation field, and small grains and PAH molecules fluctuating in temperature.

The input star formation histories are computed with the chemical evolution code described in Section 3.2 which provides the evolution of the SFR, M_{gas} and metallicity, assuming an IMF, a SF law $SFR(t)=\nu_{Sch} \cdot M_{gas}(t)^k + f(t)$ (i.e. a Schmidt-type SF with efficiency ν_{Sch}, and a superimposed analytical term to represent transient bursts possibly related to a galactic merger, and an exponential infall of gas ($dM_{inf}/dt \propto \exp(-t/\tau_{inf})$). A very short infall timescale, τ_{inf}, can be used to have a so called 'close box' chemical evolution model, which ensures that the gas going to form the galaxy is all available at the beginning. This short value of the infall timescale allows us to accrete enough mass in stars of different ages to reproduce the shape of the UV-opt-NIR SED. In our library of SFHs we consider a wide range of values for τ_{inf} from very low (0.01 Gyr) to 2-3 Gyr the latter producing longer phases of gas accretion. Here we adopt k=1, f(t) exponential, and the Salpeter IMF which is the default choice for the chemical evolution code. When comparing with other studies we converted the Salpeter IMF to the Chabrier one dividing by 1.7. Our reference library of SSPs is from Bressan et al. (1998, 2002), which directly include the effects of dusty envelopes around AGB stars.

We have used a large and fine grid of theoretical SEDs, generated by CHE_EVO+GRASIL. Our SEDs span a wide range of input parameters: star formation history; obscuration times; dust opacities etc (see Tab. 5.1). This grid is first used to explore the parameter space. Then an object-by-object analysis of the (U)LIRG SEDs was performed in order to refine the fit. We reproduced the observed broadband SEDs of our 31 (U)LIRGs, including a fit to the IRS spectra, which are useful to constrain the physical state of the warm ISM and the PAH intensity.

Figure 5.1 shows the median best-fit SFHs for the 10 $z \sim 1$ LIRGs (top) and 21 $z \sim 2$ (U)LIRGs (centre and bottom). The insets report the mass in living stars and the mass of interstellar gas.

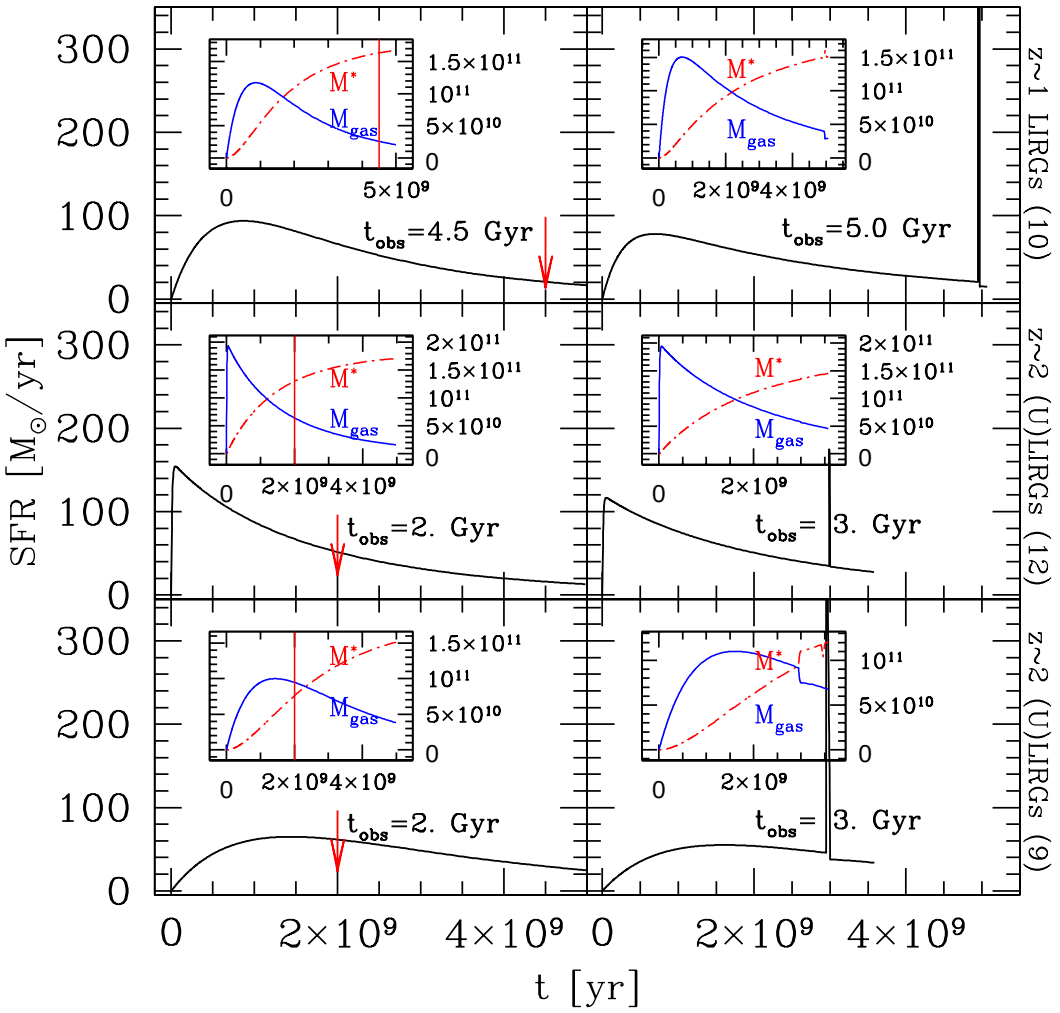

Figure 5.1 Median SFHs of $z \sim 1$ (top) and $z \sim 2$ (centre and bottom) (U)LIRGs modeled with *continuous* SF (left) or a *starburst* (right). The insets report the time evolution of the mass in living stars and the mass of interstellar gas. The median values for $\tau_{\rm inf}$ are 0.5 and 0.28 Gyr in the top-left and top-right panels respectively while they are much shorter and equal to 10 Myr for the centre panels. For the nine z∼2 (U)LIRGs requiring the SFHs represented in the bottom panels the median $\tau_{\rm inf}$ are 1 Gyr for both.

As discussed later, the fitting process appears to constrain several of the parameters ruling the SFH, in particular $\tau_{\rm inf}$ and $\nu_{\rm Sch}$. Small values for $\tau_{\rm inf}$ and high values for $\nu_{\rm Sch}$, i.e. an early fast and efficient SF phase as in the centre panels, were required for 16/31 objects, 4 LIRGs and 12 z∼2 (U)LIRGs, showing the strongest stellar bump in the rest-frame near-IR (as, for example, the ones in Fig. 5.2 top-center and bottom-left,right).

Smoother SFHs with longer $\tau_{\rm inf}$ ($\tau_{\rm inf} \gtrsim 0.2$ Gyr and $\tau_{\rm inf} \gtrsim 1$ Gyr) are instead required for the z∼1 LIRGs and 9 z∼2 (U)LIRGs shown in the top and bottom panels, respectively. These galaxies present almost 'flat' rest-frame NIR bands and higher UV fluxes. Figure 5.2 summarizes the typical best-fits SEDs of our sample showing as an example three z ∼1

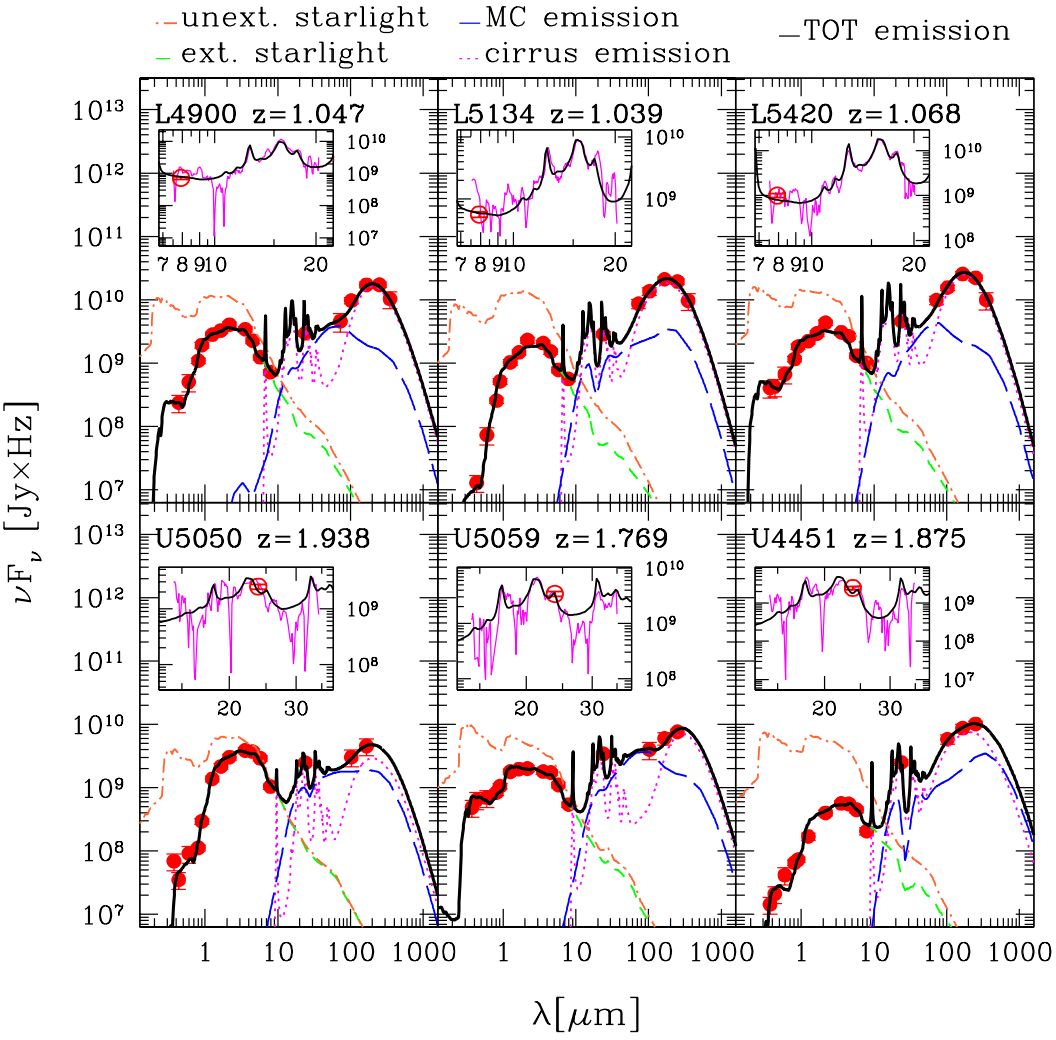

Figure 5.2 Typical GRASIL best-fits (solid black line) to the observed SED (red circles) of three $z \sim 1$ (top) and $z \sim 2$ (bottom) (U)LIRGs. IRS spectra appear in the inset window (magenta line). The color-coded lines represent the unextinguished starlight (orange dot-dashed), extinguished starlight (green dashed), cirrus emission (magenta dotted) and MC emission (blue long dashed).

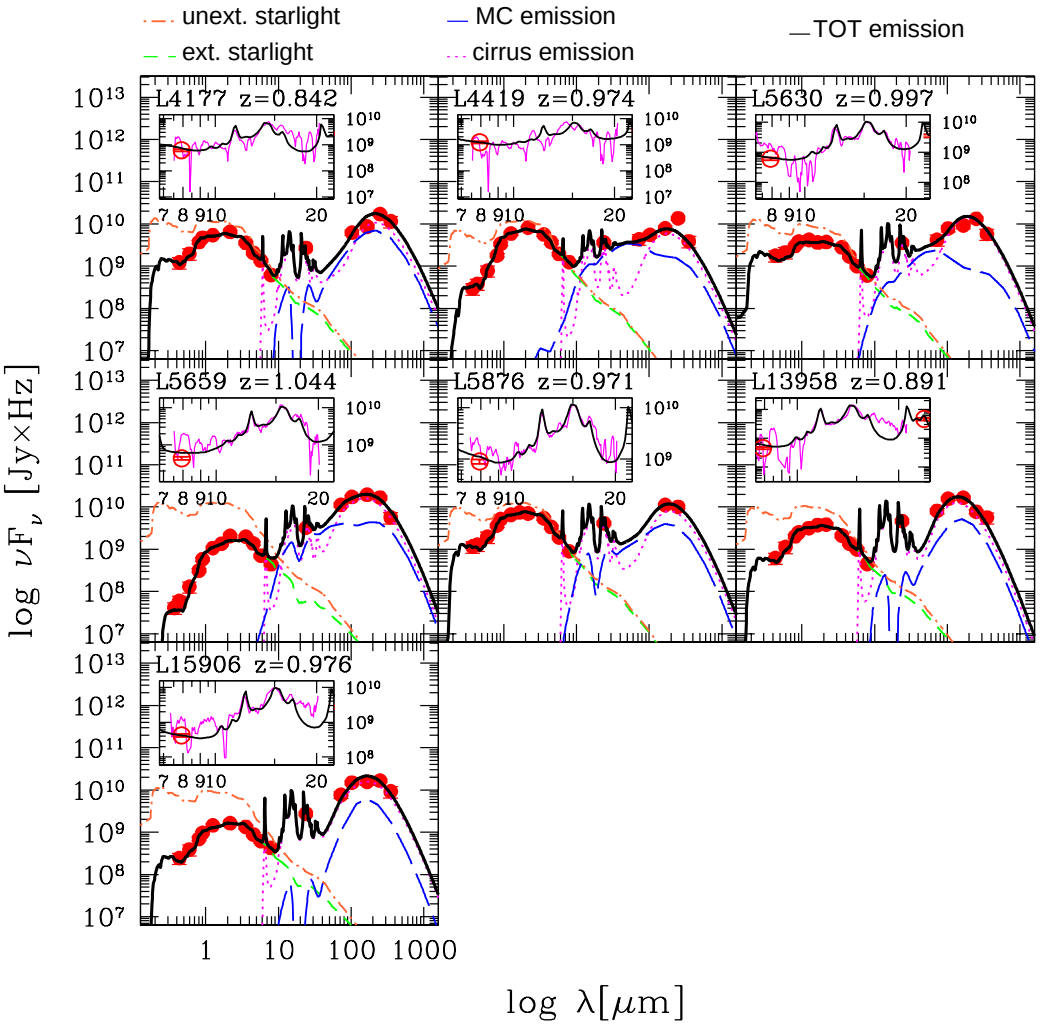

Figure 5.3 GRASIL best-fits (solid black line) to the observed SED (red circles) of $z \sim 1$ LIRGs. IRS spectra appear in the inset window (magenta line). The color-coded lines represent the unextinguished starlight (orange dot-dashed), extinguished starlight (green dashed), cirrus emission (magenta dotted) and MC emission (blue long dashed).

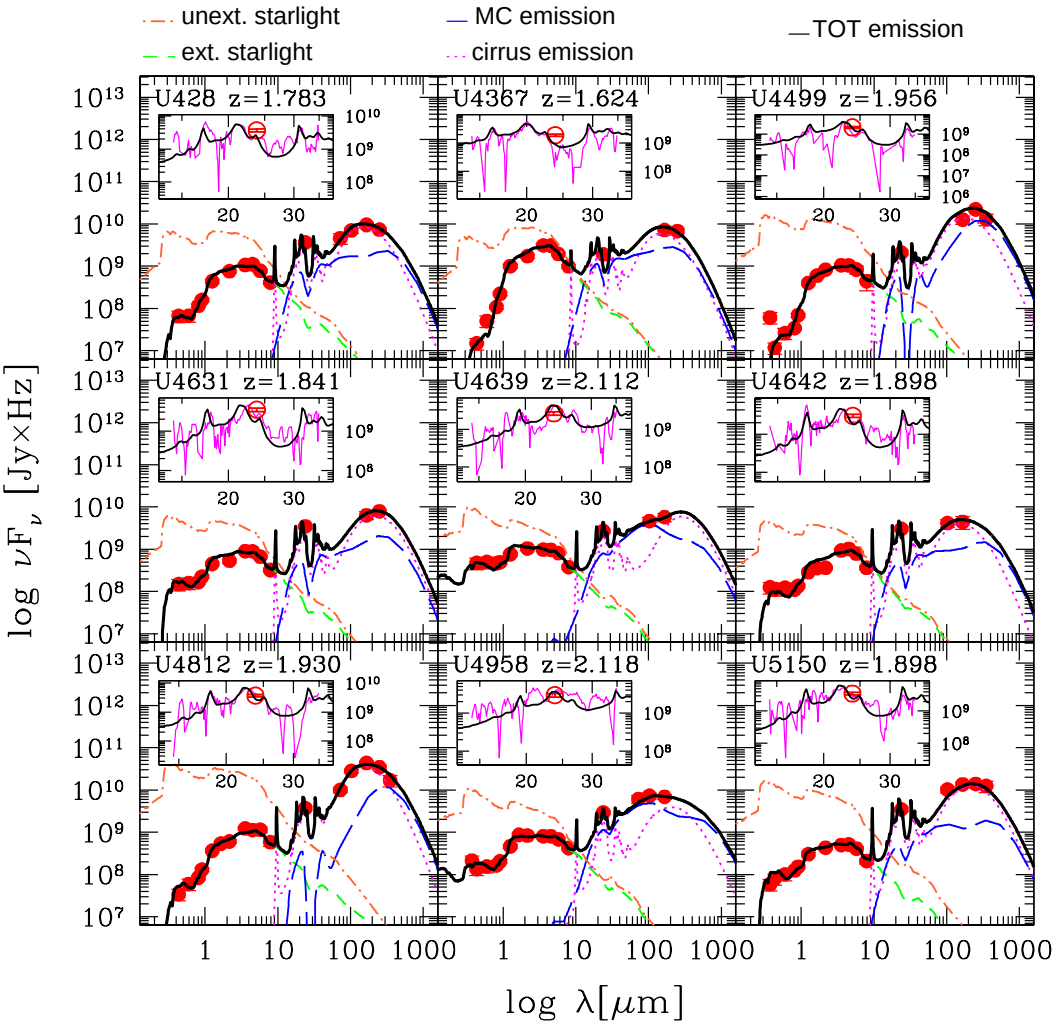

Figure 5.4 GRASIL best-fits (solid black line) to the observed SED (red circles) of $z \sim 2$ (U)LIRGs. IRS spectra appear in the inset window (magenta line). The color-coded lines represent the unextinguished starlight (orange dot-dashed), extinguished starlight (green dashed), cirrus emission (magenta dotted) and MC emission (blue long dashed).

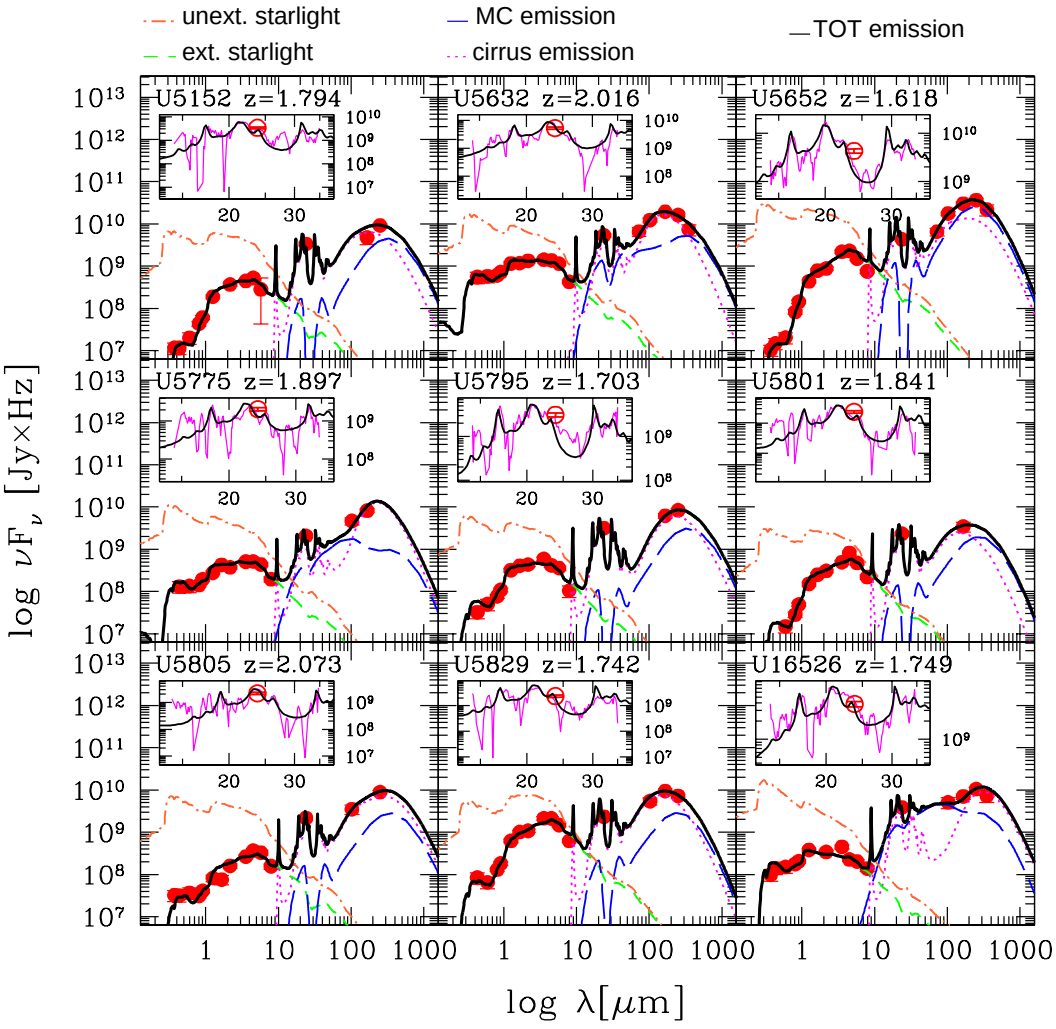

Figure 5.5 GRASIL best-fits (solid black line) to the observed SED (red circles) of $z \sim 2$ (U)LIRGs. IRS spectra appear in the inset window (magenta line). The color-coded lines represent the unextinguished starlight (orange dot-dashed), extinguished starlight (green dashed), cirrus emission (magenta dotted) and MC emission (blue long dashed).

ID	z	$L_{\rm IR}$ [L/L$_\odot$]	log$M^\star_{\rm GRASIL}$ [M$_\odot$]	log$M^\star_{\rm HYPERZ}$ [M$_\odot$]	log$M_{\rm dust}$ [M$_\odot$]	Av GRASIL	Av HYPERZ	log$SFR_{\rm K}$ [M$_\odot$/yr]	logSFR_{10} [M$_\odot$/yr]	logSFR_{100} [M$_\odot$/yr]
28-L4177	0.842	2.50E11	10.94	10.95	8.28	0.93	0.20	1.40	1.18	1.19
29-L4419	0.974	2.27E11	11.26	11.27	8.13	0.73	1.20	1.36	1.06	1.07
30-L4900	1.047	5.00E11	11.22	11.06	8.51	1.56	1.00	1.70	1.33	1.34
31-L5134	1.039	5.71E11	11.32	10.96	8.25	2.76	1.40	1.76	1.21	1.23
33-L5420	1.068	7.73E11	11.22	10.94	8.93	1.88	1.40	1.89	1.49	1.50
35-L5630	0.997	3.59E11	10.85	10.76	8.6	1.03	0.40	1.55	1.29	1.30
36-L5659	1.044	5.98E11	11.21	10.82	8.69	2.75	1.40	1.78	1.39	1.40
37-L5876	0.971	2.61E11	11.22	11.19	8.43	0.72	0.40	1.42	1.19	1.20
44-L13958	0.891	2.79E11	10.82	10.77	8.0	1.32	0.20	1.45	1.11	1.12
47-L15906	0.976	4.43E11	10.9	10.48	8.36	2.25	1.20	1.65	1.26	1.27
$\bar{x} \pm \sigma$	0.98 ± 0.07	(4.26±1.73)10^{11}	11.10 ± 0.18	10.92 ± 0.22	8.42 ± 0.26	1.59 ± 0.74	0.88 ± 0.49	1.59 ± 0.18	1.25 ± 0.12	1.26 ± 0.12
ID	z	$L_{\rm IR}$ [L/L$_\odot$]	log$M^\star_{\rm GRASIL}$ [M$_\odot$]	log$M^\star_{\rm HYPERZ}$ [M$_\odot$]	log$M_{\rm dust}$ [M$_\odot$]	Av GRASIL	Av HYPERZ	log$SFR_{\rm K}$ [M$_\odot$/yr]	logSFR_{10} [M$_\odot$/yr]	logSFR_{100} [M$_\odot$/yr]
1-U428	1.783	1.13E12	11.39	10.89	8.91	2.42	1.80	2.05	1.69	1.70
2-U4367	1.624	7.52E11	11.49	11.42	8.4	1.81	1.60	1.88	1.47	1.49
3-U4451	1.875	1.40E12	11.31	10.63	8.95	3.11	1.80	2.15	1.78	1.79
4-U4499	1.956	3.02E12	11.69	11.11	9.49	3.28	1.40	2.48	2.14	2.15
5-U4631	1.841	9.21E11	11.2	10.76	8.9	2.05	1.20	1.96	1.65	1.66
6-U4639	2.112	1.54E12	11.08	10.86	9.18	1.39	0.80	2.19	1.87	1.88
7-U4642	1.898	7.22E11	11.1	10.73	8.8	2.12	1.40	1.86	1.57	1.59
8-U4812	1.93	5.00E12	11.61	11.02	9.39	3.76	2.00	2.70	2.20	2.21
10-U4958	2.118	1.63E12	11.12	11.00	9.21	1.9	0.60	2.21	1.91	1.92
11-U5050	1.938	7.28E11	11.54	11.68	8.45	0.97	1.60	1.86	1.57	1.58
12-U5059	1.769	1.07E12	11.11	11.04	9.08	1.12	1.00	2.03	1.77	1.78
13-U5150	1.898	1.80E12	11.17	10.62	9.09	2.87	1.40	2.25	1.87	1.87
14-U5152	1.794	1.13E12	11.23	10.62	8.87	3.24	2.00	2.05	1.68	1.70
16-U5632	2.016	2.78E12	11.26	11.00	9.18	1.88	0.80	2.44	2.13	2.14
17-U5652	1.618	2.96E12	11.58	11.14	9.4	3.68	2.60	2.47	2.18	2.19
18-U5775	1.897	1.40E12	11.0	10.54	8.93	2.67	1.00	2.15	1.88	1.89
19-U5795	1.703	7.76E11	10.9	10.59	9.07	2.45	0.60	1.89	1.51	1.52
20-U5801	1.841	4.78E11	10.97	10.71	8.61	2.54	2.00	1.68	1.37	1.38
21-U5805	2.073	1.55E12	11.23	10.46	9.18	3.66	1.20	2.19	1.82	1.83
22-U5829	1.742	9.48E11	11.52	11.22	8.63	2.34	1.20	1.98	1.58	1.60
24-U16526	1.749	1.37E12	10.35	10.24	9.13	2.6	0.80	2.14	1.90	1.88
$\bar{x} \pm \sigma$	1.86 ± 0.14	(1.58±1.04)10^{12}	11.23 ± 0.29	10.87 ± 0.33	9.00 ± 0.29	2.47 ± 0.79	1.37 ± 0.52	2.12 ± 0.24	1.79 ± 0.23	1.80 ± 0.23

Table 5.2 Estimated and average values of the main physical parameters, $M_\star$, A_V and SFR, derived from the GRASIL best-fits to the 31 (U)LIRGs, compared with values based on HYPERZ.

LIRGs (top) and three z ∼2 (U)LIRGs (bottom). The best-fit SEDs of all our galaxies are shown in Figures 5.3 to 5.5.

5.3 Evaluating the Star Formation Rates and SFH

Given the detailed shape of the broadband SED, our physical analysis seems to be able not only to give an estimate of the instantaneous SFR but also to give important hints about the main parameters ruling the source's past SFH, i.e. $\tau_{\rm inf}$ and $\nu_{\rm Sch}$ as shown in fig. 5.1.

We have investigated here both SF models with and without a starburst on top of the Schmidt-type part of the SF law (see fig. 5.1). We hereafter refer to these as the *starburst* and *continuous* models, respectively. For the majority of our (U)LIRGs, a suitable calibration of the $\tau_{\rm inf}$ and $\nu_{\rm Sch}$ allowed us to obtain good fits to the observed SEDs with the continuous models. Figure 5.6 (left) compares the best-fit χ^2_ν relative to these two SFHs considered for our high-z (U)LIRGs.

If we consider first the more extreme cases, i.e., our $z \sim 2$ ULIRGs, for 5 out of 21 sources (red filled circles in Fig. 5.6), an application of the F-test to our χ^2 analysis requires the presence of a moderate *starburst*. Even in these five objects, however, the gas mass involved in the SB amounts to only a small fraction of the galactic mass, $\lesssim 4\%$, and all of them are observed just at the end of the burst event. A peak-phase SF usually produces intense far-IR spectra, with MC emission dominating the MIR and FIR spectrum. Conversely a more continuous SFH generates colder far-IR spectra with *cirrus* emission in the sub-mm and larger PAH contributions around 10 μm. Two examples are shown in Fig. 5.8. This figure shows the typical contributions to the composite SED of a highly star forming and gradually evolving galaxy (left), where the cirrus emission dominates the IR/sub-mm wavelengths, and a pure starburst (right) whose IR fluxes are dominated by MC emission. Both galaxies are taken from the sample of high-z PACS-detected off-main-sequence sources (the so called "outliers") of R11 and are modeled with GRASIL. This sample includes all the objects (∼ 50) with sSFR a factor of ∼ 8-10 higher than the one of MS galaxies. The ∼ 12 galaxies shown as magenta stars in Fig. 5.6 represent the most extreme cases with the highest SFRs. For the remaining 16 sources of our sample at $z \sim 2$, a continuous model gives a perfect account of the data, although without excluding a small starburst contribution (black filled circles in Fig. 5.6).

As illustrated in Fig. 5.1, in most of our objects the only significant effect of introducing a SB event is to slightly increase the age at which the galaxy is observed, $t_{\rm obs}$, changing from 4.5 to 5 and from 2 to 3 Gyr from left to right, for $z \sim 1$ and $z \sim 2$ (U)LIRG respectively.

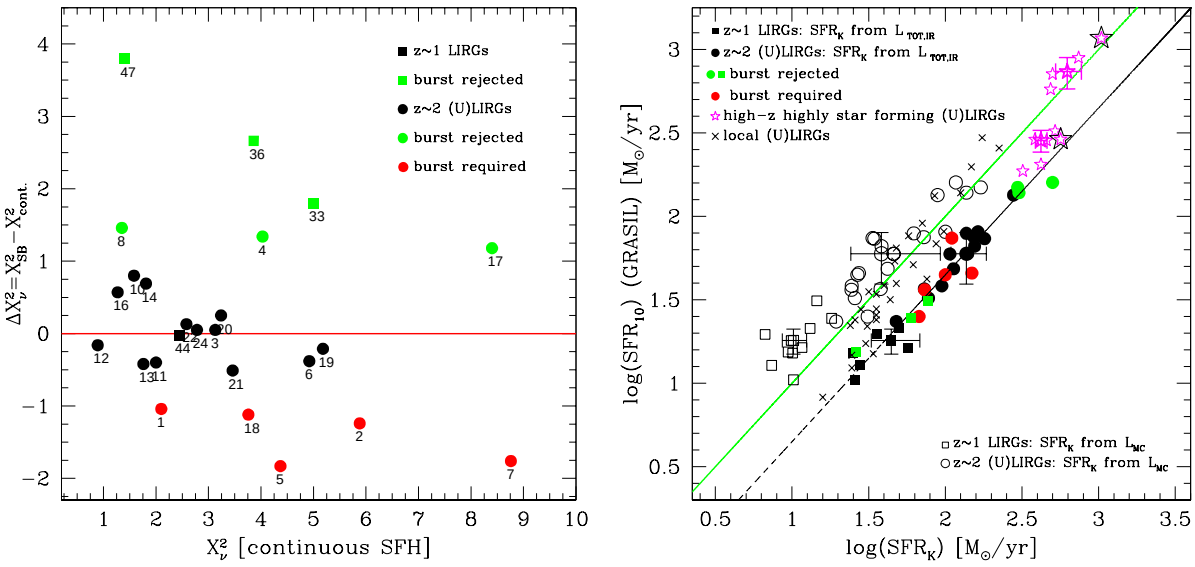

Figure 5.6 **Left**: Comparison between the best-fit χ^2_ν relative to the two different prescriptions for the SFH (*continuous* vs *starburst*) for our high-z (U)LIRGs. For 4/10 $z \sim 1$ LIRGs (shown as squares) a starburst SFH gave 'acceptable' best-fits. For the remaining 6 LIRGs a starbursting SFH was rejected with high-confidence ($\Delta\chi^2_\nu > 1$). Label numbers indicate the object IDs. **Right**: Comparison of our GRASIL-estimated SFR_{10} with the SFR derived from the 8 to 1000 μm luminosity L_{IR} using the Kennicutt (1998) calibration, SFR_K. Filled and open black squares and circles represent the different SFR_K derived by considering the total L_{IR} (cirrus + star forming MCs) and the L_{MC} (MC only), for our $z \sim 1$ and $z \sim 2$ (U)LIRGs respectively. Green filled squares and circles are $z \sim 1$ and $z \sim 2$ (U)LIRGs for which a burst is not required, while red filled circles are $z \sim 2$ ULIRGs requiring the presence of a moderate burst from an application of the F-test. Crosses are local (U)LIRGs while magenta stars are high-SFR galaxies discussed by Rodighiero et al.(2011, R11 hereafter). Datapoints with errorbars are median values with associated semi-interquartile ranges.

The effect of an ongoing SB on the galaxy SED is mimicked, in a continuous SFH, by considering the epoch of observation to be closer to the peak phase of SF.

For the $z \sim 1$ LIRGs, all objects are consistent, on the basis of the F-test application, with a continuous SFH.

Table 5.2 shows the main best-fit physical parameters derived from our analysis and their mean values and standard deviations. We report here three different estimates of SFR, SFR_K representing the SFR derived from the 8 to 1000 μm luminosity L_{IR} using the Kennicutt(1998, K98 hereafter) calibration, and our best-fit SFRs averaged over the last 10 (SFR_{10}) and 100 (SFR_{100}) Myr. Fig. 5.6 (right) shows a comparison of our SFR_{10} with SFR_K. The latter is defined in the limit of complete dust obscuration and dust heating fully dominated by young stars (see K98).

Indeed it assumes that the L_{bol} of a constant SF lasting 100 Myr is totally emitted in the IR (K98; Leitherer & Heckman 1995, LH95 hereafter). For a constant SF, the L_{bol} after the first 10 Myr evolves relatively slowly because the rate of birth and death of the most massive stars (with lifetimes $\lesssim$ 10 Myr and dominating the L_{bol}) reaches a steady state (see Fig. 2 and 8 of LH95). The K98 SFR/L_{FIR} calibration adopts the mean bolometric luminosity for a 10-100 Myr continuous SF, solar abundance, Salpeter IMF (which we have rescaled to the Chabrier one) of the starburst synthesis models of LH95, and assumes that L_{FIR}=L_{bol}. Therefore we consider SFR_{10} as the best indicator of the current SFR to be compared to this calibration.

As apparent in Fig. 5.6 (right), our inferred SFR_{10} for these high-z (U)LIRGs are systematically lower than those based on the K98 calibration (filled circles and squares). This is due to the significant contribution of cirrus emission to the total L_{IR} ($\sim$ 73% and $\sim$ 66% for z$\sim$ 1 and z$\sim$ 2 (U)LIRGs respectively) whose heating source includes already evolved stellar populations (ages older than t_{esc}). As cautioned by K98, if all of this energy is ascribed, through this calibration, to the recent SF, the SFR is overestimated. Instead, given the characteristics of the K98 calibration, a fairer comparison between SFR_{10} and SFR_K, when an ongoing starburst is not clearly dominating, is to assign to the latter the L_{IR} by MC only (empty cirles and squares in Fig 5.6 (right)). In this way most of the points spread around and above the K98 line. The spread has to be ascribed to a range of different and non constant SFR and SFH, and t_{esc} (ranging between a minimum of 3 Myr and a maximum of 90 Myr, with median values corresponding to 14 and 6 Myr for z$\sim$1 and z$\sim$2 (U)LIRGs respectively), i.e. to a spread of stellar ages contributing to L_{IR}. Averaging out our results for LIRGs and ULIRGs we find the following calibration between the total IR luminosity and SFR:

$$SFR[M_\odot/yr] \simeq (5.8 \pm 0.4) \times 10^{-11}\ L_{IR}/L_\odot, \tag{5.1}$$

approximately a factor 1.7–2.5 lower than the classical Kennicutt relation, both scaled to a Chabrier IMF.

In Fig. 5.6 (right) we also plot the SFR_{10} vs SFR_K (from total L_{IR}) derived with the same physical analysis, for a sample of local (U)LIRGs (crosses) and some of the most highly star forming objects of Rodighiero et al. (2011) (magenta stars).

The galaxies shown in this plot (excluding the open points which are the same galaxies as the filled ones, but considering only the MC contribution) seem to define a broad and continuous distribution contained between two correlation lines: an upper envelope dominated by objects with an ongoing burst of SF in MCs as for several local (U)LIRGs and peak-phase SBs, and a lower one mostly populated by secularly evolving galaxies and late starbursts

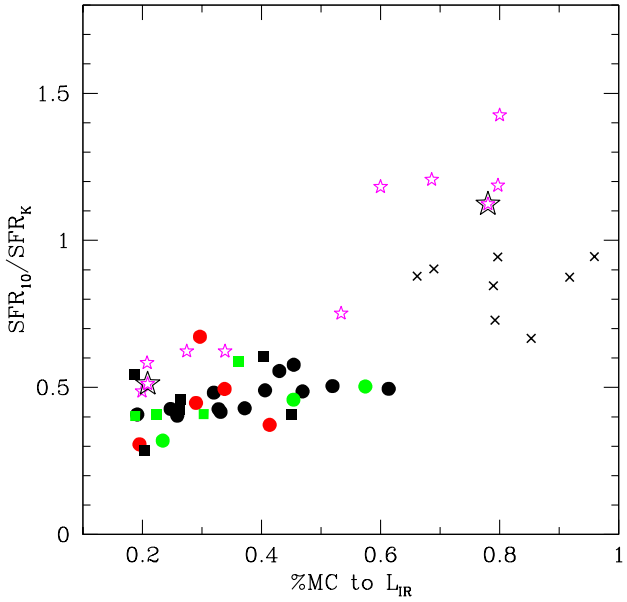

Figure 5.7 Correlation between the SFR_{10}/SFR_K ratio and the fractional contribution of MC emission to the total L_{IR}. Points are the same as in fig. 5.6. Here we show the eight local (U)LIRGs for which the fractional contributions of MC and cirrus emission have been already computed by us. Black stars are the two representative cases of R11 off-MS star forming galaxies shown in fig. 5.8. We can see here that on average galaxies with higher SFR_{10}/SFR_K ratios have total IR luminosity mostly contributed by MC emission with all of our (U)LIRGs lying on the lower relation. Of course the scatter we see in this figure as well as in fig. 5.6 is due to the wide range of ages of stellar populations.

(as the 5/21 objects of our sample discussed above), with substantial contributions of cirrus emission to the total L_{IR}.

Indeed the relative contributions of MC emission to the total L_{IR} for these sources are shown in Figure 5.7 as a function of the SFR_{10}/SFR_K ratio: galaxies falling in the lower envelope, with low values of $SFR_{10}/SFR_K \simeq 0.5$, have small contributions by MC, while those with higher SFR_{10}/SFR_K values are dominated by MC emission.

An illustration of this is reported in Fig. 5.8 for the two PACS-selected sources of R11: the one dominated by MC corresponds to the starred object in the upper figure, while that one dominated by cirrus emission falls in the lower part and shows minimal MC contribution. All these aspects will be further discussed in a forthcoming paper extending the sample to all the outliers analysed in R11 and all the local (U)LIRGs of Vega et al. (2008).

A bimodality in the star formation efficiency (SFE=SFR/M_{gas}) and Kennicutt-Schmidt relation ($\Sigma_{SFR} \propto \Sigma^N_{H_2}$) of local and high-$z$ mergers and non- or weakly-interacting star forming galaxies based on CO measurements, has been recently suggested by Genzel et al. (2010) and Daddi et al. (2010a). Our upper and lower envelopes in Fig. 3, within which all

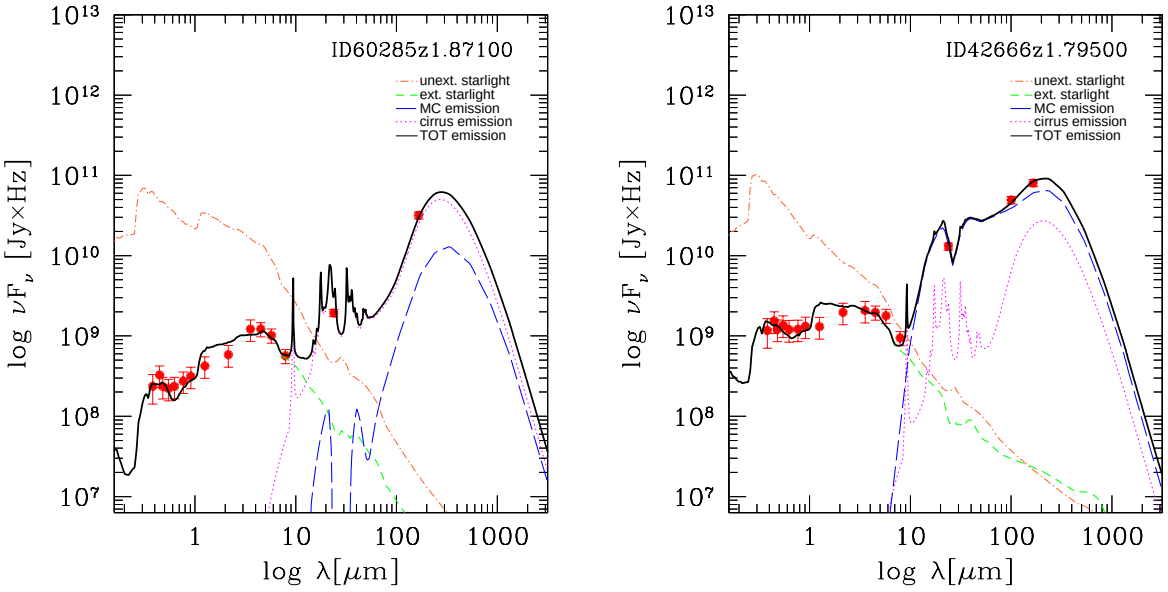

Figure 5.8 Figure shows two representative cases of the R11 outliers defined in section 5.3. Left: the galaxy is modeled as gradually evolving spheroid and have total L_{IR} dominated by cirrus emission. Right: the galaxy is dominated by an ongoing burst of star formation in MCs. While the galaxy on the right has SFR in agreement with the one estimated from L_{IR} using the Kennicutt calibration, the one on the left follows our calibration.

our sources are contained, may correspond to these two sequences. Further investigation with larger and unbiased sample of galaxies will help in this sense. The latter would be explained by the fact that, while locally galaxies with IR luminosities exceeding 10^{12} $L_{\odot}$ are predominantly associated with merging events (e.g. Dasyra et al. 2006), at high-z these high-IR luminosities may be achieved mostly via cold gas accretion (Powell et al., 2011). Our study confirms that high-z (U)LIRGs are more likely up-scaled versions of normal galaxies rather than equivalents of local (U)LIRGs in terms of the mode of SF (e.g. Rujopakarn et al. 2011, Symeonidis et al. 2009).

With our current assumptions (see § 5.2), all our mid-IR selected galaxies appear to include massive populations of old (> 1 Gyr) stars and, at the same time, to host a moderate ongoing activity of SF ($SFR_{10} \leq 100$ $M_{\odot}$/yr, cf. Fig. 5.6 (right)). The bulk of stars appear to have been formed a few Gyr before the observation in essentially all cases. Average estimates can be inferred from Fig 5.1: for the z$\sim$ 2 (U)LIRGs having the SFH shown in the central panel of Fig. 5.1, about 66-80% of the stellar mass has formed after $\sim$ 1 Gyr from the beginning of their star formation activity, proportionally higher at higher SF efficiency. For the z$\sim$2 (U)LIRGs presenting, instead, more regular SFH, as those shown in the bottom panel of Fig. 5.6, about 30-43% of stellar mass is formed after 1 Gyr. Finally for the LIRGs, on average, $\sim$ 28% of the stellar mass has already been formed after the first 1 Gyr.

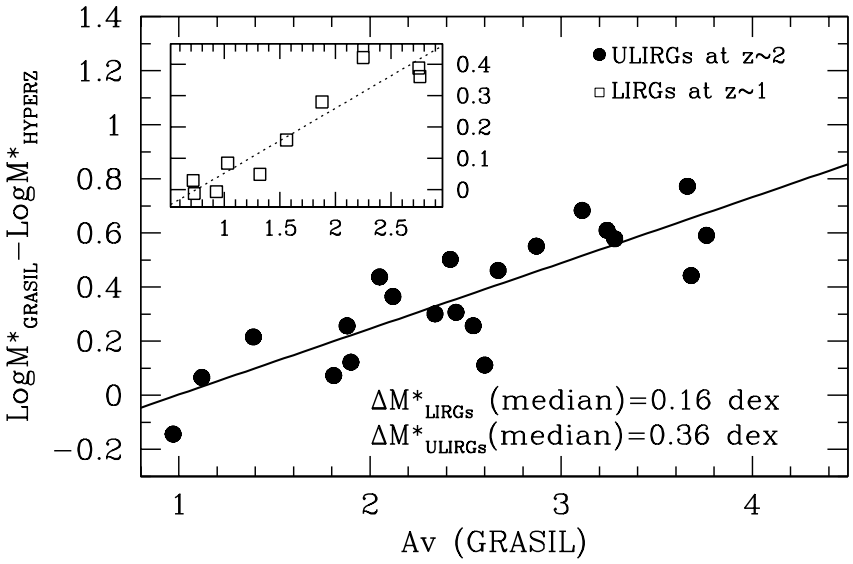

Figure 5.9 Correlation between the difference in stellar mass estimates based on the GRASIL and HYPERZ codes and the average extinction A_V. In the inset the LIRGs values are shown.

5.4 Stellar mass determinations

Another key physical parameter of high-redshift galaxies is the stellar mass $M_\star$. Our best-fit estimates appear in Table 5.2 where we compare our best-fit $M_\star$ to those derived by F10. They fit BC03 models to the optical-to-8 μm SED with the HYPERZ code (Bolzonella et al., 2000) allowing different SFHs, from a constant star formation to an exponentially declining SF with different e-folding times (τ-model), and assuming the Calzetti et al. (2000) attenuation law to account for dust extinction effects. The so called τ-model is essentially an analytical approximation of the Schmidt's law $\psi(t) \propto \exp(-t/\tau)$, with τ=1/$\nu_{\rm Sch}$. As shown in Tab. 5.2, GRASIL $M_\star$ are systematically larger than those based on HYPERZ. This discrepancy is higher for the ULIRGs at $z \sim 2$, for which it reaches a factor of ~ 6 in $M_\star$ (median factor 2.5), while it is lower for the $z \sim 1$ LIRGs whose median factor is 1.4.

5.4.1 Origin of the stellar mass discrepancy

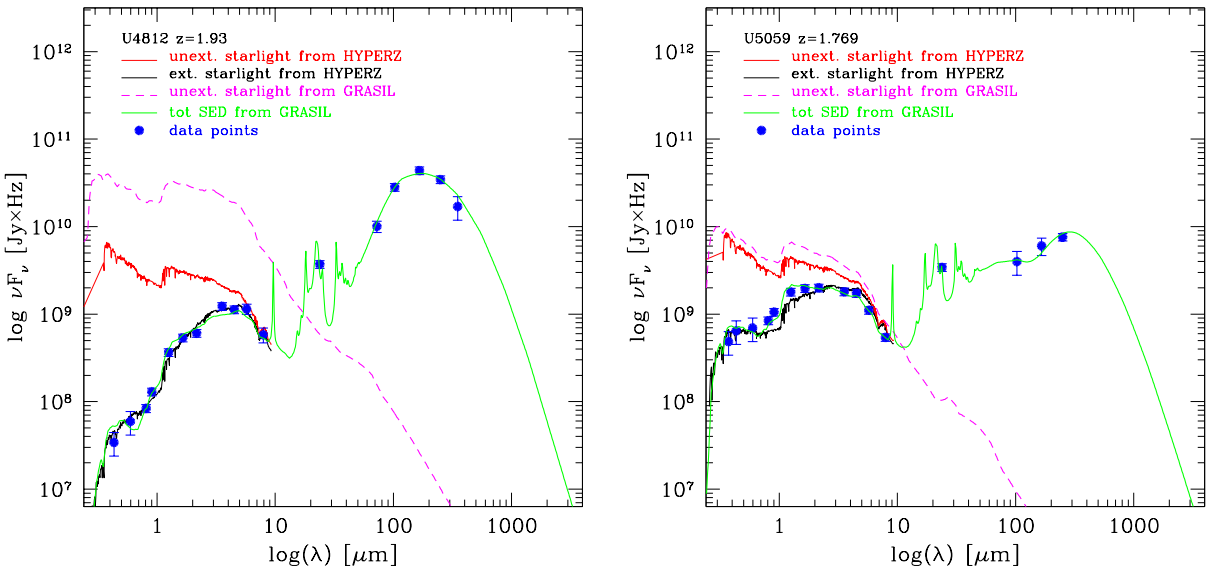

Figure 5.10 **Left**:The L_{bol} estimated from the UV to FIR fit by GRASIL is almost a factor of 4-5 higher than the L_{bol} given by the optical only fit, at least for those cases were we found large differences in stellar mass estimates. For this galaxy we estimate a $M_\star \sim 4$ times higher. **Right**: Here the effect is smaller. The average extinctions are similar and also the bolometric luminosities. For details see tab. 5.2.

Michałowski et al.(2012, M12 hereafter) found the adopted specific SFH (double component versus τ-model) to be the major factor affecting the derived stellar masses of high-z and highly star forming SMGs, accounting for a factor of ~ 2.5 in $M_\star$. We have investigated the possible origin of the larger differences in our $M_\star$ estimates by considering different models for the SFH, continuous vs starburst. In both cases we found similar $M_\star$ discrepancies with respect to the HYPERZ ones. As discussed in detail in M12, the different evoutionary models may also contribute to a factor 2.5 difference in $M_\star$ estimates when a τ-model is considered. We tested this hypothesis by modeling our (U)LIRGs with similar SFHs (tau-models), age, metallicity and A_V plus Calzetti attenuation law and by fitting the optical data alone as in the HYPERZ code. By adopting similar prescriptions we found our $M_\star$ to be in full agreement, (i.e. within 10%) with the HYPERZ estimates. Taking into account the differences in the specific parameters ruling the SFH (e.g. τ) and on the SSP libraries used (BC03 and GRASIL SSPs rely on the same Padova isochrones but the latter includes dusty envelopes around AGB stars) we can conclude that the different SFH (i.e. different τ) and SSPs cannot account for the larger discrepancies, we find among the more obscured ULIRGs at $z \sim 2$; for these the dominant factor is the dust exinction. Of course the effect of the different SFH on the stellar mass estimates becomes larger when comparing τ-models with SFH characterized by recent (last 50 Myr) burst of star formation, as shown by M12. All these galaxies are, however, normal star forming galaxies and the only five objects requiring the burst on top of the Schimdt-type SF are all observed as late-SBs.

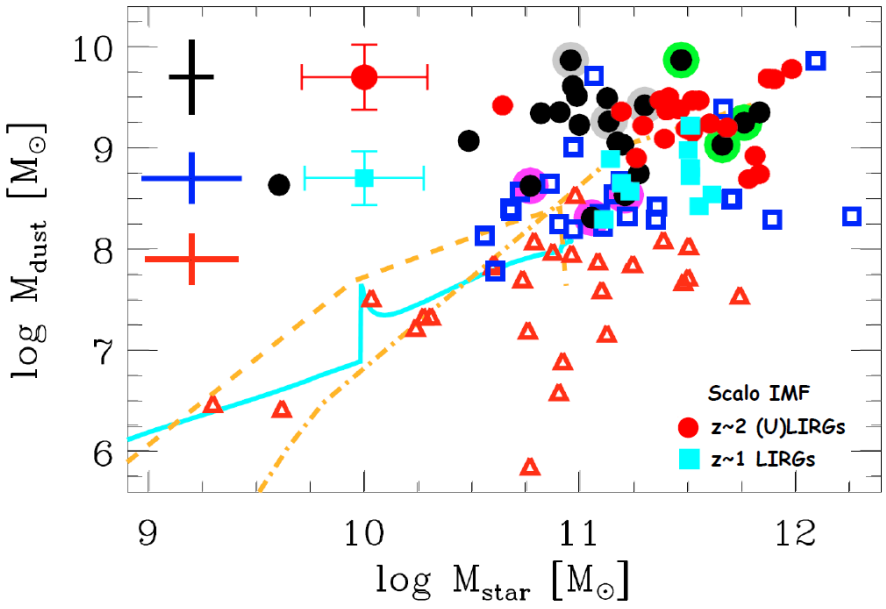

Figure 5.11 $M_\star$ vs M_{dust} (from Santini et al. (2010)). Blue squares are local ULIRGs, red triangles refer to local spirals and black circles correspond to high-z SMGs. Red filled circles and cyan filled squares represent, respectively, our z$\sim$ 2 and z$\sim$ 1 (U)LIRGs whose stellar and dust masses have been rescaled to the Scalo IMF adopted by Santini et al. Median 1σ error bars are shown on the left. Solid cyan and dashed (dot-dashed) orange lines are the predictions of Calura et al. (2008) model for spirals and proto-ellipticals with mass of 10^{11} (10^{12}) $M_\odot$.

5.4.2 Extinction as the main source of mass discrepancy

Using the GRASIL best-fits, we estimate the average total extinction in the rest-frame V-band, A_V, from the ratio of the extinguished (L_V) to the unextinguished starlight (L_V^0):

$$A_V = -2.5 log(L_V/L_V^0) \tag{5.2}$$

The average A_V values, reported in Table 5.2, are systematically higher for the $z \sim 2$ than for the $z \sim 1$ objects. These differences are traceable to the different evolutionary stages at which the two classes of sources are observed. Our best-fit A_V are also systematically higher than those obtained with HYPERZ using the Calzetti approximation in combination with the foreground screen of dust, expecially for the $z \sim 2$ ULIRGs for which the median A_V is 2.45 and 1.40 for the two cases, respectively.

As shown in fig. 5.9 we find, for our (U)LIRGs, a tight correlation ($r \sim 0.86$ for $z \sim 2$ (U)LIRGs and $r \sim 0.96$ for $z \sim 1$ LIRGs) between the difference in the $M_\star$ estimates based on GRASIL and HYPERZ solutions and the average extinction A_V, with the difference increasing as a function of the extinction A_V. This clarifies why for ULIRGs, with higher A_V on average, we see the largest stellar mass discrepancies. The stellar mass missed by

fitting optical data alone is hidden in dust. In concurrence with our results, Wuyts et al. (2009b) also found that the mass underestimate is more severe during the dusty, peak SF phase.

It is worth noting that the availability of the full wavelength coverage also plays a crucial role in constraining the models. In fact the first basic constraint that is provided by the availability of UV-to-sub-mm data is the total L_{bol} of the galaxy, which otherwise should be guessed. This is easier when the optical contains most of the total energy. The shape of the optical-UV SED indicates some level of dust, but there may be stellar populations totally obscured by dust (typically the newly born), and even less young stellar populations may be partly extinguished. Without a constraint on the optical-UV extinction, i.e. on how much is re-emitted in the IR, it is difficult to quantify how much stellar light (therefore mass) is missing from the optical. Two examples are given in Fig. 5.10 which compares the total L_{bol} inferred from the unextinguished starlight component computed with HYPERZ (in red) to that one computed with GRASIL (magenta long-dashed line) and to the total L_{IR} inferred from the GRASIL best-fits. The two objects shown in this figure represent two extreme cases, the one on the left corresponding to the largest discrepancy in stellar mass ($\sim$ a factor of 4) and the other one on the right characterized by the lowest stellar mass discrepancy ($\sim$ a factor of 1.17). Of course, due to energy balance, the energy of the pure stellar SED must be equal to that of the processed SED which fit the data. Therefore, the IR part of the SED is a further fundamental constraint when it contains an important fraction of the energy emitted by stellar populations.

Figure 5.11 shows that our stellar and dust masses are consistent with published estimates for high-z SMGs at comparable redshifts. Here dust masses are directly derived from the best-fit model by assuming a suitable dust-to-gas ratio and then using it to convert the total gas mass into dust mass. The D/G ratio can be either assumed to be proportional to the metallicity or fixed to some reasonable value. Compared to local spirals and local (U)LIRGs our $z \sim 2$ (U)LIRGs have higher dust-to-stellar mass ratios, by a factor of $\sim$ 30 and 6, respectively. Similar results were found by Santini et al. (2010) for the high-z SMGs. The $M_{dust}/M_{\star}$ of z$\sim$ 1 LIRGs are, instead, similar to those of local (U)LIRGs. $M_{\star}$ and M_{dust} of galaxies in this work appear also to be in agreement with the predictions of the Calura et al. (2008) chemical evolution models for proto-ellipticals. The distribution of our sources in this plot is also similar to that found by Rowan-Robinson et al. (2010) for the Hermes Lockman sample. These specific aspects will be dealt with in detail in one of the forthcoming papers of the series.

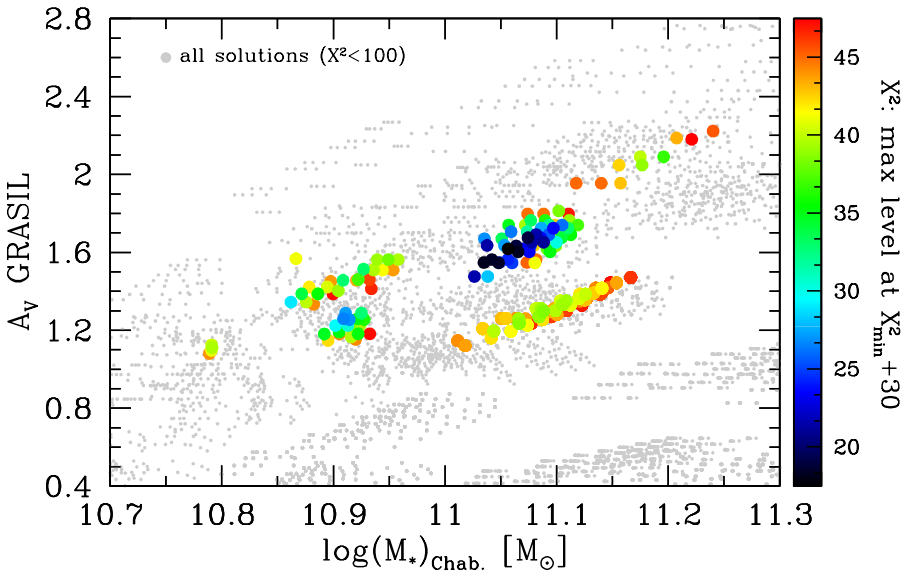

Figure 5.12 χ^2 values for spectral models of a typical z$\sim$ 2 ULIRG colour-coded (χ^2 increasing from dark to light colours) as a function of the average extinction and the stellar mass (see Tab. 5.2). We show all the solutions with $\chi^2 \leq 100$ (gray dots) in order to give an idea of the wide range of parameters (and solutions) explored, and with χ^2 within χ^2_{min}+30 (colored points). Here we assume the SFH of the galaxy to be fixed, which means that we fix the two parameters ruling the source's past SFH, and we consider only the variation of the GRASIL parameters regulating dust absorption and reprocessing.

5.5 Model Degeneracy

Another critical issue connected to this kind of physical analysis concerns model degeneracy. Figures 5.12 and 5.13 illustrate the possible degeneracy in the model solutions, between the average extinction and stellar mass, color-coded by the value of χ^2, for a typical $z \sim 2$ ULIRG. We report here two different cases. In the first case (Fig. 5.12), we assume the SFH of the galaxies to be fixed, which means that we fix $\tau_{\rm inf}$ and $\nu_{\rm Sch}$ and consider the variation only of the GRASIL parameters regulating dust absorption and reprocessing. As we see, among the many solutions considered, acceptable best-fits, within $\chi^2_{\rm min}$+30, are clearly identified in the parameter space and not much degeneracy is apparent. In particular A_V and $M_\star$ seem to be well constrained within $\Delta A_V \sim 0.1$ and $\Delta M_\star \sim 0.04$ dex. If we consider in addition to the many combinations of GRASIL parameters also the

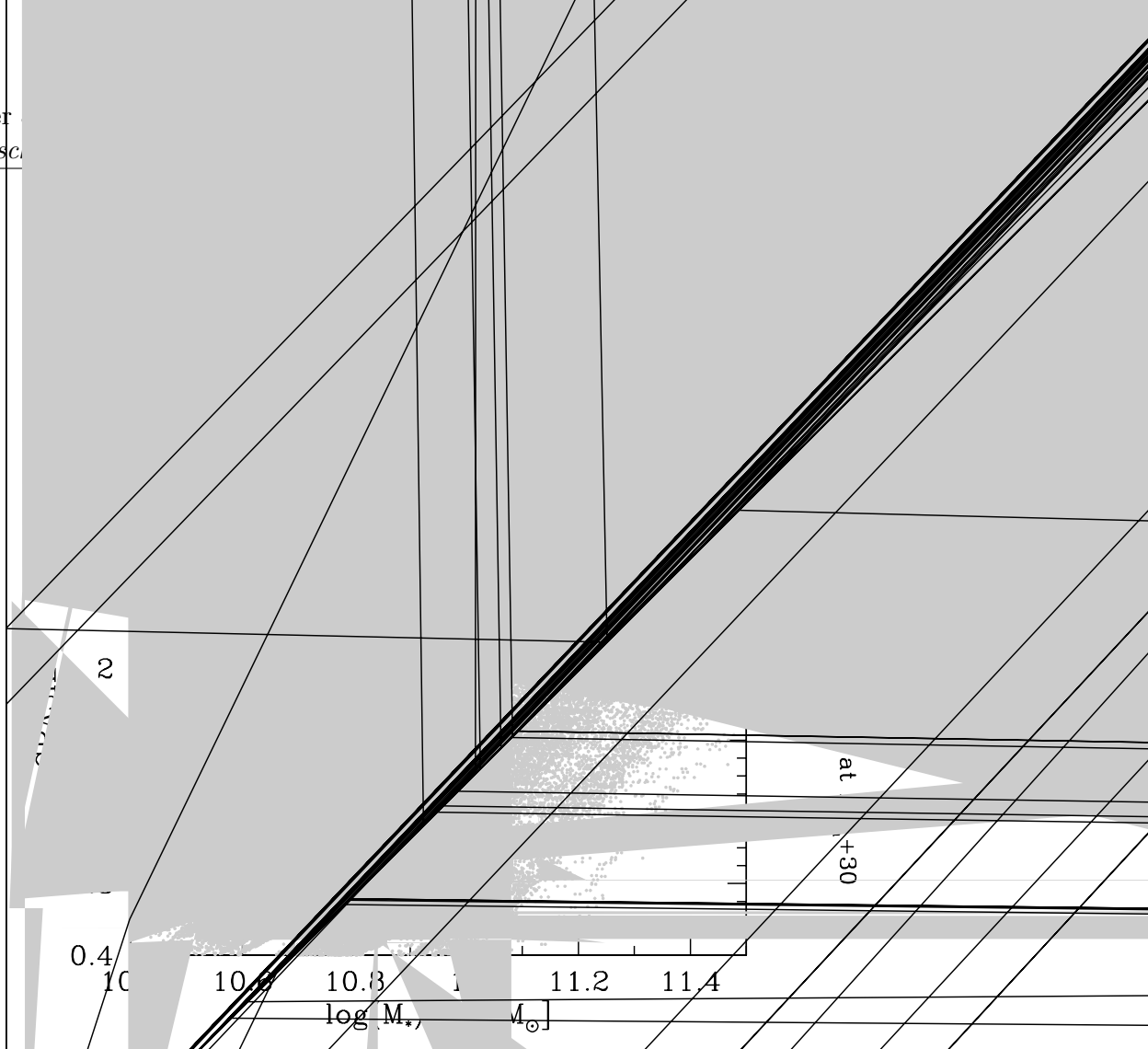

Figure 5.13 χ^2 values for spectral models of a typical z$\sim$ 2 ULIRG colour-coded (χ^2 increasing from dark to light colours) as a function of the average extinction and the stellar mass (see Tab. 5.2). We show all the solutions with $\chi^2 \leq 100$ (gray dots) in order to give an idea of the wide range of parameters (and solutions) explored, and with χ^2 within χ^2_{min}+30 (colored points). In addition to the variation of the GRASIL parameters, we consider here also the variation of the two parameters characterizing the SFH, namely ν_{Sch} and τ_{inf}. This results in a larger number of free parameters with respect to the first case and parameter combinations. As evident from the figure not much degeneracy is seen among the model parameters. Even for the second case, on the right, the typical uncertainty on the average extinction and stellar mass is $\sim$ 0.3 mag and 0.2 dex, respectively, still well within the typical uncertainties for this kind of analysis.

different combinations of parameters ruling the SFH (see Fig. 5.13), the scatter around the best-fit solution increases to $\Delta A_V \sim 0.3$ and $\Delta M_\star \lesssim 0.2$ dex, still well within the typical uncertainties for this kind of analysis. This is likely to be a result of the continuous spectral coverage from UV to sub-mm for our sample. Another likely factor is the self-consistent radiative transfer modelling, accounting for the distribution of dust with respect to young and old stars, from which both the age-dependent dust attenuation and dust reprocessing are constrained.

5.6 Further considerations: Modelled properties of the sample

In the previous sections of this Chapter we mainly focused on the self-consistent analysis of the main physical properties of dusty star forming galaxies at high-z as presented in our recent paper by Lo Faro et al. (2013). Here we intend to summarise some further results not reported in Lo Faro et al. (2013). These include the best-fit GRASIL model parameters used to reproduce the SEDs of our high-z (U)LIRGs and affecting the dust (and NIR-to-sub-mm) properties of the galaxies, (i.e. f_{MC}, t_{esc}, $r_{half-mass}$, $\tau_{1\mu m}$, β), the gas depletion timescales and star forming efficiencies and the best-fit attenuation curves of each object as computed by GRASIL by solving the radiative transfer equations for idealised but realistic geometrical distributions of stars and dust. For a detailed discussion about the parameters ruling the SFH of the galaxies (provided by the chemical evolution code), see previous Sections 5.2 and 5.3.

5.6.1 GRASIL best-fit model parameters

Table 5.3 reports, for each z$\sim$1 LIRG (top) and z$\sim$2 (U)LIRG (bottom) in our sample, the best-fit values of the main GRASIL parameters mentioned above. These have been selected by means of a standard χ^2 minimization procedure, within a large and fine grid containing thousands of different parameter combinations. The histograms of the best-fit parameters are shown in Figure 5.14 color-coded as blue horizontal line shaded areas for the z$\sim$1 LIRGs and black 45° angle line shaded areas for the z$\sim$2 (U)LIRGs. From top-left to bottom right, we give: the escaping time t_{esc}, namely the timescale for young stars to escape from their parent MCs, the fraction of gas in the molecular cloud component with respect to the diffuse one, f_{MC}, the MC optical depth at 1 μm, $\tau_{1\mu m}$ and the sub-mm spectral slope, β.

The best-fit values of t_{esc} (Fig. 5.14: top-left), range between $\sim$ 3 and 98 Myr for our (U)LIRGs, therefore, from the typical values of normal star forming galaxies to the much higher values characteristics of more dust obscured starburst objects. The median is $\sim$ 13 Myr for the z$\sim$2 (U)LIRGs and $\sim$6 Myr for the z$\sim$1 LIRGs in agreement with the typical values of high-z normal star forming objects. All the stars with ages older than the typical escaping time contribute to cirrus heating. As we have seen in previous sections this brings to an overestimate of the SFR when a Kennicutt '98 calibration is used.

The fraction of gas in the molecular cloud component (Fig. 5.14: top-right), a crucial parameter of the model as it determines also the level of dust obscuration due to the cirrus, ranges between 0.12 and 0.54 for the z$\sim$1 LIRGs and 0.2-0.98 for the z$\sim$2 (U)LIRGs.

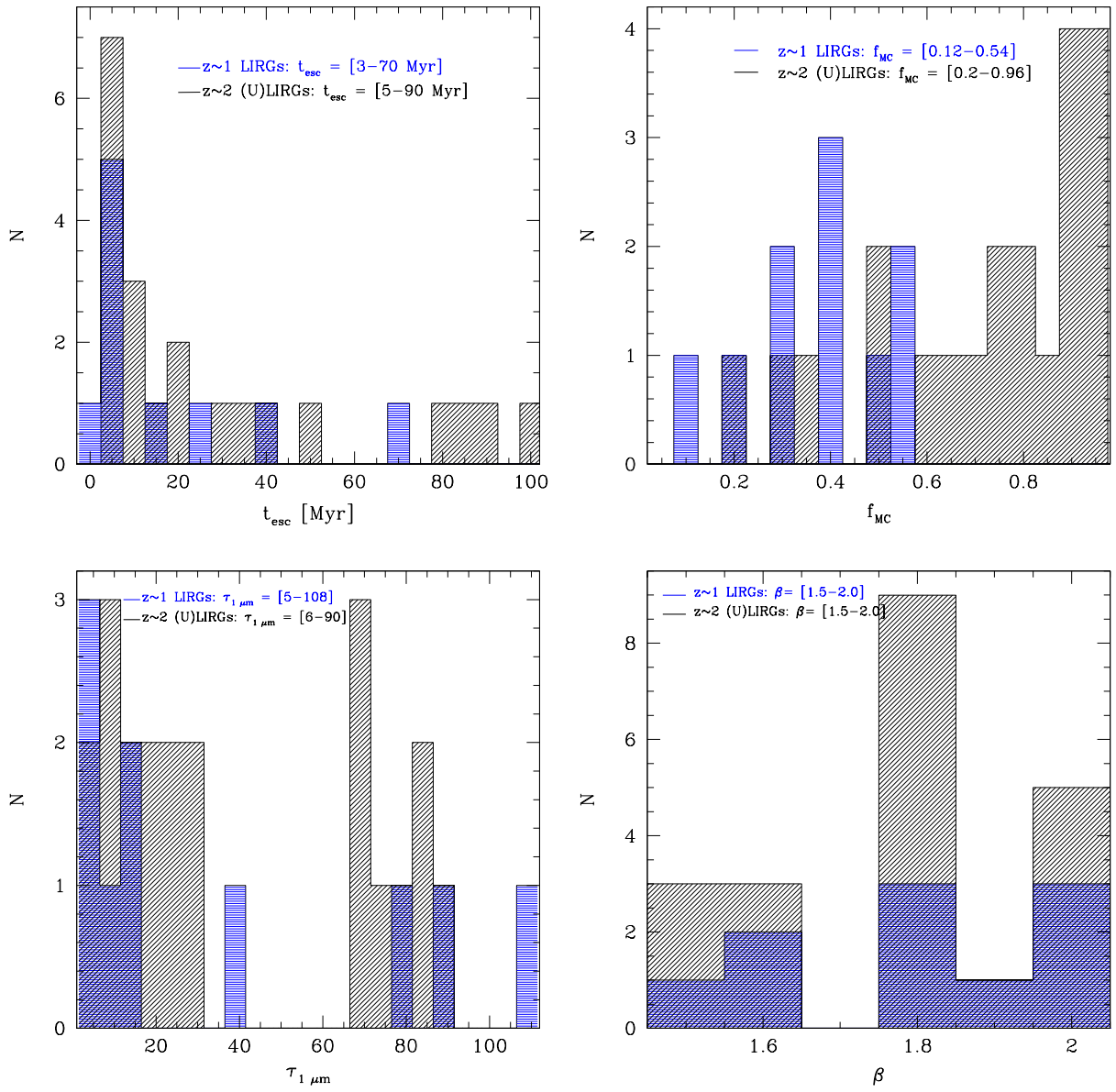

Figure 5.14 Histograms of the main GRASIL model parameters affecting the dust (and NIR-to-sub-mm) properties of our z∼1 LIRGs (blue horizontal line shaded area) and z∼2 (U)LIRGs (black 45° angle line shaded area). From top-left to bottom right there are, t_{esc}, f_{MC}, $\tau_{1\mu m}$ and β. For their meaning see text and Tab. 5.1. Their typical range of values are highlighted in each figure.

ID	name	z	χ^2_ν	$t_{\rm gal}$ (Gyr)	ν (Gyr^{-1})	$\tau_{\rm inf}$ (Gyr)	$f_{\rm MC}$	$t_{\rm esc}$ (Myr)	$\tau_{1\,\mu\,\rm m}$	$r^{\star}_{\rm half-mass}$ (kpc)	$r^{\rm diff}_{\rm half-mass}$ (kpc)	β
28	L4177	0.842	5.64	5.5	0.8	2.0	0.4	6	91	5.41	5.41	1.5
29	L4419	0.974	5.56	5.5	0.87	0.4	0.4	25	7	3.66	5.41	1.6
30	L4900	1.047	1.87	5.5	0.66	1.0	0.3	15	5	1.46	1.46	1.6
31	L5134	1.039	2.90	4.5	0.93	0.01	0.2	70	17	0.88	7.31	1.9
33	L5420	1.068	5.00	4.5	0.5	0.5	0.5	5	6	1.46	4.97	2.0
35	L5630	0.997	1.20	3.6	0.5	0.5	0.53	2	6	3.66	3.36	1.8
36	L5659	1.044	3.86	4.5	0.5	0.03	0.54	38	13	0.70	8.78	2.0
37	L5876	0.971	0.58	5.5	0.58	0.1	0.3	5	41	5.41	5.41	1.8
44	L13958	0.891	2.44	2.5	1.3	0.1	0.4	5	78	1.76	4.39	2.0
47	L15906	0.976	1.40	4.0	0.8	1.0	0.12	4	108	1.17	8.05	1.8

ID	name	z	χ^2_ν	$t_{\rm gal}$ (Gyr)	ν (Gyr^{-1})	$\tau_{\rm inf}$ (Gyr)	$f_{\rm MC}$	$t_{\rm esc}$ (Myr)	$\tau_{1\,\mu\,\rm m}$	$r^{\star}_{\rm half-mass}$ (kpc)	$r^{\rm diff}_{\rm half-mass}$ (kpc)	β
1	U428	1.783	2.1	3.0	0.83	0.01	0.91	12	17	0.15	1.61	2.0
2	U4367	1.624	5.88	3.0	1.6	0.01	0.65	80	21	0.73	16.09	1.8
3	U4451	1.875	3.13	2.3	0.9	0.01	0.81	20	29	0.45	7.55	1.5
4	U4499	1.956	4.03	2.75	0.62	0.01	0.9	86	68	0.36	5.85	2.0
5	U4631	1.841	4.37	3.6	0.78	1.0	0.5	5	28	1.46	14.63	1.8
6	U4639	2.112	4.92	2.5	0.5	1.0	0.6	35	6	3.80	9.80	1.8
7	U4642	1.898	8.76	2.5	0.8	0.1	0.93	5	24	0.58	14.63	1.8
8	U4812	1.93	1.35	2.3	0.88	0.01	0.9	10	80	0.23	2.93	2.0
10	U4958	2.118	1.58	2.5	0.5	1.0	0.96	98	8	0.88	8.78	1.5
11	U5050	1.938	2.0	2.7	1.78	0.01	0.3	50	14	0.58	11.41	1.6
12	U5059	1.769	0.89	2.6	0.5	0.5	0.34	12	6	5.41	5.41	1.8
13	U5150	1.898	1.76	2.8	0.6	1.0	0.74	5	13	0.73	7.02	1.8
14	U5152	1.794	1.81	2.35	0.9	0.01	0.92	83	8.6	0.28	4.39	1.5
16	U5632	2.016	1.27	2.0	0.9	1.0	0.96	7	25	0.58	2.93	2.0
17	U5652	1.618	8.4	2.0	0.8	0.01	0.68	90	85	0.73	17.56	1.9
18	U5775	1.897	3.76	2.0	0.9	1.0	0.75	5	7	0.58	0.58	2.0
19	U5795	1.703	5.18	2.5	0.38	0.01	0.86	18	88	0.73	2.93	1.6
20	U5801	1.841	3.24	2.7	0.78	0.01	0.93	13	75	0.44	14.63	1.8
21	U5805	2.073	3.46	2.8	0.6	0.5	0.5	5	70	0.73	17.56	1.6
22	U5829	1.742	2.58	3.2	1.23	0.01	0.81	6	70	0.44	11.70	1.8
24	U16526	1.749	2.78	0.6	0.6	1.0	0.2	38	7	2.05	5.56	1.8

Table 5.3 GRASIL best-fit Parameters for the $z\sim1$ (top) and ~2 (bottom) (U)LIRGs modeled as gradually evolving spheroids.

In agreement with other observational works (e.g. Braun et al. 2011, Combes 2013) the molecular gas fractions tend to be higher for the highest redshift (U)LIRGs. The median values are $\sim$ 0.4 and 0.8 for the z$\sim$1 and $\sim$2 sample, respectively. In particular large molecular gas reservoirs have been recently found by Daddi et al. (2010a), Magdis et al. (2012) for a sample of BzK star forming galaxies at z$\sim$1.5 (see Chapter 7). Our results for the z$\sim$2 (U)LIRGs, most of which as discussed in Section 4.4.7 are BzK galaxies, are thus in agreement with the results of the authors cited above.

The 1 μm optical depth of star forming MCs (Fig. 5.14: bottom-left), typically ranges between $\sim$ 5-100 for both samples. The median values are $\sim$17 and $\sim$25 for the z$\sim$1 and z$\sim$2 (U)LIRGs, respectively. These translate in median values for the optical depth at 100 μm approximately equal to 0.1 and 0.15 for the z$\sim$1 and 2 sample, respectively. Compared to local ULIRGs, as Arp220 for example, which appears to be optically thick out to at least 100 microns (Rangwala et al., 2011) based on Herschel data, our high-z (U)LIRGs do not show very high $\tau_{100\mu m}$. The maximum value reached is of about 0.5. Observationally speaking high values of $\tau_{100\mu m}$ make measuring the dust mass and other aspects very difficult, particularly at high redshift. Concerning our objects, even if they were very thick at 100 micron, thanks to the capability of our physical model to solve the radiative transfer for both the diffuse and dense component of the ISM, this would not be a problem. By solving the radiative transfer equations, in fact, GRASIL is able to give us well constrained and consistent estimates of both M_{dense} and M_{dust}. Anyway, as come out from our analysis, Arp220 is indeed an extreme object and it is not representative of our sample of high-z ULIRGs.

The typical sub-mm spectral slope β (Fig. 5.14: bottom-right), of our galaxies ($\sim$1.8) well agrees with the value usually measured for dusty star forming galaxies at high-z (see e.g. Magdis et al. 2012) and roughly corresponds to cold dust temperatures in the range between 11 and 30 K (e.g. Dupac et al. 2003). The range of values considered in our SED-fitting procedure is highlighted in Fig. 5.14 bottom-right. We want to emphasise here that, thanks to the availability of this rich dataset covering the FIR-to-sub-mm wavelength range, the sub-millimetre spectral slope can be accurately measured independently from the temperature distribution. This breaks the well-known T-β degeneracy usually affecting the estimates based on modified BB fit to the FIR SED.

Figure 5.15 shows the histograms of the typical scale-lengths of the assumed geometrical distribution for stars (left panel) and dust (right panel) (King's profile - see Section 3.5 for details) for the two populations of z$\sim$1 (blue horizontal line shaded area) and z$\sim$2 (black 45° angle line shaded area) (U)LIRGs. The median values of the half-mass scale lengths relative to stars and dust are highlighted in each panel. Comparing the two galaxy populations we can observe that while the distribution of stars appears to be more extended

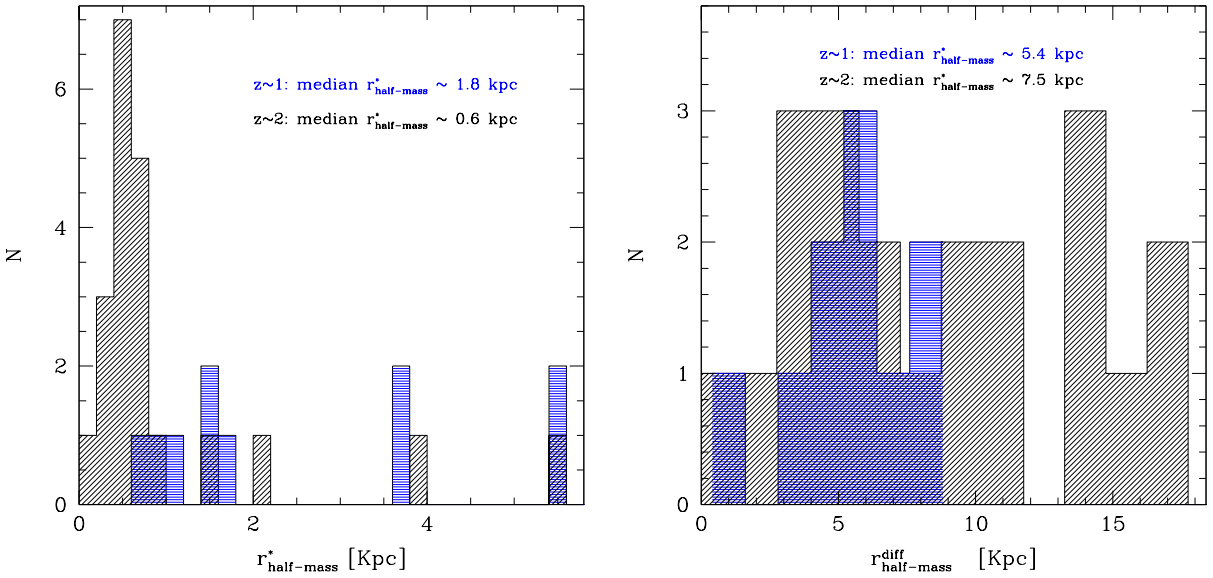

Figure 5.15 Histograms of the typical scale-lengths of the assumed geometrical distribution for stars (left panel) and dust (right panel) (King's profile - see Section 3.5 for details) for the two populations of z∼1 (blue horizontal line shaded area) and z∼2 (black 45° angle line shaded area) (U)LIRGs. The median values of the half-mass scale lengths relative to stars and dust are highlighted in each panel.

for the z∼1 LIRGs where it reaches 5.4 kpc, the dust distribution shows an inverse trend being more extended for the highest redshift (U)LIRGs for which it reaches ∼15-17 kpc. This seems to be in agreement with the recent results published by Symeonidis et al. (2013) according to which (U)LIRGs in the early Universe are typically characterised by a more extended dust distribution and/or higher dust masses than lower redshift LIRGs and local equivalent sources. This is manifested, according to the authors, as a flattening of the relation between the IR luminosity and dust temperature (L-T).

5.6.2 Gas mass, depletion timescale and star formation efficiency of dusty star forming galaxies at high redshift: model predictions

The total gas mass of the best-fit galaxy model at t_{obs} is provided by the chemical evolution code described in Sections 3.2 and 5.2. In computing the residual gas mass, the code accounts for the depletion of gas due to star formation, the injection to the ISM of processed gas by dying stars (feedback) and the infall of primordial gas forming the galaxy. The model values of the fraction of gas in the dense phase (MC component), f_{MC}, and of the dust-to-gas mass ratio provide the molecular gas and dust mass directly associated with star formation, as well as the gas and dust mass of the diffuse phase.

We have estimated, for each galaxy in our sample, the gas depletion timescale, $\tau_{\rm gas} = M_{\rm gas,MC}/SFR$, which is a measure for how long a galaxy with current total gas mass, $M_{\rm gas}$, can sustain its current SFR without being refuelled by accretion of fresh extragalactic material or by the diffuse gas. We have considered, in the computation, the molecular gas mass more directly related to the star formation activity of the galaxy. If for $\tau_{\rm gas}$ we consider instead the total gas mass, M_{gas}, we recover the inverse of the values of the star formation efficiency, ν_{Sch} parameter, listed in Tab. 5.3.

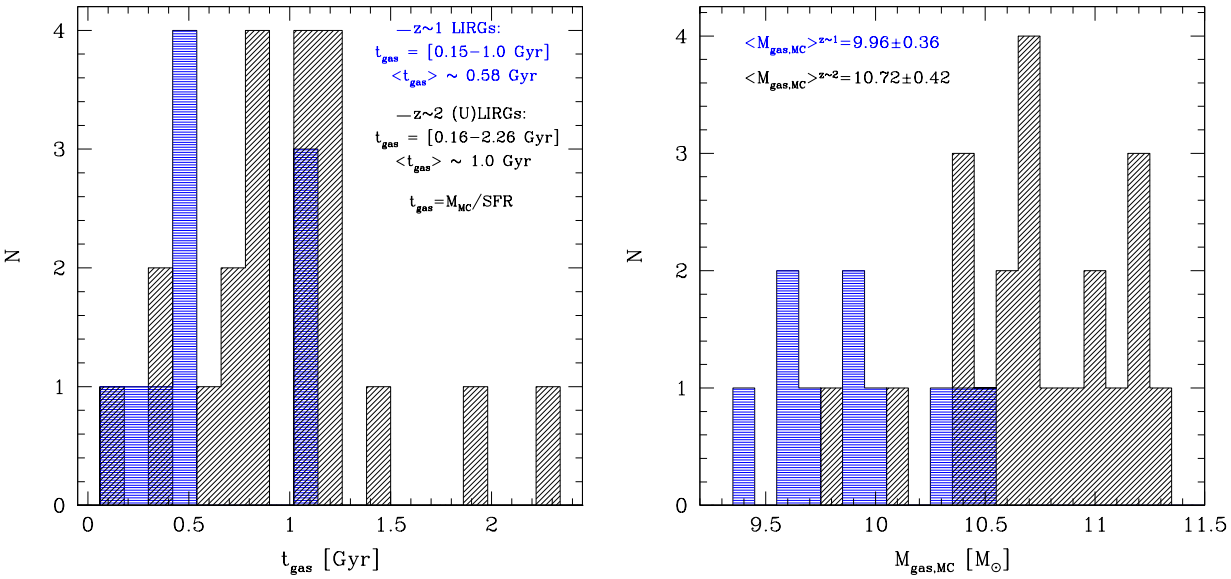

Figure 5.16 **Left**: Gas depletion timescale (t_{gas}=$M_{gas,MC}$/SFR) distributions for our best-fit z∼1 LIRGs (blue horizontal lines) and z∼2 (U)LIRGs (black 45° angled solid lines). Typical and mean values are highlighted in the top right end of the figure. **Right**: Molecular ($M_{\rm MC}$) gas mass distributions for z∼1 (blue horizontal lines) and z∼2 (black 45° angled solid lines) (U)LIRGs, respectively.

The mean depletion timescales estimated using the molecular gas mass are well in agreement with the typical duration of normal star forming galaxies duty cycle ranging between 0.5 - 1 Gyr (see e.g. Daddi et al. 2010a; here the gas mass has been estimated from CO luminosity or Magdis et al. 2012). This is much longer than the typical duration expected for starbursts ($\lesssim$100 Myr). But it is slightly lower than that of normal star forming local galaxies.

Comparing the two galaxy populations we find that the typical $t_{\rm gas}$ is longer (∼1 Gyr) for the z∼2 (U)LIRGs than for the lower redshift LIRGs (∼0.5 Gyr). If we consider these two classes of objects as the same galaxy population observed in different evolutionary stages, this result can be interpreted as due to the fact that while the highest z (U)LIRGs are in the initial phase of star formation where there are large molecular gas reservoirs (as also demonstrated by Daddi et al. 2010a) but not so high SFRs ($\lesssim 100 M_{\odot}/yr$), the lower

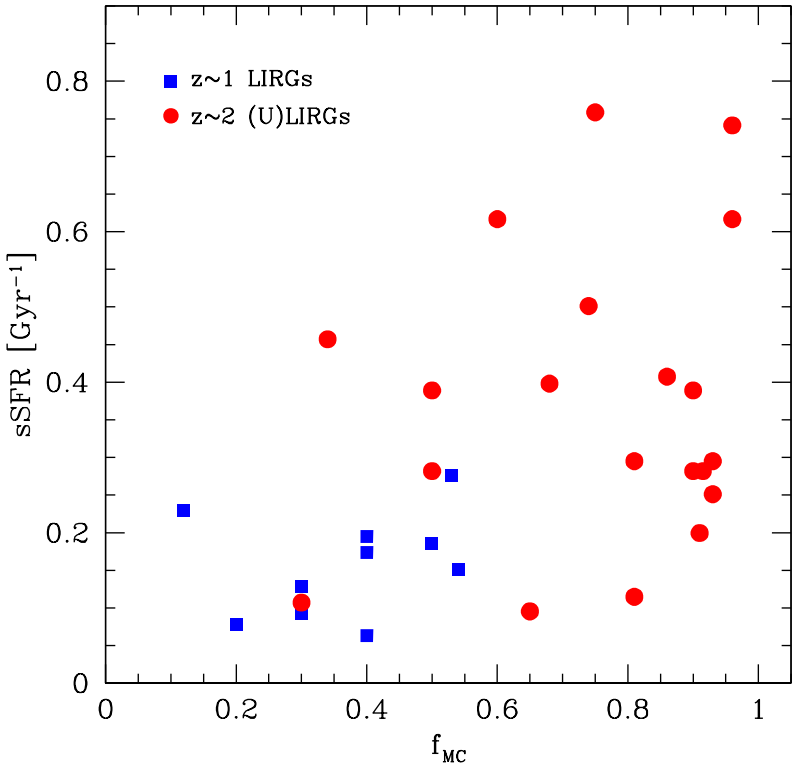

Figure 5.17 sSFR versus molecular gas fraction for our z∼ 1 LIRGs (blue filled squares) and z∼ 2 (U)LIRGs (filled red circles)

redshift LIRGs would actually be objects observed at later stages when the molecular gas reservoir has been reduced by the star formation activity and the SFR is lower. This would bring to longer depletion timescales for the z ∼ 2 (U)LIRGs, as shown in the figure. The relative distributions of M_{MC} for both samples are shown in Figure 5.16 (right). Again in agreement with observational results, we can see that the molecular gas mass is larger at higher redshifts.

Figure 5.17 shows the variation of the predicted sSFR ($SFR_{10}/M_\star$) as a function of the molecular gas fraction in the galaxy. Filled blue squares are z∼ 1 LIRGs while filled red circles are our z∼ 2 (U)LIRGs. The sSFR of the former ranges between 0.06 and 0.27 Gyr^{-1} while that one of the z ∼ 2 (U)LIRGs ranges between 0.1 and 0.76 Gyr^{-1} showing a larger variation with respect to the lower redshift LIRGs. As emphasised by the figure, the observed increase in the sSFR appears to be mainly driven by the increase of molecular gas content inside star-forming galaxies, in agreement with Daddi et al. (2010a), Magdis et al. (2012), Rodighiero et al. (2011) results. Our predictions for the sSFR tend to be lower with respect to the average sSFR estimated by Rodighiero et al. (2011) for the MS galaxies ∼ 2.6 Gyr^{-1}. This is due to the combined effect of larger stellar masses and lower SFRs obtained through our physical analysis (see detailed discussion above). Of course it

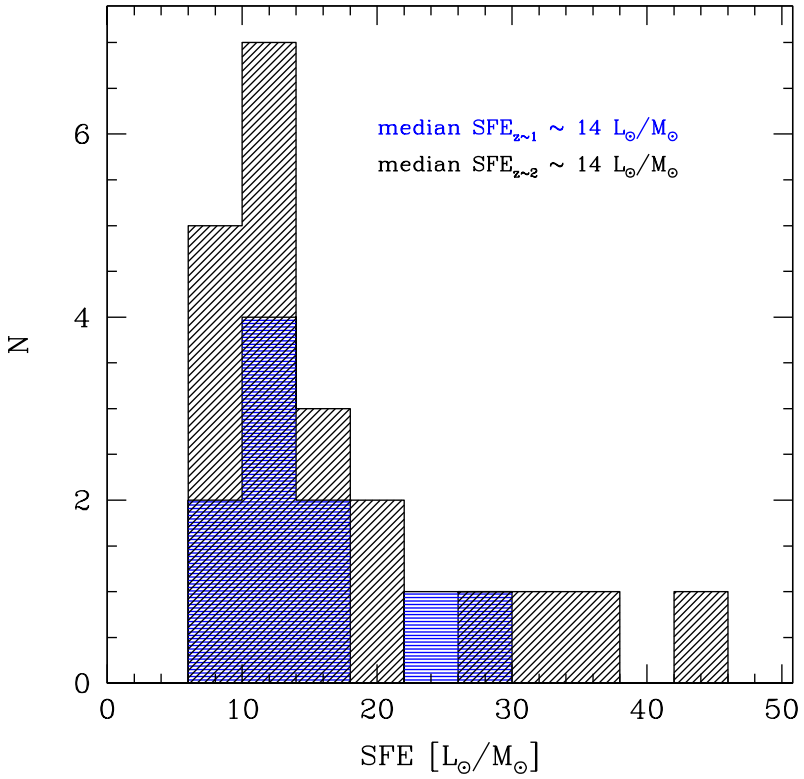

Figure 5.18 Predicted star formation efficiencies (SFE=L_{IR}/M_{gas}) of z$\sim$1 LIRGs (blue horizontal lines) and z$\sim$2 (U)LIRGs (black 45° angled solid lines). Median values for the two populations are highlighted in the figure.

is of fundamental importance to compare our estimates with those derived, by Rodighiero et al. (2011) for example, for larger statistical sample of MS and starburst galaxies. This will be discuss in the next Chapter.

While the sSFR probes the star formation mode of a galaxy only indirectly and from a statistical point of view, accurate measurements of its star formation efficiency, SFE = SFR/M_{gas}, can provide more direct and reliable information. We have thus estimated here also the star formation efficiencies of our galaxies defined by the ratio between the total IR luminosity ($\propto$SFR) and the residual gas mass. We have considered here the total gas mass instead of the molecular one to be consistent with the SFE estimates, given for a sample of z$\sim$1.5 star forming galaxies, by Magdis et al. (2012). The histograms showing the distribution of our predicted SFEs for the z$\sim$1 (blue horizontal lines) and $\sim$2 (black 45° angled solid lines) sample are given in Fig. 5.18. The median SFE of both samples is $\sim$ 14 $L_\odot/M_\odot$ which is similar to the average SFE (14 ± 2 $L_\odot/M_\odot$) found by Magdis et al. (2012) but $\sim$12 times lower than the typical value of starburst galaxies ($<$SFE$>\sim200\,L_\odot/M_\odot$) usually characterized by an accelerated mode of SF. The mean values including the standard deviation of the distribution are: 15 ± 6 and 17 ± 9 for the

z$\sim$1 and 2 (U)LIRGs, respectively, still in agreement, within the uncertainties, with the estimates given by Magdis et al. (2012). These low values of SFE may be indicative of extended molecular gas reservoirs, as discussed above (Daddi et al., 2010a).

5.6.2.1 Effects of our analysis on the SFR-M$_\star$ diagram

As we have seen in Chapter 1, many recent studies have found evidence that the SFR in galaxies correlates with their stellar mass along a Main Sequence (MS) relation which evolves with redshift (Daddi et al., 2007b, Elbaz et al., 2007, Rodighiero et al., 2011) and representing a "steady" mode of SF. Above the MS with higher sSFRs, (by a factor ranging between 4 and 10), there are the so-called outlier galaxies characterized by a "starburst" mode of SF generally interpreted as driven by merging. These off-MS (or outliers) galaxies have been found to contribute only 10% of the cosmic SFR density at $z \sim 2$ (Rodighiero et al., 2011). This has been interpreted as a further indication that most of the stellar mass forms in continuous mode of SF. Under this picture high-z LIRGs and (U)LIRGs seem to mostly reflect the high SFR typical for massive galaxies at that epoch, so they are not brief stochastic starbursts as their local counterpart. They simply represent the early gas-rich phase of smoothly declining SFH of $\geqslant L_\star$ galaxies, as demonstrated by our physical analysis.

We have investigated here also the effects of our physical analysis on the SFR-M$_\star$ relation described above. Indeed our results, in terms of larger stellar masses and lower SFRs with respect to classical estimates, have a strong impact on the SFR-M$_\star$ diagram.

Figure 5.19 shows the Stellar massstar formation rate relation for different galaxies at $1.5 < z < 2.5$. Most of the points are the same discussed in Fig. 1 of Rodighiero et al. (2011) work. The main thick black solid line represents the MS relation from Rodighiero et al. (2011) re-scaled to a Chabrier IMF. The light yellow region defines the locus occupied by objects having sSFR within a factor of 2 from the MS while the two solid lines above the yellow region mark, respectively, the loci 4 and 10 times above the MS (along the SFR axis). The small black circles are BzK galaxies from both COSMOS and GOODS catalogues. The small red and green circles represent, respectively, PACS-COSMOS and PACS-GOODS-S detected sources. For all these data-points the stellar masses have been measured by using BC03 templates in combination with the hyperz code described above. The SFRs are derived from the total IR luminosity using the Kennicutt (1998) calibration. The big red filled circles and magenta stars represent, respectively, our z$\sim$2 (U)LIRGs and some of the most extreme outliers of Rodighiero et al. (2011) (those having sSFR above a factor of 8-10 with respect to MS), for which both stellar masses and star formation rates

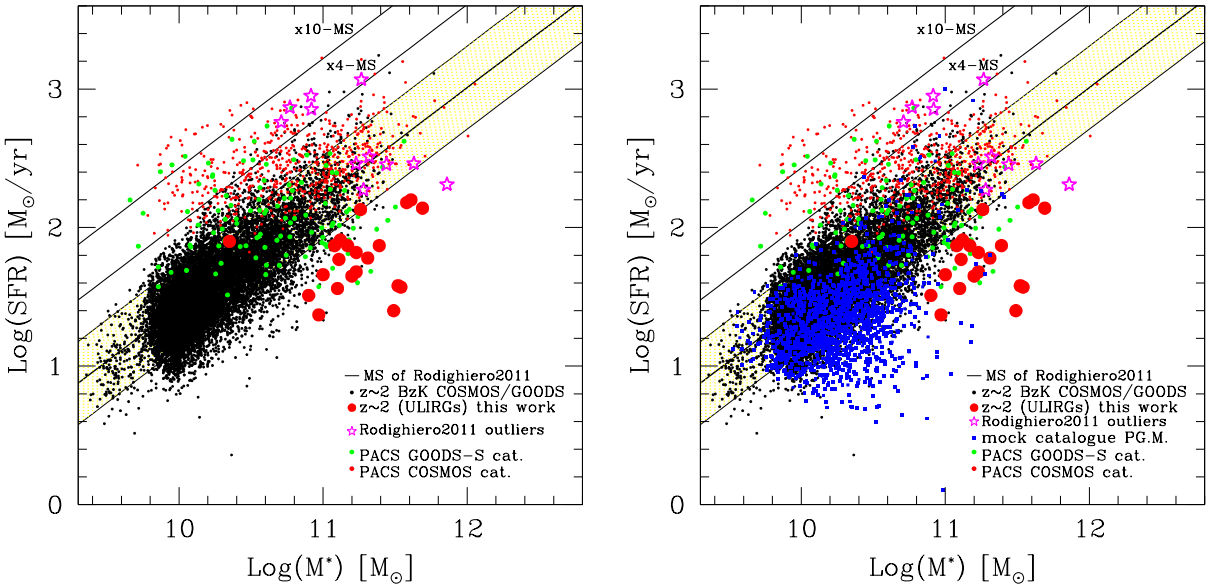

Figure 5.19 SFR-M$_\star$ diagram: model predictions vs empirical estimates based on observations. Small black circles are z*sim* 1.5-2.0 BzK galaxies from GOODS and COSMOS survey, small red and green circles are, respectively, PACS-COSMOS and PACS-GOODS-S detected sources. Black solid line represents the MS relation computed by Rodighiero et al. (2011) rescaled to Chabrier IMF, while the yellow region defines the locus occupied by objects with sSFRs within a factor of two from the MS. The other two black lines highlight the x4 and x10 off-MS regions. For all these points the stellar masses have been computed using BC03 templates in combination with Hyperz code and SFRs have been derived by using the empirical calibration by Kennicutt (1998). The big red filled circles and magenta stars represent, respectively, our z$\sim$2 (U)LIRGs and some of the outliers of Rodighiero et al. (2011), for which both stellar masses and star formation rates are self-consistently derived through our analysis. In the plot on the right the small blue squares represent the results from semi-analitical models by Fontanot et al. (2012).

are self-consistently derived through our analysis. In the plot shown on the right the small blue squares represent the results from semi-analitical models by Fontanot et al. (2012).

As evident from the figure, our physical analysis applied to high-z dusty star forming (U)LIRGs has the effect of shifting downwards, below the MS, these objects. The effect strongly depends on the level of dust obscuration of the galaxy and on its physical nature. We have seen that for the most dust obscured objects the stellar mass can be significantly larger than that derived from classical SED fitting approaches. As for the SFRs, we have found that they can be systematically lower with respect to those based on Kennicutt (1998) calibration due to significant cirrus contribution to IR luminosity by intermediate age ($t_{obs} \gtrsim 10 - 90\,Myr$) stellar populations. The combination of these two effects on the SFR-M$_\star$ relation is clearly visible when we look at the so-called outliers (magenta stars). The starting point is represented by the small red circles lying above the x10-off MS black line. After applying our physical analysis to some of those objects we get the magenta

stars. We can clearly distinguish in the figure two different situations, corresponding to the two well-distinct groups of magenta stars. For the most dust obscured objects whose IR SEDs are dominated by an ongoing burst of star formation in the MC, the SFRs derived from the model are consistent with the Kennicutt (1998) calibration, within the errors, while the stellar masses are still larger than classical predictions and for some objects reach a factor of ~ 7. The effect here is that of shifting these most extreme cases to the region between the x4- and x10-MS solid lines, still above the MS. For the dust obscured objects whose IR SED is dominated by cirrus component, thus characterized by gradual evolving SFHs, we measure SFRs lower by a factor $\sim$2-2.5 than Kennicutt calibration, in addition to large stellar masses. Here the effect of our analysis is that of bringing back to the MS these peculiar galaxies. Similar results, for a sample of high-z sub-mm galaxies, have been recently obtained also by Michałowski et al. (2012).

The question we would like to address now is: "Are these "outliers" a real population of off-MS galaxies or due to a severe mass underestimate related to their high dust obscuration, are they "simply" highly star forming MS galaxies ?". Moreover combining the two results discussed above (relative to normal star forming (U)LIRGs and starburst galaxies), it seems that the global effect of our analysis is that of simply changing the normalization of the relation. To investigate this possibility and to answer this question we need to understand, first of all, how well determined our SFRs are, in terms of different indicators for example, and then we need to apply the same physical analysis to a larger statistical sample of both MS and starburst galaxies to see whether there is a shift downwards (to larger stellar masses) of the entire sequence or only a compression due to the fact that only the most dust obscured objects have stellar masses which have been underestimated.

The first point will be discussed in detail in the next Chapter where we will compare our model predictions with radio data which are fundamental as they offer a further independent way to estimate and constrain the 'current' SFR in galaxies, mostly contributed by young massive stars.

We have compared our predictions for the SFR-M$_\star$ relation to those derived from semi-analytical model of galaxy formation (Fontanot et al., 2012, Monaco et al., 2007) (see Fig. 5.19: right). As evident from the figure, the results from semi-analytical models (small blue dots in the figure) tend to be lower, by a factor of ~ 2 on average, with respect to the MS relation defined in Rodighiero et al. (2011) and drawn by the small black points. Within the significant scatter, our computed values for our sample, represented by the big filled red circles, agree reasonably well with the models, by setting themselves at the high-mass end of the relation.

5.6.3 Dust attenuation curves: comparing GRASIL with standard prescriptions

One of the crucial points when dealing with dust obscuration in galaxies is that it strongly depends on the geometrical distribution of both stars and dust which in turn strongly depends on the age of stellar populations. Another critical issue is to understand if the adopted optical properties for the dust are well representative of the particular sample considered. It is therefore important to distinguish between the attenuation law of a galaxy and the extinction law of the dust. While the latter describes just the wavelength dependence of the optical properties of the dust mixture, the former is the ratio (expressed in magnitudes) between the observed and intrinsic starlight, as a function of wavelength (Panuzzo et al., 2007). As discussed in detail in Chapter 2 (§ 2.5), when modeling galaxy SEDs, the relevant concept is dust attenuation which, differently from extinction, takes into account two important aspects: first that the light can be scattered both out of and into a given line of sight; then that the geometrical distribution of dust with respect to the stars strongly affects the resulting SED.

Having to deal with the geometrical effects of dust, estimating dust attenuation is considerably more complex than estimating dust extinction. However several simple empirical rules are usually adopted to simplify the problem. The simplest dust geometry typically considered is that of a homogeneous foreground screen of dust, lying between us and the stellar population of the galaxy. This simple geometry yields an attenuation curve whose shape depends only weakly on the total dust column density (the weak dependence arises from the scattered light component). In this extremely idealised situation the attenuation law can provide a direct measure of the extinction law. Dust effects in classical codes (see Section 2.5), as the Hyperz one used here for comparison, are usually accounted for by following this simple prescription and adopting the Calzetti attenuation law. This law assumes a universal shape for the dependence of the attenuation on wavelength (function of $1/\lambda$), such that the UV light is the most affected by dust and it is calibrated on observations of 39 nearby UV-bright starburst galaxies.

As we have seen in Chapter 2, more complex geometries generally yield attenuation curves that become greyer (i.e., shallower) as the column density increases. Clumpy interstellar media also result in greyer attenuation curves than their homogeneous counterparts. In all cases, the total attenuation optical depth is lower than the amount of extinction that would be produced by the same column density because some scattered light is always returned to the line-of-sight.

We have demonstrated through our analysis that such extremely idealized approaches, not accounting for an age-dependent dust attenuation and based on optical-only SED-fitting

procedures, may generate unextinguished stellar SEDs unable to energetically balance the reprocessed IR emission from the galaxy due to dust (see Fig. 5.10 and discussion in the text). We have seen that for the most dust obscured objects this results in stellar mass underestimates which may reach a factor ~ 6.

By solving the radiative transfer equations for realistic geometrical distributions of stars and dust and taking advantage of a full multiwavelength coverage from far-UV to radio, our spectrophotometric code is able to break the age-extinction degeneracy (allowing for an age-dependent dust attenuation) and self-consistently reproduce the energy balance between what is absorbed at UV-optical wavelengths and what is re-emitted at longer wavelengths. This produces more physically motivated and self-consistent solutions.

In addition to the detailed discussion of § 5.4.1 we report here, in Figures 5.20 - 5.27 a comparison between the attenuation curve self-consistently computed by GRASIL by solving the radiative transfer equations for a spheroidal geometrical distribution of stars and dust (black solid line), and the Calzetti et al. (2000) attenuation curve computed using the best-fit value of A_V as given both by hyperz (red long-dashed lines) and GRASIL (blue short dashed lines).

The attenuation curve by Calzetti et al. (2000) is computed, as in hyperz, using the following relations:

$$A_\lambda = k(\lambda)E(B-V) = \frac{k(\lambda)A_V}{R_V} \tag{5.3}$$

with $R_V = 4.05 \pm 0.80$ and

$$k(\lambda) = \begin{cases} 2.659\left(-2.156 + \frac{1.509}{\lambda} - \frac{0.198}{\lambda^2} + \frac{0.011}{\lambda^3}\right) + R_V & 0.12\,\mu\mathrm{m} \leq \lambda \leq 0.63\,\mu\mathrm{m} \\ 2.659\left(-1.857 + \frac{1.040}{\lambda}\right) + R_V & 0.63\,\mu\mathrm{m} \leq \lambda \leq 2.20\,\mu\mathrm{m} \end{cases} \tag{5.4}$$

Below and above the wavelength range of validity, the slope of the reddening law is computed by interpolating $k(\lambda)$ at 1100 and 1200 $\mathring{A}$ in the first case and at 21900 and 22000 $\mathring{A}$ in the second case.

The vertical green lines shown in Fig. 5.20-5.27 indicate the position of the V band where A_V is computed. Highlighted in each panel there also are the best-fit values of the average extinction as provided by hyperz and GRASIL. In most cases due to the underprediction of the average extinction with respect to the value provided by GRASIL, the Calzetti attenuation law with A_V given by Hyperz (red long dashed lines) tend to be systematically lower at all wavelengths, with the exception of a few objects for which $\Delta A_V = A_V^{GR} - A_V^{Hyp} \lesssim 0.6$ mag. The agreement between the Calzetti empirical relation and GRASIL attenuation curve gets better when the best-fit GRASIL A_V is considered (blue short dashed line), in particular at wavelengths $\lambda \lesssim 0.6\,\mu$m. For about 15/31 objects in the sample, the increase at $\lambda \lesssim 0.6\,\mu$m of the Calzetti attenuation law computed using A_V^{GR} is too steep

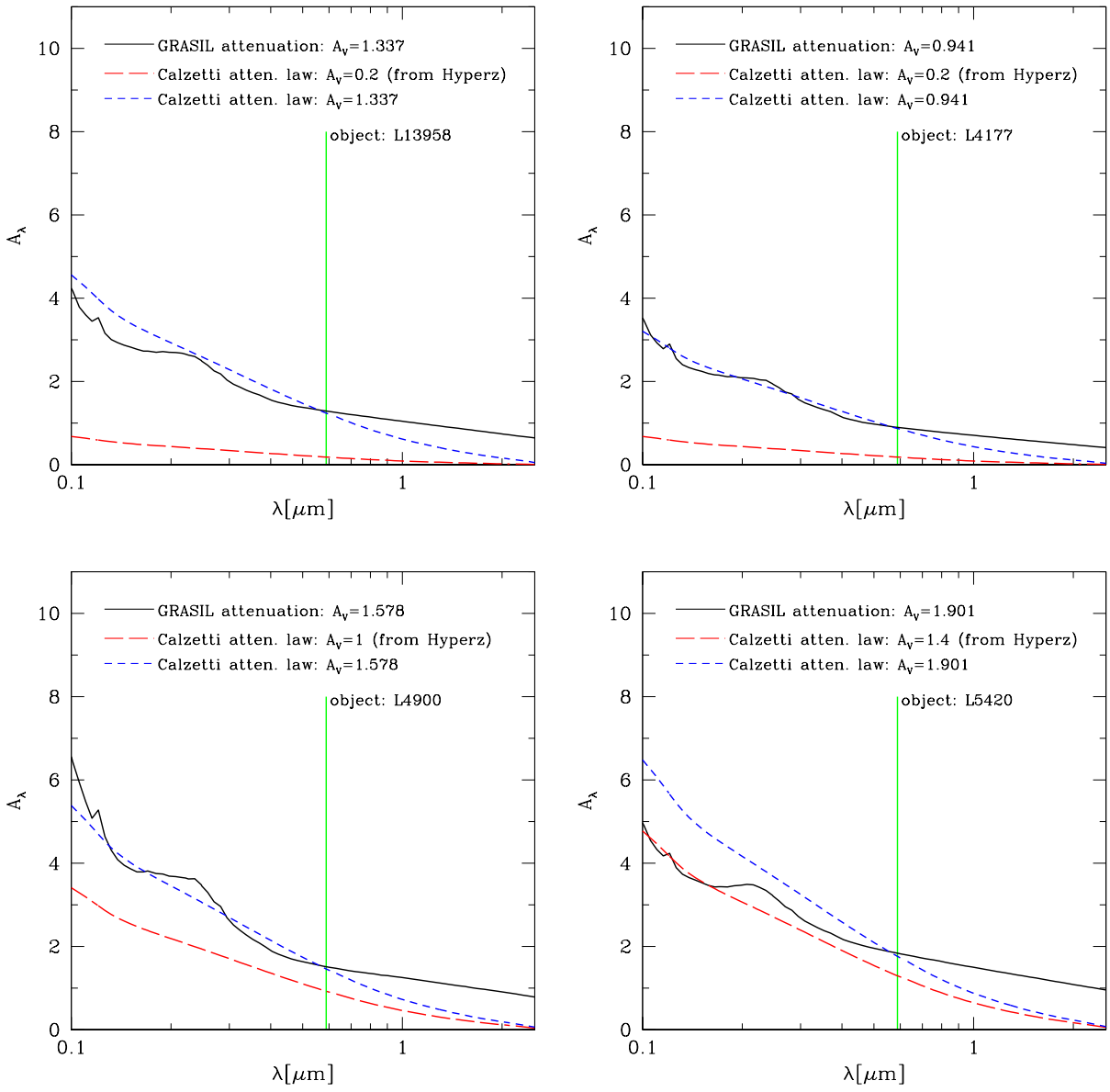

Figure 5.20 The predicted attenuation curves of each galaxy in the sample, estimated in a self-consistent way by GRASIL (black solid lines), are compared to the empirical Calzetti attenuation law computed using both the best A_V value obtained with Hyperz (red long dashed lines) and the one provided by GRASIL (blue short dashed lines). The vertical solid green lines define the V band in correspondence of which the average extinction is computed. The best-fit values of AV from both Hyperz and GRASIL are also highlighted in the figure. The specific name of the source (L for LIRGS and u for (U)LIRGs) is labelled in each panel.

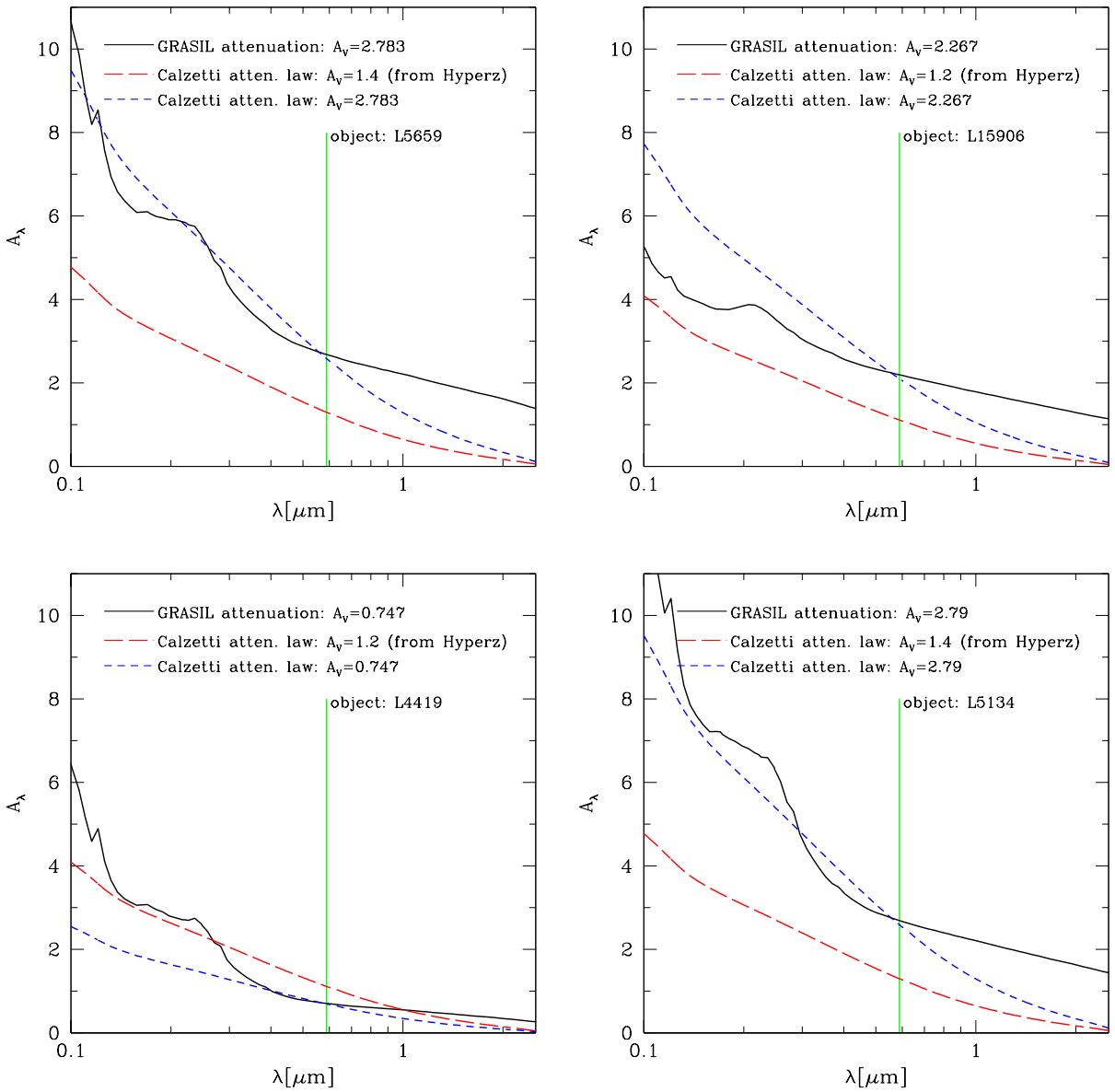

Figure 5.21 Same as in Fig. 5.20.

compared to the rise of the GRASIL curve. Granato et al. (2000), Panuzzo et al. (2007) have shown that a flattening of the attenuation curve at short wavelengths can be seen, as a function of increasing dust optical depth, due to the fact that a growing fraction of the observed UV is produced by the older stellar population.

For $\lambda > 0.6\,\mu m$ the situation is quite different. At these wavelengths and for almost all the objects in our sample, the Calzetti empirical relation is always lower than the attenuation curve estimated by GRASIL. This is of course due to the fact that the Calzetti law decreases very rapidly at longer wavelengths while in GRASIL there is still a contribution, even small, up to $\lambda \sim 5\ \mu$m to the dust attenuation.

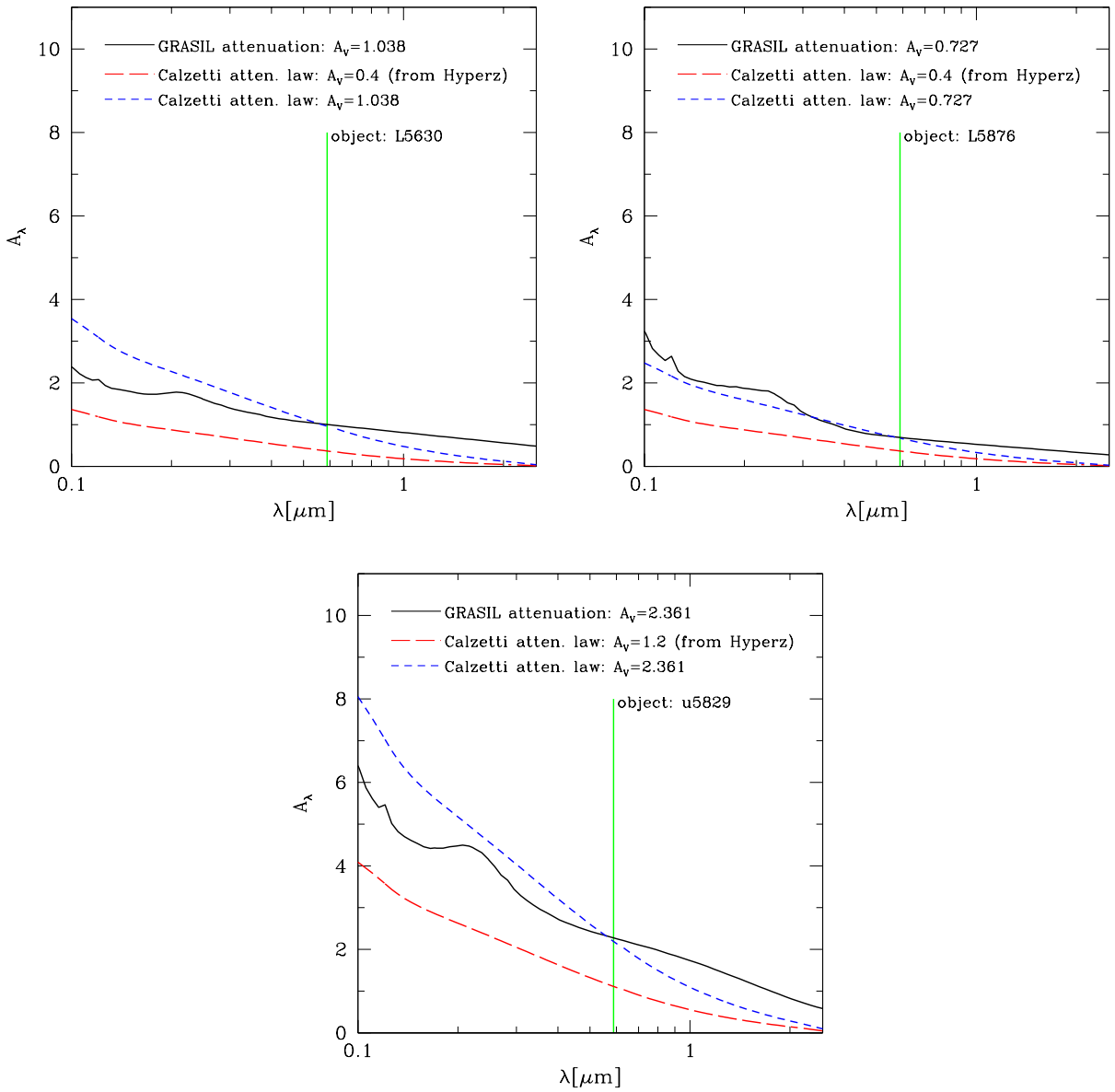

Figure 5.22 Same as Fig. 5.20.

Another major difference between our predicted attenuation curves and the Calzetti law is the total absence, in the latter, of the 2175 $\AA$ dust feature clearly present, instead, in most of our curves. A significant dilution of the feature is observable in some cases showing relatively low average extinction ($A_V \lesssim 1$) in agreement with what found by Burgarella et al. (2005b) due to the presence, in their sample, of IR-selected galaxies with a blue FUV-NUV colour and high dust attenuation. The origin and also the presence of this feature are still matter of debate. It is believed to be due to pure absorption, for this reason the effects of radiative transfer cause this feature to respond differently to geometrical effects compared to the rest of the attenuation curve.

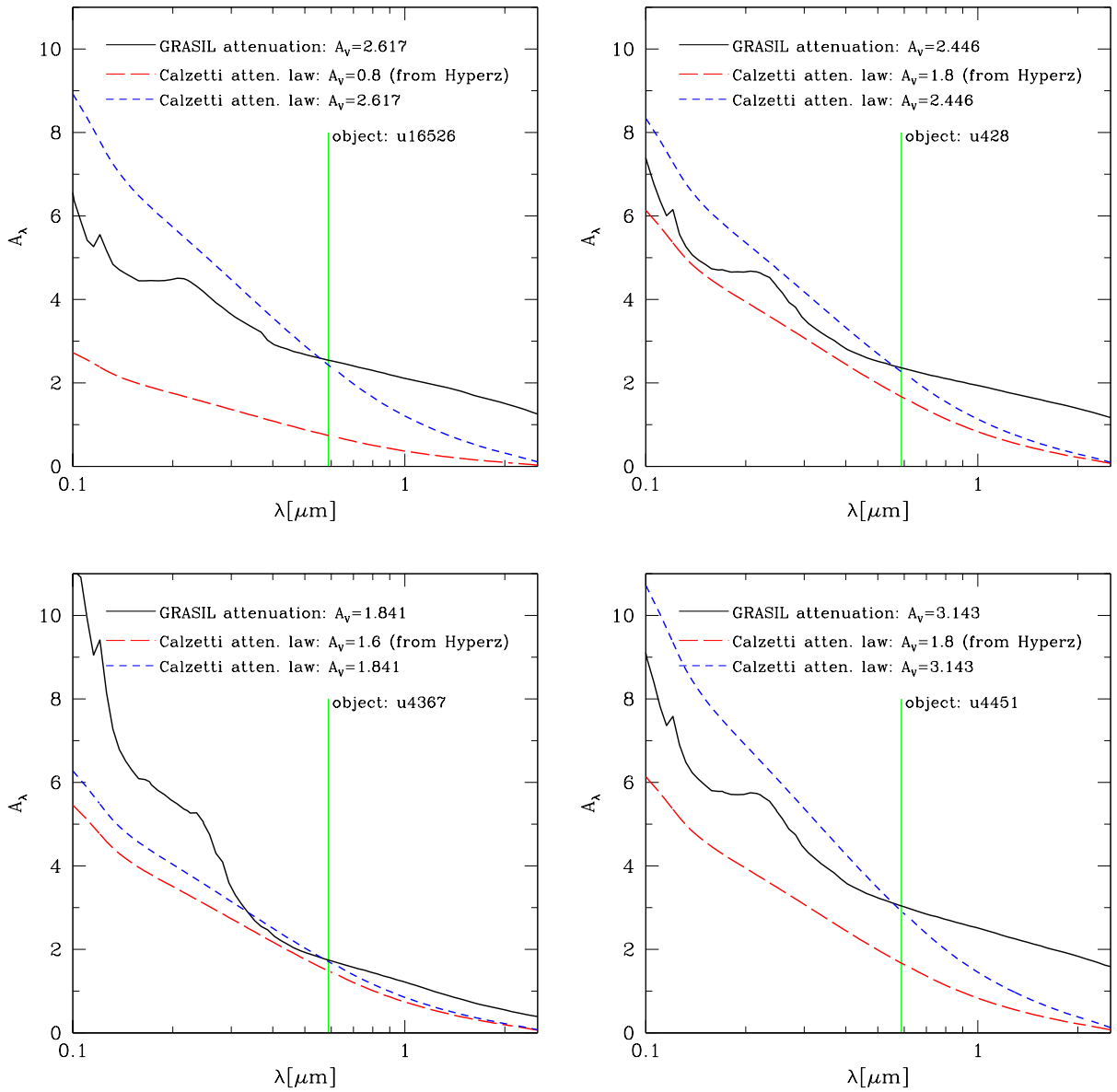

Figure 5.23 Same as Fig. 5.20.

According to Gordon et al. (1997) the observed shape of the Calzetti law can only be explained with dust that lacks the 2175-$\AA$ feature in its extinction curve. However, they only considered clumping of dust, not of stars, and assumed a spatial distribution for stars independent of stellar age. A completely different conclusion was reached by Granato et al. (2000) with GRASIL which, as we know, includes also the effect of an age-dependent extinction. They have shown that a more realistic geometry can explain the differences between the observed attenuation law of starburst galaxies and the galactic extinction law, even adopting the galactic cirrus optical properties. As cautioned by Panuzzo et al. (2007) this does not demonstrate that the optical properties of dust in starbursts are well represented by the average cirrus dust in the Galaxy, but rather than any difference may

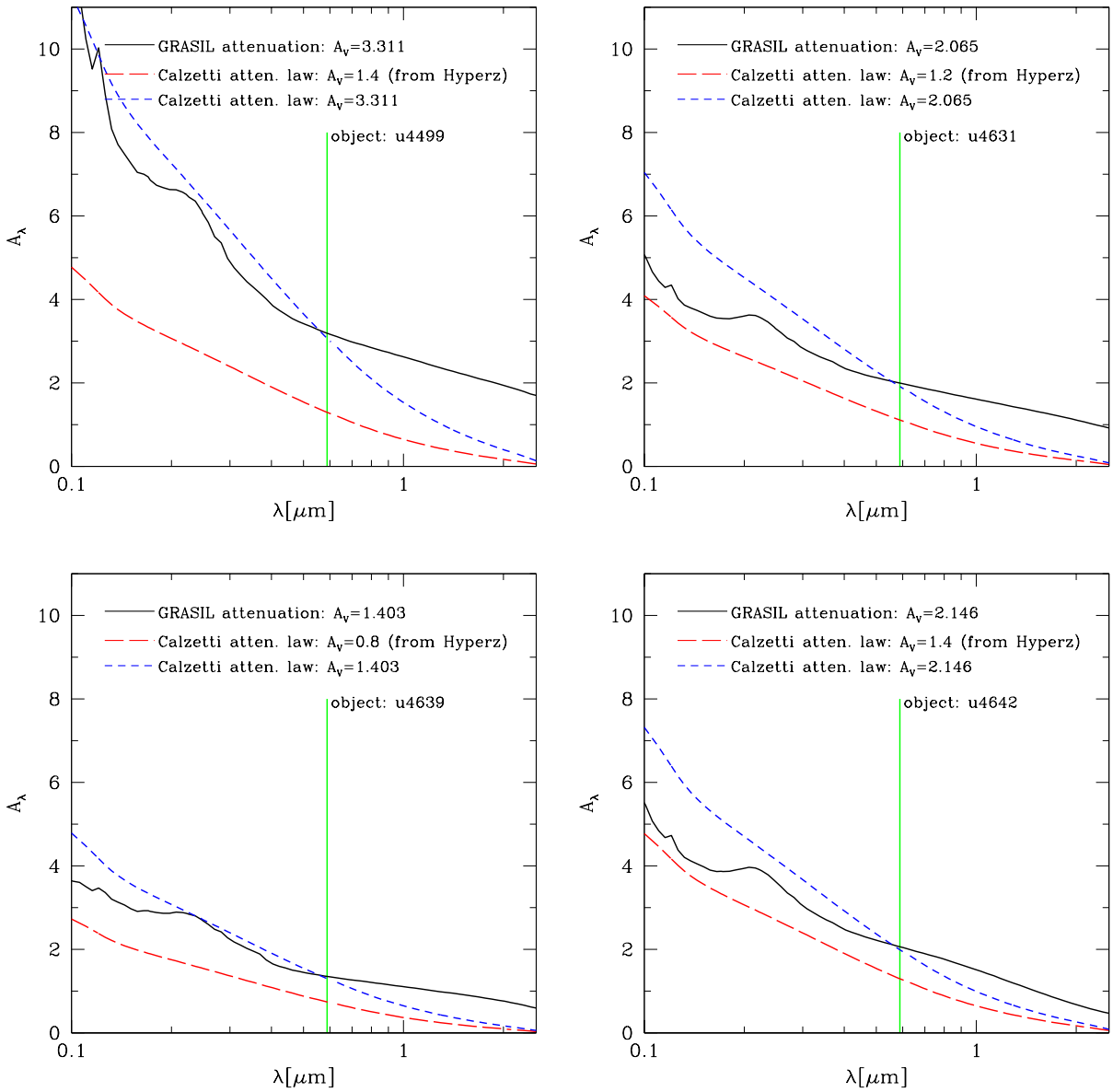

Figure 5.24 Same as Fig. 5.20.

be completely masked by geometrical effects. In this interpretation, the attenuation law of a specific stellar system arises, via the age-dependent extinction, from a complex blending of optical properties of dust, star formation history and relative geometry of stars and dust, including clumping of both components. The relative importance of these ingredients is a function of the evolutionary status of the galaxy. In very active systems the first ingredient is of little relevance, because much of the intrinsic opticalUV starlight is produced by stars embedded in molecular clouds, completely opaque at these wavelengths. Conversely, galaxies forming stars at a 'steady' rate, such as normal spirals, are expected to be better candidates to investigate variations of dust properties, provided that a sufficiently realistic geometry is used in their modelling (Panuzzo et al., 2007). In other words, as demonstrated

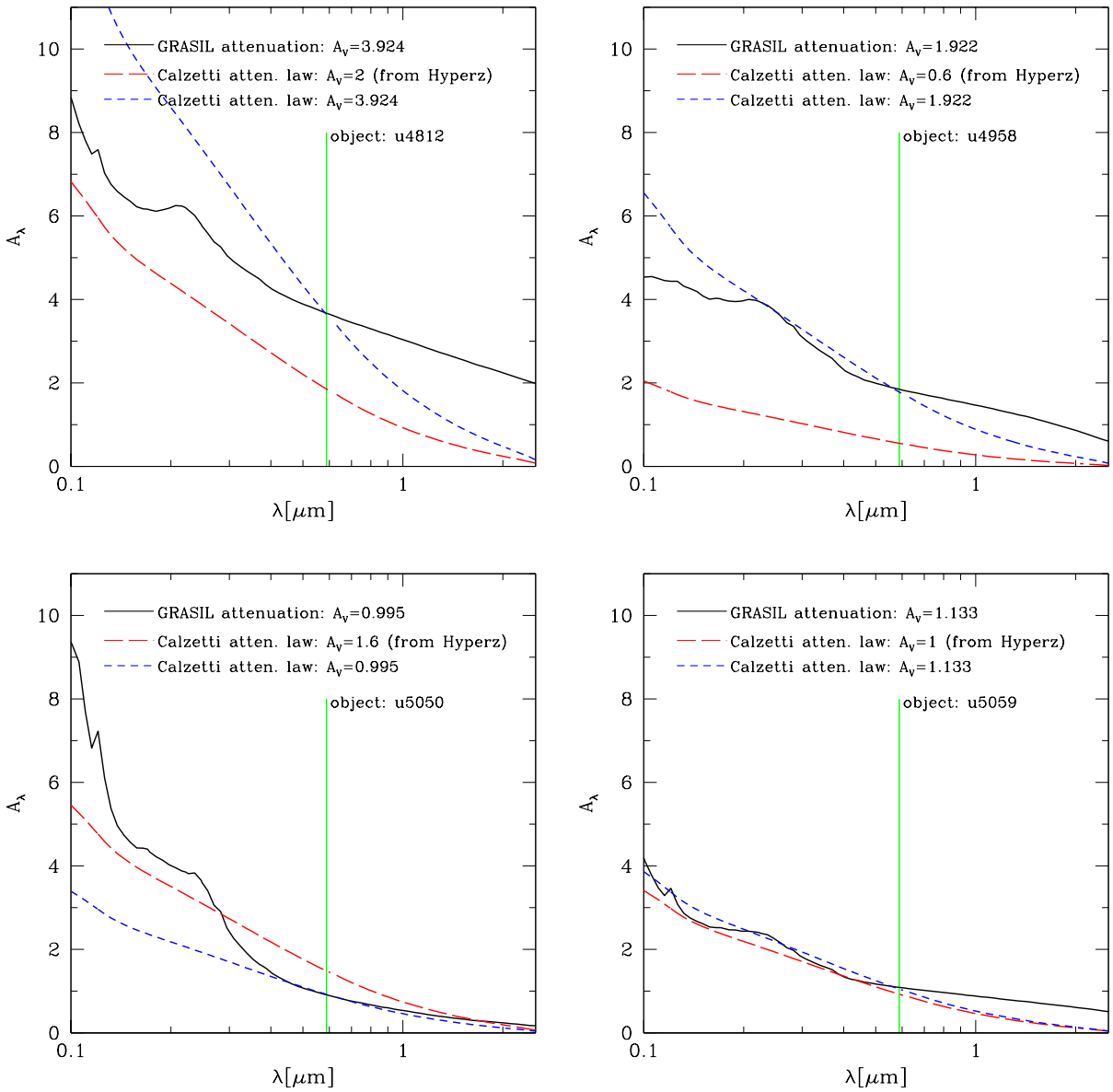

Figure 5.25 Same as Fig. 5.20.

by Granato et al. (2000) a featureless and shallow attenuation can be reproduced as a result of the complex and wavelength dependent geometry where the UV-emitting stars are heavily embedded inside MCs, while older stars, mainly emitting in the optical and NIR, suffer a smaller effect from the diffuse medium.

A further interesting aspect which is worth highlighting is the wide range of attenuations allowed by the model with respect to assuming a single attenuation low. This is clearly emphasised in Figure 5.28 which shows the V-band normalised attenuation curves computed by GRASIL (as solid black lines) compared to the Calzetti (2000) law (long dashed red line). This larger spread characterizing the models has been studied in detail by Fontanot

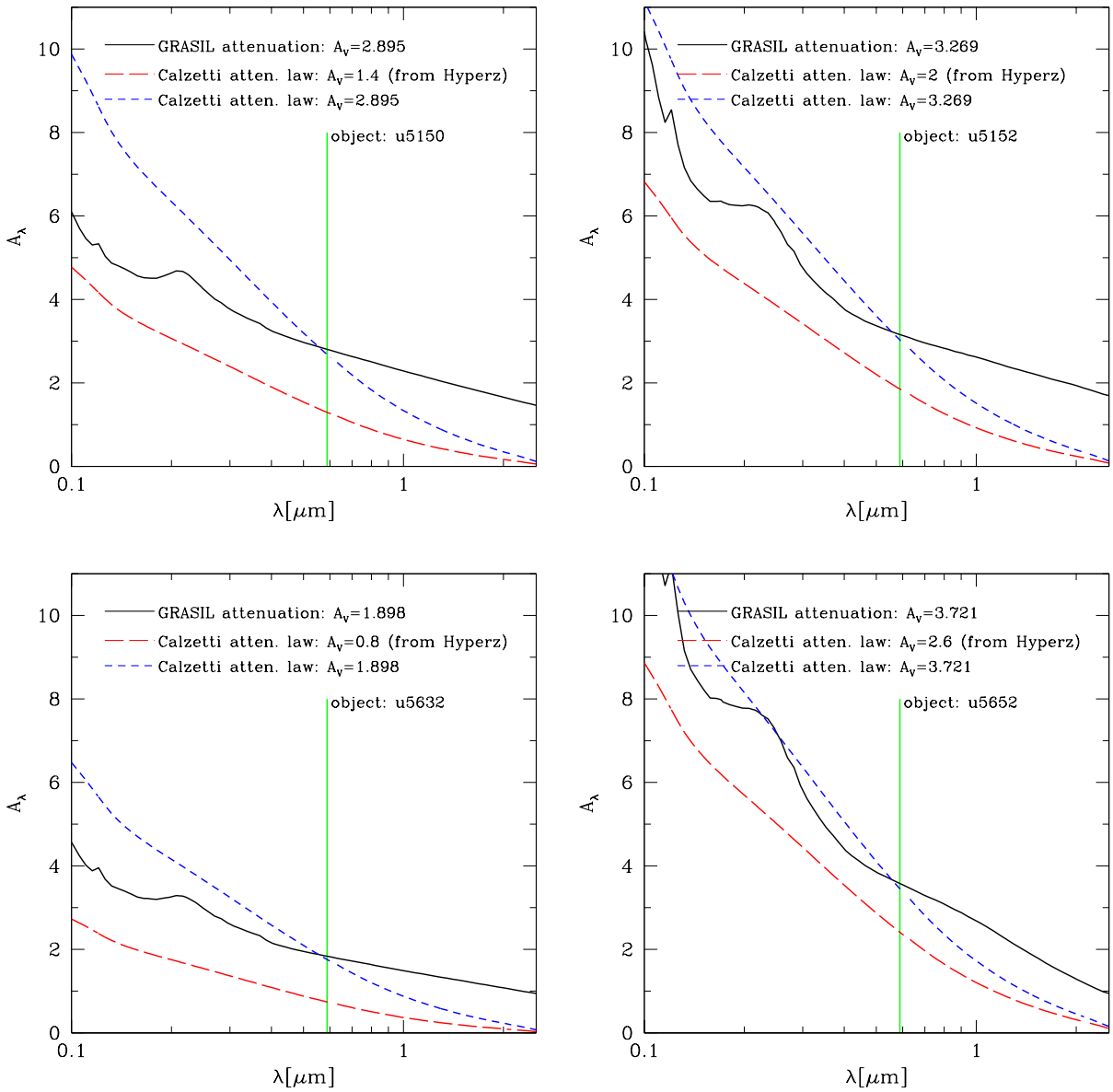

Figure 5.26 Same as Fig. 5.20.

et al. (2009b) and has to be ascribed to the accounting of the star formation histories, the geometrical distribution of stars and dust and the connection between stellar populations of different ages with different dusty environments. Indeed as stressed by Fontanot et al. (2009b) the attenuation curve obtained for each model would be exactly equal to the adopted extinction curve if we assumed that all the dust is in a foreground screen in front of the stars and there is not scattered light reaching the observer.

As stated by Conroy (2013), there is, apparently, no theoretical justification for using the same empirical relation Calzetti et al. (2000) (or attenuation curve) for a wide range of SED types. Several works (e.g. Conroy 2010; Buat et al. 2011b) have shown indeed that

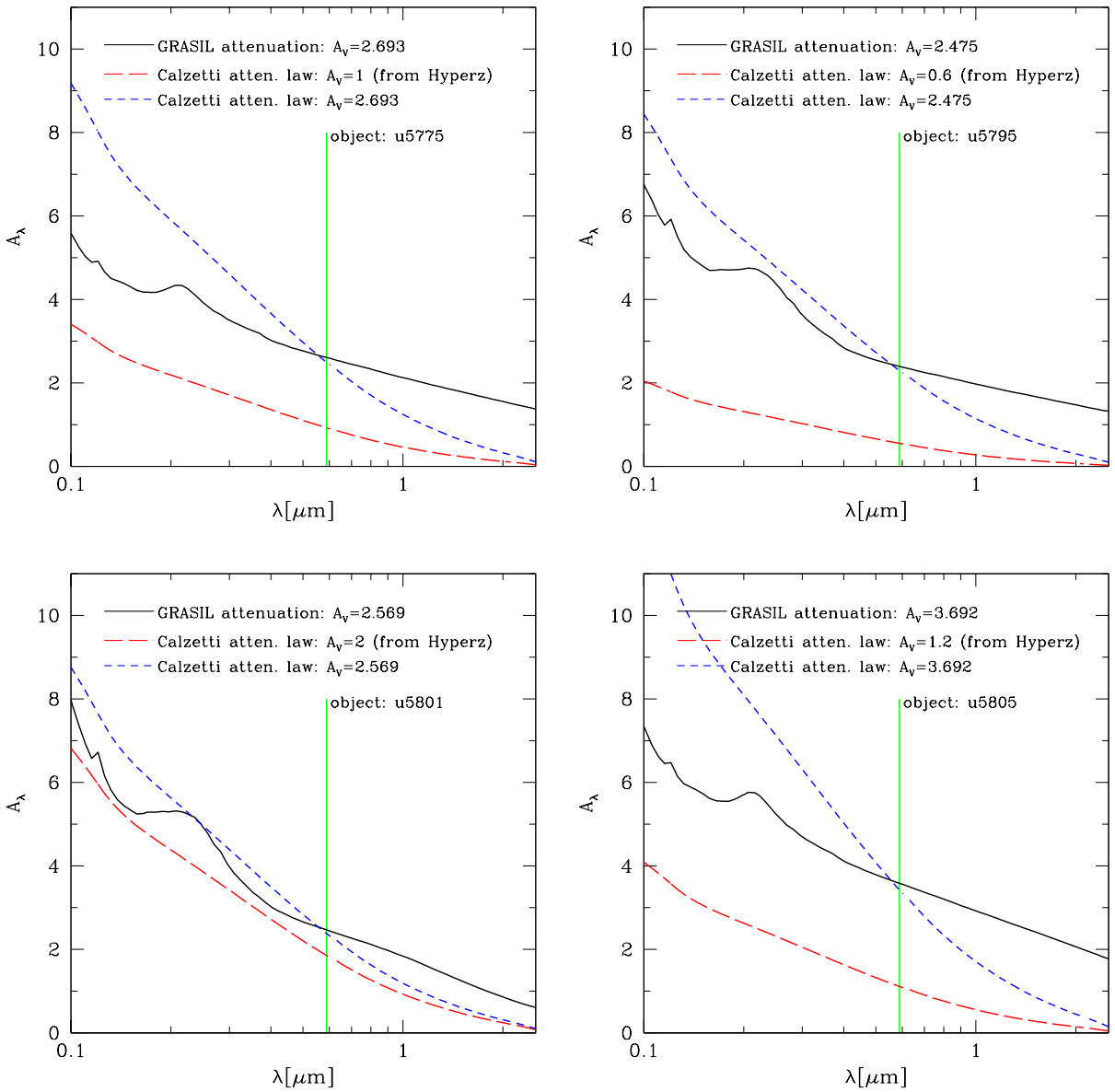

Figure 5.27 Same as Fig. 5.20.

the Calzetti law provides a poor fit to the UV colours of larger samples of nearby galaxies that have a range of star formation rates. Other observational studies also find that, at least for part of the UV-selected galaxies at $1 < z < 4$, the attenuation is not well described by the Calzetti law (Noll et al. 2009; Buat et al. 2011a, 2012; Lee et al. 2012).

IRX-A$_{FUV}$ correlation

As discussed by many authors (e.g. Buat & Xu 1996, Buat et al. 1999, Panuzzo et al. 2003, 2007), the ratio IR/UV is also a good estimator of the UV attenuation. We have thus compared our predictions for the far-UV (FUV) attenuation with those derived from the

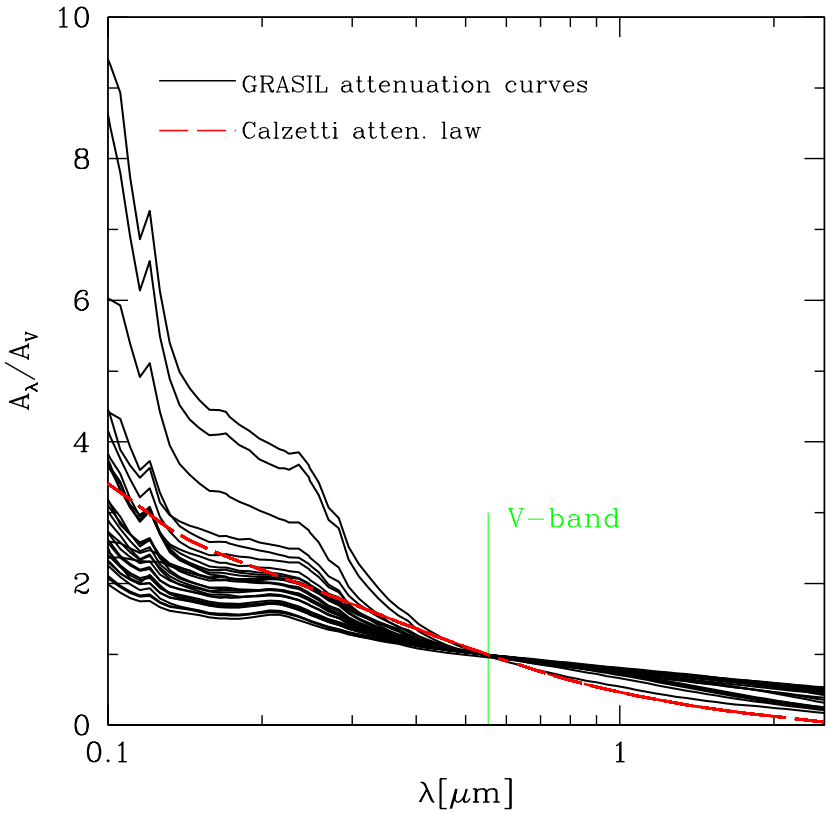

Figure 5.28 V-band normalized attenuation curves computed by GRASIL for the 31 high-z (U)LIRGs included in our sample (solid black lines), compared to the Calzetti(2000) attenuation curve (long dashed red line). The green vertical line highlights the reference V-band.

empirical relation proposed by Buat et al. (2005):

$$A_{FUV} = 0.0333IRX^3 + 0.3522IRX^2 + 1.1960IRX + 0.4967 \tag{5.5}$$

with $IRX = log\left(\frac{L_{IR}}{L_{UV}}\right)$. We have considered here the FUV filter as the near-UV (NUV) one, centred at 2310 $\mathring{A}$, is strongly affected by the presence of the 2175-$\mathring{A}$ bump in the MW extinction law (Panuzzo et al., 2007).

Figure 5.29 shows our results. z$\sim$1 LIRGs and z$\sim$2 (U)LIRGs are represented in the figure as filled blue squares and red circles, respectively. The empirical calibration by Buat et al. (2005) is highlighted as a solid green line. We have performed both a polynomial fit (as Buat2005) shown as blue long-dashed line whose coefficients are highlighted in the figure, and a linear fit (black short-dashed line) whose angular coefficient is 1.89.

As evident from the figure the agreement between our predicted relations and the empirical one by Buat et al. (2005) is good up to $log(L_{IR}/L_{FUV}) \sim 2.8$. At higher IR luminosities

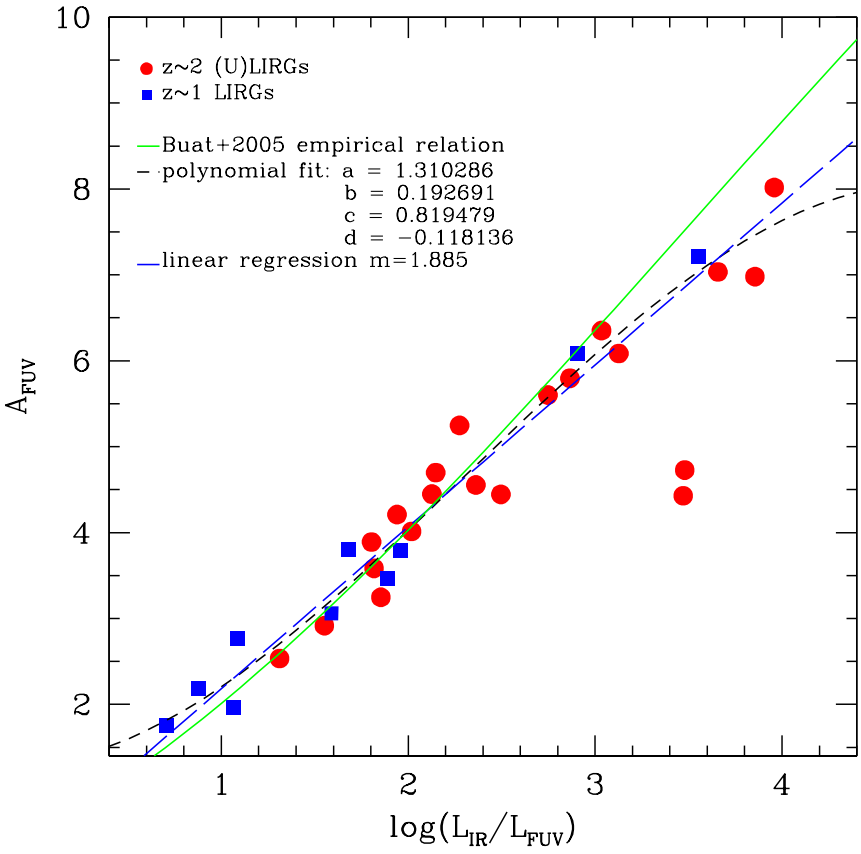

Figure 5.29 IRX-A$_{FUV}$ modeled relation (black short-dashed line for polynomial fit and blue long-dashed line for linear regression) compared to the empirical relation by Buat et al. (2005) (green solid line).

the empirical calibration of Buat2005 tends to overestimate the average FUV attenuation up to a factor of $\sim$ 2.

The empirical relation of Buat2005 has been calibrated on two different sample of local galaxies, a pure NUV-selected sample and a FIR selected sample at 60 μm built using the GALEX and IRAS sky surveys, respectively, over $\sim$ 600 deg^2. To select the sample the observed NUV and FUV fluxes have been first corrected for Galactic extinction using the Schlegel et al. (1998) dust maps and the Cardelli et al. (1989) extinction curve. Then to estimate dust attenuation for different scenarios of star formation they used the population synthesis code PEGASE (Fioc & Rocca-Volmerange, 1997) where the amount of dust emission is computed by adding all the stellar emission absorbed by the dust. Different configurations for the dust attenuation have been tested: Calzetti's screenlike attenuation law (Calzetti et al., 2000), a homogeneous mixture of dust and stars in a slab geometry with a Galactic or an LMC stellar extinction law (Buat & Xu, 1996) and a clumpy medium (Calzetti et al., 1994). Within this context the authors developed another bivariate model in which the attenuation of the light from stars younger than 10^7 yr follows the Calzetti

law whereas older stars are supposed to be homogeneously mixed with the dust or to be distributed in a clumpy medium. According to the authors, for their sample of local NUV selected star forming galaxies, all the models gave very similar results for a given star formation history, with a dispersion lower than 5%. In particular, the exact form of the extinction curve (with or without a 2175 bump) does not seem to affect the results. Only the exponentially decreasing SFR with $\tau = 2\,\mathrm{Gyr}$ seems to lead to a much lower attenuation for a given dust-to-NUV flux ratio: the dust heating by old stars becomes important, and only a fraction of the dust emission is related to the ultraviolet absorption. As they were interested in studying only SF sources they excluded this scenario more typical of elliptical or lenticular galaxies (Gavazzi et al., 2002). All the other star formation scenarios leaded to a relative error lower than 20%.

The main assumptions made by Buat et al. (2005) on dust attenuation and star and dust distribution, outlined above, are, according to me, the main driver of the difference observed between their empirical calibration and our predictions for higher IR luminosity objects. As stated also above, I believe that the crucial point here is the age-dependent dust attenuation, in terms of age-dependent spatial distribution of stars. None of the models considered above, in fact, include the clumping of stars as a function of their age. More likely, at higher IR luminosities where dust effects are larger this can bring to such discrepancies. Moreover following a 'Kennicutt-like' approach, according to which the total IR luminosity is totally contributed by young stars, they excluded the possibility for stars older than 10^7 yr to heat the cirrus, well present instead in our solutions.

5.7 Concluding Remarks

The extensive application of our self-consistent physical model to a sample of dusty star forming (U)LIRGs at high redshift has brought us various important results. The availability, for this sample, of a full multiwavelength coverage from far-UV to sub-mm, including both Herschel PACS and SPIRE photometric data and ultra-deep Spitzer IRS spectra, has prompted us to investigate the nature and the main physical properties - like stellar mass, bolometric luminosity, star-formation history, extinction, as well as the mass assembly history - for every object.

The novelty of our approach consists in modelling the data with a self-consistent physical code (GRASIL), exploiting a state-of-the-art treatment of dust extinction and reprocessing based on a full radiative transfer solution.

From the detailed shape of the broad-band best-fit SED of our galaxies, our analysis seems to be able not only to give an accurate estimate of the current SFR of galaxies but also to

give important hints on their SFH. This, in particular, seems to play a crucial role in our interpretation of galaxy spectra.

The Kennicutt's (1998) calibration of the SFR, appears to correspond to an extreme case in which SFR is constant over a time interval of 100 Myr and all the the light comes from the youngest stars. Our typical galaxies, instead, include sizeable contribution from intermediate age stars to the dust heating through cirrus emission. This brings to a factor $\sim$2 lower calibration of SFR from L_{IR}, for our moderately star-forming galaxies, with respect to the Kennicutt's calibration.

Another important result of our analysis is that the complex mixture of dust and radiant energy sources may seriously affect our interpretation of galaxies, both local and at high-redshifts. These effects might have been underestimated by past applications of empirical and simplified spectro-photometric codes. We find substantial discrepancies between our results and those based on optical-only SED fitting procedures for the same objects. Our physically consistent best-fit model solutions of the observed SEDs indicate higher extinctions (by $\Delta A_V \sim 0.81$ and 1.14) and higher stellar masses (by $\Delta \mathrm{Log}(M_\star) \sim 0.16$ and 0.36 dex) for z$\sim$1 and z$\sim$2 (U)LIRGs, respectively. The stellar mass difference is larger for the most obscured objects and correlates with the total dust extinction.

A further interesting aspect put in evidence by our analysis is the wide range of attenuations allowed by the model with respect to assuming a single attenuation low. This larger spread characterizing the models was studied in detail by Fontanot et al. (2009b) and has to be ascribed to the accounting of the star formation histories, the geometrical distribution of stars and dust and the connection between stellar populations of different ages with different dusty environments.

Our analysis thus demonstrates that a correct and self-consistent treatment of dust extinction and reprocessing, together with a full multiwavelength coverage (from far-UV to radio), is essential to get reliable estimates of the main physical parameters like stellar mass, dust extinction and SFRs.

By analysing the best-fit GRASIL model parameters used to reproduce the SEDs of our high-z (U)LIRGs and affecting the dust (and NIR-to-sub-mm) properties of the galaxies, (i.e. f_{MC}, t_{esc}, $r_{half-mass}$, $\tau_{1\mu m}$, β) we find:

(1) $\mathbf{t_{esc}}$**:** best-fit values for both galaxy populations range between $\sim$ 3 and 98 Myr, therefore, from the typical values of normal star forming galaxies to the much higher values characteristics of more dust obscured starburst objects. The median is $\sim$ 13 Myr for the z$\sim$2 (U)LIRGs and $\sim$6 Myr for the z$\sim$1 LIRGs in agreement with the

typical values of high-z normal star forming objects. All the stars with ages older than the typical escaping time contribute to cirrus heating.

(2) $\mathbf{f}_{MC}$**:** best-fit values range between 0.12 and 0.54 for the z$\sim$1 LIRGs and 0.2-0.98 for the z$\sim$2 (U)LIRGs. In agreement with other observational works (e.g. Braun et al. 2011, Combes 2013, Daddi et al. 2010a, Magdis et al. 2012) the molecular gas fractions tend to be higher for the highest redshift (U)LIRGs. The median values are $\sim$ 0.4 and 0.8 for the z$\sim$1 and $\sim$2 sample, respectively.

(3) $\tau_{1\mu m,MC}$**:** best-fit values typically range between $\sim$ 5-100 for both samples. The median values are $\sim$17 and $\sim$25 for the z$\sim$1 and z$\sim$2 (U)LIRGs, respectively. These translate in median values for the optical depth at 100 μm approximately equal to 0.1 and 0.15 for the z$\sim$1 and 2 sample, respectively. Compared to local ULIRGs, as Arp220 for example, which appears to be optically thick out to at least 100 microns (Rangwala et al., 2011) based on Herschel data, our high-z (U)LIRGs do not show very high $\tau_{100\mu m}$. The maximum value reached is of about 0.5.

(4) β**:** typical value of $\sim$1.8 well agrees with the value usually measured for dusty star forming galaxies at high-z (see e.g. Magdis et al. 2012) and roughly corresponds to cold dust temperatures in the range between 11 and 30 K (e.g. Dupac et al. 2003). It is worth emphasising that thanks to the availability of this rich dataset covering the FIR-to-sub-mm wavelength range, the sub-millimetre spectral slope can be accurately measured independently from the temperature distribution. This allows us to break the well-known T-β degeneracy usually affecting the estimates based on modified BB fit to the FIR SED.

(5) $\mathbf{r}^{\star}_{half-mass}$ **&** $\mathbf{r}^{diff}_{half-mass}$**:** these represent the typical scale-lengths, for both stars and dust, of the assumed spheroidal geometry (King's profile) for our galaxies. By comparing the two galaxy populations at z$\sim$1 and z$\sim$2 we find that while the distribution of stars appears to be more extended for the z$\sim$1 LIRGs where it reaches 5.4 kpc, the dust distribution shows an inverse trend being more extended for the highest redshift (U)LIRGs for which it reaches $\sim$15-17 kpc. This seems to be in agreement with the recent results published by Symeonidis et al. (2013) according to which (U)LIRGs in the early Universe are typically characterised by a more extended dust distribution and/or higher dust masses than lower redshift LIRGs and local equivalent sources.

No much degeneracy is observed among the model parameters. In the case where we consider the combined variation of both the SFH and GRASIL parameters, the typical uncertainties on the best-fit average extinction and stellar mass estimates are $\Delta A_V \sim 0.3$ and $\Delta M_\star \lesssim 0.2$ dex, still within the typical uncertainties for this kind of analysis.

We measure gas depletion timescales ($\tau_{gas} = M_{gas,MC}/SFR$) in agreement with the typical duration of normal star forming galaxies duty cycle ranging between 0.5 - 1 Gyr but much longer than the typical duration expected for starbursts ($\lesssim$100 Myr). Comparing the two galaxy populations we find longer depletion timescales ($\sim$1 Gyr) for the z$\sim$2 (U)LIRGs than for the lower redshift LIRGs ($\sim$0.5 Gyr). If we consider these two classes of objects as the same galaxy population observed in different evolutionary stages, this result can be interpreted as due to the fact that while the highest z (U)LIRGs are in the initial phase of star formation where there are large molecular gas reservoirs but not so high SFRs ($\lesssim 100 M_{\odot}/yr$), the lower redshift LIRGs would actually be objects observed at later stages when the molecular gas reservoir has been reduced by the star formation activity and the SFR is lower. We also measure median SFEs of $\sim$ 14 $L_{\odot}/M_{\odot}$ very similar to the average SFE (14 ± 2 $L_{\odot}/M_{\odot}$) found by Magdis et al. (2012) for normal SF galaxies at high-z but $\sim$12 times lower than the typical value of starburst galaxies ($<$SFE$>\sim 200\, L_{\odot}/M_{\odot}$) usually characterized by an accelerated mode of SF.

Chapter 6

Radio emission and SFRs of high-z dusty star forming galaxies

As discussed in the previous Chapter (§ 5.6.2.1), our results in terms of larger stellar masses and lower SFRs, with respect to classical estimates, have a strong impact on the SFR-$M_\star$ diagram. We have seen that the effect is strongly dependent on the dust obscuration and the nature of star formation, i.e. gradual evolving spheroids versus starbursts. In order to further check the reliability of our physical solutions in terms of both stellar mass and SFR estimates, we have decided to include into our analysis also radio data at 1.4 Ghz. This is fundamental because the radio continuum offers a further independent way to estimate and constrain the 'current' SFR in galaxies completely unaffected by extinction. Moreover as the radio emission probes the SFH on different timescales with respect to the IR emission, this analysis will also help us in better understanding and constraining the source's past SFHs, in particular the number of massive stars contributing to the NT component of radio emission through core-collapse SNe, another crucial point risen by our previous physical analysis.

6.1 Radio data

In addition to the availability of a spectroscopic redshift and complete FIR coverage by both Herschel PACS and SPIRE (already included in our previous analysis), we also looked for detection at 1.4 GHz.

We were initially able to recover, from the published VLA catalogue in GOODS-S by Miller et al. (2013), the radio data only for 2/31 objects of our sample, those having $> 4\sigma$ detection. More recently, we set up a collaboration with Neal Miller who has been working

on radio observations in GOODS-S, we have been able to get a radio detection for all the (U)LIRGs in our sample, although most of them at a low significance ($\lesssim 2\,\sigma$) level.

The radio flux densities have been measured at the positions of our LIRG and ULIRGs and the RMS in the vicinity of the same position. The maximum flux density within a $5''$ radius of the indicated position has been also evaluated, thus providing also the position of this maximum and its flux density.

These objects are typically faint detections, too faint for inclusion in the radio catalogue. Figure 6.1 shows a histogram representing the measured flux densities at the indicated positions. As evident from the figure the expectation of a Gaussian centered on zero and with a dispersion of the image noise (red histogram) is very different from the actual measured distribution.

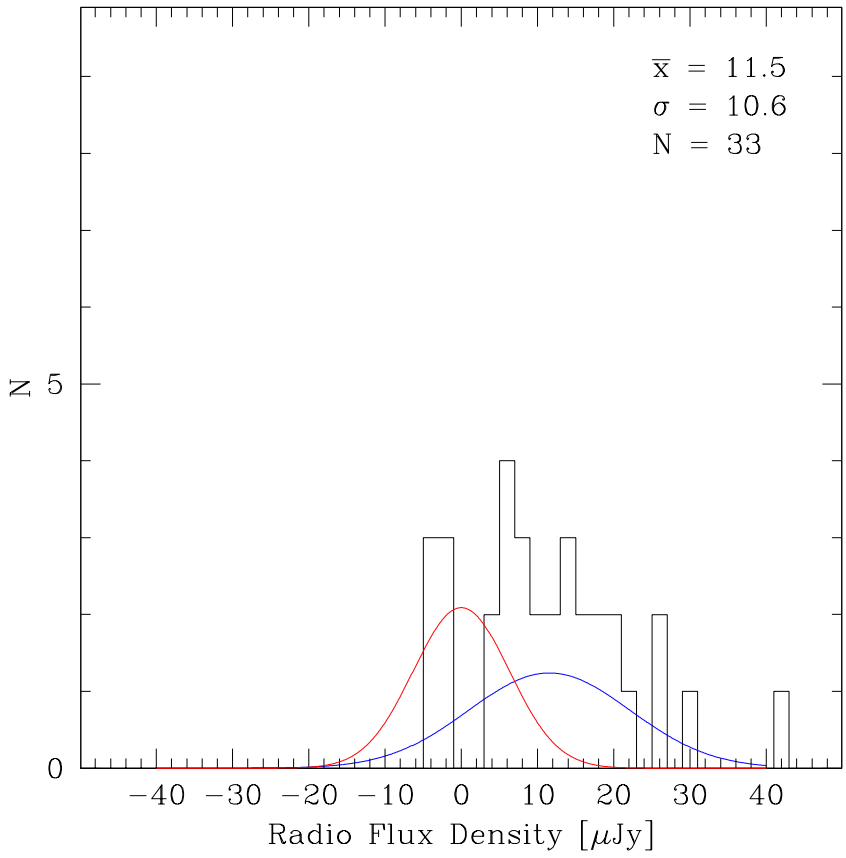

Figure 6.1 Histogram showing the measured flux densities at the indicated positions of (U)LIRGs. As evident from the figure the expectation of a Gaussian centered on zero and with a dispersion of the image noise (red histogram) is very different from the actual measured distribution [kindly provided by Neal Miller].

6.2 Modeling the Radio emission of high-z dusty star-forming galaxies with GRASIL

To model the observed SEDs of our high-z (U)LIRGs we used the same prescriptions of our previous analysis already discussed in detail in Section 5.2 of Chapter 5. We recall that among the several parameters included in the GRASIL model, through a deep study of the parameter space, we were able to limit the number of total free parameters to only 6 when dealing with gradually evolving spheroids and 9 when including also a burst on top of the secular star formation phase modelled with a Schmidt type SF law. The input star formation histories are computed with the standard chemical evolution code, described in Section 3.2, that provides the evolution of the SFR, M_{gas} and metallicity, assuming an IMF, a SF law $SFR(t)=\nu_{Sch} \cdot M_{gas}(t)^k + f(t)$ (i.e. a Schmidt-type SF with efficiency ν_{Sch}, and a superimposed analytical term to represent transient bursts possibly related to a galactic merger, and an exponential infall of gas ($dM_{inf}/dt \propto \exp(-t/\tau_{inf})$). Here we have adopted k=1, f(t) exponential, and the Salpeter IMF which is the default choice for the chemical evolution code. When comparing our estimates with other studies we converted the Salpeter IMF to the Chabrier one by dividing by a conservative value of 1.7. We used the same re-scaling factor also for the SFRs, although some works report a lower value ($\sim$ 1.58) due to the different populations dominating the energy budget of SFR and $M_\star$. We find this reliable but for consistency with our previous results we decided to keep 1.7. This value is the same as used in other works we compare with, as Daddi et al. (2010a) and Rodighiero et al. (2011), for example. Anyway we have checked that assuming the lower factor of 1.58 would result in a difference with respect to our estimates (using 1.7 instead) lower than 0.03 dex in log. scale.

The model for radio emission used here refers to the seminal work by Bressan et al. (2002) with the addition of the revised calibration first implemented by Vega et al. (2008) (see also Section 3.6). Here below we give only a brief description of the new radio calibration adopted here.

With respect to the original calibration of the $L^{NT}_{1.4Ghz}/\nu_{CCSN}$ (i.e. ratio of the non thermal radio emission to the Core-collapse SN rate) ratio by Bressan et al. (2002) we used here the revised one by Vega et al. (2008) which consists of enhancing the calibration factor by 30-40%. This is required to reproduce the radio emission of normal star forming galaxies at high redshift as well as that one of both local and high-z (U)LIRGs. The new calibration factor is a consequence of the subsequent improvements on the SSP libraries adopted here and in Vega et al. (2008) with respect to those used in the original work of Bressan2002. The updated SSPs are characterized by a finer time sampling of the ages typical of non thermal emission. This results in a lower SNII rate ($dn/dt = dn/dm \times dm/dt = IMF \times dm/dt$)

with respect to previous SSPs and therefore, for the same calibration, lower non thermal radio emission.

6.3 Spectral fits of high-z dusty star forming galaxies including radio data: Results

When reproducing the radio data we used the following prescriptions to assign them an error: (i) for the objects having $S_{1.4Ghz}/RMS \gtrsim 3\,\sigma$ we used the same error as given in the catalogue, usually of the order of $6.1 - 6.3\mu\,Jy$; (ii) for those objects having instead $S_{1.4Ghz}/RMS \lesssim 2\,\sigma - 3\,\sigma$ we assumed a $2\,\sigma$ error-bar associated to the measured flux density; (iii) finally we consider as $3\,\sigma$ upper limits all the sources having negative average flux densities measured at the position of the source. These are represented in the figure as triangles.

Figures 6.2,6.3,6.4,6.5,6.6,6.7,6.8,6.9 show the GRASIL best-fits to the far-UV-to-Radio SEDs of our z$\sim$1 LIRGs and z$\sim$2 (U)LIRGs, respectively. The 3σ upper limits are indicated as red arrows while the insets report the fit to their IRS MIR spectra. These best-fit SEDs have been obtained using the same model parameters as in the previous Chapter, except for the ULIRG *U4812* for which we considered an alternative solution based on different geometry and SFH. The best-fit SFHs of all the other (U)LIRGs are thus the same already discussed in detail in Section 5.2 of Chapter 5 (see Fig. 5.1). Here we will discuss only the SFH of the object for which the old prescription was unable to reproduce the radio data, namely *U4812*.

We recall that all these fits have been performed by assuming the simplest geometry for dust and stars, namely a King's profile, in order to limit the number of free parameters in the model. Fadda et al. (2010) have performed a rough analysis of their morphology, based on HST ACS images in the B, V, i, z filters (see Section 4.4.1). Many of these have been found to be extended sources characterized by many clumps. Some of them, instead, have been found to be very compact objects. All of them show red colors indicative of significant dust contribution. However given their high redshifts it is difficult to draw a complete picture of their morphology. We believe our approximation of spheroidal geometry to be a better choice for these objects, as further confirmed by our results.

We have also recently tested a comprehensive library of disk galaxies, allowing for different SFHs, from a bursty SFR to a more gradually evolving SFR, on this sample of high-z (U)LIRGs and found that for almost all of them a spheroidal geometry is the best

choice. Indeed, when forcing disk geometries we face the situation of un-physical parameter values for the scale-lengths of the double exponential profile (see Section 3.5.1) with the

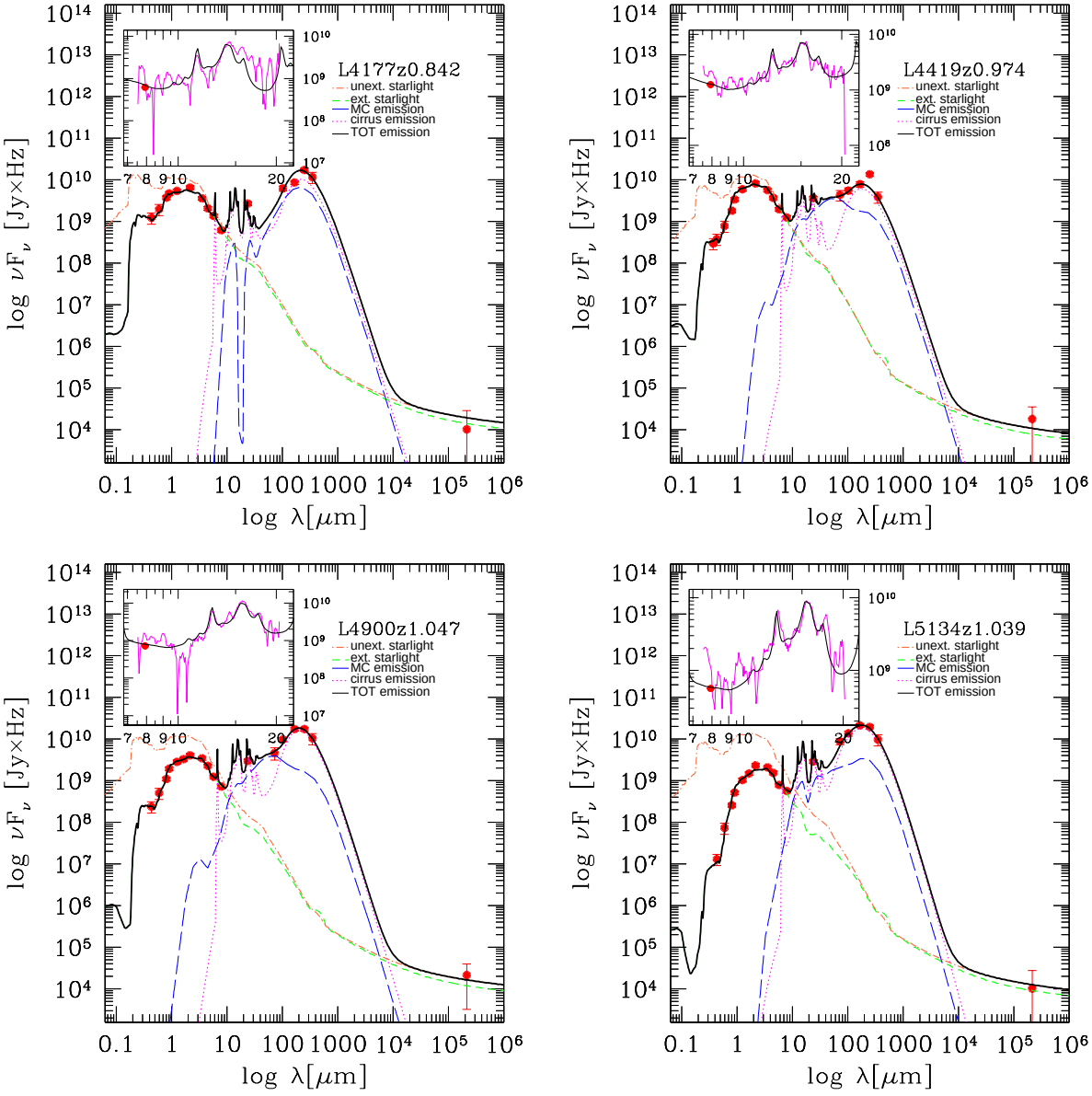

Figure 6.2 GRASIL best-fits (solid black line) to the observed SED (red circles) of $z \sim 1$ LIRGs. IRS spectra appear in the inset window (magenta line). The color-coded lines represent the unextinguished starlight (orange dot-dashed), extinguished starlight (green dashed), cirrus emission (magenta dotted) and MC emission (blue long dashed).

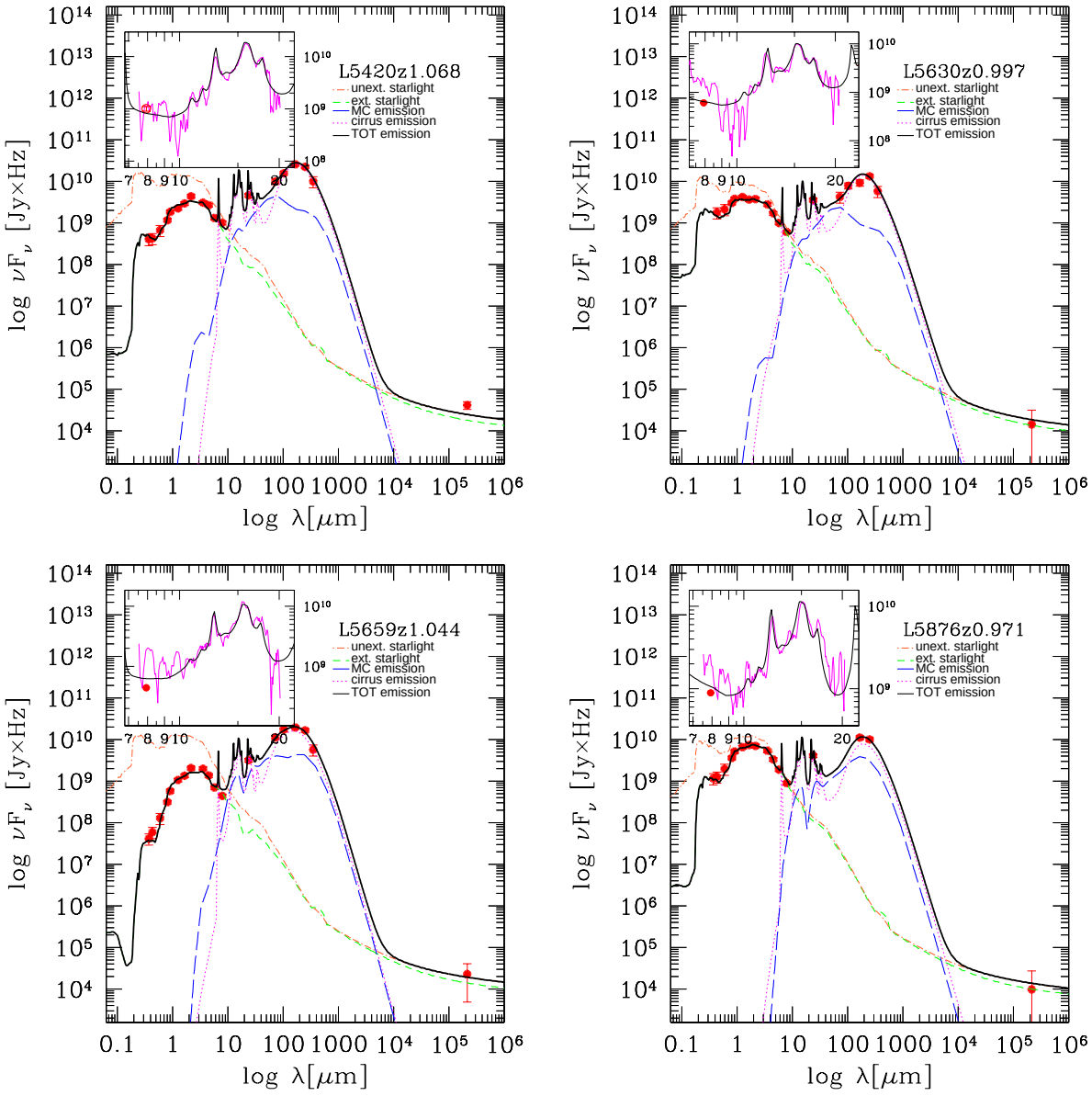

Figure 6.3 GRASIL best-fits (solid black line) to the observed SED (red circles) of $z \sim 1$ LIRGs. IRS spectra appear in the inset window (magenta line). The color-coded lines represent the unextinguished starlight (orange dot-dashed), extinguished starlight (green dashed), cirrus emission (magenta dotted) and MC emission (blue long dashed).

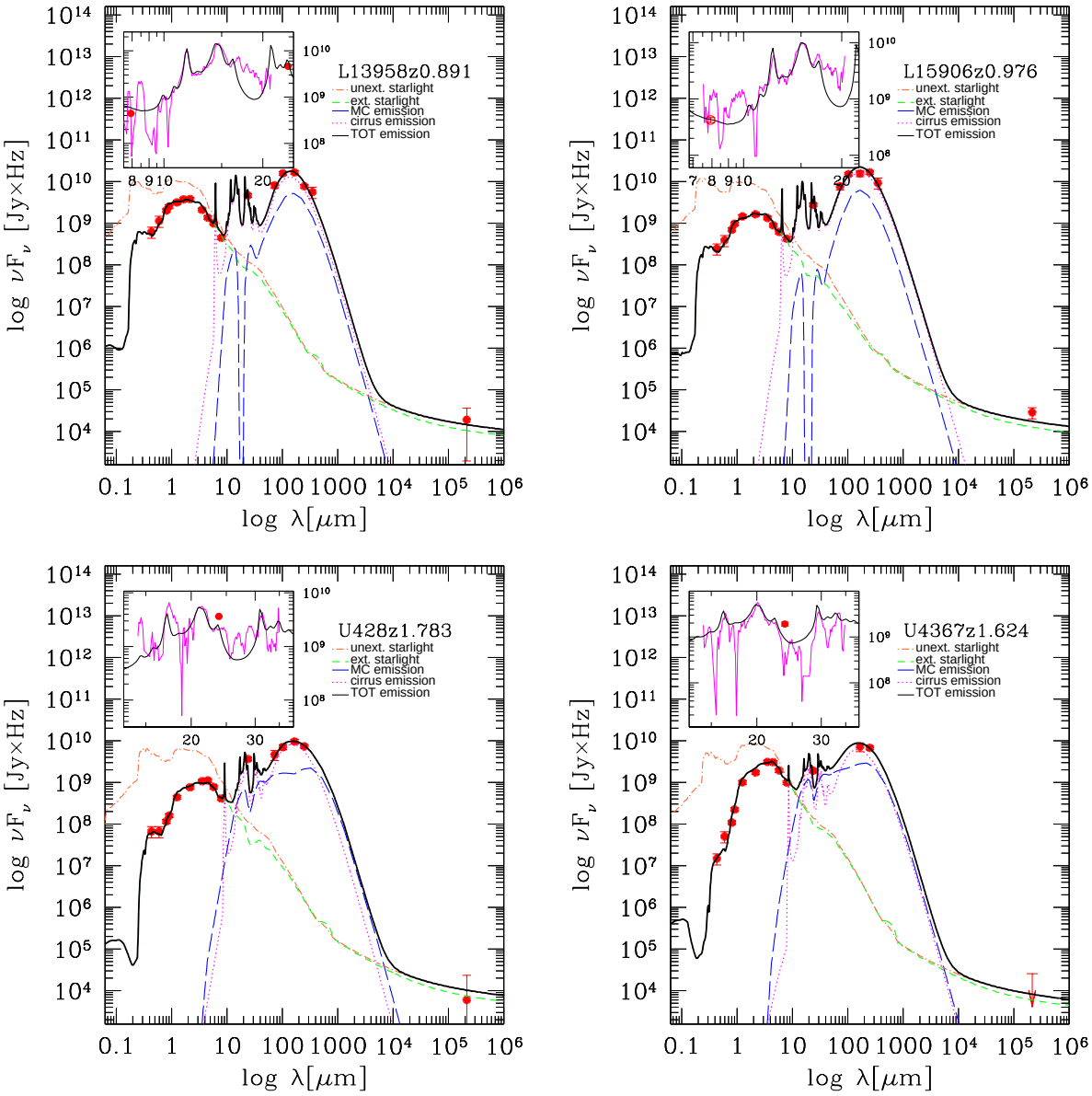

Figure 6.4 GRASIL best-fits (solid black line) to the observed SED (red circles) of $z \sim 1$ LIRGs (top) and $z \sim 2$ (U)LIRGs (bottom). IRS spectra appear in the inset window (magenta line). The color-coded lines represent the unextinguished starlight (orange dot-dashed), extinguished starlight (green dashed), cirrus emission (magenta dotted) and MC emission (blue long dashed).

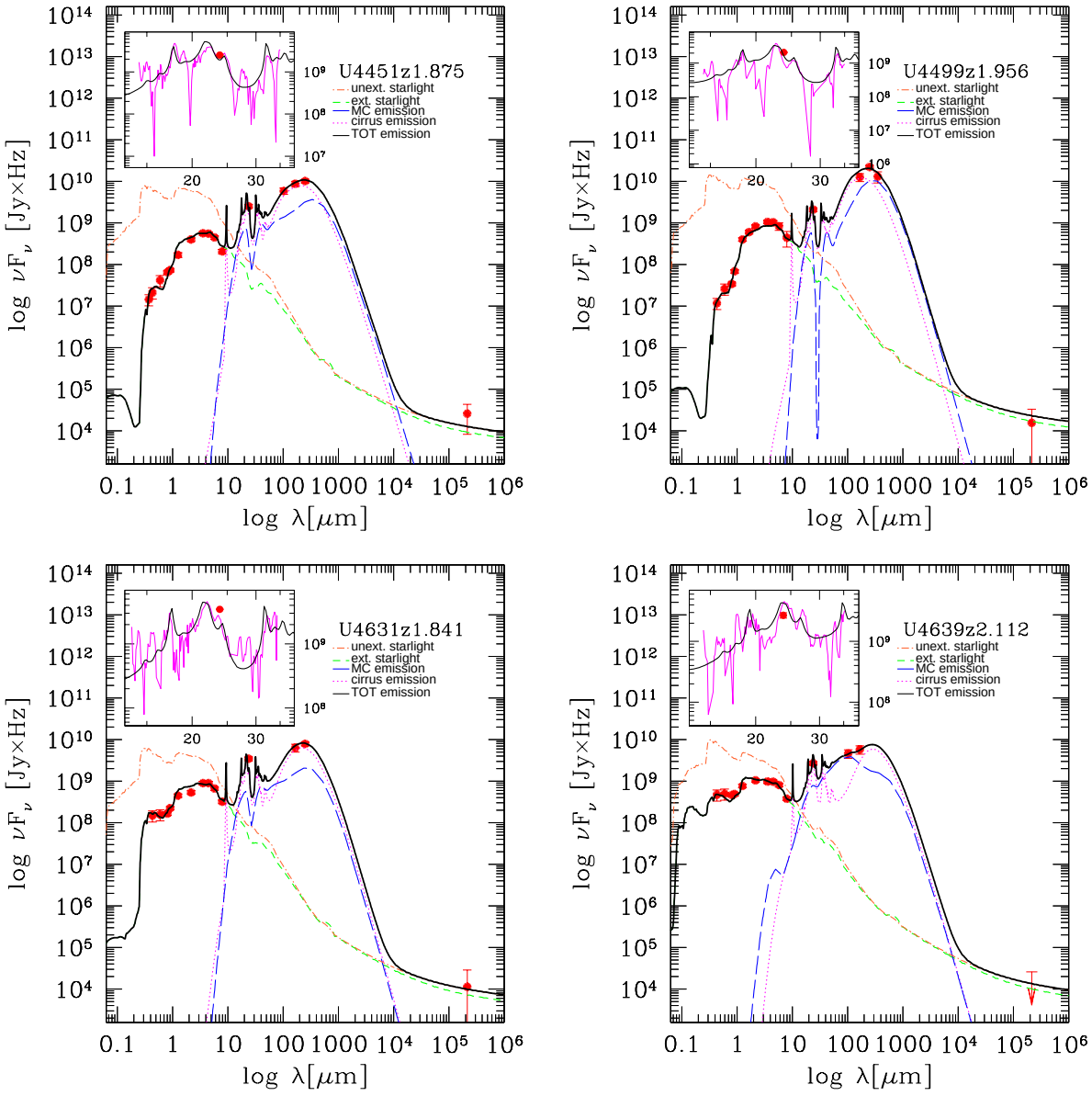

Figure 6.5 GRASIL best-fits (solid black line) to the observed SED (red circles) of $z \sim 2$ (U)LIRGs. IRS spectra appear in the inset window (magenta line). The color-coded lines represent the unextinguished starlight (orange dot-dashed), extinguished starlight (green dashed), cirrus emission (magenta dotted) and MC emission (blue long dashed).

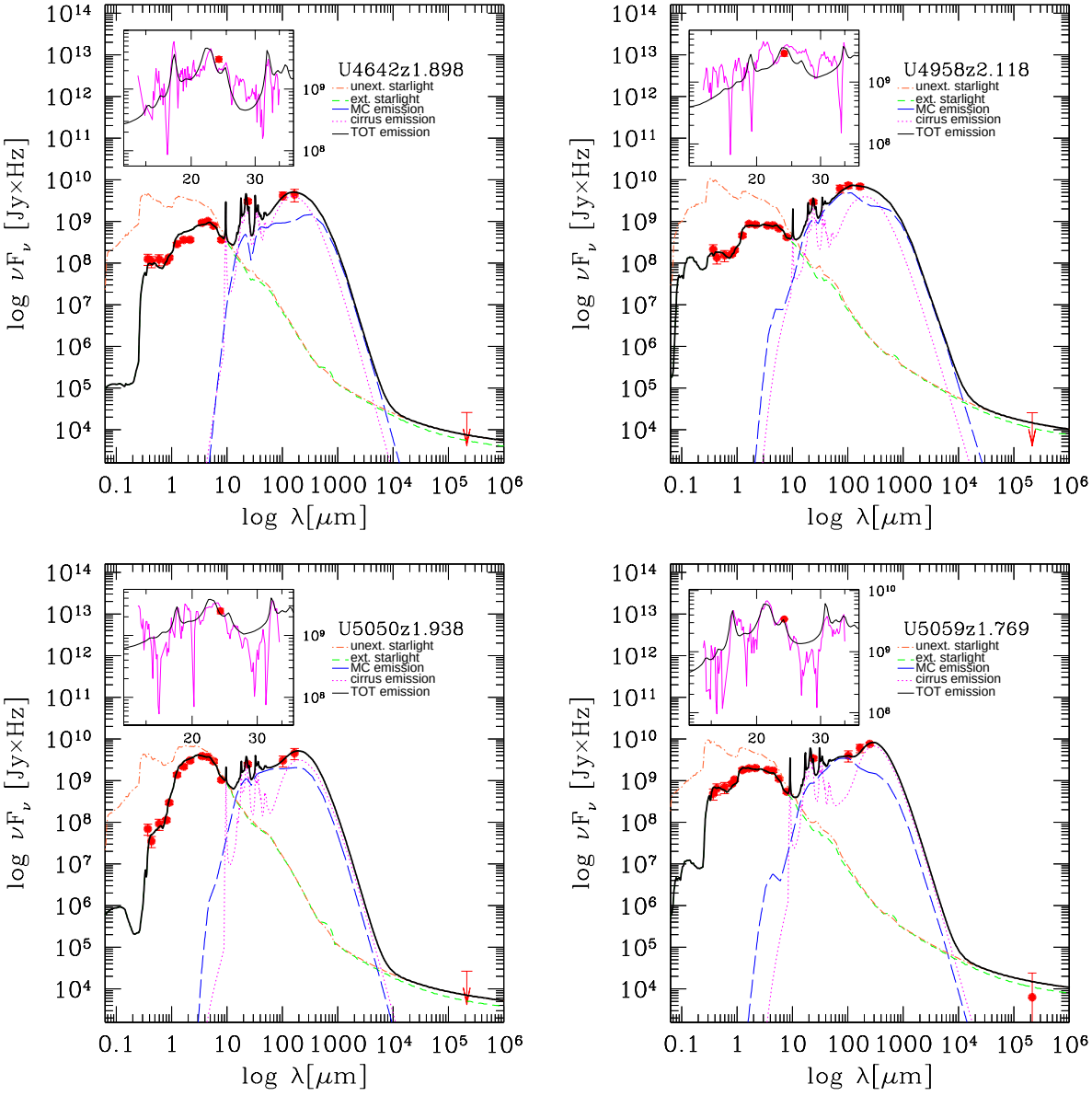

Figure 6.6 GRASIL best-fits (solid black line) to the observed SED (red circles) of $z \sim 2$ (U)LIRGs. IRS spectra appear in the inset window (magenta line). The color-coded lines represent the unextinguished starlight (orange dot-dashed), extinguished starlight (green dashed), cirrus emission (magenta dotted) and MC emission (blue long dashed).

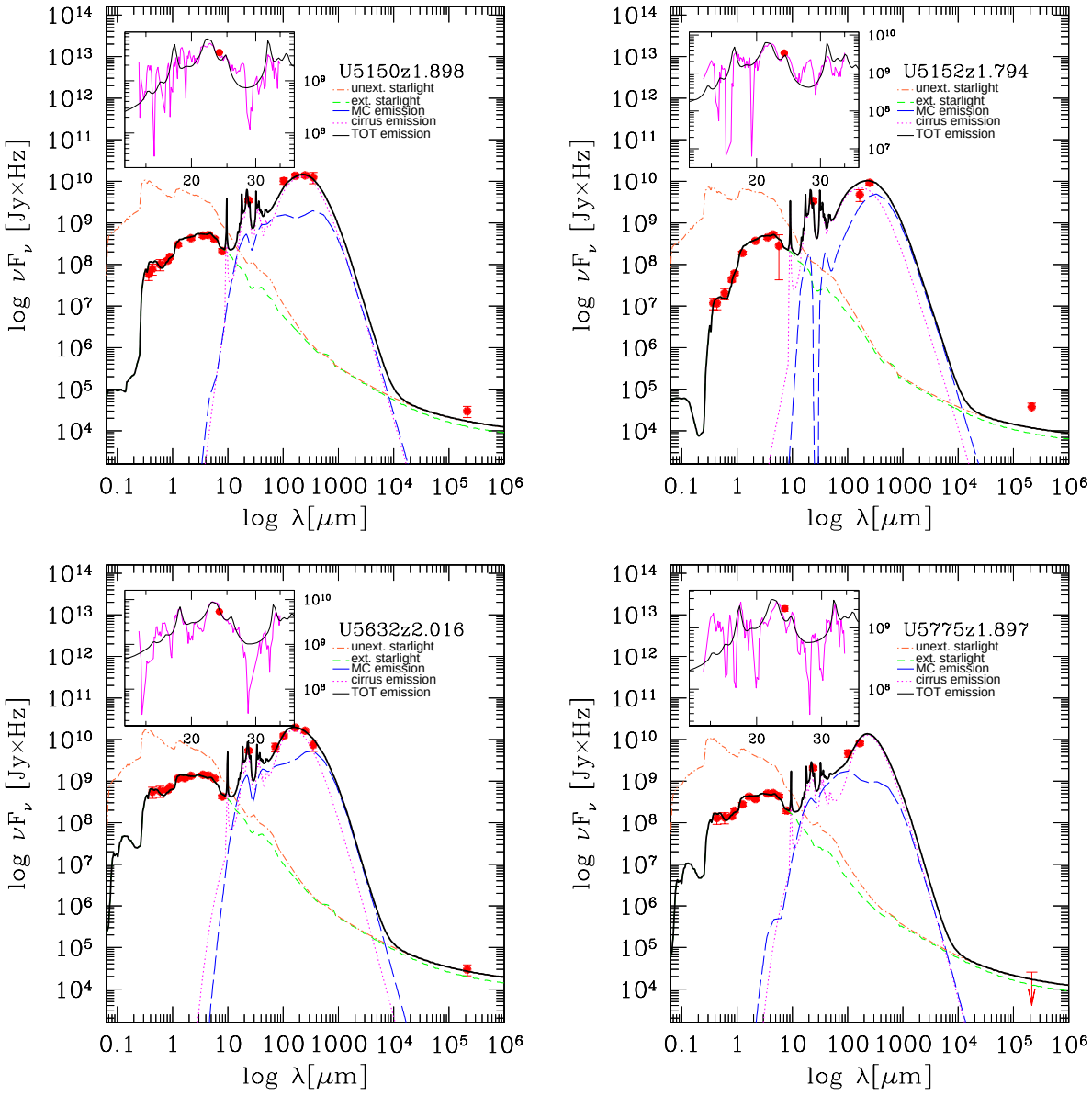

Figure 6.7 GRASIL best-fits (solid black line) to the observed SED (red circles) of $z \sim 2$ (U)LIRGs. IRS spectra appear in the inset window (magenta line). The color-coded lines represent the unextinguished starlight (orange dot-dashed), extinguished starlight (green dashed), cirrus emission (magenta dotted) and MC emission (blue long dashed).

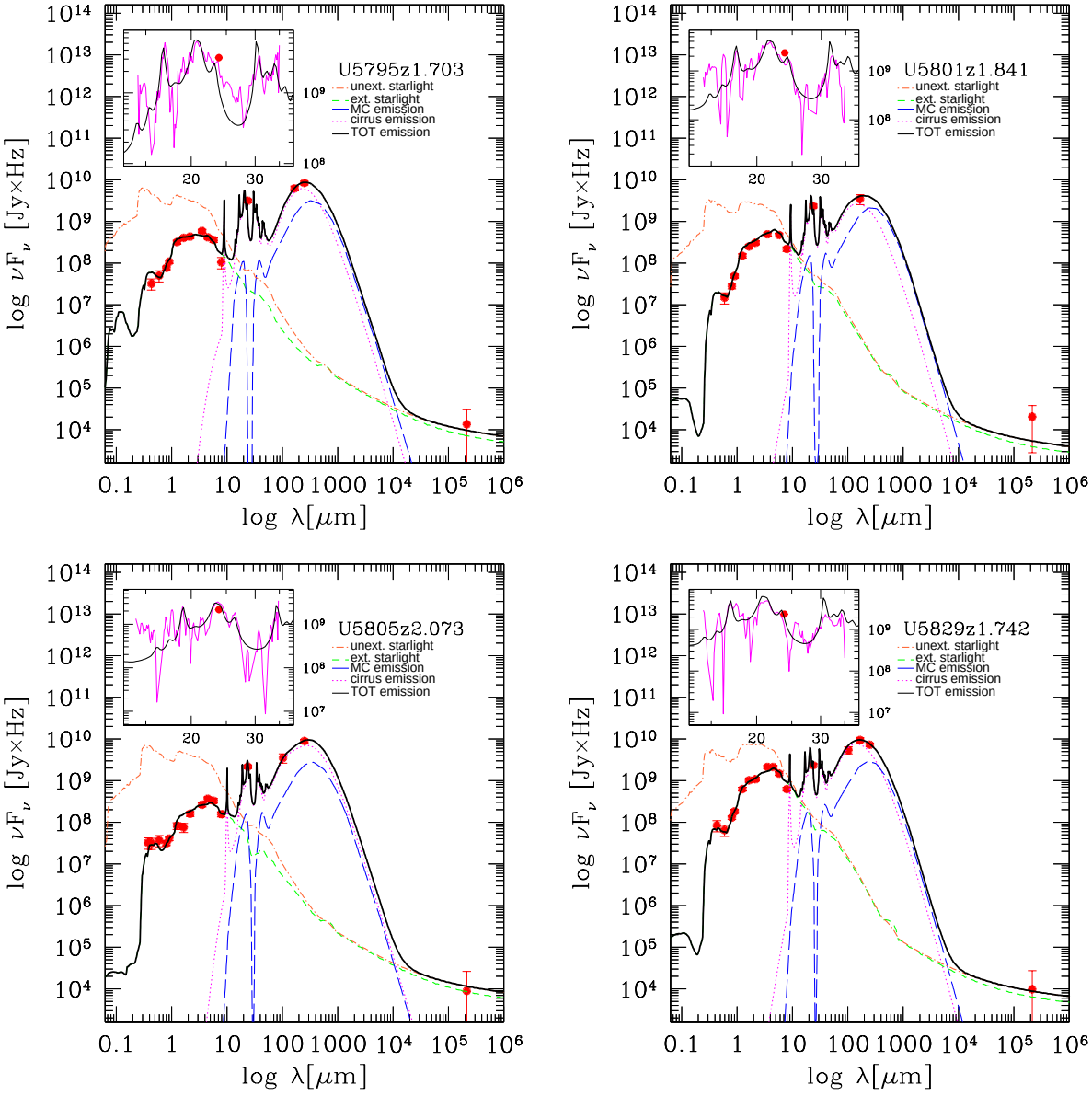

Figure 6.8 GRASIL best-fits (solid black line) to the observed SED (red circles) of $z \sim 2$ (U)LIRGs. IRS spectra appear in the inset window (magenta line). The color-coded lines represent the unextinguished starlight (orange dot-dashed), extinguished starlight (green dashed), cirrus emission (magenta dotted) and MC emission (blue long dashed).

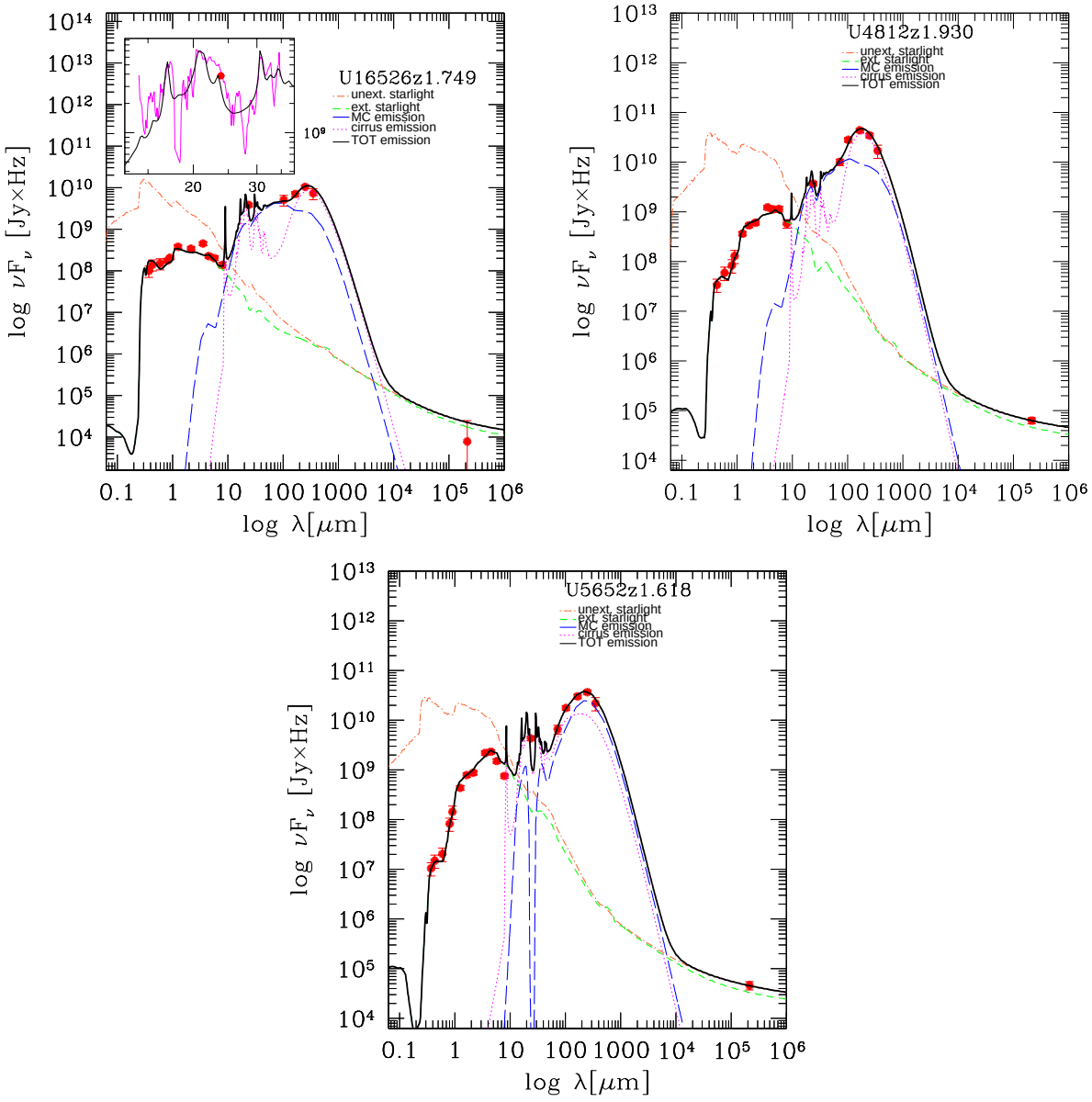

Figure 6.9 GRASIL best-fits (solid black line) to the observed SED (red circles) of $z \sim 2$ (U)LIRGs. IRS spectra appear in the inset window (magenta line). The color-coded lines represent the unextinguished starlight (orange dot-dashed), extinguished starlight (green dashed), cirrus emission (magenta dotted) and MC emission (blue long dashed).

R_d scale length being lower than z_d. This comes out when a wrong geometry is considered and it is indicative of a spheroidal one.

As evident from our best-fit SEDs, we are able to reproduce, well within a factor of two, the far-UV to radio emission for almost all the (U)LIRGs in our sample. 29/31 (U)LIRGs have modeled radio fluxes within the data error-bars. We have only four cases *U5152* - *U5801* - *U16526* - *U5059* showing a difference between the rest-frame $L_{1.4Ghz}$ model luminosity and the observed data larger than a factor of 2. The rest-frame $L_{1.4Ghz}$ luminosities have been computed using the following relation:

$$L_{1.4Ghz}[WHz^{-1}] = \frac{4\pi D_L^2(z)}{(1+z)^{1-\alpha}} S_\nu(1.4Ghz) \tag{6.1}$$

with S_ν measured in units of $\mathrm{Wm}^{-2}Hz^{-1}$ and assuming a radio spectral index $\alpha \sim 0.8$.

The first case, *U5152*, is a 'genuine' critical case because it is a 4σ detection in the catalogue. For this objects we measured a $\Delta L_{1.4Ghz} = (L^{GR}_{1.4Ghz} - L_{1.4Ghz})$ of about 0.49 dex corresponding to a factor ~ 3. Moreover for this object we also fail in well reproducing the FIR peak of the spectrum. The FIR modeled emission appears to be much broader and hotter than that suggested by the two IR data-points, in particular the PACS 160 μm flux. The UV-to-MIR part of the spectrum is instead well reproduced by our best-fit model. A possible solution for this object could be to add a little 'late' burst of SF on top of its SFH in order to burst the radio contribution without modifying the rest of the SED. We have in plan to check also this kind of solution. Of course possibilities including a different geometry and SFH have been also considered. The three objects *U5801*, *U16526* and *U5059* are indeed detections at $\lesssim 2$ and $\lesssim 1$ σ respectively so we do not consider these objects as significant failures of our SED-fitting solutions. Moreover their overall SED from far-UV to radio is very well reproduced by our model, with radio fluxes well within the error. For the object *U5801*, which shows the larger discrepancy on the radio flux, the FIR peak is defined by only one data point. This can bring to some degeneracy in the model solutions being the contribution by young stars less constrained.

Figure 6.10 shows the residuals of the difference between the rest-frame 1.4 Ghz luminosity as computed by our model and the rest-frame $L_{1.4Ghz}$ estimated from the observed flux density. As evident from the figure, neglecting for the moment the objects treated as upper limits (triangles in the figure), there are only few objects having differences larger than a factor of 2 as discussed above. The figure also shows that our solutions are scattered both above and below the $\Delta\, L_{1.4Ghz} = 0$ line, thus indicating the absence of systematics within the GRASIL solutions which appears to reproduce very well the radio emission from these galaxies.

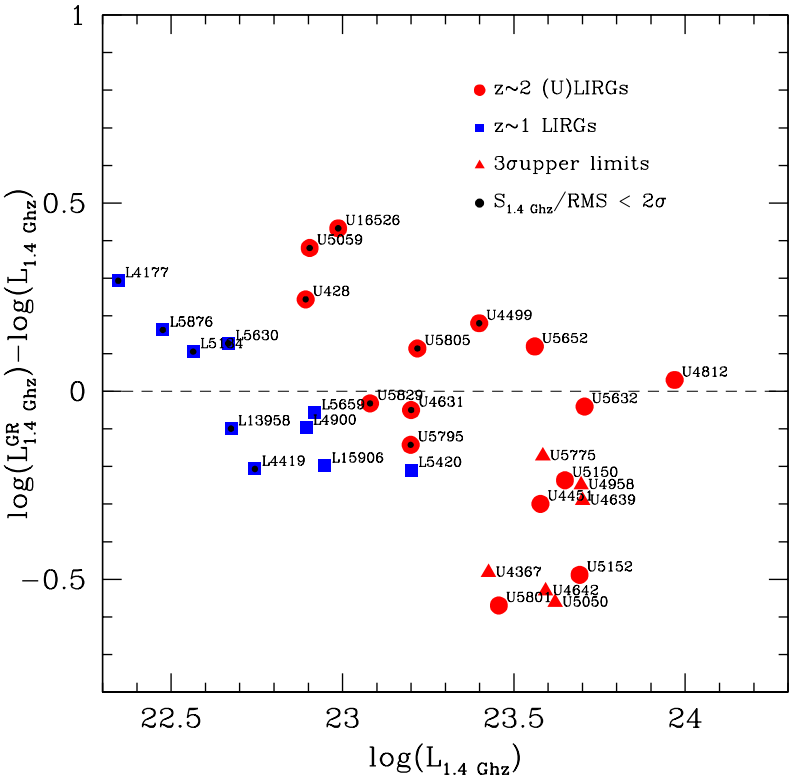

Figure 6.10 Logarithmic difference between the rest-frame $L^{GR}_{1.4Ghz}$ luminosity computed by GRASIL and that one estimated from the observed flux at 1.4 Ghz using the relation of Eq. 6.1, as a function of the rest-frame observed $L_{1.4Ghz}$. 3σ upper limits are highlighted as red triangles. Errors on luminosities are not reported here in order to avoid crowding in the figure. They are anyway shown in the best-fits.

6.3.1 *U4812*

U4812, together with *U5652* are the only two objects at z∼2 to have been detected at $\gtrsim 4\,\sigma$-level and listed in the published radio catalogue by Miller et al. (2013). These are also the objects showing the higher fluxes in the FIR Herschel bands. *U4812* has a total IR luminosity of $\sim 4.55e12 L/L_{\odot}$ corresponding to a best-fit model SFR_{10} ∼160 $M_{\odot}/yr$. This ULIRG was also the object showing the larger stellar mass discrepancy, (about a factor of 4-5), with respect to the estimate based on optical-only SED-fitting procedure, according to our previous analysis. It is also the most dust obscured with an average value of $A_V \sim 3.76$. According to our previous analysis its best-fit SFH is characterized by very short infall timescale and high efficiency of star formation ($\tau_{inf} = 0.01 Gyr$, $\nu_{Sch} = 0.88$), corresponding to an early fast and intense SF phase with an initial burst followed by a more regular SFR (see Fig. 6.11 (black solid line)). The galaxy, however, is then observed few Gyr after the peak. As shown in Figure 6.12 (left) the best-fit SED based on our previous analysis works very well in the far-UV-to-sub-mm range but tends to underpredict the radio

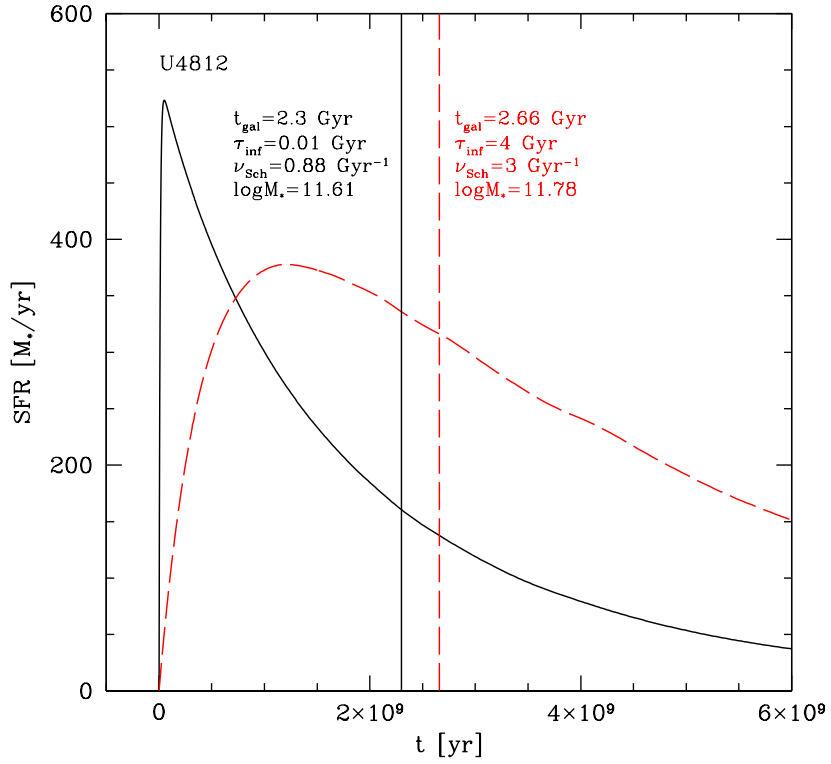

Figure 6.11 Comparison between the best-fit SFH obtained with our previous analysis (black solid line) without including the radio data and the new best-fit SFH (red dashed line) resulting from the SED-fitting in which we considered also the radio data. The best-fit galaxy age, infall timescale, SF efficiency and M$_\star$ estimates are also highlighted in the figure.

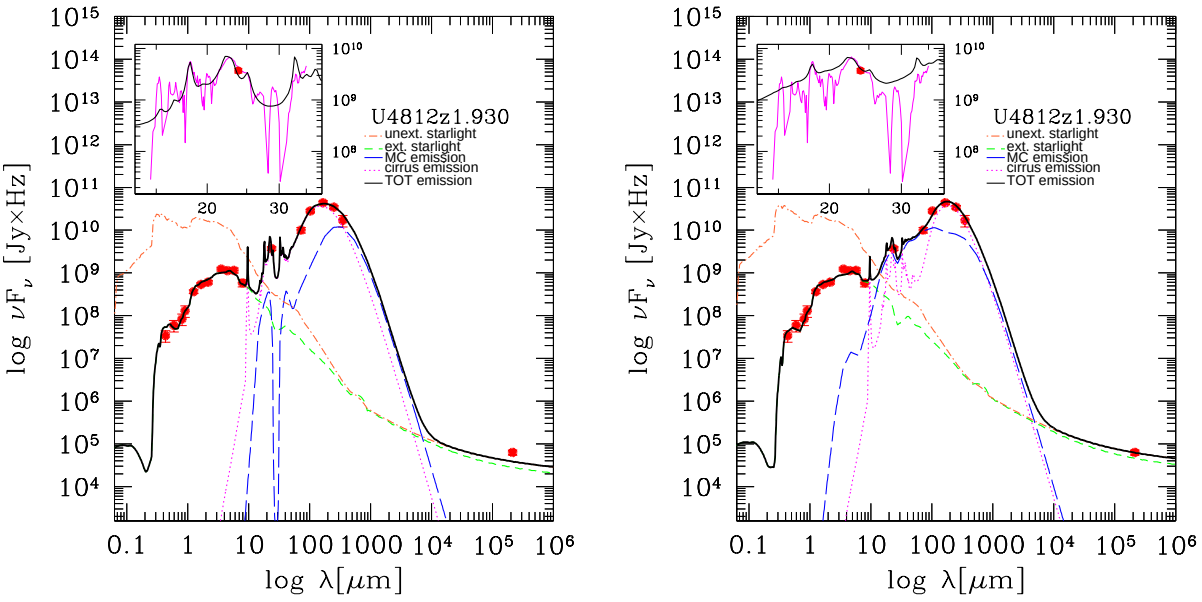

Figure 6.12 Best-fit SEDs of the ULIRG *U4812* obtained before (left) and after (right) the inclusion of radio data in the fit. They refer to a different geometry, spheroidal (left) and disk (right) and different SFHs as reported in Figure 6.11. For details see text.

flux at 1.4 Ghz. This is probably due to the significant contribution (much stronger with respect to the other objects in the sample) in our old best-fit by the cirrus component in the rest-frame MIR region. The role of cirrus in the MIR region was, indeed, required in order to reproduce the intense PAHs present in that region of the spectrum. A good compromise is given by the solution shown on the right panel of Fig. 6.12. Here the contribution of cirrus emission to the FIR remains the same as in the previous fit, but its role in the MIR part of the SED is diminished by the dominance of the MC emission which burst a young component contributing to the radio continuum. In this way we are able to reproduce the entire SED of the galaxy, included the IRS spectrum although, the depth of the Silicate feature and continuum are much better reproduced in the first case. This is due to the fact that following Vega et al. (2005) and the observational evidence of a lack of PAH emission in regions characterized by strong UV radiation fields, the abundance of PAH features in the MC component has been reduced in GRASIL by a factor of $\sim$ 1000 with respect to the cirrus component. Therefore, as in this case the dominant contribution to the MIR comes from the MC, this affects also the intensity of PAHs, which in the second solution are much more diluted. This second solution corresponds to the best-fit SFH shown in Fig. 6.11 as red dashed line. As evident, this SFH is clearly different with respect to the first one. Here the SFH is characterized by a larger infall timescale, of 4 Gyr and also larger efficiency of SF. Therefore it resemble a more gradually evolving SFH typical of BzK galaxies at high redshifts. The best galaxy age is found to be 2.66 Gyr, very close to our previous estimate of 2.3 Gyr. In this second solution the galaxy is observed closer to the peak of star formation, which contribute to enhance its SFR to 316 $M_{\odot}/yr$.

As we said above, we recently explored more complex geometries than the spheroidal one and considered also double exponential profiles typical of disk galaxies. This best-fit has been actually obtained using the disk geometry. This new geometry in combination with the SFH doesn't seem to affect significantly both the average extinction ($A_V^{disk} = 3.92$) and FIR luminosity ($L_{IR} = 4.60e12 L/L_{\odot}$) of this galaxy as our new estimates well agree with the ones discussed in our previous analysis. It affects, instead, the distribution of dust among the dense and diffuse components, enhancing the contribution from MCs and resulting in a lower dust mass ($LogM_{dust}^{disk} = 9.00$ compared to our previous estimate of $LogM_{dust}^{sph} = 9.39$). For the dust mass the difference is about a factor of 2.5. Concerning the stellar mass, another crucial issue of our analysis, the new SFH characterized by a longer infall timescale brings to a stellar mass larger by a factor $\lesssim$ 1.5 with respect to our old best-fit solution. Figure 6.11 also report the best-fit values, in logarithmic scale, of the $M_{\star}$ relative to the two best-fit solutions shown in Figure 6.12.

We recall that we have at least another two critical cases which can be further explored. However for these we already checked the new libraries including the disk geometries without success. For these objects further improvements are probably required. But for *U4812*

the radio data has been crucial in order to break the degeneracy and further constrain the current SFR and $M_\star$ of the galaxy.

6.4 Modeling the SFR of high-z dusty star forming galaxies: Reproducing the FIR-Radio correlation

Recent works by Daddi et al. (2010a, 2007b), have found very good agreement, within a factor of ~ 2, between different SFR indicators (UV dust-corrected, MIR and radio 1.4 Ghz) for a GOODS sample of BzK-selected galaxies including both individual sources and stacked sources. All these SFR estimates, however, rely on calibrations based on similar assumptions, namely Kennicutt (1998). This calibration assumes that the L_{bol} of a constant SF lasting 100 Myr is totally emitted in the IR (K98; Leitherer & Heckman,1995 LH95 hereafter). For a constant SF, the L_{bol} after the first 10 Myr evolves relatively slowly because the rate of birth and death of the most massive stars (with lifetimes $\lesssim 10$ Myr and dominating the L_{bol}) reaches a steady state (see Fig. 2 and 8 of LH95). The K98 SFR/L_{IR} calibration adopts the mean bolometric luminosity for a 10-100 Myr continuous SF, solar abundance, Salpeter IMF of the starburst synthesis models of LH95, and assumes that L_{IR}=L_{bol}. The relation is:

$$SFR_{Kennicutt}(M_\odot/yr) = 1.70 \times 10^{-10} L_{IR} \tag{6.2}$$

where L_{IR} is the 8 to 1000 μm integrated luminosity derived from the best-fit SED. For the radio band the SFR is usually estimated from the 1.4 Ghz flux using the calibration of Bell et al. (2003). This calibration is based on the IR-radio correlation. It assumes that non-thermal radio emission directly tracks the SFR, and it is chosen so that the radio SFR matches the IR SFR for $L \geqslant L^\star$ galaxies. The SFR calibration is given by the following relation:

$$SFR^{Bell}_{1.4GHz}(M_\odot/yr) = 5.52 \times 10^{-22} L_{\nu,\,1.4GHz} \tag{6.3}$$

where $L_{\nu,\,1.4GHz}$ is in units of $W \times Hz^1$ and a Salpeter IMF is assumed. With respect to the original calibration by Condon (1992) this one is found to be lower by a factor of two (Kurczynski et al., 2012). Indeed the calibration of Condon (1992) explicitly models the thermal and non thermal emission mechanisms, whereas the calibration of Bell et al. (2003) relies upon the IR-Radio correlation. Thus we expect agreement between $SFR^{Bell}_{1.4Ghz}$ and IR-based SFR estimates, if the IR-radio correlation continues to hold at high redshift, as it has indeed been suggested in the literature

Our main goal here is to further test our physical solutions (discussed in Chapter 5) and therefore SFR estimates against radio estimates based on the Bell et al. (2003) calibration

and compare these also to those derived from the infrared luminosity using the Kennicutt calibration. Secondly, we would like to investigate the best indicator of the 'current' star formation rate, the one minimizing the contribution from intermediate-to-older stellar populations. In this way we would be able to recover the relative proportion of old and young stars in the galaxies thus providing an indirect proof of our $M_\star$ and A_V estimates.

In the previous Chapter we have shown that, due to the significant contribution of cirrus emission to the total L_{IR} whose heating source includes already evolved stellar populations (ages older than t_{esc}, typically ranging between $\sim$3 Myr and $\sim$90 Myr), our inferred SFR_{10} are systematically lower than those based on the K98 calibration, by a factor $\sim$2-2.5.

Averaging out our results for LIRGs and ULIRGs we have found the following calibration between the total IR luminosity and SFR:

$$SFR[M_\odot/yr] \simeq (5.46 \pm 0.6) \times 10^{-11}\ L_{IR}/L_\odot, \tag{6.4}$$

assuming a Chabrier IMF. The important point here, given the dominant role of cirrus emission to L_{IR}, is to understand if the predictions for the FIR are consistent with those from the radio emission.

The radio emission from normal star forming galaxies is usually dominated by the non-thermal component (up to $\sim$90%) which is due to the synchrotron emission from relativistic electrons accelerated into the shocked interstellar medium, by core-collapse Supernova (CCSN) explosions (Condon, 1992). Both the SN rate and FIR emission are strictly related to the recent star formation rate, sampling typical timescales of $\sim 10^7 - 10^8$ yr, respectively. The FIR emission, however, depends on the dominant population of stars heating the dust. There are in fact few issues concerning the SFR estimates based on the FIR: first of all, dust may also be heated by older stellar populations, as actually confirmed by our study, then there could be a fraction of the UV-optical emission escaping the galaxy and so not re-processed by the dust.

The inclusion of radio emission is crucial to understand if this conspicuous cirrus component contributing to the FIR is an 'effect' of a poor parameter exploration or if it is real, and required in order to reproduce the NIR-to-FIR properties of our galaxies. One possibility in fact is that, forcing a contribution by intermediate age ($\gtrsim$ 50 Myr) stellar populations in order to reproduce the NIR peaked fluxes of our galaxies, we get the right FIR emission as the integrated luminosity (mass) of these stars is large, but we lack in SNII production. This increases the $L_{FIR}/L_{1.4Ghz}$ ratio of the model but fitting the FIR we underpredict the radio. It is important, therefore, to check any possible systematics within the model.

Figure 6.13 compares our model SFRs averaged over the last 10 Myr, thus sampling the most recent SF activity, to the SFR obtained from the rest-frame radio luminosities at 1.4

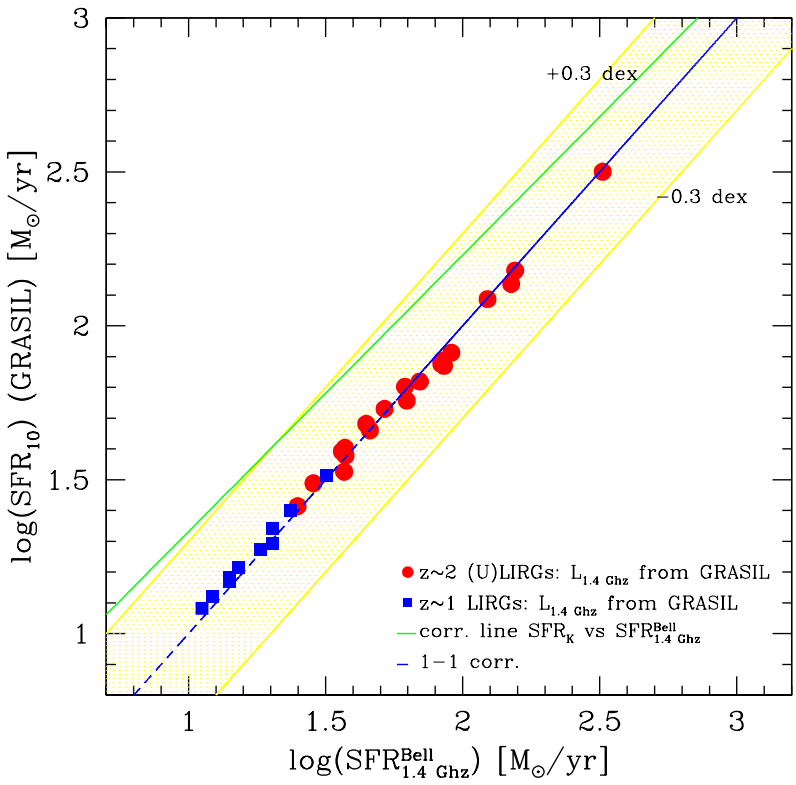

Figure 6.13 Comparison of our GRASIL-estimated SFR_{10} with the SFR derived from the modeled (filled points) rest-frame $L_{1.4Ghz}$ luminosity using the Bell (2003) calibration (eq. 6.3). The 1-1 correlation is shown as blue dashed line. The green solid line represents the SFR estimates provided by the Kennicutt (1998) calibration plotted as a function of the radio SFRs derived from the modeled $L_{1.4Ghz}$. The slope of the green line is ~ 0.90. The yellow shaded area highlights the region of the plot where the SFR estimates are within a factor of ~ 2 from the 1-1 corr. line.

Ghz, as provided by the best-fit physical model, using the Bell (2003) calibration of eq. 6.3. For the comparison we have re-scaled this relation, originally computed for a Salpeter IMF with [0.1-100 $M_\odot$], to a Chabrier IMF. Red filled circles and blue squares represent, respectively, our z$\sim$2 and $\sim$1 (U)LIRGs. The green solid line represents the SFR estimates based on the Kennicutt (1998) calibration plotted as a function of the $SFR^{Bell}_{1.4Ghz}$ derived from the modeled rest-frame radio luminosity. Its slope is ~ 0.90. The dashed blue line is the 1-1 correlation while the yellow shaded area highlights the region of the plot where the SFR estimates are within a factor of ~ 2 from the 1-1 corr. line.

As evident from the figure our SFR_{10} (from GRASIL) are in perfect agreement with the $SFR^{Bell}_{1.4Ghz}$ (from Bell 2003) derived from the best-fit $L^{GR}_{1.4Ghz}$. For our model predictions we have derived the calibration factor between modeled SFR and radio rest-frame luminosity, corresponding to the ratio $SFR^{Salp.}_{10}/L^{GR}_{1.4Ghz}$, and compared it to the same factor as derived by Bell et al. (2003) (i.e. 5.52×10^{-22}). For the filled points of Figure 6.13 we have measured

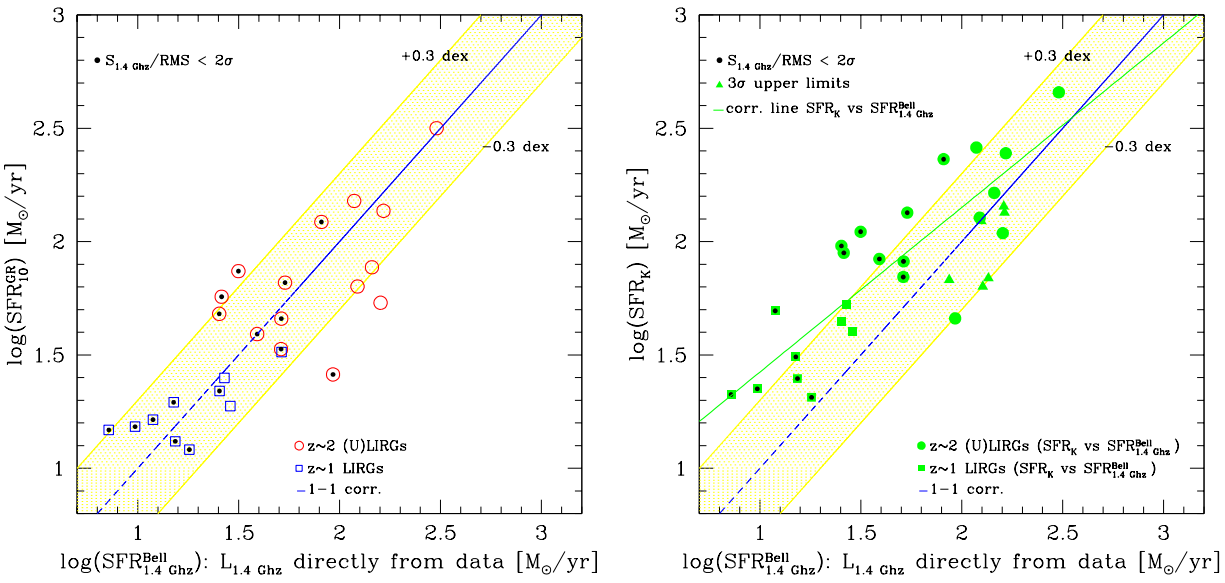

Figure 6.14 Left: Comparison of our GRASIL-estimated SFR_{10} with the SFR derived from the observed (open points) rest-frame $L_{1.4Ghz}$ luminosity using the Bell (2003) calibration (eq. 6.3). The 1-1 correlation is shown as blue dashed line. In both panels the yellow shaded area identifies the region of the plot where the SFRs are within a factor of 2 from the 1-1 correlation line. Right: Comparison between the SFR estimates provided by the Kennicutt (1998) calibration and the $SFR^{Bell}_{1.4Ghz}$ derived directly from the observed rest-frame radio luminosity. The green filled circles and squares represent, respectively, the z$\sim$2 and z$\sim$1 (U)LIRGs. The green solid line is the linear regression of the green points. Its slope is $\sim$0.73.

a factor of $(5.53 \pm 0.38) \times 10^{-22}$.

The estimates from Kennicutt are, instead, systematically off-set with respect to those provided by radio luminosity, by a factor ranging between 1.5 and $\gtrsim$2. In particular we observe that the discrepancy between the FIR- and radio-based SFRs is $\gtrsim$2 up to z$\sim$2.5 then larger than 1.5 up to z$\sim$2.5 and lower than 1.5 at higher redshifts. In other words the discrepancy seems to be larger at lower redshifts.

In Figure 6.14 we compare our model SFR_{10} (left) and those based on the Kennicutt calibration, SFR_K (right), to the radio estimates where the rest-frame radio luminosity is computed directly from the observed flux density using the relation specified in eq. 6.1 (Left: open blue squares and red circles; Right: filled green circles and squares). The blue dashed line represents, in both panels, the 1-1 corr. line, while the green solid line is the linear regression for the filled green points.

As shown in Fig. 6.14 (Left) a larger scatter around the 1-1 correlation line is evident when considering the $SFR^{Bell}_{1.4Ghz}$ estimated from the observed rest-frame radio luminosity. This scatter reflects the scatter of our best-fit solutions already discussed in Fig. 6.10 and

pertains mostly to the z$\sim$2 2σ - $\lesssim$ 3σ detections. It is, in fact, lower for the z$\sim$1 LIRGs. As discussed above, only one ULIRG, *U5152*, shows a significant (larger than a factor of 2) discrepancy between our model and observed radio fluxes and most of our predictions are well within a factor of $\sim$2 (yellow shaded area) from the 1-1 corr. line. Averaging out our results here, we have measured a calibration factor between our model SFRs and the observed rest-frame radio luminosity of $\sim$ $(6.06 \pm 3.00) \times 10^{-22}$, with the 6/31 (19%) 3$\sigma$ upper limits excluded from this computation. Also in this case our solutions are in agreement, within the errors, with the empirical calibration provided by Bell et al. (2003).

The important point here is that there is no systematic effect in our solutions which tend to scatter both above and below the empirical calibration. On the contrary, compared to the SFRs estimated from the FIR using the Kennicutt calibration, we are systematically lower by a factor of $\sim$2. Therefore, this seems to go in the direction of confirming our physical predictions and it gives an indication that radio emission more than FIR is able to accurately predict the current SFR mostly contributed by young massive stars. It doesn't seem to suffer from contamination by intermediate-age stellar populations, as it happens for the FIR where, in our solution, cirrus dominates. Of course we have to take into account the large errors associated to the radio data, but even with this in mind our results are in good agreement.

In the right panel of Fig. 6.14 we compare the SFR_K based on the Kennicutt calibration and FIR luminosity (filled green circles and squares), to the radio estimates derived from the observed rest-frame radio luminosity. Also here there is a large scatter of the data points mostly above the 1-1 correlation line. The slope of the green line is $\sim$0.73. What's evident here is that the FIR-based SFRs tend to be higher with respect to the radio ones by a factor larger than 2 up to z$\sim$1.5. Moreover, up to z$\sim$1.8 most of the points tend to lie above the 1-1 corr. line. Beyond redshift 1.8 the discrepancy between the FIR- and radio-based SFRs decreases up to a factor below 1.5. So it seems to be, in the trend shown in this Figure, a redshift dependence of the SFR based on Kennicutt calibration and on the radio flux, already highlighted in Fig.6.13.

As we have discussed above, the FIR, differently from the radio emission, depends on the dominant population of stars heating the dust. We have demonstrated, trough our physical analysis, that when the cirrus emission dominates at FIR wavelengths the Kennicutt calibration can overestimate the current SFR of galaxies. We have thus investigated the correlation between the logarithmic difference of the FIR- and radio-based SFRs and the fractional contribution of cirrus emission to the total IR luminosity computed as $L_{IR}^{cirr}/L_{IR}^{TOT}$. The results are shown in Figure 6.15 as filled green circles (z$\sim$2) and squares (z$\sim$1). There is not a clear correlation in the first (left) plot, due to the large scatter, rather a 'trend' showing that the discrepancy between the two different SFR estimates becomes larger for

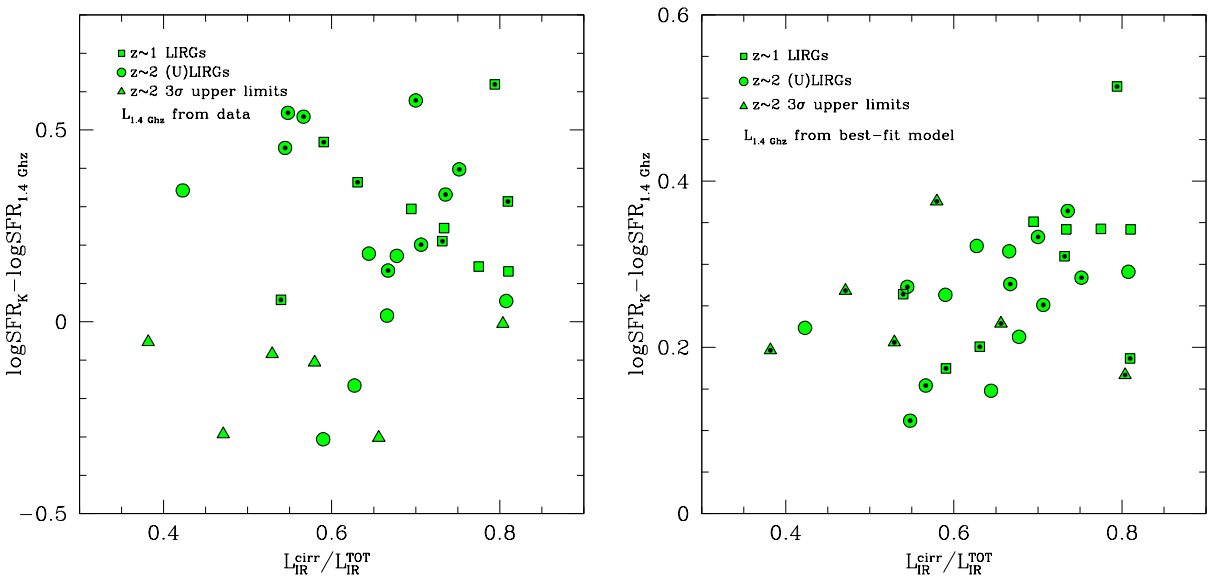

Figure 6.15 Logarithmic difference of the SFR estimated from the rest-frame IR luminosity using the Kennicutt (1998) calibration, SFR_K, and that one derived from the rest-fame radio luminosity using the Bell (2003) empirical relation, $SFR^{Bell}_{1.4Ghz}$, as a function of the fractional contribution of cirrus emission to the total IR luminosity as provided by the best-fit model. In the left panel $L_{1.4Ghz}$ is directly derived from the observed data using the relation 6.3, while on the right panel it comes from the best-fit model. There is not a clear correlation in the left panel, due to the large scatter, rather a 'trend' showing that the discrepancy between the two different SFR estimates becomes larger, on average, for higher fractional contributions of cirrus emission to the IR luminosity. The correlation becomes, instead, more clear in the right panel where the scatter is strongly reduced as all the quantities are derived from the model. seems to be also a redshift dependence in the sense that being z∼ 1 LIRGs (filled squares) characterised by higher cirrus fractions, on average, they also show the larger discrepancies.

higher fractional contributions of cirrus emission to the IR luminosity. A correlation appears to be more evident in the second (right) plot where the scatter is strongly reduced as all the quantities are derived from the model. There seems to be also a redshift dependence in the sense that being z∼ 1 LIRGs (filled squares) characterised by higher cirrus fractions, on average, they also show the larger discrepancies. Of course the extension of our analysis also to low redshift main sequence galaxies is necessary in order to draw a more complete picture of the variation of the two different SFR estimators as a function of both redshift and cirrus content. This will be part of our future works.

Table 6.1 finally summarises all the best-fit physical and radio properties of our high-z (U)LIRGs.

ID	z	χ^2	L_{IR}	$L_{IR,cirr}$	$L_{IR,MC}$	SFR_{10}	SFR_{100}	SFR_K	$M_\star$	M_{gas}	A_V	$AFUV$	A_{FUV}^{Buat05}	q_{TIR}	B03fac	$L_{1.4Ghz}^{GR}$	$L_{1.4Ghz}$
U428	1.783	1.79	9.60E11	6.70E11	2.84E11	48	49	96	2.38E11	5.77E10	2.45	4.73	7.52	2.86	5.96E-22	1.37E23	7.80E22
U4367	1.624	6.53	6.78E11	3.93E11	2.81E11	31	32	68	3.18E11	1.92E10	1.84	6.08	6.66	2.9	5.95E-22	8.79E22	2.66E23
U4451	1.875	3.47	1.27E12	8.48E11	4.23E11	63	65	127	2.14E11	7.02E10	3.14	5.80	6.03	2.84	5.68E-22	1.90E23	3.78E23
U4499	1.956	2.26	2.31E12	1.26E12	1.05E12	122	124	231	4.24E11	1.96E11	3.31	7.03	7.95	2.80	5.47E-22	3.79E23	2.50E23
U4631	1.841	4.18	8.18E11	5.78E11	2.37E11	46	46	82	1.59E11	5.85E10	2.07	3.58	3.63	2.78	5.50E-22	1.41E23	1.58E23
U4639	2.112	4.74	1.34E12	7.10E11	6.28E11	75	76	134	1.20E11	1.50E11	1.40	2.92	3.07	2.73	4.96E-22	2.57E23	5.02E23
U4642	1.898	8.87	6.33E11	4.15E11	2.15E11	38	39	63	1.27E11	4.72E10	2.15	3.89	3.60	2.75	5.59E-22	1.15E23	3.91E23
U4812	1.93	1.27	4.55E12	2.93E12	1.61E12	316	319	455	6.04E11	1.05E11	3.92	6.98	8.43	2.67	5.39E-22	9.98E23	9.31E23
U4958	2.118	1.58	1.43E12	5.46E11	8.80E11	82	82	143	1.31E11	1.63E11	1.92	4.01	4.07	2.72	4.96E-22	2.80E23	4.97E23
U5050	1.938	3.17	6.90E11	3.25E11	3.58E11	40	42	69	3.76E11	2.25E10	1.00	4.43	7.5	2.79	5.96E-22	1.15E23	4.17E23
U5059	1.769	1.04	8.91E11	5.05E11	3.83E11	57	58	89	1.22E11	1.14E11	1.13	2.53	2.60	2.68	5.04E-22	1.93E23	8.02E22
U5150	1.898	1.91	1.64E12	1.32E12	3.13E11	77	78	164	1.53E11	1.28E11	2.89	4.55	4.85	2.81	5.07E-22	2.58E23	4.46E23
U5152	1.794	2.74	1.90E12	6.83E11	4.04E11	54	55	109	1.88E11	5.95E10	3.27	6.35	6.44	2.85	5.71E-22	1.60E23	4.92E23
U5632	2.016	1.21	2.45E12	1.66E12	7.86E11	137	138	245	1.82E11	1.52E11	1.90	3.25	3.71	2.74	5.02E-22	4.63E23	5.08E23
U5652	1.618	7.89	2.60E12	1.10E12	1.49E12	151	154	260	3.81E11	1.89E11	3.72	8.02	8.68	2.75	5.37E-22	4.78E23	3.64E23
U5775	1.897	3.76	1.23E12	9.91E11	2.40E11	76	77	123	1.01E11	8.48E10	2.69	4.21	3.90	2.69	5.02E-22	2.59E23	3.84E23
U5795	1.703	5.00	6.98E11	4.66E11	2.31E11	34	34	70	8.21E10	8.82E10	2.47	4.70	4.36	2.8	5.0E-22	1.14E23	1.58E23
U5801	1.841	4.0	4.58E11	2.70E11	1.86E11	26	26	46	1.02E11	3.32E10	2.57	5.25	4.65	2.79	5.73E-22	7.70E22	2.86E23
U5805	2.073	3.04	1.34E12	1.01E12	3.31E11	66	67	134	1.70E11	1.10E11	3.69	5.60	5.75	2.81	5.21E-22	2.15E23	1.65E23
U5829	1.742	2.48	8.38E11	6.17E11	2.17E11	39	40	84	3.34E11	3.17E10	2.36	4.44	5.16	2.90	5.95E-22	1.12E23	1.20E23
U16526	1.749	3.10	1.10E12	6.06E11	4.99E11	74	71	110	2.08E10	1.24E11	2.62	4.45	4.31	2.64	4.79E-22	2.63E23	9.71E22
L4177	0.842	4.69	2.11E11	1.25E11	8.54E10	15	15	21	8.38E10	1.84E10	0.94	2.18	1.79	2.70	5.76E-22	4.35E22	2.21E22
L4419	0.974	5.81	2.06E11	1.11E11	9.27E10	12	12	20	1.86E11	1.39E10	0.75	3.06	3.15	2.79	5.96E-22	3.45E22	5.55E22
L4900	1.047	1.89	4.46E11	3.27E11	1.17E11	22	22	45	1.70E11	3.32E10	1.58	3.80	3.94	2.87	5.97E-22	6.25E22	7.83E22
L5134	1.039	2.59	4.95E11	3.93E11	1.00E11	16	17	49	2.08E11	1.76E10	2.79	7.22	7.69	3.04	5.96E-22	4.67E22	3.67E22
L5420	1.068	5.39	6.98E11	5.66E11	1.31E11	32	33	70	1.73E11	6.50E10	1.90	3.46	3.79	2.87	5.65E-22	9.79E22	1.59E23
L5630	0.997	1.09	3.10E11	2.51E11	5.76E10	19	20	31	7.06E10	3.90E10	1.04	1.75	1.51	2.71	5.35E-22	6.21E22	4.64E22
L5659	1.044	3.80	5.30E11	3.68E11	1.60E11	25	25	53	1.63E11	5.00E10	2.78	6.09	6.13	2.87	5.86E-22	7.26E22	8.28E22
L5876	0.971	0.44	2.24E11	1.41E11	8.10E10	15	15	22	1.63E11	2.63E10	0.73	1.97	2.13	2.72	6.00E-22	4.35E22	3.00E22
L13958	0.891	2.58	2.49E11	1.82E11	6.57E10	13	14	245	6.68E10	1.01E10	1.34	2.76	2.17	2.83	5.95E-22	3.76E22	4.72E22
L15906	0.976	1.75	4.01E11	3.11E11	8.94E10	19	19	40	8.22E10	2.35E10	2.27	3.81	3.35	2.87	5.70E-22	5.610E22	8.86E22

Table 6.1 Best-fit physical parameters of high-z (U)LIRGs including radio data.

6.4.1 FIR-Radio correlation in high-z dusty star forming (U)LIRGs

Despite the FIR/radio correlation, which is one of the tightest correlation in Astrophysics, is now well established up to high redshifts (e.g. Ivison et al. 2010, Sargent et al. 2010), its physical origin is still debated. We have seen in Section 3.6 that it is natural when the synchrotron mechanism dominates over the inverse Compton, and the electron cooling time is shorter than the fading time of the supernova rate. Both conditions are met in star forming galaxies, from normal spirals to obscured starbursts. However, since the radio nonthermal (NT) emission is delayed, deviations are expected both in the early phases of a starburst, when the radio thermal component dominates, and in the post-starburst phase, when the bulk of the NT component originates from less massive stars.

By taking advantage of the full FIR coverage provided by both Herschel PACS and SPIRE instruments together with the radio detection at 1.4 Ghz, we have estimated for each galaxy in our sample the ratio, q_{TIR}, of the rest-frame 8-1000 μm luminosity to the rest-frame radio luminosity at 1.4 Ghz directly derived from our model. The logarithmic total IR (TIR)/radio flux ratio q_{TIR} (Helou et al., 1985) has been computed according to the following relation:

$$q_{TIR} = log\left(\frac{L_{TIR}}{3.75 \times 10^{12} W}\right) - log\left(\frac{L_{1.4Ghz}}{W Hz^{-1}}\right) \tag{6.5}$$

We have then compared our predictions to observational estimates by Sargent et al. (2010), for galaxy samples selected at far-infrared and radio wavelengths at the same redshift and in the same luminosity range as our high-z (U)LIRGs.

Figure 6.16 shows the distribution of the predicted q_{TIR} values for both the z$\sim$1 LIRGs (blue horizontal lines) and z$\sim$2 (U)LIRGs (black 45° angled solid lines). The two distributions are quite similar with the lower redshift LIRGs reaching higher values of q_{TIR}. Mean values and standard deviations are also highlighted in the figure and compared to the observational estimates provided by Sargent et al. (2010) (in red). Sargent et al. (2010) studied the evolution of the IR/radio relation out to z$\sim$2 for a statistically significant volume-limited sample of IR-luminous galaxies selected in the COSMOS field. Their sample includes $\sim$1,692 star forming ULIRGs and $\sim$3000 SF 'IR bright' ($L_{\rm TIR} \geq L_{TIR}^{knee}(z)$) COSMOS sources up to z$\sim$2. They found no evolution of the median TIR/radio ratio among the ULIRG sample, with a median value at z$\sim$2 of $2.672^{+\infty}_{-0.121}(2.892)$. The value within brackets represents the median in high-redshift bins before the correction ($\Delta\, q_{TIR} \sim 0.22$), needed in order to compensate for the relative offset between medians at high and low redshift that arises artificially due to the increased scatter (σ_{TIR}) in the data at $z \gtrsim 1.4$ (Sargent et al., 2010).

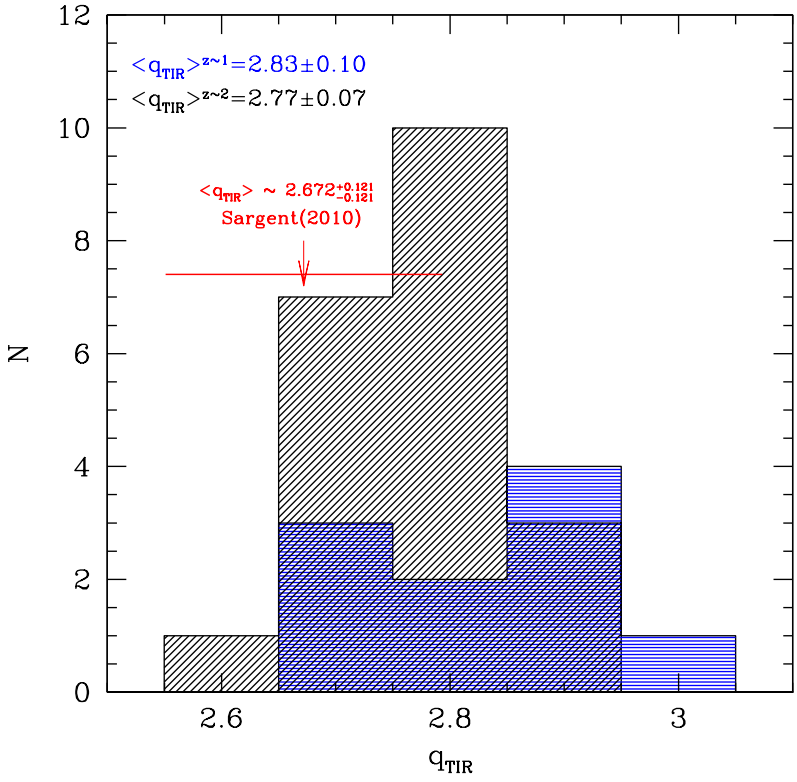

Figure 6.16 Distributions of the predicted q_{TIR} values for both the z$\sim$1 LIRGs (blue horizontal lines) and z$\sim$2 (U)LIRGs (black 45° angled solid lines). Mean values and standard deviations are also highlighted in the figure. The red arrow and horizontal line indicate the typical q_{TIR} of z$\sim$1-2 (U)LIRGs, as computed by Sargent et al. (2010), and its range of values.

Our predicted q_{TIR} for z$\sim$2 (U)LIRGs (2.83 ± 0.10), well agrees, within the errors, with the results from Sargent et al. (2010) discussed above and also with the median q_{TIR} measured by the authors for local (U)LIRGs ($\langle q_{TIR} \rangle 2.703^{+0.050}_{-0.050}$). Our results thus confirms, from a modellistic point of view and in line with theoretical and numerical simulation expectations, that ULIRGs should follow the local IRradio relation until at least z$\sim$2 (Lacki & Thompson, 2010, Murphy et al., 2009). This implies that that magnetic fields are sufficiently strong to ensure cosmic-rays electrons to predominantly lose energy through synchrotron radiation rather than inverse Compton scattering off the CMB.

Good agreement, within the errors, is found also between our predicted q_{TIR} for z$\sim$1 LIRGs and the median q_{TIR} derived by Sargent et al. (2010) for z$\sim$1 SF IR-bright sources ($2.672^{+0.069}_{-0.061}$). These are actually very similar to the median q_{TIR} measured for z$\sim$2 SF ULIRGs. In Figure 6.16 this is emphasised with the two samples showing very similar q_{TIR} distributions. No strong evolution of the FIR/radio correlation is thus observed also between our z$\sim$1 and $\sim$2 $L \gtrsim 10^{11}\, L_{\odot}$ objects.

Our physical model thus seems to be able to reproduce the radio properties of high-z (U)LIRGs including the FIR-radio correlation up to z$\sim$1-2. This provides a further important constraint to model the SFR and SFHs underlying the observed SED.

6.5 Concluding Remarks

The analysis presented in this Chapter has emphasized a potentially important role of radio flux data in further constraining our modellistic solutions based on the GRASIL code.

In Chapter 5 we have found that the interpretation of the optical to far-IR emissions in terms of the rate of star formation was subject to some uncertainties depending on the age of stars responsible for the dust heating and reprocessing. If intermediate-age stars significantly contribute to it, we may have even factors of 2 difference on the ongoing rate of SF compared to standard calibrations as from Kennicutt (1998). The addition of radio luminosity to the spectral multi-band fitting offers a tight constraint on the SFR, considering that only stars younger than about 10 Myr produce the galactic cosmic rays responsible for the non-thermal radio emission.

We have investigated the correlation between the logarithmic difference of the FIR- and radio-based SFRs and the fractional contribution of cirrus emission to the total IR luminosity computed as $L_{IR}^{cirr}/L_{IR}^{TOT}$. We find that the discrepancy between the two different SFR estimates becomes larger for higher fractional contributions of cirrus emission to the IR luminosity and at lower redshift. In the sense that being z$\sim$1 LIRGs characterised by higher cirrus fractions, on average, they also show the larger discrepancies. Of course the extension of our analysis also to low redshift main sequence galaxies is necessary in order to draw a more complete picture of the variation of the two different SFR estimators as a function of both redshift and cirrus content.

The inclusion of the radio data in our analysis significantly modified in particular our solution for the source U4812: the improved solution implies a SFH in which the time of observation is closer to that of the peak of SFR.

Unfortunately, the radio data available for our analysis come from VLA observations that were not completely matched in sensitivity to our Herschel and Spitzer data, and consequently only a few sources have reliable radio detections. Our analysis points towards the radio flux as an essential information for interpreting star-forming galaxies at high redshifts and for recovering reliable SFH's. The currently operational and much improved sensitivity of J-VLA promises to add important data as soon as the relevant cosmological fields will be surveyed at faint enough limits. And, of course, forthcoming facilities like Meerkat,

or future ones like SKA, will provide the full extensive radio coverage needed for all the relevant use.

Chapter 7

Modeling the molecular gas and dust properties of high-z normal star forming galaxies

In this Chapter we present the first results of an ongoing investigation focused on the physical modelling of the interstellar media (molecular gas and dust in particular) of normal star-forming high-z galaxies selected with a BzK criterion on the main sequence (MS), in the GOODS field. We start here with a small but representative 'test' sample of six SF BzK galaxies at $z \sim 1.5$, selected from Daddi et al. (2010a), characterised by a rich dataset of photometric and spectroscopic data including Spitzer and Herschel (PACS + SPIRE) observations, radio detection and CO emission line measurements. The information provided by this rich dataset is essential to constrain the molecular gas reservoirs in high-z star forming galaxies and to investigate the nature of star formation, the parameters that regulate it and its possible dependence on local and global galaxy properties.

Given the interesting results obtained through this first analysis, we have in plan to extend the ongoing investigation to a larger statistical sample of BzK galaxies having CO-line observations in order to put stronger constraints on the total and molecular gas masses of MS star forming galaxies. The results will be discussed in detail in a forthcoming paper in preparation.

7.1 Introduction

As emphasized in our previous Chapters, a correct and self-consistent treatment of dust extinction and reprocessing together with a full multiwavelength coverage (from far-UV to radio), is essential to get reliable estimates of the main physical parameters like stellar mass,

dust extinction and SFRs. Concerning the stellar mass determination, in particular, we have shown how the absence of an age-dependent dust attenuation, in terms of age dependent spatial distribution of stars, can bring to a significant underestimate of the stellar masses with respect to classical estimates based on optical only SED-fitting procedures. On the other hand radio emission has revealed to be of crucial importance to further constrain the recent star formation activity of galaxies and in combination with the information given by the entire SED, also their past SFH. The shape of the galaxy SED, however, is not sufficient alone to put strong constraints on the total and molecular gas mass of galaxies. A tighter constraint on these quantities is provided by comparing our physical solutions to dynamical and molecular gas mass estimates from CO line observations.

Probing the properties of molecular gas reservoirs in high-z star forming galaxies is essential to understand how stellar formation proceeds in distant galaxies and shed light on the origin of the $M_\star$- and M_{gas}-SFR correlation since it is the molecular gas out of which stars form.

Schmidt (1959) was the first to suggest the existence of a power-law relation between surface densities of SFR and gas masses. Later Kennicutt (1998, hereafter K98) presented a calibration of the Schmidt law with a slope of 1.4 in log space, which has since been the most widely used in the literature. K98 fits the local populations of spiral galaxies and IR-luminous galaxies (LIRGs/ULIRGs), with the gas mass including both neutral (HI) and molecular (H_2) hydrogen for spirals, and molecular gas only for (U)LIRGs (as their HI content is likely negligible).

Figure 7.1, taken from Daddi et al. (2010b) shows the relation between the infrared luminosity L_{IR} and the molecular gas mass M_{H2} for several samples in the literature including high-z SMGs, $z\sim1.5$ BzK galaxies, normal galaxies, local (U)LIRGs etc. We have added to the original plot by Daddi et al. (2010b) also the objects analysed in our previous work, namely, $z\sim1$ LIRGs (blue filled squares), $z\sim2$ (U)LIRGs and off-MS galaxies (cyan filled circles and magenta stars, respectively) and the local (U)LIRGs taken from the sample of Vega et al. (2008) (black filled hexagons). Our molecular gas masses have been derived using GRASIL. As discussed in Chapter 4, the sample of $z\sim2$ (U)LIRGs consists mostly of BzK selected galaxies. The z∼1.5 BzK galaxies from Daddi et al. (2010a, D10 hereafter) are represented in the figure as red filled circles. As you can see our galaxies overlap very well the BzK studied by D10, and put themselves in the region of the plot typical of normal star forming galaxies characterized by quasi-steady long-lasting mode of SF (see Section 1.10). However here we are comparing galaxies of similar nature but selected in different fields. Our galaxies have been selected from the GOODS-S field while D10 BzK refer to the GOODS-N. They are very similar but of course a fairer comparison would be that one between the M_{H2} estimates we would get for the same BzK galaxies from our

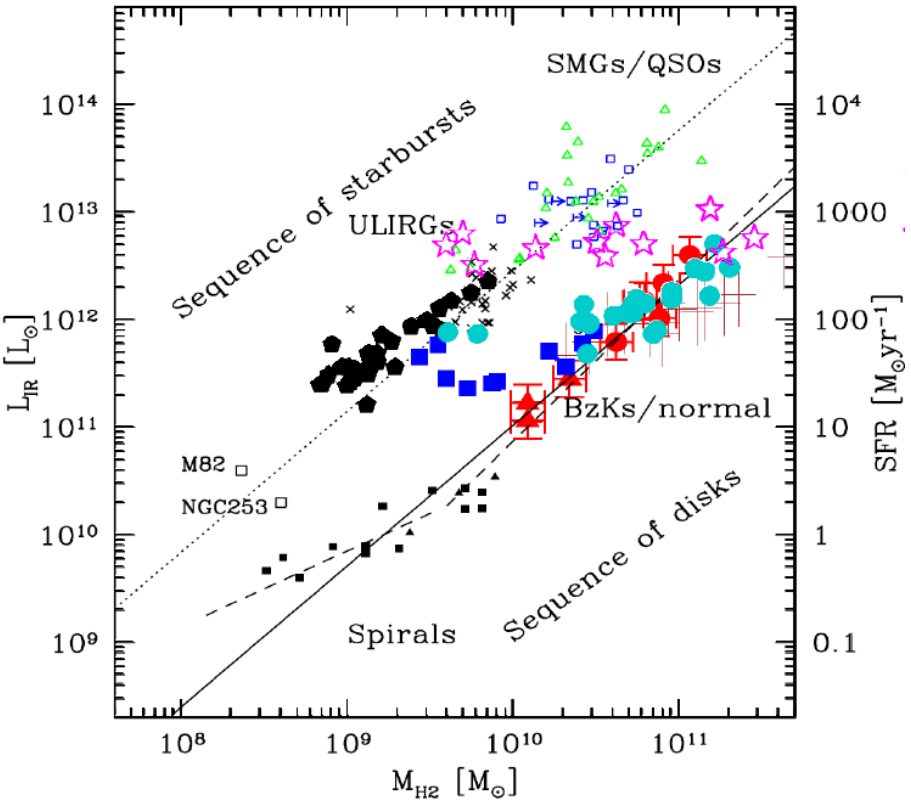

Figure 7.1 Comparison of molecular gas masses and total IR bolometric luminosities: BzK galaxies (red filled circles; D10), z ∼ 0.5 disk galaxies (red filled triangles; F. Salmi et al. 2010), z = 1-2.3 normal galaxies (Tacconi et al. 2010; brown crosses), SMGs (blue empty squares; Greve et al. 2005; Frayer et al. 2008; Daddi et al. 2009a, 2009b), QSOs (green triangles; see Riechers et al. 2006), local ULIRGs (black crosses; Solomon et al. 1997), and local spirals (black filled squares, Leroy et al. 2009; black filled triangles, Wilson et al. 2009). The two nearby starbursts M82 and the nucleus of NGC 253 are also shown (data from Houghton et al. 1997; Kaneda et al. 2009). The solid line represents a fit to local spirals and BzK galaxies and the dotted line is the same relation shifted in normalization by 1.1 dex. The dashed line is a possible double power-law fit to spirals and BzK galaxies. The image is taken from Daddi et al. (2010b). The objects analysed in Chapter 5 are overplotted in the figure as cyan filled circles (z∼2 (U)LIRGs), blue filled squares (z∼1 LIRGs), black filled pentagons (local (U)LIRGs) and z∼2 off-MS galaxies (magenta stars).

physical analysis and the "observed" estimates given by D10 and based on the CO line luminosity.

With this goal in mind we have decided to investigate the far-UV to radio properties, including molecular gas and dust, of this well studied and representative sample of z∼1.5 BzK galaxies selected from D10. This sample has been studied in detail, from an observational point of view, more recently by Magdis et al. (2012, M12 hereafter) who provided robust estimates of dust masses (useful check for our modeled dust properties) based on Herschel PACS and SPIRE fluxes, and also 1.3 mm continuum data derived as a by-product from the

CO[5-4] emission line observations (Dannerbauer et al., 2009). In addition M12 also provided independent estimates of the molecular gas content and CO-to-H_2 conversion factors (α_{CO}) based on the the correlation of gas to dust mass with metallicity (M_{gas}/M_{dust}-Z). This rich dataset therefore provides a unique tool to constrain the capabilities of our code in reproducing the physical properties of star forming galaxies at high redshift.

7.2 The BzK data sample

We briefly review here the main properties of a sample of z∼1.5 BzK star forming galaxies whose molecular gas reservoirs have been investigated in detail by D10 and whose molecular gas and dust properties have been accurately modeled with our physical model.

The six normal star forming galaxies presented here were originally selected from the sample of Daddi et al. (2007a,b) in GOODS-N. These are NIR-selected galaxies with K < 20.5 (Vega scale; or K < 22.37 AB), to which it has been applied the BzK color selection criterion of Daddi et al. (2004) together with the requirement of a detection in deep Spitzer 24 μm imaging, in order to select a sample of star forming galaxies at $1.4 < z < 2.5$.

The BzK technique is a simple two-color selection method based on B-, z-, and K-band photometry aimed at culling galaxies at $1.4 \lesssim z \lesssim 2.5$ in K-selected samples and classifying them as star-forming or passive systems. The method has been calibrated on the highly complete spectroscopic redshift database of the K20 survey. The requirement of BzK = $(z - K)_{AB} - (B - z)_{AB} > -0.2$ allows to select actively star-forming galaxies at $z \gtrsim 1.4$, independently of their dust reddening. On the other hand, objects with BzK < -0.2 and $(z - K)_{AB} > 2.5$ colors include passively evolving galaxies at $z \gtrsim 1.4$, often characterized by spheroidal morphologies.

Among the BzK galaxies selected using the criteria specified above, only those having a pre-determined spectroscopic redshift have been considered as required for follow-up observations in CO. Currently, 89 BzK galaxies of the Daddi et al. (2007a,b) sample in GOODS-N have a spectroscopic redshift, from various observing campaigns and from the literature.

Among the six targeted galaxies, five redshifts were obtained through the GOODS-N campaigns at Keck using DEIMOS (D. Stern et al. 2010). The redshift for *BzK-12591* was instead derived by Cowie et al. (2004). This galaxy, having a strong bulge evident from Hubble Space Telescope (HST) imaging (see Fig. 7.2), has a possible detection of [NeV]λ 3426 $\mathring{A}$ emission line, suggesting the presence of an active galactic nucleus (AGN). This galaxy is not detected in hard X-ray emission in Alexander et al. (2003) but exhibits some soft X-ray emission.

In addition to the availability of a spectroscopic redshift, D10 also required the detection of the galaxies at 1.4 GHz. This is important because the radio continuum provides an independent estimate of the current SFR in the sources.

For these sources D10 presented PdBI CO[2-1] emission line detections. All observed galaxies were detected with high S/Ns and their spectroscopic redshifts confirmed by multiple CO detections. High spatial resolution observations allowed to resolve the CO emission in four of them, implying sizes of the gas reservoirs of the order of 6-11 kpc and suggesting the presence of ordered rotation. Their UV morphologies are consistent with clumpy, unstable disks, and UV sizes are consistent with those measured in CO.

Total IR luminosities and SFRs were derived using all the available SFR indicators, including dust corrected UV luminosities, mid-IR continuum luminosities from 24 Spitzer imaging and the VLA 1.4 Ghz radio continuum. The SFRs of the galaxies were then computed by averaging among the three different indicators. The typical uncertainty on SFR is $\sim 0.17dex$. Stellar masses were computed from synthetic template fitting procedures, by fitting the M05 models to the UV-to-NIR bands of galaxy SEDs. The Stellar masses range from $3.3 \times 10^{10}\,M_{\odot}$ for BzK-25536 to $1.1 \times 10^{11}\,M_{\odot}$ for BzK-12591. The $1\,\sigma$ error on $M_{\star}$ is of the order of 0.10-0.15 dex. When plotted in the SFR-$M_{\star}$ diagram, the six BzK galaxies tend to lie right on top (high-mass and high-SFR end) of the SFR-$M_{\star}$ relation. The reason why they are massive is the requirement by D10 of radio continuum detection. The typical $5\,\sigma$ limit of 20 μ Jy in their 1.4 Ghz VLA maps (Morrison et al., 2010) corresponds to SFR of 66 $M_{\odot}$/yr at z=1.4 and SFR=156 $M_{\odot}$/yr at z=2.0.

All the BzKs have redshift in the range $1.4 \lesssim z \lesssim 1.6$, that is in the lower redshift regime probed by BzK selection. This is due to the requirement of a radio detection coupled with the choice of observing the CO[2-1] transition. Its rest-frame frequency of 230.538 Ghz can be observed with the PdBI only up to z=1.87.

The star formation efficiencies are homogeneously low (84 ± 12 $L_{\odot}$ K^{-1} km^{-1} s pc^{-2}) within the sample and similar to those of local spirals. The resulting gas depletion times (M_{gas}/SFR) are $\sim$0.5 Gyr, much higher than those of high-z submillimeter galaxies and quasars. The typical error on CO luminosities is $\sim$ 0.15 dex. D10 also used new dynamical models of clumpy disk galaxies to derive dynamical masses for the sample. Typical uncertainties on dynamical masses are between 30%-50%. By subtracting the contribution of the stellar and dark matter (25%) masses from the dynamical mass (within r_e), D10 derived molecular gas reservoirs with masses of $(0.4 - 1.2) \times 10^{11} M_{\odot}$. The uncertainty in the total gas mass estimate is about 30% for *BzK-4171* and *BzK-17999* and 50% for *BzK-21000*. These were the three objects having resolved CO emission. The implied conversion (CO luminosity-to-gas mass) factor is very high: $\alpha_{CO} = 3.6 \pm 0.8$, consistent with a Galactic conversion factor but 4 times higher than that of local ultra-luminous IR galaxies that is

typically used for high-redshift objects. Their gas masses are often comparable to or larger than the stellar mass, and the gas accounts for an impressive 50%-65% of the baryons within the galaxies' half-light radii.

All six sources (*BzK-21000*, *BzK-17999*, *BzK-4171*, *BzK-16000*, *BzK-12591* and *BzK-22536*) were observed during the Herschel campaign with both PACS and SPIRE (see Magdis et al. 2012). Four of them also benefit from 1.3 mm continuum data derived from the CO[5-4] emission line observations (Dannerbauer et al., 2009). In addition to IRAC and MIPS 24 μm data, the sources are also seen in the 16 μm InfraRed Spectrograph peak-up image (Teplitz et al., 2011). Using the data from MIR to mm wavelengths M12 have recently provided robust estimates of dust masses using the realistic models by Draine & Li (2007). They also provided independent estimates of the CO-to-H_2 conversion factor (α_{CO}), molecular gas masses and SFEs by exploiting the correlation of gas-to-dust mass with metallicity ($M_{gas}/M_{dust} - Z$). The SFRs have been computed using the information coming from the full coverage from MIR to sub-mm offered by Herschel data and therefore do not suffer from the same bias of SFR estimates from 24 μm only. It has been shown, in fact, that the L_{IR} from 24 μm can be up to a factor $\sim$2 higher than the 'real' L_{IR} from Herschel (see e.g. Oliver et al. 2012, Canalog et al. 2013 in prep.).

The results derived by D10 and M12 are listed in Tables 7.1, 7.2 and 7.3.

7.3 Best-fit SEDs and SFHs of z $\sim$ 1.5 BzK star forming galaxies

We have explored for these galaxies, in addition to the well tested library of star forming spheroids discussed above and widely in Chapter 5, new disk geometries and SFHs. Disk galaxies are modelled using a double exponential of the distance from the polar axis and from the equatorial plane (see Eq. 3.7), with the scale lengths R_d and z_d left as free parameters. In the code the scale lengths R_d and z_d can be independently set for the three components. Nevertheless we simplify the problem by assuming identical values for them, thus reducing the number of free parameters in case of disk geometry to two: $R_d^{\star}=R_d^{mc}=R_d^{c}$ and $z_d^{\star}=z_d^{mc}=z_d^{c}$. Several values for these scale lengths have been explored in combination with the other model parameters discussed in Section 3.8. Concerning the SFH, we considered both SFHs typical of normal SF galaxies, namely longer infall timescales (1-5 Gyr) and moderate to high star formation efficiencies (0.5-3.0 Gyr^{-1}), and more 'bursty' SFHs characterized by shorter infall timescales. We have built in this way a library including more than 400,000 disk spectra. For each galaxy in this sample we then performed the SED-fitting procedure on both the old spheroidal and new disk library. Based on the χ^2

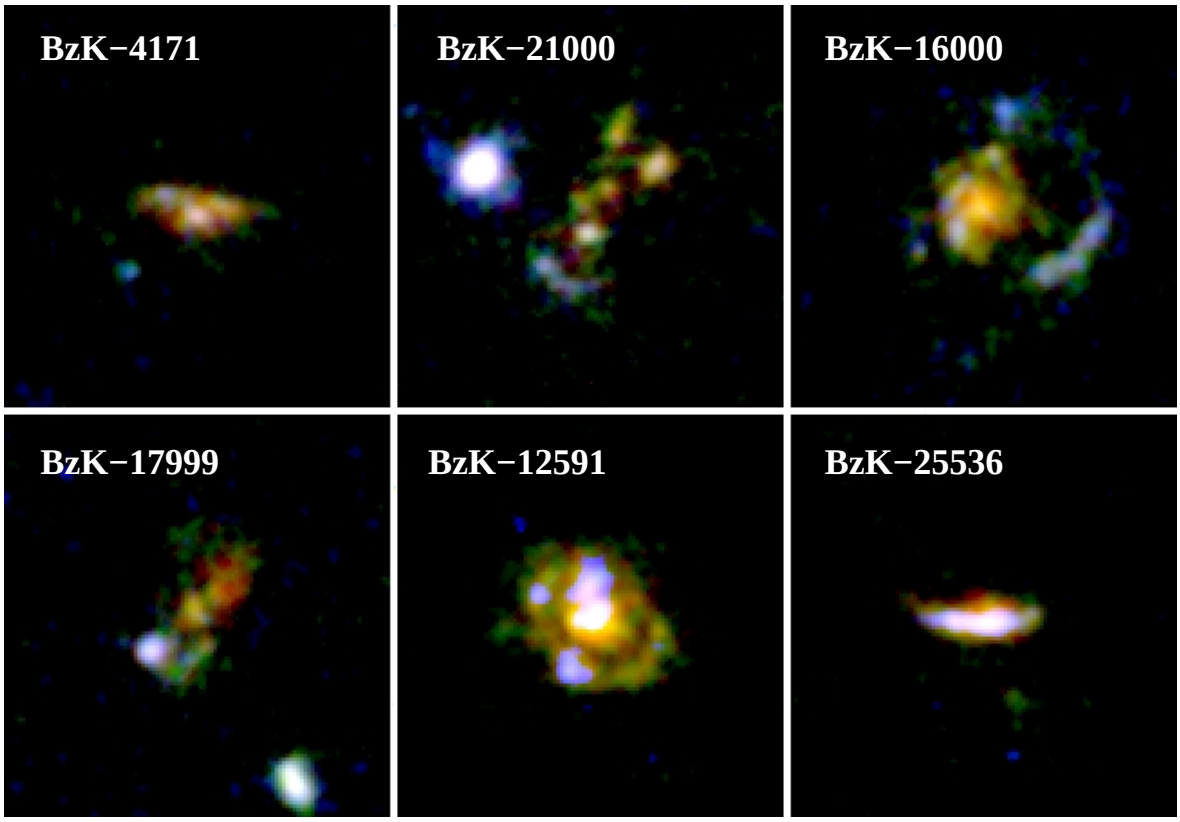

Figure 7.2 Three-color RGB imaging of the six CO-detected BzK galaxies, based on ACS imaging of Giavalisco et al. (2004), release 2.0. Red is *F850LP*, green is *F775W*, and blue is *F435W*. A two-pixel top-hat smoothing has been used to improve the source visibility. Images are $3''$ in size [image from Daddi et al. (2010a)].

minimization procedure and physical parameter analysis, we obtained the best-fits shown in Figures 7.4 and 7.5 all based on disk geometry, in agreement with D10 morphological analysis.

For all the six BzK galaxies in the sample, we were able to reproduce the observed SEDs from far-UV-to-sub-mm very well. Among these galaxies, 3/6 (*BzK-16000, BzK-21000, BzK-17999*) have radio data also in perfect agreement with our best-fit solutions, 1/6 (*BzK-4171*) has radio data in agreement with our estimates within a factor of $\lesssim 1.5$ and 2/6 (*BzK-12591, BzK-25536*) have radio data underpredicted by our models by a factor larger than ~ 2. The latter, namely *BzK-12591* and *BzK-25536*, are the two objects showing the lowest observed q_{TIR} value (both ~ 2.06, much lower also than the typical local value by Condon (1992) of 2.35). The observed q_{TIR} has been measured following the eq. 6.5 with $L_{1.4Ghz}$ computed from the observed flux at 1.4 Ghz using the Eq. 6.1 and L_{TIR} estimated from the GRASIL best-fit by integrating the IR luminosity in the wavelength range between 8-1000 μm. The galaxy *BzK-12591*, as discussed above, shows a strong bulge in HST imaging (see Fig. 7.2) and has a possible detection of [NeV]λ 3426 $\AA$ emission line, indicative of the presence of an AGN. This galaxy is not detected in hard X-rays

ID	z	L_{IR} [$L/L_\odot$]	SFR_{10} [$M_\odot$/yr]	SFR_K [$M_\odot$/yr]	SFR_{D10} [$M_\odot$/yr]	SFR_{M12} [$M_\odot$/yr]	$LogM_\star^{GR}$ [$M_\odot$]	$LogM_\star^{D10}$ [$M_\odot$]	$LogM_\star^{D10,\%60}$ [$M_\odot$]
bzk16000	1.522	8.10E11	75	81	152	74	11.25	10.63	10.84
bzk12591	1.600	2.95E12	205	295	400	275	11.65	11.04	11.25
bzk21000	1.523	2.40E12	163	240	220	209	11.35	10.89	11.10
bzk17999	1.414	1.27E12	96	127	148	115	11.43	10.59	10.79
bzk25536	1.459	3.58E11	28	36	62	29	10.90	10.52	10.72
bzk4171	1.465	1.22E12	71	122	103	95	11.28	10.60	10.81

Table 7.1 Best-fit physical parameters of BzK galaxies compared to estimated values from Daddi et al. (2010a) (D10) and Magdis et al. (2012) (M12). The last column reports the stellar mass computed by D10 using the M05 stellar libraries corrected by a factor of $\sim 60\%$ corresponding to the difference with respect to BC03 models.

ID	z	$LogM_{gas}^{GR}$	$LogM_{dense}^{GR}$	$LogM_{gas,mol}^{D10}$	$LogM_{gas,mol}^{M12}$	f_{mol}	L_{CO}	α_{CO}^{D10}	α_{CO}^{M12}
bzk16000	1.522	10.97	10.67	10.77	11.19	0.50	1.6E10	3.6 ± 0.8	9.7 ± 3.1
bzk12591	1.600	11.53	11.49	11.08	11.08	0.90	3.2E10	3.6 ± 0.8	3.8 ± 2.0
bzk21000	1.523	11.31	11.21	10.91	11.10	0.80	2.2E10	3.6 ± 0.8	5.7 ± 2.0
bzk17999	1.414	10.84	10.74	10.80	10.82	0.80	1.7E10	3.6 ± 0.8	3.9 ± 1.2
bzk25536	1.459	10.30	10.18	10.62	10.57	0.76	1.2E10	3.6 ± 0.8	3.1 ± 2.1
bzk4171	1.465	10.94	10.72	10.89	10.72	0.60	2.1E10	3.6 ± 0.8	2.5 ± 1.1

Table 7.2 Best-fit physical parameters of BzK galaxies compared to estimated values from Daddi et al. (2010a) (D10) and Magdis et al. (2012) (M12).

by Alexander et al. (2003) but exhibits some soft X-ray emission. As our model does not include an AGN component, we tend to underpredict the radio emission for this object. The other galaxy, *BzK-25536*, has no explicit indication for a presence of an AGN but shows the same low value of q_{TIR}. Low values of this parameter are usually typical of AGN dominated objects. We suggest this object could be dominated by an optically-obscured radio loud AGN. A 'radio excess' of the data with respect to models, for these two objects, has been also observed independently by Magdis and collaborators, (private communication), thus supporting our results. The predicted and observed q_{TIR} values of each BzK galaxy in the sample, estimated according to the eq. 6.5, are listed in Table 7.3.

From the detailed shape of the broad-band best-fit SED of these 6 BzK galaxies we have derived the SFHs shown in Figure 7.3. As evident from the figure, 3/6 objects (top-left and top- and bottom-centre panels) show relatively long infall timescales ($\tau_{inf} \sim 4$ Gyr) typical of gradually evolving star forming disks at high redshift. Two of them also have high SF efficiencies ($\nu_{Sch} = 1.4$ Gyr^{-1}) while one of them shows a lower SF efficiency of 0.6 Gyr^{-1} typical of normal SF spiral galaxies. The remaining three BzK show SFHs characterized by shorter infall timescales ($\tau_{inf} \sim 0.5$ Gyr) and moderate SF efficiencies ($\nu_{Sch} = 0.8$ Gyr^{-1}), typical of objects in earlier phases of SF. The latter also show lower ages with respect to the former, typically in the range between 1.78 and 2.66 Gyr. All of them are observed within 2 Gyr from the peak of SF activity. Anyway the statistics of the sample is still too low to draw a self-consistent picture of their SFHs. A detailed analysis of a larger sample of BzK galaxies including CO line observations and radio detections is in plan.

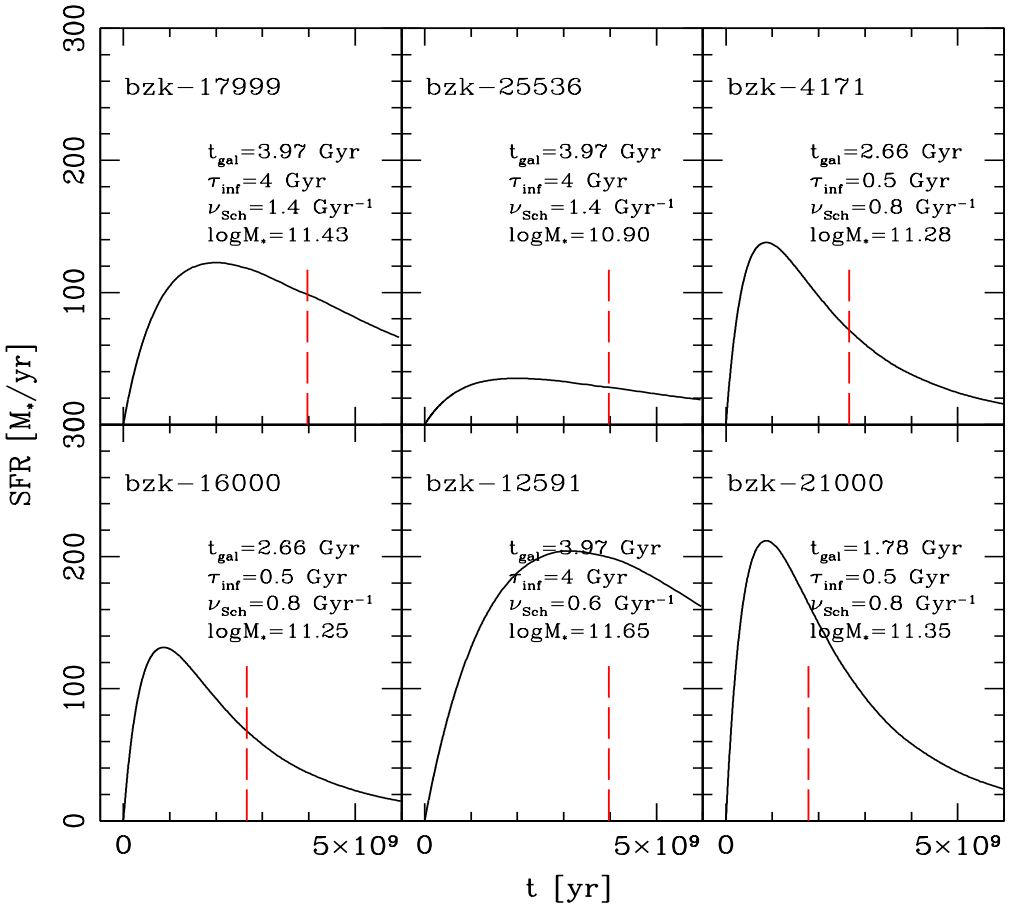

Figure 7.3 Best-fit SFHs of z ∼ 1.5 SF Bzk galaxies. The long dashed red vertical lines indicate the age at which the galaxy is observed.

ID	z	χ^2	LogM$_{dust}$	LogM$_{dust}^{M12}$	A$_V$	A$_{FUV}$	q$_{TIR}^{GR}$	q$_{TIR}^{obs}$
bzk16000	1.522	0.96	8.95	9.11	1.42	3.41	2.59	2.54
bzk12591	1.600	4.85	9.52	9.09	1.78	4.42	2.65	2.06
bzk21000	1.523	1.35	9.29	9.07	2.36	4.06	2.65	2.66
bzk17999	1.414	2.22	8.82	8.78	2.60	5.19	2.64	2.64
bzk25536	1.459	2.00	8.29	8.52	1.18	2.84	2.62	2.07
bzk4171	1.465	2.66	8.93	8.70	2.57	5.10	2.75	2.51

Table 7.3 Best-fit physical parameters of BzK galaxies compared to estimated values from Daddi et al. (2010a) (D10) and Magdis et al. (2012) (M12).

7.4 Physical Properties of z ∼ 1.5 BzK galaxies: SFR & M$_\star$

Tables 7.1-7.3 summarise the main results of our analysis and compare them to the observational estimates provided by D10 and M12. Differently from D10, whose SFR estimates rely only on 24 μm, the SFRs from M12 have been computed using the information coming from the full coverage from MIR to sub-mm offered by Herschel. They are thus more reliable with respect to the former. As already stated above, the L$_{IR}$ from 24 μm can be up to

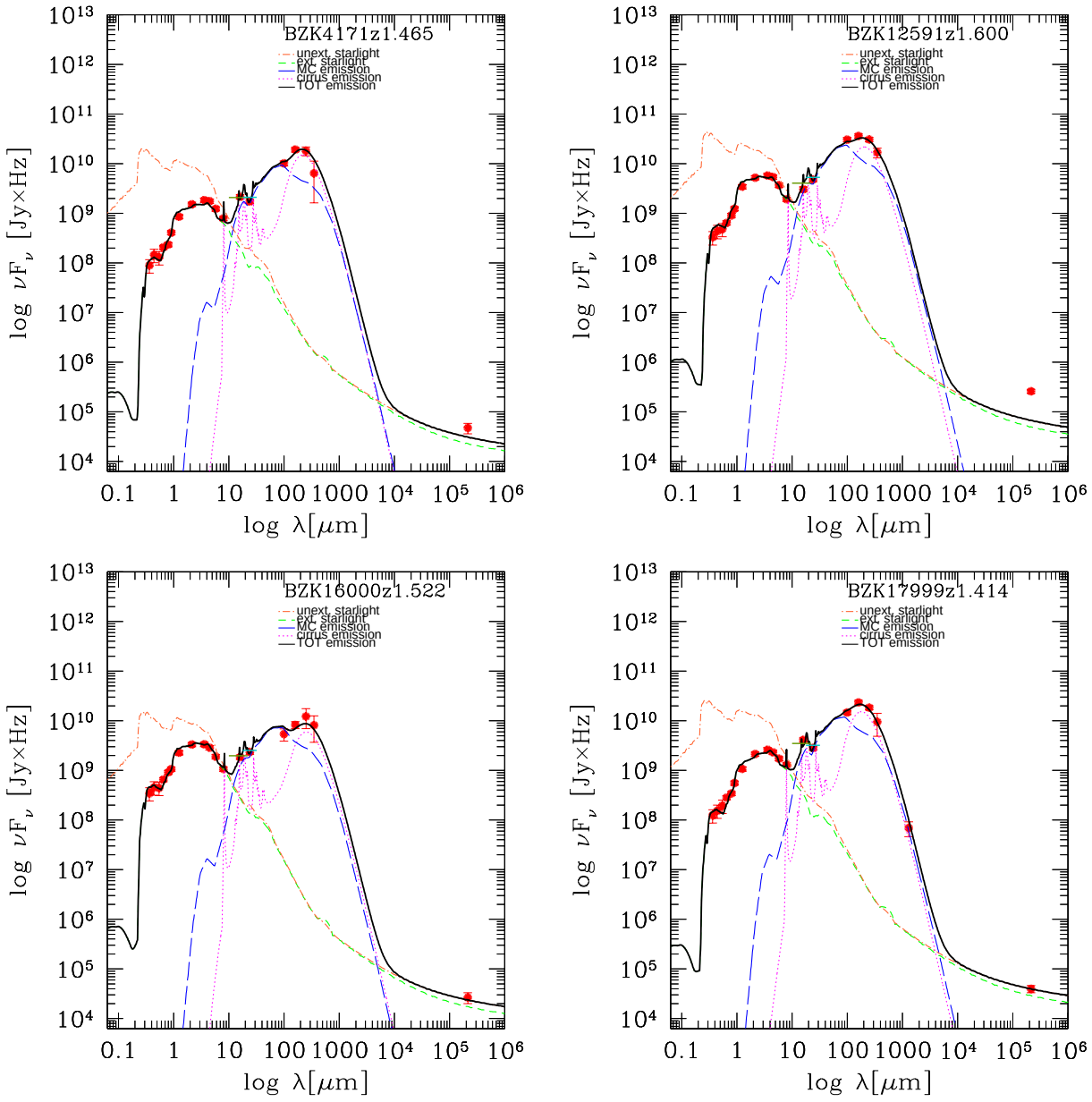

Figure 7.4 Best-fits to the observed SEDs (red filled circles) of z ∼ 1.5 BzK star forming galaxies. The short green and cyan segments at 16 and 24 μm, respectively, represents the modeled fluxes integrated over the filter bands. These are required by the presence of several spectral features ascribed to PAHs falling in these wavelength range.

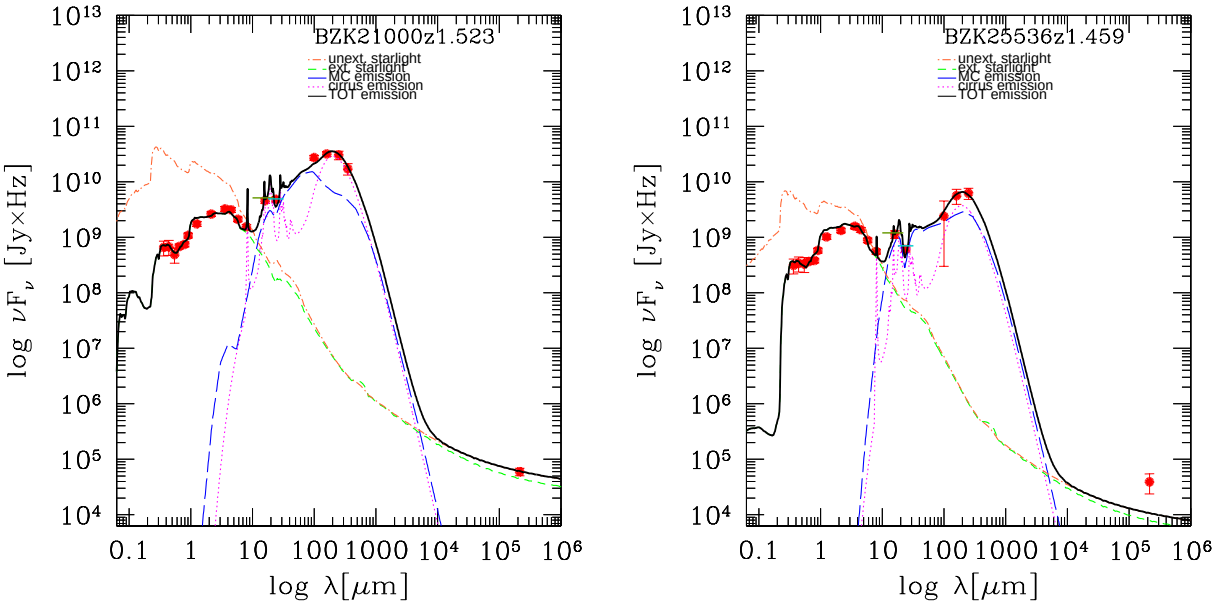

Figure 7.5 Same as in Fig. 7.4.

a factor $\sim$2 higher than the 'real' L_{IR} measured with Herschel (see e.g. Oliver et al. 2012, Canalog et al. 2013 in prep.). As evident from Tab. 7.1 our SFRs, averaged over the last 10 Myr, well agree with those derived by M12. For comparison we also report the SFRs based on the Kennicutt calibration. These differ with respect to our estimates less than $\sim$1.4, on average, well within the typical uncertainties for this kind of measure. According to our analysis these galaxies seem to host a moderate ongoing activity of SF with SFRs $\lesssim$107 $M_{\odot}$/yr, typical of MS star forming galaxies (Daddi et al., 2010a).

The stellar masses derived from the best-fit SED (SFH) of these objects are also listed in Tab. 7.1 and compared to the estimates provided by D10. Our $M_{\star}$ are computed following the procedure described in Chapters 2 and 5, adopting a Salpeter IMF then rescaled to a Chabrier IMF and the updated stellar libraries by Bressan et al. (1998, 2002). These include the effects of dusty envelopes around the AGB stars and the radio emission by stars. Except for the treatment of the dusty AGB phase, our SSPs are based on the same Padova stellar isochrones as the BC03 ones.

Stellar masses in D10 (column n. 9 of Tab. 7.1) are derived, instead, by fitting the M05 template libraries to the UV-optical-NIR (up to 5.8 μm) band of each galaxy. M05 templates include a strong contribution of AGB emission, much larger than in BC03 (see Section 2.1.1 for details). Given that all the galaxies in the sample are star forming, a constant SFR in combination with a large range of ages, a Chabrier (2003) IMF and different metallicities from half solar to twice solar, is adopted by D10. Dust effects are accounted for by assuming an homogeneous foreground screen of dust and the Calzetti (2000) reddening law. The 1 σ error on D10 stellar masses is of the order of 0.10-0.15 dex. As clearly evident from Tab. 7.1,

D10 $M_\star$ are much lower than our estimates by a factor ranging between 2.4 up to ~ 7 (for *bzk-17999*). We have seen in Section 2.1.1 that the differences in the (1) Stellar Evolutionary models used to construct the isochrones, (2) the treatment of the TP-AGB phase and (3) the specific procedure used for computing the integrated spectra can lead to large differences in terms of stellar ages and masses when comparing the BC03 stellar models to the M05 ones. In particular M05 SSPs are typically brighter and redder than BC03 ones, this results in lower ages and lower stellar masses with respect to BC03 by a factor $\sim 60\%$. We have applied this factor to the D10 $M_\star$ estimates getting the results shown in the last column of Tab. 7.1. In this case the average difference between our estimates and those provided by D10 decreases to ~ 2.5, with a maximum corresponding to a factor of ~ 4 (for *bzk-17999*). The object showing the largest stellar mass discrepancy is also, accordingly to the results discussed in Chapter 5, the one with the largest average extinction ($A_V \sim 2.6$). We believe that, once corrected for the use of different stellar population models, the combination of a different SFH and dust attenuation treatment is again the major source of discrepancy.

We have in program to test, within our code, different libraries of SSPs, among which the Maraston (2005), the updated libraries by Bruzual & Charlot and those by Marigo (2013). The major difference between these libraries concerns the implementation of the AGB phase. It will be interesting in this respect to investigate, given the same radiative transfer treatment of dust effects, how the different prescriptions for stellar evolution and chemical enrichment affect the SEDs of our galaxies and, above all, their stellar mass determination.

7.5 The Schimdt-Kennicutt plot

As described in detail in Section 5.6.2, the total gas mass of the best-fit model at t_{obs} is provided, in GRASIL, by the chemical evolution code described in Section 3.2. The model values of the fraction of gas in the dense phase (MC component), f_{MC}, and of the dust-to-gas mass ratio provide the molecular gas and dust mass directly associated with star formation, as well as the gas and dust mass of the diffuse phase.

In D10 the gas mass of the BzK galaxies having resolved CO images is estimated from the dynamical mass, (derived from dynamical models of clumpy disk galaxies), by subtracting the contribution of stellar and dark matter masses. The stellar mass is computed using the procedure described in Sec. 7.4 and M05 templates, while the latter is estimated by assuming a dark matter fraction within the effective radius r_e of 25%. In this way D10 derive molecular gas masses independently from the CO-line luminosity. Taking the ratio of the gas mass estimate and CO luminosity, the α_{CO} conversion factor is then estimated. For the galaxies not resolved in CO this factor is used to estimate the gas mass from the CO luminosity. Indeed the α_{CO} so computed traces the total amount of gas, including

molecular and atomic hydrogen as well as helium in their respective proportions within the galaxy half-light radii. However D10 assume that more than 90% of the gas mass is molecular based on the results of hydrodynamical simulations (Bournaud et al., 2010). The typical uncertainty on total gas masses estimated following the procedure described above ranges between 30% and 50%. We believe it could be even higher than this.

In order to understand how GRASIL and D10 molecular gas masses compare one to each other we need to define the 'critical density' at which the radiative molecule suffers collisions. Briefly, the excitation for the rotational levels of molecules like CO observed at mm and submm wavelengths is provided by collisions with the homonuclear H_2 molecule. If these collisions are sufficiently frequent (compared to the spontaneous decay rate) the levels will come into thermal equilibrium with the H_2 and their excitation temperature will approach the gas kinetic temperature ($T_B(CO) \simeq T_k(H_2)$). For any molecular transition this occurs at the 'critical density' $n_{H_2,crit} = A_{UL}/\sigma\,\nu_{UL}$ where A_{UL} is the Einstein spontaneous decay rate ($7 \times 10^{-8}\,\mathrm{sec}^{-1}$ for CO, J=1-0), and the $\sigma\,\nu_{UL}$ is the collisional de-excitation rate averaged over the Maxwellian distribution of H_2 thermal velocities. For the CO(J=2-1) transition considered by D10, the critical density is ~ 6000 cm^{-3}. Transitions with high emission coefficients as for example the HCN (hydrogen cyanide) J=1-0 line at $\nu \approx 88.63$ Ghz are collisionally excited only at very high densities ($n_{crit} \approx 4 \times 10^4 - 10^5\,cm^{-3}$), therefore they are more directly connected with the star forming cores in galaxies.

As the molecular gas mass provided by GRASIL is directly linked to the highest density star forming regions (Vega et al., 2008), the best observational indicator to be compared with would be the HCN luminosity instead of low excitation CO luminosity which is a better tracer of the overall distribution of H_2 in galaxies. However given the large uncertainties in the D10 gas mass estimates and the effectively high molecular gas fraction of high-z SF galaxies, we can still consider this as a good approximation of the molecular gas mass.

We have estimated, for each BzK in the sample, the gas depletion timescale ($\tau_{\rm gas} = M_{\rm gas,MC}/SFR$) and we have compared our predictions to the observational estimates provided by D10. Given the assumptions made by D10 in order to derive the molecular gas reservoirs for these galaxies, we have considered, in the computation of the depletion timescale, the molecular gas mass instead of the total gas mass as more directly connected to the star formation activity of the galaxy. Results are given in Figure 7.6. Our estimates, based on GRASIL best-fits, are shown as black 45° angle line shaded area, those based on D10 results as red horizontal line shaded area. We show here also the estimates by D10 'corrected' by a factor of 2 (blue dotted line shaded area), based on the consideration that their SFRs are, on average, a factor of ~ 2 larger than our predictions and observational estimates by M12 both based on the full MIR to sub-mm coverage provided by Spitzer and Herschel (see text for details). The mean t_{depl} and SD, colour-coded accordingly to the

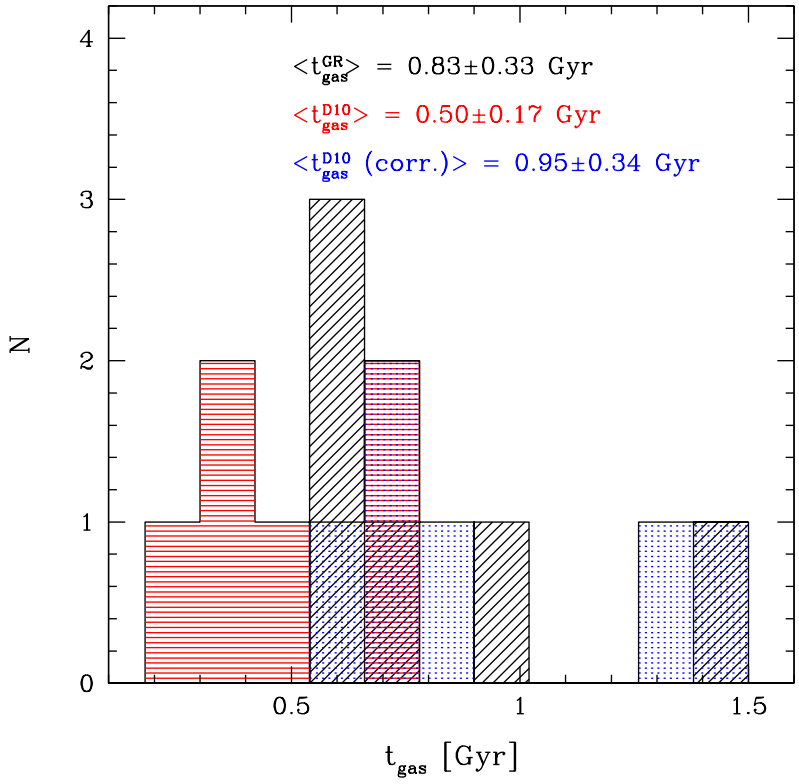

Figure 7.6 Gas depletion timescale distributions for z ∼ 1.5 BzK galaxies. We compare here our predictions (black 45° angle line shaded area) to those provided by D10 (red horizontal line shaded area). We consider here also the estimates by Daddi (2010) 'corrected' by a factor of 2 (blue dotted line shaded area), based on the consideration that their SFRs are, on average, a factor of ∼ 2 larger than our predictions and observational estimates by M12 based on the full MIR to sub-mm coverage provided by Spitzer and Herschel (see text for details). The mean values and SD are also highlighted in the figure colour-coded according to specific case.

specific case considered, are also highlighted in the figure. With respect to the mean depletion timescale reported by D10, t_{depl}^{D10} ∼ 0.5 Gyr, our estimates tend to be slightly higher with a mean t_{depl}^{GR} ∼ 0.83 Gyr. The agreement is better when we consider the D10 t_{depl} corrected for the factor of ∼ 2 cited above. Anyway considering the typical uncertainties associated to these estimates we can still consider our predictions in good agreement also with the un-corrected mean t_{depl} computed by D10. Moreover our resulting gas depletion timescales, in the range between 0.5 - 1.0 Gyr, well agree with the typical duration of MS normal star forming galaxies duty cycle.

The main aim of this 'still ongoing' work is that of reproducing the Schmidt-Kennicutt-like diagram of these 6 BzK galaxies taking advantage of the full multiwavelength coverage from far-UV to radio provided by Spitzer, Herschel and VLA combined to the availability of CO-line detections for these objects. These in fact are useful to constrain the gas and molecular

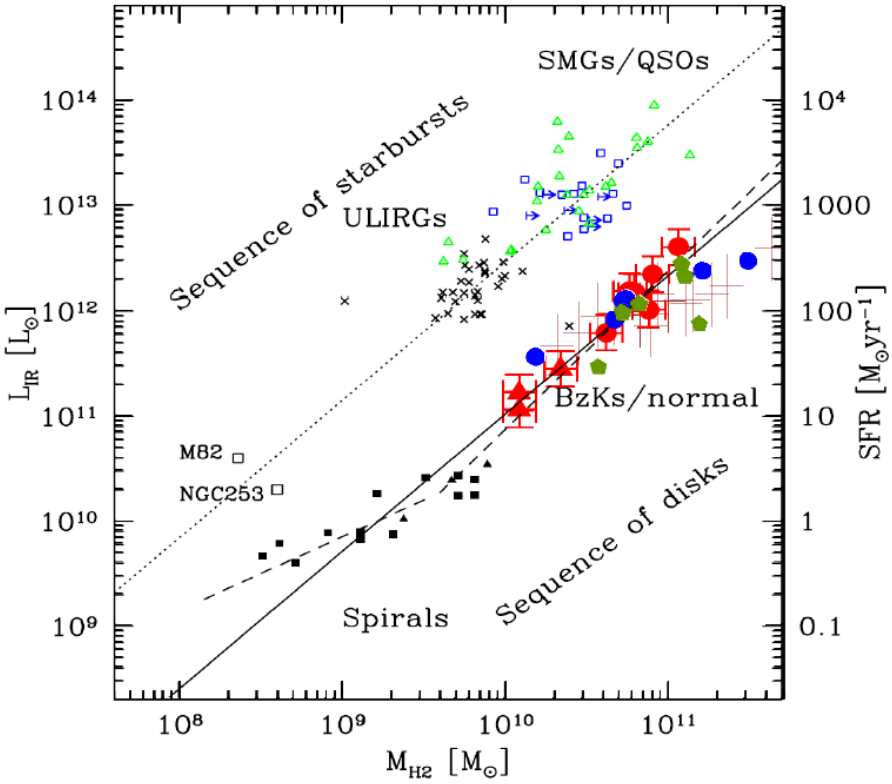

Figure 7.7 Same as in Fig. 7.1 but without our high-z (U)LIRGs and with, overplotted, our modeled solutions for the 6 BzK analysed in this work (blue filled cirles). Only 1/6 BzK fall-off the region occupied by the observed BzK galaxies from Daddi et al. (2010a) (red filled circles). This is *BzK-12591*, the one confirmed to be AGN dominated for which, the absence of an AGN component in our model, forces the MC contribution to the power-low MIR. The observed estimates by M12 are also overplotted as dark green pentagons. As evident from the figure our solutions agree very well with both D10 and M12 estimates within the errors.

gas mass of these galaxies. Figure 7.7 shows, again, the relation between the infrared luminosity L_{IR} and the molecular gas mass M_{H2} for several galaxy samples in the literature including high-z SMGs (blue empty squares), z$\sim$0.5 disk galaxies (red filled triangles), z$\sim$1-2.3 normal galaxies (brown crosses), local (U)LIRGs (small black crosses) and local spirals (black filled squares). The solid line represents a fit to local spirals and BzK galaxies and the dotted line is the same relation shifted in normalization by 1.1 dex. Overplotted as filled red circles, green pentagons and blue circles there are, respectively, D10, M12 and our estimates for the sample of z$\sim$1.5 BzK galaxies discussed in this work. As evident from the figure, our solutions agree very well with both D10 and M12 estimates within the errors. All of our modelled BzKs lie in the region of the plot populated by normal star forming galaxies characterized by a quasi-steady long-lasting mode of SF. This result is interesting as the three sets of points (D10, M12 and our work), rely on independent methods to estimate the molecular gas masses. In M12 the CO-to-H_2 conversion factors (α_{CO}) have been estimated on the basis of the correlation of gas to dust mass with metallicity (M_{gas}/M_{dust}-Z). With

respect to D10 and M12 we cover a wider range in molecular gas mass but still consistent with the range covered by the brown crosses representing z = 1-2.3 normal SF galaxies from Tacconi et al. (2010). The object reaching, according to our analysis, the largest gas mass in the plot is *BzK-12591*, the one confirmed to be AGN dominated for which, the absence of an AGN component in our model, forces the MC contribution to the power-low MIR.

Given the low statistics of the sample studied here, we cannot draw strong conclusions from this analysis. We can give, however, some hints on the GRASIL capability in reproducing the molecular gas properties of high-z SF galaxies. As already stated above, we have actually in plan to extend the ongoing investigation to a larger statistical sample of BzK galaxies having CO-line observations, in order to put stronger constraints on the total and molecular gas masses of MS star forming galaxies. The results are going to be discussed in detail in a forthcoming paper in preparation.

7.6 Predicted M_{dust} distribution of $z \sim 1.5$ BzK galaxies

The other main aim of this work is the physical modelling of the dust properties of high-z star forming BzK galaxies. We give here only a brief overview on some preliminary results we got for this small sample of 6 BzKs.

In our procedure, dust and gas masses are derived from the best-fit model and related one to the other by assuming a suitable dust-to-gas ratio. The D/G ratio can be either assumed to be proportional to the metallicity or fixed to some reasonable value (for more details about the dust model see Chapter 3). We have compared our M_{dust} estimates to those provided by M12.

Dust masses in M12 have been computed considering both the physically motivated Draine & Li (2007, DL07 hereafter) models and the more simplistic, but widely used, modified blackbody (MBB) model. In the DL07 models the interstellar dust is described as a mixture of carbonaceous and amorphous silicate grains, whose size distributions are chosen to mimic the observed extinction law in the MW, the LMC, and the SMC bar region. The properties of these grains are parameterized by the PAH index, q_{PAH}, defined as the fraction of the dust mass in the form of PAH grains. The majority of the dust is supposed to be located in the diffuse ISM heated by a radiation field with a constant intensity U_{min}. A smaller fraction γ of the dust is exposed to starlight with intensities ranging from U_{min} to U_{max}, representing the dust enclosed in photodissociation regions (PDRs). According to DL07 the spectrum of a galaxy can be thus described by a linear combination of one stellar component approximated by a blackbody with color temperature $T_\star = 5000$K and two dust components, one arising from dust in the diffuse ISM, heated by a minimum radiation

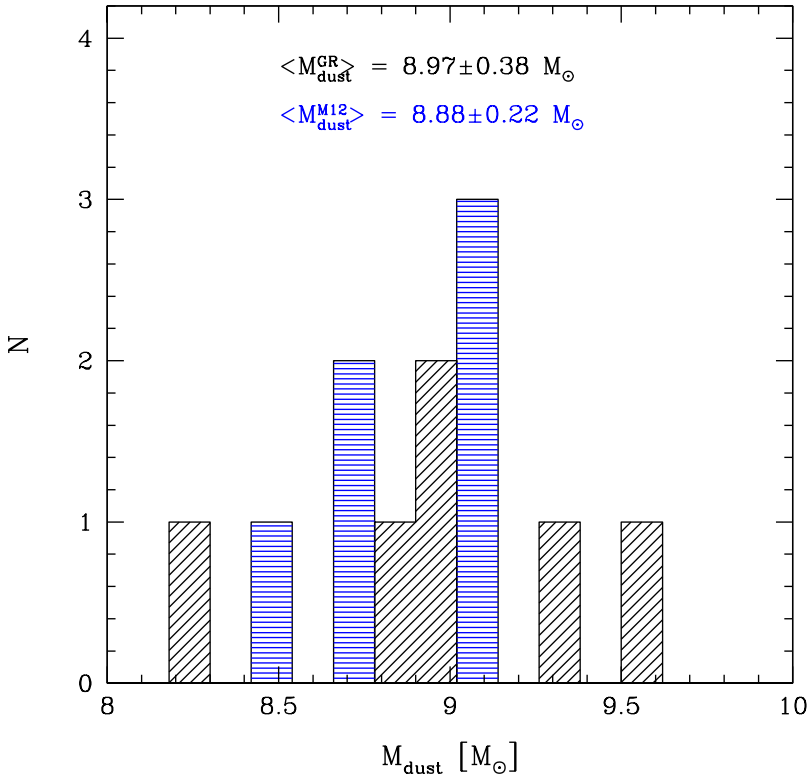

Figure 7.8 Comparison of the predicted dust masses (black 45° angle line shaded area) of z ∼ 1.5 BzK galaxies with observational estimates (blue horizontal line shaded area), provided by M12 following the procedure described in the text. Mean values and standard deviations are also highlighted in the figure.

field U_{min} ("diffuse ISM" component), and the other from dust heated by a power-law distribution of starlight, associated with the intense PDRs ("PDR" component).

In the MBB method the dust mass, temperature (T_d) and emissivity index (β) are estimated by fitting the far-IR to submillimeter SED of the galaxies with a single-temperature MBB. Then from the best-fit model the dust mass is obtained from the relation:

$$M_d = \frac{S_\nu D_L^2}{(1+z) k_{rest} B_\nu(\lambda_{rest}, T_d)}, \qquad with \quad k_{rest} = k_0 \left(\frac{\lambda_o}{\lambda_{rest}}\right)^\beta, \tag{7.1}$$

where S_ν is the observed flux density, D_L is the luminosity distance, and k_{rest} is the rest-frame dust mass absorption coefficient at the observed wavelength. M12 found the MBB dust masses to be lower by a factor of ∼2 on average, than those derived based on DL07 models. This is due to the fact that grains of a given size and chemical composition are exposed to different intensities of the interstellar radiation field and thus attain different equilibrium temperatures, which will contribute differently to the SED. The single-temperature models cannot account for this range of T_d in the ISM and attempt to simultaneously fit

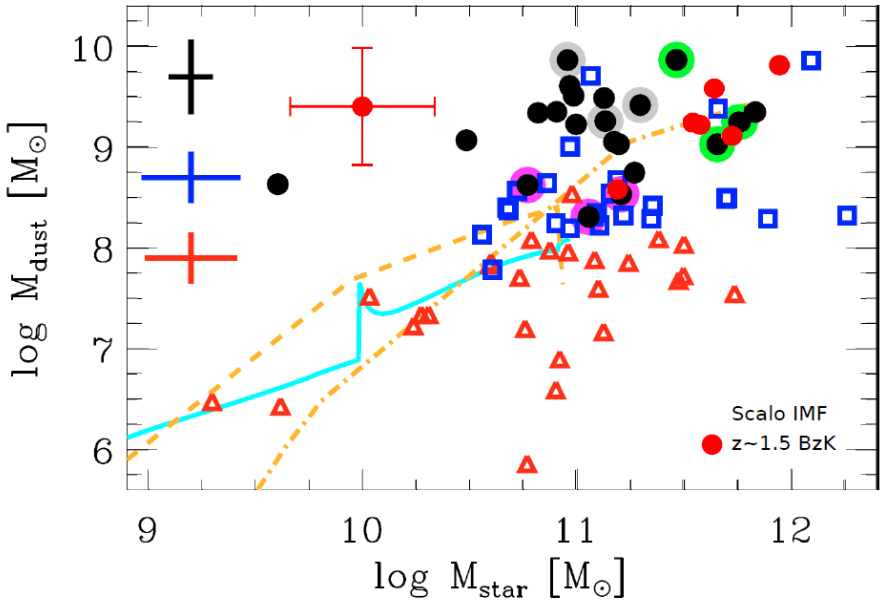

Figure 7.9 $M_\star$ vs M_{dust} (from Santini et al. (2010)). Blue squares are local ULIRGs, red triangles refer to local spirals and black circles correspond to high-z SMGs. Red filled circles are $z \sim 1.5$ BzKs whose stellar and dust masses have been rescaled to the Scalo IMF adopted by Santini et al. Median 1σ error bars are shown on the left. Solid cyan and dashed (dot-dashed) orange lines are the predictions of Calura et al. (2008) model for spirals and proto-ellipticals with mass of 10^{11} (10^{12}) $M_\odot$.

both the Wien side of the gray-body, which is dominated by warm dust, and the Rayleigh-Jeans tail, sensitive to colder dust emission. The net effect here is that the temperatures are driven toward higher values, consequently resulting in lower dust masses. This problem is overcome when a two-temperature blackbody fit is considered.

Figure 7.8 shows a comparison between the dust masses of $z \sim 1.5$ BzK galaxies self-consistently estimated by GRASIL (black 45° angle line shaded area) and those based on DL07 models as reported by M12 (blue horizontal line shaded area). Mean values and SD are also highlighted in the figure. As evident from the figure our predictions (average $M_{dust} \sim 8.97$) well agree within the errors, with the estimates provided by M12 (average $M_{dust} \sim 8.88$). There seems to be, therefore, a good agreement between our radiative transfer based code and the semi-empirical, but physically motivated, code by DL07.

As done in Section 5.4.2 for our high-z (U)LIRGs, also here we compare our stellar and dust masses to those of several galaxy populations discussed in Santini et al. (2010). Figure 7.9 reports our results where our $z \sim 1.5$ BzK galaxies are shown as filled red circles. As evident from the figure once again our stellar and dust masses are consistent with published estimates for high-z SMGs at comparable redshifts. Only one object, the *BzK-25536*, seems to show stellar and dust masses more compatible with local (U)LIRGs (blue open squares). This galaxy is also the one showing the lowest q_{TIR}, possibly indicative of the presence of

an AGN. Similarly to the z ∼ 2 (U)LIRGs discussed in Chapter 5, our z ∼ 1.5 BzK galaxies show higher dust-to-stellar mass ratios, by a factor of ∼ 30 and 6, compared to local spirals and local (U)LIRGs, respectively. The only exception, again, is the object discussed above which shows $M_{dust}/M_{\star}$ similar to those of local (U)LIRGs. Our estimated $M_{\star}$ and M_{dust} for these BzKs appear also to be in agreement with the predictions of the Calura et al. (2008) chemical evolution models for proto-ellipticals.

7.7 Concluding Remarks

In this Chapter we presented the first results from an ongoing work focused on the physical modelling of molecular gas and dust properties of high-z BzK selected galaxies. We concentrated here on a small but well representative sample of 6 BzK galaxies at z ∼ 1.5 selected in GOODS-N characterised by a rich dataset of photometric and spectroscopic data including Spitzer and Herschel (PACS + SPIRE) observations, radio detection and CO emission line measurements.

Our analysis includes also a deep exploration of a different geometrical distribution for stars and dust, in a disk-like profile, in combination with different SFHs ranging from that typical of normal star forming galaxies to the one more typical of starbursts.

Through our SED-fitting procedure we are able to reproduce fairly well the far-UV to sub-mm SED of all the BzK in our sample and, simultaneously, the radio emission for 4/6 objects. For the remaining 2 BzKs, showing very low values of q_{TIR} (∼ 2.04) we find a radio excess of data with respect to models. This has to be ascribed to the possible presence of an AGN bursting the radio flux. For one object this has been also confirmed, independently, by Cowie et al. (2004).

Best-fit SFHs closely resemble those typical of normal star forming galaxies at high redshift characterised by infall timescales ranging between 0.5 and 4 Gyr and high SF efficiencies, with the former being observed at earlier phase of SF. We find, for these objects, a moderate ongoing activity of star formation with SFRs $\lesssim$ 107 $M_{\odot}$/yr, typical of MS star forming galaxies and in good agreement with the estimates provided by Magdis et al. (2012).

Our predicted molecular gas masses for these galaxies are found to be in good agreement, within the errors, with both Daddi et al. (2010a) and Magdis et al. (2012) estimates based on different methods. All of our modelled BzKs lie in the region of the Schmidt-Kennicutt plot populated by normal star forming galaxies characterized by a quasi-steady long-lasting mode of SF.

The dust masses obtained from the GRASIL best-fit (average $M_{dust} \sim 8.97$), are found to be in good agreement, within the errors, with the estimates derived by Magdis et al. (2012) (average $M_{dust} \sim 8.88$), by fitting the DL07 templates to the full MIR-to-sub-mm SEDs provided by Spitzer and Herschel. There seems to be, therefore, a good agreement between our radiative transfer based code and the semi-empirical, but physically motivated, code by DL07. Stellar and dust masses appear also to be consistent with published estimates for high-z SMGs at comparable redshifts (Santini et al., 2010). Only one object, the *BzK-25536*, seems to show stellar and dust masses more compatible with local (U)LIRGs (blue open squares). This galaxy is also the one showing the lowest q_{TIR}, possibly related to the presence of an AGN. Compared to local spirals and local (U)LIRGs, our $z \sim 1.5$ BzK galaxies show higher dust-to-stellar mass ratios, by a factor of ~ 30 and 6, respectively. The only exception, again, is the object discussed above which shows $M_{dust}/M_{\star}$ similar to those of local (U)LIRGs.

Given the low statistics of the sample studied here, we cannot draw strong conclusions from this analysis. We can give, however, some hints on the GRASIL capability in reproducing the molecular gas properties of high-z SF galaxies. We have actually in plan to extend the ongoing investigation to a larger statistical sample of BzK galaxies having CO-line observations in order to put stronger constraints on the total and molecular gas masses of MS star forming galaxies.

Chapter 8

Conclusions & Future Perspectives

The main focus of my PhD research project was that of investigating the nature and mass assembly history of dusty star forming galaxies at high redshift ($0.8 < z < 2.5$), observed with Herschel, through the modelling of their main physical properties like stellar, gas and dust mass, SFR and SFH, and dust attenuation.

The power of the approach presented in this thesis lies in the combination of a full multi-wavelength coverage for our selected galaxies, including the FIR from 70 to 500 micron by Herschel PACS and SPIRE and ultra-deep IRS Spitzer spectra where available, with a self-consistent spectral synthesis code GRASIL (Silva et al., 1998) used to interpret galaxy SEDs. This code computes the SEDs of galaxies from far-UV to radio including a state-of-the-art treatment of dust extinction and reprocessing based on a full radiative transfer solution.

8.1 Physical Models of LIRGs and ULIRGs at high redshift

We have started focusing our physical analysis on a small (31 objs) but well representative sample of dusty star forming (U)LIRGs at z$\sim$ 1-2. The availability, for this sample, of a full multiwavelength coverage from far-UV to sub-mm, including both Herschel PACS and SPIRE photometric data and ultra-deep Spitzer IRS spectra, has prompted us to investigate the nature and the main physical properties - like stellar mass, bolometric luminosity, star-formation history, extinction, as well as the mass assembly history - for every object.

According to our analysis all of our galaxies appear to require massive populations of old (> 1 Gyr) stars and, at the same time, to host a moderate ongoing activity of SF ($SFR_{10} \leq 100$ $M_{\odot}$/yr with SFR_{10} being the SFR averaged over the last 10 Myr). Our detailed analysis appears to give important hints also on the past history of SF with the bulk of stars consistent with having been formed a few Gyr before the observation in essentially

all cases. Only five galaxies of the sample seem to require, on the basis of an application of the F-test to our χ^2 analysis, a recent starburst superimposed on a low-level, secularly evolving star formation history. Even in these five objects, however, the gas mass involved in the SB amounts to only a small fraction of the galactic mass, $\lesssim 4\%$, and all of them are observed just at the end of the burst event (i.e. late SBs).

We also find substantial discrepancies between our results and those based on optical-only SED fitting for the same objects. Our physically consistent best-fit model solutions of the observed SEDs indicate higher extinctions (by $\Delta A_V \sim 0.81$ and 1.14) and higher stellar masses (by $\Delta \mathrm{Log}(M_\star) \sim 0.16$ and 0.36 dex) for z$\sim$1 and z$\sim$2 (U)LIRGs, respectively. The stellar mass difference is larger for the most obscured objects and correlates with the total dust extinction. This is in agreement with the results of Wuyts et al. (2009b) who also found that the mass underestimate is more severe during the dusty, peak SF phase.

We also find lower SFRs, by a factor ~ 2 on average, than those computed from the total $L_{\rm IR}$ using the Kennicutt (1998) calibration due to the significant contribution to the dust heating by intermediate-age (i.e. with ages larger than the typical escape time) stellar populations through 'cirrus' emission: only $\sim$27% and $\sim$34% of the total $L_{\rm IR}$ appears to be due to ongoing SF in MCs for $z \sim 1$ and $z \sim 2$ (U)LIRGs, respectively. The Kennicut's (1998) calibration seems to correspond instead to an extreme case in which all the the light comes from the youngest stars.

We have investigated the degeneracy in model solutions by considering two different cases. A first case where the SFH of the galaxy is fixed, i.e. the two parameters ruling the source past SFH are fixed, and we consider the variation only of the GRASIL model parameters regulating dust effects. In this case we find stellar masses and average extinctions to be constrained within $\Delta A_V \sim 0.1$ and $\Delta M_\star \sim 0.04$ dex. Therefore no much degeneracy is present in this case in the model solutions. Then we have considered in addition to the many combinations of GRASIL parameters also the different combinations of parameters ruling the SFH. In this case the scatter around the best-fit solution increases to $\Delta A_V \sim 0.3$ and $\Delta M_\star \lesssim 0.2$ dex, still well within the typical uncertainties for this kind of analysis. This is likely to be a result of the continuous spectral coverage from UV to sub-mm for our sample. Another likely factor is the self-consistent radiative transfer modelling, accounting for the distribution of dust with respect to young and old stars, from which both the age-dependent dust attenuation and dust reprocessing are constrained.

By analysing the best-fit GRASIL model parameters used to reproduce the SEDs of our high-z (U)LIRGs and affecting the dust (and NIR-to-sub-mm) properties of the galaxies, (i.e. f_{MC}, t_{esc}, $r_{half-mass}$, $\tau_{1\mu m}$, β) we find:

(1) $\mathbf{t}_{esc}$**:** best-fit values for both galaxy populations range between $\sim$ 3 and 98 Myr, therefore, from the typical values of normal star forming galaxies to the much higher values characteristics of more dust obscured starburst objects. The median is $\sim$ 13 Myr for the z$\sim$2 (U)LIRGs and $\sim$6 Myr for the z$\sim$1 LIRGs in agreement with the typical values of high-z normal star forming objects. All the stars with ages older than the typical escaping time contribute to cirrus heating.

(2) $\mathbf{f}_{MC}$**:** best-fit values range between 0.12 and 0.54 for the z$\sim$1 LIRGs and 0.2-0.98 for the z$\sim$2 (U)LIRGs. In agreement with other observational works (e.g. Braun et al. 2011, Combes 2013, Daddi et al. 2010a, Magdis et al. 2012) the molecular gas fractions tend to be higher for the highest redshift (U)LIRGs. The median values are $\sim$ 0.4 and 0.8 for the z$\sim$1 and $\sim$2 sample, respectively.

(3) $\tau_{1\mu m,MC}$**:** best-fit values typically range between $\sim$ 5-100 for both samples. The median values are $\sim$17 and $\sim$25 for the z$\sim$1 and z$\sim$2 (U)LIRGs, respectively. These translate in median values for the optical depth at 100 μm approximately equal to 0.1 and 0.15 for the z$\sim$1 and 2 sample, respectively. Compared to local ULIRGs, as Arp220 for example, which appears to be optically thick out to at least 100 microns (Rangwala et al., 2011) based on Herschel data, our high-z (U)LIRGs do not show very high $\tau_{100\mu m}$. The maximum value reached is of about 0.5.

(4) β**:** typical value of $\sim$1.8 well agrees with the value usually measured for dusty star forming galaxies at high-z (see e.g. Magdis et al. 2012) and roughly corresponds to cold dust temperatures in the range between 11 and 30 K (e.g. Dupac et al. 2003). It is worth emphasising that thanks to the availability of this rich dataset covering the FIR-to-sub-mm wavelength range, the sub-millimetre spectral slope can be accurately measured independently from the temperature distribution. This allows us to break the well-known T-β degeneracy usually affecting the estimates based on modified BB fit to the FIR SED.

(5) $\mathbf{r}^{\star}_{half-mass}$ **&** $\mathbf{r}^{diff}_{half-mass}$**:** these represent the typical scale-lengths, for both stars and dust, of the assumed spheroidal geometry (King's profile) for our galaxies. By comparing the two galaxy populations at z$\sim$1 and z$\sim$2 we find that while the distribution of stars appears to be more extended for the z$\sim$1 LIRGs where it reaches 5.4 kpc, the dust distribution shows an inverse trend being more extended for the highest redshift (U)LIRGs for which it reaches $\sim$15-17 kpc. This seems to be in agreement with the recent results published by Symeonidis et al. (2013) according to which (U)LIRGs in the early Universe are typically characterised by a more extended dust distribution and/or higher dust masses than lower redshift LIRGs and local equivalent sources.

The gas depletion timescales ($\tau_{gas} = M_{gas,MC}/SFR$) of our objects, computed considering the molecular gas mass as more directly related to the star formation activity of the galaxy, well agree with the typical duration of normal star forming galaxies duty cycle ranging between 0.5 - 1 Gyr but they are much longer than the typical duration expected for starbursts ($\lesssim$100 Myr). Comparing the two galaxy populations we find longer depletion timescales ($\sim$1 Gyr) for the z$\sim$2 (U)LIRGs than for the lower redshift LIRGs ($\sim$0.5 Gyr). If we consider these two classes of objects as the same galaxy population observed in different evolutionary stages, this result can be interpreted as due to the fact that while the highest z (U)LIRGs are in the initial phase of star formation where there are large molecular gas reservoirs but not so high SFRs ($\lesssim 100 M_{\odot}/yr$), the lower redshift LIRGs would actually be objects observed at later stages when the molecular gas reservoir has been reduced by the star formation activity and the SFR is lower.

Both our samples show median SFEs of $\sim$ 14 $L_{\odot}/M_{\odot}$ very similar to the average SFE (14 ± 2 $L_{\odot}/M_{\odot}$) found by Magdis et al. (2012) but $\sim$12 times lower than the typical value of starburst galaxies ($<$SFE$>\sim 200$ $L_{\odot}/M_{\odot}$) usually characterized by an accelerated mode of SF.

We have also compared the attenuation curves self-consistently computed by GRASIL, by solving the radiative transfer equations for a spheroidal geometrical distribution of stars and dust, with the Calzetti et al. (2000) attenuation curve. This comparison has revealed several crucial aspects related to the modelling of dust effects in galaxies, all focused on the importance of an age-dependent dust attenuation.

One of the crucial points risen by our analysis is that dust obscuration in galaxies strongly depends on the geometrical distribution of both stars and dust particularly in terms of the age of stellar populations, in the sense the younger stars embedded in the MCs will be more extinguished than older stars. We have also demonstrated that extremely idealized approaches (homogeneous foreground screen of dust + single extinction law), not accounting for an age-dependent dust attenuation and based on optical-only SED-fitting procedures, may generate unextinguished stellar SEDs unable to energetically balance the reprocessed IR emission from the galaxy due to dust. For the most dust obscured objects this can result in stellar mass underestimates which may reach a factor $\sim$6. On the contrary a more realistic geometry, like the one adopted in GRASIL, is able to explain, for example, the differences between the observed attenuation law of starburst galaxies and the galactic extinction law, even adopting the galactic cirrus optical properties. A further interesting aspect put in evidence is the wide range of attenuations allowed by the model with respect to assuming a single attenuation law. This larger spread characterizing the models was studied in detail by Fontanot et al. (2009b) and has to be ascribed to the accounting of the

star formation histories, the geometrical distribution of stars and dust and the connection between stellar populations of different ages with different dusty environments.

Our analysis thus demonstrates that a correct and self-consistent treatment of dust extinction and reprocessing together with a full multiwavelength coverage (from far-UV to radio), is essential to get reliable estimates of the main physical parameters like stellar mass, dust extinction and SFRs.

We have investigated the strong impact of our results, in terms of larger stellar masses and lower SFRs, on the SFR-$M_\star$ diagram. In particular our physical analysis applied to high-z dusty star forming (U)LIRGs has the effect of shifting downwards, below the main sequence (MS), these objects. The effect strongly depends on the level of dust obscuration of the galaxy and on the nature of star formation (starburst vs gradually evolving SF). The combination of these two effects on the SFR-$M_\star$ relation is clearly visible when we look at some of the off-MS galaxies of Rodighiero et al. (2011). After applying our physical analysis to some of those 'outliers' we get two different situations: for the most dust obscured objects whose IR SEDs are dominated by an ongoing burst of star formation in the MC, the SFRs derived from the model are consistent with the Kennicutt (1998) calibration, within the errors, while the stellar masses are still larger than classical predictions and for some objects reach a factor of $\sim$7. The effect here is that of shifting these most extreme cases to the region between the x4- and x10-MS galaxies, still above the MS. For the dust obscured objects whose IR SED is dominated by cirrus component, thus characterized by gradual evolving SFHs, we measure SFRs lower by a factor $\sim$2-2.5 than Kennicutt calibration, in addition to large stellar masses. Here the effect of our analysis is that of bringing back to the MS these peculiar galaxies, accordingly to Michałowski et al. (2012).

The net effect of our analysis thus would seem that of simply changing the normalization of the relation, maybe leaving some outliers surviving to our analysis. To investigate this possibility and further check the reliability of our physical solutions in terms of both stellar mass and SFR estimates, we have decided to include into our analysis also radio data at 1.4 Ghz. This is fundamental because the radio continuum offers a further independent way to estimate and constrain the 'current' SFR in galaxies completely unaffected by extinction. Moreover the inclusion of radio emission is crucial to understand if the conspicuous cirrus component contributing to the FIR is an 'effect' of a poor parameter exploration or if it is real, and required in order to reproduce the NIR-to-FIR properties of our galaxies.

We have been able to collect radio detections for all the objects in our sample although only $\sim$13% are detection at a high S/N level.

We have modelled the far-UV to radio SEDs of our high-z (U)LIRGs using the same prescriptions of our previous analysis. We have also tested a recently developed library of disk

galaxies, allowing for different SFHs, from a bursty SFR to a more gradually evolving SFR and found that for almost all of them a spheroidal geometry is the best representation. We are able to reproduce, well within a factor of two, the far-UV to radio emission for almost all the (U)LIRGs in our sample. 29/31 (U)LIRGs have modeled radio fluxes within the data error-bars. We have only four cases *U5152* - *U5801* - *U16526* - *U5059* showing a difference between the rest-frame $L_{1.4Ghz}$ model luminosity and the observed data larger than a factor of 2, but three of them are faint (RMS $\lesssim 2\,\sigma$) detections and we do not consider them as a significant failure of our procedure. For the remaining object, *U5152*, we argue that a possible solution could be to add a little 'late' burst of SF on top of its SFH in order to burst the radio contribution without modifying the rest of the SED. We have in plan to check also this kind of solution.

We have compared our star formation rate estimates averaged over the last 10 Myr, SFR_{10}, to radio estimates based on the Bell et al. (2003) calibration and also to those derived from the infrared luminosity using the Kennicutt calibration. We find very good agreement between our SFR_{10} and the $SFR^{Bell}_{1.4Ghz}$ (from Bell 2003) derived from the best-fit $L^{GR}_{1.4Ghz}$. For our model predictions we have derived a calibration factor between modeled SFR and radio rest-frame luminosity, (corresponding to the ratio $SFR^{Salp.}_{10}/L^{GR}_{1.4Ghz}$), of $(5.53 \pm 0.38) \times 10^{-22}$ very similar to the one from Bell et al. (2003) (i.e. 5.52×10^{-22}). The estimates from Kennicutt are, instead, systematically off-set with respect to those provided by radio luminosity, by a factor ranging between 1.5 and $\gtrsim 2$. In particular we observe that the discrepancy between the FIR- and radio-based SFRs is $\gtrsim 2$ up to z$\sim$ 2.5 then larger than 1.5 up to z$\sim$ 2.5 and lower than 1.5 at higher redshifts. In other words the discrepancy seems to be larger at lower redshifts.

A larger scatter in the SFR^{GR}_{10}-$SFR^{Bell}_{1.4Ghz}$ plot is seen when considering the $SFR^{Bell}_{1.4Ghz}$ estimated directly from the observed rest-frame radio luminosity. This scatter reflects the scatter of our best-fit solutions with respect to radio data and pertains mostly to faint detections and $3\,\sigma$ upper limits.

The important conclusion here is that there is no systematic effect in our solutions which tend to scatter both above and below the empirical calibration. On the contrary, compared to the SFRs estimated from the FIR using the Kennicutt calibration, we are systematically lower by a factor of ~ 2.

Another crucial point of our analysis rises when comparing the SFR_K based on the Kennicutt calibration and FIR luminosity to the radio estimates derived from the observed rest-frame radio luminosity. We find here that the FIR-based SFRs tend to be higher with respect to the radio ones by a factor larger than 2 up to z$\sim$ 1.5. Moreover, up to z$\sim$ 1.8 most of the points tend to lie above the 1-1 corr. line. Beyond redshift 1.8 the discrepancy

between the FIR- and radio-based SFRs decreases up to a factor below 1.5. So it seems to be a redshift dependence of the SFR based on Kennicutt calibration and on the radio flux.

Differently from the radio emission, the FIR depends on the dominant population of stars heating the dust. We have demonstrated, trough our physical analysis, that when the cirrus emission dominates at FIR wavelengths the Kennicutt calibration can overestimate the current SFR of galaxies. We have thus investigated the correlation between the logarithmic difference of the FIR- and radio-based SFRs and the fractional contribution of cirrus emission to the total IR luminosity computed as $L_{IR}^{cirr}/L_{IR}^{TOT}$. We find that the discrepancy between the two different SFR estimates becomes larger for higher fractional contributions of cirrus emission to the IR luminosity. Moreover we also find a redshift dependence in the sense that being z$\sim$1 LIRGs characterised by higher cirrus fractions, on average, they also show the larger discrepancies. Of course the extension of our analysis also to low redshift main sequence galaxies is necessary in order to draw a more complete picture of the variation of the two different SFR estimators as a function of both redshift and cirrus content. This will be part of our future works.

Our results on the comparison of SFRs derived from different indicators (and methods) seem to go in the direction of confirming our physical predictions and give an indication that radio emission more than FIR is able to accurately predict the current SFR mostly contributed by young massive stars. It doesn't seem to suffer from contamination by intermediate-age stellar populations, as it happens for the FIR where, in our solution, cirrus dominates. Of course we have to take into account the large errors associated to the radio data, but even with this in mind our results are in good agreement.

By taking advantage of the full FIR coverage provided by both Herschel PACS and SPIRE instruments together with the radio detection at 1.4 Ghz, we have also estimated for each galaxy in our sample the ratio, q_{TIR}, of the rest-frame 8-1000 μm luminosity to the rest-frame radio luminosity at 1.4 Ghz directly derived from our model. We have then compared our estimates with those provided for samples of high-z (U)LIRGs and IR-bright galaxies by Sargent et al. (2010). Our mean values of q_{TIR} equal to 2.83 ± 0.10 and 2.77 ± 0.07 for the z$\sim$1 and $\sim$2 sample, respectively, well agree, within the errors, with the typical value of $\sim$2.672 derived by Sargent et al. (2010) thus confirming from a modellistic point of view that ULIRGs should follow the local IRradio relation until at least z$\sim$2 (Lacki & Thompson, 2010, Murphy et al., 2009).

Our physical model thus seems to be able to reproduce the radio properties of high-z (U)LIRGs including the FIR-radio correlation up to z$\sim$1-2. This provides a further important constraint to model the SFR and SFHs underlying the observed SED.

8.2 Normal star forming (BzK selected) galaxies at high redshift

In addition to the analysis of the high-z (U)LIRGs discussed above, we have investigated here also the molecular gas and dust properties of a sample of high-z BzK star forming galaxies selected in the GOODS field. The basic reason of this analysis is that while the shape of galaxy SED can provide direct information on the dust mass, SFH, SFR and $M_\star$ of galaxies, it is not sufficient alone to put strong constraints on the total gas and molecular gas mass of galaxies. Here we concentrated on a small but well representative sample of 6 BzK galaxies at $z \sim 1.5$ selected in GOODS-N. These galaxies are characterised by a rich dataset of photometric and spectroscopic data including Spitzer and Herschel (PACS + SPIRE) observations, radio detection and CO emission line measurements. The information provided by this rich dataset has revealed essential to constrain the molecular gas reservoirs in high-z star forming galaxies and to investigate the nature of star formation, the parameters that regulate it and its possible dependence on local and global galaxy properties.

We have explored for these galaxies, in addition to the well tested library of star forming spheroids discussed above, new disk geometries and SFHs. This new parameter exploration allows us to reproduce fairly well the far-UV to sub-mm SED of all the BzK in our sample and, simultaneously, the radio emission for 4/6 objects. For the remaining 2 BzKs, showing very low values of q_{TIR} (~ 2.04) we find a radio excess of data with respect to models. This has to be ascribed to the possible presence of an AGN bursting the radio flux. For one object this has been also confirmed, independently, by Cowie et al. (2004).

We find, for these objects, SFHs typical of normal star forming galaxies at high redshift characterised by infall timescales ranging between 0.5 and 4 Gyr and high SF efficiencies, with the former being observed at earlier phase of SF. They show a moderate ongoing activity of star formation with SFRs $\lesssim 107$ $M_\odot$/yr, typical of MS star forming galaxies and in good agreement with the estimates provided by Magdis et al. (2012).

Our predicted molecular gas masses for these galaxies are found to be in good agreement, within the errors, with both Daddi et al. (2010a) and Magdis et al. (2012) estimates based on different methods. All of our modelled BzKs lie in the region of the Schmidt-Kennicutt plot populated by normal star forming galaxies characterized by a quasi-steady long-lasting mode of SF.

We have also compared our predicted dust masses, for these BzK galaxies, to those derived by Magdis et al. (2012) by fitting the DL07 templates to the full MIR-to-sub-mm SEDs provided by Spitzer and Herschel. We find our predictions (average $M_{dust} \sim 8.97$) to

be in good agreement, within the errors, with the estimates provided by M12 (average $M_{dust} \sim 8.88$). There seems to be, therefore, a good agreement between our radiative transfer based code and the semi-empirical, but physically motivated, code by DL07. Stellar and dust masses appear also to be consistent with published estimates for high-z SMGs at comparable redshifts (Santini et al., 2010). Only one object, the *BzK-25536*, seems to show stellar and dust masses more compatible with local (U)LIRGs (blue open squares). This galaxy is also the one showing the lowest q_{TIR}, possibly related to the presence of an AGN. Compared to local spirals and local (U)LIRGs, our $z \sim 1.5$ BzK galaxies also show higher dust-to-stellar mass ratios, by a factor of ~ 30 and 6, respectively. The only exception, again, is the object discussed above which shows $M_{dust}/M_{\star}$ similar to those of local (U)LIRGs.

Given the low statistics of the sample studied here, we cannot draw strong conclusions from this analysis. We can give, however, some hints on the GRASIL capability in reproducing the molecular gas properties of high-z SF galaxies. We have actually in plan to extend the ongoing investigation to a larger statistical sample of BzK galaxies having CO-line observations in order to put stronger constraints on the total and molecular gas masses of MS star forming galaxies.

8.3 Future Perspectives

(1) Further constraints on the SFH: testing different synthetic stellar libraries and IMFs, aand exploring as far as possible the parameter degeneracies

(2) The impact of our physical modelling on the SFR-M* relation. It will be very interesting to investigate the effects of physically-motivated estimates of fundamental galaxy parameters, like the SFR and stellar mass, on large samples of both local and high redshift galaxies and studying how this would impact on the claimed relation between the SFR and stellar mass.

(3) Future exploitation of deep radio photometry: new, forthcoming and future radio facilities promise to offer a dramatic improvement in deep radio photometric imaging.

(4) High resolution observations of diffuse media at high redshift (ALMA, JWST) and model interpretations

(5) Physical modelling of spectral lines. Spectral lines trace in a different way the interstellar media of galaxies and require some dedicated modelling effort.

Appendix A

Evidence for Holmberg Effect in high redshift close major merger pairs selected in the COSMOS field

Chapter based on a paper in preparation by B. Lo Faro, C. Kevin Xu et al.

A.1 ABSTRACT

The aim of this project is the study of the star formation properties of major-merger galaxy pairs at $z < 1$ selected in the COSMOS field with Herschel. More specifically, my work is focused on finding evidence for the so-called "Holmberg effect" in the selected high-redshift close major-merger pairs, and in investigating its evolution with cosmic time.

The "Holmberg Effect" (Holmberg, 1958), refers to the correlation between physical properties of the primary and secondary component of a major-merger pair. This is observed in star formation indicators of very different timescales: $t_{SFR} \sim 10^7$ yr for H_{alpha} emission, $\sim 10^8$ yr for IR emission, $\sim 10^9$ yr for (B-V) colors. According to Xu et al. (2010) the physical mechanism responsible for this correlation is related to the local environment within/around the DMH surrounding the pairs which has the effect of modulating the sSFR of the galaxies. We found evidence of this effect in $z \sim 1$ galaxies and we are now doing the same analysis for local SDSS galaxies. Due to blending effects we are now performing new photometric analysis in order to compute the isophotal magnitudes of the galaxies avoiding for interference on the colors by each other. This is part of a paper in preparation.

A.2 Introduction

Interacting and merging galaxies are among the most fascinating astronomical objects in the Universe. These systems can present in a wide range of different configurations. Along the so-called Toomre merger sequence, Toomre (1977), showing the main stages of a typical merging process between two disk galaxies, we can distinguish five different phases, corresponding to five different configurations. From the phase in which the two galaxies are approaching each other but are still separable to the formation of the merger remnant which shows no outward sign of its violent origin. This scenario can be tested by observing galaxies at these phases to see if they represent a transition between disk galaxies and ellipticals. Along the merger sequence galaxies in close pairs are usually mergers in the early stages when the two galaxies are still separable.

According to hierarchical galaxy formation and evolution models, (ΛCDM), galaxy interactions and mergers are one of the primary drivers in galaxy evolution. Nevertheless their role in the star formation history of galaxies is still debated and poorly understood.

Numerical and theoretical models cannot explain yet the main properties of merger-induced starbursts, including their intensity and their spatial extent. Usually the mechanism invoked in merger-induced starbursts is a global inflow of gas towards the central kpc, resulting in a nuclear starburst (Bournaud et al., 2010). According to the standard models, in an interacting galaxy pair, usually the gas content of one component undergoes tidal forces from the companion galaxy, but this is actually not the main direct driver of the gas response. According to the mechanism described in Bournaud et al. (2010), the gas distribution becomes non-axisymmetric, because of the asymmetry in the gravitational field itself introduced by the companion. This results in gravitational torquing of the gas. Gas initially inside the corotation radius (tipically a radius of a few kpc) undergoes negative gravity torques and flows inwards in a more and more concentrated central component. While the gas outside the corotation radius, i.e. initially in the outer disk, undergoes positive gravity torques and gains angular momentum, forming long tidal tails.

Tidal interactions between galaxies can trigger star formation which contributes to the global star formation rate density of the Universe. Star formation triggered by these tidal interactions may also consume much of the galaxies' cold gas and this could be a key factor in the transformation of blue star forming galaxies into red and quiescent galaxies. This coupling between galactic dynamics and star formation processes provides a unique tool for a deeper understanding of galactic evolution.

On the other hand, observations have suggested that major interactions and mergers between galaxies may account for many of the changes seen over the history of the Universe, from morphological transformations to the assembly of mass in galaxies.

Galaxy pairs constitute about 10% of the noncluster population (Xu & Sulentic, 1991). For paired galaxies current ideas suggest that most of them are morphologically concordant, that is, with component galaxies showing similar initial star formation and angular momentum properties.

One of the first quantitative indications of this correlation comes from Holmberg (1958), as a by-product of his famous photometric survey of nearby galaxies. By comparing the photographic $(B-V)$ colors of paired galaxies, he found a significant correlation between the colors of pair components (with a linear correlation coefficient of $R = 0.80 \pm 0.06$). This phenomenon has since been referred to as the "Holmberg Effect". Today with Holmberg Effect we refer to the correlation between the physical properties, (not only the colors), of the primary and secondary component of a major-merger pair.

Later studies (Demin et al., 1981, Reshetnikov, 1998, Tomov, 1978, 1979, Vardanian & Tomov, 1980) have confirmed this result, finding typical linear correlation coefficients of $R \approx 0.8$ for the $B-V$ colors of paired galaxies.

Hernández-Toledo & Puerari (2001) by studying multicolor broad band $(BVRI)$ photometry of a sample of 33 spiral-spiral (S+S) binary galaxies drawn from the Karachentsev Catalogue of Isolated Pairs of Galaxies (KPG), found that more than half of their pairs showed morphological concordance which could explain, in part, the strong correlation observed in the $(B-V)$ colour indices (Holmberg effect) between pair components (with a correlation coefficient $r \sim 0.77$ and a residual sigma $\sigma \sim 0.18$). All the above studies, however, used very small samples of paired galaxies, none of them, in fact, contained more than 100 galaxy pairs.

Allam et al. (2004) studied the Holmberg Effect for a sample of 1479 merging pairs in the Sloan Digital Sky Survey Early Data Release (SDSS EDR; Stoughton et al. (2002)) at redshift $0 \lesssim z \lesssim 0.35$ with few galaxies beyond $z = 0.25$. They computed the linear correlation coefficients for different color indices, ($u-g$,$g-r$,$r-i$ and $i-z$), and noted that the level and significance of the correlation depends on the color indices. This is the highest ($r \sim 0.38 \pm 0.03$) and has the greatest significance ($> 12\sigma$) for $g-r$ index (which is the closest SDSS analog to $B-V$), while it is the lowest and has the minimum significance ($< 2\sigma$) for $i-z$ index, which is not surprising since most galaxies have very similar $i-z$ colors. After checking, they confirmed that these measured correlations are due to a physical effect rather than systematic errors in their measurements.

Xin-Fa et al. (2006) studied the Holmberg Effect for 1158 merging pairs selected in the SDSS Data Release 4 with a median redshift of 0.1. As Allam et al. (2004), they also computed the linear correlation coefficients for the different color indices seen above obtaining the highest correlation for the $g-r$ index ($r \sim 0.571$) and the lowest one for the $i-z$. Except for the $i-z$ color, their linear correlation coefficients are apparently higher than those found by Allam et al. (2004). They explained the different results arguing that since Allam et al. (2004) identified pairs by selection criteria based on projected sky separations and galaxy diameter, their pair catalogue may include some optical pairs or non-merging associated pairs. So the lower significance of their results is probably due to contamination by paired galaxies that are either optical pairs or non-merging associated pairs.

More recently, Xu et al. (2010), (hereafter Xu10), in their analysis about the cosmic evolution of close major merger pairs selected from cross-matches between the Two Micron All Sky Survey and SDSS Data Release 3, found evidence for a correlation ($\rho \sim 0.58$) between the global star formation activities (but not the nuclear activities) of the component galaxies in massive ($M \geqslant 10^{10.7} M_{\odot}$) S+S major-merger pairs (Holmberg Effect). SFRs for galaxies both in the Pair sample and in the Control sample have been computed using Spitzer observations. Their sample includes 27 K-band selected and spectroscopically confirmed spiral-spiral (S+S) and spiral-elliptical (S+E) pairs.

The Holmberg Effect they observed on SFR/M of massive S+S pairs is in agreement with the result of Kennicutt et al. (1987) derived from the integrated H_{α} fluxes, and that of Hernández-Toledo & Puerari (2001) based on (B-V) colors. So, apparently, this effect is present in star formation indicators of very different timescales ($\sim 10^{7} yr$ for the H_{α} emission, $\sim 10^{8} yr$ for the IR emission, and $\sim 10^{9} yr$ for the (B-V) color). However it has been found only in global star formation indicators for entire galaxies, but not in those for the nuclear star formation activity (Joseph et al., 1984). The SFR dependence on interaction parameters has been invoked to explain both the presence of the correlation between the SFR of the two components (Kennicutt et al., 1987) and the absence of it (Joseph et al., 1984). Xu10, on the contrary, show that for spirals in close major merger pairs, interaction parameters such as the separation between the two components are not important factors in determining whether a galaxy has enhanced SFR/M or not (refer to fig. 17 of Xu10). It is possible that nuclear starbursts have shorter time scales, and therefore lower chance to occur simultaneously in both galaxies in a pair.

Although a physical explanation of this effect is complex and still uncertain, two possible mechanisms have been recently invoked in order to explain this correlation. The first mechanism is based on the ideas of Kennicutt et al. (1987) according to which pairs induce parallel evolution as manifested by the star formation history. The Holmberg effect in this case may be due to the dominance of interaction parameters of pair over parameters

that are specific for each component galaxy. For example, paired galaxies in close and slow passages should have more enhanced star formation than other interacting galaxies. But this is, apparently, in contrast with the results by Xu10 who found no evidence for a correlation of the Holmberg Effect on interaction parameters such as galaxy separations and local density.

The second mechanism is based on the ideas of Xu et al. (2010) according to which the concordant star formation behavior of galaxies in a close major-merger pair is due to the modulation of the sSFR by the IGM in the dark matter halo (DMH) that the two galaxies share (environment). In this case the low sSFR of spirals in quiescent S+S or S+E pairs could be explained by two different ipothesis: it is possible that the SFR is suppressed in those quiescent S+S pairs because of the presence of a diffuse hot IGM gas in the DMH (as in S+E pairs) or, in a related scenario, it might be because the DMHs of these quiescent S+S pairs have not "cold streams" of IGM gas to fuel the star formation in the companion galaxy (Kereš et al., 2009).

Xin-Fa et al. (2010), by investigating the dependence of the Holmberg effect of paired galaxies on three-dimensional separations find a weak tendency for correlation coefficients of color indices to increase with decreasing three-dimensional separations, but such a tendency does not exist for those of luminosity and size. Then they conclude that it is still very difficult to clearly affirm the dependence of the Holmberg Effect of paired galaxies on their separations.

So far the Holmberg Effect has been studied only for major merger pair samples at low redshift (none of the previous works, in fact, goes beyond $z \sim 0.2$ with a statistically significant sample). In this paper we investigate the Holmberg Effect for a sample of 444 high redshift ($0.2 \leqslant z_{phot} \leqslant 1.0$) (S+S) and (S+E) close, ($5\ h^{-1}\ kpc \leqslant s_{proj} \leqslant 20\ h^{-1}\ kpc$), major merger pairs selected in the COSMOS field from the stellar mass limited sample of Drory et al. (2009, herafter D09), and compare the results with the Holmberg Effect estimated for a sample of local SDSS galaxie pairs, selected from Domingue et al. (2009) and Xu10, and also with previous works.

The COSMOS sample has the advantage of having the best photo-z's, because of the availability of photometric data for $\sim$ 30 bands covering the entire range from UV to infrared, for more than 100,000 galaxies with nearly 100% completeness (Ilbert et al., 2009). This allows us to obtain a sample which is $\sim$ 80% complete. We confine our study to galaxy pairs of $z \leqslant 1.0$, because the photo-z's and stellar mass estimates of COSMOS galaxies of $z > 1$ are less accurate, (D09, Ilbert et al. 2010).

In order to avoid mass and redshift dependence on the estimate of the Holmberg Effect we adopt two strategies: we first subdivide the entire pair sample, covering the redshift

interval between 0.2 and 1.0, into four redshift bins (i.e. $[0.2-0.4], [0.4-0.6], [0.6-0.8]$ and $[0.8-1.0]$) and compute the Holmberg Effect in each of these bins; and secondly we also apply a mass cut-off subdividing the sample into two mass bins, $10.0 \leqslant LogM(M_{\odot}) \leqslant 10.5$ (low mass bin) and $10.5 < LogM(M_{\odot}) \leqslant 11$ (high mass bin). Then we calculate the Spearman's correlation cefficients for each subsample. This strategy makes our results and findings very robust with respect to these effects.

As only late-type galaxies contribute significantly to the total SFR, as confirmed by Xu10, our analysis is concentrated mainly on S+S and S+E pairs. On one hand S+S pairs have been largely studied by many authors and have revealed very interesting properties such as a tight correlation between their color indices, (Holmberg Effect), and an enhanced specific star formation strongly dependent on galaxy mass and probably due to tidal interactions between the two components (Wong et al., 2011, Xu et al., 2010). On the other hand S+E pairs have been less studied than S+S pairs but also revealed very interesting features. Domingue et al. (2003) analysed H_{α} and ISO mid- and far-IR observations for a sample of mixed-morphology galaxy pairs revealing both the stellar and nonstellar signatures of the interaction process. Their observations revealed that most of the early-type galaxies in their sample exhibit weak (low equivalent width) emission, as often observed in field elliptical galaxies, but some of the early-type components of their mixed-morphology pairs, especially the lenticular galaxies, show evidence for significant star formation, with H_{α} equivalent widths and $15\mu m$ luminosities comparable to or exceeding those of their often much larger spiral companions. This is not in contrast with the results of Xu10 because their early-type components were pure elliptical galaxies.

As to the Holmberg Effect, there has also been evidence for this correlation in mixed-morphology pairs, (that is S+E pairs), (Demin et al., 1984, Reduzzi & Rampazzo, 1995) and also, indirectly, in Xu10. For example, Xu10 found that massive spiral galaxies in spiral-elliptical pairs have systematically lower sSFR enhancement than those in spiral-spiral pairs.Arguably, this can also be interpreted as another Holmberg Effect, in the sense that the very low sSFR of the elliptical component is matched by the relatively low sSFR of the spiral component in the S+E pair.

All the cosmological quantities used in this work have been computed adopting the Λ-cosmology with Ω_m=0.24, Ω_{Λ}=0.76 and H_0= 73 ($Kms^{-1}Mpc^{-1}$).

A.3 Sample Selection

A.3.1 Real Pairs

The selection procedure used to define the sample of close major-merger pairs studied in this work is fully described in Xu et al. (2011), (hereafter Xu11). Anyway the main features of the sample are here below summarized.

Our stellar mass limited sample of COSMOS major-merger pair candidates, (hereafter CPAIR sample), has been constructed from the parent sample of D09 which consists of 138001 sources, with $i^+_{AB} < 25$ and $K_s < 24$, selected in a 1.7 square degrees area of the COSMOS field with photometric redshifts in the interval $0.2 \leqslant z_{phot} \leqslant 1.0$, derived from the ~ 30 broad and medium bands described in Ilbert et al. (2009) and Capak et al. (2007). This provides us with a large sample of galaxies with defined stellar masses and computed photometric redshifts which is $\sim 80\%$ complete. The accuracy of the photo-z is $\sigma_{\Delta z}/(1+z) = 0.007$ at $i^+_{AB} < 22.5$, and $\sigma_{\Delta z}/(1+z) = 0.012$ at $i^+_{AB} < 24.$, with the percentage of catastrophic failures (i.e. $\mid z_{phot} - z \mid /(1+z) > 0.15$) less than 1% (Ilbert et al., 2009). The sample is divided into 4 redshift bins of width $\delta z = 0.2$, and into "active" (star forming galaxies , SFGs) and "passive" (red quiescent galaxies, RQGs) populations according to the SED type of the best fitting template (Ilbert et al., 2009). The stellar masses, $M_\star$, are derived through a stellar population synthesis model fitting, (with Chabrier IMF), using the photo-z and photometric data in the $u^*(CFHT), B_J, V_J, g^+, r^+, i^+, z^+(Subaru), J(UKIRT)$ and $K_s(CFHT)$ bands. Uncertainties on $M_\star$ are between 0.1 dex and 0.3 dex at 68% confidence level, depending on spectral type, the S/N of photometry, and other factors (Xu et al., 2011).

In the four redshift bins the completeness limits for SFGs are $log(M_\star/M_\odot) = [8.3,8.9,9.2,9.4]$ and for the RQGs, $log(M_\star/M_\odot) = [8.9,9.2,9.8,10.1]$.In order to guarantee the completeness for all types of galaxies, the following minimum mass limits to the parent sample in the corresponding redshift bins have been introduced: $log(M_{min}/M_\odot) = [9.0,9.4,9.8,10.2]$.

Table A.1 is taken from Xu11 and lists the number of galaxies above these limits computed for each redshift bin.

Following D09, also the CPAIR sample have been subdivided into the four redshift bins listed above. Then, in order to define our sample starting from the parent sample of D09, we applied the following selection criteria:

Table A.1 Parent Sample

z_{min}	z_{max}	Volume ($10^6 Mpc^3$)	$log(M_{min})$ ($M_\odot$)	Number of Galaxies * SFGs	RQGs	Total
0.2	0.4	0.56	9.0	6787	2039	8826
0.4	0.6	1.23	9.4	6169	1526	7695
0.6	0.8	1.92	9.8	6745	1981	8726
0.8	1.0	2.53	10.2	6610	2287	8897

(*) Number of Galaxies with $log(M_\star) \geqslant log(M_{min})$

1. The primary, (defined as the brighter component of the pair), must have $log(M_\star) \geqslant log(M_{lim})$, where $log(M_{lim})/M_\odot) = 9.4$,9.8,10.2,10.6 for the four redshift bins, respectively. Note that M_{lim}'s are 0.4 dex above the M_{min}'s of the parent sample (see A.1).

2. The difference between stellar masses, $M_\star$ of primary and secondary component must be lower than 0.4 dex: $\delta log(M_\star) \leqslant 0.4$ (i.e. Stellar Mass ratio $\leqslant 2.5$).

3. The projected separation is in the range of $5\ h^{-1}\ kpc \leqslant s_{proj} \leqslant 20\ h^{-1}\ kpc$, (h=$H_0/(100\ km\ s^{-1}\ Mpc^{-1})$). Many studies have found that only major mergers with separations comparable to the size of galaxies (i.e., $\lesssim 20\ h^{-1}\ kpc$) show significant SFR enhancements (Alonso et al., 2004, Barton et al., 2007, 2000, Ellison et al., 2008, Lambas et al., 2003, Nikolic et al., 2004, Woods et al., 2006, Xu & Sulentic, 1991).

4. The photo-z difference between the two components, $\delta z_{phot} = \mid z_{phot}^{pri} - z_{phot}^{sec} \mid$, satisfies the condition of $\delta z_{phot}/(1 + z_{phot}) \leqslant 0.03$.

With respect to the selection criteria (1) and (2) defined in Xu et al. (2004) and used by Xu10 to select local SDSS pairs, here the rest-frame K-band selection is replaced by a stellar mass selection. As emphasized in Xu11, this is because data in the Spitzer-IRAC 3.6 μm and 4.5 μm bands, which encompass the rest-frame K-band emission for galaxies at $0.6 \lesssim z \leqslant 1$, have relatively lower angular resolution than the HST/ground-based optical and NIR data. Using IRAC data would result in larger confusion errors in the stellar mass for pairs with separation $\lesssim 2''$. D09 also show that for field galaxies at redshift $z \leqslant 1$ the stellar masses derived using the HST/ground-based optical and NIR data are nearly identical to those derived using data including also the IRAC fluxes (Ilbert et al., 2010). This is also the reason why our pairs have not been selected using the larger sample of Ilbert et al. (2010) whose stellar masses have been computed including the IRAC data.

Criteria (1) and (2) ensure that, by construction, our pair sample does not suffer for the so-called bias 'missing the secondary'. This is the most common bias affecting the selection of close pair galaxies (Xu et al., 2004). For flux-limited (= apparent magnitude limited)

samples or luminosity limited (= absolute magnitude limited) samples, a paired galaxy brighter than the limit can be missed if its companion is fainter than the limits. The amplitude of this incompleteness can vary with the redshift, and cause significant bias in the measurements of the evolution of the merger rate (see also Xu10).

Criterion (3) makes the comparison between local pairs (e.g. Xu10; see also A.7), and the high redshift pairs in this sample robust. As emphasized in Xu10, for high-z galaxies it is difficult to distinguish a galaxy pair from a single galaxy if the separation is lower than 5 h^{-1} *kpc*, and the probability for chance pairs is significantly higher if the projected separation is much larger than 20 h^{-1} *kpc* (Kartaltepe et al., 2007).

Criterion (4) is set to minimize the incompleteness due to the photo-z error while ensuring that the reliability of the sample is not significantly compromised. This issue is fully addressed in Section 3 of Xu11, where they discuss the reliability and completeness of the pair sample both in terms of incompleteness due to missing very close pairs and of incompleteness and spurious pairs due to photo-z errors. Our CPAIR sample results to be highly reliable (reliability=0.93) and complete (completeness = [0.86,0.82,0.80,0.70]) for the four subsamples in the four redshift bins [0.2-0.4],[0.4-0.6],[0.6-0.8] and [0.8-1.0]. The slightly higher incompleteness in high-z bins is mostly due to the missing of very close pairs of angular separation $\lesssim 2''$ (Xu et al., 2011).

Using the selection criteria specified above, 417 pair candidates have been selected. In order to exclude spurious pairs due to artifacts in the parent sample, visual inspections on the HST-ACS images (in the F814 band, Koekemoer et al. (2007)) have been carried out by Xu11. Among the 417 pair candidates, 335 were covered by the HST survey. Pair candidates without ACS images (82/417 = 19.7%) have been omitted from the final pair sample. In addition further fourteen spurious pairs have been identified using ACS images and then removed from the final sample. Also galaxies belonging to multiple systems, (55 galaxies), have been identified and isolated from the final sample of simple major-merger pairs used here to study the Holmberg Effect at high redshift.

The final CPAIR sample includes 280 isolated pairs, (i.e. a total of 560 objects). Among these 139 are S+S pairs, 83 S+E pairs and 58 E+E pairs.

Component galaxies have been classified as either 'S' or 'E' according to the SED type of the best fitting template (Ilbert et al., 2009), as reported in D09. Among the 560 component galaxies, 362 are classified as Spirals (SFGs) and 198 as Ellipticals (RQGs).

A.3.2 Control sample of (S+S) and (S+E) pairs

In order to understand how interactions and mergers between galaxies affect galaxy properties, we compare our sample of paired galaxies with a sample of control pairs made up of isolated, (i.e. non-interacting), Spiral and Elliptical galaxies. Given that many observed properties of galaxies are redshift dependent, and that the intrinsic galaxy properties are known to correlate with stellar mass (e.g., Abbas & Sheth (2006)), the control sample is defined by matching in terms of mass and redshift the real one (see below).

As the CPAIR sample, also the sample of control pairs has been selected from the stellar mass limited parent sample of D09, by requiring the following criteria to be satisfied:

1. The M_{star} difference between the pseudo and the real pair component must be within 0.1 dex: $\delta log(M_\star) \leqslant 0.1$.
2. The photo-z difference between the pseudo and the real pair component, $\Delta z_{phot} \leqslant 0.03$.
3. The pseudo pair components must be of the same type, 'S' (SFGs) or 'E' (RQGs), as those in the CPAIR sample.
4. Among all the single spiral or elliptical galaxies fulfilling requirements (1) and (2), the chosen one has the minimum redshift difference from that of the paired galaxy.
5. Each single galaxy belonging to the control sample can be used once, namely if it is matched to a paired galaxy, then it cannot be matched to another one.

The control pair candidates selected according to these criteria are then visually inspected, by looking at their HST-ACS images, in order to see whether they are (a) artifacts, (b) galaxies belonging to interacting systems or (c) peculiar galaxies. If they are, then we exclude them from the sample and perform a new match.

The final sample of control pairs consists of 139 S+S and 83 S+E pseudo-pairs. As the control pairs have been selected in terms of the matches of their masses and photo-z's to those of the CPAIR sample, the same limits and constraints we defined for the CPAIRs holds here.

A.4 Statistical Properties of (S+S) and (S+E) pairs

The isolated (S+S) and (S+E) pairs have been selected from a 1.7 square degrees area of the COSMOS field with photometric redshifts in the interval $0.2 \leqslant z_{phot} \leqslant 1.0$ and stellar masses $M_\star$ in the range $9.0 < log(M_\star)[M_\odot] < 11.5$.

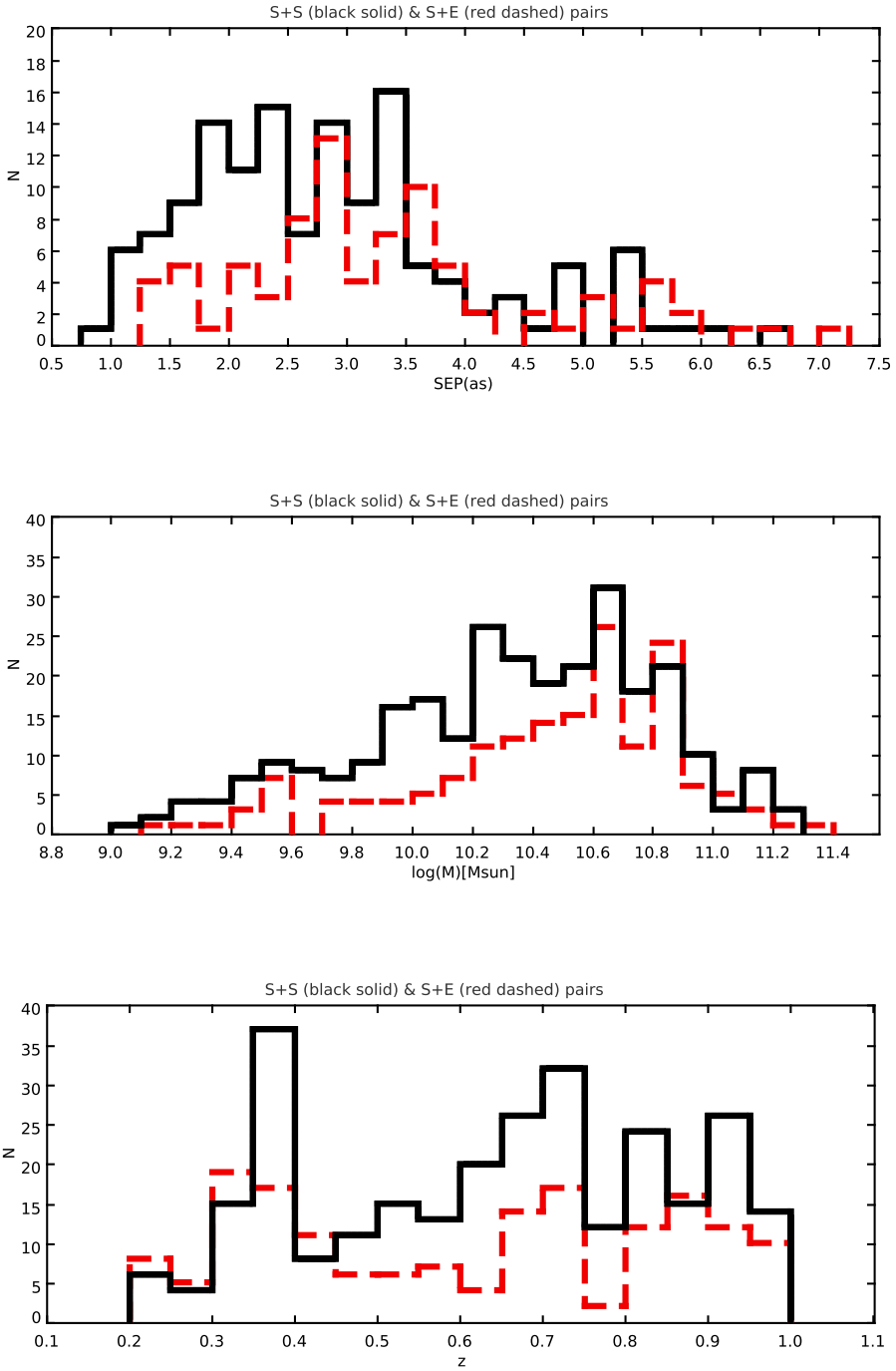

Figure A.1 Histograms of the angular SEP distribution (TOP), stellar mass distribution, ($log(M_\star)[M_\odot]$), (CENTER) and redshift distribution (BOTTOM) of close (S+S) (black solid line) and (S+E) (red dashed line) pairs.

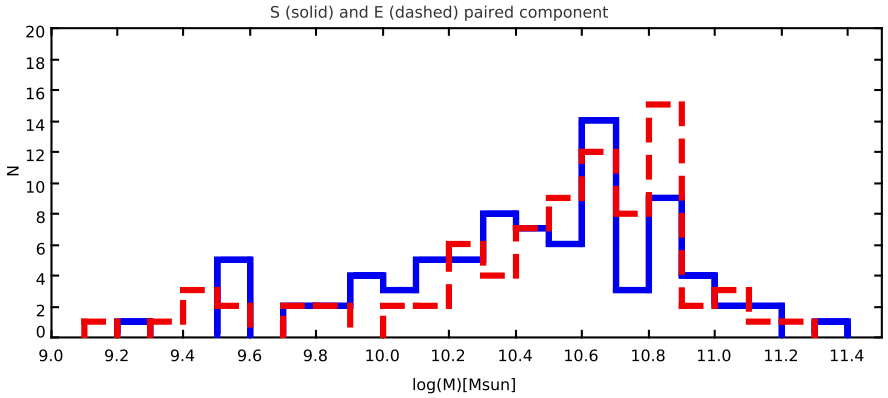

Figure A.2 Histogram of the stellar mass distribution, $(log(M_{\star})[M_{\odot}])$, of Spiral (blue solid line) and Elliptical (red dashed line) component of (S+E) pairs.

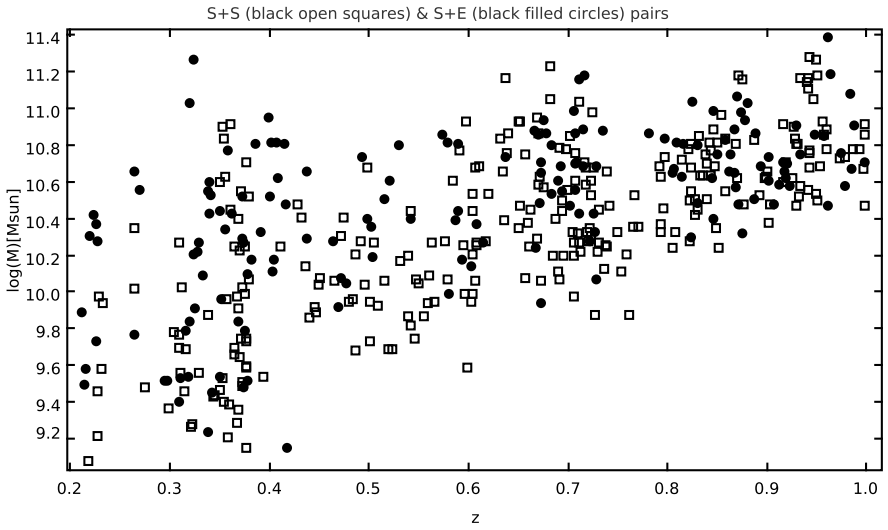

Figure A.3 The figure shows the $logM_{\star}(M_{\odot})$ versus redshift z of both (S+S) (black open squares) and (S+E) (black filled circles) COSMOS pairs.

Figure A.1 shows the histograms of the angular SEP (top), stellar mass (center) and redshift (bottom) distribution of both the (S+S) (black solid line) and (S+E) (red dashed line) CPAIRs.

The typical median and mean values for the three distributions are here below itemized:

SEP: CPAIR angular SEP are in the range $0.95 \lesssim \epsilon \lesssim 6.5$, $(5h^{-1}Kpc \leqslant s_{proj} \leqslant 20h^{-1}Kpc)$. The *median* values for (S+S) and (S+E) pairs are, respectively, at $SEP_{S+S} \sim 2.72$, (with mean $SEP_{S+S} = 2.85 \pm 1.19$), and at $SEP_{S+E} \sim 3.18$, (with mean $SEP_{S+E} = 3.37 \pm 1.31$).

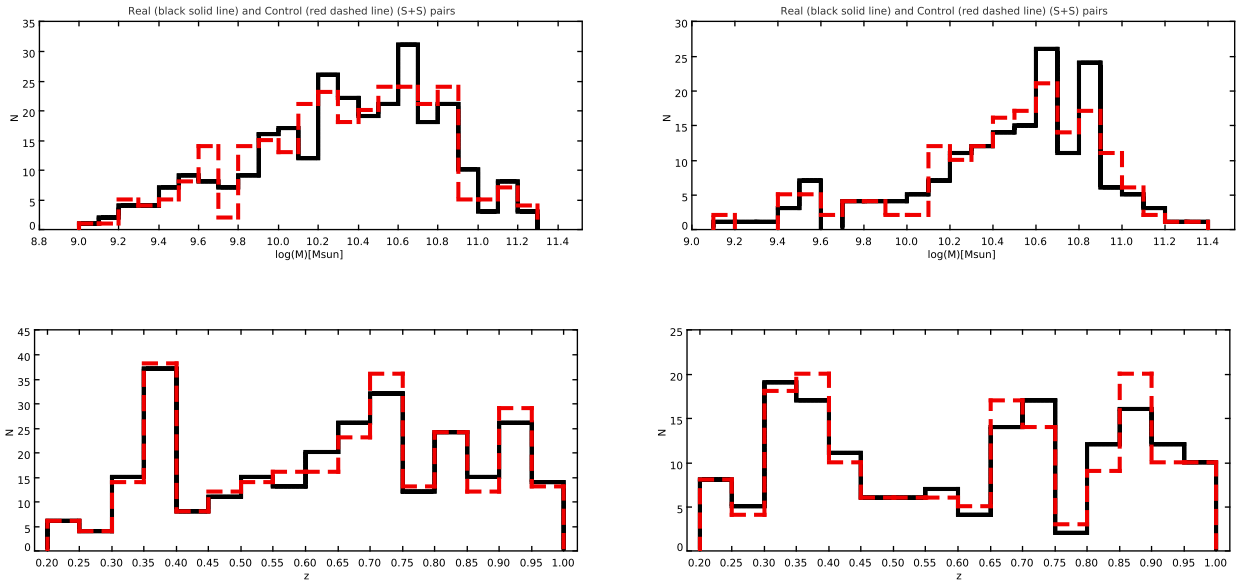

Figure A.4 Histograms of the stellar mass distribution, ($log(M_\star)[M_\odot]$), (TOP) and redshift distribution (BOTTOM) of both Real (black solid line) and Control (red dashed line) (S+S) (left) and (S+E) (right) pairs.

$M_\star$: The *median* values for the stellar masses of (S+S) and (S+E) pairs are, respectively, at $log(M_\star)[M_\odot] \sim 10.38$, (with mean $log(M_\star)_{S+S} = 10.33 \pm 0.47$) and at $log(M_\star)[M_\odot] \sim 10.55$, (with mean $log(M_\star)_{S+E} = 10.46 \pm 0.44$). With the Spiral component of the (S+E) pairs having the median at $log(M_\star)_S[M_\odot] \sim 10.48$ and the Elliptical component having the median value at $log(M_\star)_E[M_\odot] \sim 10.60$ (see fig. A.2).

z: The median values for the redshift distributions of (S+S) and (S+E) pairs are, respectively, $z \sim 0.670$, (with mean $z = 0.64 \pm 0.21$) and $z \sim 0.667$, (with mean $z = 0.61 \pm 0.24$).

Figure A.3 shows the distribution of $logM_\star(M_\odot)$ versus redshift z of both (S+S), (black open squares) and (S+E), (black filled circles) COSMOS pairs. The distribution increases at higher redshifts due to the well-known "Malmquist Bias". This is an observational selection effect in which for flux-limited samples an increase in average luminosity with distance is seen. This is, of course, due to the fact that less luminous sources at large distances are not detected.

All these properties are then compared with those of control (S+S) and (S+E) pairs. Figure A.4 shows the histograms of the stellar mass (top) and redshift (bottom) distribution of both (S+S) (left) and (S+E) (right) (black solid line) CPAIRs, compared to the same distributions of (S+S) and (S+E) control pairs (red dashed line).

The typical *median* and mean values for the $logM_\star$ and z distributions of control (S+S) and (S+E) pairs are, respectively, at $log(M_\star)[M_\odot] \sim 10.4$, (with mean $log(M_\star)_{S+S} = 10.32 \pm 0.47$) and at $z \sim 0.67$ (with mean $z = 0.64 \pm 0.21$) for the (S+S) control pairs and at $log(M_\star)[M_\odot] \sim 10.54$, (with mean $log(M_\star)_{S+E} = 10.46 \pm 0.44$) and $z \sim 0.65$ (with mean $z = 0.61 \pm 0.24$) for the (S+E) pairs.

Table A.2 summarizes the median and mean values of the different distributions seen above for both the populations of real and control (S+S) and (S+E) pairs.

	Median			*mean & sigma*		
	$SEP[as]$	$log(M_\star)[M_\odot]$	z	$SEP[as]$	$log(M_\star)[M_\odot]$	z
$(S+S)_{real}$	2.72	10.38	0.67	2.85 ± 1.19	10.33 ± 0.47	0.64 ± 0.21
$(S+S)_{control}$		10.40	0.67		10.32 ± 0.47	0.64 ± 0.21
$(S+E)_{real}$	3.18	10.55	0.667	3.37 ± 1.31	10.46 ± 0.44	0.61 ± 0.24
$(S+E)_{control}$		10.54	0.65		10.46 ± 0.44	0.61 ± 0.24

Table A.2 Typical *median* and *mean* values of angular SEP, $log(M_\star)$ and z distributions of both (S+S) and (S+E) real and control pairs.

A.5 Photometry and color estimates

In order to get the multiband data relative to our major merger pairs we cross-correlated our sample taken from D09 with the COSMOS intermediate and broad band photometry catalogue (DR2008) by matching the photoz-IDs of each galaxy component. COSMOS multiband photometry includes the following 33 bands (Ilbert et al., 2009): ***Subaru*** (B_j, V_j, $g+$, $r+$, $i+$, $z+$, $NB816$, $NB711$ + 12 IA bands), ***CFHTLS*** (u^*, i^*, Ks^*), ***KPNO/CTIO*** (Ks), ***SDSS*** (u, g, r, i, z), ***HST*** ($F814W$), ***UKIRT*** (J) and ***GALEX*** ($FUV + NUV$). The wealth of photometric data points in the spectral range between UV and NIR allows us to get robust estimates of galaxy rest-frame $(B-V)_J$ colors over the entire redshift range of our pairs, $0.2 \leqslant z \leqslant 1.0$, by using simple interpolation methods (see A.5.1). This catalog is an I band selected multi-color catalog for 2 square degrees centered on the COSMOS field at 10:00:28.6, +02:12:21.

Photometry has been done using SExtractor in dual mode (Bertin & Arnouts, 1996). The source detection has been run on the deepest image ($i^+ \sim 26.2$ for a point source detected at 5σ). All the total magnitudes (SExtractor mag_auto) listed in the catalogue, for a source must have an AB magnitude of less than $i^+ < 25$. All photometry is in the AB magnitude system and measured in a 3" aperture on PSF-matched images. A magnitude of -99 indicates a photometric measurement was not possible due to lack of data, a large number of bad pixels, or saturation. A magnitude of 99.0 indicates no detection. In the case of no detection the error given for the object is the 1 sigma limiting magnitude at the position of the source.

The Photometric Redshifts included in this catalog are described in Mobasher et al. (2007) and have an accuracy of $dz/(1+z) < 0.031$ at $z < 1.2$ and $I < 24$.

For most of COSMOS sources ($z > 0.4$), 3" corresponds to $\sim 20kpc$, while for the nearest source of $z = 0.2$, it is $\sim 10kpc$. This means that our colors estimated from 3" apertures are well representative of galaxy colors because they reflect the major stellar population in the source.

Finally, in order to get a measurement of the rest-frame intrinsic $(B-V)$ colors of galaxies, all magnitudes have been corrected for galactic extinction, estimated for each object individually using dust map images from Schlegel et al. (1998).

For a complete description of the observations, data reduction and the photometry catalogue please refer to (Capak et al., 2007, Ilbert et al., 2009).

A.5.1 $(B-V)$-color computation

To compare our results for the Holmberg Effect with previous works (see A.2) rest-frame intrinsic $(B-V)^J_{RF,0}$ colors have been computed by using the following procedure:

1. Given the wealth of photometric data points available in the range between UV and NIR wavelengths, we assumed the photometric points to be sufficient to sample the "real" SED of the galaxy. We also tested this hypothesis by modeling some paired galaxy SED by using the spectro-photometric code GRASIL (Silva et al., 1998), and the resulting rest-frame B_J and V_J luminosities are concordant with those estimated directly from the observed photometric data points.

2. As the COSMOS photometric catalogue doesn't include the Jhonson B and V bands, we considered their filter transmission curves, whose effective wavelengths and zero-points are, respectively, 450 nm and $F_{0,B} = -11.18$ for the B_J band and 550 nm and $F_{0,V} = -11.42$ for the V_J band. Here the zero-point fluxes are given in unit of $log(F_\lambda)$ in $W/cm^2/\mu m$. The filter response curve are then convolved with the rest-frame Luminosities $L_{\nu,RF}$.

3. Starting from the observed fluxes $f_\nu(\nu_o)$ in $erg/cm^2/s/Hz$, for each source in our catalogue we calculated the rest-frame luminosities as $L_\nu(\nu_e) = \frac{4\pi d_L^2}{(1+z)} f_\nu(\nu_o)$, with ν_o and $\nu_e = (1+z)\nu_o$ representing the observed and the rest-frame frequencies, respectively, and d_L being the luminosity distance of the source. The rest-frame luminosities so computed are then convolved with the B_J and V_J filter response curves in order to get the rest-frame L_{RF,B_J} and L_{RF,V_J} luminosities. The luminosities are given in units of the bolometric luminosity of the Sun, $L_\odot = 3.83 \times 10^{33} ergs^{-1}$.

4. The rest-frame $(B-V)^J_{RF}$ colors are then computed as $(B-V)^J_{RF} = -2.5 \times log_{10}(L^B_{\nu_e}/L^V_{\nu_e}) + 2.5 \times log_{10}(F_{0,B}/F_{0,V})$.

5. The Galactic extinction corrections, $E(B-V)$, in magnitudes at the position of each object are computed following Schlegel et al. (1998). The intrinsic colors are then defined as $(B-V)^J_0 = (B-V)^J_{obs} - E(B-V)$. For the extinction corrected observed fluxes we used the following relation: $F(\lambda, obs) = F(\lambda, intrinsic) \times 10^{-0.4E(B-V)k(\lambda)}$ with F equal to flux or luminosity, $E(B-V) = A(B) - A(V)$ being the galactic extinction, and $k(\lambda) = A(\lambda)/E(B-V)$ being the extinction curve. We also took into account the conversion relations: $A(V) = 3.1 \times E(B-V)$, $B_J = B_{AB} + 0.163$ and $V_J = V_{AB} + 0.044$.

The above procedure to compute galaxy colors has been applied to both the CPAIR and Control Pair sample.

A.6 Results: The Evolution of the Holmberg Effect up to $z \leqslant 1.0$ in COSMOS

Figure A.5 shows the "global" Holmberg effect, obtained by correlating the rest-frame and dust-extinction corrected (B-V) colors of primary e secondary component of all the S+S (left) and S+E (right) real (black filled circles) and control (black open squares) pairs without applying any mass cut-off or redshift binning. The black solid and dashed lines represent the linear correlation to the observed data of, respectively, real and control pairs. These plots emphasize that when appropriate cut-offs on both mass and redshift are not taken into account, unreliable correlations between galaxy colors can be obtained. If, in fact, we look at the control pairs, represented in the figure as black open squares, we can see a tight correlation among their colors, which is unreal because, as specified in section A.3.2, control pairs are isolated and therefore non-interacting galaxies which should not present any interaction-driven correlation among their colors. This correlation is due to redshift and mass dependence ("richness effect"), the latter being also dominated by the well-known Malmquist bias effect and it is not real. This strong mass and redshift dependence is clearly visible in figure A.6, which shows the rest-frame and dust extinction corrected (B-V) colors of both real (top) and control (bottom) S+S (left) and S+E (right) pairs as a function of the stellar mass, with the different redshift bins highlighted with different symbols and colors.

In order to avoid this mass and redshift dependence the Holmberg Effect has been re-computed separately for the four redshift bins, $[0.2-0.4]$,$[0.4-0.6]$,$[0.8-1.0]$ and $[0.8-1.0]$ and into the two narrow mass bins, $10.0 \leqslant logM_\star[M_\odot] < 10.5$ and $10.5 < logM_\star[M_\odot] \leqslant 11$.

Figure A.7, shows the Holmberg Effect for real (black filled circles) and control (black open squares) S+S pairs computed for the high mass-bin and into the last two redshift bins. The first two redshift bins, $[0.2-0.4]$ and $[0.4-0.6]$ have not been considered here because of the very low statistics. The black solid and dashed lines are the linear correlation to the observed data for, respectively, real and control S+S pairs.

The ρ and σ values highlighted in the plots, define the Spearman's rank correlation coefficient and significance of the correlation. These values are also tabulated in Tab. A.3. In each plot is also specified the statistics, that is the number of pairs, relative to each redshift bin. For the statistically significant redshift bin, ($[0.8-1.0]$) (Fig. A.7b), we get a ρ-value for the real pairs of 0.51 with a probability for the null hypothesis of only 0.02 while no correlation is found between the $(B-V)$ colors of their matches in the control sample, as it is expected. In particular for the control pairs we get a ρ-value of -0.07 and a probability for the null hypotesis of 0.74 which means no-correlation. The Holmberg Effect we find is in agreement with the results of Xu10 derived from the IR emission, those of Kennicutt et al. (1987) derived from H_α fluxes and those one of Hernández-Toledo & Puerari (2001) derived from $(B-V)$ colors.

For the Holmberg Effect shown in Fig. A.7a and relative to the redshift bin $[0.6-0.8]$ we cannot draw strong conclusions given the low statistics but also the low significance which is of about 0.12 for the real pairs and 0.18 for the control pairs. The values of the Spearman's rank correlation coefficient and significance for the redshift bin, $[0.6-0.8]$ are, anyway, reported in Tab.A.3 for completeness.

Figure A.8 shows the Holmberg Effect for the low mass, $(10.0 \leqslant logM_\star[M_\odot] \leqslant 10.5)$, real (black filled circles) and control (black open squares) S+S pairs and for the four redshift bins. The black solid and dashed lines represent the linear correlation to the data for, respectively, real and control pairs. In this case too, due to the very low statistics, (with a total number of pairs per redshift bin lower than 10 objects), we cannot draw strong conclusions for the two low-z redshift bins even if the values of the significance (intended as probability for the null hypothesis), are good. The Spearman's rank correlation coefficients and significance for the two statistically significant samples, that is $[0.6-0.8]$ and $[0.8-1.0]$, are: $\rho_{[0.6-0.8]} \sim 0.04$ with $\sigma_{[0.6-0.8]} \sim 0.86$ and $\rho_{[0.8-1.0]} \sim 0.10$ with $\sigma_{[0.8-1.0]} \sim 0.71$ for the real pairs and $\rho_{[0.6-0.8]} \sim 0.09$ with $\sigma_{[0.6-0.8]} \sim 0.66$ and $\rho_{[0.8-1.0]} \sim -0.02$ with $\sigma_{[0.8-1.0]} \sim 0.76$ for the control pairs. These values are also tabulated in tab. A.4.

While for the control pairs these results are not surprising because, as expected, there is no correlation among their colors, for the real pairs we get very interesting results. What we have found here is that there is a clear difference between high-mass and low-mass close pairs, with low mass pairs being less or not correlated with respect to the high-mass pairs. In this case the high correlation among the colors of massive spirals could be connected to

the local environment within and around the DMH surrounding the pairs as mentioned in the Introduction.

In order to check whether this difference is real and also present in local major-merger pairs, and not due to some systematics or selection effects, we compare our results obtained for the COSMOS pairs with the Holmberg Effect estimated for a local sample of SDSS close pairs (see section A.7). To make the local SDSS sample consistent in terms of pair selection and photometry, (color estimates), we have decided to make our own computation of the correlation starting from the small sample of S+S and S+E pairs presented in Xu10 and then including all the S+S and S+E pairs from the parent catalogue of D09 satisfying the pair selection criteria specified in section A.7.

Spearman's rank correlation coefficient ρ and significance σ for S+S pairs

Redshift bin	$[0.2-0.4]$	$[0.4-0.6]$	$[0.6-0.8]$	$[0.8-1.0]$
N.pairs	low stat.	low stat.	12(24 objs)	22(44 objs)
real	"	"	$\rho = 0.46$ & $\sigma \sim 0.12$	$\rho = 0.51$ & $\sigma \sim 0.02$
control	"	"	$\rho = 0.44$ & $\sigma \sim 0.18$	$\rho = -0.07$ & $\sigma \sim 0.74$

Table A.3 For each bin of redshift and for the high-mass cut-off, ($10.5 < logM_{\star}[M_{\odot}] \leqslant 11.$), the Spearman's rank correlation coefficient and relative significance are here tabulated. In the second row the statistics relative to each redshift bin is shown, with the total number of objects given in parenthesys.

Redshift bin	$[0.2-0.4]$	$[0.4-0.6]$	$[0.6-0.8]$	$[0.8-1.0]$
N.pairs	7(14 objs)	8(16 objs)	27(54 objs)	16(32 objs)
real	$\rho = 0.61$ & $\sigma \sim 0.15$	$\rho = -0.05$ & $\sigma \sim 0.91$	$\rho = 0.04$ & $\sigma \sim 0.86$	$\rho = 0.10$ & $\sigma \sim 0.71$
control	$\rho = -0.03$ & $\sigma \sim 0.96$	$\rho = -0.24$ & $\sigma \sim 0.51$	$\rho = 0.09$ & $\sigma \sim 0.66$	$\rho = 0.09$ & $\sigma \sim 0.76$

Table A.4 As in Tab. A.3 but for $10 \leqslant logM_{\star}[M_{\odot}] \leqslant 10.5$ (low mass cut-off).

A.7 SDSS pairs

A.7.1 Sample Selection

For a more detailed description of local SDSS pair selection refer to Xu10. Here we only provide a brief description of the sample with particular emphasys on the criteria used to select the local close major-merger pairs. We have started considering the small sample of 27 S+S and S+E pairs presented in Xu10 which has been selected from cross-matches between the 2MASS Extended Source Catalogue (XSC; Jarrett et al. (2000)) and the galaxy catalogue of SDSS-DR5 (put reference), following the selection procedure described in Xu et al. (2004) and D09. We then enlarged that sample to cover the whole sample of D09-DR5 by including all the remaining pairs fulfilling the requirements specified below.

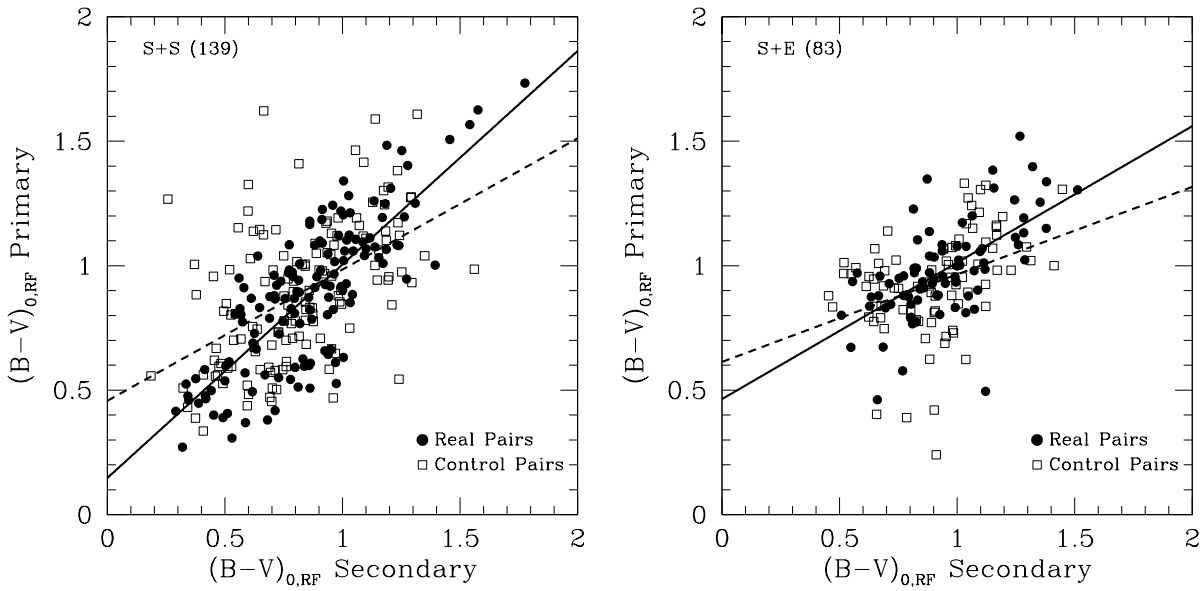

Figure A.5 These figures show the "global" Holmberg Effect computed for both real (black filled circles) and control (black open squares) S+S (left) and S+E (right) pairs. This is given by the correlation between the rest-frame and dust extinction corrected (B-V) colors of secondary and primary component of the pair, computed following the procedure specified in section A.5.1. With "global" we mean without applying any mass cut-off or redshift binning. The black solid and dashed lines represent the linear correlation to the data-points relative, respectively, to the real (solid line) and control (dashed line) S+S and S+E pairs.

To be considered in the pair selection all galaxies have to satisfy the following two criteria:

1. Galaxies must be brighter than $K_s = 13.5$ mag, which is the completeness limit of the XSC (Jarrett et al., 2000). The default K_{20} magnitude is used for the K_s-band (2.16 μm) fluxes, where the K_{20} magnitude is taken from D09 for which the photometric error due to the blending of close neighbors has been corrected. As in Xu et al. (2004), a uniform -0.2 mag correction is applied to the K_{20} when extrapolation to total K-band magnitude is necessary (Xu et al., 2010).

2. Galaxies must have a redshift completeness index $c_z > 0.5$, where c_z is the ratio between the number of galaxies with measured redshifts within $1^{\rm deg}$ radius from the center of the galaxy in question and the number of all the galaxies within the same radius (Xu et al., 2004). This confines the pair selection to region where the SDSS-DR5 has a good spectroscopic coverage.

At this point, close pair galaxies are selected by using the selection criteria described in detail in Xu et al. (2004):

1. The K_s magnitude of the primary must be brighter than 12.5 mag.

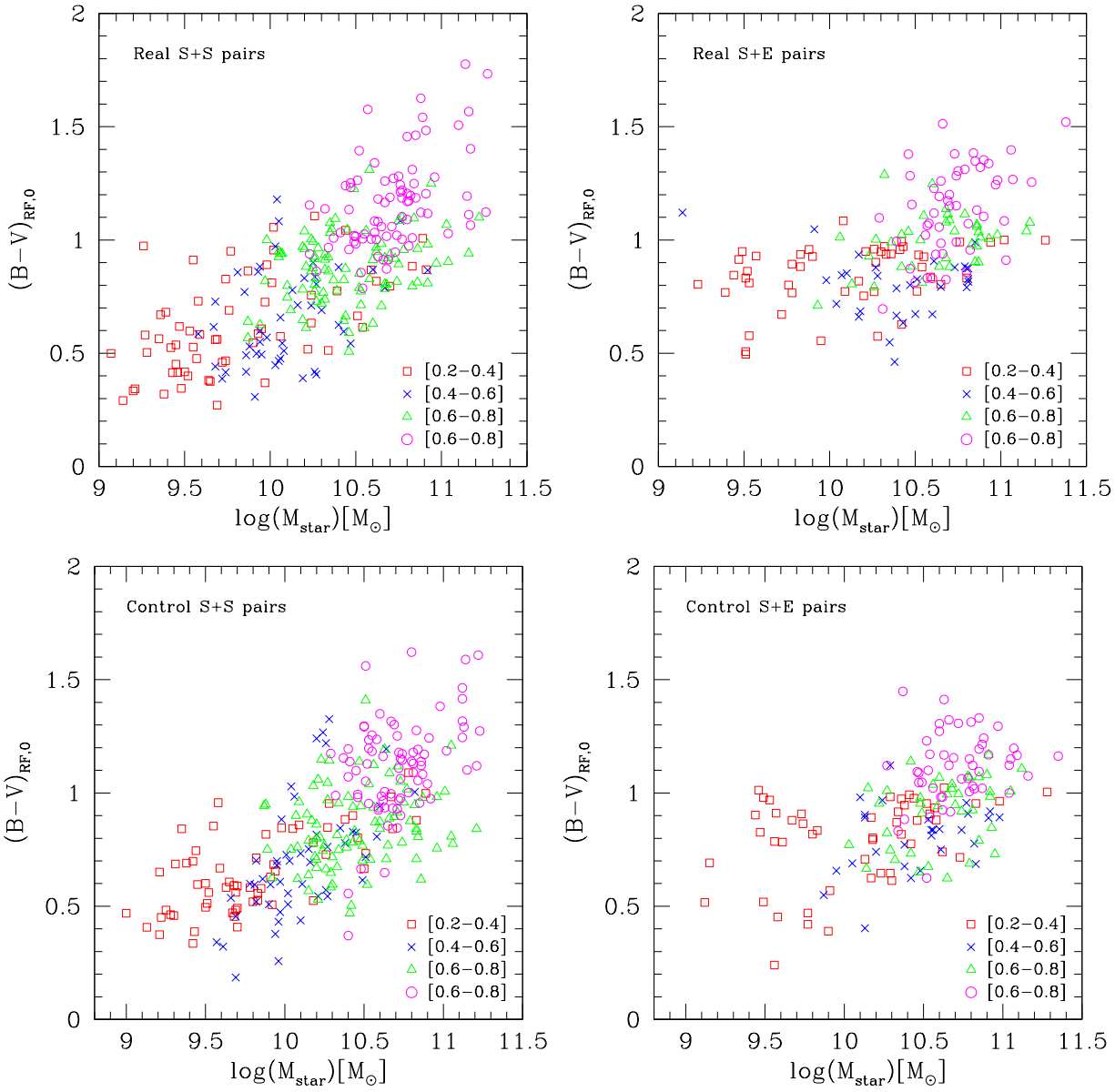

Figure A.6 Plot of the rest-frame and dust extinction corrected (B-V)-colors as a function of stellar mass in logarithmic scale and solar units for both real (top) and control (bottom) S+S (left) and S+E (right) pairs. The different symbols in different colors represent the four redshift bins in which the entire sample has been subdivided: $[0.2-0.4]$ (open red squares), $[0.4-0.6]$ blue crosses, $[0.6-0.8]$ open green triangles and $[0.8-1.0]$ open magenta circles. This figure emphasizes the strong dependence on both mass and redshift and therefore the importance, in order to avoid such dependences, of applying a mass cut-off and redshift binning.

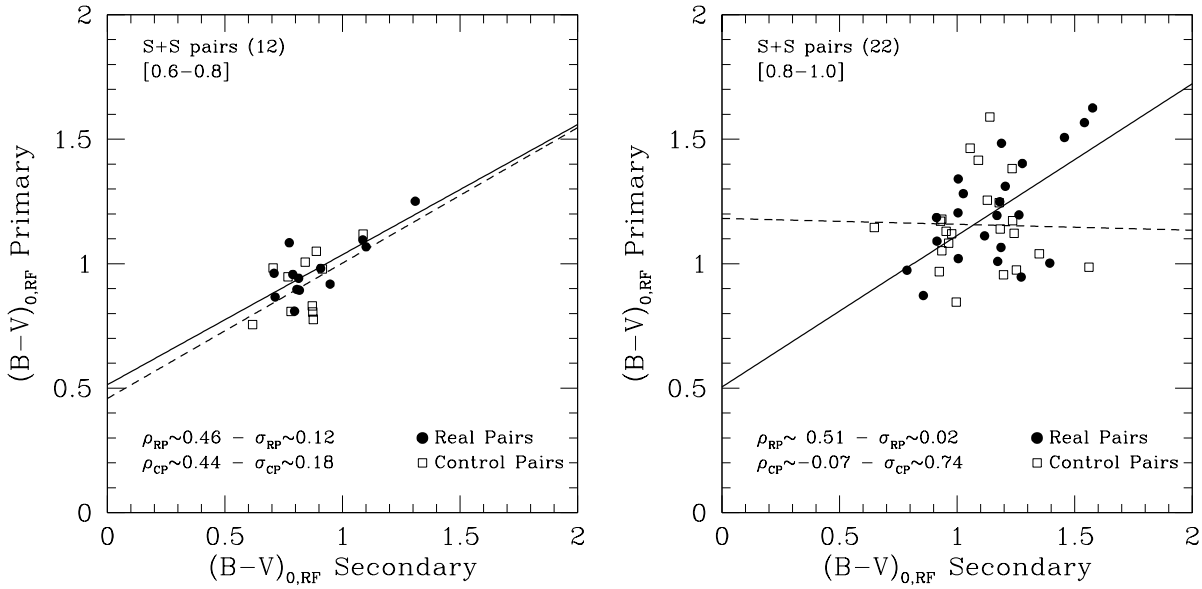

Figure A.7 This figure shows the Holmberg Effect on real (filled black circles) and control (open black squares) S+S pairs, computed for the high mass bin ($10.5 < logM_{\star} \leqslant 11.$) and, into the two higher redshift bins: $[0.6-0.8]$ (left) and $[0.8-1.0]$ (right). The two low redshift bins, ($[0.2-0.4]$ and $[0.4-0.6]$), have not been considered here because of the very low statistics due to the well-known "Malmquist Bias" effect. The black solid and dashed lines represent the linear correlation to the data for, respectively, the real (solid) and control (dashed) pairs. The Spearman's rank correlation coefficient and relative significance, (which gives the probability for the null hypothesis), are are shown in the bottom left of each figure and are also tabulated in tab. A.3.

2. The K_s difference between the two components must be lower than 1 mag: $\delta K_s \leqslant 1mag$.

3. At least one component must have spectroscopic redshift

4. The projected separation s is in the range $5h^{-1}kpc \leqslant s \leqslant 20h^{-1}kpc$ (i.e. close pairs).

5. The velocity difference between primary and secondary $\delta v \leqslant 500kms^{-1}$.

These criteria are very similar to those used to select our COSMOS pairs, (see section A.3.1), with the stellar mass selection replaced by the rest-frame K-band selection in criteria (1) and (2). Stellar masses of the primary and secondary component of the pair are derived from the K_{20} magnitude. Component galaxies are classified as either "S" or "E" by combining to different methods: the classical "eyeball" classification carried out independently by two members of the group by inspecting the SDSS optical image of every galaxy in the sample and by assigning a type to it according to its morphology and an automatic classification based on galaxy colors and Petrosian fluxes. The final sample, after applying the criteria specified above, consists of 246 objects: 98 S+S, 100 S+E and 48 E+E pairs including also

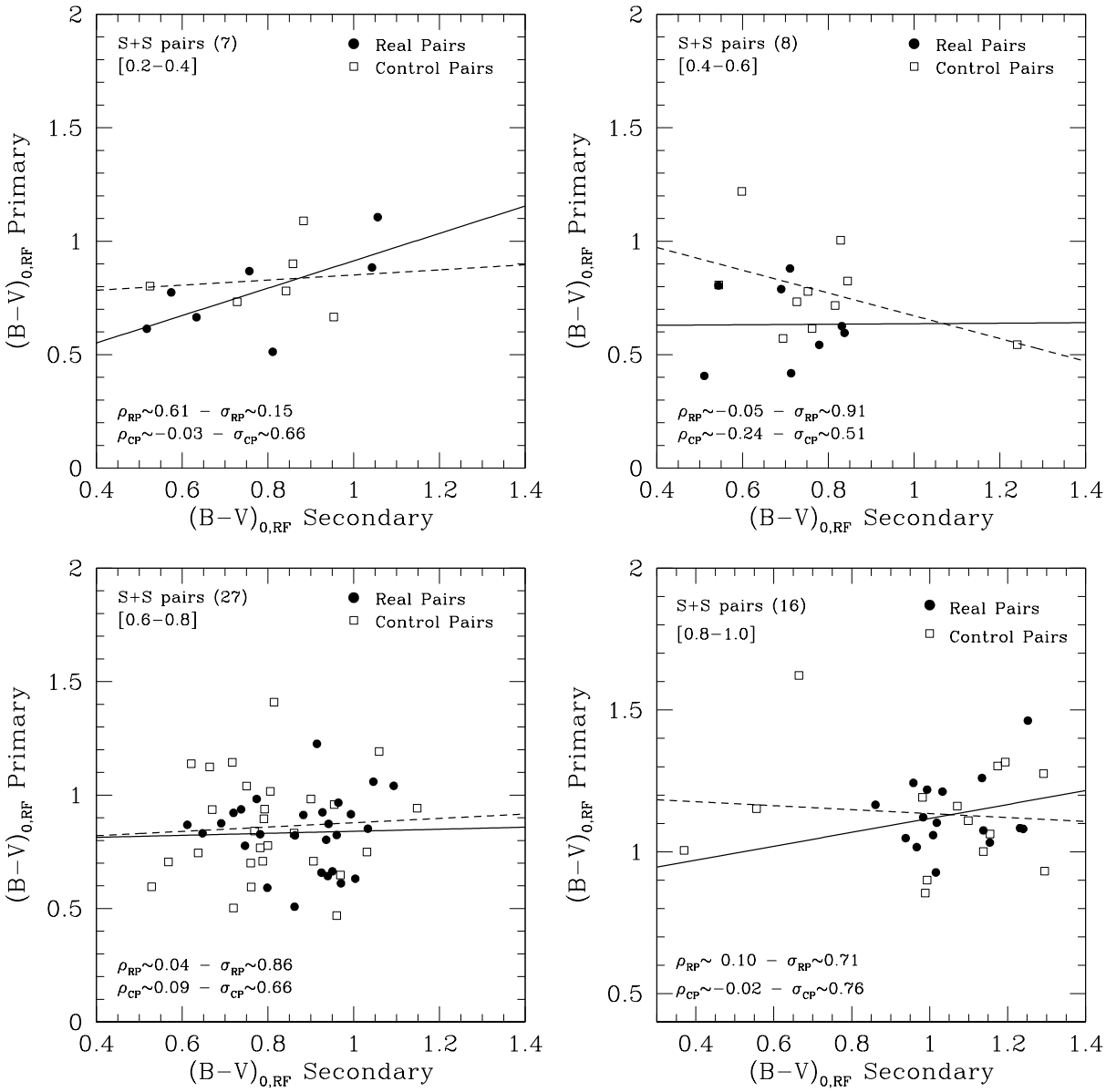

Figure A.8 These plots show the Holmberg Effect on real (filled black circles) and control (open black squares) S+S pairs, for the low mass bin ($10 \leqslant logM_{\star} \leqslant 10.5$) and, for the four redshift bins: $[0.2-0.4]$ (top left), $[0.4-0.6]$(top right), $[0.6-0.8]$ (bottom left) and $[0.8-1.0]$ (bottom right). The black solid and dashed lines represent the linear correlation to the data for, respectively, the real (solid) and control (dashed) pairs. The Spearman's rank correlation coefficient and relative significance are shown in each figure and tabulated in tab. A.4.

the 27 S+S and S+E pairs analyzed by Xu10. For the computation of the local Holmberg Effect we will consider only the S+S pairs.

As for the control sample, the selection has been confined to two Spitzer data archives. (1) The SWIRE survey of Lockman field, ELAIS-N1 field and ELAIS-N2 field (Lonsdale et al., 2003), which provides an IRAC 3.6 μm band selected sample of field galaxies (Surace et al., 2005). (2) The SINGS survey of nearby galaxies, (Kennicutt et al., 2003), which observed a heterogeneously selected sample of 75 well-known galaxies, including normal late and early types, AGNs and starbursts.

The control sample, made up of isolated Spirals and Ellipticals, is then defined by matching each pair galaxy with a galaxy in the SWIRE samples using the following criteria:

1. The $M_\star$ difference between control and real pair components must be within 0.1 dex: $\delta log(M_\star) \leqslant 0.1$.
2. When there are multiple matches, the chosen one is the one having the minimum δz.
3. Control galaxies are 1-to-1 mass matched to paired galaxies, namely if a galaxy is matched to a paired galaxy then it cannot be matched to another one.
4. Control galaxies must be of the same morphologycal type as the paired galaxies.

The control pair candidates selected according to these criteria are then visually inspected, by looking at their SDSS images, in order to check whether they are (a) artifacts, (b) galaxies belonging to interacting systems or (c) peculiar galaxies as done for the COSMOS pairs.

A.7.2 SDSS Photometry

The photometric analysis of local SDSS galaxy pairs is still ongoing due to significant blending which causes low or absent correlation among their colors. Here below I give just a schematic overview on what we have in plan for these objects.

After a brief description of DR7 photometric catalogue and model magnitudes we will discuss in detail the blending problem affecting the colors of local SDSS pair galaxies, referring to the works by Patton et al. (2011) and Simard et al. (2011), with particular emphasis on the fact that this doesn't seem to depend on the particular magnitude system considered. To better visualise the problem it could be interesting to consider the Holmberg effect computed for these galaxies with and without the mass cut-off. Our strategy to solve the problem, is to compute isophotal magnitudes by using the *ellipse* task of IRAF masking the blended pixels of the image.

A.8 Summary

Here below we give a very schematic view on the main results and conclusions obtained, with the present study, up to now.

- High-z COSMOS pairs ($z_{phot} \lesssim 1.0$):
  - Evidence for the Holmberg Effect at high redshift ($0.2 \lesssim z_{phot} \lesssim 1.0$) for both S+S and S+E COSMOS-PAIRs
  - To avoid mass and redshift dependence on the estimate of the Holmberg Effect we subdivided the sample into 4 redshift bins and considered two mass cut-off (low and high-mass cut)
  - **High-mass pairs**: show strong correlation among their (B-V) rest-frame and dust extinction corrected colors with higher significance (~ 0.02) for the last redshift bin [0.8-1.0]. This conclusion holds for both S+S and S+E pairs
  - **Low-mass pairs**: show no or very low correlation in all redshift bins except for the first one [0.2-0.4] which have indeed very low (only 7 pairs) statistics and significance
- Local SDSS pairs $z < 0.1$:
  - Apparently no correlation (Holmberg effect) is seen among SDSS local major-merger pairs. This does not seem to be due to the particular choice of the SDSS magnitude system. This is found to be due, instead, to the 'blending problem' affecting the colors of these galaxies. It is still present in the Petrosian Magnitude system and in the GM2D system by Simard et al. (2011) and Patton et al. (2011), revealing an SDSS poor galaxy photometry for closely separated pairs.
  - Fiber magnitudes do provide a better probe of central colors rather than global colors
  - Our strategy to solve the problem, is to compute isophotal magnitudes by using the *ellipse* task of IRAF masking the blended pixels of the image and use them to estimate unblended galaxy colors.

Appendix B

Combining GRASIL with semi-analytical model of galaxy formation and evolution (MORGANA)

based on the paper: "Faint Lyman-break galaxies as a crucial test for galaxy formation models" by Lo Faro et al. 2009

B.1 Abstract

It has recently been shown that galaxy formation models within the ΛCDM cosmology predict that, compared to the observed population, small galaxies (with stellar masses $< 10^{11}$ $M_{\odot}$) form too early, are too passive since $z \sim 3$ and host too old stellar populations at $z = 0$. We then expect an overproduction of small galaxies at $z > 4$ that should be visible as an excess of faint Lyman-break galaxies. To check whether this excess is present, we use the MORGANA galaxy formation model and GRASIL spectro-photometric + radiative transfer code to generate mock catalogues of deep fields observed with HST-ACS. We add observational noise and the effect of Lyman-alpha emission, and perform color-color selections to identify Lyman-break galaxies. The resulting mock candidates have plausible properties that closely resemble those of observed galaxies. We are able to reproduce the evolution of the bright tail of the luminosity function of Lyman-break galaxies (with a possible underestimate of the number of the brightest i-dropouts), but uncertainties and degeneracies in dust absorption parameters do not allow to give strong constraints to the model. Besides, our model shows a clear excess with respect to observations of faint Lyman-break galaxies, especially of $z_{850} \sim 27$ V-dropouts at $z \sim 5$. We quantify the properties

of these "excess" galaxies and discuss the implications: these galaxies are hosted in dark matter halos with circular velocities in excess of 100 km s^{-1}, and their suppression may require a deep re-thinking of stellar feedback processes taking place in galaxy formation.

B.2 Introduction

Despite the large observational and theoretical efforts of the last decade, the formation of galaxies in the context of the ΛCDM cosmology is still an open problem. In fact, the wealth of multi-wavelength data on deep fields, coupled with wide local surveys, has produced new constraints on number densities, stellar masses, star formation rates and metallicities of galaxies in the redshift range from 0 to ~ 7. From the phenomenological point of view, a remarkable behaviour of observed galaxies is their "downsizing" trend in star formation rates, stellar masses, chemical enrichment, reconstructed age of stellar populations, reconstructed duration of the main star formation episode (see references in Fontanot et al., 2009a). For "downsizing" here we mean that more massive galaxies tend to be older than less massive ones in terms of either stellar ages or mass assembly, a behaviour that is at variance with that of dark matter halos.

These constraints are a strong challenge to theoretical models of galaxy formation. In a recent paper, Fontanot et al. (2009a) compared the predictions of three galaxy formation models (Monaco et al., 2007, Somerville et al., 2008, Wang et al., 2008) with observational data which showed downsizing trends. This analysis allowed the authors to highlight a significant discrepancy between models and data that pertains to relatively small galaxies, with stellar masses in the range $10^9 - 10^{10.5}$ $M_\odot$. In all three models these galaxies are formed at high redshift and are rather old and passive at late times, while the population of real galaxies in the same stellar mass range builds up at low z, growing in number by a factor of ~ 3 from $z \sim 1$ to the present time, and shows higher specific star formation rates up to $z \sim 3 - 4$. Similar conclusions are obtained considering the age of stellar populations in local galaxies: real galaxies host much younger stars on average than model galaxies. The consistency of results coming from stellar masses, star formation rates and reconstructed stellar ages makes this trend robust. Previous comparisons, focused on stellar mass downsizing, showed that this discrepancy is not limited to the three models tested in that paper but extends to many semi-analytic and N-body codes (see the comparisons to models in Cirasuolo et al., 2008, Fontana et al., 2006, Marchesini et al., 2008).

This is a severe discrepancy because, as we will discuss later in this paper, it cannot be easily solved by a simple fine-tuning of parameters. Also, it is not directly related to the well-known tendency of semi-analytic models to produce steep luminosity functions, because all the model stellar mass functions have roughly the correct slope at $z = 0$, or

to the well-known problem of overquenching of satellite galaxies, which are too red and passive in models (see, e.g., the recent analysis of Kimm et al., 2008). Clearly the solution of this problem amounts to understanding why do small galaxies form so early and why do they stop forming stars later. The second problem is most likey a byproduct of the first one: once too many small galaxies are produced at high redshift, strong stellar feedback must be invoked to suppress their star formation at lower redshift, so as to recover the correct number density at $z = 0$. Then, the crucial objects that are at the origin of this discrepancy are the small star-forming galaxies at $z > 3$. Unfortunately, with presently available facilities only the rest-frame UV radiation of such galaxies is accessible; these are visible as distant faint Lyman-break galaxies. Their name takes origin from the technique used to select them, also known as "dropout technique". This technique selects galaxies over a specific redshift interval by detecting the drop of the UV flux observed in correspondence with the Lyman limit at $\lambda < 912$ Å, the wavelength below which the ground state of neutral hydrogen may be ionized.

In this paper we use the MORGANA + GRASIL model of galaxy formation to generate predictions of B-, V- and i-dropouts to be compared with the results of (i) the GOODS-S photometric and spectroscopic data by Giavalisco et al. (2004) and Vanzella et al. (2008), (ii) the GOODS-MUSIC sample (Grazian et al., 2006) with photometric redshifts, (iii) the results of Bouwens et al. (2007), where many HST-ACS deep fields were analysed and scaled to the depth of the Hubble Ultra Deep Field (HUDF, Beckwith et al., 2006).

Several previous theoretical studies addressed the properties of Lyman-break galaxies using both semi-analytical models (Baugh et al., 2005, Blaizot et al., 2004, Gao et al., 2008, Guo & White, 2008, Lee et al., 2008, Mao et al., 2007, Overzier et al., 2008, Poli et al., 2003, 2001, Somerville et al., 2001) and cosmological simulations (Finlator et al., 2006, Harford & Gnedin, 2003, Nagamine, 2002, Nagamine et al., 2008, 2004, Night et al., 2006, Weinberg et al., 2002). These papers checked how models within the ΛCDM cosmology are able to reproduce the properties of Lyman-break galaxies and their clustering, often reporting satisfactory agreement. Despite some authors (namely Finlator et al., 2006, Night et al., 2006, Poli et al., 2003, 2001) noticed that models tend to overproduce faint high-redshift Lyman Break Galaxies with respect to observations, no quantitative claim had been possible at that time, given the uncertainties on the observational constraints. As an example, Finlator et al. (2006) found that their predicted steep faint-ends of the luminosity function were still in agreement with the available data, which spanned a range of values from -2.2 to -1.6. This wide range has recently been revised by (Bouwens et al., 2007), so that the most recent determinations give a slope $\sim 1.7 \pm 0.1$ from $z \sim 2$ to $z \sim 6$, which implies a disagreement with the theoretical predictions.

The aim of this paper is a careful revision of this comparison, in the light of the improved observational constraints, based on the generation of reliable and improved mock galaxy catalogues through state-of-the-art semi-analytical and spectro-photometric models. This approach will allow us to test the impact of the selection criteria, as well as different theoretical ingredients (with particular emphasis on the modeling of dust attenuation). Moreover, we aim to include this comparison in a cosmological context, and to discuss its implications for current models of galaxy formation and the so-called "downsizing" scenario (see e.g. Fontanot et al. (2009c)).

The plan of the paper is the following. Section B.3 presents the model, which contains some improvements with respect to previous versions. Section B.4 describes the adopted procedure to select Lyman-break galaxies from the simulated galaxy catalogues and to tune the free parameters connected to dust extinction. Section B.5 presents the comparison of model and data in terms of number counts, redshift and color distributions and luminosity functions of B,V and i-dropouts, while Section B.6 quantifies the properties of the model "excess" galaxies and discusses future observational tests that can help shedding light on this population. Section B.7 gives the conclusions.

B.3 The MORGANA + GRASIL model

B.3.1 MORGANA

The MOdel for the Rise of GAlaxies aNd Agns (MORGANA) is described in full detail in Monaco et al. (2007). The model follows the general scheme of semi-analytic models (see Baugh, 2006, for a review); here we only mention how the main processes are implemented. (i) Each dark matter halo hosts a central galaxy and many satellite galaxies, contained within dark matter substructure that has not yet been destroyed by orbital decay due to dynamical friction. Baryons are subdivided into stellar halo, bulge and disc components. Each component has cold, hot and stellar phases. (ii) Merger trees of dark matter halos are obtained using the PINOCCHIO tool (Monaco et al. 2002; Monaco, Theuns, & Taffoni 2002; Taffoni et al. 2002). (iii) After a merging of dark matter halos, galaxy merging times are computed using the results of Taffoni et al. (2003), which are tuned on N-body simulations that include dynamical friction, tidal stripping and tidal shocks. (iv) At each merger a fraction of the satellite stellar mass is moved to the diffuse stellar component of the stellar halo, as explained in Monaco et al. (2006). (iv) The evolution of the baryonic components and phases is performed by numerically integrating a system of equations for all the mass, energy and metal flows. (v) The intergalactic medium infalling on a dark matter halo is shock-heated to a specific thermal energy equal to 1.2 times that of dark matter. (vi) At

each time-step of the numerical integration, the hot gas component is assumed to be in hydrostatic equilibrium with the dark matter halo. (vii) Cooling flows are computed with a new cooling model, tested against simulations of isolated halos in Viola et al. (2008), which takes into account mass and energy input from feedback sources. (viii) The cooling gas is let infall on the central galaxy on a dynamical time-scale. It is divided between disc and bulge according to the fraction of the disc that lies within the half-mass radius of the bulge. (ix) The gas infalling on the disc keeps its angular momentum; disc sizes are computed with an extension of the Mo, Mao & White (1998) model that includes the contribution of the bulge to the disc rotation curve. (x) Disc instabilities and major mergers of galaxies lead to the formation of bulges. In minor mergers the satellite mass is given to the bulge component of the larger galaxy. (xi) Star formation and feedback in discs are inserted following the model of Monaco (2004), while in bulge components the Kennicutt (1998) law is used. In both cases, hot gas is ejected to the halo (in a hot galactic wind) at a rate equal to the star-formation rate. (xii) Feedback from star formation heats the hot halo phase. When its temperature gets significantly higher than the virial one, it leaves the dark matter halo in a galactic hot super-wind. The matter is re-acquired later, when the virial temperature of the descendant halo gets as high as that of the hot superwind gas. (xiii) In star-forming bulges cold gas is ejected in a cold galactic wind by kinetic feedback due to the predicted high level of turbulence driven by SNe. Analogously to the hot superwind, cold halo gas can be ejected out of the dark matter halo if its kinetic energy is high enough. (xiv) Accretion of gas onto massive black holes (starting from small seeds present in all galaxies) is connected to the ability of cold gas to loose angular momentum by some (unspecified) mechanisms driven by star formation. This is explained in full detail in Fontanot et al. (2006). (xv) The kind of feedback from the AGN depends on the accretion rate in Eddington units: whenever this is higher than 1 per cent the AGN can trigger a massive galaxy wind, (see Monaco & Fontanot, 2005) which leads to the complete removal of Inter-Stellar Medium (ISM) from the galaxy, while at lower accretion rates the energy is ejected through jets that feed back on the hot halo gas; this can lead to quenching of the cooling flow.

B.3.2 The improvements with respect to the earlier version

The version of the model used here presents a few improvements with respect to that of Monaco et al. (2007). The most important difference lies in the treatment of star formation in the bulge component. In the earlier version, the size of the starburst, used to compute the gas surface density and then the star formation rate through the Kennicutt (1998) relation, was assumed to be equal to the bulge effective radius R_b. As a consequence, a starburst declines very slowly because the residual gas has a decreasingly low surface density, and then a long star formation time-scale. This is a clearly naive estimate, because

the dissipational gas settles in the centre of the galaxy. In this version we assume that the size of the starburst is determined by the level of turbulence that the gas acquires. The velocity dispersion $\sigma_{\rm cold}$ due to turbulence is:

$$\sigma_{\rm cold} = \sigma_0 \left(\frac{t_\star}{1 \text{ Gyr}} \right)^{-1/3} \tag{B.1}$$

where the parameter σ_0 is set to 60 km s^{-1}. Fontanot et al. (2006) show that this value allows a good reproduction of the evolution of the AGN population. The time-scale of star formation $t_\star$ is:

$$t_\star = 4 \left(\frac{\Sigma_{\rm cold}}{1 \text{ M}_\odot \text{ pc}^{-2}} \right)^{-0.4} \text{ Gyr} \tag{B.2}$$

where $\Sigma_{\rm cold}$ is the (cold) gas surface density. The size of the startburst is determined as the radius for which the turbulence-driven velocity dispersion equals that of the host bulge computed at the same radius. For the Young mass profile used in the model, the bulge velocity curve is roughly constant (assuming a value $\sim 0.707 V_{\rm bulge}$, where $V_{\rm bulge}$ is the circular velocity of the bulge) down to 0.04 times the effective radius R_b, where it quickly drops to zero. Consequently, the size of starbursts in bulges is estimated as:

$$R_{\rm gas} = \left(\frac{\sigma_{\rm cold}(R_b)}{0.707 V_b} \right)^{3.75} R_b \tag{B.3}$$

where $\sigma_{\rm cold}(R_b)$ is computed using R_b to determine the surface density (equation B.2). The radius $R_{\rm gas}$ is not allowed to be smaller than $0.04 R_b$.

A second difference is that we optimized this version of the model for a Chabrier (2003) mass function instead of the Salpeter one used before. To achieve the same level of agreement with data as with Salpeter we perform the following parameter changes (please refer to Monaco et al. (2007) for all details): (i) the stellar mass per supernova is $M_{\star,\rm SN} = 84$ M$_\odot$, the restoration rate is $f_{\rm rest} = 0.44$, while the metal yield per generation is set to $Y = 0.016$; (ii) the preferred values of some parameters change to: $n_{\rm quench} = 0.3$, $n_{\rm dyn} = 0.3$, $f_{\rm wind} = 2.0$, $f_{\rm th,B} = 0.1$, $f_{\rm th,D} = 0.32$, $f_{\rm jet,0} = 3.0$. Quasar-triggered galaxy winds are present as in Fontanot et al. (2006); dark matter halo concentrations are not rescaled to improve the fit of the baryonic Tully-Fisher relation. Moreover, the threshold for disc instability is relaxed from $\epsilon_{\rm limit} = 0.9$ to 0.7; this allows to remove the excess of small bulges present in the previous version of the model (see Figure 7 of Monaco et al., 2007).

Finally, to slow down the merger-driven evolution of the most massive galaxies, at each merger a fraction $f_{\rm scatter} = 0.8$ of the stellar mass of each satellite is given to the halo

diffuse stellar component; however, this is done only at $z < 1$, as suggested by Conroy et al. (2007). This is not a physically acceptable solution of the problem raised by Monaco et al. (2006), but has the advantage of giving realistic results.

B.3.3 GRASIL

For each galaxy modeled by MORGANA the corrisponding UV-to-radio SED is computed with the spectro-photometric + radiative transfer code GRASIL (Silva et al., 1998, please refer to this paper for a detailed description of this code). According to this model, stars and dust are distribuited in a bulge (King profile) + disc (radial and vertical exponential profiles) axisymmetric geometry. Three different dusty environments are taken into account: (1) dust in interstellar HI clouds heated by the general interstellar radiation field of the galaxy (the "cirrus" component), (2) dust associated with star-forming molecular clouds and HII regions, and (3) circumstellar dust shells produced by the windy final stages of stellar evolution. These environments have different importance in different galactic systems at various evolutionary stages. Therefore the residual gas fraction in the galaxy is divided into two phases: the dense giant molecular clouds (MCs) and the diffuse medium ("cirrus"). The fraction of gas in the molecular phase, $f_{\rm mol}$, is a model parameter. The molecular gas is subdivided into clouds of given mass and radius: the stars are assumed to be born within the optically thick MCs and gradually to escape from them, as they get older, on a time-scale $t_{\rm esc}$. To compute the emitted spectrum of the star-forming molecular clouds a radiative transfer code is used. The diffuse dust emission is derived by describing the galaxy as an axially symmetric system, in which the local dust emissivity is consistently computed as a function of the local field intensity due to the stellar component.

For each galaxy modelled by MORGANA, star formation histories, together with gas and metal contents at the "observation" time for both bulge and disc component, are then given as an input to GRASIL. Unobscured stellar SEDs are generated by using again a Chabrier (2003) IMF with stellar masses in the limit [0.15-120] $M_{\odot}$. In the radiative transfer computation the effect of dust is limited to absorption; dust emission, which is very expensive from the point of view of computational time, is irrelevant in the rest-frame UV spectral regions sampled here. Absorption from the Inter-Galactic Medium (IGM) is taken into account by applying to the redshifted SEDs the Madau (1995) attenuation, as explained in Fontanot et al. (2007).

Here below the GRASIL parameters that are not provided by MORGANA and which play an important role in the dust parametrization are briefly discussed. We also recall the values used in Fontanot et al. (2007) to compare with K-band and sub-mm selected galaxies.

(i) t_{esc} represents the time-scale for young O-B stars to escape from their parent MCs. In Fontanot et al. (2007) we fixed the value of t_{esc} to $10^7 yr.$. This is an intermediate value between those found by Silva et al. (1998) to well describe the SED of spirals ($\sim$ a few Myr) and starburst ($\sim$ a few 10 Myr), and it is of the order of the estimated destruction time-scale of MCs by massive stars. (ii) The cold gas mass provided by MORGANA is subdivided between the dense and diffuse phases. In Fontanot et al. (2007) we fixed the fraction of gas in MCs $f_{\rm mol}$ to 0.5.. (iii) The total (i.e., cirrus + MCs) dust content of a galaxy ISM is obtained by the residual gas mass and the dust-to-gas mass ratio δ which is assumed to scale linearly with the metallicity ($\delta = 0.45Z$). The optical depth of MCs depends on their mass and radius only through the relation $\tau \propto \delta M_{MC}/r_{MC}^2$,. In Fontanot et al. (2007) we assumed $M_{MC} = 10^6 M_\odot$, $r_{MC} = 16pc$. (iv) The bulge and disc scale radii for stars and gas are given by MORGANA, while the disc scale-heights, h_d^* and h_d^d for stars and dust, respectively, are set as in Fontanot et al. (2007) to 0.1 the corresponding scale radii. The dust grain size distribution and abundances are set so as to match the mean Galactic extinction curve and emissivity as in Silva et al. (1998) and Vega et al. (2005) and are not varied here.

Because the rest-frame UV emission is especially sensitive to dust attenuation, there is no guarantee that the parameters used in Fontanot et al. (2007) are suitable for Lyman-break galaxies (see Fontanot et al., 2009c, for a discussion on dust attenuation at low and high redshift). In this paper we will explore the effect of changing the values of the two parameters t_{esc} and f_{mol} keeping fixed the other ones. These parameters, in fact, by definition, are those which can play a fundamental role in the attenuation of the UV emission from young massive stars. This will be discussed in more detail in the next section.

B.3.4 Lyman-α emission line

Many Lyman-break galaxies show a prominent Lyman-α emission line, which may influence galaxy colors. This is especially true at the highest redshift, where the i-z color can get significantly bluer, so that the selection of a galaxy as an i-dropout is shifted to higher redshift. Modeling the effect of such emission is very difficult due to the resonant scattering of Lyman-α photons by neutral hydrogen which implies that even a small amount of dust is sufficient to absorb many emitted photons and attenuate the Lyman-α line. The observed lines are generally ascribed to the presence of galactic winds which allow Lyman-α photons to escape the galaxy after a few scatterings. Radiative transfer calculations of Lyman-α through winds have shown that this process can explain the observed asymmetric line profiles (e.g. Shapley et al., 2003, Vanzella et al., 2006, Verhamme et al., 2008). Due to this complexity, we prefer to make an empirical estimate of the possible influence of the Lyman-α line on galaxy colors and number counts.

To this aim, we add a Lyman-α emission line to the produced spectra, with specified EW. Given the relatively coarse wavelength sampling used (sufficient to compute magnitudes over standard filters), this line is added to one single wavelength bin. With the VLT/FORS2 spectroscopic campaign of the GOODS-S field the number of Lyman-break candidates with observed Lyman-α emission lines is 25 over 85 for the B-dropouts, 19 over 52 for the V-dropouts, 24 over 65 for the i-dropouts. The median EW for the three cases are 15^{+19}_{-12} Å, 22^{+56}_{-12} Å and 64^{+100}_{-48} Å (Vanzella et al., 2009). These numbers should be taken with a grain of salt, because most dropout candidates (mainly the fainter ones) are safely confirmed only when a Lyman-α emission line is found, so it is not easy either to compute an unbiased estimate of the fraction of emitters with respect to *confirmed* dropouts or to assess the completeness limit on the EW distribution. As a rough guess we assume that 1/3 of the galaxies have emission lines, and assume for the EW either the median values reported above for the three dropout categories, applying them at redshifts $[3, 4.5]$, $[4.5, 5.5]$ and $[5.5, \infty]$, or the V-dropout value of 22 Å for all emitters. These values are roughly consistent with those assumed by Bouwens et al. (2007) in their analysis.

We will show result of this procedure only for one combination of GRASIL parameters; analogous results are obtained in other cases.

B.4 Simulations of deep fields

To run MORGANA we use merger trees from a 1000^3 particles PINOCCHIO run in a 200 Mpc box with the WMAP3 (Spergel, 2005) cosmology $\Omega_0 = 0.24$, $\Omega_\Lambda = 0.76$, $\Omega_b = 0.0456$, $H_0 = 73$ km/s/Mpc, $\sigma_8 = 0.8$, $n_s = 0.96$. The power spectrum was computed using the fit by Eisenstein & Hu (1998). The particle mass in this run is $2.84 \cdot 10^8$ $M_\odot$, so the smallest used dark matter halo is $1.42 \cdot 10^{10}$ $M_\odot$ (50 particles) and the smallest resolved progenitor is $2.84 \cdot 10^9$ $M_\odot$ (10 particles).

To simulate a deep field, we need to pass from a time sampling of galaxies in the box to a pencil beam where time is translated to redshift, then compute galaxy SEDs in the observer frame.

We transform the output from MORGANA into a pencil beam as follows. The model gives as an output, for each galaxy and in a fixed time grid, its physical properties like mass and metal content of each phase in each component, bulge and disc sizes and circular velocities, bulge and disc star formation rates (see Fontanot et al., 2007, for details). The time grid length has been set to $\Delta t = 10$ Myr, and the run has been stopped at $z = 3$.

As specified in Paper I, the mass function of dark matter halos is sparse-sampled, computing the evolution of at most 300 halos per bin of 0.5 dex in log mass. This results in an

oversampling of small satellite galaxies compared to the central galaxies of similar stellar mass. To correct this oversampling, satellites are further sparse-sampled so as to be as abundant, at the final redshift ($z = 3$), as the corresponding central galaxies of the same stellar mass. An approximately constant number of galaxies in logarithmic intervals of mass is thus obtained from this procedure. This way, the number of produced galaxies is anyway very high, because each galaxy can be "observed" at each output time, i.e. each 10 Myr. A further sparse sampling (1 over 100) is then applied to all galaxies, so as to select a sufficiently large sample of roughly 35,000 galaxies. Each of these sparse samplings define a weight for the galaxies, equal to the inverse of the selection probability. All the statistical quantities are then computed by weighted sums over the galaxies. Our procedure, explained in full detail in Fontanot et al. (2007), is different from, e.g., Kitzbichler & White (2007), where information on the spatial position of the halos in the simulated box is retained. Our procedure has the advantadge of being simpler and, by averaging over the box (redshift does not depend on the position of the galaxy in the box), giving results insensitive to large scale structure, while the procedure of Kitzbichler & White (2007) is necessary to address, for instance, the clustering of high-redshift galaxies.

The galaxy sample is then transformed into a pencil beam by assigning to each galaxy "observed" at time t a redshift z and proper, luminosity and diameter distances $r(z)$, d_L and d_D. The comoving volume associated to each galaxy is computed as the comoving area of the simulation box times the $\Delta r(z)$ distance associated to the cosmic time interval Δt of 10 Myr. The solid angle to be associated to the galaxy is that subtended by the box at the "observed" redshift z.

The apparent (AB) magnitudes of the galaxies are computed by convolving the resulting redshifted SEDs from GRASIL with the ACS filters B_{435}, V_{606}, i_{775} and z_{850} (in the following for simplicity we drop the pedices from the magnitudes, with the exception of z_{850} in order to avoid confusion with the redshift).

In order to better reproduce the observed number counts of Lyman-break galaxies and their color distributions, photometric scatter has been associated to each galaxy magnitude. Modeling this scatter is important because of the tendency for fainter, lower signal-to-noise sources to scatter into the selection through a Malmquist-like effect. To quantify this scatter it is necessary, first of all, to obtain an estimation of the flux error associated to the apparent magnitude of the observed galaxies.

Observational errors are assigned to magnitudes on the basis of the ACS GOODS catalogue, version 2.0. Details of the ACS observations, as well as major features of the GOODS project, can be found in Giavalisco et al. (2004); additional information about the latest v2.0 release of the GOODS ACS images and source catalogues can be found

at `http://www.stsci.edu/science/goods/v2.0` and will be described in detail in an upcoming paper. Here we only mention that we use the best guess for the total magnitude for comparison with the model, while galaxy colours of real galaxies are always computed using isophotal magnitudes. Source detection for this catalog has been performed on the z_{850} band, the isophotes defined by the z_{850} image have been then used as apertures for all other bands. Using this catalogue we compute for each band (B, V, i, z_{850}) the average signal-to-noise ratio as a function of the AB apparent magnitude of the observed galaxies. For B, V and i bands this has been done down to 1-σ detection limit, because it is important to set proper upper limits in order to select faint drop-outs. For the reference band, z_{850}, where by definition the sources are detected above 5-σ, we use the i band error to have a good guess of the 1-σ error. Then, given the AB magnitude of a model galaxy, its flux f is perturbed with a Gaussian-distributed random error with width σ_f equal to the corresponding average 1-σ error flux computed above from the GOODS catalogue. Fluxes are finally transformed back to magnitudes. Whenever the theoretical magnitude is larger (fainter) than that corresponding to $S/N = 1$, which means that such objects are not detectable in that band ($S/N < 1$), we put their magnitude equal to the corresponding 1-σ limit. The new magnitude represents therefore the lower limit, (upper limit if we are looking at the flux of the object), at 1-σ to the real value. The corresponding 1-σ limit magnitudes are 30.45 (B_{435}), 30.56 (V_{606}) and 30.19 (i_{775} and z_{850}).

This procedure is tuned to reproduce ACS deep fields, so we will compare our predictions to the spectroscopic sample of GOODS-S Lyman-break galaxies (Vanzella et al., 2009), to the GOODS-MUSIC sample with photometric redshifts (Grazian et al., 2006), which is based on the version 1.0 of the ACS GOODS catalogue including deep J and K data of VLT-ISAAC and mid-IR data of Spitzer-IRAC, with photometric redshifts, and with the results of Bouwens et al. (2007). The latter authors measured number counts and luminosity functions of Lyman-break galaxies in various ACS deep fields, homogenizing the samples and scaling all results to the depth of the HUDF (Beckwith et al., 2006).

Selection of Lyman break galaxies is then applied to the apparent magnitudes computed as explained above. We use the following criteria respectively for the B-, V- and i-dropout (Giavalisco et al., 2004):

$$(B-V>1.1)\ \text{AND}\ [B-V>(V-z_{850})+1.1]\ \text{AND}\ (V-z_{850})<1.6$$

$$[V-i>1.5+0.9\,(i-z_{850})]\ \text{OR}\ (V-i>2)\ \text{AND}\ (V-i>1.2)\ \text{AND}\ (i-z_{850})<1.3$$

$$(i-z_{850})>1.3\ \text{AND}\ S/N(B)<1\ \text{AND}\ S/N(V)<1 \tag{B.4}$$

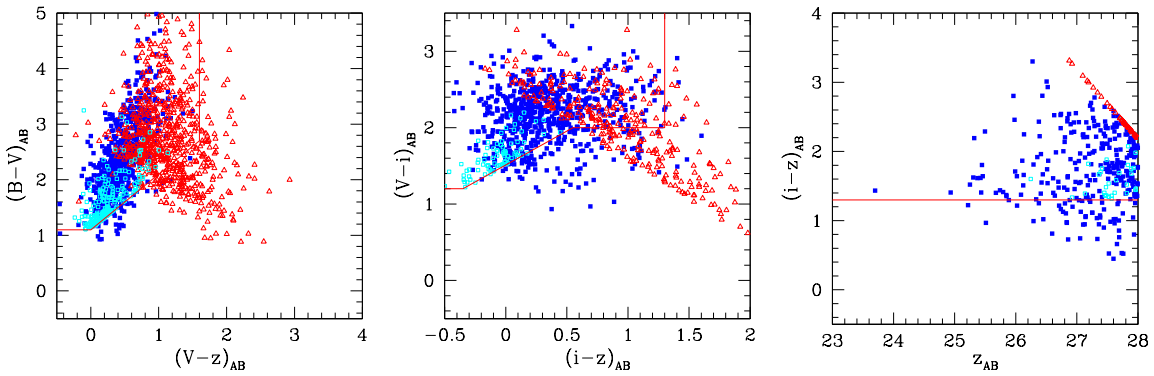

Figure B.1 Color-color diagrams of B-, V- and i-dropouts for the `std.f095.e03` model. (Blue) filled squares are galaxies with redshift in the specific interval of the selection, that is, [3.5-4.5], [4.5-5.5] and [5.5-6.5] for B-, V- and i-dropouts respectively. The open (cyan) squares represent the interlopers (see text for details), while the (red) open triangles are upper-limits in B,V and i. For sake of clarity only the central galaxies (see Section B.3.1) are here considered, (satellite galaxies have very similar colors).

B.4.1 Tuning GRASIL

The prediction of galaxy apparent magnitudes critically depends on dust attenuation, for which several uncertain parameters must be specified in GRASIL. Among all the parameters, we identify two of them as the crucial ones, namely $f_{\rm mol}$, the fraction of gas in molecular clouds, and $t_{\rm esc}$, the time after which OB stars get out of the highly obscured molecular cloud. In Fontanot et al. (2007) values of $f_{\rm mol} = 0.5$ (typical of the Milky Way) and $t_{\rm esc} = 10$ Myr were used to make predictions in the K and sub-mm bands. However, when applied to our (much more dust-sensitive) Lyman-break candidates they give dust attenuations of more than 2 mag, definitely larger, e.g., than the values of 1.4, 1.15 and 0.8 mag assumed by Bouwens et al. (2007) for B-, V- and i-dropouts. Such parameter values may not be suitable for compact, gas-rich starbursting galaxies as our Lyman-break candidates are. In fact, higher molecular fractions are observed in galaxies where the ISM is more pressurized (see, e.g., Blitz & Rosolowsky, 2004); this would imply much lower attenuation by diffuse dust in the ISM (cirrus component).

We then run grasil using all combinations of $f_{\rm mol} = 0.5$, 0.90, 0.95, 1.0 and $t_{\rm esc} = 10$, 3, 1 Myr. Table B.1 gives a list of all the runs performed. We use the model described in Section B.3.1 with quasar-triggered galaxy winds (`std`), but perform also a few runs without winds (`nowind`) to check the effect of this (very uncertain) ingredient of the model. For sake of completeness we also show results for the same model (`old`) presented in Monaco et al. (2007) and Fontanot et al. (2007), with GRASIL run with a Salpeter IMF, but with $f_{\rm mol} = 0.50$ and $t_{\rm esc} = 3$ Myr, a combination which gives a best-fit of the Lyman-break luminosity functions.

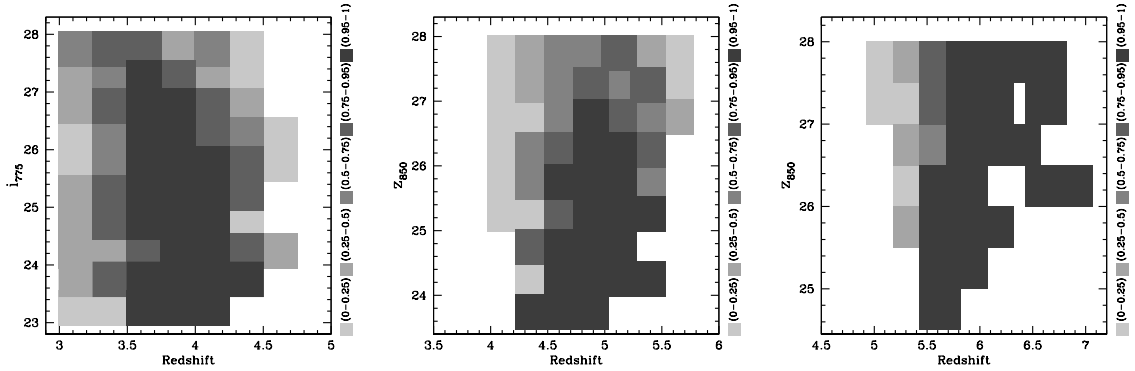

Figure B.2 Selection function for B-, V- and i-dropouts for the `std.f095.e03` model. The fraction of selected galaxies is computed in bins of redshift and apparent magnitude, and is reported as a tone of gray, as indicated in the right of each panel.

name	$f_{\rm mol}$	$t_{\rm esc}$ (Myr)	MORGANA run
`std.f050.e10`	0.50	10	with quasar winds
`std.f090.e10`	0.90	10	”
`std.f095.e10`	0.95	10	”
`std.f100.e10`	1.00	10	”
`std.f050.e03`	0.50	3	”
`std.f090.e03`	0.90	3	”
`std.f095.e03`	0.95	3	”
`std.f100.e03`	1.00	3	”
`std.f050.e01`	0.50	1	”
`std.f090.e01`	0.90	1	”
`std.f095.e01`	0.95	1	”
`std.f100.e01`	1.00	1	”
`std.f095.e03.lya1`	0.95	3	with Lyα in emission
`std.f095.e03.lya2`	0.95	3	”
`nowind.f090.e03`	0.90	3	without quasar winds
`nowind.f090.e01`	0.90	1	”
`nowind.f095.e03`	0.95	3	”
`old.f050.e03`	0.50	3	2007 model

Table B.1 Runs performed for this paper, with values of GRASIL parameters (see Section B.3.3 for a brief description of the parameters) and indication of the MORGANA model used.

For one of the models (`std.f095.e03`) we perform two runs with the addition of the Lyman-α emission line, either assuming a redshift-dependent EW (`std.f095.e03.lya1`) or assuming a constant EW (`std.f095.e03.lya2`), as motivated in Section B.3.4

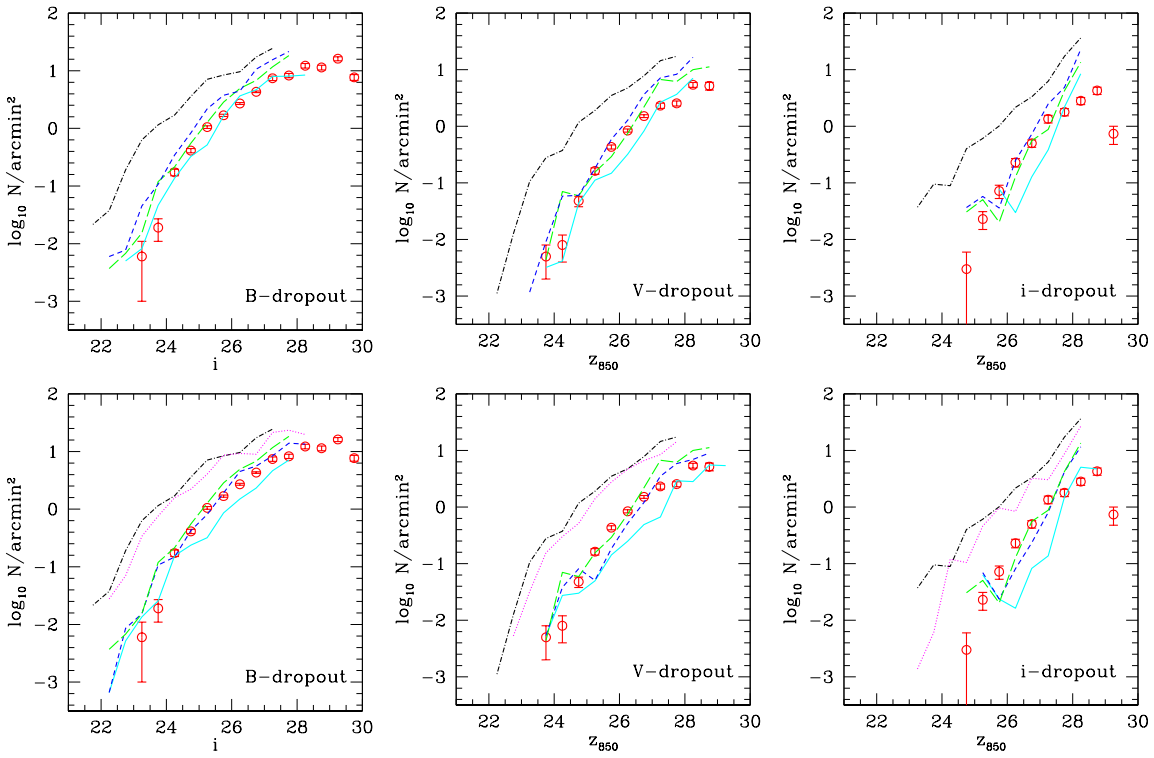

Figure B.3 Number counts of B-, V- and i-dropouts. (Red) points are from Bouwens et al. (2007). Upper panels: models with $f_{\rm mol} = 0.95$, `std.f095.e10` (cyan solid lines), `std.f095.e03` (green long-dashed lines) and `std.f095.e01` (blue dashed lines) compared to the model without dust attenuation (black dot-dashed lines). Lower panels: models with $t_{\rm esc} = 0.3$, `std.f050.e03` (cyan solid lines), `std.f090.e03` (blue dashed lines) and `std.f095.e03` (green long-dashed lines) and `std.f100.e03` (magenta dotted lines) also compared to the model without dust attenuation (black dot-dashed lines).

B.5 Results

Figure B.1 shows the color-color plots for the selection of the model B-, V- and i-dropouts, according to the criteria defined above. Here and in the next figure we use the `std.f095.e03` model; here for sake of clarity only central galaxies with $z_{850} < 28$, the resolution limit of the model, are used (satellite galaxies have very similar colors). All galaxies in the redshift intervals of the selection [3.5-4.5], [4.5-5.5] and [5.5-6.5] for B-,V- and i-dropouts respectively, are shown as full blue squares, or red triangles if they are upper limits. These are the same redshift intervals identified by Bouwens et al. (2007) as typical of Lyman-break galaxies at mean redshift of $z \sim 4$, $z \sim 5$ and $z \sim 6$. The few interlopers falling in the selection areas are marked as cyan open squares. For interlopers we mean galaxies with redshift in the interval [3.0-3.4] for the B-dropouts, [4.0-4.4] for the V-dropouts and [5.0-5.4] for the i-dropouts. Clearly, most galaxies in the relevant redshift interval are selected. Those that scatter out of the selection region are mostly faint galaxies with upper limits in the band from which they drop out; their colors are made less red by the upper limits.

Figure B.2 shows the selection function as a function of redshift and i (B-dropouts) or z_{850} (V- and i-dropouts) magnitude. Selected galaxies clearly tend to reside in the expected redshift range, though some B- and V-dropouts are lost at magnitudes fainter than ~ 26.

We first compare model predictions of B-, V- and i-dropouts with observed number counts, which are the directly observable quantity when complete spectroscopic samples are not available.

Figure B.3 shows the effect of changing the GRASIL parameters $t_{\rm esc}$ and $f_{\rm mol}$ compared to the standard model without dust attenuation (black dot-dashed lines). We consider both the effect of changing $t_{\rm esc}$ keeping fixed the value of $f_{\rm mol}$ (upper panel), and the effect of varying $f_{\rm mol}$ at fixed $t_{\rm esc}$ (bottom panel). Model predictions for unabsorbed spectra drop at a magnitude ~ 27.5 (fainter for the i-dropouts). This is the typical magnitude of the central galaxy contained in the smallest resolved dark matter halo ($1.42 \cdot 10^{10}$ $M_\odot$), fainter galaxies would be hosted in smaller, unresolved halos and are thus under-represented. It is worth noting that HUDF data are deeper than this limit[1] Clearly this limit magnitude increases when dust attenuation is considered. When compared to Bouwens et al.'s observations (open red points in the Figure), number counts in absence of dust attenuation clearly overshoot the data (by about 2 mag). This shows how a correct modeling of attenuation is fundamental to best-fit the data. This feature clearly limits the predictive power of the model, because small variations of dust parameters within the allowed range give very large differences in the results.

The figure shows that the two parameters are degenerate; we identify the two combinations $(t_{\rm esc}, f_{\rm mol}) = (3\ {\rm Myr}, 0.95)$ (model `std.f095.e03`) and $(1\ {\rm Myr}, 0.90)$ (model `std.f090.e01`) as the best-fitting ones. This degeneration concerns the extinction, we in fact, expect to find differences in the IR due to the different distributions of temperature and optical depth of the two phases. The attenuations given by these best-fit models are roughly similar to the ones used by Bouwens et al. (1.4, 1.15 and 0.8 mag for B-, V- and i-dropouts) but are systematically higher for brighter galaxies. This is in line with the findings of Shapley et al. (2001): these authors reported for a large sample of Lyman-break galaxies at $z \sim 3$ an average $E(B-V)$ attenuation of 0.15 that correlates with magnitude, brighter objects being more absorbed. Expressed in terms of the same $E(B-V)$ quantity, our attenuation is 0.1 at the bright end and declines to ~ 0.05 for the faint objects.

Figure B.4 shows number counts for the two best-fit models. As expected, while the bright end is well reproduced with its redshift evolution (with a modest excess for the B-dropouts

[1] It would be easy too reach deeper magnitudes by running the model on a smaller box. However, here we are interested in understanding whether the *same* model that produces small galaxies that are too old at $z = 0$ (Fontanot et al., 2009a) is also over-producing faint star-forming galaxies at high redshift. To achieve this, the requirement is that observations probe at least as deep as the model's limiting magnitude.

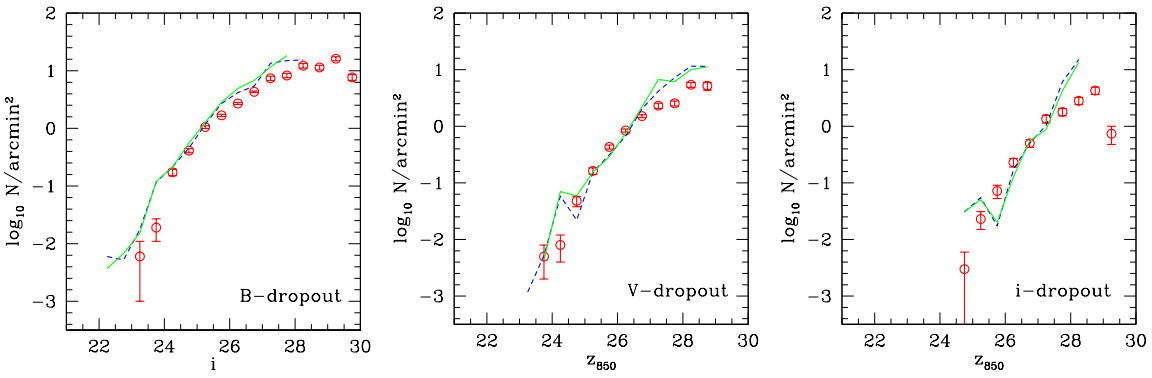

Figure B.4 Number counts of B-, V- and i-dropouts. (Red) points are from Bouwens et al. (2007), the (blue) dashed and (green) solid lines give the predictions of the two best-fit models, respectively `std.f090.e01` and `std.f095.e03`.

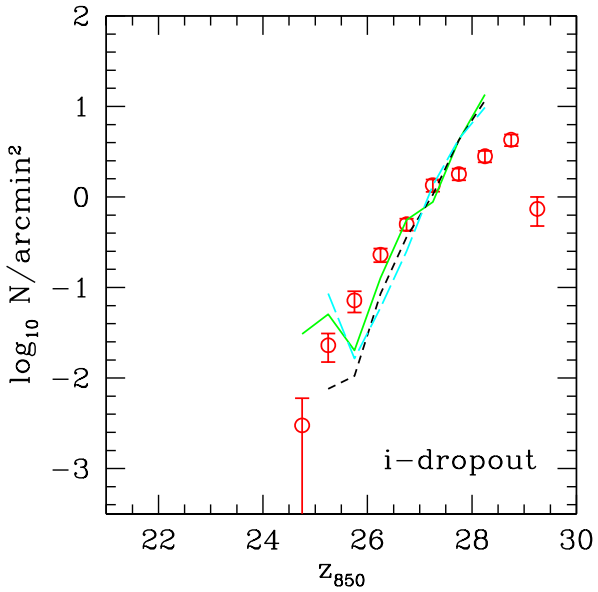

Figure B.5 Number counts of i-dropouts. (Red) points are from Bouwens et al. (2007), the (green) solid line gives the predictions of the best-fit model `std.f095.e03`, the (black) dashed and the (cyan) long-dashed lines correspond to the same combination of parameters but with the contribution of Lyα emission line in the two different prescription discussed in Section B.3.4 (black: `std.f095.e03.lya1`, cyan: `std.f095.e03.lya2`).

and possibly a dearth of bright i-dropouts), a clear excess of faint objects is present at $z_{850} \gtrsim 27$, especially for the V-dropouts.

The inclusion of the Lyman-α line does not change much the predicted number counts of Lyman-break galaxies, with the exceptions of the i-dropouts, which are especially sensitive to the line. Figure B.5 shows the effect of including the Lyman-α line, as explained in Section B.3.4, to the `std.f095.e03` best-fit model. As expected, the effect of the Lyman-α emission line is to make the i-z_{850} color bluer, thus shifting the entrance in the selection criterion to slightly higher redshift and decreasing the number counts. This decrease is

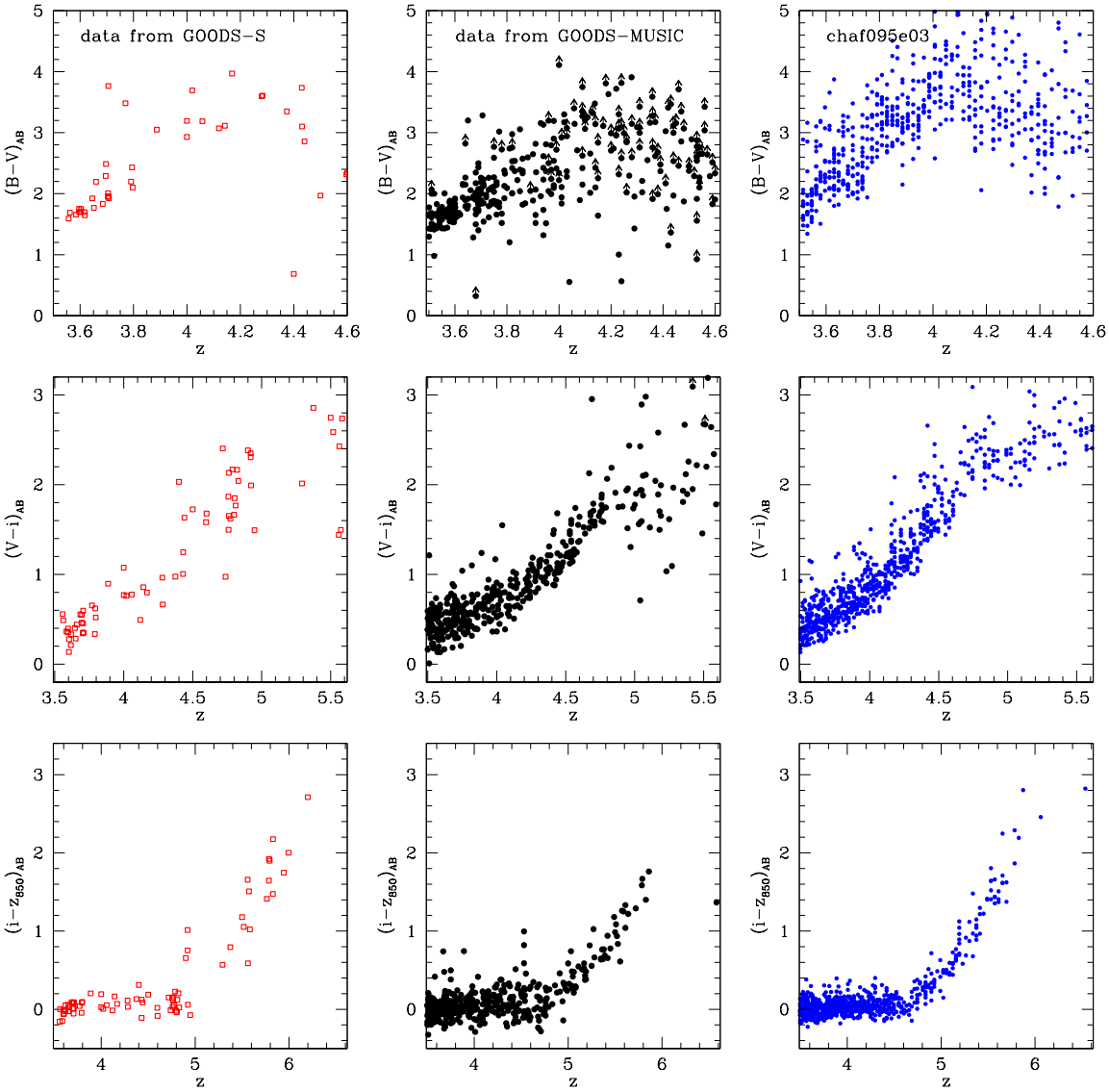

Figure B.6 B-V, V-i and i-z_{850} colors of galaxies with $z_{850} < 26.2$ as a function of redshift. Left panels: GOODS-S galaxies with spectroscopic redshift. Mid panels: GOODS-MUSIC galaxies with photometric redshifts. Black arrows indicate that the magnitude estimation is based on an upper limit at 1-σ. Right panels: model galaxies (`std.f095.e03`).

significant at the bright end, which is then underestimated by the model (in one case it also removes the kink at bright luminosity, which is due to the presence of few, high-weight galaxies - see Section B.4), while the faint end is not strongly influenced. This conclusion does not change much with the choice of the EW. The inclusion of the Lyman-α emission line performed here is clearly tentative, but this test shows that our results are robust with respect to the inclusion of Lyman-α emission line under reasonable assumptions.

We then concentrate on the `std.f095.e03` model, to understand to what extent model Lyman-break galaxies resemble the real ones.

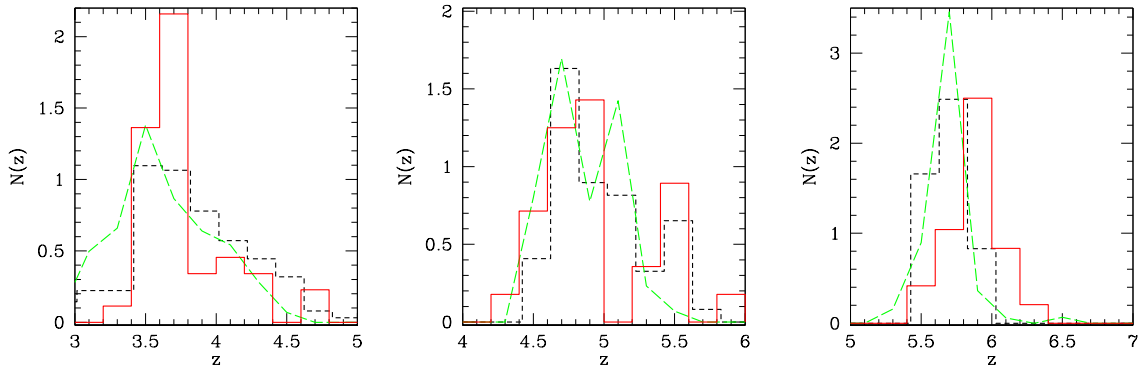

Figure B.7 Redshift distribution for B-, V- and i-dropouts in the GOODS-S (red solid lines) and GOODS-MUSIC (black dashed lines) data samples ($z_{850} < 26.2$) and in the `std.f095.e03` model (green long-dashed lines).

Figure B.6 shows the B-V, V-i and i-z_{850} colours of model and real galaxies as a function of redshift. Observed galaxies are shown both from the GOODS-S catalogue, with spectroscopic redshift, and for the GOODS-MUSIC catalogue, with photometric redshift, which clearly has many more galaxies. Only the galaxies brighter than $z_{850} < 26.2$ are here considered, because of the 90 per cent completeness limit of the GOODS-MUSIC catalogue. As already noticed in Fig. B.1, model galaxies present colours that closely resemble the observed ones, though they tend to be slightly redder, especially in B-V at z$\sim$4 (at least compared to GOODS-MUSIC). Analogous conclusions can be drawn by considering the other best-fit model, `std.f090.e01`. This means that colours cannot be used to constrain the parameters. This conclusion is strenghtened by noting that the strong reddening of all colors with redshift is driven by IGM absorption.

Figure B.7 shows the redshift distributions of model Lyman-break galaxies. We compare these predictions with the spectroscopic redshift distribution of GOODS-S galaxies (red solid lines) which constitute an incomplete sample (see Vanzella et al., 2008, 2009, for details) and with the photometric redshift distributions of GOODS-MUSIC (black dashed lines) and consider only galaxies brighter than $z_{850} = 26.2$, the range where the GOODS-MUSIC sample is complete. The agreement is good though not perfect; this can be seen by comparing the average and standard deviation of the predicted redshift distributions, (3.71$\pm$0.35; 4.88$\pm$0.27; 5.67$\pm$0.22; for B-,V- and i-dropout respectively), with those derived from Giavalisco et al. (2004), (3.78 ± 0.34; 4.92 ± 0.33; 5.74 ± 0.36; for the three candidates respectively), the GOODS-S spectroscopic sample (3.78 ± 0.37; 4.98 ± 0.39; 5.92 ± 0.20) and GOODS-MUSIC photometric sample (3.81 ± 0.40; 4.95 ± 0.37; 5.74 ± 0.10); however sample variance in the 150 arcmin^2 GOODS-S field is not negligible, so the level of agreement is considered satisfactory, especially if we consider that a confirmation of the validity of the redshift distribution is represented by the consistency between number counts and luminosity functions. Anyway, since the uncertainty related to the redshift measurements

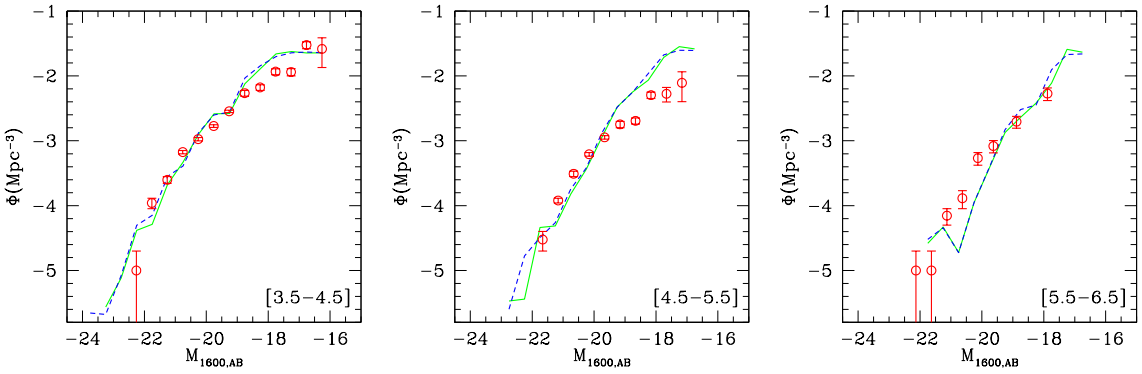

Figure B.8 Luminosity function of B-, V- and i-dropouts. (Red) points are the estimate by Bouwens et al. (2007), (green) solid and (blue) dashed lines give predictions for the `std.f095.e03` and `std.f090.e01` models.

increases at higher redshifts where the detection is more difficult, this comparison should be taken with grain of salt. In particular, the number of available photometric redshifts of i-dropout galaxies is very low, because only few such galaxies are bright enough to be detected in J and K bands.

Bouwens et al. (2007) estimated the luminosity function of Lyman-break galaxies by scaling all observations to the HUDF (5-σ) depth of 29 in the z_{850} band. Assuming that the B-dropout technique selects all star-forming (and not severely obscured) galaxies in the redshift interval $3.6 < z < 4.5$, they obtained selection functions of V- and i-dropouts by degrading images of low-z B-dropout galaxies to reproduce observational biases at higher redshift, then estimating how many of them would be selected. As shown in figures B.1 and B.2, most model galaxies in that redshift range with high enough z_{850} flux are B-dropouts, so it is fair to compare Bouwens et al.'s estimate to the luminosity function of all model galaxies in the redshift range $3.5 < z < 4.5$, $4.5 < z < 5.5$ and $5.5 < z < 6.5$. Figure B.8 shows the luminosity function of the two best-fit models, compared to the Bouwens et al. (2007) determination, adjusted to take into account the slightly different cosmology. The agreement is again good at high luminosities (with a possible underestimate of the i-dropout bright tail), while a clear excess is visible in the faint tail, especially in the V-dropouts. We stress that this result is different from the one of figure B.4 relative to number counts, because the two comparisons follow two different approaches: in the first case the model tries to reproduce exactly the observed quantity, in the second case the observers try to reconstruct a quantity more directly comparable with models, i.e. the luminosity function. The good agreement of data and model in terms of both number counts and luminosity functions cofirms that model galaxies closely resemble the observed population and their selection function. Moreover, the model follows very well the positive evolution (with time) of the knee of the luminosity functions, and this allows us to support

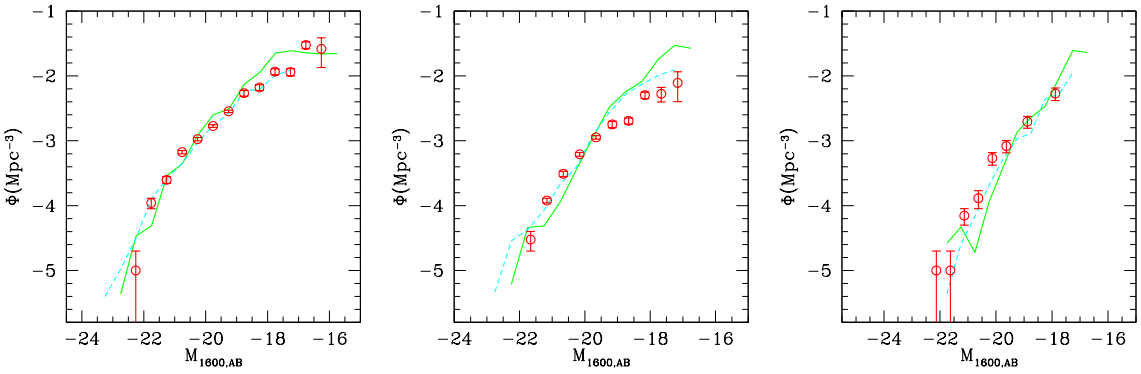

Figure B.9 Luminosity function of B-, V- and i-dropouts. (Red) points are the estimate by Bouwens et al. (2007), (green) solid and (cyan) dashed lines give predictions for the `nowind.f095.e03` and `old.f050.e03` models.

Bouwens et al.' conclusion that we are indeed witnessing the hierarchical build-up of the population of young galaxies.

Summing up, the MORGANA model reproduces the main observational properties (number counts, colours, selection functions, redshift distributions and estimated luminosity functions) of bright Lyman-break star-forming galaxies at $z > 3.5$, (though a possible underestimate of the number of bright i-dropouts may be present); fainter galaxies, with $z_{850} \gtrsim 27$, have acceptable properties but are over-produced. However, dust attenuation heavily depends on uncertain parameters of the ISM like $t_{\rm esc}$ and $f_{\rm mol}$, so that multiple solutions are equally acceptable.

B.6 A population of excess galaxies

Degeneracies in model predictions do not allow us to draw strong conclusions from the good agreement shown above between model and real Lyman-break galaxies at the bright end of the luminosity function. Indeed, parameter degeneracy is not due only to GRASIL; two MORGANA parameters, namely $n_{\rm dyn}$ and $n_{\rm quench}$ (see section B.3.2) influence the star-formation rate density at $z > 3$ but give small difference at lower redshift, where more constraints are available. To strengthen this point, we show in Figure B.9 the prediction for the luminosity function of a model run without quasar-triggered galaxy winds (`nowind.f095.e03`) and the `old.f090.e03` used in Fontanot et al. (2007), where a Salpeter IMF is used in place of Chabrier, and a slightly different cosmology with $\sigma_8 = 0.9$ is adopted. The last model is run on a 512^3 box with slightly worse mass resolution. The fit is very similar to our best fits in all cases, and this confirms that bright Lyman-break galaxies cannot give strong constraints to models as long as dust attenuation is so uncertain. The reason why quasar winds do not affect this observable is the following. In our implemented scheme

for quasar-triggered winds (Fontanot et al., 2006) radiation from an accreting black hole can evaporate some cold gas in the star-forming bulge; if the putative evaporation rate is higher than the star formation rate, then all the cold mass in the host bulge is removed. Quasar winds are then able to quench star formation in bulges (mergers), and this could lead to a suppression of star formation. However, due to the (modeled) delay between star formation and black-hole accretion, quasar winds take place when the star formation episode that has triggered accretion is almost over. The independence of the Lyman-break luminosity function on winds is a further demonstration of this.

Previous papers (Cirasuolo et al., 2008, Fontana et al., 2006, Fontanot et al., 2009a, Marchesini et al., 2008) have shown that MORGANA presents a deficit of massive galaxies at $z > 3$, when compared to the stellar mass function or to the K-band luminosity function. At the same time, MORGANA is able to reproduce the sub-mm counts of $z \sim 2$ starburst galaxies (Fontanot et al., 2007), and even shows a modest excess of bright B-dropouts (fig. B.4). The two evidences of low stellar masses and a correctly high SFR are not contradictory: compared with similar models, MORGANA produces stronger cooling flows and then stronger bursts of star formation that are readily quenched by stellar feedback, so that the high levels of star formation are maintained for short times and *do not* produce higher amounts of stellar mass. Moreover, the apparent underestimate of stellar masses by MORGANA may be at least in part due to systematics in stellar mass estimates. Tonini et al. (2008) showed that inclusion of TP-AGBs in the Simple Stellar Population libraries give a significant downward revision of stellar masses at high redshifts or, equivalently, a boost to the K-band magnitude of model galaxies. According to Marchesini et al. (2008), our stellar mass function at $z \sim 3$ remains low at the $\sim 2\sigma$ level, but when we compare stellar masses of our model Lyman-break galaxies with estimates of Stark et al. (2009), which take into account TP-AGBs, we find a slight over-prediction, in contrast with the evidences mentioned above. It is then difficult at this stage to assess to what extent a good match of the bright end of the luminosity function of Lyman-break galaxies at $z \sim 4 - 5$ is in contrast with the apparent underestimate of the high end of the stellar mass function at $z \sim 3$.

Once the bright tail is matched, the model shows a clear excess of faint dropouts. Is this excess robust? From the one hand, as explained in the Introduction, the excess is expected: Fontanot et al. (2009a) demonstrated that galaxies with stellar masses (at $z = 0$) in the $10^9 - 10^{10}$ $M_\odot$ range are formed too early and are too passive since $z \sim 3$, and this is the main cause of the lack of (stellar mass and archaeological) downsizing in models. It follows that an excess of small star-forming galaxies must be present at higher redshift, and because the data go deeper than the completeness limit of the model, this excess must be visible. On the other hand, number counts at such deep magnitudes may well be incomplete. The use of the HUDF, and the careful analysis of Bouwens et al. to determine the selection functions, makes it unlikely that the model excess is purely due to sample incompleteness.

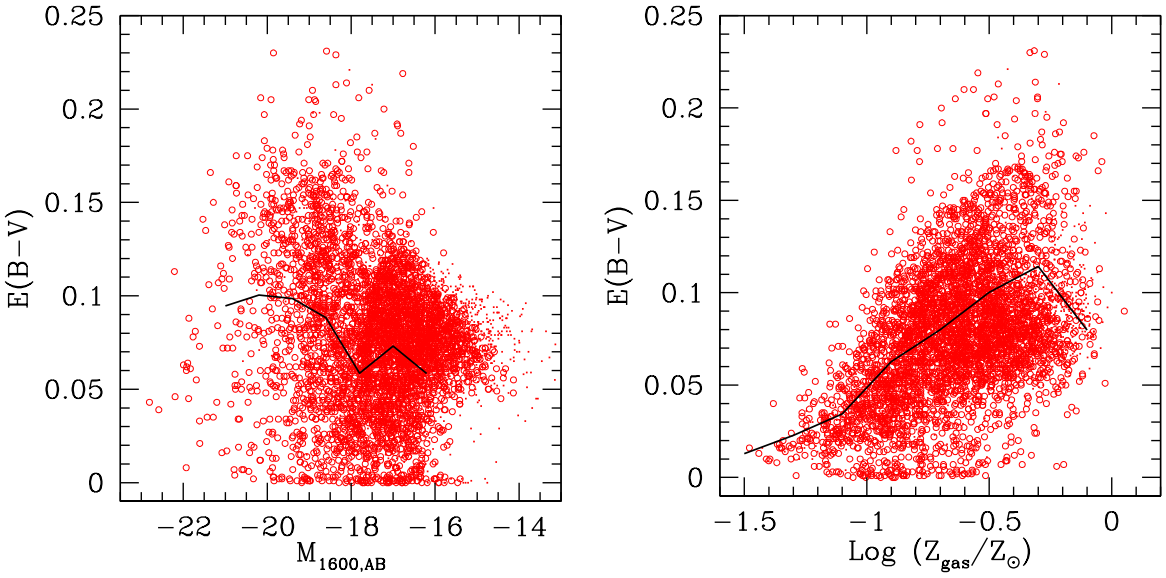

Figure B.10 $E(B-V)$ attenuation as a function of the UV rest-frame luminosity $M_{1600,AB}$ (left panel) and gas-metallicity (referred to solar metallicity)(right panel). All model V-dropout galaxies at redshift about 5 and with $Log(M_\star) > 7.75$, are here considered. Open circles refer to central galaxies. The black solid lines represent the 'weighted' mean values of $E(B-V)$ computed, respectively, for each bin of magnitude and gas-metallicity. B- and i-dropouts show a similar trend.

Moreover, the reconstructed faint slope of the luminosity function is ~ -1.7, in agreement with many other determinations both at $z \geq 3$ (Beckwith et al., 2006, Oesch et al., 2007, Yoshida et al., 2006) and at $z \sim 2$ (Reddy & Steidel, 2008), while the slope of model luminosity functions is significantly steeper, in excess of -2.0.

Is this excess an artifact of dust extinction? in other words, is it possible that MORGANA is underestimating the star formation rate of bright galaxies (as well as stellar masses) but our *ad-hoc* tuning of dust parameters absorbs this discrepancy, creating an excess of faint galaxies? Figure B.10 shows the $E(B-V)$ attenuation as a function of UV rest-frame luminosity $M_{1600,AB}$ (left panel) and gas-metallicity (right panel) for model V-dropout galaxies at $z \sim 5$ and with $Log(M_\star) > 7.75$; central galaxies are highlighted as empty circles. The solid black lines represent the 'weighted' mean values of $E(B-V)$ computed, respectively, for each bin of magnitude and gas-metallicity. For B- and i-dropouts we obtain a similar trend. The figure shows that the attenuation we obtain is only slightly lower ($E(B-V) \sim 0.1$ in place of 0.15) than what found by Shapley et al. (2001) at lower redshift, (but we are not using the same SED template of those authors because every galaxy in our model has its own SED), while, as mentioned above, the attenuation in the observed i and z_{850} bands is very similar to that used by Bouwens et al. (2007); the excess remains if we attenuate our galaxies as suggested in that paper. Moreover, the faint-end slope of model luminosity functions, in excess of -2.0, is inconsistent with the latest and

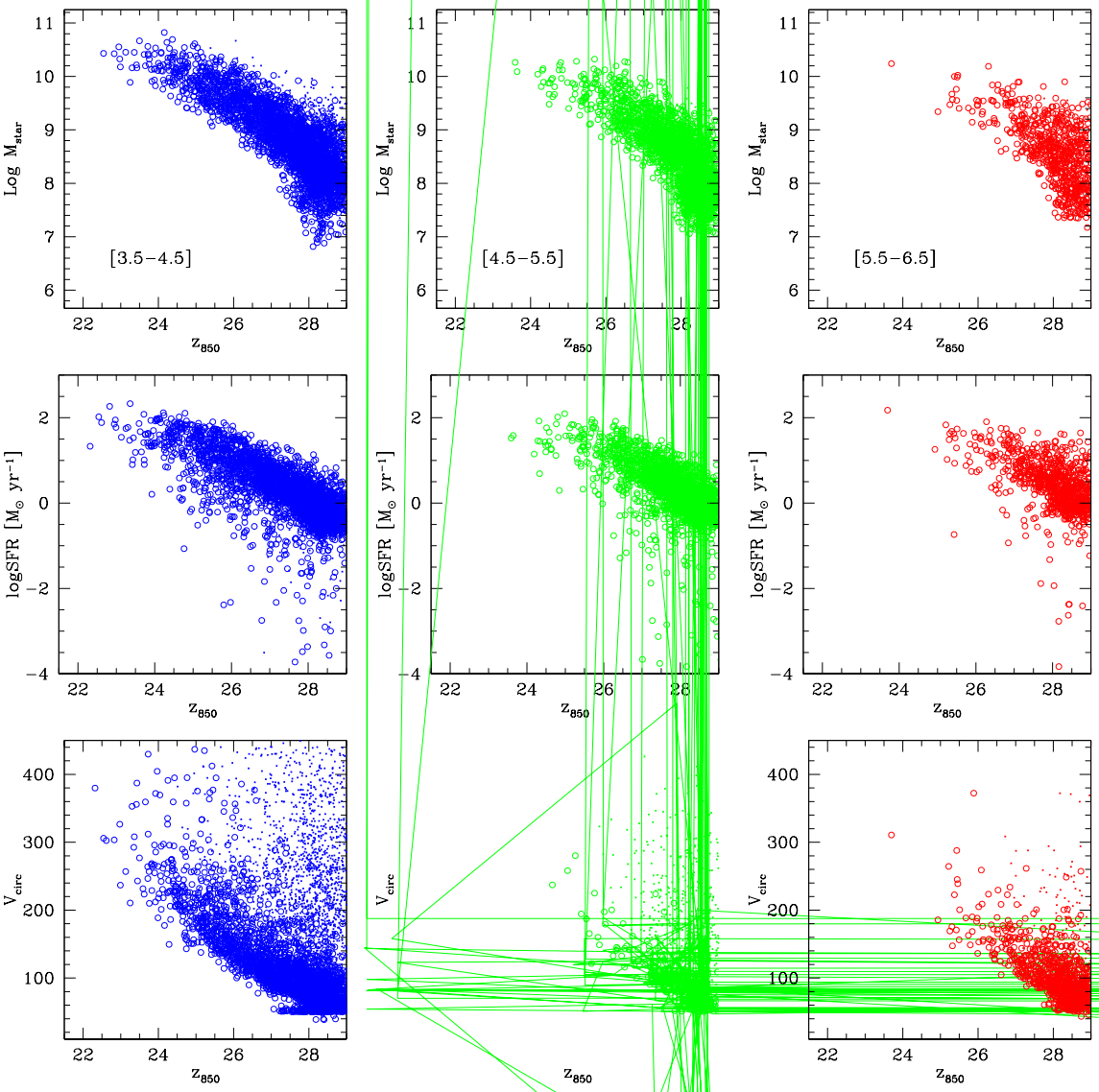

Figure B.11 Properties of model Lyman-break galaxies as a function of z_{850} magnitude, for the model `std.f095.e03`. Upper panels give stellar masses, mid panel give star formation rates, lower panels give dark matter halo circular velocities. Bigger open points refer to central galaxies.

very stable -1.7 value; with such a difference, an excess of faint galaxies will be obtained even if the bright tail is underestimated. This steep slope is in part due to to the fact that faint galaxies are less absorbed than bright ones, something that is well known in literature (see, e.g., Sanders & Mirabel, 1996), and is consistent with the trend found by Shapley et al. (2001) at $z \sim 3$. We conclude that it is unlikely that this excess is due to a peculiar behaviour of dust attenuation as predicted by GRASIL.

Other theoretical groups have compared their predictions of Lyman-break galaxies to data (see the reference list in the Introduction), but no group has clearly claimed to find a similar excess, with the exception of Poli et al. (2003, 2001), who compared the predictions of a

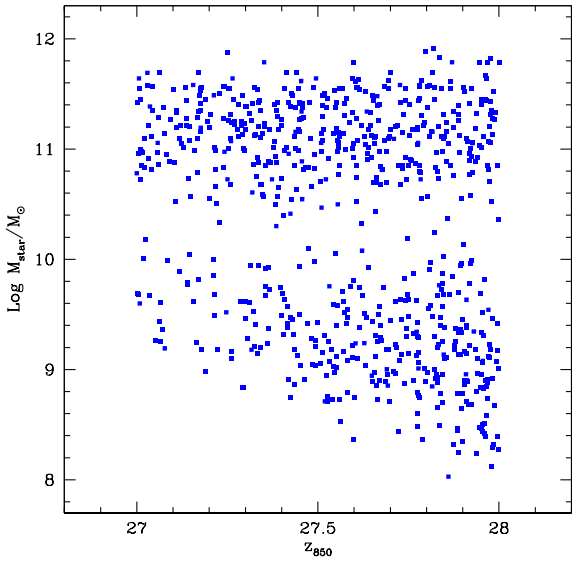

Figure B.12 Stellar masses of the $z = 0$ descendant galaxies of V-dropouts with $27 < z_{850} < 28$.

semi-analytical model (Menci et al., 2002) with the reconstructed luminosity function of I and K-selected samples (*not* color selected). They reported an excess of faint $I \sim 27$ galaxies at lower redshift, $z \sim 3$, which is even stronger than the one we find here. Also, Night et al. (2006) and Finlator et al. (2006), extracting catalogues of Lyman-break galaxies from N-body simulations, find rather steep luminosity functions, with slopes ~ -2. Night et al. (2006) discuss in some detail the implications of this steep slope, but claim broad consistency with available data; compared to the more recent determination of Bouwens et al., such steep slopes are nominally ruled out. There are two reasons why many groups may have not noticed such an excess: first, very deep fields like GOODS and the HUDF are required to reliably sample the $z_{850} \sim 27 - 28$ magnitude range, and these have been made available only recently. Second, a simple (and over-simplistic) magnitude-independent attenuation makes the excess less visible, so a more advanced tool as GRASIL is needed to notice it.

In the following of this section we try to assess whether the excess can be fixed simply by a better fine-tuning of model parameters, without spoiling the good match with local galaxies. To answer this question, we focus on the properties of the excess population. Figure B.11 shows stellar masses, star formation rates and dark matter circular velocities of B-, V- and i-dropout galaxies as a function of apparent z_{850} magnitude, for the best-fit model `std.f095.e03`; central galaxies are highlighted as empty circles. Excess galaxies with $z_{850} \sim 27 - 28$ are characterized by star formation rates of order of $\lesssim 10$ $M_{\odot}$ yr^{-1}, stellar masses growing from $10^8 - 10^9$ $M_{\odot}$ at $z \sim 6$ to a factor of ~ 3 higher at $z \sim 4$, and the central ones are hosted in dark matter halos with masses in the range from 10^{11}

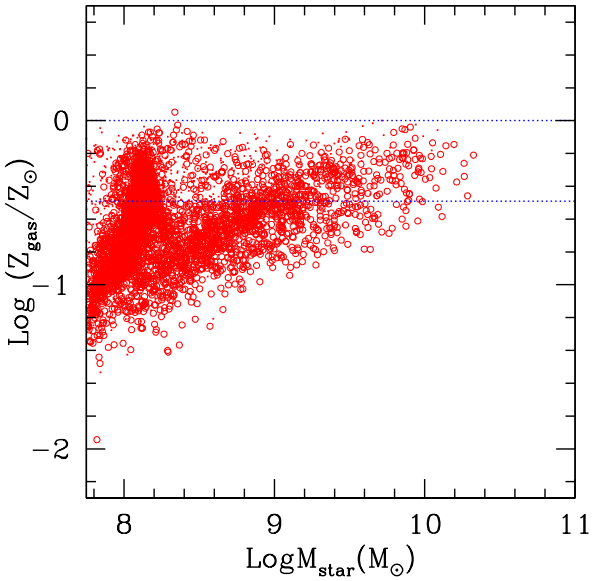

Figure B.13 Stellar mass – gas metallicity relation for model galaxies at $z = 5$. In this plot all galaxies in the box are used. Bigger open points refer to central galaxies. The two horizontal lines mark solar and 1/3 solar metallicities. We removed galaxies with less than 10 per cent gas fraction.

to 10^{12} $M_\odot$, whose circular velocities are in excess of 100 km s^{-1}. Figure B.12 shows the stellar mass of the $z = 0$ descendant galaxies of V-dropouts with $27 < z_{85} < 28$. Roughly half of them do not grow much in mass since $z \sim 5$, thus falling in the stellar mass range of galaxies that are too old in models. The other half merge with larger galaxies to end up at the knee of the stellar mass function. In many papers, like e.g. Santini & et al. (2008), the observed specific star formation rates of massive galaxies is found to be higher than model predictions by a factor at least of ~ 4, which is apparently at variance with the good match of the growth of stellar mass in the same galaxies since $z \sim 3$ (Fontana et al., 2006). The puzzle may be solved if the excess population of small galaxies contributes to inflate the growth of massive galaxies by minor mergers, thus compensating for the lower star formation rates. We propose this as a plausible explanation, although more stable estimates of star formation rates in galaxies are necessary to assess this problem.

An important hint on the mechanism responsible for the excess of faint galaxies comes from their metallicities Z. Observations show that metallicities measured from emission lines decline with redshift, and this decline is stronger for smaller galaxies. This has been measured at $z \sim 2$ by Savaglio et al. (2005) and by Erb et al. (2006), Erb (2007), and at $z \sim 3$ by Maiolino et al. (2008), but some measures exist at higher redshift (Ando et al., 2007) that seem to confirm the trend up to $z \sim 6$. Besides, Pettini et al. (2001) report a value of 1/3 solar as the typical metallicity of $z \sim 3$ Lyman-break galaxies. We show in figure B.13 the predicted metallicities of the gas component of galaxies at $z = 5$ as a

function of their galaxy stellar mass. We show gas metallicities because these are measured from emission lines. A mass-metal relation is visible, but with a very high normalization, for which 10^{10} $M_\odot$ galaxies are already enriched above 1/3 solar, the typical gas metallicity of $z \sim 3$ Lyman-break galaxies. Moreover, a blob of small, highly enriched galaxies is visible, that is probably absent in the real world. These high metallicities justify the slightly redder colours of model galaxies and the shift toward lower redshift of the selection function, and may be at the origin of the underestimate of the number of bright i-dropouts. High metallicities at high redshift are a common problem of galaxy formation models, as pointed out in Maiolino et al. (2008); relatively high metallicities at $z \sim 2-3$ are reported by Guo & White (2008), and studying model predictions for the Milky Way De Lucia & Helmi (2008) noticed a dearth of low metallicity halo stars, due to excessive enrichment of small galaxies (before they become Milky Way satellite) at high redshift. Can this mismatch in gas metallicity create the excess of faint galaxies? Observations (Maiolino et al., 2008) suggest a downsizing trend for metal enrichment, with the stellar mass-gas metallicity relation steepening at high redshift. Our relation is rather flat, so that we are probably overestimating gas metallicity more in fainter objects. If more metals give higher attenuation, this mismatch would lead to an artificial *flattening* of the LF, thus decreasing the excess of faint Lyman-break galaxies rather than creating it.

There is a broad consensus among modelers on the fact that AGN feedback is most effective in massive galaxies at low redshift, so the excess galaxies should be suppressed by stellar feedback. This should work in the direction of creating strong gas and metal outflows, so as to keep low both stellar mass and metallicity. Coming back to the question on whether this excess can be suppressed by fine-tuning model parameters, it is easy to do it by increasing the efficiency of stellar feedback, but at the cost of destroying the good fit of the stellar mass function at low redshift. Indeed, as clear in Figure B.11, such galaxies, though small, are hosted in relatively large dark matter halos with circular velocities well in excess of 100 km s^{-1}. Because the efficiency of gas removal mainly scales with halo circular velocity (as found since the seminal work of Dekel & Silk, 1986), this would be done at the cost of suppressing also star formation in those 10^{12} $M_\odot$ halos at $z = 0$ in which star formation efficiency is highest, thus destroying the good agreement with the local stellar mass function (and luminosity functions as well).

Stellar feedback is manily driven by SNe, and each SN produces roughly 10^{51} erg of energy, which translates into 10^{49} erg per $M_\odot$ of stars formed if roughly 1 SN explodes each 100 $M_\odot$ of solar masses. If a fraction ε of SN energy is injected in the ISM instead of being quickly radiated away ($\varepsilon \sim 0.3$ in our model), the velocity $v_{\rm eject}$ at which a mass $M_{\rm eject}$ can be accelerated by a mass $M_\star$ of stars formed is $v_{\rm eject} \sim 500\sqrt{(\varepsilon/0.3)M_\star/M_{\rm eject}}$ km s^{-1}. As a result, one $M_\odot$ of stars can not eject much more than one $M_\odot$ of gas out of a halo with circular velocity of $\sim$ 200 km s^{-1} (and escape velocity higher by the canonical factor of

$\sqrt{2}$). In order to limit the number and metal content of faint Lyman-break galaxies hosted in 100 km/s halos at $z \sim 5$, $v_{\rm eject}$ must be higher than it is at $z \sim 0$, and this can be obtained as follows: (i) increasing energy feedback efficiency ε (if not the SN energy), (ii) increasing the number of SNe per solar mass of stars formed, (iii) decreasing halo circular velocities (or their number at fixed V_c). The first solution would imply that feedback works differently in such starburst, with the paradoxical conclusion that feedback can be most efficient in the densest environments. Anyway, the gain factor is unlikely to be very high, because if 32 per cent of SN energy (in discs) is available for feedback, as assumed in this paper, the gain cannot be higher than a factor of three in energy (or $v^2_{\rm eject}$). Things would change if such SNe were more energetic than their low-redshift and high-metallicity counterparts. Solution (ii) would be obtained by assuming a different, more top-heavy IMF in these galaxies, while solution (iii) would require that dark matter is not completely cold and collisionless as assumed.

In all cases, a solution of this discrepancy, and a proper reproduction of stellar mass and archaeological downsizing, requires some deep change in the models, be it a more sophisticated feedback scheme, more energetic SNe at high redshift, a varying IMF or a different dark matter theory. Moreover, this question is of great interest because, due to their steep luminosity function, such galaxies would contain most produced metals, so they are very important contributors to metal pollution of the IGM.

While theoretical progress can be achieved by exploring the ideas given above, observational breakthroughs will have to wait the next generation of telescopes. Indeed, while the photometric selection of Lyman-break galaxies is feasible with the current facilities up to magnitude z_{850} ∼28, even though on a relatively small field like GOODS, the spectroscopic observations of relevant features like the break of the continuum blueward the $Ly\alpha$ line and the detection of the ultraviolet absorption lines is still challenging for sources fainter than $z_{850} \sim 25.5$. Beyond this limit the main spectral feature is the Lyman α emission line (if present), often observed without continuum; only composite spectra allow to increase the signal-to-noise. Future observations in the next decade with ground-based 30-40m class telescopes (e.g. TMT, E-ELT), with ALMA and from the space with JWST will be crucial to make an observational breakthrough; one of the main goals of these facilities is to perform spectroscopic surveys of faint sources, reaching easily $z_{850} \sim 27$. Not only the precise estimation of the redshift will be possible, but the validation of the dropout technique at that level and information on the total mass (from the stellar velocity dispersion), mass distribution and rotation curve, metallicity, dust content, galactic wind energetics and stellar population distribution will be straightforward to derive from 30-40m spectra of the galaxies already discovered in the 8-10m surveys. The rich phenomenology revealed by these spectra will give us new insight on the formation of galaxies, that will complement the theoretical efforts made in the next years.

B.7 Summary

We have compared the predictions of MORGANA+GRASIL (Fontanot et al., 2007, Monaco et al., 2007, Silva et al., 1998) with data of Lyman-break galaxies at $z \sim 4-6$. Model predictions have been produced by simulating deep ACS-HST fields, taking into account photometric errors as in the GOODS-S survey (Giavalisco et al., 2004), and the effect of Lyman-alpha emission line. They have been compared to number counts of B- V- and i-dropouts, scaled to the HUDF sensitivity by Bouwens et al. (2007), colour evolution, redshift distributions and selection function of GOODS-S (Vanzella et al., 2009) and GOODS-MUSIC (Grazian et al., 2006) galaxies, and luminosity functions estimated by Bouwens et al. (2007).

Model galaxies closely resemble the observed ones in terms of sizes, stellar masses, colors, dark matter halo properties and spatial distribution but have significantly higher metallicities. However for such galaxies, observed at rest-frame UV wavelengths, dust attenuation is as important as uncertain. We find that reasonable tuning of GRASIL parameters, namely escape time $t_{\rm esc}$ of stars from the parent molecular cloud and fraction $f_{\rm mol}$ of gas in the molecular phase, can result in more than a magnitude difference. The two parameters are also degenerate, i.e. decreasing the first has a similar effect as increasing the second and *vice versa*. These parameters are also degenerate with model parameters that regulate the amount of star formation in high-redshift halos.

Fixing the parameters it is possible to reproduce the bright end of the number counts and luminosity functions, with a modest overestimate of the number of bright B-dropouts and a possible underestimate of bright i-dropouts. We then notice an excess of faint ($z_{850} \gtrsim 27$) star-forming galaxies, especially when considering V-dropouts at $4.5 < z < 5.5$. This excess is unlikely to be due to sample incompleteness or to some peculiar behaviour of GRASIL dust attenuation. Fontanot et al. (2009a), found a serious discrepancy between models of galaxy formation (including MORGANA) and data for galaxies in the mass range $10^9 - 10^{10.5}$ $M_\odot$ at $z = 0$. These form too early in the models, are too passive at $z < 3$ and host too old stellar populations at low redshift. This clearly implies an excess of small star-forming galaxies at high redshift that forces modelers to suppress star formation at later time, so as to recover the correct number of small galaxies at $z = 0$.

We define a class of galaxies which are over-produced by the model. These faint Lyman-break galaxies, forming stars at $\lesssim 10$ $M_\odot$ yr^{-1}, have masses that grow in stellar mass from $z \sim 6$, where their mass is $\sim 3 \times 10^8 - 3 \times 10^9$ $M_\odot$, to $z \sim 4$, where their mass has grown to $\sim 10^9 - 10^{10}$ $M_\odot$. They are hosted in relatively massive dark matter halos, with masses in the range $10^{11} - 10^{12}$ $M_\odot$ and circular velocities in excess of 100 km s^{-1}. These galaxies show a stellar mass – gas metallicity relation which is too high compared to the (sparse)

available evidence. At $z = 0$ roughly half of them are found in small galaxies, the other half having evolved into more massive objects.

We conclude that some feedback mechanism should be at play, causing star formation in these galaxies to be suppressed by strong gas and metal outflows. These metals would then be important polluters of the IGM, and because this pollution takes place before the peak of cosmic star formation, constraining this process is of great importance also for IGM studies. As originally shown by Dekel & Silk (1986), the amount of ejected mass mainly scales with the halo circular velocities, and this is true for most semi-analytic galaxy formation models. In this way, under very simple assumptions, a suppression of these galaxies implies a suppression of star formation in those 10^{12} $M_{\odot}$ halos for which the peak of efficiency of star formation is expected at $z = 0$. Solving this discrepancy requires either some form of feedback that, surprisingly, is most effective at the highest gas densities, or some more exotic solution, like higher SN energy in dense environments with low metallicity, a top-heavy IMF or a not perfectly cold and collisionless dark matter which suppresses such compact halos. Observational breakthroughs able to clarify the phisical processes responsible for the suppression of these "excess" galaxies may be obtained with the future 30-40m optical telescopes, ALMA and JWST; a strong theoretical and numerical effort on this topic should be carried out in the next future to produce predictions that can be tested by future observations.

Bibliography

Abbas, U. & Sheth, R. K. 2006, MNRAS, 372, 1749

Alexander, D. M., Bauer, F. E., Brandt, W. N., et al. 2003, AJ, 126, 539

Allam, S. S., Tucker, D. L., Smith, J. A., et al. 2004, AJ, 127, 1883

Alonso, M. S., Tissera, P. B., Coldwell, G., & Lambas, D. G. 2004, MNRAS, 352, 1081

Ando, M., Ohta, K., Iwata, I., et al. 2007, PASJ, 59, 717

Appleton, P. N., Fadda, D. T., Marleau, F. R., et al. 2004, ApJS, 154, 147

Armus, L., Bernard-Salas, J., Spoon, H. W. W., et al. 2006, ApJ, 640, 204

Armus, L., Charmandaris, V., Bernard-Salas, J., et al. 2007, ApJ, 656, 148

Arnouts, S., Cristiani, S., Moscardini, L., et al. 1999, MNRAS, 310, 540

Baldry, I. K., Balogh, M. L., Bower, R., Glazebrook, K., & Nichol, R. C. 2004a, in American Institute of Physics Conference Series, Vol. 743, The New Cosmology: Conference on Strings and Cosmology, ed. R. E. Allen, D. V. Nanopoulos, & C. N. Pope, 106–119

Baldry, I. K. & Glazebrook, K. 2003, ApJ, 593, 258

Baldry, I. K., Glazebrook, K., Brinkmann, J., et al. 2004b, ApJ, 600, 681

Balogh, M. L., Baldry, I. K., Nichol, R., et al. 2004, apjl, 615, L101

Balogh, M. L., Morris, S. L., Yee, H. K. C., Carlberg, R. G., & Ellingson, E. 1999, ApJ, 527, 54

Barton, E. J., Arnold, J. A., Zentner, A. R., Bullock, J. S., & Wechsler, R. H. 2007, ApJ, 671, 1538

Barton, E. J., Geller, M. J., & Kenyon, S. J. 2000, ApJ, 530, 660

Bauer, A. E., Drory, N., Hill, G. J., & Feulner, G. 2005, ApJ, 621, L89

Bauer, F. E., Yan, L., Sajina, A., & Alexander, D. M. 2010, ApJ, 710, 212

Baugh, C. M. 2006, Reports of Progress in Physics, 69, 3101

Baugh, C. M., Lacey, C. G., Frenk, C. S., et al. 2005, MNRAS, 356, 1191

Beckwith, S. V. W., Stiavelli, M., Koekemoer, A. M., et al. 2006, AJ, 132, 1729

Bell, E. F. & de Jong, R. S. 2001, ApJ, 550, 212

Bell, E. F., McIntosh, D. H., Katz, N., & Weinberg, M. D. 2003, ApJS, 149, 289

Bell, E. F., Papovich, C., Wolf, C., et al. 2005, ApJ, 625, 23

Bell, E. F., Wolf, C., Meisenheimer, K., et al. 2004, ApJ, 608, 752

Bender, R., Burstein, D., & Faber, S. M. 1992, ApJ, 399, 462

Bendo, G. J., Wilson, C. D., Pohlen, M., et al. 2010, A&A, 518, L65

Bertelli, G., Bressan, A., Chiosi, C., Fagotto, F., & Nasi, E. 1994, A&AS, 106, 275

Bertin, E. & Arnouts, S. 1996, A&AS, 117, 393

Bertoldi, F., Carilli, C., Aravena, M., et al. 2007, ApJS, 172, 132

Bessell, M. S., Brett, J. M., Scholz, M., & Wood, P. R. 1991, A&AS, 89, 335

Blain, A. W. & Longair, M. S. 1993, MNRAS, 264, 509

Blain, A. W., Smail, I., Ivison, R. J., Kneib, J.-P., & Frayer, D. T. 2002, Phys. Rep., 369, 111

Blaizot, J., Guiderdoni, B., Devriendt, J. E. G., et al. 2004, MNRAS, 352, 571

Blanton, M. R., Lupton, R. H., Schlegel, D. J., et al. 2005, apj, 631, 208

Blitz, L. & Rosolowsky, E. 2004, ApJ, 612, L29

Bolzonella, M., Miralles, J.-M., & Pelló, R. 2000, A&A, 363, 476

Boquien, M., Calzetti, D., Kennicutt, R., et al. 2009, ApJ, 706, 553

Boulanger, F., Abergel, A., Bernard, J. P., et al. 1998, in Astronomical Society of the Pacific Conference Series, Vol. 132, Star Formation with the Infrared Space Observatory, ed. J. Yun & L. Liseau, 15

Boulanger, F., Abergel, A., Cesarsky, D., et al. 2000, in ESA Special Publication, Vol. 455, ISO Beyond Point Sources: Studies of Extended Infrared Emission, ed. R. J. Laureijs, K. Leech, & M. F. Kessler, 91

Bournaud, F., Elmegreen, B. G., Teyssier, R., Block, D. L., & Puerari, I. 2010, MNRAS, 409, 1088

Bouwens, R. J., Illingworth, G. D., Franx, M., et al. 2009, ApJ, 705, 936

Bouwens, R. J., Illingworth, G. D., Franx, M., & Ford, H. 2007, ApJ, 670, 928

Bowen, G. H. & Willson, L. A. 1991, ApJ, 375, L53

Brandl, B. R., Bernard-Salas, J., Spoon, H. W. W., et al. 2006, ApJ, 653, 1129

Braun, R., Popping, A., Brooks, K., & Combes, F. 2011, MNRAS, 416, 2600

Bressan, A., Chiosi, C., & Fagotto, F. 1994, ApJS, 94, 63

Bressan, A., Granato, G. L., & Silva, L. 1998, A&A, 332, 135

Bressan, A., Silva, L., & Granato, G. L. 2002, A&A, 392, 377

Brinchmann, J. & Ellis, R. S. 2000, ApJ, 536, L77

Bruzual, G. & Charlot, S. 2003, MNRAS, 344, 1000

Bruzual A., G. 1983, ApJ, 273, 105

Buat, V., Donas, J., Milliard, B., & Xu, C. 1999, A&A, 352, 371

Buat, V., Giovannoli, E., Burgarella, D., et al. 2010, MNRAS, 409, L1

Buat, V., Giovannoli, E., Heinis, S., et al. 2011a, A&A, 533, A93

Buat, V., Giovannoli, E., Takeuchi, T. T., et al. 2011b, A&A, 529, A22

Buat, V., Iglesias-Páramo, J., Seibert, M., et al. 2005, ApJ, 619, L51

Buat, V., Noll, S., Burgarella, D., et al. 2012, A&A, 545, A141

Buat, V. & Xu, C. 1996, A&A, 306, 61

Burgarella, D., Buat, V., & Iglesias-Páramo, J. 2005a, MNRAS, 360, 1413

Burgarella, D., Buat, V., & Iglesias-Páramo, J. 2005b, MNRAS, 360, 1413

Calura, F., Pipino, A., & Matteucci, F. 2008, A&A, 479, 669

Calzetti, D. 2001, New Astron. Rev., 45, 601

Calzetti, D., Armus, L., Bohlin, R. C., et al. 2000, ApJ, 533, 682

Calzetti, D., Kennicutt, R. C., Engelbracht, C. W., et al. 2007, ApJ, 666, 870

Calzetti, D., Kinney, A. L., & Storchi-Bergmann, T. 1994, ApJ, 429, 582

Capak, P., Aussel, H., Ajiki, M., et al. 2007, ApJS, 172, 99

Caputi, K. I., Dunlop, J. S., McLure, R. J., & Roche, N. D. 2004, MNRAS, 353, 30

Caputi, K. I., Lagache, G., Yan, L., et al. 2007, ApJ, 660, 97

Caputi, K. I., McLure, R. J., Dunlop, J. S., Cirasuolo, M., & Schael, A. M. 2006, MNRAS, 366, 609

Cardelli, J. A., Clayton, G. C., & Mathis, J. S. 1989, ApJ, 345, 245

Carilli, C. L. & Yun, M. S. 2000, ApJ, 530, 618

Cassisi, S. 2004, in Astronomical Society of the Pacific Conference Series, Vol. 310, IAU Colloq. 193: Variable Stars in the Local Group, ed. D. W. Kurtz & K. R. Pollard, 489

Cassisi, S., Castellani, M., & Castellani, V. 1997, A&A, 317, 108

Cassisi, S., Marín-Franch, A., Salaris, M., et al. 2011, A&A, 527, A59

Cava, A., Rodighiero, G., Pérez-Fournon, I., et al. 2010, MNRAS, 409, L19

Cenarro, A. J., Peletier, R. F., Sánchez-Blázquez, P., et al. 2007, MNRAS, 374, 664

Chabrier, G. 2001, ApJ, 554, 1274

Chabrier, G. 2003, ApJ, 586, L133

Chapman, S. C., Blain, A. W., Smail, I., & Ivison, R. J. 2005, ApJ, 622, 772

Charlot, S. & Bruzual, A. G. 1991, ApJ, 367, 126

Chary, R. & Elbaz, D. 2001, ApJ, 556, 562

Chiosi, C., Bertelli, G., & Bressan, A. 1988, A&A, 196, 84

Cimatti, A., Cassata, P., Pozzetti, L., et al. 2008, A&A, 482, 21

Cimatti, A., Daddi, E., Mignoli, M., et al. 2002, A&A, 381, L68

Cirasuolo, M., McLure, R. J., Dunlop, J. S., et al. 2008, ArXiv e-prints, 804

Coelho, P. 2009, in American Institute of Physics Conference Series, Vol. 1111, American Institute of Physics Conference Series, ed. G. Giobbi, A. Tornambe, G. Raimondo, M. Limongi, L. A. Antonelli, N. Menci, & E. Brocato, 67–74

Coelho, P., Barbuy, B., Meléndez, J., Schiavon, R. P., & Castilho, B. V. 2005, A&A, 443, 735

Coelho, P., Bruzual, G., Charlot, S., et al. 2007, MNRAS, 382, 498

Collison, A. J. & Fix, J. D. 1991, ApJ, 368, 545

Combes, F. 2013, ArXiv e-prints

Condon, J. J. 1974, ApJ, 188, 279

Condon, J. J. 1992, in American Institute of Physics Conference Series, Vol. 254, American Institute of Physics Conference Series, ed. S. S. Holt, S. G. Neff, & C. M. Urry, 629–639

Condon, J. J., Anderson, M. L., & Helou, G. 1991, ApJ, 376, 95

Condon, J. J. & Yin, Q. F. 1990, ApJ, 357, 97

Conroy, C. 2010, MNRAS, 404, 247

Conroy, C. 2013, ArXiv e-prints

Conroy, C. & Gunn, J. E. 2010, ApJ, 712, 833

Conroy, C., Gunn, J. E., & White, M. 2009, ApJ, 699, 486

Conroy, C. & van Dokkum, P. G. 2012, ApJ, 760, 71

Conroy, C., Wechsler, R. H., & Kravtsov, A. V. 2007, ApJ, 668, 826

Contursi, A., Lequeux, J., Cesarsky, D., et al. 2000, A&A, 362, 310

Cortese, L., Boselli, A., Buat, V., et al. 2006, ApJ, 637, 242

Cowie, L. L., Barger, A. J., Hu, E. M., Capak, P., & Songaila, A. 2004, AJ, 127, 3137

da Cunha, E., Charlot, S., & Elbaz, D. 2008, MNRAS, 388, 1595

da Cunha, E., Charmandaris, V., Díaz-Santos, T., et al. 2010, A&A, 523, A78

Daddi, E., Alexander, D. M., Dickinson, M., et al. 2007a, ApJ, 670, 173

Daddi, E., Bournaud, F., Walter, F., et al. 2010a, ApJ, 713, 686

Daddi, E., Cimatti, A., Renzini, A., et al. 2004, ApJ, 617, 746

Daddi, E., Dannerbauer, H., Elbaz, D., et al. 2008, ApJ, 673, L21

Daddi, E., Dickinson, M., Morrison, G., et al. 2007b, ApJ, 670, 156

Daddi, E., Elbaz, D., Walter, F., et al. 2010b, ApJ, 714, L118

Dale, D. A. & Helou, G. 2002, ApJ, 576, 159

Dale, D. A., Helou, G., Contursi, A., Silbermann, N. A., & Kolhatkar, S. 2001, ApJ, 549, 215

Dannerbauer, H., Daddi, E., Riechers, D. A., et al. 2009, ApJ, 698, L178

Dasyra, K. M., Tacconi, L. J., Davies, R. I., et al. 2006, ApJ, 651, 835

Dasyra, K. M., Yan, L., Helou, G., et al. 2008, ApJ, 680, 232

Davis, M., Newman, J., Faber, S., & Phillips, A. 2000, The DEEP2 Redshift Survey

de Graauw, T., Helmich, F. P., Phillips, T. G., et al. 2010, A&A, 518, L6

de Jong, T., Klein, U., Wielebinski, R., & Wunderlich, E. 1985, A&A, 147, L6

De Lucia, G. & Helmi, A. 2008, MNRAS, 391, 14

Dekel, A. & Silk, J. 1986, ApJ, 303, 39

Demarque, P., Woo, J.-H., Kim, Y.-C., & Yi, S. K. 2004, ApJS, 155, 667

Demin, V. V., Dibay, E. A., & Tomov, A. N. 1981, AZh, 58, 925

Demin, V. V., Zasov, A. V., Dibai, E. A., & Tomov, A. N. 1984, Soviet Ast., 28, 367

Desert, F.-X., Boulanger, F., & Puget, J. L. 1990, A&A, 237, 215

Devriendt, J. E. G., Guiderdoni, B., & Sadat, R. 1999, A&A, 350, 381

Dickinson, M., Giavalisco, M., & The Goods Team. 2003, in The Mass of Galaxies at Low and High Redshift, ed. R. Bender & A. Renzini, 324–+

Dole, H., Lagache, G., Puget, J.-L., et al. 2006, A&A, 451, 417

Domingue, D. L., Sulentic, J. W., Xu, C., et al. 2003, AJ, 125, 555

Domingue, D. L., Xu, C. K., Jarrett, T. H., & Cheng, Y. 2009, ApJ, 695, 1559

Draine, B. T. 2003, ApJ, 598, 1017

Draine, B. T. & Lee, H. M. 1984, ApJ, 285, 89

Draine, B. T. & Li, A. 2007, ApJ, 657, 810

Drory, N., Bundy, K., Leauthaud, A., et al. 2009, ApJ, 707, 1595

Dunne, L., Eales, S., Edmunds, M., et al. 2000, MNRAS, 315, 115

Dupac, X., Bernard, J.-P., Boudet, N., et al. 2003, A&A, 404, L11

Dwek, E. 1998, ApJ, 501, 643

Dwek, E., Arendt, R. G., Fixsen, D. J., et al. 1997, ApJ, 475, 565

Eales, S., Dunne, L., Clements, D., et al. 2010, PASP, 122, 499

Efstathiou, A. & Rowan-Robinson, M. 2003, MNRAS, 343, 322

Efstathiou, A., Rowan-Robinson, M., & Siebenmorgen, R. 2000, MNRAS, 313, 734

Egami, E., Dole, H., Huang, J.-S., et al. 2004, ApJS, 154, 130

Eisenstein, D. J. & Hu, W. 1998, ApJ, 496, 605

Elbaz, D., Cesarsky, C. J., Chanial, P., et al. 2002, A&A, 384, 848

Elbaz, D., Daddi, E., Le Borgne, D., et al. 2007, A&A, 468, 33

Elbaz, D., Dickinson, M., Hwang, H. S., et al. 2011, A&A, 533, A119

Eldridge, J. J. & Stanway, E. R. 2012, MNRAS, 419, 479

Ellis, R. S. 2008, Observations of the High Redshift Universe, ed. A. Loeb, A. Ferrara, & R. S. Ellis, 259–364

Ellison, S. L., Patton, D. R., Simard, L., & McConnachie, A. W. 2008, AJ, 135, 1877

Elmegreen, B. G. 2006, ApJ, 648, 572

Erb, D. K. 2007, in EAS Publications Series, Vol. 24, EAS Publications Series, ed. E. Emsellem, H. Wozniak, G. Massacrier, J.-F. Gonzalez, J. Devriendt, & N. Champavert, 191–202

Erb, D. K., Shapley, A. E., Pettini, M., et al. 2006, ApJ, 644, 813

Faber, S. M., Willmer, C. N. A., Wolf, C., et al. 2007, ApJ, 665, 265

Fadda, D., Flores, H., Hasinger, G., et al. 2002, A&A, 383, 838

Fadda, D., Yan, L., Lagache, G., et al. 2010, ApJ, 719, 425

Fagotto, F., Bressan, A., Bertelli, G., & Chiosi, C. 1994, A&AS, 104, 365

Fazio, G. G., Hora, J. L., Allen, L. E., et al. 2004, ApJS, 154, 10

Ferraro, F. R., Origlia, L., Testa, V., & Maraston, C. 2004, ApJ, 608, 772

Ferreras, I., Pasquali, A., Malhotra, S., et al. 2009, ApJ, 706, 158

Finlator, K., Davé, R., & Oppenheimer, B. D. 2007, MNRAS, 376, 1861

Finlator, K., Davé, R., Papovich, C., & Hernquist, L. 2006, ApJ, 639, 672

Fioc, M. & Rocca-Volmerange, B. 1997, A&A, 326, 950

Fluks, M. A., Plez, B., The, P. S., et al. 1994, A&AS, 105, 311

Fontana, A., Salimbeni, S., Grazian, A., et al. 2006, A&A, 459, 745

Fontanot, F., Cristiani, S., Santini, P., et al. 2012, MNRAS, 421, 241

Fontanot, F., De Lucia, G., Monaco, P., Somerville, R. S., & Santini, P. 2009a, MNRAS, 397, 1776

Fontanot, F., Monaco, P., Cristiani, S., & Tozzi, P. 2006, MNRAS, 373, 1173

Fontanot, F., Monaco, P., Silva, L., & Grazian, A. 2007, MNRAS, 382, 903

Fontanot, F., Somerville, R. S., Silva, L., Monaco, P., & Skibba, R. 2009b, MNRAS, 392, 553

Fontanot, F., Somerville, R. S., Silva, L., Monaco, P., & Skibba, R. 2009c, MNRAS, 392, 553

Franceschini, A. 2000, ArXiv Astrophysics e-prints

Franceschini, A., Aussel, H., Bressan, A., et al. 1997, in ESA Special Publication, Vol. 401, The Far Infrared and Submillimetre Universe., ed. A. Wilson, 159

Franceschini, A., Aussel, H., Cesarsky, C. J., Elbaz, D., & Fadda, D. 2001, A&A, 378, 1

Franceschini, A., Mazzei, P., de Zotti, G., & Danese, L. 1994, ApJ, 427, 140

Franceschini, A., Rodighiero, G., Vaccari, M., et al. 2009, ArXiv e-prints

Franx, M., Labbé, I., Rudnick, G., et al. 2003, ApJ, 587, L79

Frayer, D. T., Fadda, D., Yan, L., et al. 2006a, AJ, 131, 250

Frayer, D. T., Huynh, M. T., Chary, R., et al. 2006b, ApJ, 647, L9

Frayer, D. T., Sanders, D. B., Surace, J. A., et al. 2009, AJ, 138, 1261

Frogel, J. A., Terndrup, D. M., Blanco, V. M., & Whitford, A. E. 1990, ApJ, 353, 494

Galliano, F., Madden, S. C., Jones, A. P., et al. 2003, A&A, 407, 159

Gao, L., Navarro, J. F., Cole, S., et al. 2008, MNRAS, 387, 536

Garrett, M. A. 2001, in Astronomical Society of the Pacific Conference Series, Vol. 249, The Central Kiloparsec of Starbursts and AGN: The La Palma Connection, ed. J. H. Knapen, J. E. Beckman, I. Shlosman, & T. J. Mahoney, 652

Garrett, M. A. 2002, A&A, 384, L19

Garrett, M. A., Wrobel, J. M., & Morganti, R. 2003, New Astron. Rev., 47, 385

Gavazzi, G., Bonfanti, C., Sanvito, G., Boselli, A., & Scodeggio, M. 2002, ApJ, 576, 135

Gawiser, E., van Dokkum, P. G., Herrera, D., et al. 2006, ApJS, 162, 1

Genzel, R. & Cesarsky, C. J. 2000, ARA&A, 38, 761

Genzel, R., Lutz, D., Sturm, E., et al. 1998, ApJ, 498, 579

Genzel, R., Tacconi, L. J., Gracia-Carpio, J., et al. 2010, MNRAS, 407, 2091

Giallongo, E., Salimbeni, S., Menci, N., et al. 2005, apj, 622, 116

Giavalisco, M., Ferguson, H. C., Koekemoer, A. M., et al. 2004, ApJ, 600, L93

Girardi, L., Bressan, A., Bertelli, G., & Chiosi, C. 2000, A&AS, 141, 371

Gordon, K. D., Calzetti, D., & Witt, A. N. 1997, ApJ, 487, 625

Granato, G. L. & Danese, L. 1994, MNRAS, 268, 235

Granato, G. L., Lacey, C. G., Silva, L., et al. 2000, ApJ, 542, 710

Grazian, A., Fontana, A., de Santis, C., et al. 2006, A&A, 449, 951

Gregg, M. D., Silva, D., Rayner, J., et al. 2004, in Bulletin of the American Astronomical Society, Vol. 36, American Astronomical Society Meeting Abstracts, 1496

Greggio, L. & Renzini, A. 2011, Stellar Populations. A User Guide from Low to High Redshift

Greve, T. R., Bertoldi, F., Smail, I., et al. 2005, MNRAS, 359, 1165

Griffin, M. J., Abergel, A., Abreu, A., et al. 2010, A&A, 518, L3

Groves, B., Dopita, M. A., Sutherland, R. S., et al. 2008, ApJS, 176, 438

Guhathakurta, P. & Draine, B. T. 1989, ApJ, 345, 230

Guo, Q. & White, S. D. M. 2008, ArXiv e-prints

Guzman, R., Gallego, J., Koo, D. C., et al. 1997, ApJ, 489, 559

Harford, A. G. & Gnedin, N. Y. 2003, ApJ, 597, 74

Harwit, M. & Pacini, F. 1975, ApJ, 200, L127

Hatziminaoglou, E., Omont, A., Stevens, J. A., et al. 2010, A&A, 518, L33

Helou, G. 1986, ApJ, 311, L33

Helou, G., Soifer, B. T., & Rowan-Robinson, M. 1985, ApJ, 298, L7

Hernández-Toledo, H. M. & Puerari, I. 2001, A&A, 379, 54

Hirashita, H., Buat, V., & Inoue, A. K. 2003, A&A, 410, 83

Hogg, D. W. 2001, AJ, 121, 1207

Holmberg, E. 1958, Meddelanden fran Lunds Astronomiska Observatorium Serie II, 136, 1

Hony, S., Van Kerckhoven, C., Peeters, E., et al. 2001, A&A, 370, 1030

Hopkins, A. M. 2004, ApJ, 615, 209

Hopkins, A. M. & Beacom, J. F. 2006, ApJ, 651, 142

Houck, J. R., Roellig, T. L., van Cleve, J., et al. 2004, ApJS, 154, 18

Howell, J. H., Armus, L., Mazzarella, J. M., et al. 2010, ApJ, 715, 572

Hoyle, F. 1949, Nature, 163, 196

Hoyle, F. & Wickramasinghe, N. C. 1991, Earth Moon and Planets, 52, 161

Hughes, D. H., Serjeant, S., Dunlop, J., et al. 1998, Nature, 394, 241

Hummel, E., Davies, R. D., Pedlar, A., Wolstencroft, R. D., & van der Hulst, J. M. 1988, A&A, 199, 91

Iglesias-Páramo, J., Buat, V., Takeuchi, T. T., et al. 2006, ApJS, 164, 38

Ilbert, O., Capak, P., Salvato, M., et al. 2009, ApJ, 690, 1236

Ilbert, O., Salvato, M., Le Floc'h, E., et al. 2010, ApJ, 709, 644

Ivison, R. J., Alexander, D. M., Biggs, A. D., et al. 2010, MNRAS, 402, 245

Ivison, R. J., Greve, T. R., Dunlop, J. S., et al. 2007, MNRAS, 380, 199

Jarrett, T. H., Chester, T., Cutri, R., et al. 2000, AJ, 119, 2498

Jonsson, P. 2006, MNRAS, 372, 2

Joseph, R. D., Meikle, W. P. S., Robertson, N. A., & Wright, G. S. 1984, MNRAS, 209, 111

Kannappan, S. J. & Gawiser, E. 2007, ApJ, 657, L5

Karim, A., Schinnerer, E., Martínez-Sansigre, A., et al. 2011, ApJ, 730, 61

Kartaltepe, J. S., Sanders, D. B., Scoville, N. Z., et al. 2007, ApJS, 172, 320

Kauffmann, G., Heckman, T. M., White, S. D. M., et al. 2003, MNRAS, 341, 54

Keller, S. C. & Wood, P. R. 2006, ApJ, 642, 834

Kennicutt, Jr., R. C. 1983, ApJ, 272, 54

Kennicutt, Jr., R. C. 1998, ApJ, 498, 541

Kennicutt, Jr., R. C., Armus, L., Bendo, G., et al. 2003, PASP, 115, 928

Kennicutt, Jr., R. C., Roettiger, K. A., Keel, W. C., van der Hulst, J. M., & Hummel, E. 1987, AJ, 93, 1011

Kereš, D., Katz, N., Fardal, M., Davé, R., & Weinberg, D. H. 2009, MNRAS, 395, 160

Kimm, T., Somerville, R. S., Yi, S. K., et al. 2008, ArXiv e-prints

Kitzbichler, M. G. & White, S. D. M. 2007, MNRAS, 376, 2

Klein, U. & Graeve, R. 1986, A&A, 161, 155

Klein, U., Wielebinski, R., & Morsi, H. W. 1988, A&A, 190, 41

Koekemoer, A. M., Aussel, H., Calzetti, D., et al. 2007, ApJS, 172, 196

Kormendy, J. & Sanders, D. B. 1992, ApJ, 390, L53

Kriek, M., van Dokkum, P. G., Franx, M., et al. 2008, ApJ, 677, 219

Kroupa, P. 2001, MNRAS, 322, 231

Kroupa, P., Tout, C. A., & Gilmore, G. 1993, MNRAS, 262, 545

Krugel, E. & Siebenmorgen, R. 1994, A&A, 282, 407

Kurczynski, P., Gawiser, E., Huynh, M., et al. 2012, ApJ, 750, 117

Kurucz, R. L. 1992, in IAU Symposium, Vol. 149, The Stellar Populations of Galaxies, ed. B. Barbuy & A. Renzini, 225

Kurucz, R. L. 1993, VizieR Online Data Catalog, 6039, 0

Kurucz, R. L. 2005, Memorie della Societa Astronomica Italiana Supplementi, 8, 86

Labbé, I., Huang, J., Franx, M., et al. 2005, ApJ, 624, L81

Lacki, B. C. & Thompson, T. A. 2010, ApJ, 717, 196

Lada, C. J. & Adams, F. C. 1992, ApJ, 393, 278

Lagache, G., Dole, H., & Puget, J.-L. 2003, MNRAS, 338, 555

Lagache, G., Dole, H., Puget, J.-L., et al. 2004, ApJS, 154, 112

Lambas, D. G., Tissera, P. B., Alonso, M. S., & Coldwell, G. 2003, MNRAS, 346, 1189

Lançon, A., Hauschildt, P. H., Ladjal, D., & Mouhcine, M. 2007, A&A, 468, 205

Lançon, A., Mouhcine, M., Fioc, M., & Silva, D. 1999, A&A, 344, L21

Laor, A. & Draine, B. T. 1993, ApJ, 402, 441

Larson, R. B. 1998, MNRAS, 301, 569

Larson, R. B. & Tinsley, B. M. 1978, ApJ, 219, 46

Le Borgne, J. F., Paschke, A., Vandenbroere, J., et al. 2007, A&A, 476, 307

Le Fèvre, O., Vettolani, G., Garilli, B., et al. 2005, A&A, 439, 845

Le Fèvre, O., Vettolani, G., Paltani, S., et al. 2004, A&A, 428, 1043

Le Floc'h, E., Papovich, C., Dole, H., et al. 2005, ApJ, 632, 169

Lee, K.-S., Alberts, S., Atlee, D., et al. 2012, ApJ, 758, L31

Lee, S.-K., Ferguson, H. C., Somerville, R. S., Wiklind, T., & Giavalisco, M. 2010, ApJ, 725, 1644

Lee, S.-K., Idzi, R., Ferguson, H. C., et al. 2008, ArXiv e-prints

Lee, S.-K., Idzi, R., Ferguson, H. C., et al. 2009, ApJS, 184, 100

Leger, A., D'Hendecourt, L., & Defourneau, D. 1989, A&A, 216, 148

Leger, A. & Puget, J. L. 1984, A&A, 137, L5

Leitherer, C. & Heckman, T. M. 1995, ApJS, 96, 9

Leitherer, C., Ortiz Otálvaro, P. A., Bresolin, F., et al. 2010, ApJS, 189, 309

Lejeune, T. & Schaerer, D. 2001, A&A, 366, 538

Li, A. & Draine, B. T. 2001, in Bulletin of the American Astronomical Society, Vol. 33, American Astronomical Society Meeting Abstracts, 1451

Li, Y., Calzetti, D., Kennicutt, R. C., et al. 2010, ApJ, 725, 677

Lo Faro, B., Franceschini, A., Vaccari, M., et al. 2013, ApJ, 762, 108

Lo Faro, B., Monaco, P., Vanzella, E., et al. 2009, MNRAS, 399, 827

Longhetti, M. & Saracco, P. 2009, MNRAS, 394, 774

Lonsdale, C., Polletta, M. d. C., Surace, J., et al. 2004, ApJS, 154, 54

Lonsdale, C. J., Farrah, D., & Smith, H. E. 2006, Ultraluminous Infrared Galaxies, ed. J. W. Mason, 285

Lonsdale, C. J., Lonsdale, C. J., Smith, H. E., & Diamond, P. J. 2003, ApJ, 592, 804

Lonsdale Persson, C. J. & Helou, G. 1987, ApJ, 314, 513

Lotz, J. M., Davis, M., Faber, S. M., et al. 2008, ApJ, 672, 177

Lotz, J. M., Primack, J., & Madau, P. 2004, AJ, 128, 163

Marigo, P., Bressan, A., & Chiosi, C. 1996, A&A, 313, 545

Marigo, P. & Girardi, L. 2007, A&A, 469, 239

Marigo, P., Girardi, L., Bressan, A., et al. 2008, A&A, 482, 883

Marinoni, C., Monaco, P., Giuricin, G., & Costantini, B. 1999, apj, 521, 50

Marleau, F. R., Fadda, D., Storrie-Lombardi, L. J., et al. 2004, ApJS, 154, 66

Martins, L. P. & Coelho, P. 2007, MNRAS, 381, 1329

Martins, L. P., González Delgado, R. M., Leitherer, C., Cerviño, M., & Hauschildt, P. 2005, MNRAS, 358, 49

Mathis, J. S. 1990, ARA&A, 28, 37

Matsuura, S., Shirahata, M., Kawada, M., et al. 2011, ApJ, 737, 2

Matteucci, F. 1996, Fund. Cosmic Phys., 17, 283

Mattila, K., Lemke, D., Haikala, L. K., et al. 1996, A&A, 315, L353

Melbourne, J., Williams, B. F., Dalcanton, J. J., et al. 2012, ApJ, 748, 47

Menci, N., Cavaliere, A., Fontana, A., Giallongo, E., & Poli, F. 2002, ApJ, 575, 18

Menci, N., Fontana, A., Giallongo, E., & Salimbeni, S. 2005, apj, 632, 49

Meurer, G. R., Heckman, T. M., & Calzetti, D. 1999, ApJ, 521, 64

Meurer, G. R., Heckman, T. M., Leitherer, C., et al. 1995, AJ, 110, 2665

Mezger, P. G. & Henderson, A. P. 1967, ApJ, 147, 471

Michałowski, M. J., Dunlop, J. S., Cirasuolo, M., et al. 2012, A&A, 541, A85

Mignoli, M., Cimatti, A., Zamorani, G., et al. 2005, A&A, 437, 883

Miller, G. E. & Scalo, J. M. 1979, ApJS, 41, 513

Miller, N. A., Bonzini, M., Fomalont, E. B., et al. 2013, VizieR Online Data Catalog, 220, 50013

Mobasher, B., Capak, P., Scoville, N. Z., et al. 2007, ApJS, 172, 117

Monaco, P. 2004, MNRAS, 352, 181

Monaco, P. & Fontanot, F. 2005, MNRAS, 359, 283

Monaco, P., Fontanot, F., & Taffoni, G. 2007, MNRAS, 375, 1189

Monaco, P., Murante, G., Borgani, S., & Fontanot, F. 2006, ApJ, 652, L89

Monaco, P., Theuns, T., & Taffoni, G. 2002a, MNRAS, 331, 587

Monaco, P., Theuns, T., Taffoni, G., et al. 2002b, ApJ, 564, 8

Morrison, G. E., Owen, F. N., Dickinson, M., Ivison, R. J., & Ibar, E. 2010, ApJS, 188, 178

Murphy, E. J., Chary, R.-R., Alexander, D. M., et al. 2009, ApJ, 698, 1380

Murphy, E. J., Chary, R.-R., Dickinson, M., et al. 2011a, ApJ, 732, 126

Murphy, E. J., Condon, J. J., Schinnerer, E., et al. 2011b, ApJ, 737, 67

Murphy, E. J., Helou, G., Braun, R., et al. 2006, ApJ, 651, L111

Murphy, E. J., Helou, G., Kenney, J. D. P., Armus, L., & Braun, R. 2008, ApJ, 678, 828

Muzzin, A., Marchesini, D., van Dokkum, P. G., et al. 2009, ApJ, 701, 1839

Nagamine, K. 2002, ApJ, 564, 73

Nagamine, K., Ouchi, M., Springel, V., & Hernquist, L. 2008, ArXiv e-prints

Nagamine, K., Springel, V., Hernquist, L., & Machacek, M. 2004, MNRAS, 350, 385

Night, C., Nagamine, K., Springel, V., & Hernquist, L. 2006, MNRAS, 366, 705

Nikolic, B., Cullen, H., & Alexander, P. 2004, MNRAS, 355, 874

Noeske, K. G., Faber, S. M., Weiner, B. J., et al. 2007a, ApJ, 660, L47

Noeske, K. G., Weiner, B. J., Faber, S. M., et al. 2007b, ApJ, 660, L43

Noll, S., Pierini, D., Cimatti, A., et al. 2009, A&A, 499, 69

Nordon, R., Lutz, D., Genzel, R., et al. 2012, ApJ, 745, 182

Nordstroem, B., Andersen, J., & Andersen, M. I. 1997, A&A, 322, 460

Oesch, P. A., Stiavelli, M., Carollo, C. M., et al. 2007, ApJ, 671, 1212

Oliver, S. J., Bock, J., Altieri, B., et al. 2012, MNRAS, 424, 1614

Omont, A. 1986, A&A, 164, 159

Overzier, R., Guo, Q., Kauffmann, G., et al. 2008, ArXiv e-prints

Panagia, N. 2003, Chinese Journal of Astronomy and Astrophysics Supplement, 3, 64

Pannella, M., Carilli, C. L., Daddi, E., et al. 2009, ApJ, 698, L116

Panuzzo, P., Bressan, A., Granato, G. L., Silva, L., & Danese, L. 2003, A&A, 409, 99

Panuzzo, P., Granato, G. L., Buat, V., et al. 2007, MNRAS, 375, 640

Papovich, C., Dickinson, M., & Ferguson, H. C. 2001, ApJ, 559, 620

Papovich, C., Finkelstein, S. L., Ferguson, H. C., Lotz, J. M., & Giavalisco, M. 2011, MNRAS, 412, 1123

Papovich, C., Moustakas, L. A., Dickinson, M., et al. 2006, ApJ, 640, 92

Patanchon, G., Ade, P. A. R., Bock, J. J., et al. 2009, ApJ, 707, 1750

Patton, D. R., Ellison, S. L., Simard, L., McConnachie, A. W., & Mendel, J. T. 2011, MNRAS, 412, 591

Pauldrach, A. W. A., Hoffmann, T. L., & Lennon, M. 2001, A&A, 375, 161

Peeters, E., Spoon, H. W. W., & Tielens, A. G. G. M. 2004, ApJ, 613, 986

Pellerin, A. & Finkelstein, S. L. 2010, in IAU Symposium, Vol. 262, IAU Symposium, ed. G. R. Bruzual & S. Charlot, 283–286

Peng, Y.-j., Lilly, S. J., Kovač, K., et al. 2010, ApJ, 721, 193

Peng, Y.-j., Lilly, S. J., Renzini, A., & Carollo, M. 2012, ApJ, 757, 4

Pérez-González, P. G., Rieke, G. H., Egami, E., et al. 2005, ApJ, 630, 82

Pettini, M., Shapley, A. E., Steidel, C. C., et al. 2001, ApJ, 554, 981

Pforr, J., Maraston, C., & Tonini, C. 2012, MNRAS, 422, 3285

Pietrinferni, A., Cassisi, S., Salaris, M., Percival, S., & Ferguson, J. W. 2009, ApJ, 697, 275

Pilbratt, G. L., Riedinger, J. R., Passvogel, T., et al. 2010, A&A, 518, L1

Piovan, L., Tantalo, R., & Chiosi, C. 2006, MNRAS, 370, 1454

Poggianti, B. M., Bressan, A., & Franceschini, A. 2001, ApJ, 550, 195

Poggianti, B. M. & Wu, H. 2000, ApJ, 529, 157

Poglitsch, A., Waelkens, C., Geis, N., et al. 2010, A&A, 518, L2

Poli, F., Giallongo, E., Fontana, A., et al. 2003, ApJ, 593, L1

Poli, F., Menci, N., Giallongo, E., et al. 2001, ApJ, 551, L45

Popescu, C. C., Misiriotis, A., Kylafis, N. D., Tuffs, R. J., & Fischera, J. 2000, A&A, 362, 138

Popescu, C. C., Tuffs, R. J., Dopita, M. A., et al. 2011, A&A, 527, A109

Popesso, P., Dickinson, M., Nonino, M., et al. 2009, A&A, 494, 443

Portinari, L., Chiosi, C., & Bressan, A. 1998, A&A, 334, 505

Powell, L. C., Bournaud, F., Chapon, D., et al. 2011, in IAU Symposium, Vol. 277, IAU Symposium, ed. C. Carignan, F. Combes, & K. C. Freeman, 234–237

Pozzi, F., Gruppioni, C., Oliver, S., et al. 2004, ApJ, 609, 122

Pozzi, F., Vignali, C., Gruppioni, C., et al. 2012, MNRAS, 423, 1909

Prugniel, P., Koleva, M., Ocvirk, P., Le Borgne, D., & Soubiran, C. 2007, in IAU Symposium, Vol. 241, IAU Symposium, ed. A. Vazdekis & R. Peletier, 68–72

Prugniel, P. & Soubiran, C. 2001, A&A, 369, 1048

Puget, J. L. & Leger, A. 1989, ARA&A, 27, 161

Ranalli, P., Comastri, A., & Setti, G. 2003, A&A, 399, 39

Rangwala, N., Maloney, P. R., Glenn, J., et al. 2011, ApJ, 743, 94

Reddy, N. A. & Steidel, C. C. 2008, ArXiv e-prints

Reddy, N. A., Steidel, C. C., Fadda, D., et al. 2006, ApJ, 644, 792

Reduzzi, L. & Rampazzo, R. 1995, Astrophysical Letters and Communications, 30, 1

Renzini, A. 2006, ARA&A, 44, 141

Renzini, A. 2009, MNRAS, 398, L58

Renzini, A. & Buzzoni, A. 1986, in Astrophysics and Space Science Library, Vol. 122, Spectral Evolution of Galaxies, ed. C. Chiosi & A. Renzini, 195–231

Renzini, A., Greggio, L., Ritossa, C., & Ferrario, L. 1992, ApJ, 400, 280

Reshetnikov, V. P. 1998, Astronomy Letters, 24, 153

Rieke, G. H., Alonso-Herrero, A., Weiner, B. J., et al. 2009, ApJ, 692, 556

Rieke, G. H., Young, E. T., Engelbracht, C. W., et al. 2004, ApJS, 154, 25

Rix, H.-W., Barden, M., Beckwith, S. V. W., et al. 2004, ApJS, 152, 163

Rodighiero, G., Cimatti, A., Franceschini, A., et al. 2007, A&A, 470, 21

Rodighiero, G., Daddi, E., Baronchelli, I., et al. 2011, ApJ, 739, L40

Rodighiero, G., Vaccari, M., Franceschini, A., et al. 2010, A&A, 515, A8

Roseboom, I. G., Oliver, S., Parkinson, D., & Vaccari, M. 2009, MNRAS, 400, 1062

Roseboom, I. G., Oliver, S. J., Kunz, M., et al. 2010, MNRAS, 409, 48

Rowan-Robinson, M. 1980, ApJS, 44, 403

Rowan-Robinson, M. 2001, ApJ, 549, 745

Rowan-Robinson, M. 2009, MNRAS, 394, 117

Rowan-Robinson, M. 2012, in IAU Symposium, Vol. 284, IAU Symposium, ed. R. J. Tuffs & C. C. Popescu, 446–455

Rowan-Robinson, M., Babbedge, T., Surace, J., et al. 2005, AJ, 129, 1183

Rowan-Robinson, M. & Crawford, J. 1989, MNRAS, 238, 523

Rowan-Robinson, M., Roseboom, I. G., Vaccari, M., et al. 2010, MNRAS, 409, 2

Rujopakarn, W., Rieke, G. H., Eisenstein, D. J., & Juneau, S. 2011, ApJ, 726, 93

Rybicki, G. B. & Lightman, A. P. 1979, Radiative processes in astrophysics

Salpeter, E. E. 1955, ApJ, 121, 161

Sánchez-Blázquez, P., Peletier, R. F., Jiménez-Vicente, J., et al. 2006, MNRAS, 371, 703

Sanders, D. B. & Mirabel, I. F. 1996, ARA&A, 34, 749

Santini, P. & et al. 2008, submitted to A&A

Santini, P., Fontana, A., Grazian, A., et al. 2009, A&A, 504, 751

Santini, P., Maiolino, R., Magnelli, B., et al. 2010, A&A, 518, L154

Sargent, M. T., Schinnerer, E., Murphy, E., et al. 2010, ApJ, 714, L190

Savage, R. S. & Oliver, S. 2007, ApJ, 661, 1339

Savaglio, S., Glazebrook, K., Le Borgne, D., et al. 2005, ApJ, 635, 260

Scalo, J. 1998, ArXiv Astrophysics e-prints

Scalo, J. M. 1986, Fund. Cosmic Phys., 11, 1

Schaller, G., Schaerer, D., Meynet, G., & Maeder, A. 1992, A&AS, 96, 269

Scheuer, P. A. G. 1957, Proceedings of the Cambridge Philosophical Society, 53, 764

Schinnerer, E., Carilli, C. L., Scoville, N. Z., et al. 2004, aj, 128, 1974

Schlegel, D. J., Finkbeiner, D. P., & Davis, M. 1998, ApJ, 500, 525

Schmidt, M. 1959, ApJ, 129, 243

Scoville, N., Abraham, R. G., Aussel, H., et al. 2007, ApJS, 172, 38

Scoville, N. Z. 2012, ArXiv e-prints

Searle, L., Sargent, W. L. W., & Bagnuolo, W. G. 1973, ApJ, 179, 427

Shapley, A. E., Steidel, C. C., Adelberger, K. L., et al. 2001, ApJ, 562, 95

Shapley, A. E., Steidel, C. C., Pettini, M., & Adelberger, K. L. 2003, ApJ, 588, 65

Siebenmorgen, R. & Krügel, E. 2007, A&A, 461, 445

Silva, L. 1999, PhD thesis, SISSA - Trieste, Italy

Silva, L., Granato, G. L., Bressan, A., & Danese, L. 1998, ApJ, 509, 103

Silva, L., Schurer, A., Granato, G. L., et al. 2011, MNRAS, 410, 2043

Simard, L., Mendel, J. T., Patton, D. R., Ellison, S. L., & McConnachie, A. W. 2011, ApJS, 196, 11

Smail, I., Ivison, R. J., Blain, A. W., & Kneib, J.-P. 2002, MNRAS, 331, 495

Smith, J. D. T., Draine, B. T., Dale, D. A., et al. 2007, ApJ, 656, 770

Smith, L. J., Norris, R. P. F., & Crowther, P. A. 2002, MNRAS, 337, 1309

Smith, M. W. L. & Spire Sag2 Consortium. 2011, in Astronomical Society of the Pacific Conference Series, Vol. 446, Galaxy Evolution: Infrared to Millimeter Wavelength Perspective, ed. W. Wang, J. Lu, Z. Luo, Z. Yang, H. Hua, & Z. Chen, 35

Soifer, B. T. 1988, in Bulletin of the American Astronomical Society, Vol. 20, Bulletin of the American Astronomical Society, 1067

Soifer, B. T., Helou, G., & Werner, M. 2008, ARA&A, 46, 201

Soifer, B. T. & Neugebauer, G. 1991, AJ, 101, 354

Somerville, R. S., Hopkins, P. F., Cox, T. J., Robertson, B. E., & Hernquist, L. 2008, MNRAS, 391, 481

Somerville, R. S., Primack, J. R., & Faber, S. M. 2001, MNRAS, 320, 504

Spergel, D. N. 2005, in Astronomical Society of the Pacific Conference Series, Vol. 344, The Cool Universe: Observing Cosmic Dawn, ed. C. Lidman & D. Alloin, 29–+

Spoon, H. W. W., Marshall, J. A., Houck, J. R., et al. 2007, ApJ, 654, L49

Stark, D. P., Ellis, R. S., Bunker, A., et al. 2009, ArXiv e-prints

Stothers, R. B. 1991, ApJ, 383, 820

Stoughton, C., Lupton, R. H., Bernardi, M., et al. 2002, AJ, 123, 485

Strateva, I., Ivezić, Ž., Knapp, G. R., et al. 2001, aj, 122, 1861

Sturm, E., Lutz, D., Tran, D., et al. 2000, A&A, 358, 481

Sullivan, M., Mobasher, B., Chan, B., et al. 2001, ApJ, 558, 72

Surace, J. A., Shupe, D. L., Fang, F., et al. 2005, in Bulletin of the American Astronomical Society, Vol. 37, American Astronomical Society Meeting Abstracts, 1246

Symeonidis, M., Page, M. J., Seymour, N., et al. 2009, MNRAS, 397, 1728

Symeonidis, M., Vaccari, M., Berta, S., et al. 2013, MNRAS, 431, 2317

Szokoly, G. P., Bergeron, J., Hasinger, G., et al. 2004, ApJS, 155, 271

Tacconi, L. J., Genzel, R., Neri, R., et al. 2010, Nature, 463, 781

Taffoni, G., Mayer, L., Colpi, M., & Governato, F. 2003, MNRAS, 341, 434

Taffoni, G., Monaco, P., & Theuns, T. 2002, MNRAS, 333, 623

Takagi, T., Arimoto, N., & Hanami, H. 2003a, MNRAS, 340, 813

Takagi, T., Vansevicius, V., & Arimoto, N. 2003b, PASJ, 55, 385

Takeuchi, T. T., Buat, V., & Burgarella, D. 2005, A&A, 440, L17

Tantalo, R., Chiosi, C., Bressan, A., & Fagotto, F. 1996, A&A, 311, 361

Teplitz, H. I., Chary, R., Elbaz, D., et al. 2011, AJ, 141, 1

Tielens, A. G. G. M., Hony, S., van Kerckhoven, C., & Peeters, E. 1999, in ESA Special Publication, Vol. 427, The Universe as Seen by ISO, ed. P. Cox & M. Kessler, 579

Tinsley, B. M. 1972, A&A, 20, 383

Tinsley, B. M. 1980, Fund. Cosmic Phys., 5, 287

Tomov, A. N. 1978, AZh, 55, 944

Tomov, A. N. 1979, AZh, 56, 949

Tonini, C., Maraston, C., Devriendt, J., Thomas, D., & Silk, J. 2008, ArXiv e-prints

Toomre, A. 1977, ARA&A, 15, 437

Trentham, N., Sampson, L., & Banerji, M. 2005, MNRAS, 357, 783

Tully, R. B. & Fisher, J. R. 1977, aap, 54, 661

Turner, J. L. & Ho, P. T. P. 1983, ApJ, 268, L79

Turner, J. L. & Ho, P. T. P. 1985, ApJ, 299, L77

Turner, J. L. & Ho, P. T. P. 1994, ApJ, 421, 122

Valdes, F., Gupta, R., Rose, J. A., Singh, H. P., & Bell, D. J. 2004, ApJS, 152, 251

van Dokkum, P. G., Franx, M., Förster Schreiber, N. M., et al. 2004, ApJ, 611, 703

VandenBerg, D. A. & Stetson, P. B. 2004, PASP, 116, 997

Vanzella, E., Cristiani, S., Dickinson, M., et al. 2008, A&A, 478, 83

Vanzella, E., Cristiani, S., Dickinson, M., et al. 2006, A&A, 454, 423

Vanzella, E., Giavalisco, M., Dickinson, M., et al. 2009, ArXiv e-prints

Vardanian, R. A. & Tomov, A. N. 1980, Soobshcheniya Byurakanskoj Observatorii Akademiya Nauk Armyanskoj SSR Erevan, 52, 3

Vassiliadis, E. & Wood, P. R. 1993, ApJ, 413, 641

Vega, O., Clemens, M. S., Bressan, A., et al. 2008, A&A, 484, 631

Vega, O., Silva, L., Panuzzo, P., et al. 2005, MNRAS, 364, 1286

Veilleux, S., Rupke, D. S. N., Kim, D.-C., et al. 2009, ApJS, 182, 628

Ventura, P. & Marigo, P. 2010, MNRAS, 408, 2476

Verhamme, A., Schaerer, D., Atek, H., & Tapken, C. 2008, A&A, 491, 89

Viola, M., Monaco, P., Borgani, S., Murante, G., & Tornatore, L. 2008, MNRAS, 383, 777

Voit, G. M. 1992, MNRAS, 258, 841

Walcher, C. J., Coelho, P., Gallazzi, A., & Charlot, S. 2009, MNRAS, 398, L44

Walcher, J., Groves, B., Budavári, T., & Dale, D. 2011, Ap&SS, 331, 1

Wang, J., De Lucia, G., Kitzbichler, M. G., & White, S. D. M. 2008, MNRAS, 384, 1301

Weinberg, D. H., Hernquist, L., & Katz, N. 2002, ApJ, 571, 15

Weiss, A. & Schlattl, H. 2008, Ap&SS, 316, 99

Werner, M., Fazio, G., Rieke, G., Roellig, T. L., & Watson, D. M. 2006, ARA&A, 44, 269

Werner, M. W., Roellig, T. L., Low, F. J., et al. 2004, ApJS, 154, 1

Westera, P., Lejeune, T., Buser, R., Cuisinier, F., & Bruzual, G. 2002, A&A, 381, 524

Williams, R. E., Blacker, B., Dickinson, M., et al. 1996, aj, 112, 1335

Willson, L. A. 2000, ARA&A, 38, 573

Wolf, C., Meisenheimer, K., Kleinheinrich, M., et al. 2004a, aap, 421, 913

Wolf, C., Meisenheimer, K., Kleinheinrich, M., et al. 2004b, A&A, 421, 913

Wong, K. C., Blanton, M. R., Burles, S. M., et al. 2011, ApJ, 728, 119

Woods, D. F., Geller, M. J., & Barton, E. J. 2006, AJ, 132, 197

Wunderlich, E., Wielebinski, R., & Klein, U. 1987, A&AS, 69, 487

Wuyts, S., Förster Schreiber, N. M., Lutz, D., et al. 2011, ApJ, 738, 106

Wuyts, S., Franx, M., Cox, T. J., et al. 2009a, ApJ, 700, 799

Wuyts, S., Franx, M., Cox, T. J., et al. 2009b, ApJ, 696, 348

Wuyts, S., Labbé, I., Franx, M., et al. 2007, ApJ, 655, 51

Wuyts, S., Labbé, I., Schreiber, N. M. F., et al. 2008, ApJ, 682, 985

Wuyts, S., van Dokkum, P. G., Franx, M., et al. 2009c, ApJ, 706, 885

Xin-Fa, D., Xin, Y., Peng, J., & Wu, P. 2010, Astrophysics, 53, 342

Xin-Fa, D., Xin-Sheng, M., Con-Gen, H., Cheng-Hong, L., & Ji-Zhou, H. 2006, ArXiv Astrophysics e-prints

Xu, C. & de Zotti, G. 1989, A&A, 225, 12

Xu, C. & Sulentic, J. W. 1991, ApJ, 374, 407

Xu, C. K., Appleton, P., Dopita, M., et al. 2004, Spitzer Proposal, 3440

Xu, C. K., Domingue, D., Cheng, Y.-W., et al. 2010, ApJ, 713, 330

Xu, K. S., Kliger, M., & Hero, III, A. O. 2011, ArXiv e-prints

Yan, L., Chary, R., Armus, L., et al. 2005, ApJ, 628, 604

Yan, L., McCarthy, P. J., Weymann, R. J., et al. 2000, AJ, 120, 575

Yoshida, M., Shimasaku, K., Kashikawa, N., et al. 2006, ApJ, 653, 988

Zibetti, S., Gallazzi, A., Charlot, S., Pasquali, A., & Pierini, D. 2012, in IAU Symposium, Vol. 284, IAU Symposium, ed. R. J. Tuffs & C. C. Popescu, 63–65